Departamento de Física Teórica

Structure, Kinematics and Evolution of Elliptical Galaxies from Hydrodynamical Simulations

Memoria presentada para optar al grado
de Doctor en Ciencias Físicas por
José Oñorbe Bernis

Dirigida por **Rosa Domínguez Tenreiro**

Madrid, Marzo 2009

"Me lo contaron y lo olvidé.
Lo vi y lo recordé.
Lo hice y lo aprendí."
Confucio, 551 a.C. - 479 a.C.

"I hear and I forget.
I see and I remember.
I do and I understand."
Confucius, 551 B.C. - 479 B.C.

A mis padres
y a mi hermana

Agradecimientos

Si ahora lees este texto pagano es probable que me seas cercano, y que hallamos compartido otoño, invierno, primavera o verano. No te preocupes, no emplearé tu tiempo en vano y te hablaré yendo al grano. El *librillo* que tienes en mano reúne mi trabajo cotidiano, desde un tiempo, ahora lejano, compartido más o menos sano. Por eso me gustaría de veras que seas quien seas, no dejes esto a medias y te leas el resto de este pequeño texto, que presento solo como gesto honesto y grita al viento mi más profundo agradecimiento para todo el regimiento al que, no miento, le pertenece un trozo de todo esto. Y es que ahora que tras el sacrificio, observo desde la cima del precipicio, confirmo, ya sin resquicio, que en estos años de ejercicio, toda mi gente fuisteis mi mayor beneficio.

Agradecer a Rosa lo primero, la oportunidad de iniciar el sendero, por contagiar ese entusiasmo sincero y por su consejo certero, ante cualquier quebradero.

Sigo con Héctor, genio y figura, primer compañero de esta aventura, mentor de informática pura, en torno a la que, por ventura, se forjó una amistad que aún dura. Fran fue mi siguiente colega del frente en esta guerra tan diferente. Y aunque DEVA es enemigo potente, compartimos congreso, casa, cena caliente pasando algún rato más que decente. Agradecer también a Arturo el sacarme de algún apuro pero sobretodo aseguro no olvidar en el futuro donde encontrar arroz de lujo puro. Cesar, penúltimo fichaje, gran físico y mejor personaje, compartimos amistad, en cada comida y viaje, paciente para escucharme en algún momento salvaje. Con M^{a} Angeles y Latifa estos años, he compartido buenos ratos, charlas, consejos, amaños, combatiendo el desengaño, creo que con bastante buen apaño. A Paola, más que digna heredera, que acaba de lanzarse a la trinchera, le deseo de forma sincera que, mientras sube su escalera, disfrute de la carrera tanto o más que este calavera.

Al resto de gente que con su trabajo hizo posible este fajo, le debo un mínimo agasajo. Gracias a JuanCarlos, Lola, José y demás personal, incluido el centro computacional que me ayudó en más de un berenjenal. Incluso al Ministerio de Educación y Ciencia que me dio algo de opulencia en esto años de física y demencia.

Gracias también a todos los comensales: Frabice, Sara, Nacho y el resto de ocasionales por los debates reales y las sobremesas sociales, que salvaron el día a día con sensaciones geniales.

Otra prueba de mi suerte de primera fue que, persiguiendo esta quimera, me siguieron amigos de la carrera: Ernesto, amigo fuera donde fuera, y gran anfitrión en mi visita extranjera, Nico (el Mar de Bering nos espera), Mariluz, colega astrofísica y genial compañera, y María con su filosofía de la manzana y la pera. También tuve el honor de compartir buen humor, despacho (y mucho calor) con Enrique, genial conversador, Fouad, todo un señor, Iñaki, (desayunos con sabor) y Javi (¡adelante chacho!, ¡ten

valor!). Además rondando por despachos y pasillo, encontré buena gente a porrillo. Con Matteo ser amigos fue sencillo (la siguiente nada de oreja, solomillo). Alberto a base de no dar cuartelillo, enseguida me tuvo en el bolsillo. Conocí al genial LuisFer (gracias por todo crack), a Jorge y Jorge junior, un simpático pack, y a Ignacio, Sara y a un gran compa, Sergio (¡sack!). Con Fernando, Jacobo y otros mercenarios redescubrí los deportes minoritarios y con el resto de precarios, Willy, Raúl, Rubén, Javi, África, Jose, Tomás, Ana... compartí congresos varios, riesgos legendarios, y estupendas noches larios.

Agradecer también a mi prima María, por la experiencia compartida, a Edu, amigo de y para toda la vida, a Manu y Laura (¿para cuando otra partida?), a Pablo, Pedro y toda la gente curtida, en la casa más divertida. A Ba, por la locura divina de tanta ida y venida. A la memoria de Hortensia y mis abuelos (mi pequeña herida).

A Eva, Oscar, Alex-san, Esti, JP, ¡todo el clan!, son muchos años compartiendo plan y aguantando a este rufián. Espero que sigamos en conexión y que, vea o no Japón, *trae ese ron* siga siendo la canción.

A Javi, Euke, Pablo... mi gente del "Ruíz", *años ha* compartiendo parque y tapiz, ahora más de cócteles y perdiz, pero no cambia ni un matiz, a vuestro lado siempre feliz. Por supuesto que en breve un bis y gracias porque nunca huis, de la lucha contra un día gris.

No puedo no hacer mención, a la gente del Unión, unidos por un balón, hoy ya, herman@s de corazón: Aunque seáis un montón cada uno, en mi opinión, merece mínimo una canción. Un grupo de amigos de sólidos cimientos, de sinceridad sin miramientos, con los que he vivido grandísimos momentos y que según varios cuentos engloba máximo a unos 300.

Por último y con gana, agradecer el cariño y apoyo constante de mi hermana, papá y mama, que sin afán de fama, consiguen que no me falte calma, y vaya tranquilo a la cama. Porque sé que ante cualquier drama, sea cual sea la llama, que suceda en el mañana, solo tendría que hacer reclama.

Gracias.

Contents

List of Figures

List of Tables

Chapter 1

Introduction

This work presents an original approach to the study of the formation and evolution of elliptical galaxies in a cosmological context.

The first section of this introduction is concerned with the motivation for the present work. The second section lists the theoretical issues that are encountered when analyzing the problem. A short description of the chosen approach is then presented. Finally, the overview section provides the reader with a bird's view of the organization and contents of the work itself.

1.1 Motivation

Ever since the 1930s when galaxies were confirmed as the fundamental building blocks of the universe, their origin and evolution have remained as one of the most important challenges at the interface between Astronomy and Cosmology. It also turned out that they were some of the most difficult to discern mainly because of two reasons: First, galaxies take very long to evolve, so it is impossible to study one galaxy from birth to death. Therefore astronomers have been faced with the task of studying galaxies by looking at snapshots. It has now turned possible for astronomers to collect a huge number of these snapshots and maybe even more important, to see distant galaxies, thanks to the new generation of telescopes and spectrographs.

The second reason was that, as in any physical problem, the study of galaxy formation needed some solid initial conditions in the frame of current theories. Cosmology has dealt with this issue during the ultimate seven decades. However, the last few years have seen the emergence of an observationally consistent cosmological model based on firm physical ideas. The hot big bang model of the expanding universe, whose structure and dynamics can be described by general relativity, has a number of cosmological parameters that are now well constrained by numerous observations: WMAP measurements of the cosmic microwave background radiation (CMB Dunkley et al., 2009), supernova data (Riess et al., 2007), measurements of large scale structure (Massey et al., 2007;

Percival et al., 2007), among others have settled on a concordance model of a spatially flat universe with matter density about 30% of critical.

This model predicts that the large scale structure galaxy distribution that we observe in galaxy surveys must have formed through gravitational collapse of the small fluctuations left over from that earlier time. The properties of these large-scale mass densities can be predicted from the initial conditions as observed in the CMB combined with our understanding of gravity as described by General Relativity. Large scale studies of comprehensive surveys as SDSS (York et al., 2000) or 2dF (Folkes et al., 1999) confirm this idea. While the theory of origin of structure at large scale is more than promising, there are still some open questions at lower levels that the standard model has to answer. One of them is galaxy formation where the model has to address for a huge set of observational data available.

Actually, the amount of observational data nowadays is indeed so huge that studying the origin and evolution of galaxies in detail encourages to focus on some *particular* cases. As the term galaxy comprises a wide variety of types of galaxies with different properties, one way to deepen into this topic during the last decades has been to try to know how each of these different types of galaxies were formed, because sharing the same physical properties, their formation process should experience some common features.

From all the population of galaxy classes, elliptical galaxies are the easiest to study and are those that show the most precise empirical regularities, some times in the form of very tight correlations among their observable parameters (Djorgovski & Davis, 1987; Faber et al., 1987; Caon et al., 1993; Bernardi et al., 2003a). The interest of these regularities lies in that they may encode a lot of relevant information on the physical processes underlying elliptical formation and evolution. All the new advances make it possible for the first time to address meaningfully key questions about the way in which elliptical galaxies were formed and evolved over 10 billion years of cosmic history. When did they appear? What triggered the process of their formation? Do all form at a single, well defined epoch or is their formation spread out in time? Were the early proto-ellipticals similar to present-day Es? What is the connection between this population and the physics of the early universe? And perhaps, most interestingly of all, what are the processes that establish the observed relations between the various structural and kinematical properties?

Self-consistent hydrodynamical simulations constitute a powerful tool to work out these questions, since they make possible to accurately follow the evolution of the dynamical and thermodynamical properties of matter in the Universe. The general idea is to solve simultaneously the gravitational and hydrodynamical evolution equations. Therefore, they are a key tool in connecting the initial conditions offered by cosmology and all the available data from observations. So, in some sense, they play the role of

the *laboratory* experiments of astrophysics.

The main advantage of this kind of simulations is that physics is introduced at the most general level, and the dynamical processes relevant to galaxy assembly, such as collapse, gas infall, interactions, mergers, etc, emerge naturally, rather than by assumption, and can be followed in detail. Only the subscale physics needs to be modeled. These considerations emphasize the interest in hydrodynamical simulations as a very convenient tool in order to understand the formation and evolution of galaxies from the field of primordial fluctuations.

Therefore, this was the motivation for the present work: using self-consistent hydrodynamical simulations to build a consistent theoretical framework to interpret and study the different observations of elliptical galaxies.

1.2 Theoretical Issues

The approach that has been outlined in the motivation section involves several fields of knowledge. Part I of this thesis, Theoretical Framework provides an introduction to each of these fields. This section provides an overview of the contents of Part I, presenting short descriptions of each field and the reasons to include them.

From the moment that theoretical models gave some initial conditions it was a matter of time that scientists started to study their evolution and compare it with observations. The complex evolution of the primordial inhomogeneities made cosmological pure N-Body simulations, which computed only gravitational force, a powerful tool to study them in the non-linear regime. First attempts to use this technique in the study of the formation of large structure started during the 70's (Peebles, 1974; Press & Schechter, 1974; Miyoshi & Kihara, 1975; Aarseth et al., 1979), obtaining a great success and motivating several cosmological N-body simulations all over the world.

From these first approaches up to nowadays, all the different algorithms and ideas that this technique englobes have been continuously refined. In this sense, and first of all, it is worth to say that simulators are in deep debt with all the incredible advances in computer technology developed during the last decades.

Incorporation of hydrodynamics in cosmological simulations has made it possible to study not only the gravitational formation of dark matter halos, but also the properties of baryonic matter, and thus the formation of galaxies associated with those halos. First self-consistent hydrodynamical simulations were done in the late 80s (Evrard, 1988; Hernquist & Katz, 1989; Navarro & White, 1994).

To date, no code has sufficient dynamic range to compute both the large scale cosmological evolution on scales of many hundreds of megaparsecs and the formation of stars from baryons, but physical heuristics have been successfully incorporated into some codes to model the conversion of baryons into stars (Cen, 1992; Tissera et al.,

1997; Thacker & Couchman, 2000). Since the beginning of this new millennium several groups have obtained great success in modeling the formation of galaxies using self-consistent simulations which take into account the dynamics of DM and gas, radiative cooling, star formation and some other sub-resolution physic (Sommer-Larsen et al., 2002; Murali et al., 2002; Meza et al., 2003; Sáiz et al., 2003; Kawata & Gibson, 2003; Sáiz et al., 2004).

Anyway, to do a proper analysis we have not only to understand the way these simulations technique works, its limits and advantages, but also we need to know how to compare correctly their results with theory and observations. To this end, we need to deepen into the available data of real elliptical galaxies to discover what it is really known about them. Maybe even more important is how all this information was obtained in order to be able to mimic as far as possible the same methods, facilitating the comparison.

Furthermore, we also have to study the different models that have been proposed for the formation and evolution of elliptical galaxies. A set of observations suggested that ellipticals formed at higher redshift and on short timescales, in what has been called the *monolithic collapse scenario* (Eggen et al., 1962; Larson, 1974; Matteucci, 2003). On the other hand, another set of observations suggests that mergers at intermediate and low redshift could have played an important role in the assembly of this type of galaxies pointing to, what is called, the *hierarchical scenario* (White & Rees, 1978; Cole et al., 1994; Bundy et al., 2005). These observational results are paradoxical and challenging, making the study of the problem in connection with the global cosmological model a clear must do and a very promising method.

1.3 Approach

Inspired by all the prior art on self-consistent hydrodynamical simulations mentioned above, and specially by the work of Sáiz et al. (2004), we have tried to go one step further in the study of elliptical galaxies using this method. To this end, we have worked on obtaining both, a large sample of systems from simulations to study, to have significant statistics, and also that the resolution of these systems would be high enough to do a proper structural and kinematical analysis.

A critical issue regarding the code used to perform the simulations is that conservation laws are accurately verified. Particularly, an appropriate numerical code must satisfy all the conservation laws for physical quantities such as momentum, energy, or entropy. In this thesis we have used the `DEVA` code (Serna et al., 2003) and its parallel version `P-DEVA` which fulfills all these requirements.

As we intend to use these simulations as tools to better understand the real Universe, it is essential to have a more or less direct way to compare between simulation outputs

and observations. To carry out the comparison we must rely on galaxy properties which are measurable both on the simulations outputs and in observations.

In this work, we have studied the strong correlation observed between different structural and dynamical parameters of ellipticals. Using hydrodynamical simulations we have arranged, in addition to the equivalent observable measurements, the 3-D stellar object parameters and halo scale parameters for our elliptical-like objects. With the information obtained from this study, we want to deepen into the origin of these correlations, address their evolution with redshift and its implications in the formation of elliptical galaxies.

To this end, we have first dealt with the design of all the different characteristics of the simulations that we needed to achieve our goal of statistics and resolution. We had to take into account that there are finite resources available, in the sense not only of computer power but also in real time.

Once we had all the details about the simulations configured, we have built a set of analysis tools aimed at a proper comparison with both, observational data and theoretical (analytical and simulations) results. As it can be seen along this work, there are a lot of different parameters and properties of our simulated ellipticals in which we are interested so, we needed to develop a significant amount of computer programs and algorithms. However, the general idea behind our implementation has been to create a solid pipeline of analysis which can be useful not only to analyze these simulations but also the future ones. We have made its architecture highly modular, to facilitate the inclusion of more functions and/or the improvement of older ones. To improve the usability for beginner users, different global parameters which can be tuned readily have been defined.

1.4 Overview

This work is organized as follows:

Part I – Theoretical Framework: Provides the groundwork for the results presented in Part III, with an introduction to each of the fields of knowledge touched by the present work. Terms and concepts used in the results are introduced and described. Chapter 2 gives introduction to self-consistent hydrodynamical simulations. In particular we present the code we have used to run our simulations, `DEVA`. Chapter 3 gives a short overview of present galaxy formation theory, models and observational constrains.

Part II – Simulations and Tools: Includes Chapter 4 in which we present a detailed description of the different simulations under study, how they have been analyzed and the different technical issues concerning the study of elliptical-like object properties.

Part III – Results: We present the results of our study of galaxy formation using hydrodynamical simulations divided in two separate blocks. The first one includes Chapters 5, 6 and 7, and deeps into several kinematical and structural properties of nearby ellipticals. The second block is concerned about the characteristics of elliptical galaxies at younger epochs. In particular, Chapter 8 presents a study of the evolution of the different fundamental relations of these type of galaxies at redshift below 1.5. Finally, Chapter 9, provides some insights into elliptical galaxies formation and evolution scenarios.

Part IV – Conclusions and Outlook: Contains the conclusions, a brief discussion of important aspects and outlines future work.

Additionally, Appendix A contains a translation of this first chapter into Spanish. Appendix B contains a translation into Spanish of the conclusions part. As a general frame for this work, Appendix C summarizes the Standard Cosmological Model introducing several concepts that are used throughout this thesis. For the sake of clarity and ease for the reader, Appendix D includes several long data tables that would be referenced along this thesis.

Finally, some of the work that is presented in this manuscript has appeared on a set of refereed journals (Oñorbe et al., 2005; Domínguez-Tenreiro et al., 2006; Oñorbe et al., 2006; Oñorbe et al., 2007; González-García et al., 2009)[1] and conference proceedings (Oñorbe et al., 2006; Oñorbe et al., 2006, 2007; Domínguez-Tenreiro et al., 2008; Oñorbe et al., 2008) in which I have participated during the development of this thesis as would be indicated on each chapter when appropriate.

[1]First four articles can be found in Appendix E. Last article has been included in Section 8.5

Part I

Theoretical Framework

Chapter 2

Method: Self-Consistent Hydrodynamical Simulations

2.1 Introduction

Structures like galaxies and clusters of galaxies are believed to have formed by amplification of small perturbations (Peebles, 1980; Peacock, 1999; Liddle & Lyth, 2000; Bernardeau et al., 2002). Galaxies are highly over-dense systems. Matter density, ρ, in galaxies is thousands of times larger than the average density, $\bar{\rho}$, in the universe. Thus in this scenario the problem of galaxy formation and the large scale distribution of galaxies is essentially one of evolving density perturbations from small initial values to the large values we encounter today. In this sense, advances in computer science have brought us the possibility of making these extremely complex calculations in a reasonable time.

The present chapter is devoted to give a general picture of the main tool used in this thesis, the self-consistent hydrodynamical simulations. First, Section 2.2, introduces the theoretical issues of this method and the main problems that it has to face. Thereafter, in Section 2.3, we briefly examine the last advances in this topic during the past years. In Section 2.4 a detailed description of `DEVA`, the code used in all our numerical experiments, is given. Section 2.5 is the summary.

2.2 Description of the Method

Equations that describe the evolution of density perturbations in non-relativistic matter due to gravitational interaction in an expanding Universe have been known for a long time (Peebles, 1980). The fundamental idea is that due to the Birkhoff theorem, as long as in a region $v/c \ll 1$ and $r <$ horizon, Newtonian approximation continues to be a valid framework (see Peacock, 1999, for a more detailed explanation). Then, the dynamical equations that described the evolution of these inhomogeneities in a pressure-less and

self-gravitating Newtonian fluid are: the equation of continuity for mass conservation (Eq. 2.1), Euler's equation for momentum conservation (Eq. 2.2) and Poisson's equation that accounts for the Newtonian gravity (Eq. 2.3). Considering that the phase-space distribution function of the fluid is given by $f(r,p,t)$, where r is the position and p the momentum ($p = mv$), ρ is the proper mass density, $\rho(r,t) = \int f(r,p,t)d^3p$, Φ is the gravitational potential and $d/dt = \partial/\partial t + v \cdot \nabla_r$ is the usual convective derivative, then these equations can be written as:

$$\frac{d\rho}{dt} = -\nabla_r \cdot (\rho v) \quad (Equation\, of\, continuity) \tag{2.1}$$

$$\frac{dv}{dt} = -\nabla_r \Phi \quad (Euler's\, equation\, presureless) \tag{2.2}$$

$$\nabla_r^2 \Phi = 4\pi G\rho \quad (Poisson's\, equation) \tag{2.3}$$

Here, we have written the three last equations in Eulerian coordinates, this is, they are fixed in an inertial reference frame. The alternative approach to fluid dynamics is to use Lagrangian coordinates, which are fixed to a given parcel of fluid but move in space. They have the property that the Lagrangian position of a fluid element does not change with time. In cosmology, a type of Lagrangian coordinates is used by the name of comoving coordinates. These label observers who follow the Hubble expansion in an unperturbed universe. In this case, comoving coordinates and physical coordinates are related by the scale factor $a(t)$. For a more detailed description of the underlying cosmology and related issues as the scale factor, see Appendix C. The comoving position $\vec{x}$ and the physical position $\vec{r}$ are related by $\vec{r}(t) = a(t)\vec{x}$. The comoving time coordinate is the elapsed time since the Big Bang according to a clock of a comoving observer and is a measure of cosmological time. Physical velocity, $\vec{v} = d\vec{r}/dt$, and comoving velocity, $\vec{u} = d\vec{x}/dt$, coordinates are linked by the following expression $\vec{v} = \frac{da(t)}{dt}\vec{x} + a(t)\vec{u}$. ∇_x is the comoving gradient, which is related with the physical gradient as $\nabla_r = \nabla_x/a(t)$.

It is useful to rewrite equations (2.1), (2.2) and (2.3) in comoving coordinates when working in an expanding universe framework because it allows us to focus on perturbations in density and velocity. For this purpose it is also helpful to express the density as a first order perturbation magnitude[1], $\rho(r,t) = \rho_0(t) + \delta\rho(r,t)$, because $\rho_0(t)$ behaves like $\rho_0(t) \propto a(t)^{-3}$ in comoving coordinates. If we also define the density contrast $\delta_\rho \equiv \delta\rho/\rho_0$ we get the following relation:

$$\rho(x,t) = \rho_0(1 + \delta_\rho) \tag{2.4}$$

[1]Nonetheless it is important to remark that once we consider a perturbed universe, the comoving coordinates formed by dividing the eulerian coordinates by the scale factor $a(t)$ are no longer pure Lagrangian because gravity will cause a non-uniform distribution of the fluid to grow increasingly irregular. In other words, when $\delta\rho \neq 0$ then $x \to x(t)$.

as the expression for density in comoving coordinates. From this definition and using Eq. (2.3), the gravitational potential can be expressed as $\Phi(x,t) = \Phi_0(t) + \delta\Phi(x,t)$, where $\delta\Phi$ is called the peculiar gravitational potential. Therefore, equations (2.1), (2.2) and (2.3) in comoving coordinates to first order in the perturbations (linear regime) are written as:

$$\dot{\delta_\rho} = -\nabla_x[(1+\delta\rho)u] \quad (Equation\, of\, continuity) \tag{2.5}$$

$$\ddot{x} + 2\frac{\dot{a}}{a}\dot{x} = -\frac{1}{a^2}\nabla_x\delta\Phi \quad (Euler's\, equation\, presureless) \tag{2.6}$$

$$\nabla_x^2\delta\Phi = 4\pi G a^2\rho_0\delta_\rho \quad (Poisson's\, equation) \tag{2.7}$$

where dot stands for d/dt and two dots for d^2/dt^2 and we have used the unperturbed solution for Euler equation (2.6), this is, if $\delta_\rho \to 0 \Longrightarrow (\ddot{a}/a)x = -a^{-2}\nabla_x\Phi_0$ (see Peacock, 1999, for a full demonstration). These equations can be solved analytically for a small density contrast, and for highly symmetric situations. There are many approximate solutions in the quasi-linear regime that are useful for understanding the evolution of perturbations in this regime (Zel'Dovich, 1970; Gurbatov et al., 1989; Bernardeau et al., 2002) but fail when density contrast become large ($\delta_\rho \gg 1$).

Taking into account that clusters have typical overdensities of $\sim 10^3$ and galaxies around $\sim 10^6$ (Ettori et al., 2002), it seems that the use of numerical methods to study how galaxies are assembled within a cosmological scenario from field of primordial fluctuations is a convenient approach. The exact solution of the density field can be performed by means of a numerical simulation, in which the density field is represented by the sum of a set of fictious discrete points. The basic steps in this type of simulations can be summarized as follows:

(i) implementation of initial conditions. See below for a brief discussion on initial conditions.

(ii) Calculation of the force by solving the Poisson equation.

(iii) Update of positions and velocities of particles.

(iv) Diagnostics, e.g. tests of energy conservation.

(v) Go back to (ii) until simulation is completed.

So, numerical simulations are basically a Monte-Carlo method of solving these equations, with the number of bodies per volume governing the accuracy of the method.

We have shown the equations that govern the motion of a pressure-less fluid. This is valid for dark matter only simulations (often called N-Body simulations) which are very useful to understand the large scale structure formation. However, at galactic scales,

gas dynamic plays an important role and it needs to be taken into account for a proper solution of the problem. In this case we have to extend the Euler equation for motion (Eq. 2.2) to the baryons, adding a pressure term:

$$\frac{dv}{dt} = -\nabla_r \delta\Phi - \frac{\nabla_r P}{\rho} \quad (Euler\ equation\ for\ baryons) \tag{2.8}$$

where P is the pressure. Also the first law of thermodynamics takes a more elaborated form, from $de/dt = 0$ it now stands as:

$$\frac{de}{dt} = -\frac{P}{\rho}\nabla_r \cdot v - \frac{\Lambda(e,\rho)}{\rho} \quad (First\ law\ of\ thermodynamics) \tag{2.9}$$

where e is the internal energy per unit mass and $\Lambda(e,\rho)$ is the cooling function which accounts for the radiative losses of baryons. Finally these five equations are closed by an equation of state, relating the pressure, the density and the internal energy:

$$P = (\gamma - 1)\rho e \tag{2.10}$$

Assuming an ideal, monoatomic gas, γ equals 5/3. The simulations that introduce baryon particles and therefore solve not only equations (2.1), (2.2), (2.3) for pressureless fluid but also equations (2.1), (2.3), (2.8) and (2.9) to follow the baryonic fluid, are called hydrodynamical simulations.

The history of hydrodynamical simulations, and more generally of numerical simulations, is the search for algorithms that solve these equations, or their comoving equivalents, as fast as possible and even more important, with enough accuracy.

2.2.1 Algorithms

The advance in numerical simulations has become possible both by the rapid growth of computer performance and by the implementation of ever more sophisticated numerical algorithms. We can differentiate two crucial points in hydrodynamical simulations concerning numerical algorithms. First one is to compute the Poisson term, $\nabla\Phi$, a problem that is shared with N-Body simulations. The second one is to solve the motion of the collisional baryonic matter. These are the two bottlenecks of any hydrodynamical simulation regarding the computational cost. Here, we briefly describe how physicists have deal with them.

Gravitational force in the Newtonian limit falls as $1/r^2$, hence it is a long range force and we cannot ignore force due to distant particles. This makes the calculation of the Poisson equation (2.3) one of the most time consuming tasks in numerical simulations. Early simulations (White, 1976; Fall, 1978; Aarseth et al., 1979) employed the direct summation method, also known as Particle-Particle (PP) method, for the gravitational N-Body problem. This is, to sum directly the contributions of all individual particles

to the gravitational potential

$$\Phi(r) = -G \sum_{\mathrm{j}} \frac{m_{\mathrm{j}}}{(|r - r_{\mathrm{j}}|^2 + \epsilon^2)^{\frac{1}{2}}} \tag{2.11}$$

It is important to remark that in the simulations used in astrophysics, the particles do not represent individual dark matter or baryonic particles, but should be considered as Monte Carlo realizations of the mass distribution, and therefore only collective, statistical properties can be considered. In this kind of simulations, close encounters between individual particles are irrelevant to the physical problem under consideration, and the gravitational force between two particles is smoothed by introducing the gravitational softening ϵ. This softening reduces the spurious two-body relaxation which occurs when the number of particles in the simulation is not large enough to represent correctly a collisionless fluid and in some sense, determines the spatial resolution of the simulation. Typically, ϵ is chosen to be $1/20 - 1/50$ of the mean inter-particle separation within the simulation.

However, the PP method scales like $O(N(N-1))$. Therefore one needs to bypass the increase in computational time for large numbers of particles with a more sophisticated treatment when calculating the forces. One option is to organize the particles in a tree-like structure. The force of a distant group of particles can be approximated by the force due to a single pseudo-particle located at the center of mass of the group, with mass equal to the total mass of the group of particles (Barnes & Hut, 1986; Dehnen, 2000). This method, usually called Tree method, scales as $O(NlogN)$. Another way for obtaining the forces is to numerically integrate Poisson equation. The idea is to use the Fourier transform of this equation (a simple algebraic equation) combined with Fast Fourier Transforms (FFT). This technique demands the introduction of a grid in order to define the density. That is why this method is usually known as the Particle-Mesh method (PM). It also scales as $O(NlogN)$. From these three approaches (PP, Tree and PM) have grown several hybrid methods that combine and/or improve them: TreePM, PPPM (also known as P^3M), Adaptative P^3M (AP^3M), ATreePM, etc.

The methods to solve the problem of adding the baryonic matter to the simulations have been developed in the past decades. They fall into two categories: Lagrangian methods or particle methods, which discretize mass, and Eulerian methods or grid-based methods, which discretize space. Eulerian methods are based on the so-called Godunov's scheme for solving partial differential equations. In these methods the equation of motion for the brayon component (Eq. 2.8) is solved based on structured or unstructured grids, representing the fluid. The conservative variables are considered as piecewise constant over the mesh cells at each time step and the time evolution is determined by the exact solution of the Riemann problem (shock tube) at the inter-cell boundaries. On the other hand most of the lagrangian methods used in astrophysics are based on the

smoothed particle hydrodynamics (SPH) algorithm (Lucy, 1977; Gingold & Monaghan, 1977; Monaghan, 1992). The basic idea of SPH is to discretize the fluid by mass elements (e.g. particles), rather than by volume elements as in the Eulerian methods. Therefore the fluid properties like pressure, density, temperature, etc at any point can be found by averaging over particles in the region using a weight function W. This weight function (or kernel) leads to the definition of an individual smoothing length, $h_{\rm i}$, for each particle, it is normalised and collapses to a delta function if the smoothing lenght approaches zero. This length must be adapted such that each particle has a constant number of neighbors, leading to a constant mass resolution independent of the density of the flow. For a finite number of particles, N, the resulting estimate of the field, $\langle f(r)\rangle_{\rm i}$, is then given by:

$$f(r_{\rm i}) = \sum_{j=1}^{N} \frac{m_{\rm j}}{\rho_{\rm j}} f(r_{\rm j}) W(r_{\rm ij}, h_{\rm i}, h_{\rm j}) \tag{2.12}$$

where $r_{\rm ij} = |r_{\rm i} - r_{\rm j}|$, $m_{\rm j}$ is the mass of particle j, ρ_j is the density at the location of particle j, and h_j is the smoothing length for the j-th particle, which specifies the extent of the averaging volume around it. As a particular case of Equation 2.12, the smoothed estimate of the local density would be

$$\rho(r_{\rm i}) = \sum_{j=1}^{N} m_{\rm j} W(r_{\rm ij}, h_{\rm i}, h_{\rm j}) \tag{2.13}$$

For a complete review on different techniques and algorithms applied in N-Body simulations and hydrodynamical simulations, see Bagla (2005); Dolag et al. (2008) and references therein. For a more historical perspective see Yepes (2001) and Suto (2003).

2.2.2 Initial Conditions

Once we have our code prepared, we need to provide it with an initial condition or initial configuration for all the different particles. There are two main approaches to set the initial conditions depending on how we plan to use hydrodynamical cosmological codes. First one is called the pre-prepared scheme where the initial conditions are usually set from analytical models based on observations. These initial conditions try to model situations that would have arisen along the evolution of the systems under consideration. This kind of simulations move in a huge range of scales from planet formation (see Mayer et al., 2004, as a recent example) up to the interaction of galaxies (see González-García et al., 2006, and references therein). This method has proved to be a very powerful instrument to deepen into the physics of these problems with a very high resolution.

The other approach, which is the one employed in this thesis, is the self-consistent or cosmological scheme. This kind of simulations use the good agreement between

observations of the large-scale distribution of galaxies and the CMB that link the growth of structures with a Gaussian random field of initial density fluctuations (see Appendix C.6 for more details). The two-point correlation function or its Fourier transform, the power spectrum contain all the statistical properties of this field. The standard ad-hoc procedure for setting up cosmological initial conditions is described in Efstathiou et al. (1985) and references therein. The basic (but not trivial) idea is that given an unperturbed particle/grid distribution, any desired linear fluctuation distribution can be in principle generated using the Zeldovich approximation.

The main advantage of this method (i.e. self-consistent simulations), is that the physics is introduced at a very general level, and the system evolves as a consequence. We can follow the evolution of the dynamical and hydrodynamical properties of matter in the Universe. These simulations play a very significant role in cosmology because they can be considered as an experiment to verify theories of the origin and evolution of the Universe. Self-consistent gravo-hydrodynamical simulations are useful not only as tools for evolving complex systems, these can also be used to understand which effects play a more important role in different phases of this evolution.

Of course this technique has some difficulties. Just to mention, one of the most important complications is the discreteness effect, this relates with the problem of sampling the continuous initial density field with a discrete distribution. The other one is the possible effect that the perturbations at scales larger than the box size and at scales smaller than the resolution (not taken into account) can have in the specific subject of study of the simulation. For a more detailed description on how to generate cosmological initial conditions and how to minimize these problems see Sirko (2005); Lukić et al. (2007); Dolag et al. (2008).

2.2.3 Additional Physics

A realistic simulation should give us, at least, the same information as the one obtained by observations. However there are several key effects that are important in the final result but occur in regions that have a size many orders of magnitude smaller than the spatial resolution of the simulation. They are, for example, the radiative cooling, the star formation, supernova explosions and a large etcetera, most of them involved with baryonic physics. In general these effects are difficult to include as vastly different scales of relevance are involved. As a result, much of the treatment of them has remained phenomenological.

One of the first relevant processes that need to be added is the radiative cooling. This is the main process leading to the condensation of gas in the matter potential wells and consequently to star and structure formation. We have already mentioned it above including the cooling function in equation (2.9). In standard implementations the cooling rates are estimated, making several simplification assumptions, directly as

a function of local gas density and temperature $\Lambda(\rho_g, T) = \rho_g^2 \Lambda(T)$ (Cen, 1992; Katz et al., 1996). However this parameterization has been improved along time and now the methods are more complex, taking into account more physics, as the molecular cooling or the metal dependence. See Maio et al. (2007) for a current review on this topic.

Including radiative losses in simulations however, can cause an *overcooling* problem. This is, as gas cools it tends to collapse but, as cooling depends on density this can make that a very large fraction of the baryonic component can cool down and condense. To deal with these issues, one has to include in the code a suitable recipe to convert the reservoir of cold and dense gas into collisionless stars. Star formation is still a really open issue in astrophysics (McKee & Ostriker, 2007) therefore its inclusion in hydrodynamical simulations is a matter of debate. Even first attempts, Katz et al. (1992), showed that the dynamics of the system is strongly altered with respect to simulations without star formation. The scheme to transform gas into stars has not been changed since that date. It has been widely tested and implemented in different kind of hydrodynamical codes (see Stinson et al., 2006; Saitoh et al., 2008, and references therein). A more detailed discussion about the star formation algorithm in the context of its implementation in `DEVA` and its motivation can be found in Section 2.4.

Of course, once star formation is also included, one would like to model all the feedback associated with star evolution: metal enrichment, supernova explosions, stellar winds, ultraviolet (UV) radiation from stars, black holes, UV cosmic background (QSO and AGN). Also, magnetic fields (Roettiger et al., 1999; Dolag et al., 1999), radiative transfer (Iliev et al., 2006) and a very long etcetera are other interesting issues. A huge range of these effects have been implemented in different codes with very interesting results. Anyway, a full description of these processes is far outside of this thesis and we point the interested reader to the recent reviews Thacker & Couchman (2000); Yepes (2001); Dolag et al. (2008) and references therein.

2.3 State of the Art

Numerical simulations in astrophysics have turn to be a key tool for theoreticians and observers in the last twenty years. Definitely, the most important step in numerical simulation of the last years has been the appearance of parallel codes that allow running simulations with an important increase in the number of particles (or mesh resolution) (e.g. Springel et al., 2005; Gottlöeber et al., 2006). Taking into account that the future of supercomputers points towards an increase in the number of accessible CPUs rather than on the speedup of individual CPUs, it is clear that this technique is going to be basic in the future of numerical simulations. It is important to remark that this future not only involves the run of numerical simulations by themselves but also, and maybe even more important, their analysis pipelines.

In regard to hydrodynamical simulations, it is clear that one focus in future will be on incorporating further effects so that more complex problems can be studied in detail. However, historically the implementation of more and more sub-scale effects in cosmological simulations has responded to the rise of new problems concerning previous inclusions of sub-scale physic, e.g. star formation for the overcooling problem, stellar feedback to regulate the star formation (angular momentum catastrophe, low mass halos problem, high star formation at low redshifts), etc (Moore et al., 1999a; Ceverino & Klypin, 2007). As long as these issues are not fully understood by themselves and we have a detailed theory for them, their phenomenological treatment would be, at least, controversial and subject to continuous changes and improvements. In the next years hydrodynamical simulations of the interstellar medium promise to be a key element in shedding some light on these issues (Slyz et al., 2005; de Avillez & Breitschwerdt, 2007). Besides, it is interesting to remark that pure N-Body simulations have found in the semi-analytical method (SAM) a very powerful ally to introduce baryon and sub-scale physics in their results. It turns out that this method is very helpful, and complementary to the hydrodynamical simulations, in the study of the effects of these processes (see Baugh, 2006, and references therein).

The new era of precision cosmology requires new standards for the reliability and accuracy of numerical simulations. Code comparison plays a crucial paper in this task. A global comparison between N-body codes, hydrodynamical algorithms and different additional physic implementations is mandatory. First serious attempts to do this have started not a few years ago (Frenk et al., 1999). Last results show that although it seems that we are going into the right direction, still much work is needed in order to attain the required accuracy for upcoming surveys both in pure N-body and hydrodynamical methods (Heitmann et al., 2005, 2007; Agertz et al., 2007). As a starting point, the present agreement over a broad range of tests is gratifying, nevertheless, the lack of a rigorous quantification of error is a serious barrier to future progress. As error control requirements become more severe, the need for such a theory becomes further manifest. In addition, as more (uncontrolled) physics is added, and subgrid modeling incorporated as an essential part of the simulations, it becomes ever harder to extract error-controlled results. The resulting uncertainties introduced by the parameterization of sub-resolution physics have not yet been deeply explored in the context of code comparison, and any comparison seems that would test the agreement between the recipes rather than identify any computational error.

In the future, the demand on precision in both simulation techniques and captured complexity of the physical processes within the simulations guarantee the computational astrophysics as a challenge field.

2.4 The Deva Code

In this Section we briefly describe DEVA, a Langrangian multistep AP3M-like-SPH code designed to study galaxy formation and evolution in connection with the global cosmological model, that uses a formulation of SPH equations ensuring energy, entropy, momentum and angular momentum conservation (Serna et al., 2003; Sáiz et al., 2004). All simulations analyzed in this thesis have been performed using the DEVA code. In designing DEVA, particular attention has been paid that conservation laws of physics (energy, entropy and momentum) are correctly implemented in the code, so that they hold at all scales and under physical conditions relevant for galaxy assembly in a cosmological context. A parallel version of DEVA, P-DEVA has also been used in this thesis (Serna et al. in preparation). This version shares the same fundamental algorithms with DEVA and has been implemented in **OpenMP**, i.e., it is designed for shared memory multiprocessing.

2.4.1 Gravity and Gas Dynamics

To solve the Poisson equation (Eq. 2.3) DEVA uses an AP^{3}M algorithm. This method combines two basic ideas over the PM algorithm (see previous Section for more details). It adds a Particle-Particle correction for close neighbors to the force computed using the PM. Also it uses spatially adaptive mesh refinements in regions with high particle density where the clustering makes the number of neighbors to increase and the short-range force computation starts to dominate, making the pure P^{3}M algorithm to scale as $O(N(N-1))$ (Couchman, 1991).

Concerning the hydrodynamical motion, in DEVA conventional SPH formulation is improved in order to overcome an important problem found related with the entropy violation of the dynamical equation (Hernquist, 1993). The origin of these errors can be found in overlook relevant terms in the dynamical equations associated with the space dependence of the smoothing length, h. The idea in DEVA is to calculate these additional terms, previously neglected.

Another important particularity of DEVA is the attention paid to angular momentum conservation, a key point to enable disc formation in simulations (Domínguez-Tenreiro et al., 1998). The code uses a formulation of SPH equation that is consistent with the smoothed estimate for the different properties (density, etc) of the local gas (Eq. 2.12). However this equation is symmetrized to ensure that the reciprocity principle holds (that is, if at a given time the j^{th} particle belongs to the neighbor list of the i^{th} particle, then it is mandatory that, at this same time, the i^{th} particle belongs to the neighbor list of the j^{th} particle), so that momentum and angular momentum are conserved. The way to solve this issue is to use a symmetric kernel $W(r_{\rm ij}, h_{\rm i}, h_{\rm j}) = \bar{W}_{\rm ij}$ that is usually

built as the kernel average:

$$\bar{W}_{\rm ij} = \frac{1}{2}[W(r_{\rm ij}, h_{\rm i}) + W(r_{\rm ij}, h_{\rm j})] \tag{2.14}$$

The implementation of this principle in an SPH code increases considerably the CPU time per integration step, because a double loop on gas particles is necessary to evaluate smoothing lengths.

Finally to get an accurate enough time integration scheme, and, at the same time, to avoid that particles in denser volumes slow down the simulation, a PEC (predict-evaluate-correct) scheme with individual timesteps has been developed and implemented in the code. We refer the reader to Serna et al. (2003) for a detailed description of the implementation of all these algorithms in `DEVA`.

2.4.2 Additional Physics

Cooling is also implemented in `DEVA`, taking the cooling curve from Tucker (1975) and Bond et al. (1984) for an optically thin primordial mixture of H and He (X=0.76, Y=0.24) in collisional equilibrium and in absence of any significant background radiation field. Also, as we have pointed out, ideally a gravo-hydrodynamical code should describe star formation (SF) at small scales as a result of evolution, and the possible ensuing feedback effects. However, this would require an enormous dynamical range and very high mass, time and space resolution, and these conditions cannot be met by the present status of computer technology, and so, stellar processes have to be modeled, either inspired in kpc or pc scale hydrodynamical simulations or other considerations (Katz et al., 1992; Vázquez-Semadeni et al., 2000; Padoan et al., 2001; Avila-Reese & Vázquez-Semadeni, 2001). One of these approaches and the one used in this thesis, is *The turbulent sequential star formation scenario* (Elmegreen, 2002).

The interstellar medium (ISM) is assumed to be structured into different regions characterized by specific values of their physical variables. These structures are thought to form a multiscale hierarchy with different levels. The turbulent sequential star formation scenario propounds that different physical processes operate at different levels of this hierarchy to produce the interstellar medium gas structure. In particular, giant molecular clouds and molecular clouds are supported against gravity by turbulence and magnetic fields. Turbulence has a second role at this level: it produces gas compressions at lower scales. Compressed volumes can then fragment into clumps and dense cores, even if the cloud is globally stable because the average rms speed is large enough to give global stability. The final step of the sequence is SF from dense core collapse, locally triggered at this scale by SNe explosions and expanding shells, among other possibilities.

Not any dense core collapses into stars. A given core collapses when gravity overcomes its kinetic energy support. A density threshold for core collapse appears at this

scale, ρ_c, as well as a SF efficiency, ϵ_c. The ISM gas structure can be described by means of the probability distribution function (pdf). Wada & Norman (2001) in their simulations of whole galaxy models found a log-normal pdf. Stellar processes (stellar winds, SNe explosions and so on) inject energy, momentum and metals into the ISM. This very likely results into molecular cloud destruction. However, as the bulk ISM could be stable and cloud-forming instabilities still operate in the cool phase, caused by turbulent compressions, this stellar self-regulation of SF could not be very effective. Despite its complexity, SF (at least in disk galaxies) follows two simple empirical laws that any deeper understanding of SF processes must explain: 1) the Kennicutt-Schmidt law for the SF rate (Kennicutt, 1998). It represents an average over ∼disk scales, and, as an average, takes into consideration the whole complex physical processes involved into SF at disk scales. 2) Moreover, a density threshold at this scale appears empirically (Martin & Kennicutt, 2001). Concerning the explanation of these empirical laws, Elmegreen (2003) propounds that the Kennicutt-Schmidt law can be linked to the SF processes at the scale of dense cores through the pdf: the SF efficiency at a given scale is proportional to the fraction of gas at this scale verifying $\rho_{\rm gas} > \rho_c$. Li, Mac Low, & Klessen (2005a,b), on their turn, have reproduced the observed global and local Kennicutt-Schmidt laws, and, also, have obtained star formation thresholds in disk galaxies in their three dimensional SPH simulations of SF in disk galaxies where no stellar explicit feedback has been implemented. These works indicate that an agreement of astronomers about the precise role of stellar feedback in the setting up of the two laws above, among other SF characteristics, is far from being reached.

This scenario is implemented in `DEVA` through a parameterization similar to those used by Katz et al. (1992) and Tissera et al. (1997). To allow a gas particle to be converted into stars it has to fulfill two conditions. First one is that ρ_{gas} must be lower than a critical density ρ_{crit} (as mentioned above this ρ_{crit} is obtained empirically). Also it has to be in a convergent flow, $\nabla\vec{v} < 0$. Once a particle of gas satisfies these requirements, it is transformed into stars according with an inefficient Schmidt-law-like transformation rule,

$$\frac{d\rho_g}{dt} = -\frac{d\rho_*}{dt} = -\frac{c_*\rho}{t_g} \tag{2.15}$$

where c_* is a dimesionless star-formation efficiency parameter, and t_g is a characteristic time-scale chosen to be equal to the maximum of the local gas-dynamical time $t_{dyn} = (4\pi G\rho_g)^{-1/2}$, and the local cooling time, $t_{cool} = u/\dot{u}$ ($u \equiv thermalenergy$). Using Eq. (2.15) expression for the star formation rate, the probability p that a gas particle forms stars in a time Δt is

$$p = 1 - e^{-c_*\Delta/t_g} \tag{2.16}$$

p is computed at each time step for all eligible gas particles and draw random numbers

to decide which particles actually form stars.

2.5 Summary

Numerical simulations of three-dimensional self-gravitating fluid have become an indispensable tool in cosmology. They are now routinely used to study from the non-linear gravitational clustering of dark matter up to the evolution of the intergalactic gas. Simulations have provided us with an invaluable insight into the physical processes responsible for the formation and evolution of galaxies and other structures in the Universe. But, despite the advances made in the last decades, much remains to be done to fully understand the formation of all these structures. It is clear that much of the near future of this technique points more into the direction of a proper description and modelization of the baryonic physic and into code comparison projects than to any bottleneck due to the parallel computation technology.

Finally we have introduced `DEVA`, a Lagrangian code that uses an AP3M algorithm to resolve gravity and a SPH implementation to compute hydrodynamics in which particular attention has been paid in that the conservation laws of physics (energy, entropy, momentum) were correctly implemented in the code. `DEVA` has been used to run all the simulations analyzed in this thesis.

Chapter 3

Formation and Evolution of Elliptical Galaxies

3.1 Introduction

It is not easy to answer the question, what is a galaxy? One possible definition could be: *A galaxy is a self-gravitating system composed of an interstellar medium, stars, and dark matter.* Another definition, may be: *A galaxy is the environment in which stars are born and die.* Our galaxy, the Milky Way, is one of billions of such systems. Why matter in the universe should be organized around such clear characteristic units is one of the most outstanding cosmological questions.

The origin of cosmic structures, including galaxies of all types, is currently described through the gravitational collapse of infinitesimal density fluctuations (the dynamical evolution of these perturbations and the equations that govern them are discussed in Chapter 2). After a decade of spectacular breakthroughs in physical cosmology, the focus is beginning to shift away from determining the values of the basic cosmological parameters towards attacking the problem of galaxy formation. A combination of factors is responsible for this change. Firstly, the *concordance* ΛCDM model have been consolidating in the past years by a new generation of observational data sets concerning the cosmic microwave background radiation, galaxy clustering and high redshift supernovas (Spergel et al., 2007) giving a solid pillar to develop a complete theory of galaxy formation and evolution[1]. Secondly, the 1990s saw the first detections of sizeable populations of galaxies at high redshifts (Abraham et al., 1996; Ferguson et al., 2000; Blain et al., 2002; Beckwith et al., 2006; Scoville et al., 2007), allowing evolutionary trends to be established. Finally, the increase in readily available computing power coupled with the development of powerful new techniques, such as the one used in this thesis, self-consistent hydrodynamical simulations (a full description of this method is given

[1]Further explanation of the standard cosmological model, its physical implication and its observational successes can be found in Appendix C

in chapter 2), means that we are a in position to generate accurate predictions for the properties of galaxies in hierarchical cosmologies.

This chapter introduces the Elliptical Galaxies in which this thesis is centered. We also try to convince why the study of these objects is so exciting and compelling for those who want to deepen into the galaxy formation and evolution process. In Section 3.2, we start by providing the reader with a general overview of the last nearby observations on this type of galaxies concerning their structural and kinematical profiles and making a special emphasis in the Fundamental Plane relation. We also try to give the theoretical framework to deal with all these data. The next Section 3.3 makes an historical introduction of the two main scenarios of galaxy formation. We define several important concepts on this subject and discuss the last observational and theoretical constraints on this topic, focusing on the ones given by the observed evolution of the elliptical population. A summary can be found in the last Section 3.4.

3.2 Elliptical Galaxies

Since the seminal work by Hubble (1936), we distinguish between three main classes of galaxies based on their optical aspect: elliptical galaxies, disk galaxies and irregular. Elliptical galaxies have nearly-featureless oval forms with approximately elliptical isophotes. Disk galaxies generally resemble the Milky Way; much of their luminosity is contained in thin, rotating disks of stars. Irregular/peculiar galaxies follow neither the disk nor elliptical plans; they lack any apparent symmetry. From these years we have discovered much more information about all these types of galaxies and found that a lot of other general properties are correlated with this morphological classification.

Among the different galaxy families, ellipticals are the easiest to study and those that show the most precise regularities in their empirical properties, some times in the form of tight correlations among their observable parameters. The interest of these regularities lies in that they could encode a lot of relevant information on the physical processes underlying the ellipticals formation and evolution. Elliptical galaxies exhibit far less evidence for young stars, gas, or dust than do spiral galaxies, and have larger random motion of stars than in spiral galaxies where the motion is a more ordered rotation. In fact, they are dominated by old stellar populations, giving them red colors and being also classified in the group of early-type galaxies (ETGs).

Despite of their interest, very few is known, both from the theoretical or observational points of view, about the mass or velocity distributions of the different elliptical mass components (stars, dark matter, and hot and cold gas).

3.2.1 Structure and Kinematical Profiles

3.2.1.1 Mass Distribution

There has been, nevertheless, an important recent progress on the photometric characterization of elliptical galaxies, and, in fact, authors now agree that the Sérsic law adequately describes the optical surface brightness profiles of most of them (Caon et al., 1993; Trujillo et al., 2001; Bertin et al., 2002; Ravindranath et al., 2006). The Sérsic law (Sérsic, 1968) can be written

$$I^{\rm light}(R) = I_0^{\rm light} exp[-b_n(R/R_e^{\rm light})^{1/n}], \tag{3.1}$$

where $I^{\rm light}(R)$ is the surface brightness at projected distance R from the ellipticals center, $R_e^{\rm light}$ is the effective half-light radius, encompassing half the total galaxy luminosity, $b_n \simeq 2n - 1/3 + 0.009876/n$, and n is the Sérsic shape parameter. Putting $n = 4$ the largely used de Vaucouleurs $R^{1/4}$ law (de Vaucouleurs, 1948) is recovered.

It is generally assumed that galaxies of any type are embedded in massive haloes of dark matter. However, from the observational point of view, the importance and the distribution of dark matter in elliptical galaxies is still a matter of a living debate. Data on stellar kinematics from integrated-light spectra are very scarce beyond $2R_e^{\rm light}$, making it difficult even to establish the presence of a dark matter halo (Kronawitter et al., 2000; Magorrian & Ballantyne, 2001) through this method. Otherwise, the lack of mass tracers at larger distances that can be interpreted without any ambiguity, has historically hampered the proper mapping of the mass distribution at the outer regions of elliptical galaxies. The situation is changing and a dramatic improvement is expected in the near future. In fact, several ongoing projects have already produced high quality data on samples of ellipticals through different methods, for example: stellar kinematics from integral-field spectroscopic measurements SAURON (de Zeeuw et al., 2002; Cappellari et al., 2006); strong gravitational lensing CLASS (Myers et al., 1995); LSD (Koopmans & Treu, 2003; Treu & Koopmans, 2004); SLACS (Koopmans et al., 2006); stellar kinematics from planetary nebulae, PNs (Douglas et al., 2002), or globular cluster (Bergond et al., 2006) observations; and X-rays (O'Sullivan & Ponman, 2004b,a). In particular, the combination of high-quality stellar spectroscopy and strong lensing analyses breaks the so-called mass-anisotropy degeneracy, giving strong indications that constant mass-to-light ratios can be ruled out at $> 99\%$ confidence level, consistent with the presence of massive and extended dark matter haloes around, at least, the massive lens ellipticals analyzed so far (Treu & Koopmans, 2004; Koopmans et al., 2006). Moreover, these authors have also found that the dark matter and the baryons mass density profiles combine in such a way that the total mass density profiles can be fit by power-law expressions within their Einstein radii, whose slopes are consistent with isothermality. Similar conclusions on the important amounts of dark matter

inside the virial radii of ellipticals have been reached from weak lensing of L_* galaxies (Guzik & Seljak, 2002; Hoekstra et al., 2004), dynamical satellite studies (van den Bosch et al., 2004) and X-ray analyses (Humphrey et al., 2006). Other observational results or some of their interpretations, however, could suggest that the amounts of dark matter in the haloes of some ellipticals are not that important. For example, Napolitano et al. (2005) have analyzed the mass-to-light gradients of a sample of elliptical + SO galaxies, and found that these are positive and important in massive, boxy elliptical galaxies, but no very important for faint, disky elliptical galaxies. This has been confirmed by Ferreras et al. (2005) using lensing analyses. This result is similar to what Romanowsky et al. (2003) (see also, Romanowsky, 2006) have propounded from the study of random velocities at the outskirts of elliptical galaxies through PN, found to be low, and first interpreted by these authors as proving a dearth of dark matter in elliptical galaxies, while Dekel et al. (2005) explain these large-radii low velocity dispersions as an effect of anisotropy and triaxiality of the halo stellar populations of these galaxies.

Assuming that ellipticals are embedded in massive haloes of dark matter, a second important concern is the possibility that their profiles have near-universal shapes. Here most inputs come from numerical simulations because observational inputs are scarce. When no dissipative processes are taken into account, spherically averaged dark matter density profiles of relaxed haloes produced in N-body simulations have been found to be well fitted by analytical expressions such that, once rescaled, give essentially a unique mass density profile, determined by two parameters. These two parameters are usually taken to be the total mass, $M_{\rm vir}$, and the concentration, c, or the energy content, E. These two parameters are, on their turn, correlated (i.e., the mass-concentration relation, see, for example, Bullock et al., 2001; Wechsler et al., 2002; Manrique et al., 2003). When hydrodynamical forces and cooling processes enter the assembly of these haloes and the baryonic objects they host, the dark matter profiles could be modified in the regions where baryons are dynamically dominant, due to the so-called adiabatic contraction (see, for example, Blumenthal et al., 1986; Dalcanton et al., 1997; Tissera & Dominguez-Tenreiro, 1998; Gnedin et al., 2004; Gustafsson et al., 2006). So, the shapes of dark matter haloes in ellipticals could deviate from the near-universal behavior of dark matter haloes produced in purely N-body simulations.

Another important issue concerns the three dimensional cold baryon mass (i.e., stellar mass and cold gas) distribution, and, more particularly, its distribution relative to the dark matter haloes: are ellipticals homologous systems or is the homology broken in their stellar mass distribution or in their *relative* dark- versus bright-mass distribution?

In regard to the other baryon component, the hot gas, galaxy formation scenarios generally predict that galaxies are embedded in haloes of hot diffuse gas, extending well beyond the distribution of stars. These haloes are thought to consist of gravitationally trapped gas with a temperature of millions of Kelvin. X-ray emission from elliptical

galaxies (Matsushita, 2001; Humphrey et al., 2006), and more recently also from spirals (Pedersen et al., 2006), confirms these predictions and proofs the presence of such hot halos around galaxies. The new generation of X-ray instruments (Chandra, XMM) confirms and extends previous findings in ellipticals. Recent Chandra measurements (Humphrey et al., 2006) have determined their total baryon fractions inside their virial radii. These fractions indicate that these systems, despite having stellar masses $>5 \times 10^{12} M_{\odot}$, are not baryonically closed at virial radius, i.e., their baryon fraction is lower than the average cosmological one. Put in other words, as occurs for clusters (Allen et al., 2004; Zhang et al., 2006), ellipticals miss baryons inside their virial radii. So, we would need to answer a set of questions related with these issues: where the missing baryons are? How did hot gas haloes form? Where and when is the gas heated?

3.2.1.2 Kinematics

Studies on the global kinematics have established that elliptical galaxies as a class are supported by anisotropic velocity dispersions (Binney, 1976, 1978, e.g.). However, concerning the three dimensional velocity distributions of the different elliptical components, very few is known either. In particular, the anisotropy of the stellar three-dimensional velocity dispersion tensor is hard to be observationally characterized. This is an important issue, however, not only because anisotropy plays an important role in the analyses of the elliptical dark matter content at several effective radii, but also because it could keep fossil information about the physical processes involved in mass assembly and stellar formation in elliptical galaxies. The relative behavior of the three-dimensional velocity dispersion tensors for the stellar and the dark mass components (i.e., the so-called kinematical segregation) is still more uncertain. There is not an unambiguous observational input about its presence in ellipticals, or about its possible systematic dependence with the elliptical mass scale. However, it is possible to measure the shape of absorption lines, hence the Line-Of-Sight Velocity Distribution (LOSVD), which will tell us about the velocity anisotropy and hence constrain the orbital families (Bender & Nieto, 1990; Rix & White, 1992; van der Marel & Franx, 1993). Only for a limited number of ellipticals are the $V_{\rm los}(R)$ or $\sigma_{\rm los}(R)$ profiles available.

The LOSVD is often parameterized by the mean velocity in the line of sight V_{los} and velocity dispersion σ_{los}, plus higher order moments ($h3$, $h4$, ...) of a Gauss-Hermite series. The $h3$ and $h4$ offer extra information on the asymmetric and symmetric deviation, respectively, away from a perfect Gaussian. Detailed kinematic studies often reveal kinematic distinct cores (Emsellem et al., 2004, e.g.) and non-relaxed structures (e.g. Balcells & González, 1998) which may be related to the way the galaxy is formed and to its merger history.

Observationally, a useful characterization of the velocity dispersion of an E galaxy is provided by its central stellar line-of-sight velocity dispersion, σ_0. Due to its interest, σ_0

has deserved an important attention in literature and it had been measured for several E galaxy samples (Faber et al., 1987; Djorgovski & Davis, 1987; Dressler et al., 1987; Lucey et al., 1991; Jorgensen et al., 1993, 1996; Kelson et al., 1997, 2000; Bernardi et al., 2002, 2003a). Recently integral field (or 2D) spectroscopy has opened the possibility for analyses of large scale kinematics and stellar population of galaxies (Bacon et al., 2001).

In what follows we will deepen into the different observed correlations between photometric and kinematical parameters obtained for elliptical galaxies.

3.2.2 Parameter Correlations: The Fundamental Plane

Elliptical galaxies exhibit a bewildering variety of correlations between their kinematical and photometrical data. The strongest relation (i.e., with less scatter) found up the moment is the one that relates the projected effective radius, $R_{\rm e}^{\rm light}$ (as measured from the brightness profile), the mean surface brightness within the effective radius, $< I^{\rm light} >_{\rm e}$, and the central velocity dispersion, σ_0 (Djorgovski & Davis, 1987; Dressler et al., 1987; Faber et al., 1987). In fact, this correlation is so tight that it is usually said that elliptical galaxies lie on a Fundamental Plane (FP). The FP relation can be written as

$$\log_{10} R_{\rm e}^{\rm light} = a \log_{10} \sigma_0 + b \log_{10} < I^{\rm light} >_{\rm e} + c. \tag{3.2}$$

Some previous known relation for ellipticals can be seen as a projection onto any two axes out of the three variables. Examples of this projections are the effective radius and surface brightness relation (Kormendy, 1977), the Faber-Jackson relation (Faber & Jackson, 1976) between luminosity and velocity dispersion. The $D_n - \sigma$ relation is another example, as it was constructed as a nearly edge-on projection of the FP (Dressler et al., 1987).

In the last years, the Sloan Digital Sky Survey (SDSS, York et al., 2000) has substantially improved the statistics on elliptical samples. The sample selected by Bernardi et al. (2003a) from the SDSS database in the summer of 2001, using morphological and spectral criteria, contains 9000 ellipticals in the redshift range $0.01 \leq z \leq 0.3$ and in every environment from voids to groups to rich clusters. This is a larger number of ellipticals than in all the previously considered samples. Analyzes of their structural and dynamical parameters have shown that the distributions of their luminosities L, radii at half projected light, $R_{\rm e}^{\rm light}$, and central line-of-sight velocity dispersions, σ_0 (Bernardi et al., 2003b,c), are approximately gaussian at any z. Moreover, a maximum likelihood analysis indicates that the pairs of parameters σ_0—L and $R_{\rm e}^{\rm light}$—L, or their combinations, such as the mass-to-luminosity ratio within the effective radii $M_{\rm e}/L$ and L (where $M_{\rm e}$ is the dynamical mass defined as $M_{\rm e} = 2R_{\rm e}^{\rm light}\sigma_0^2/G$), show correlations consistent with those previously established in literature, obtained from individual galaxy spectra of smaller samples, such as the Faber-Jackson relation (Faber & Jackson, 1976); the

D_n—σ_0 relation (Dressler et al., 1987); and the surface brightness —R_e^{light} relation (Kormendy, 1977; Kormendy & Djorgovski, 1989), among others. Furthermore, early-type galaxies in the SDSS have been found to have roughly constant stellar-mass-to-light ratios (Kauffmann et al., 2003b,a; Padmanabhan et al., 2004). The values of the FP coefficients for the SDSS elliptical sample are $a \simeq 1.5$, similar in the four SDSS bands, $b \simeq -0.77$, and $c \simeq -8.7$ (see their exact values in Bernardi et al., 2003c, Table 2) with a small scatter. These SDSS results confirm previous ones, either in the optical (Lucey et al., 1991; de Carvalho & Djorgovski, 1992; Bender et al., 1992; Jorgensen et al., 1993; Prugniel & Simien, 1996; Jorgensen et al., 1996) or in the near-IR wavelengths (Recillas-Cruz et al., 1990, 1991; Pahre et al., 1995; Mobasher et al., 1999), even if the published values of a show larger values in the K-band than at shorter wavelengths (see, for example, Pahre et al., 1998). La Barbera et al. (2008) have also confirmed these results using a sample of ∼1500 ETGs studied both in the optical (Data Release 5 of the SDSS) and the near infrared (UKIRT Infrared Deep Sky Survey, UIDSS). The invariance of the FP with wave band is in agreement with Cappellari et al. (2006), who found for 25 ETGs from the SAURON project the M/L versus L relation to have the same slope in both the I and K bands.

Recently Hyde & Bernardi (2008a,b) have studied the Fundamental Plane using a sample of 50000 early-type galaxies based on the Data Release Fourth of the SDSS. They selected galaxies with velocity dispersions $60 < \sigma_0 < 400\ km \times s^{-1}$ These authors have confirmed previous results on the slope of the Fundamental Plane and pointed out a possible dependence of the fit parameters on the range of L or σ_0 in the sample which may explain some of the relatively wide range of Fundamental Plane coefficients in the literature. They also showed that the intrinsic scatter around this plane becomes broader at low sizes/masses.

The existence of the FP and its small scatter has the important implication that it provides us with a strong constraint when studying elliptical galaxy formation and evolution (Bender et al., 1992; Guzman et al., 1993; Renzini & Ciotti, 1993). The physical origin of the FP is not yet clear, but it must be a consequence of the physical processes responsible for galaxy assembly. These processes built up early type galaxies as dynamically hot systems whose configuration in phase space are close to equilibrium. For this reason, the general framework to explain this relation is the virial theorem, which relates the moment of inertia of a self-gravitating system with its kinetic energy and potential energy. The scalar form of the virial theorem, for which one assumes that the system is in steady state, so its moment of inertia is constant in time, can be written as (see Binney & Tremaine, 1987, for the full demonstration):

$$2T + V = 0 \tag{3.3}$$

where T is the kinetic energy of the system and V its potential energy.

The kinetic energy of an isolated system with mass, $M_{\rm vir}$, is just $T = \frac{1}{2} M_{\rm vir} < (v_3^{\rm tot})^2 >$, where $< (v_3^{\rm tot})^2 >$ is the mean-square speed of the whole system, including both dark and baryonic matter, and $M_{\rm vir}$ is its virial mass. We also use the definition of a characteristic gravitational radius, related with the system's mass and potential energy as $r_g^{\rm tot} = \frac{G {M_{\rm vir}}^2}{|V|}$ (Binney & Tremaine, 1987, chapter 2.5). Using these relations in the scalar virial equation, we obtain:

$$M_{\rm vir} = c_{\rm f} \frac{< (v_3^{\rm tot})^2 > r_{\rm g}^{\rm tot}}{G} \tag{3.4}$$

where $c_{\rm f}$ is a form factor of order unity.

All the quantities that appear in Equation (3.4) can be related with available observables. The virial mass with the luminosity L

$$M_{\rm vir} = \frac{M_{\rm vir}}{M_*} \cdot \frac{M_*}{L} \cdot L \tag{3.5}$$

where we have also introduced the stellar mass of the galaxy, M_*. Therefore we can distinguish between the well known stellar-mass-to-light ratio M_*/L and the total-to-stellar mass ratio $M_{\rm vir}/M_*$.

For the mean-square speed of the system, using the arithmetic mean, $\bar{v}_3^{\rm tot}$, and the standard deviation $\sigma_3^{\rm tot}$ we have that $< (v_3^{\rm tot})^2 > = < \bar{v}_3^{\rm tot} >^2 + (\sigma_3^{\rm tot})^2$. As pointed out before, observations indicate that ellipticals are systems that are supported by velocity dispersion, so we can neglect the ordered motion term, $\bar{v}_3^{\rm tot} \sim 0$. In this case, we can just utilize the standard deviation to sample the kinetic energy, and, introducing its observational equivalent, the central line-of-sight velocity dispersion of the stellar component, σ_0, obtain the following expression

$$< (v_3^{\rm tot}) >^2 \cong (\sigma_3^{\rm tot})^2 = 3 \cdot c_{\rm v} \cdot \sigma_0^2 \tag{3.6}$$

where the $c_{\rm v}$ is a constant that relates the standard deviation of the whole system with the observational line-of-sight velocity dispersion.

Additionally we define $c_{\rm r}$, to relate the gravitational radius with the observed effective radius, this is the projected effective radius obtained from the light curve of the galaxy:

$$r_g^{\rm tot} = c_{\rm r} \cdot R_{\rm e}^{\rm light} \tag{3.7}$$

Before going any further, to simplify, we can define a unique constant, $c_{\rm vir}^{\rm M}$, that group together the different ones defined in Equations (3.4), (3.6) and (3.7)

$$c_{\rm vir}^{\rm M} = c_{\rm f} \cdot c_{\rm v} \cdot c_{\rm r} \tag{3.8}$$

It is important to remark for future discussions in this thesis that to do this transfor-

mations, we have made three clearly different steps. Firstly considering the visible light instead of the whole virialized system, implies that we need to go from the halo-virial mass scale to the observed light galaxy scale. Therefore we have to take into account two issues, the change of scales from the halo to the galaxy and the relation between the stellar mass of this galaxy and the light that it produces, which is what we really see. The third one is the fact that we have to use projected quantities, so a projection effect is also included. All the constants and ratios introduced in the last equations account for our ignorance of these effects.

If we replace in Equation (3.5) the last luminosity term, L, with the relation $L = 2\pi < I^{\rm light} >_{\rm e} {R_{\rm e}^{\rm light}}^2$ and use it with Equations (3.6) and (3.7) in Equation (3.4) we obtain

$$R_{\rm e}^{\rm light} = \frac{3}{2\pi G} \cdot c_{\rm vir}^{\rm M} \cdot (\frac{M_{\rm vir}}{M_*})^{-1} \cdot (\frac{M_*}{L})^{-1} \cdot \sigma_0^2 \cdot < I^{\rm light} >_{\rm e}^{-1} \tag{3.9}$$

that is, from the virial theorem we have predicted a relation between the same observables that are involved in the Fundamental Plane (see Equation 3.2). Besides, if one assumes that $M_{\rm vir}/M_* \cdot M_*/L$ is independent of the elliptical luminosity or mass scale and that the galaxies form a homologous family (i.e. c_{vir}^{M} is also constant) the application of the virial theorem predicts the FP relation to be $R_{\rm e}^{\rm light} \propto \sigma_0^2 < I^{\rm light} >_{\rm e}^{-1}$. But the observational results, described above, obtain a FP relation tilted respect to the virial relation: $R_{\rm e}^{\rm light} \propto \sigma_0^{1.2} < I^{\rm light} >_{\rm e}^{-0.8}$. This effect is known as the *tilt* of the Fundamental Plane and it is supposed to be caused by the falsification of one (or both) hypothesis made above.

Different authors interpret the tilt of the FP relative to the virial relation as caused by different misassumptions that we comment briefly. Firstly we consider the M_*/L and the $M_{\rm vir}/M_*$ ratios:

1.1) A first possibility is that the tilt is due to systematic changes of stellar age and metallicity with galaxy mass, or, even, to changes of the slope of the stellar initial mass function with galaxy mass, resulting in systematic changes in the *stellar*-mass-to-light ratios, M_*/L, with mass or luminosity (Zepf & Silk, 1996; Pahre et al., 1998; Mobasher et al., 1999). But these effects could explain at most only one third of the tilt value in the B-band (Tinsley, 1978; Dressler et al., 1987; Prugniel & Simien, 1996; Renzini & Ciotti, 1993; Trujillo et al., 2004). Furthermore, early-type galaxies in the SDSS have been found to have roughly constant stellar-mass-to-light ratios (Kauffmann et al., 2003b,a). Anyhow, the presence of a tilt in the K-band FP, where population effects are no important, indicates that it is very difficult that the tilt is caused by stellar physics processes alone, as Bender et al. (1992); Renzini & Ciotti (1993); Guzman et al. (1993); Pahre et al. (1998); La Barbera et al. (2008), among other authors, have suggested.

1.2) A second possibility is that $M_{\rm vir}/L$ changes systematically with the mass scale

because the total dark-to-visible mass ratio, $M_{\rm vir}/M_*$ changes (see, for example, Renzini & Ciotti, 1993; Pahre et al., 1998; Ciotti et al., 1996; Padmanabhan et al., 2004; Cappellari et al., 2007; Hyde & Bernardi, 2008b; Tortora et al., 2009).

Otherwise, a dependence of $c_{\rm M}^{\rm vir}$ on the mass scale could be caused by systematic differences in:

2.1) the dark versus bright matter spatial distribution,

2.2) the kinematical segregation, the rotational support and/or velocity dispersion anisotropy in the stellar component (dynamical non-homology),

2.3) systematic projection or other geometrical effects.

Taking into account these effects in the FP tilt, it is mandatory to model the galaxy mass and velocity three-dimensional distributions and comparing the outputs with high quality data.

Bender et al. (1992) considered effects 2.1) and 2.2); Ciotti et al. (1996) explore 1.2) - 2.2) and conclude that a systematic increase in the dark matter content with mass, or differences in its distribution, as well as a dependence of the Sérsic shape parameter for the luminosity profiles with mass, may by themselves formally produce the tilt; Padmanabhan et al. (2004) find evidence of effect 1.2) in SDSS data. Other authors have also shown that allowing for broken homology, either dynamical (Busarello et al., 1997), in the luminosity profiles (Trujillo et al., 2004), or both (Prugniel & Simien, 1997; Graham & Colless, 1997; Pahre et al., 1998), brings the observed FP closer to Eq. (3.9).

One important source of ambiguity in observational data analysis comes from the impossibility to get accurate measurements of the elliptical three-dimensional mass distributions (either dark, stellar or gaseous) and velocity distributions. Analytical models give very interesting insights into these distributions as well as the physical processes causing them, but are somewhat limited by symmetry considerations and other necessary simplifying hypotheses. Self-consistent gravo-hydrodynamical simulations are a very convenient tool to work out this problem, as they *directly* provide with complete 6-dimensional phase-space information on each constituent particle sampling a given galaxy-like object formed in the simulation, that is, they give directly the mass and velocity distributions of dark matter, gas and stars of each objet. This phase space information would allow us to test whether or not the $c_{\rm M}^{\rm vir}$ (that is, the $c_{\rm f}, c_{\rm v}$ and $c_{\rm r}$) coefficient, as well as the $M_{\rm vir}/M_*$ ratios, do or do not systematically depend on the mass scale. This is the issue addressed in Section 6.2, where we analyze whether the dependence is such that the tilt and the scatter of the observed FP can be explained in terms of the regularities in the structural and dynamical properties of ELOs formed in self-consistent hydrodynamical simulations.

3.2.2.1 Rotation versus Shape. Two kinds of Elliptical Galaxies?

Still under the scope of the virial theorem, we can also get a lot of information about the internal motions of elliptical galaxies from the knowledge of their shapes and speeds of rotation. The tensor virial theorem (see Binney & Tremaine, 1987) relates the kinetic energy tensor T_{ij}, the potential energy tensor,V_{ij}, and the moment of inertia tensor I_{ij}. It is useful to split the kinetic energy tensor in the K_{ij} and Π_{ij} tensors, that account for the ordered and random motions respectively, in the following form: $T_{ij} = K_{ij} + \frac{1}{2}\Pi_{ij}$. The tensor virial theorem can be written

$$\frac{1}{2}\frac{d^2 I_{ij}}{dt^2} = 2K_{ij} + \Pi_{ij} + V_{ij} \tag{3.10}$$

The classical example is an axisymmetric system that rotates about its symmetry axis (that we call the z-axis) and the system is seen edge-on (from the x-axis, for example). In this case, thanks to the symmetry of the problem, we have $V_{xx} = V_{yy}$ and $V_{ij} = 0\,(if\ i \neq j)$ and similar relations for Π and K tensors. Assuming that the galaxy is in equilibrium ($d^2 I_{ij}/dt^2 = 0$) the tensor virial Equation (3.10) yields to only two nontrivial equations: $2K_{xx} + \Pi_{xx} + V_{xx} = 0$ and $2K_{zz} + \Pi_{zz} + V_{zz} = 0$. Dividing the first equation by the second, we obtain

$$\frac{2K_{xx} + \Pi_{xx}}{2K_{zz} + \Pi_{zz}} = \frac{V_{xx}}{V_{zz}} \tag{3.11}$$

Also if the only streaming motion is the rotation about z-axis we can write

$$2K_{ij} = \frac{1}{2} M v_{los}^2 \begin{pmatrix} 1 & 0 & 0 \\ 0 & 1 & 0 \\ 0 & 0 & 0 \end{pmatrix} \tag{3.12}$$

where M is the mass of the system and v_{los}^2 is the mass-weighted mean-square rotation speed. Now for the tensor associated with the random motion, Π,

$$\Pi_{ij} = M\sigma_{los}^2 \begin{pmatrix} 1 & 0 & 0 \\ 0 & 1 & 0 \\ 0 & 0 & 1-\delta \end{pmatrix} \tag{3.13}$$

where δ is the anisotropy parameter that accounts for the possibility that the random dispersion in the z-axis is different from the dispersions in the x and y-axis. M is again the mass of the system and σ_{los}^2 is the mass-weighted random velocity along the line of sight.

We can now use Equations (3.12) and (3.13) in (3.11) and rewrite it as

$$\frac{V_{xx}}{V_{zz}} = \frac{\frac{1}{2}V_{los}^2 + \sigma_{los}^2}{(1-\delta)\sigma_{los}^2} \tag{3.14}$$

In systems whose isodensity surfaces are similar concentric ellipsoids, any ratio of terms like V_{xx}/V_{zz} depends only on the ellipticity, ϵ_{3d}, of these surfaces. This shape parameter, $\epsilon_{3d} \equiv 1 - \frac{c}{a}$, is determined by measuring the major and minor axes, a and c, of the ellipsoid. So $V_{xx}/V_{zz} = f(\epsilon)$ and Equation (3.14)

$$\frac{V_{los}}{\sigma_{los}} = \sqrt{2 \cdot f(\epsilon_{3d}) \cdot (1-\delta) - 2} \tag{3.15}$$

A reasonably accurate approximation for $f(\epsilon_{3d})$ (see Binney & Tremaine, 1987, Tables 2.1 and 2.2) is

$$f(\epsilon_{3d}) \simeq 1 + \frac{\epsilon_{3d}}{2(1-\epsilon_{3d})} \tag{3.16}$$

additionally there are some interesting easy examples that can be illustrative. For a non rotating galaxy $v_{los} = 0$ then $1 - \delta = \frac{1}{f(\epsilon_{3d})} \simeq \frac{2-2\epsilon_{3d}}{2-\epsilon_{3d}}$. In the case of an isotropic rotating galaxy, $\delta = 0$, then

$$\frac{V_{los}}{\sigma_{los}} \simeq \sqrt{\frac{\epsilon_{3d}}{1-\epsilon_{3d}}} \tag{3.17}$$

The observational application of these relationships is somewhat complicated by projection effects. Instead of v_{los} and σ_{los} one has to use their observational counterparts. These are V_{max}, the maximum of the line-of-sight rotation curve and σ_0, the central l.o.s. velocity dispersion. The apparent ellipticity, ϵ, is determined by measuring the major and minor axes, a and b, of a chosen isophote where $\epsilon \equiv 1 - \frac{b}{a}$. However, for isotropic rotators ($\delta = 0$) projection diminishes apparent ellipticity and rotation velocity alike in such a way that Eq. (3.17) is still roughly correct (Binney & Tremaine, 1987).

Davies et al. (1983) studied the now classical V_{max}/σ_0 vs. ϵ diagram[2] for spheroids (Illingworth, 1977; Binney, 1978). They found that luminous (and massive) elliptical galaxies were characterized by low V_{max}/σ_0 and a fairly round aspect (low ϵ), while ellipticals with intermediate luminosity tend to have larger values of V_{max}/σ_0 and ϵ. Some observations of near-by elliptical galaxies corroborate this division in two flavors according to their luminosity (Lauer, 1985; Bender, 1988; Bender et al., 1989; Nieto & Bender, 1989; Bender et al., 1994; Gerhard et al., 2001; Pellegrini, 2005; Cappellari et al., 2007; Emsellem et al., 2007). On the one hand, high luminosity elliptical galaxies show boxy isophotal deviations from perfect ellipses, low rotation and high velocity dispersion. They are powerful emitters in X-rays and radio. On the other hand, low to

[2]Another successful formulation for this diagram is $(V/\sigma)^*$ vs ϵ, where $(V/\sigma)^* = \frac{(V_{max}/\sigma_0)_{obs}}{(V_{max}/\sigma_0)_{theo}}$. Here $(V_{max}/\sigma_0)_{obs}$ is the observed relation while $(V_{max}/\sigma_0)_{theo}$ is the theoretical value obtained from Equation (3.17), this is, if the system is an oblate rotator supported by rotation. Note that $(V/\sigma)^* \simeq 1$ for a rotationally flattened galaxy, and < 1 for a galaxy flattened by velocity anisotropy.

intermediate luminosity elliptical galaxies show disky isophotal deviations with a fair to important contribution of rotation as compared with velocity dispersion. Finally, they are not associated to extended X-ray emission or radio loud objects. Because of all these multiple correlations, Kormendy & Bender (1996) have proposed that boxyness or diskyness be adopted as the primary classification criterion for elliptical galaxies. Cappellari et al. (2007); Emsellem et al. (2007) proposed to use the rotational support and to name them as slow and fast rotators. However, it is worth to mention that the largest homogeneous set of V_{max}/σ_0 and ellipticity values is currently around 90 early-type objects. In this sense, Rothberg & Joseph (2006) has also studied this relation in a sample of 51 nearby ellipticals classified as merger remnants finding some interesting results which indicate that this picture is not so clear and that it is far from being closed. Concerning the study of this diagram at higher redshifts, recently van der Marel & van Dokkum (2007) presented evidences of evolution of the rotation support of spheroidal systems since $z = 0.5$ pointing towards a decrease in the rotational support as the redshift decreases. Present formation schemes should explain this dichotomy and its possible evolution.

3.2.2.2 The Photometric Plane

Finally, since the first statistical studies of galaxies, a big effort has been done in looking for empirical correlations involving only the photometric parameters, given the observational difficulties in measuring σ_0 and other kinematical descriptors. An interesting example is the Kormendy relation between $R_{\rm e}^{\rm light}$ and $\mu_{\rm e}$ (Kormendy, 1977) already discussed in previous sections under the Fundamental Plane framework. However, in the last years, the fact that the projected luminosity profile of elliptical galaxies appears to be universal and can be parameterized by the Sérsic law has generated a lot of interest in the shape parameter n that characterize these profiles (see Section 3.2.1).

The shape parameter, n, is related to both the curvature of light profiles and to the degree of concentration of light. It soon became clear that, in local elliptical samples, n correlates with global quantities such as the total luminosity and effective radius (Caon et al., 1993; Prugniel & Simien, 1997; Khosroshahi et al., 2000; D'Onofrio, 2001), or $\sigma_{\rm los,0}^{\rm star}$ (Graham, 2002; Vazdekis et al., 2004). Just as the Kormendy relation is a projection of the FP, both the $R_{\rm e}^{\rm light} - \mu_{\rm e}$ and the $R_{\rm e}^{\rm light} - n$ relations may be seen as projections of a more fundamental law among these three photometric parameters. In logarithmic units, such a relation indeed exists and it is a plane referred to as the Photometric Plane (PhP) recently detected in both near infrared (Khosroshahi et al., 2000) and optical (Graham, 2002). The PHP has an intrinsic scatter that is only slightly larger than that of the FP, therefore making this relation an interesting tool to analyze the properties of galaxies at different redshifts. However, a definitive theoretical interpretation is still lacking. Modeling the stars in ETG as a self-gravitating gas, Lima

Neto et al. (1999) have recovered a PhP like relation (referred to as the entropic plane) by assuming that the specific entropy (i.e., the entropy by mass unit) is constant for all ETGs. Later, Márquez et al. (2001) derived an energy - entropy (or mass - entropy) line giving a possible explanation for the structural relations among photometric parameters. Moreover, they also found out that the specific entropy increases as a consequence of merging processes so offering a possible way to test the model against the observed variation of the PhP with redshift. In this sense, even if still very incomplete, new data (Coe et al., 2006; Ravindranath et al., 2006) pointed to an extension of these correlations towards higher zs, that is, to a homogeneity of the elliptical population with z, except that the objects became on average more compact, at fixed stellar mass, with increasing z (Trujillo et al., 2007; Buitrago et al., 2008; van der Wel et al., 2008).

Some authors have recently argued that these two relations could be the projection of a more fundamental one between the four parameters involved in them, following the idea of underlying more general relations that gave rise to the Fundamental Plane and the Photometric Plane (see Graham, 2002; Capozziello et al., 2007). However, as with the Photometric Plane the theoretical interpretation of this *Sersic Virial hyperplane* is still not clear.

3.2.3 Observational Problems, Theoretical Improvements

We see that the mass or velocity distributions of the different elliptical mass components encode a lot of information about the physical origin of the different parameter correlations observed, and, consequently, on the physics of their formation. We see also that, unfortunately, observational methods, by themselves, suffer from some drawbacks to deepen into these issues. A major problem is that the information on the intrinsic mass distribution is not directly available: we see the projected distributions (not three-dimensional mass) either dark, stellar or gaseous. Another major caveat is that the intrinsic 3D velocity distribution of galaxies is severely limited by projection, only the line-of-sight velocity distributions can be inferred from galaxy spectra. And, so, the interpretation of observational data is not always straightforward. To complement the information provided by data and circumvent these drawbacks, analytical modeling is largely used in literature (Kronawitter et al., 2000; Gerhard et al., 2001; Romanowsky & Kochanek, 2001; Borriello et al., 2003; Padmanabhan et al., 2004; Mamon & Łokas, 2005a,b). They give very interesting insights into mass and velocity distributions, as well as the physical processes causing them, but are somewhat limited by symmetry considerations and other necessary simplifying hypotheses. These difficulties and limitations could be circumvented should we have at our disposal complete information on the phase-space of the galaxy constituents. This is not possible through observations, but can be attained by numerical simulations.

The first authors who studied the formation and properties of elliptical galaxies by

means of numerical methods used purely gravitatory pre-prepared simulations. Capelato et al. (1995) first addressed the origin of the FP by analyzing the remnants of the dissipationless mergers of two equal-mass one-component King models, and varying their relative orbital energy and angular momentum, they showed that their merger remnants lie in the FP. This result was extended by Dantas et al. (2003), who used one- and two-component Hernquist models as progenitors, González-García & van Albada (2003), based on Jaffe (1983) models; and by Boylan-Kolchin et al. (2005), who used Hernquist+NFW models, confirming that further dissipationless mergers of objects on the FP produce new objects in the FP. Nipoti et al. (2003) showed, in turn, that the FP is well reproduced by dissipationless hierarchical equal-mass merging of one- and two-component galaxy models, and by accretion with substantial angular momentum, with the merging zero-order generation placed at the FP itself. They also found that both the Faber-Jackson and the Kormendy relations are not reproduced by the simulations, and conclude that dissipation must be a basic ingredient in elliptical formation. That further dissipationless mergers preserve the Fundamental Plane but not its projections, was also pointed out by Boylan-Kolchin et al. (2005). In agreement with this conclusion, Dantas et al. (2002, 2003) showed that the end products of dissipationless collapse generally do not follow a FP-like correlation. Bekki (1998) first considered the role of dissipation in elliptical formation through pre-prepared simulations. He adopted the merger hypothesis (i.e.., ellipticals form by the mergers of two equal-mass gas-rich spirals) and he focused on the role of the timescale for star formation in determining the structural and kinematical properties of the merger remnants. He concluded that the slope of the FP reflects the difference in the amount of dissipation the merger end products have experienced according with their luminosity (or mass). Recently, Robertson et al. (2006) have confirmed this conclusion on the role of dissipative dynamics to shape the FP, again through pre-prepared mergers of disk galaxies.

Apart from the origin of the FP, other aspects of the formation and evolution of elliptical galaxies have been analyzed through pre-prepared simulations. For example, a number of recent numerical simulations of galaxy encounters have dealt with the population of the classical V_{max}/σ_0 vs ϵ diagram and the formation of boxy and disky objects (Naab & Burkert, 2003; González-García & Balcells, 2005; González-García & van Albada, 2005; Bournaud et al., 2005; Naab et al., 2006; Robertson et al., 2006; Cox et al., 2006; González-García et al., 2006; Jesseit et al., 2007). These studies indicate that mergers between disk galaxies tend to produce too large rotation when compared with present day massive elliptical galaxies. Besides, mergers between elliptical galaxies do reproduce the observed characteristics. Khochfar & Burkert (2003); Kang et al. (2007) (and references there in) present first attempts of semi-analytical modeling to address the origin of the observed dichotomy in early type galaxies.

We see that pre-prepared simulations of merger events provide a very useful tool

to work out the mass and velocity distributions of elliptical galaxies. They allow also to find out their links with the processes involved in galaxy assembly, but they are somewhat limited, for example by the fact that the probability of a particular initial setup at a given z is not known a priori, and that mergers involving more than two objects also occur and are frequent at high zs, so that some complementary information must be provided, for example through semi-analytical models (Khochfar & Burkert, 2005; Naab et al., 2006).

To overcome these limitations, a convenient method is to study the processes involved in galaxy formation in a *cosmological context* through *self-consistent* gravo-hydrodynamical simulations (a description of this technique and the state of the art can be found in Chapter 2).

Kobayashi (2005) has simulated the chemodynamical evolution of 74 fields with different cosmological cold dark matter initial spectra set in slowly rotating spheres, each of them with a 1.5 Mpc comoving radius and vacuum boundaries. So, these simulations are not yet fully self-consistent. She succeeded in reproducing the observed global scaling relations shown by elliptical galaxies, and, in particular, the FP relation, and the surface-brightness profiles, as well as the color-magnitude and the mass-metallicity relations. She also analyzed the role of major merger events and the timescales for star formation in shaping the mass and sizes of remnants.

Concerning self-consistent hydrodynamical simulations, Sommer-Larsen et al. (2002) presented first results on early-type galaxy formation in a cosmological context. Meza et al. (2003) presented results of the dissipative formation of a compact elliptical galaxy in the ΛCDM scenario. Kawata & Gibson (2003, 2005) and Gibson et al. (2007) studied the X-ray and optical properties of virtual ellipticals formed in different simulations run with their chemodynamical Tree/SPH code. Romeo et al. (2005) analyzed the galaxy stellar populations formed in their simulations of galaxy clusters. Naab et al. (2007) got, from cosmological initial conditions, a spheroidal system whose photometric and kinematical properties agree with observations of ellipticals, in a scenario not including feedback from supernovae or AGN and not requiring recent major mergers. Interesting results on elliptical formation have also been obtained by De Lucia et al. (2006), from a semi-analytic model of galaxy formation grafted to the *Millennium Simulation*.

However, detailed analyses of the mass and velocity distributions of samples of virtual ellipticals formed in fully self-consistent hydrodynamical simulations, and, in particular, of the amount and distribution of dark matter relative to the bright matter distribution, as well as of the kinematics of the dark and bright components, and their successful comparison with observational data, are still missing. Filling this gap is one of the aims of this thesis.

3.3 Monolithic Collapse vs Hierarchical Merging

The data discussed in the previous section provide us with a valuable tool that we can use not only for asking us how are elliptical galaxies today but also to try to dig into how they have been formed. As we have pointed out in the introduction of this chapter, now that we have a solid framework, the *concordance* cosmological model, we should try to go one step further and investigate the origin of the Hubble sequence. However, understanding the formation of every type of galaxies and how they have evolved is still controversial and an issue of living debate in the astrophysical community (Ellis & Silk, 2007).

In current ΛCDM galaxy formation and evolution scenarios at least two physical phenomena could contribute to the mass assembly: spherical collapse and hierarchical mergers (Peebles, 2002). Two main families of models may be recognized depending of the importance of each of these phenomena: the *monolithic scenario* (Eggen et al., 1962; Larson, 1974) and the hierarchical scenario (White & Rees, 1978; Cole et al., 1994).

Although the picture of spherical collapse is quite simple, it is very useful when studying collapsed objects like galaxies. The physical description of the processes that follow from primordial fluctuations can only be done analytically in cases of particular symmetry. The simplest one is the collapse of an overdensity of dark matter, with a spherical density profile given by the step function and a radius lower than the horizon. In this case, we can use a Newtonian approach that shows that mass shells with negative total energy expand up to a maximum radius and then recolapse, reaching the equilibrium through violent relaxation. However, in the real world, radial symmetry is not exact and the halo reaches a virial equilibrium state after a violent relaxation phase (Peebles, 1980). Numerical simulations show the basic scalings derived from this approach to be roughly correct and useful for making simple analytic estimates (Bryan & Norman, 1998; Silk & Bouwens, 2001). However, the general picture of spherical collapse has been evolved during the last years to a more sophisticated one. Now, collapse as a physical process involved in galaxy formation is a non symmetrical mechanism where star formation occurs in small clumps of gas during a short phase of time. The modern version of the classical monolithic collapse scenario puts the stress on elliptical assembly out of gaseous material (that is, with dissipation), either in the form of a unique cloud or of many gaseous clumps, but not out of pre-existing stars, with the stellar populations forming at high z and on short timescales relative to spirals (Matteucci, 2003).

On the other hand, in the Cold Dark Matter scenario, halos form hierarchically by the merging of smaller halos and accretion (see Chapter C for more details on this subject) and the role of these mergers in the galaxy formation models cannot be ignored. Then the hierarchical merging scenario propounds that galaxies form hierarchically through successive, random mergers of subunits (the so-called galaxy merger tree) over a wide redshift range, in such a way that more massive ones form more likely at late

time. The importance of mergers as an essential element in galaxy assembly, and their evolution, is becoming more significant as soon as new observations are giving more information of their frequency (below we will address the observational data available on this subject).

3.3.1 Different Observational Constraints

In the monolithic collapse scenario, galaxies of different morphological types (spirals and ellipticals) are born intrinsically different, whereas in the hierarchical merging scenario, galaxies end up as spirals or ellipticals depending on the details of their merger history. The hierarchical formation of giant galaxies is predicted in models to be the natural outcome of major mergers (Barnes & Hernquist, 1992). Some indications are the visible signs of past merging activity around giant elliptical galaxies, such as the so-called shells or ripples found around 10% of all massive galaxies (e.g., Michard & Prugniel, 2004). A significant number of central cluster galaxies also show evidence for recent merger activity in the form of multiple nuclei and tidal features (e.g., Conselice et al., 2005). Another piece of evidence for merger activity are decoupled cores found in the centers of a great number of ellipticals (e.g., de Zeeuw et al., 2002). Results at high redshift shows that a typical galaxy with a stellar mass of $M_* > 10^{10} M_\odot$ undergoes between 1-2 major mergers at $z < 1.2$ (Conselice et al., 2008). These authors also found that for galaxies selected by $M_* > 10^{10} M_\odot$, the merger fraction can be parameterized by $f_m(z) = f_0 \times (1+z)^m$ with the power-law slope $m = 2.3 \pm 0.4$. They also found that the merger rate of these galaxies increases linearly between $z = 0.7$ and $z = 3$. Other methods of finding mergers through galaxy pair counts, either kinematic or spatially projected (Le Fèvre et al., 2000; Patton et al., 2002; Kartaltepe et al., 2007; Bluck et al., 2009), agree with this result out to $z \sim 1$ (see De Propris et al., 2007, for a comparison between the two methods). The fact that mergers are not rare events in the universe and they are even more frequent at high redshifts, aims to indicate that they play an important role in galaxy assembly.

Attempts to discriminate between the two models focus mostly on elliptical galaxies, which are easier to study than spiral ones. As we have seen above, present-epoch ellipticals form a very homogeneous family, with very similar intrinsic properties, compared with the heterogeneous family of spirals. Furthermore, they are mostly composed of old stellar populations, about as old as the universe (Thomas et al., 2005; Jimenez et al., 2007). This fact is responsible for the most distinctive property of ellipticals: their color. Ellipticals are the reddest galaxies in the local universe. They have little or no star formation activity.

Due to their different formation times for ellipticals, these scenarios also yield remarkably different predictions for the evolution in the number density of early-type galaxies as a function of redshift.

Joint gravitational lensing and dynamical analyses of elliptical lens galaxies have evidenced their lack of significant structural and dynamical evolution at least out to $z \sim 1$ (Treu & Koopmans, 2004), and, moreover, that the evolution of their average stellar mass-to-light ratio, $M^{\rm star}/L_B$, is consistent with the predictions of a scenario of pure luminosity evolution of their stellar populations (Treu, 2004). Analyses of the combined evolution of the luminosity-size and stellar mass-size relations (Trujillo et al., 2004; McIntosh et al., 2005) provide similar results on elliptical homogeneity. In fact, these analyses show that the luminosity-size distribution evolves in a manner that, by itself, is consistent with a passive evolution of the red early-type galaxy populations since high z, but they do not find evidence of any strong structural evolution in the stellar mass-size relation. However, it is important to remark that some recent results point to an evolution in the mass-size relation for the very massive elliptical galaxies since redshift $z \simeq 2$ (Trujillo et al., 2007; Buitrago et al., 2008; van der Wel et al., 2008).

Weak lensing (Heymans et al., 2006) and optical studies of the Fundamental Plane of early-type galaxies out to $z \sim 1$ (van Dokkum et al., 2001; van de Ven et al., 2003; Wuyts et al., 2004; di Serego Alighieri et al., 2005; Treu et al., 2005; van Dokkum & van der Marel, 2007) have traditionally described its evolution in terms of the evolution of their stellar populations (see, however discussion in di Serego Alighieri et al., 2005). An important convergent result is the confirmed existence of a population of old, relaxed, massive ($M^{\rm star} > 10^{11}{\rm M}_{\odot}$) spheroidal galaxies at intermediate zs ($z \sim 1-2$). The K20 survey has first shown (Moriondo et al., 2000) that a high fraction of the so-called Extremely Red Object sample are in fact old spheroidal galaxies, found out to $z \sim 1$, with formation redshifts of no later than $z_f \sim 2.5-3.4$ if a unique starburst is assumed or even earlier on if this hypothesis is relaxed (Cimatti et al., 2002). Cimatti et al. (2004) have identified four massive ($M^{\rm star} > 10^{11}{\rm M}_{\odot}$) fully assembled spheroidal galaxies at $1.6 < z < 1.9$ with old stellar populations and Stanford et al. (2004) a larger sample in HDF-NICMOS data. Otherwise, recent studies of red galaxies in random cosmological volumes (Bell et al., 2004; Drory et al., 2004; Fontana et al., 2004; McCarthy et al., 2004; Wiklind et al., 2008) inferred that red massive galaxies existed at all observational epochs, and that their stellar populations at each epoch were predominantly old. Mobasher et al. (2005) identified a candidate for a massive, evolved galaxy at $z = 6.5$. These convergent results on elliptical homogeneity strongly suggest that i), a population of massive, relaxed spheroids with old stellar populations (i.e., formed at a redshift of $z_f > 2.4$) was already at place by $z \sim 1.5$ or even by $z \sim 2$, ii) this population lacks of significant structural and dynamical evolution, and, iii), their average luminosity evolution is consistent with a passive evolution of their stellar populations.

Elliptical galaxies show age effects in their stellar populations, as inferred from the observed correlation of the $\alpha/<$Fe$>$ ratios with mass (Thomas et al., 2002; Caldwell et al., 2003; Bernardi et al., 2003d). More massive elliptical galaxies seem to have older

means and narrower spreads in the age distributions of their stellar populations than less massive ones (such effect is also known as the downsizing phenomenon, Thomas et al., 2005). This result have been confirmed from different results on the FP evolution, see for example (van der Wel et al., 2004; Treu et al., 2005; di Serego Alighieri et al., 2005; Faber et al., 2007) and from estimations of the star formation rate for ellipticals (Jimenez et al., 2005; Juneau et al., 2005; Thomas et al., 2005; Gallazzi et al., 2006; Clemens et al., 2009). These age effects link elliptical dynamical properties with the characteristics of their stellar populations, and are another manifestation of the physical regularities underlying elliptical galaxy populations.

These results on elliptical homogeneity and regularity can be easily interpreted in the context of a formation scenario where most elliptical mass assembles with dissipation out of gaseous material and their stellar populations form at high z on short timescales relative to spirals (i.e., the so-called *monolithic collapse scenario*). However, this scenario does not recover all the currently available observations on ellipticals either. Important examples are: i), the growth of the total stellar mass bound up in bright red galaxies by a factor of ~ 2 since $z = 1$ (Bell et al., 2004; Conselice et al., 2005; Fontana et al., 2004; Drory et al., 2004; Bundy et al., 2005; Faber et al., 2007), implying that the mass assembly of most ellipticals continued below $z = 1$, ii), the signatures of merging activity observed out to intermediate zs (Le Fèvre et al., 2000; Patton et al., 2002; Conselice, 2003; Cassata et al., 2005; Conselice et al., 2008), in particular of major dry mergers between spheroidal galaxies (van Dokkum et al., 1998; Bell et al., 2006), that translate into a relatively high merger rate for massive galaxies even below $z = 1$, iii), the need for a young stellar component in some elliptical galaxies (van Dokkum & Ellis, 2003; van der Wel et al., 2004; Schiavon et al., 2006), or, more particularly, the finding of blue cores (that is, recent star formation at the central regions), and inverse color gradients in a 30% - 40% of the spheroidal galaxies in some samples out to $z \sim 1.2$ (Abraham et al., 1999; Menanteau et al., 2001, 2004, 2005; Lee et al., 2006), and, iv), the observation by the Spitzer Space Telescope that an important fraction of massive galaxies are undergoing at $z \sim 0.7$ a period of star formation above their past-averaged star formation rate (Bell et al., 2005).

So, why we obtain this paradox? Before answering, we would like to address an important point: a solid definition for galaxy formation. Some misunderstandings have arisen because of defining galaxy formation with different concepts linked with just one physical process and using the results to reinforce or discard a model. For example, stellar age studies have been sometimes used to justify a monolithic collapse scenario, while merger rates measurements to discuss the hierarchical scenario. We will see that both physical processes can occur in a ΛCDM universe so although possible, it is very difficult to really discard one or other model with these analyses. Probably this problem has its origin on the facility for obtaining direct observational data of both

physical phenomena. But, in this sense it is necessary to make a more general study, trying to focus on measurements that really distinguish between models not only to check the frequency of one physical process. Of course the drawback of this approach is that this kind of measurements are harder to obtain from direct observations.

Anyway, defining galaxy formation will help us to look for a better observational approximation and to know the frame where we have to keep our results. A common proper definition is that one galaxy has "formed" when around half of this mass was already assembled (Peebles, 2002; Domínguez-Tenreiro et al., 2004). So, we saw that in ΛCDM model both processes, collapse and hierarchical merging *do occur* but the question would be which one of them, if any, is more important than the other and dictates the time of assembly. At high redshift, assembly with a passive evolution is postulated by a monolithic collapse scenario, while in hierarchical scenario major mergers put time for assembly to lower redshifts.

3.4 Summary

The observational results above demand spheroids with passively evolving stellar populations and, at the same time, assembling their stellar mass and undergoing some star formation below $z \sim 1$. The question then arises why elliptical galaxies had their star formation almost quenched at high z and when this happened relative to their mass assembly. The lack of structural and dynamical evolution at intermediate zs of ellipticals and the high formation redshift of most of their stars could result from the same physical processes involved in their formation, namely, the occurrence of dissipation mostly at high z, with further mass assembly at intermediate and lower zs mainly through non-dissipative processes.

One important clue for explaining how ellipticals were assembled is the very strong correlations between their photometric and spectroscopic parameters that, as we pointed out, make these galaxies a homogeneous population. Therefore, the first step in understanding how these galaxies formed should be to understand well these how correlations arise.

Part II

Simulations and Tools

Chapter 4

Analysis of the Simulations

4.1 Introduction

The very first step of our work, and of the most compelling ones, is to select and run the appropriate simulations in order to achieve our objectives. In what follows we will explain all the phases from the point of deciding which simulations to run and why, up to obtain robust samples of elliptical-like-objects. So, this chapter presents the roots of this thesis. We would discuss all the important steps that have to be done between these two points and stress up the relevance of the ones that can introduce significant errors in the final results.

This chapter is organized as follows: the next section, 4.2, describes and discuss what kind of simulations has been used in this thesis and why. Section 4.3 introduce the Galaxy-like objects that appear in our hydrodynamical simulations and the different techniques and problems to identify them. In section 4.4 is explained how Elliptical-like objects (ELOs) are selected and their two fundamental scales are defined. Section 4.5 goes into detail about the different tools and algorithms used to calculate the physical properties of ELOs. Finally section 4.6 summarizes the main ideas and results of this chapter.

4.2 Simulations runs under study

As explained in chapter 2, self-consistent hydrodynamical simulations have a great computational cost so it is very important to decide and program what kind of simulations will be needed before starting to run them. This is one of the most important steps when working with cosmological simulations. Having in mind the final goals of the project while designing it, is crucial for its final success or failure.

The aim of this thesis is to study in depth the structural and kinematical properties of early-type galaxies, so we want enough resolution to look inside these types of galaxies. On the other hand we would like to make some reliable statistics. Then we want a

significant sample of this kind of objects that extend in some orders of magnitude in mass. Ideally we would like to run a very large box simulation with a resolution of less than one kpc (i.e. with thousands of millions of particles), but sadly, this is not possible nowadays even in the best computational centers of the world. Fixing the number of particles of a simulation, something that is given by the computational resources available, you can choose between a large box simulation (loosing resolution) or a small box of great resolution simulation (loosing statistics). In the last years galaxy formation and evolution have been studied by n-body simulations using these two different approaches. For a more detailed explanation on this topic and the historical options in different astrophysical problems see 2.1.

Taking into account all these aspects and considering last works in this field, including previous runs with the `DEVA`code (see Sáiz et al., 2004; Domínguez-Tenreiro et al., 2004), we decide to go for another approach. We have built the main set of our sample by running five simulations (*EA* simulations) using 64^3 dark matter and 64^3 baryon particles, with a mass of 1.29×10^8 and $2.67\times10^7 M_\odot$, respectively, to homogeneously sample the density field in a periodic box of 10 Mpc side. In any run we use the framework of a flat ΛCDM cosmological model, with $\Omega_\Lambda = 0.65$, $\Omega_{\rm baryon} = 0.06$ and $h = 0.65$. These values are in 1σ of the cosmological concordance model values when simulations were run, see Spergel et al. (2003) and Tegmark et al. (2004) for details. Observational data in the last four years has changed very little the general framework of this concordance model, specially these parameters (Ω_Λ,$\Omega_{\rm baryon}$,h) but for a more precise knowledge of their exact values (see Spergel et al., 2007; Dunkley et al., 2009). We always used a fixed smoothing length in physical coordinates that in this case takes the value of $\epsilon = 0.0015$ ($h_{100}^{-1}Mpc$), so the maximum spatial resolution for all these simulations was 2.3 (h_{65}^{-1} kpc). Therefore with this size of box and number of particles we reach a resolution high enough to fulfill our objectives of studying the structure and kinematics of early-type galaxies. Furthermore to solve also the statistics issue, apart from running up to five simulations, we have tried to simulate the areas of the universe where ellipticals are more abundant. The power spectrum normalization, σ_8, has been set up to mimic an active region of the universe (Evrard, Silk, & Szalay, 1990) in which elliptical galaxies are more frequent. All these simulations also share the same star formation parameters ($\rho_{\rm thres} = 6\times10^{-25}$ gr cm^{-3}, $c_* = 0.3$) and differ in the seed used to build up the initial conditions.

As important as building the sample is studying the different systematics that we can have in our results. Consequently we have also run several simulations in order to check for the four more important ones: variations in the star formation parameters, variations in the cosmological model, resolution effects and box size. We will try to discuss their possible importance in all the different results of this thesis. For a general overview on how these and other systematics errors could affect the results on this thesis,

see section 6.5.

To test the role of SF parameterization, the same initial conditions have been run with different SF parameters ($\rho_{\rm thres} = 1.8 \times 10^{-24}$ gr cm^{-3}, $c_* = 0.1$) making SF more difficult, contributing another set of five simulations (hereafter, the *EB* simulations). We have also run a cosmological test simulation (*EC* simulation) with slight variations in the cosmological values but with the same star formation parameters as *EA*.

Concerning spatial resolution we run three simulations (*ED* simulations). First we made two simulations that share the same initial conditions, cosmological parameters and box size but differ in the number of particles. One of them uses the same amount of particles as all the previous runs (7705), 2×64^3 particles, and the other one uses eight times more particles (6705), this is 128^3 dark matter and 128^3 baryon particles, with a mass resolution of 1.67×10^7 and $2.58 \times 10^6 {\rm M}_\odot$, respectively. The smoothing length used in the low resolution simulation was $\epsilon = 0.0015$ ($h_{100}^{-1} Mpc$) and in the high resolution simulation was $\epsilon = 0.00075$ ($h_{100}^{-1} Mpc$), hence having a spatial resolution of 2.14 (h_{70}^{-1} kpc) and 1.07 (h_{70}^{-1} kpc) respectively. We have also run one simulation (7714) that share all cosmology and SF parameters with *EA* simulations but with eight times more particles, in order to have results that can be directly compared with the *EA* sample.

We are also interested in testing the effect of increasing the box size, $L_{\rm box}$ of the simulation. It is a well established fact (see, for example, Bagla, 2005) that L_{box} affects the two-point correlation function and the mass function (and, consequently, the global tidal field is also changed), because reducing L_{box} is equivalent to putting a large-scale cut-off to the power spectrum of perturbations.

An important point to note is that L_{box} has an impact on the $R_\sigma = \sigma_{8in}/\sigma_{8eff}$ ratio, where σ_{8in} is the input normalization parameter in the algorithm used to build-up the initial conditions of the simulation, and σ_{8eff} is the linear mass variance in spheres of radius $8h^{-1}$ Mpc at $z = 0$. In fact σ_{8eff} decreases with decreasing L_{box} (see discussion in Sirko, 2005), so that R_σ increases (Power & Knebe, 2006; Gelb & Bertschinger, 1994). These differences can already be appreciated in the initial conditions as numerically set by any standard algorithm. We have found that kept σ_{8in} and changing L_{box}, the normalized distribution of initial peculiar velocities changes and convergence is only attained for $L_{box} > 100$ Mpc. Note that this effect can be compensated for by tuning σ_{8in} (see below).

As a consequence of the power spectrum cut-off, when L_{box} decreases there is a deficit of massive objects, and the clustering length decreases, so that simulations with large L_{box} (> 100 Mpc) are required in order to correctly get convergence on the results for the two-point correlation, σ_{8eff} and mass functions.

However, this does not imply that the modification of these global properties of the large scale structure has necessarily an impact on the inner properties of the small scale

systems (galaxies and their halos). This problem has been addressed in detail for dark matter halos by Power & Knebe (2006). They have established that the box size of the simulations has an impact on i) σ_{8eff}, ii) the masses of the most massive halos. Both are reduced as the box size decreases, confirming previous findings. That is, lowering L_{box} implies a reduction of the number of massive systems, that are formed in the more active environments. Consequently, lower L_{box} also implies a deficit of massive environments (groups and clusters of galaxies) relative to larger L_{box} simulations.

These authors also found that these modifications have relatively little effect on the internal properties of the halos (concentration, spin parameter, triaxiality, see Figures 6 to 11 of Power & Knebe, 2006). There is only a small effect on the spin parameter, independent of halo mass and L_{box} size. This is small: they found that the halo spin parameter is on average only a 15 percent lower.

These authors interpret their results about shape invariance on the L_{box} size (or power spectrum truncation) in the light of the existence of a universal dark matter mass profile (Navarro et al., 1996; Manrique et al., 2003, see the two last sections of their paper). The small effects noted in the spin distribution are interpreted as an imprint of the angular momentum acquired during the linear growth of the perturbations (Navarro et al., 2004a). An important point to note is that in their work, Power & Knebe (2006) use the same input σ_{8in} irrespective the power spectrum cut-off.

Our work has to do with virtual elliptical galaxies, stellar systems placed inside massive dark matter halos. To our best knowledge, there does not exist by the moment a study on how L_{box} affects the shape and rotation properties of these objects. However, because their mass assembly process reflects that of dark matter halos (see Chapter 9), we cannot expect that the impact of decreasing L_{box} is that important.

Therefore, to test this point we run two simulations in a periodic box of 20 Mpc side (twice that of EA and EB runs) and using 8 times more particles ($EF1$ and $EF2$ runs) fixing the cosmological and star formation parameters as in EA simulations.

We have also used one simulation with a periodic box of 80 Mpc side ($EF3$). Cosmological parameters were set using last observational results[1] (Dunkley et al., 2009). However due to computational costs this simulation only include hydrodynamical calculation in a sub-box of 27 Mpc side. The number of dark matter and baryonic particles in this volume is fixed to obtain the same resolution as for the other EF simulations. Moreover, in order to do a proper comparison, we will study just a sub-box of 20 Mpc side of this simulation. It is important to remark that this simulation is the first result of a major ongoing project in which the full box of 80 Mpc side, including the hydrodynamical calculation, is also being simulated. However, as this simulation takes too long to reach redshift zero and also in order to have some test samples, we are running a total of nine simulations as the $EF3$ one and five simulations with an hydrodynamical

[1] http://lambda.gsfc.nasa.gov/product/map/current/params/lcdm_sz_lens_run_wmap5_bao_snall_lyapost.cfm

sub-box of 40 Mpc side. These simulations cover different subvolumes of the bigger box and by the time of closing this thesis, only $EF3$ has reached redshift zero.

Due to the effect of L_{box} on R_σ (see above), one has to be careful when analyzing the effects of varying L_{box}, and try to disentangle as much as possible the effects due to the changes of the effective normalization (that can be overcome to some extent by tuning σ_{8in} relative to L_{box}), to the changes induced by the presence of longer wave perturbations as L_{box} increases.

The values of the parameters used in each simulation defining the global cosmological models, star formation parameterization, box side, etc. are given in Table 4.1.

Initial conditions are set at high z as a Monte Carlo realization of the field of primordial fluctuations in a given cosmological model. For all these simulations they were performed using the same scheme used by Couchman et al. (1995) which follows the basic ideas explained in Section 2.2. Concretely, we have used *MPGRAFIC* (Prunet et al., 2008) to create the initial conditions of the $EF3$ run and *INITDEVA* (Bertschinger, 1995) for the rest of simulations. All the simulations with $L_{\rm box} = 10Mpc$ started at $z = 0$ and were run up to $z = 0$ using the sequential version of `DEVA`, but for the ED sample simulations which were performed using the parallelized version `P-DEVA`. ED, $EF1$ and $EF2$ simulations run in an Altix 3700 machine of the Centro de Computación Científica (UAM, Spain)[2] up to $z = 0$ using `P-DEVA`. $EF3$ also used `P-DEVA` code but run in the Leibniz Supercomputing Centre[3]. The initial redshift for the EF simulations was calculated using *GRAFIC2* (Bertschinger, 2001). They started before any mode simulated become non-linear ($z = 33$ for the $EF1$-2 runs and $z = 50$ for the $EF3$ run respectively).

All the important information of the simulation is saved at different redshifts in a file. This file contains a header with all the global parameters concerning the simulation followed by the positions, velocities, mass, etc. for each particle. We have saved around 40 timesteps for each simulation in our sample at redshifts in which we were interested. For the simulation 8716 (EB) we have saved around 2000 timesteps to have a high temporal resolution simulation. This will allow us to perform detailed temporal studies and videos. In Figure 4.1 it is shown all the gas particles of one of the EA simulations when it has reached redshift $z = 0$.

[2]See http://www.uam.es/investigacion/servicios/computacion/ for more details.
[3]http://www.lrz-muenchen.de/wir/intro/en/

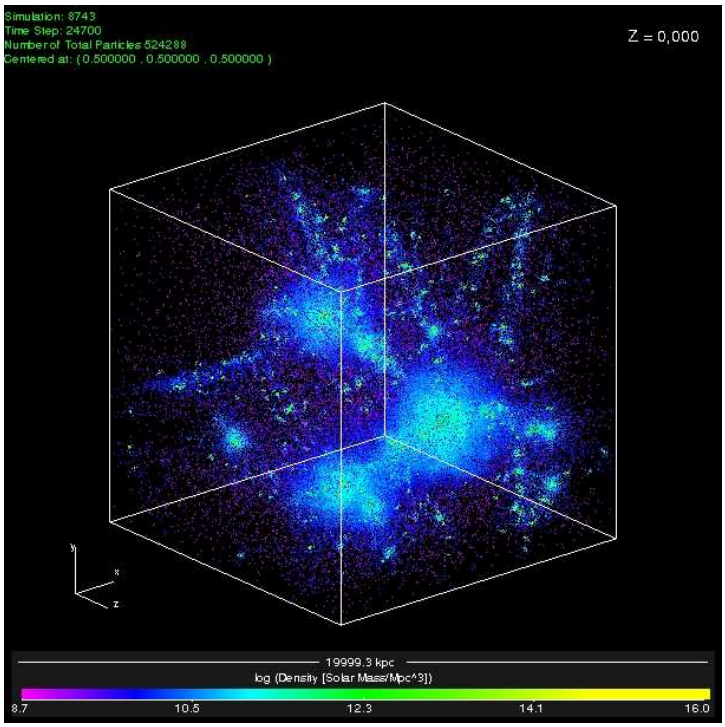

Figure 4.1: View of all the gas particles of one of the *EA* simulations at $z = 0$. Color of the gas particles stands for their SPH density.

Simulation (1)	I.C. (2)	h (3)	Ω_m (4)	Ω_b (5)	Ω_Λ (6)	σ_8 (7)	ρ_{thres} (8)	c_* (9)	$N_{DM}+N_{bar}$ (10)	$L_{\rm box}$ (11)	ϵ (12)	$z_{\rm initial}$ (13)	CODE (14)
EA													
S8714	#1	0.65	0.35	0.06	0.65	1.18	6×10^{-25}	0.3	64^3+64^3	10	0.0015	20	DEVA
S8747	#2	0.65	0.35	0.06	0.65	1.18	6×10^{-25}	0.3	64^3+64^3	10	0.0015	20	DEVA
S8741	#3	0.65	0.35	0.06	0.65	1.18	6×10^{-25}	0.3	64^3+64^3	10	0.0015	20	DEVA
S8742	#4	0.65	0.35	0.06	0.65	1.18	6×10^{-25}	0.3	64^3+64^3	10	0.0015	20	DEVA
S8743	#5	0.65	0.35	0.06	0.65	1.18	6×10^{-25}	0.3	64^3+64^3	10	0.0015	20	DEVA
EB													
S8716	#1	0.65	0.35	0.06	0.65	1.18	1.8×10^{-24}	0.1	64^3+64^3	10	0.0015	20	DEVA
S8717	#2	0.65	0.35	0.06	0.65	1.18	1.8×10^{-24}	0.1	64^3+64^3	10	0.0015	20	DEVA
S8721	#3	0.65	0.35	0.06	0.65	1.18	1.8×10^{-24}	0.1	64^3+64^3	10	0.0015	20	DEVA
S8722	#4	0.65	0.35	0.06	0.65	1.18	1.8×10^{-24}	0.1	64^3+64^3	10	0.0015	20	DEVA
S8723	#5	0.65	0.35	0.06	0.65	1.18	1.8×10^{-24}	0.1	64^3+64^3	10	0.0015	20	DEVA
EC													
S5714	#1	0.72	0.27	0.046	0.73	1.18	6×10^{-25}	0.3	64^3+64^3	10	0.0015		DEVA
ED													
S7705	#6	0.70	0.30	0.04	0.70	1.00	6×10^{-25}	0.3	64^3+64^3	10	0.0015	20	P-DEVA
S6705	#6	0.70	0.30	0.04	0.70	1.00	1×10^{-24}	0.3	128^3+128^3	10	0.00075	20	P-DEVA
S7714	#7	0.65	0.35	0.06	0.65	1.18	6×10^{-25}	0.3	128^3+128^3	10	0.00075	20	P-DEVA
EF													
S8935 (*EF*1)	#8	0.65	0.35	0.06	0.65	0.95	6×10^{-25}	0.3	128^3+128^3	20	0.002	33	P-DEVA
S8914 (*EF*2)	#9	0.65	0.35	0.06	0.65	0.7463	6×10^{-25}	0.3	128^3+128^3	20	0.0015	33	P-DEVA
S2100 (*EF*3)	#11	0.694	0.295	0.0476	0.705	0.852	4.8×10^{-25}	0.3	see text	80	0.0015	50	P-DEVA

Table 4.1: Parameters of the simulations. (1): Simulation run; (2): Initial Condition number; (3): $H_0/100\,km\,s^{-1}$; (4): Matter density; (5): Baryon density; (6): Cosmological constant energy density; (7): Power spectrum normalization; (8): Density threshold; (9): Star formation efficiency; (10) Number of dark matter and baryonic particles; (11) Box side ($h_{100}^{-1}\times Mpc$); (12) Smoothing length ($h^{-1}Mpc$); (13) Initial redshift; (14) Code used.

4.3 Galaxy-like objects in the simulations

SPH simulations with CDM initial conditions and radiative cooling lead to the formation of dense groups of baryonic particles that have sizes and masses comparable to the luminous regions of observed galaxies (Cen, 1992; Katz et al., 1992; Evrard et al., 1994). If star formation is included, these dense groups are the regions where stars form and tend to group in Galaxy-like objects (hereafter GLOs, Katz et al., 1996; Domínguez-Tenreiro et al., 2003, for DEVA code). The structure and kinematical properties of these objects and their formation and evolution are the main topic of this thesis, so the identification of distinct particle groups at different redshifts underlies all of our subsequent analysis.

Many different algorithms to identify groups of particles in N-Body simulations have been proposed. We want to address here the question of how the choice of an algorithm can affect the properties of GLOs. To do this, we have used two of the most popular algorithms: FOF (friends-of-friends Huchra & Geller, 1982; Davis et al., 1985) and SKID (Stadel et al., 1997; Weinberg et al., 1997). With FOF, particles are joined into groups if the separation to the nearest neighbor is less than a given threshold, called the linking length, b, which is the only free parameter for this algorithm. We will express b in units of the mean particle separation. The mean particle separation between N^3 baryon particles uniformly distributed in a simple cubic lattice over a cube box of size L, is L/N. Then, $1/b^3$ corresponds to an overdensity, and FOF approximately groups together particles which lie inside the corresponding level surfaces. On the other hand, SKID is a multiple-step process. The basic algorithm consists of, first determining the smoothed density field, then moving particles upward along the gradient of this density field using a heuristic equation of motion that forces them to collect at local density maxima. Afterwards, it defines the approximate group to be the set of particles identified with a FOF algorithm with a linking length, b, and finally, particles that are not gravitationally bound to the groups identified in the previous step are removed. So, SKID has more than one free parameter, being the most important ones: the linking length, b, the number of nearest neighbors used in calculating the density gradients, N_{neigh}^{SKID}, and just for gas particles, a minimum density threshold, ρ_{min}^{SKID}, and a maximum temperature threshold, T_{max}^{SKID}.

To make our study, we have first looked at one of the simplest quantity that characterizes the galaxy populations in the simulations: the mass function. Although, as pointed above, our aim is not to make a study of all the galaxies that appear in our simulations, examining this characteristic can show a first idea of the numerical factors that come into play in the identification of galaxies in cosmological simulations. Also, this kind of analysis has been used before to compare group identification algorithms in the context of dark matter halos finding (Bertschinger & Gelb, 1991; Goetz et al., 1998). Following the work of these last authors, we have run several times the FOF

and SKID algorithms over the same simulation varying their free parameters (see Table 4.2). We have chosen *ED* simulations because it will also allow us to control for possible resolution effects. First of all we have run FOF algorithm using $b = 0.1$ (run I), $b = 0.2$ (run II), $b = 0.25$ (run III) and $b = 0.02$ (run IV), in units of the mean particle separation. The three first values cover the range used in the literature. The last one is a test run to see what happens if the linking length is decreased up to a few percent of the mean particle separation. In the *ED* simulation of 64^3 baryonic particles and 10 $h_{70}^{-1}Mpc$ box, the mean particle separation is 156.25 ($h_{70}^{-1}kpc$). The tests with SKID were done in the following way: first we study the two more important parameters of this algorithm, b and N_{neigh}^{SKID} (runs V, VI, VII, VIII, IX, X, XIII) and after we study the effects of the density and temperature limits for gas particles, ρ_{min}^{SKID} and T_{max}^{SKID} (runs XI, XII and XIV). All the runs were done using eight particles as the lower limit of a group. The same tests have been also done with the *ED* high resolution simulation (for which the mean particle separation is 78.13 ($h_{70}^{-1}kpc$)). First we present results for the 2×64^3 particles *ED* simulation. Afterwards it will be discussed the high resolution results.

Run	Algorithm	b	N_{neigh}^{skid}	ρ_{min}^{skid}	T_{max}^{skid}
(1)	(2)	(3)	(4)	(5)	(6)
I	FOF	0.1	–	–	–
II	FOF	0.2	–	–	–
III	FOF	0.25	–	–	–
IV	FOF	0.02	–	–	–
V	SKID	0.1	60	0	1×10^{30} K
VI	SKID	0.1	40	0	1×10^{30} K
VII	SKID	0.1	20	0	1×10^{30} K
VIII	SKID	0.2	40	0	1×10^{30} K
IX	SKID	0.2	20	0	1×10^{30} K
X	SKID	0.25	40	0	1×10^{30} K
XI	SKID	0.1	40	0	3×10^4 K
XII	SKID	0.1	40	$10^3\Omega_b\rho_{crit}$	3×10^4 K
XIII	SKID	0.02	40	0	1×10^{30} K
XIV	SKID	0.02	40	$10^3\Omega_b\rho_{crit}$	3×10^4 K

Table 4.2: Parameters for the different test runs of the group finding algorithms.

Results for FOF tests can be seen in Figure 4.2(a). The mass function obtained with FOF does not depend upon the typical values of b, these are 0.1, 0.2 and 0.25. Even with a lower value of b, as 0.02, we found no significant variations in the mass function. Concerning the SKID tests we found that, as well as in the FOF tests, variations of the linking length parameter do not produce significant changes in the mass function as long as all the other free parameters are keep constant. However we found a strong dependence of the mass function upon the resolution at which the density gradients

are calculated, that is, the number of nearest neighbors used by the SKID algorithm, N_{neigh}^{SKID}. A low resolution of the density field (large number of neighbors) produces preferably large halos, since, there are few density maxima present inside the volume towards which all the particles are moved. Each of the density maxima will then end up with a large number of particles, and hence larger groups are formed. On the other hand, with high resolution of the density field (small number of neighbors), it becomes bumpy, and, except for the densest regions, each particle will correspond to a density maximum at its location. In this case the SKID algorithm become close to plain FOF, specially in the more massive part of the mass function but this bumpy effect make that the number of low mass halos increases. In Figures 4.2(b) and 4.2(c) we show the relevant results of the SKID tests. We also found that the temperature and density threshold can play a key role in the final mass function. Both quantities, specially the temperature, seem to diminish the amount of low mass groups, indicating that there were some of these groups that were formed by high temperature and low density particles. As pointed above this problem is due the way SKID calculates the maximum density points, so it is important to try to minimize its effects by using these two limits.

Similar conclusions are also observed by Goetz et al. (1998) in their tests of these algorithms in the context of dark matter halos finding and the reconstruction of the dark matter halo mass function. The main difference is that the dependence of the mass function with the linking length parameter is much more important in the context of dark matter halos. This is because dissipation greatly increases the density of cooled baryons with respect to the local background. However is important to remark that even in this situation, we have seen that the mass function depends on the group finding algorithm and, especially for SKID, in the parameters used.

Once we have studied the mass function obtained from the different algorithms, we have calculated the center of mass of all the GLOs found in the simulations. Focusing on the forty more massive GLOs, we have observed that the order of them varies a little depending on each run and that some of them disappear in high linking length tests because they are linked to a close bigger GLO. However the center of mass obtained in general agrees between different tests. Considering that this work is primary interested in the most massive GLOs of the simulations, we have decided to go one step further and make a more detailed comparison between the masses of the GLOs obtained by different algorithms. In order to have a proper mass estimation to compare with, we have calculated one by one, the real baryonic mass of the fifteen more massive GLOs of the simulation that are found in all the tests (see next Section, 4.4, for more details on this calculation for GLOs). Figure 4.3 shows the normalized difference between the mass given by one of the different algorithm tests, M_{alg}, and the mass calculated *manually* object by object, M_{man}, versus M_{man}. The results are really interesting. The masses obtained by the algorithms can differ by more than a 100% in the most massive objects

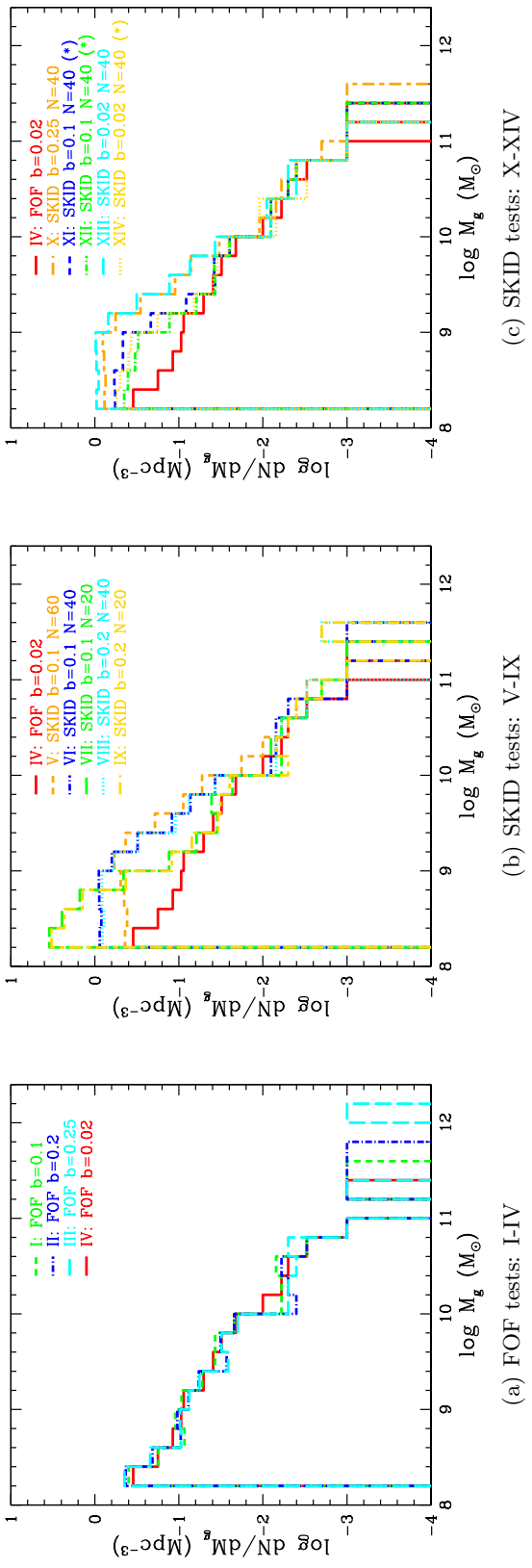

(a) FOF tests: I-IV

(b) SKID tests: V-IX

(c) SKID tests: X-XIV

Figure 4.2: Mass functions obtained from different runs of group finding algorithms over the same simulation changing their free parameters. SKID runs marked by (*) used the parameters T_{max}^{SKID} and/or ρ_{max}^{SKID}. See text and Table 4.2 for more details on the parameters used on each run.

and are in general quite far from the real values. The origin of this systematic in the estimation of mass is due to the presence of satellites. These satellites are close enough to be not separated from the main object by the algorithms if b is too big. Although with errors between 1% and 20% (or even 60% in one extreme case), the best results are obtained by test IV and test XIV, the tests of lower linking length values used for both algorithms.

We have confirmed that the most basic property of a GLO, as its mass, depends upon the choice of group finding algorithm and its free parameters. Also we cannot talk about a better group finding algorithm but about a good selection of the free parameters. In this framework, we want to notice that analyzing just the mass function can induce to wrong conclusions about the goodness of the group finding algorithms. For example, the linking length parameter plays an important role in the final mass of the galaxy-like objects but this role is not appreciated when the mass function is built. Some direct measurements, as the mass or the velocity dispersion (Murante et al., 2007), should be done before arising to any conclusion.

In regard to the high resolution tests we show main results in Figure 4.4. First, FOF tests give identical mass functions irrespective of the resolution of the simulation. SKID results are more complex. The dependence of the mass function with b and N_{neigh}^{SKID} shows exactly the same trends that we had found before. The density and temperature thresholds also produce same effects. In other words, high resolution mass functions are exactly the same as the ones presented in Figure 4.2 but rescaled to a higher resolution. However, there are some interesting facts that deserve to be mentioned. The number of neighbors used by the SKID algorithm should be also rescaled depending of the resolution of the simulation.

We want to stress out the importance of these results in the context of some recent works that use the mass obtained by these algorithms to study the evolution, merger history or gas accretion history of galaxy-like objects (see, for example Murali et al., 2002). Taking into account that in this kind of studies it is impossible to do a one-by-one object analysis, it is important to try to take into account the possible errors that may came from the use of these algorithms. The best approximation should be to make the same study using different parameters of the group finding algorithms to find out the systematics in the final results.

However, from our analysis we have reached some general conclusions. In the case of just using the FOF algorithm, we have found that it is better to make the runs with a low linking length value, between 0.02 and 0.05. Mass function is not significantly affected by this quantity and the best mass estimations are obtained with low values of b. Just for the same reasons, we have also found that for SKID the use of low values of b are preferable too. Concerning, N_{neigh}^{SKID}, the best option is the one suggested by Murante et al. (2007). Run SKID using three different values of N_{neigh}^{SKID} (20, 40

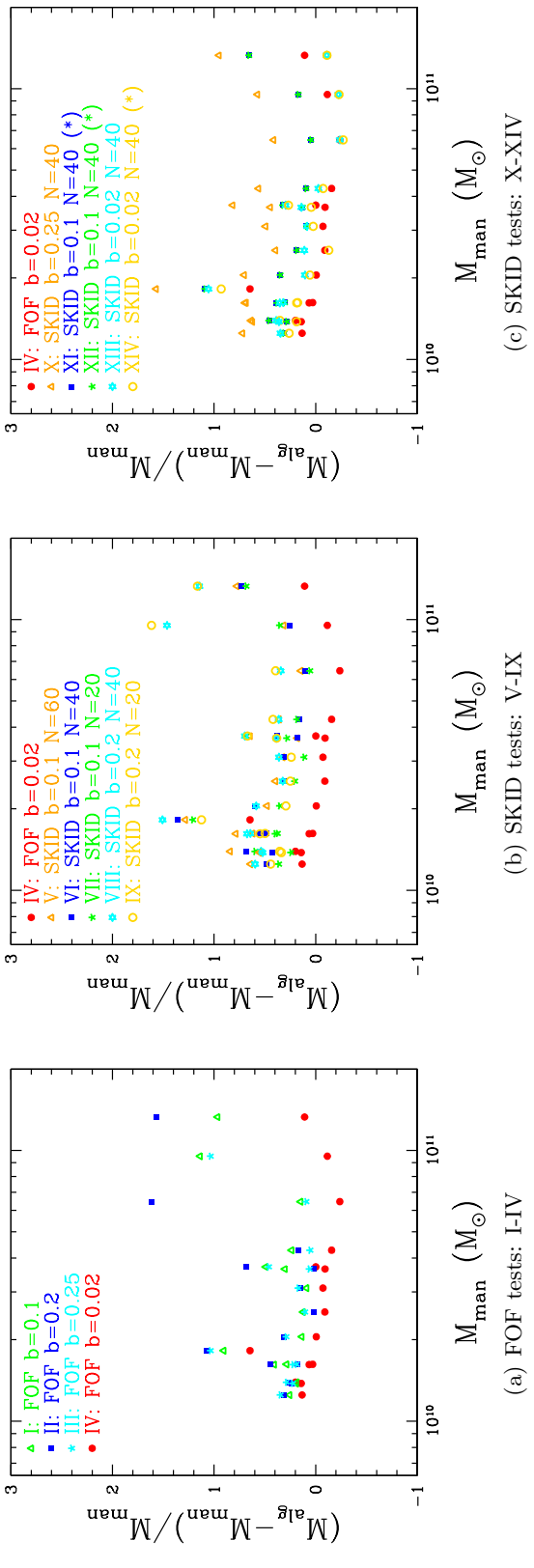

(a) FOF tests: I-IV

(b) SKID tests: V-IX

(c) SKID tests: X-XIV

Figure 4.3: Direct mass estimations obtained from different runs of group finding algorithms over the same simulation changing their free parameters. SKID runs marked by (*) use the parameters T_{max}^{SKID} and/or ρ_{max}^{SKID}. See text and Table 4.2 for more details on the parameters used on each run.

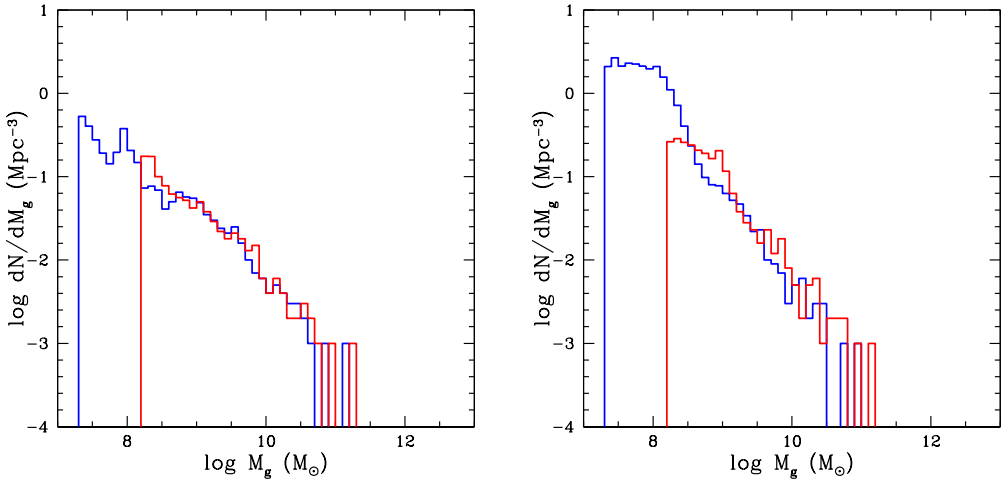

Figure 4.4: Mass function profiles obtained in test IV (left) and test XIV (right) from the *EC* simulations. Red line stands for 2×64^3 particles simulation and blue line for the 2×128^3 simulation.

and 60 for example) and define a galaxy to be the set of particles which belong to a SKID group with anyone of the above N_{neigh}^{SKID} values. We also think that using the temperature and density thresholds for gas particles is a must, in order to control the high increase of low mass GLO of high temperature and low density particles that this method produces. This will be especially important as we go to higher redshifts where gas is more abundant and can enclose or be adjacent of different clumps of star particles. Therefore, we encourage using just star particles for GLOs identification at these high redshifts (see Murante et al., 2007, for similar conclusions).

Finally, all these tests and investigations with the group finding algorithms convinced us to use them just as a tool to obtain the mass centers of the GLOs in our simulations. We have decided to do a one-by-one analysis of our objects in order to determine their mass and all their fundamental parameters. Even to optimize calculations of the coordinates centers of GLOs obtained from the algorithms a *sigma-clipping* algorithm was used. This type of algorithm minimizes the phase-space of a group of particles and helps to obtain better values of the mass center especially in very close systems that are dynamically linked.

4.4 Building Elliptical-Like-Objects (ELO) Samples

GLOs that appear in DEVA simulation span a range of morphologies: disk-like objects (DLOs), spheroid or elliptical objects (ELOs) and irregular objects. See Figures 4.5, 4.6 and 4.7 for some visual examples.

We are interested in building a large sample of elliptical-like objects (hereafter ELOs)

at different redshifts: $z = 0$, $z = 0.5$, $z = 1$ and $z = 1.5$ redshifts. Obviously we have studied $z = 0$ to compare our data with nearby elliptical galaxy observations. We built our higher redshift samples to study the evolution of this type of galaxies. Our choice for higher redshift values is also related with the available observations for ellipticals. ELOs have been identified as those galaxy-like objects having a prominent, dynamically relaxed spheroidal component made out of stars, with no extended discs and very low gas content. For this purpose we combined several techniques.

A *visual* approach allow us to eliminate galaxy-objects suffering major mergers or with prominent disks. Some examples of this approach can be seen in (4.5) (4.6) and (4.7). At the same time we used a combination of statistical and numerical techniques. We built for each GLO a mass versus radius profile for all mass components: hot gas, cold gas, stars, baryons, dark matter and total. Masses were obtained by calculating the mass contained in spheres of increasing radius. First one can address for the presence of large amounts of gas. Also we can look for satellites and any presence of an ongoing merger. In this sense we put the limit for major merger definition when the quotient between baryon masses of the satellite and the main object was greater than 0.25 (Gottlöber et al., 2001; Solanes et al., 2005). Related with interacting signals, we have looked for:

- The presence of tidal tails, loops, and shells, which are induced by strong gravitational interaction.
- A single nucleus, which, based on numerical studies, marks the completion of the merger. This criterion is important because it marks the point at which the merger should begin to exhibit properties in common with elliptical galaxies.
- The absence of nearby companions that may induce the presence of tidal tails and make the object appear to be in a more advanced stage of merging.

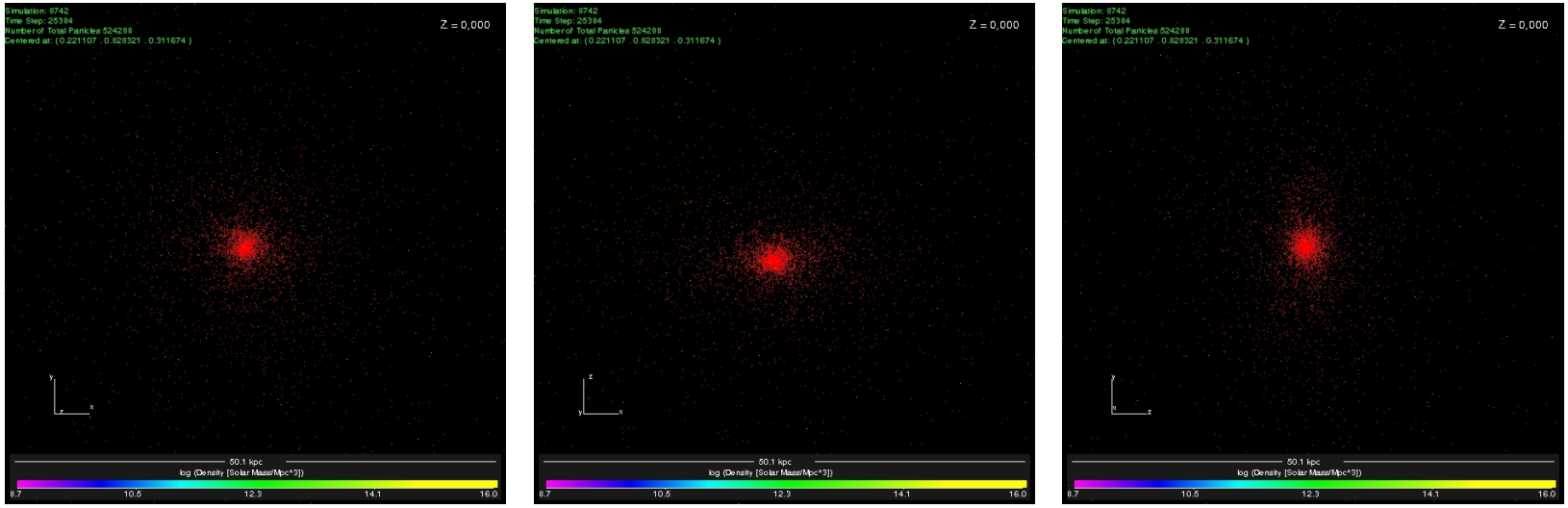

Figure 4.5: Three orthogonal projection of the stellar and gas components of an Elliptical-like object.

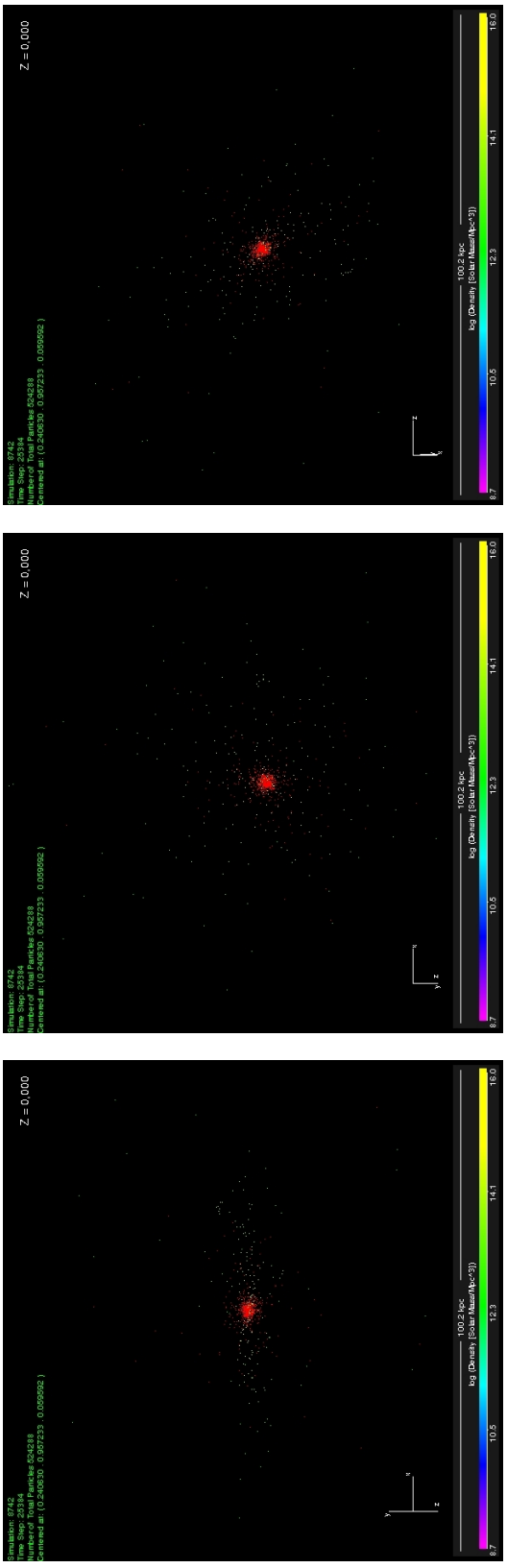

Figure 4.6: Three orthogonal projection of the stellar and gas components of a Disk-like Object.

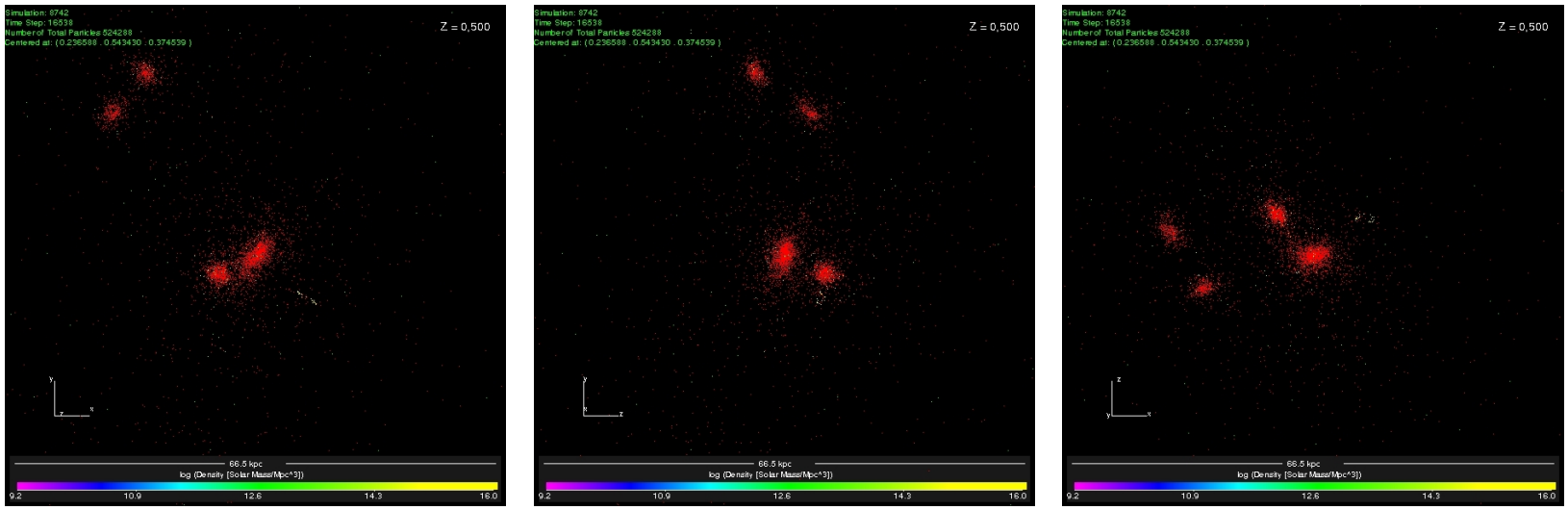

Figure 4.7: Three orthogonal projection of the stellar and gas components of an irregular object.

4.4.1 The halo and stellar scales of an ELO

Following the identification of an ELO, to characterize its structural and dynamical properties, two scales have been defined on it: the halo scale, and the stellar scale. Note that along this work we have used superscripts to mean the different ELO constituents (total, dark, stars, etc), and subscripts to distinguish between halo (h) or baryonic object (bo) scales.

The virial halo scale This scale describes the ELO size at the scale of its dark matter halo. It is usually defined in terms of a characteristic overdensity, Δ_c. The value of Δ_c is taken from the solution of a spherical top-hat perturbation under the assumption that it has just virialized and the model of spherical collapse (Padmanabhan, 1993; Peebles, 1980). The exact calculation of its value is not trivial because it has a dependence on cosmology. In this work we have used the solution from Bryan & Norman (1998) for a flat universe:

$$\Delta_c(z) = 18\pi^2 + 82x(z) - 39x(z)^2 \tag{4.1}$$

where,

$$x(z) = \frac{\Omega_m(1+z)^3}{\Omega_m(1+z)^3 + \Omega_\Lambda} - 1 \tag{4.2}$$

We define the virial radius, $r_{\rm vir}$, as the radius of a spherical volume within which the mean density is Δ_c times the critical density at that redshift. The total mass inside $r_{\rm vir}$ is the virial mass $M_{\rm vir}$. Therefore we obtain very solid characteristic length and mass parameters at the halo scale.

We will say that the halo scale is *well defined* for the simulated elliptical as long as the total and dark matter halo profiles do not have several irregularities due to on-going mergers up to $r_{\rm vir}$ or satellite infall. In Figure 4.8 several clear examples of well and ill defined ELOs are shown.

The stellar or galaxy scale This scale is defined by the stellar mass of the ELO, $M_{\rm bo}^{\rm star}$ which was calculated using spherical mass profiles. We calculate the stellar mass inside spheres of different radius, from zero to at least $r_{\rm vir}$. For each sphere we sum all stellar masses inside it. In these profiles we see a very characteristic pattern, a fast grow from lower to higher radius up to a point where the curve seems to flatten out (see Figures 4.9). We define the radius of the baryonic object, $r_{\rm bo}$, as the distance from the center of the object to some point of this flat part of the curve. The mass inside the sphere of radius $r_{\rm bo}$ is $M_{\rm bo}^{\rm star}$. We will say that this scale is well defined as long as the ELO is not suffering a major merger. This is, the stellar mass profile flattens out before we found any other GLO that satisfies the major merger criterion defined upwards. We also need that we can define the characteristic radius without including any possible satellite that will affect the analysis. Finally we define a more solid length scale estimator, the effective stellar radius, $r_{\rm e,bo}^{\rm star}$, as the radius enclosing half of the stellar

mass, $M_{\rm bo}^{\rm star}$. This scale estimator is used to make a final filter in the ELO samples. To avoid the lack of resolution in the internal properties of ELO samples, we selected just objects that have a $r_{\rm e,bo}^{\rm star}$ equal or greater than the resolution of the simulation. We have also defined a more solid total length scale estimator $r_{\rm 90,bo}^{\rm star}$ characterized as those radii enclosing 90% of the $M_{\rm bo}^{\rm star}$ mass.

The masses used to compare different group finding algorithms in Section, 4.3, called M_{man}, was calculated following this method for each object but taking into account all the baryonic particles (filtered by the gas temperature and density threshold if necessary).

From the analysis of these two scales we have build all ELO samples at different redshift that will be studied in the following chapters. We have decided to build two different samples types. The *stellar* ELO sample type (also defined as -STAR sample), include all ELOs that are well defined at the stellar scale. ELOs in these samples can be embedded in a dark matter halo that it is not relaxed, making the halo properties ill-defined. This happens because the halo is suffering a merger at this scale. In these cases there can be some other significant stellar objects around the main ELO below the virial radius. The *stellar & halo* ELO sample type, include all ELOs that are well defined at the stellar and at the halo scale. This subsample will be important in order to study the link between halo and stellar fundamental parameters. The final total number of ELOs found in each simulation sample is given in Table 4.3. Note that due to their respective SF implementations, galaxy-like objects formed in *EA* type simulations tend to be of earlier type than their counterparts formed in *EB* type simulations. Moreover, gas has had more time to lose energy along *EB* type ELO assembly than in their *EA* type counterparts, and, consequently, the former have smaller sizes than the latter (see discussion in Section 6.2).

Simulations	Scale	Number of ELOs			
		$z = 0$	$z = 0.5$	$z = 1$	$z = 1.5$
EA-STAR	Stellar	56	56	57	56
EA	Stellar & Halo	26	19	21	16
EB-STAR	Stellar	26	25	23	24
EB	Stellar & Halo	17	14	16	16
EC	Stellar & Halo	6	7	7	5
ED (7705)	Stellar	7	–	–	–
ED (6705)	Stellar	7	–	–	–
ED (7714)	Stellar&Halo	4	–	–	–
*EF*1-STAR (8935)	Stellar	31	25	22	18
*EF*1 (8935)	Stellar & Halo	21	–	–	–
*EF*2-STAR (8914)	Stellar	38	26	18	20
*EF*3-STAR (2100)	Stellar	22	–	14	–
*EF*3 (2100)	Stellar & Halo	11	–	8	–

Table 4.3: The number of ELOs found in the simulations for the different redshifts analyzed. For each sample, we indicate the number of ELOs well defined at the stellar scale (-STAR) and the number of these objects that are **also** well defined at the halo scale.

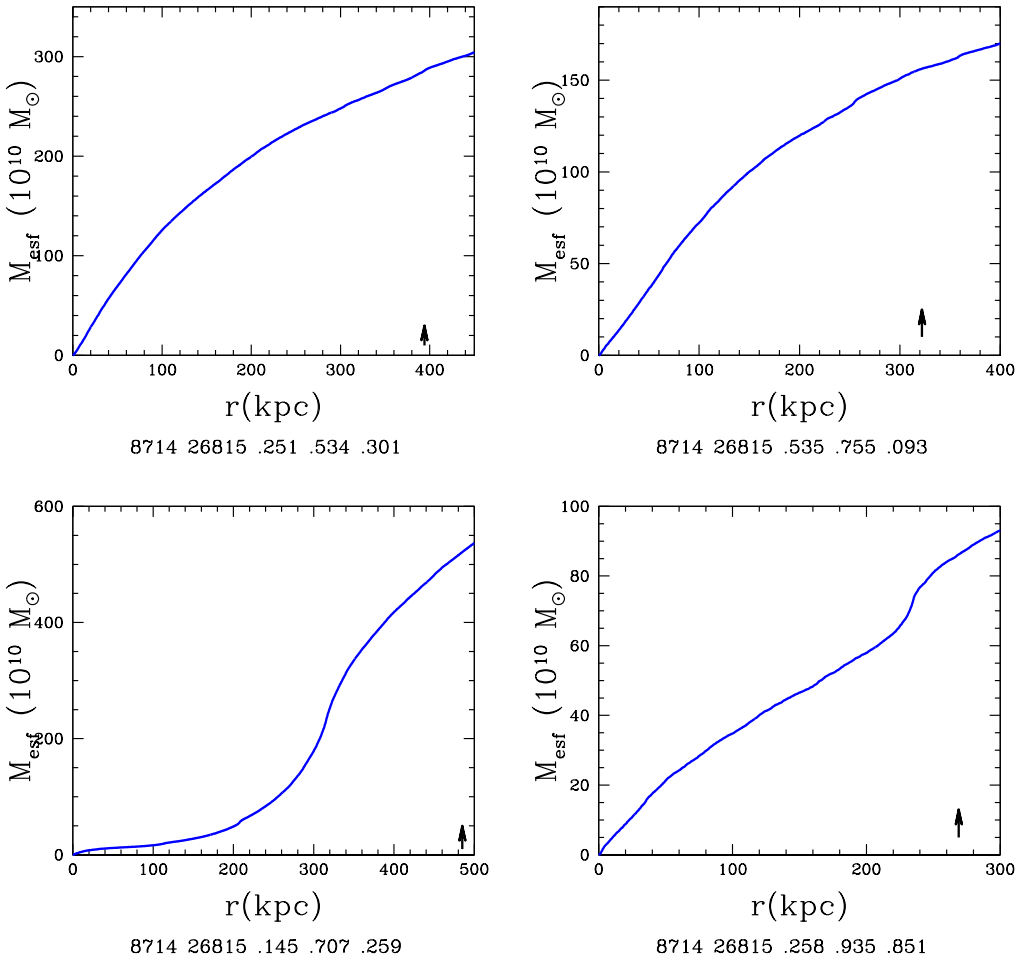

Figure 4.8: Four examples of total mass profiles. Arrows stand for the $r_{\rm vir}$ obtained by the Bryan & Norman (1998) algorithm (see text for details). In the top, two examples of *well defined* ELOs at the halo scale. Bottom Figures show two examples of ELOs that are not well defined at the halo scale. They are not isolated, making the virial parameters ill defined.

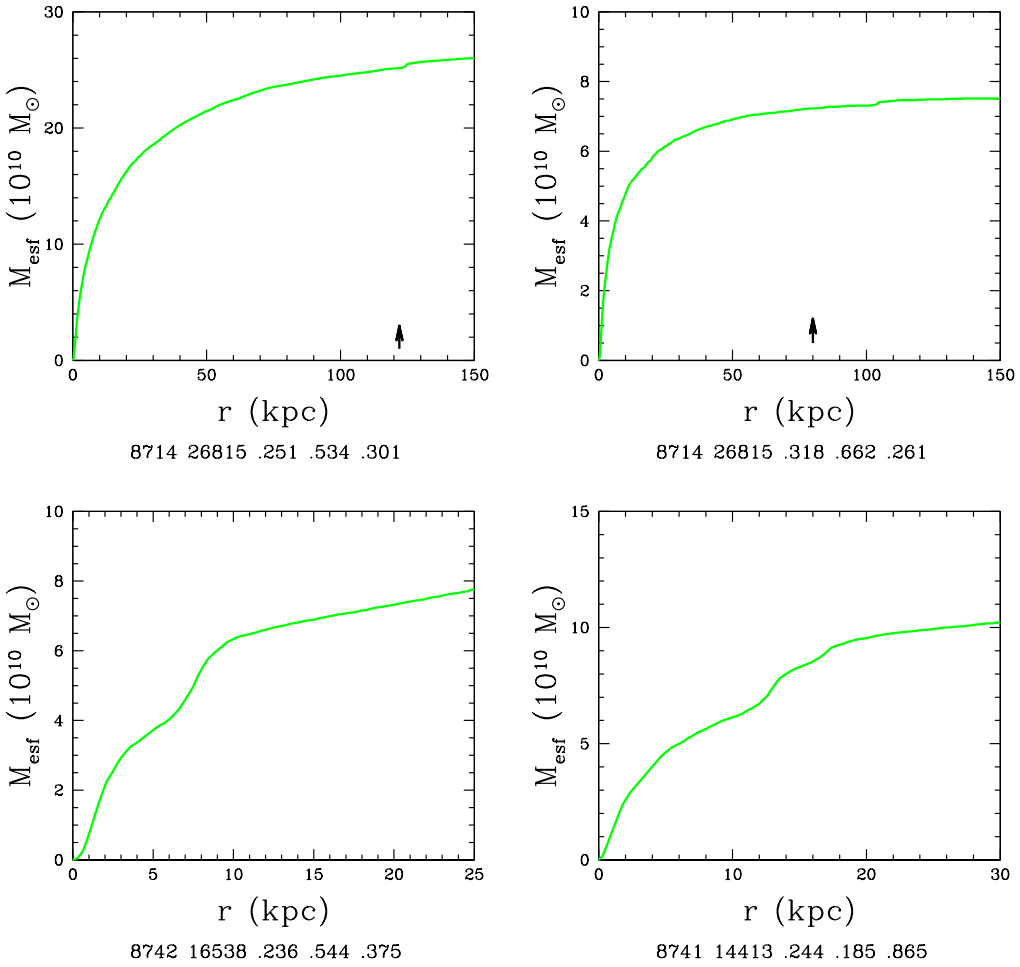

Figure 4.9: Four examples of stellar mass profiles. Arrows stand for the $r_{\rm bo}$ obtained for each ELO as long as it is well defined at the stellar scale. In the top, two examples *well defined* ELOs at the stellar scale. Bottom Figures show two examples of ELOs that are ill-defined at this scale because of merger events.

4.5 Calculating global properties

We have defined already the two scales that characterize all the global properties of the elliptical-like objects of our simulations. In order to make the following chapters of results easier to read and to stress their main findings, this Section describes in detail the different tools developed to obtain the structural and kinematical information of each simulated elliptical at its different main scales.

4.5.1 The halo scale properties

In the case of the total mass structure of galaxies, last results from lensing (Koopmans et al., 2006) have found that the internal part of total matter density profiles can be described by a power law expression $\rho^{\rm tot}(r) \propto r^{-\gamma}$. Following these results, we have built the total matter density profiles of our elliptical-like objects and fit them to a power law expression using the least squares fitting technique. We have done this fits up to the virial radius, $r_{\rm vir}$ and other lower characteristic radius that will be discussed in the following chapters. In general, we have developed tools to calculate the matter density profiles by fixing the bin length (lineal or logarithmic) or by imposing a number of particles in each bin. In the case of this analysis, we found the binning by a logarithmic scale the most appropriate because of its low noise at the inner and outer parts of the object.

Concerning the dark matter, spherically averaged dark matter density profiles of relaxed halos formed in N-body simulations have been found to be well fitted by analytical expressions such that, once rescaled, give essentially a unique mass density profile i.e., a two parameter family. These two parameters are usually taken to be the total mass, $M_{\rm vir}$, and the concentration, c or the energy content, E. These two parameters are, on their turn, correlated (i.e., the mass-concentration relation, see, for example Bullock et al., 2001; Wechsler et al., 2002; Manrique et al., 2003) because the assembly process implies a given correlation between $M_{\rm vir}$ and E. Different authors propound slightly different fitting formulae, see Einasto (1969, Eina) or Navarro et al. (2004b), Hernquist (1990, Hern), Navarro et al. (1996, NFW), Tissera & Dominguez-Tenreiro (1998, TD), Moore et al. (1999b) and Jing & Suto (2000, JS), that can be written as:

$$\rho_{\rm h}^{\rm dark}(r) = \rho_{\Delta}^{\rm aver} \times \frac{c^3 \tilde{\rho}(r/a_h)}{3g(c)} \tag{4.3}$$

where $\rho_{\Delta}^{\rm aver}$ is the average density within the virial radii, a_h is a characteristic radius and $c \equiv r_{\rm vir}/a_h$ is the so-called concentration parameter. Using $y = r/a_h$

$$\tilde{\rho}(y) = y^{-\alpha}(1+y)^{-\beta}, \tag{4.4}$$

where $(\alpha, \beta) = (1, 3)$ for Hern; $(\alpha, \beta) = (1, 2)$ for NFW; $(\alpha, \beta) = (2, 2)$ for TD, and

$\beta = 3-\alpha$, with α left free, for the general formula found by Jing & Suto (2000) (note that NFW can be considered as JS with $\alpha = 1$). In these fitting formulae α is the inner slope ($r << a_h$), the outer slope ($r >> a_h$) is $\alpha+\beta$ (3 for JS or NFW), so that a_h characterizes the scale where the slope changes. Other interesting scale is r_{-2}, the r value where the logarithmic slope, $d\ln\rho/d\ln r = -2$. We have $r_{-2} = a_h(2-\alpha)/(\alpha+\beta-2)$ for a profile given by Eq. 4.4, with $r_{-2} = a_h(2-\alpha)$ for JS and $r_{-2} = a_h$ for NFW. Navarro et al. (2004b) propound a different fitting formula of the form:

$$\tilde{\rho}(y) = \exp(-2\mu y^{1/\mu}). \tag{4.5}$$

where $d\ln\rho/d\ln r = -2(r/a_h)^{1/\mu}$ and $r_{-2} = a_h$. Note that this last fitting formula is similar to the Sérsic formula (Eq. 3.1), as Merritt et al. (2005) first pointed out. It was first used by Einasto (1969), see also Einasto & Haud (1989), so that we will refer to it as the *Einasto model* (Eina), in consistency with the terminology used by other authors (Merritt et al., 2006).

One great advantage of using the formulation stated in Equation (4.3) for the density profile is that the mass profile function can be easily obtained as

$$M^{\rm dark}(r) = \frac{g(y)}{g(c)} M_{\rm h}^{\rm dark} \tag{4.6}$$

and for each proposed formulae the g functions can be written as:

$$g(y) = \frac{y^2}{2(y+1)^2} \ (Hern) \tag{4.7}$$

$$g(y) = \ln(y+1) - \frac{y}{y+1} \ (NFW) \tag{4.8}$$

$$g(y) = \frac{9y}{1+y} \ (TD) \tag{4.9}$$

$$g(y) = (3-\alpha)^{-1} y^{3-\alpha} \, {}_2F_1(3-\alpha, 3-\alpha, 4-\alpha, -y) \ (JS) \tag{4.10}$$

$$g(y) = \frac{1}{2}(2\mu)^{1-3\mu}\gamma(3\mu, 2\mu y^{1/\mu}) \ (Eina) \tag{4.11}$$

where ${}_2F_1(a,b,c,d)$ is the hypergeometric function and $\gamma(a,b)$ is the lower incomplete gamma function.

We have used the *integrated* dark matter density profiles as fitting formulae instead of the dark matter density profiles themselves because these latter are binning dependent, more noisy and with fewer points to fit. The optimal fit has been obtained by minimizing the statistics:

$$\chi^2 = \Sigma_{i=1}^{N} [\log M(r_i) - \log M^{\rm dark}(r_i)]^2 / N \tag{4.12}$$

where $M^{\rm dark}(r_i)$ is the ELO dark matter mass within a sphere of radius r_i centred at its center of mass, $M(r_i)$ is the integrated mass density profile corresponding to the different formulae above, and the virial radii $r_{\rm vir}$ have been taken as outer boundaries of the fitting range. The minimum radius for the fit was set at the resolution of the simulation. The reason of selecting a $\log - \log$ statistics is mainly because of the difficulty of calculating proper errors of any quantity from the simulations. Without this normalization, in the classical form of the χ^2 statistics, the higher values of the outer part of the profiles take to much statistical weight. However, as we have seen before, the main differences between the different authorś formulae are in the inner parts of the dark matter. Therefore to improve the fits in the inner part of the mass profiles we have selected a $\log - \log$ statistics. An updated version of the MINUIT software from the CERN library has been used to make these fits as well as any other in this thesis.

The $V_{\rm cir}(r)$ profiles provide another measure of the mass distribution. We have to take into account that the gravity interaction in the simulations is modified by a softening term (see discussion in Chapter 2). Therefore we calculate these profiles using the following equation:

$$V_{\rm cir}(r) = \sqrt{\frac{G \cdot M(r) \cdot r^2}{(r^2+\epsilon^2)^{1.5}}} \tag{4.13}$$

where G is the gravitational constant, $M(r)$ is the mass profile and ϵ is the softening used in the simulation. The formal definition of circular velocity is recovered when $\epsilon \to 0$. Some examples of these profiles can be seen in Section 5.2.

At the halo scale we also calculate $\sigma^{\rm tot}_{\rm 3,h}$, as the velocity dispersion at halo scale. For this calculation all particles (baryonic and dark matter) inside a sphere of radius $r_{\rm vir}$ were used. To eliminate some possible under resolution effects, particles placed at a distance lower than the resolution of the simulation from the center were excluded. This was made in every velocity dispersion calculation made in this work, at all scales. Velocity dispersion is calculated in the following way, as we know velocity dispersion is given by the following equation $\sigma^2 = \bar{v^2} - \bar{v}^2$. Situate ELO variables in the center of mass system coordinates makes $\bar{v}^2 = 0$ so

$$\sigma^2 = \bar{v^2} = \frac{\sum_i^N (v_i - \bar{v})^2}{N-1} \tag{4.14}$$

This brings us also the possibility to test our center of mass finding algorithm as we can check if $\bar{v}^2 = 0$ for the number of particles we have select. This deviation effect makes corrections of less than 1% in the σ^2 calculations. Some examples can be seen in Section 5.3.

4.5.2 The stellar scale properties

To quantify the stellar three-dimensional mass density profiles of ELOs, we will fit them to the JS and Einasto analytical formulae (see Equations 4.4, 4.3, 4.11 and 4.10) through the statistics defined in Eq. 4.12 where $M^{\rm dark}(< r_i)$ has been replaced by the ELO stellar mass within a sphere of radius r_i, $M^{\rm star}(< r_i)$. As the maximum radius of these fits we have selected the radius of the baryonic object, $r_{\rm bo}$, and a more solid total length scale estimator, $r^{\rm star}_{\rm 90,bo}$, characterized as those radii enclosing 90% of the $M^{\rm star}_{\rm bo}$ mass. The minimum radius for the fit, as in the dark matter mass profiles fit, was set at the resolution of the simulation.

Another historical approximation to the study of the structure of the stellar objects is by assuming that it can be characterized by an ellipsoid with principal axes $a \geq b \geq c$. There are a few different ways found in the literature to model mass systems as ellipsoids. They all differ in details, but most methods model them using the eigenvectors from some form of the inertia tensor (Allgood et al., 2006, see,). We have computed these values from the eigenvalues ($\lambda_1 \geq \lambda_2 \geq \lambda_3$) of the inertia tensor of the particles inside a specific maximum radius r_{max}, $I_{ij}(< r_{max}) = \sum_{k=1}^{N} m_k(r_k^2\delta_{ij} + x_i x_j)$ following González-García & van Albada (2005). For an ellipsoid of uniform density,

$$a = \sqrt{\frac{5(\lambda_2 - \lambda_1 + \lambda_3)}{2M^{\rm star}_{\rm rmax}}} \quad b = \sqrt{\frac{5(\lambda_3 - \lambda_2 + \lambda_1)}{2M^{\rm star}_{\rm rmax}}} \quad c = \sqrt{\frac{5(\lambda_1 - \lambda_3 + \lambda_2)}{2M^{\rm star}_{\rm rmax}}} \tag{4.15}$$

To check how the 3D shape parameters, a, b and c, depend on the maximum radius used we compute it, for each baryonic object, at the effective stellar radius, $r^{\rm star}_{\rm e,bo}$, at the 90% stellar mass radius, $r^{\rm star}_{\rm 90,bo}$ and at the radius of the baryonic object, $r_{\rm bo}$.

Concerning kinematics at the stellar scale, we calculate velocity dispersion inside $r_{\rm bo}$, $\sigma^{\rm star}_{\rm 3,bo}$, in a very similar way as the velocity dispersion in the halo scale but just using stellar particles. As long as $r_{\rm bo}$ is well defined (see above), changes of even a 10% in the radio produce changes lower than 1% in $M^{\rm star}_{\rm bo}$ and $\sigma^{\rm star}_{\rm 3,bo}$. Another relevant quantity is the anisotropy of the 3D velocity distributions of the ELO sample, defined as:

$$\beta_{\rm ani} = 1 - \frac{\sigma_{\rm t}^2}{2\,\sigma_{\rm r}^2}, \tag{4.16}$$

where $\sigma_{\rm r}$ and $\sigma_{\rm t}$ are the radial and tangential velocity dispersions ($\sigma_{\rm t}^2 = \sigma_\theta^2 + \sigma_\phi^2$), relative to the center of the object. Some examples of these profiles can be seen in Section 5.2.

Concerning the organized motion of the elliptical-like objects, we have developed several tools to measure the possible rotation of these objects. We compute the total angular momentum, $\vec{L} = \vec{r} \times \vec{p}$ using all the star particles that satisfies $r_{max} > r > r_{min}$, where r_{min} was set at the resolution of the simulation and as r_{max} we utilized the characteristic radii, $r^{\rm star}_{\rm e,bo}$, $r^{\rm star}_{\rm 90,bo}$ and $r_{\rm bo}$, in a similar way as the 3D shape study described

above. However, once we knew the angular momentum, we have built another set of tools that also measure the amount of rotation of our elliptical-like objects in order to make better comparisons with observational data. From our calculation of $\vec{L} = (L_x, L_y, L_z)$, we determine the main axis of rotation of the simulated ellipticals. In spherical coordinates, the direction of this axis are set by $\theta = L_z/|\vec{L}|$, $\phi = \arctan(L_y/L_x)$, where θ is referred to as the zenith, colatitude or polar angle, while ϕ is referred to as the azimuth. We have rotated the whole system to make this axis the z-axis. This rotation can be done in several ways, in this work we have used the following matrix:

$$\mathbb{R} = \begin{pmatrix} 1 + (\cos(\theta) - 1) \cdot \cos(\phi)^2 & (\cos(\theta) - 1) \cdot \sin(\phi) \cdot \cos(\phi) & -\sin(\theta) \cdot \cos(\phi) \\ (\cos(\theta) - 1) \cdot \sin(\phi) \cdot \cos(\phi) & 1 + (\cos(\theta) - 1) \cdot \sin(\phi)^2 & -\sin(\theta) \cdot \sin(\phi) \\ \sin(\theta) \cdot \cos(\phi) & \sin(\theta) \cdot \sin(\phi) & \cos(\theta) \end{pmatrix} \tag{4.17}$$

which has been built to make $\mathbb{R} = \mathbb{1}$ whenever $\theta = 0$.

Once we have set the z-axis as the axis of rotation, we have calculated the mean tangential velocity, V_ϕ, at the different characteristic radii that we have for our elliptical-like objects: $r^{\rm star}_{\rm e,bo}$, $r^{\rm star}_{\rm 90,bo}$ and $r_{\rm bo}$.

4.5.3 The observational stellar scale properties

In addition, at the stellar scale we measured a *observational* scale. To compare with observations we have to try to mimic as much as possible the data that is obtained through telescopes. This is, we have to take into account projection and concentration effects. Projected stellar mass, $M^{\rm star}_{\rm cyl,bo}$ and projected stellar half-mass radii[4], $R^{\rm star}_{\rm e,bo}$, are calculated again by building a mass profile. We first select the particles of the simulation for the study using a sphere of radius $r_{\rm bo}$ (i.e.; a limiting radius for each object). Nevertheless this time we want a projected mass profile. For this, instead of using spheres as in previous cases, we have to choose a direction of projection and place cylinders of increasing radii along it. We sum all stellar mass particles inside each cylinder to obtain the projected mass profile, $M_{\rm cyl}(R)$. The observationally relevant size scales are the *projected* half-mass radii. They are determined from $M_{\rm cyl}(R)$, the integrated projected mass density in concentric cylinders of radius R for the different constituents. For example, $R^{\rm cb}_{\rm e,bo}$ and $R^{\rm star}_{\rm e,bo}$ are the projected radii where $M^{\rm cb}_{\rm cyl}(R)$ and $M^{\rm star}_{\rm cyl}(R)$ are equal to $M^{\rm cb}_{\rm cyl,bo}/2$ and to $M^{\rm star}_{\rm cyl,bo}/2$, respectively. Note that, as $r_{\rm bo}$ is used to cut a sphere that afterwards is being projected, we have that $M^{\rm star}_{\rm cyl,bo} \backsimeq M^{\rm star}_{\rm bo}$.

Before going any further on observational scale parameters, it is important to clarify an important point. The first step in calculating the observational parameters described here is the definition of a line-of-sight axis. To account for the possible projection effects we have generated one hundred random projections. We have calculated all

[4]Hereafter we will use capital R to mean projected radii

the observational scale parameters for these one hundred random projections for each object to really include all the range of possible observational data. The random line of sight axes have been set by the generation of random pairs of the spherical coordinates (θ,ϕ). The system is rotated to make the axis defined by these coordinates the z-axis using the rotation matrix described above (see Equation 4.17). For purposes of clarity, **we reserve the formal definition terms used in this Section for the observational parameters** (as $M^{\rm star}_{\rm cyl,bo}$, $R^{\rm star}_{\rm e,bo}$, etc.) **for the averages values over these one hundred random projections**. Anyway, in the following chapters of this thesis we will remind this definition if necessary and indicate properly any other uses.

The next step is the description of the projected mass density profiles. Authors now agree that the Sérsic law given in Eq. 3.1 (Sérsic, 1968) is an adequate empirical representation of the optical surface brightness profiles of most ellipticals (see, for example, Caon et al., 1993; Bertin et al., 2002). Assuming that the stellar mass-to-light ratio $\gamma^{\rm star}$ does not appreciably change with ELO projected radius R, the projected stellar *mass* profile, $\Sigma^{\rm star}(R)$ can be taken as a measure of the surface *brightness* profile and be written as

$$\Sigma^{\rm star}(R) = \gamma^{\rm star} I^{\rm light}(R). \tag{4.18}$$

One can then expect that $\Sigma^{\rm star}(R)$ can be fitted by a Sérsic-like law. Following Equation (3.1), the Sérsic law for the projected stellar mass profile can be written as

$$\Sigma^{\rm star}(R) = \Sigma^{\rm star}_0 \exp[-(R/R^{\rm star}_{\rm s})^{1/n}] \tag{4.19}$$

where $R^{\rm star}_{\rm s}$ is the Sérsic scale parameter, n the Sérsic shape parameter and $\Sigma^{\rm star}_0$ is projected central stellar mass density. But this equation can be rewritten in terms of more familiar factors, as the projected stellar half-mass radius, $R^{\rm star}_{\rm e,bo}$, and the projected stellar mass density within this radius, $\Sigma^{\rm star}_{\rm e}$,

$$\Sigma^{\rm star}(R) = \Sigma^{\rm star}_{\rm e} \exp[-b_{\rm n}((R/R^{\rm star}_{\rm e})^{1/n} - 1)] \tag{4.20}$$

where we have introduced the term $b_{\rm n}$, defined as $R^{\rm star}_{\rm e} = R^{\rm star}_{\rm s}(b_{\rm n})^n$ and $\Sigma^{\rm star}_0 = \Sigma^{\rm star}_{\rm e} \exp[b_{\rm n}]$ and that can be obtained by $b_{\rm n} = 2n - 1/3 + 0.009876/n$ (Prugniel & Simien, 1997). We have calculate the $\Sigma^{\rm star}(R)$ profiles by averaging on concentric rings centered at the projection of the center-of-mass of the corresponding ELO. Obviously we are interested in how the projected structure of our elliptical-like objects adjust to the Sérsic profile so we have developed all the necessary tools to do it. The fitting set of parameters depend on the methodology used to obtain them (see interesting discussions in Lima Neto et al. 1999 and Aceves et al. 2006). Therefore some remarks on how our fits have been made are in order. Since the projected densities are binning dependent and somewhat noisy, the integrated projected mass density in concentric cylinders of

radius R and mass $M^{\rm star}_{\rm cyl}(R) = 2\pi \int_0^R \Sigma^{\rm star}(R')R'dR'$ has been used as a fitting function, instead of $\Sigma^{\rm star}(R)$ itself. Finally, using the formulation of Equation (4.20) for the Sérsic law we can obtain the following equation for the projected mass profiles:

$$M^{\rm star}_{\rm cyl}(R) = M^{\rm star}_{\rm cyl}(R_{max}) \frac{P[2n, b_{\rm n}(R/R^{\rm star}_{\rm e})^{1/n}]}{P[2n, b_{\rm n}(R_{max}/R^{\rm star}_{\rm e})^{1/n}]} \tag{4.21}$$

where $P[a, x]$ is the regularized gamma function. In this case we have used the statistics defined as

$$\chi^2 = \Sigma_{i=1}^{N}[M_{cyl}(R_i) - M^{\rm star}_{cyl}(R_i)]^2/N \tag{4.22}$$

since we want to directly compare with observational results. However we have also studied the effects of using the statistics stated in Eq. (4.12).

Concerning the fitting range, we have adopted an outer boundary $R_{\rm max}$ such that the corresponding surface brightness $I^{\rm light}(R_{\rm max})$ (see Eq. 4.18) gives the standard value of $\mu_B(R_{\rm max}) = 27$ mag arcsec^{-2} which is a typical limit of resolution in the Johnson B Band for nowadays telescopes (D'Onofrio, 2001). To obtain $I^{\rm light}$ in $L_\odot pc^{-2}$ we have used that $\log I^{\rm light}_B(R_{\rm max}) = -0.4[\mu_B(R_{\rm max}) - k_B]$ taking $k_B = 27$ for nearby observations in the Johnson B band (Jorgensen et al., 1996). Using these parameters we obtain a surface brightness limit of $I^{\rm light}_B(R_{\rm max}) \simeq 1 L_\odot pc^{-2}$. Moreover, the values for the stellar mass-to-blue-light $\gamma^{\rm star}_B$ span a range from $\gamma^{\rm star}_B = 2$ to 12, depending on the details of its determination (see discussion in Mamon & Łokas, 2005a), and best values of $\gamma^{\rm star}_B = 5$ to 8. Their geometric mean $\gamma^{\rm star}_B = 6.3$ and the lower and higher best values have been used to make the fits. These limits translate into $\Sigma^{\rm star}_{\rm lim} = 6.32 \times 10^{12} M_\odot/Mpc^2$ for the best value and $5 \times 10^{12} M_\odot/Mpc^2$ and $8 \times 10^{12} M_\odot/Mpc^2$ for lower and upper $\gamma^{\rm star}_B$ limits. We will call the outer boundary obtained from this method, R_{27}.

Just as in the 3D case of the stellar object, we have used another classic tool to study the shape of the projected simulated galaxy and compare it with observations. We have calculated the apparent ellipticity, ϵ of the projected mass profiles. Concerning the point of view, we have calculated ϵ for one hundred random projections and also for a point of view chosen to be perpendicular to the spin angular momentum vector of the stellar matter because we are interested in studying the shape versus rotation relation (see Section 3.2). This particular point of view should maximize the effects of rotation where this is present (see Binney, 2005; Burkert & Naab, 2005). We project the particle distribution along the line of sight to derive the ellipticity for each point of view. Following the same approach used to obtain the 3D shape parameters, we compute ϵ from the eigenvalues ($\lambda_1 \geq \lambda_2$) of the projected inertia tensor of the particles inside a specific maximum radius, where $\epsilon = 1 - \lambda_2/\lambda_1$. We will also analyze the effects of selecting different maximum radius for computing ϵ as $R^{\rm star}_{\rm e,bo}$ or $R^{\rm star}_{\rm 90,bo}$.

We have measured the stellar line-of-sight velocity and the stellar velocity dispersion profiles, $V^{\rm star}_{\rm los}(R)$ and $\sigma^{\rm star}_{\rm los}(R)$, along one hundred random projections for all ELOs in

the sample. We have taken into account only star particles as this quantity is measured through stellar spectra or other observables, as the planetary nebulae, linked with stars (observational profiles can be found, for example in Douglas et al., 2007). Some examples for our ELOs can be seen in Section 5.2.

Obtaining an equivalent to the observational central l.o.s velocity dispersion, $\sigma^{\rm star}_{\rm los,0}$, is not straightforward. Again, the direction of projection has been selected and the particles are binned using cylinders of increasing radii. We compute it by calculating the accumulated velocity dispersion just using the velocity component along the line of sight. To improve the drawback of resolution, the maximum of all these values for different radii up to stellar effective radii, is chosen as the line-of-sight velocity dispersion, $\sigma^{\rm star}_{\rm los,0}$. To eliminate some possible under resolution effects, particles placed at a distance lower than the resolution of the simulation from the center were excluded.

To mimic other observational techniques used in stellar kinematics of elliptical galaxies, we have measured these profiles placing a slit along the major and minor axes of projected ELOs, where the major axis is defined as that orthogonal to the ELO spin vector projected on the plane normal to the LOS, and the minor axis is parallel to the spin projection onto the plane of the sky (see Figure 4.10). Only those particles below $r_{\rm bo}$ and above the resolution of the simulation are selected. In this way we obtain the classical $\tilde{V}^{\rm star}_{\rm los}(R)$ and $\tilde{\sigma}^{\rm star}_{\rm los}(R)$ obtained in observations (see for example Hau & Forbes, 2006). Some examples can be seen in Section 5.3.

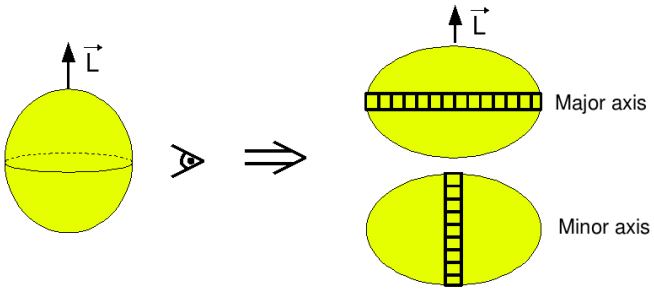

Figure 4.10: Slit position to mimic observational observations and compute stellar kinematic profiles.

Finally, we are interested in the maximum of the velocity curve, $V_{\rm max}$, of these line-of-sight velocity profiles. This quantity has been largely used as an observational indicator of the amount of rotation in ellipticals (see discussion in Section 3.2). As with the projected ellipticity, we have used a point of view chosen to be perpendicular to the spin angular momentum vector of the stellar matter which maximizes the effects of rotation where this is present (see above). We have placed a slit along the major axis of the projected system and we have obtained the projected velocity and velocity dispersions curves. The value of $V_{\rm max}$ is obtained from the mean value of the maximum

velocity (positive) and the minimum velocity (negative) of the profile inside $R^{\rm star}_{\rm e,bo}$ and $R^{\rm star}_{\rm 90,bo}$.

4.6 Summary

This chapter describes a set of samples of virtual ellipticals, formed in different cosmological simulations roughly consistent with observations. The normalization parameter has been taken slightly high, $\sigma_8 = 1.18$, as compared with the average fluctuations of 2dFGRS or SDSS galaxies to mimic an active region of the Universe. Newton laws and hydrodynamical equations have been integrated in this context, with a standard cooling algorithm and a star formation parameterization through a Kennicutt-Schmidt-like law, containing our ignorance about its details at sub-kpc scales. No further hypotheses to model the assembly processes have been made. Individual galaxy-like objects naturally appear as an output of the simulations, so that the physical processes underlying mass assembly can be studied. Five out of the total simulations (the *EA* type simulations) share the SF parameters and differ in the seed used to build up the initial conditions. To test the role of SF parameterization, the same initial conditions have been run with different SF parameters making SF more difficult, contributing another set of five simulations (the *EB* type simulations). We have also run different simulations in order to test the effect in our results of different parameters as the cosmological model (*EC*), resolution (*ED*) and box size (*EF*).

We have seen that the search for GLOs in hydrodynamical simulations and the study of their properties is not a trivial issue. The group finding algorithms give different results depending on the parameters used. In this context we have obtained from our analysis some results that will help in order to minimize these effects and to obtain more robust identifications. However we have decided to go for an object-by-object study of the most massive GLOs of the simulations in order to build our elliptical-like object samples. Although this is a really more tedious work, it guarantees the robustness of our samples.

During this object-by-object analysis we have studied the halo and stellar scale of GLOs and selected those satisfying the ELO identification criteria. In all these simulation ELOs have been identified as those galaxy-like objects having a prominent, dynamically relaxed spheroidal component made out of stars, with no extended discs and very low gas content. This stellar component is embedded in a dark matter halo that contributes an important fraction of the mass at distances from the ELO center larger than $\sim 10 - 15$ kpc. ELOs have also an extended halo of hot, diffuse gas. We have described all the analysis done in order to get robust ELO samples. Then, at the end of this phase, we have obtained several ELOs in our different simulation samples that are well defined by a characteristic radius at each scale, the virial radius, $r_{\rm vir}$ and

the baryonic object radius, $r_{\rm bo}$. These two radius define two characteristic masses, the virial mass, $M_{\rm vir}$, and the stellar mass of the object, $M_{\rm bo}^{\rm star}$. Finally we have developed a set of tools in order to study the structure and kinematics of these objects at the different scales and to compare them with observational data.

To help the reader, in Table 4.4 and Table 4.5 we give a list of the parameter names and symbols introduced in this chapter to be used in the following ones.

Name	Symbol
Halo scale parameters	
Virial mass	$M_{\rm vir}$
Virial radius	$r_{\rm vir}$
Dark mass inside virial radius	$M_{\rm h}^{\rm dark}$
Baryon mass inside virial radius	$M_{\rm h}^{\rm bar}$
Cold baryon mass inside virial radius	$M_{\rm h}^{\rm cb}$
Stellar mass inside virial radius	$M_{\rm h}^{\rm star}$
Total half-mass radius	$r_{\rm e,h}^{\rm tot}$
Cold baryon half-mass radius	$r_{\rm e,h}^{\rm cb}$
Stellar half-mass radius	$r_{\rm e,h}^{\rm star}$
Einasto shape parameter	μ
Total 3D velocity dispersion	$\sigma_{\rm 3,h}^{\rm tot}$
Baryonic-object scale parameters	
Baryonic object radius	$r_{\rm bo}$
Stellar mass	$M_{\rm bo}^{\rm star}$
Cold baryon mass	$M_{\rm bo}^{\rm cb}$
Stellar half-mass radius	$r_{\rm e,bo}^{\rm star}$
Stellar 90%-mass radius	$r_{\rm 90,bo}^{\rm star}$
Cold baryon half-mass radius	$r_{\rm e,bo}^{\rm cb}$
3D ellipticity	$\epsilon_{\rm 3D}$
Mean stellar 3D velocity dispersion	$\sigma_{\rm 3,bo}^{\rm star}$
tangential stellar velocity	V_ϕ
Observational baryonic-object scale parameters	
Projected stellar half-mass radius	$R_{\rm e,bo}^{\rm star}$
Projected stellar mass	$M_{\rm cyl,bo}^{\rm star}$
Mean projected stellar mass density within $R_{\rm e,bo}^{\rm star}$	$\Sigma_{\rm e}^{\rm star}$
Projected 27 $mag \times arcsec^{-2}$ radius	$R_{27}^{\rm star}$
Sérsic shape parameter	n
Stellar projected ellipticity	ϵ
Central LOS stellar velocity dispersion	$\sigma_{\rm los,0}^{\rm star}$
Maximum of the velocity curve	$V_{\rm max}$

Table 4.4: Parameter names and symbols. See text for details.

Profiles	
Name	Symbol[a]
Mass profile	$M(r)$
Circular velocity profile	$V_{\rm cir}(r)$
3D velocity dispersion profile	$\sigma_{3D}(r)$
Anisotropy profile	$\beta_{\rm ani}(r)$
Projected mass density profile	$\Sigma(R)$
Line-of-sight velocity profile	$V_{\rm los}(R)$
Line-of-sight velocity dispersion profile	$\sigma_{\rm los}(R)$
Ratios	
Ratio definition	Ratio symbol
$GM_{\rm vir}/(\sigma^{\rm tot}_{\rm 3,h})^2 r^{\rm tot}_{\rm e,h}$	$c_{\rm f}$
$r^{\rm tot}_{\rm e,h}/r^{\rm star}_{\rm e,bo}$	$c_{\rm rd}$
$r^{\rm star}_{\rm e,bo}/R^{\rm star}_{\rm e,bo}$	$c_{\rm rp}$
$(\sigma^{\rm tot}_{\rm 3,h})^2/\sigma^{\rm star}_{\rm 3,bo})^2$	$c_{\rm vd}$
$(\sigma^{\rm star}_{\rm 3,bo})^2/3(\sigma^{\rm star}_{\rm los,0})^2$	$c_{\rm vpc}$
$GM_{\rm vir}/3(\sigma^{\rm star}_{\rm los,0})^2 R^{\rm star}_{\rm e,bo} = c_{\rm F} c_{\rm rd} c_{\rm rp} c_{\rm vd} c_{\rm vpc}$	$c^{\rm vir}_{\rm M}$

Table 4.5: Profile and ratio names and symbols.
(a) To specify the constituent, a superindex has been added in the text to the profile symbols: dark for dark matter, bar for baryonic matter, hb just for hot baryons, cb for cold baryons and star for stars. For example $M^{\rm star}(r)$ for the stellar mass profile.

Part III

Results

Chapter 5

Ellipticals at z = 0: Profiles [1]

5.1 Introduction

In what follows, we present our work on the structural and kinematical description of our simulated nearby ellipticals ($z = 0$). The information about position and velocity distributions of the ELO particles of different kinds (dark matter, stars, cold gas, hot gas) provided by the simulations, allows a detailed study of the parameters characterizing their structure and dynamics. This Chapter is focused on the structural and kinematical profiles of the different components, dark matter, star and gas, of the $z = 0$ samples. Next Chapter would focus on the study of the different relations of the fundamental parameters that characterize these profiles.

All this study has been done for the different simulations discussed in 4.2. However for the sake of clarity, in this and in the following chapter we would center our analysis on the *EA*-Z0 and *EB*-Z0 ELO main samples. We would discuss deeply robustness of results and possible caveats between all the samples at the end of the next chapter 6.5.

The organization of this chapter is as follows: Next section 5.2 is focused on the 3D and 2D structural profiles and we would try to address the important issue of the amount and distribution of dark, stellar and total matter in virtual ellipticals. In section (5.3) we would focus on the kinematical profiles trying to deepen into the kinematics of the dark matter component and its relationship with the kinematics of the bright matter component. Finally in Section (5.4) we present our conclusions.

5.2 Structure Profiles

A quantitative description of ELO mass distributions is given by their 3D density profile and the structure their constituent particles. We first address the structure of the baryonic particles. To help the reader, we remind that in Table 4.4 and Table 4.5 a list

[1] Based on Oñorbe, Domínguez-Tenreiro, Artal, & Serna (2006); Oñorbe, Domínguez-Tenreiro, Sáiz, & Serna (2007)

of the parameter names and symbols used in this thesis can be found.

5.2.1 Three Dimensional Structure for Gas Particles

The gas structure is drawn in Figure 5.1 for the second more massive object formed in a *EB*-Z0 type simulation. The 3D density at a given distance, r, from the center of the object has been calculated by binning on concentric spherical shells around r. In this Figure, the line is the density profile of dark matter around the object, multiplied by $\Omega_{\rm b}/\Omega_{\rm m}$. Points represent gas density at the positions of SPH particles, and colors stand for gas particle temperatures according with the scale at the bottom of the Figure.

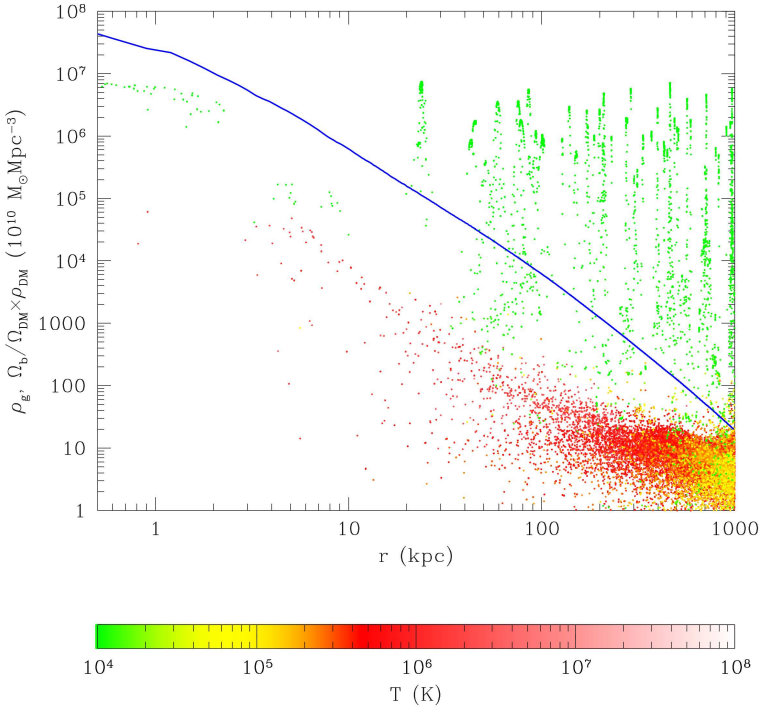

Figure 5.1: 3D gas (points) and dark matter (blue line) density for a typical ELO. Note the dense cold gas clumps embedded in the diffuse hot gas component. See text for an explanation. This figure is courtesy of A. Sáiz.

We see in this Figure that very few gas is left at positions with $r \leq 30$ kpc where stars dominate the mass density, that cold gas at $r \geq 30$ kpc is dense and clumpy, while hot gas (that is, gaseous particles with $T > 3 \times 10^4$K) is diffuse with an almost isothermal component at 100 kpc $\leq r \leq$ 400 kpc, and a warm component at the outskirts of the configuration, reaching outside the virial radius (395.0 kpc). Two scales stand out in this configuration: the *ELO scale* or stellar component, with a size in this case of $\sim$ 30 kpc, and the *halo scale*, a halo of dark matter of 395.0 kpc. Cold dense gas particles

are associated in most cases with small dark matter halos (not seen in the Figure); both gaseous particles in cold clumps and dark matter particles in their (sub)halos are *shocked* particles, using the terminology of the adhesion model (see, for example, Vergassola et al., 1994). The configuration illustrated by this Figure is generic for ELOs: we can distinguish an *ELO or baryonic object scale*, with typical sizes of no more than $\sim$ 10 - 40 kpc, and the *halo scale*, a halo of dark matter typically ten times larger in size.

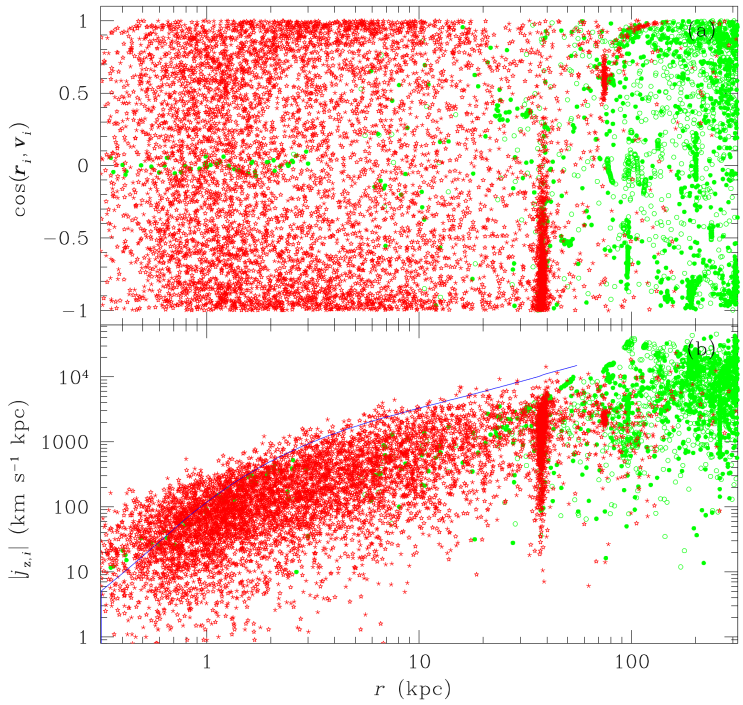

Figure 5.2: Upper panel: the cosine of the angle formed by the position and the velocity vectors for each gaseous (green circles) and stellar (starred red symbols) particle belonging to a typical ELO. Filled (open) symbols stand for particles in (counter) co-rotation with the small inner disc. This figure is courtesy of A. Sáiz.

5.2.2 Stellar and Gaseous Particle Orbits

ELO constituent particles of different kinds travel on orbits that have different characteristics. To analyze this point, in the upper panel of Figure 5.2 we plot, for each star particle and each gaseous particle of a typical ELO, the cosine of the angle formed by its position ($\vec{r_i}$) and its velocity ($\vec{v_i}$) as a function of r_i. Positions and velocities have been taken with respect to the center of mass of the main baryonic object. In this plot radial orbits have cosines $= \pm 1$, while circular orbits have cosines $= 0$. Starred (circular) symbols stand for stellar (gaseous) particles. We see that cold gas particles at $r \leq 4$

kpc form a disc in coherent circular motion; filled (open) symbols represent particles in co-rotation (counterrotation) with respect to this small disc. We can also see that stellar particle orbits at ≤ 3 kpc scales do not show any preference, while those further away, as well as gaseous particles outside the disc, show a slight tendency to be on radial orbits providing anisotropy to the velocity dispersion. Stellar particles constitute a disordered or dynamically hot component, showing an important velocity dispersion, and, also, in some cases, a coherent net rotation. In 5.3 these issues will be addressed in detail.

5.2.3 Dark Matter Profiles

All our virtual ellipticals are embedded in a well defined dark matter halo up to the virial radius. As we have seen in Section 3.2, pure N-Body simulations had played a very important role in the study of the properties of these halos, and different authors had propound different analytical fitting formulas such that, once rescaled give essentially a unique mass density profile. However, when processes other than gravitational are involved in mass assembly (for example, cooling or heating), the dark matter density profiles could be modified (see Blumenthal et al., 1986; Dalcanton et al., 1997; Tissera & Dominguez-Tenreiro, 1998; Gnedin et al., 2004). To analyze this point, in Figure 5.3 we plot the dark matter density profiles for several typical ELOs, along with their best fit to different analytical profiles: Einasto (1969, Eina) or Navarro et al. (2004b), Hernquist (1990, Hern), Navarro et al. (1996, NFW), Tissera & Dominguez-Tenreiro (1998, TD), Moore et al. (1999b) and Jing & Suto (2000, JS). All the details of the fitting procedure and the exact parameterization of these profiles can be found in 4.5. As a test to check the consistency of the fits, we have compared the virial effective radius, $r_{\rm e,h}^{\rm tot}$, and the virial mass, $M_{\rm vir}$, obtained from the different fits versus the ones obtained directly from the profiles and find very similar results.

Note in Figure 5.3 that the quality of the fits differs from one analytical profile to another. To quantify this effect, in Figure 5.4 we plot the distributions of the χ^2 per d.o.f. statistics, normalized to $(\log M_{\rm vir})^2$, resulting from the fits to the different profiles above. We see that the lower χ^2 per d.o.f. values generally correspond to either the Eina or the JS profiles, with the TD profiles in the third position and NFW profiles in fourth. In Figure 5.5 we draw the values of the μ (for Eina profiles) and α (for JS profiles) slopes corresponding to the optimal fits of EA-Z0 sample DM halos. A slight mass effect can be appreciated with lower mass ELOs having steeper DM halos than more massive ones, presumably due to a more important pulling in of baryons onto dark matter as they fall to the ELO center with decreasing ELO mass. That is, massive halos are less concentrated than lighter ones, i.e., the mass-concentration relation. In any case, the profiles are always steeper than $\alpha = 1$ (i.e., the NFW profile; see Mamon & Łokas, 2005a; Stoehr, 2006).

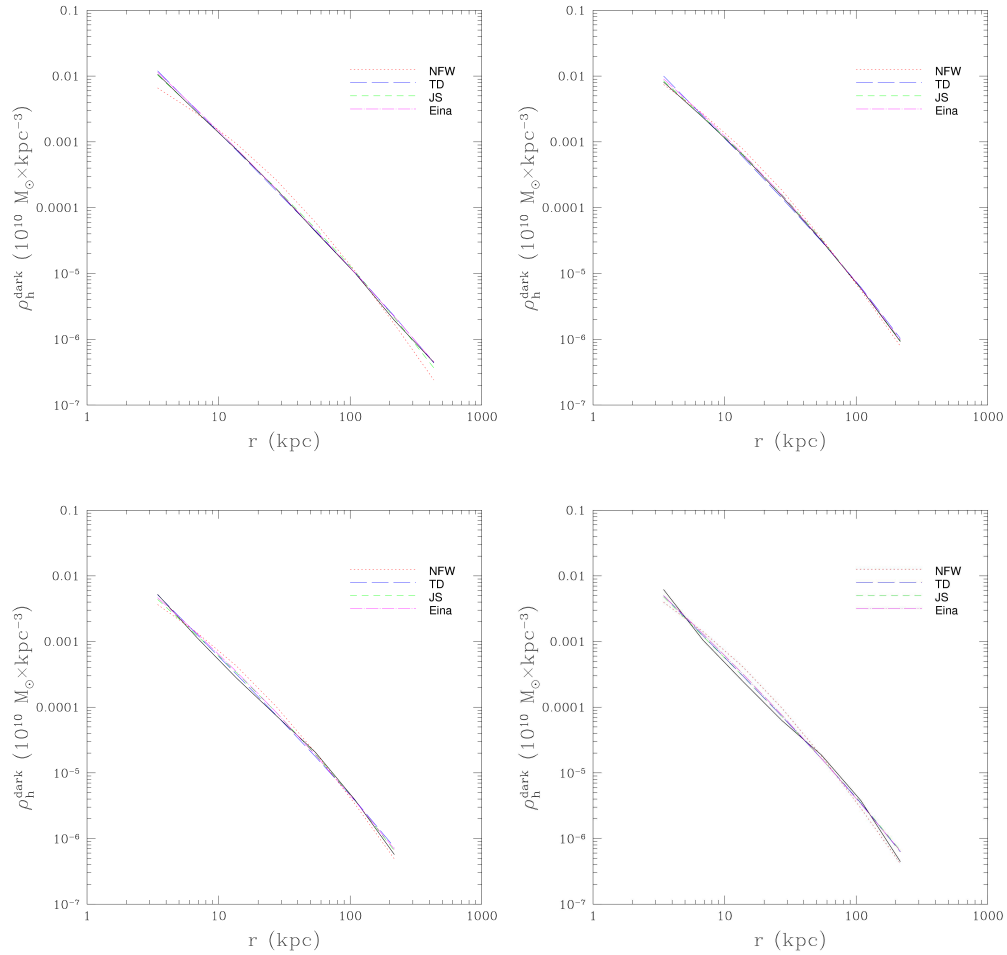

Figure 5.3: Dark matter density profiles (black full line) for several typical ELOs from *EA*-Z0 and *EB*-Z0 samples along with their best fits to different analytical profiles: NFW (red point line), TD (blue long-dashed line), JS (green short-dashed line) and Eina (magenta point-dashed line).

To further analyze this effect, we plot in Figure 5.6 the ρ_{-2} density parameter versus the r_{-2} scale obtained from fits to the Einasto model. Green triangles are measurements by Navarro et al. (2004b) onto halos formed in N-body simulations and the green line is their best fit. We see that at given r_{-2}, ρ_{-2} is higher in our hydrodynamical simulations than in those of Navarro et al. (2004b), presumably due to the pulling in of dark matter by baryon infall. We also see that at given $M_{\rm vir}$, r_{-2} is shorter in hydrodynamical simulations than in purely gravitatory ones, by the same reason. It is worth to mention that in the work of these authors, the virial radius and virial mass is defined by fixing an overdensity of $\Delta_c = 200$, which is much greater than the one obtained from Bryan & Norman (1998) algorithm (see details in Section 4.4.1) for *EA*and *EB*cosmologies Δ_c 106. This issue produces lower virial masses and radius. Virial masses of our ELO

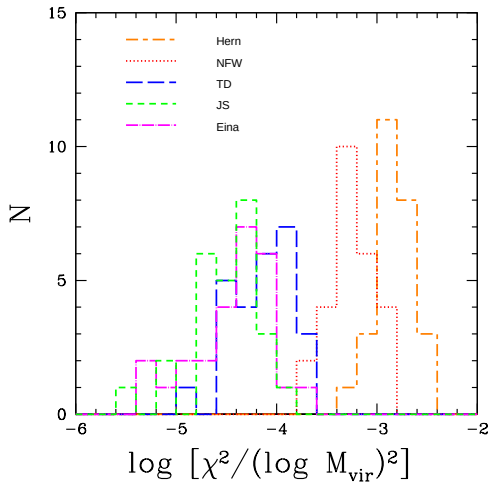

Figure 5.4: The distributions of the χ^2 per d.o.f., normalized to the logarithm of their respective mass square, for the fits of the DM density profiles of ELO halos (*EA*-Z0 and *EB*-Z0 samples) to different analytical profiles.

samples plotted in Figure 5.6 have been adjusted to this issue. In addition, our test fits using a much shorter radius as the maximum limit of the fit, lead to very similar r_{-2} and ρ_{-2} values and exactly the same conclusions.

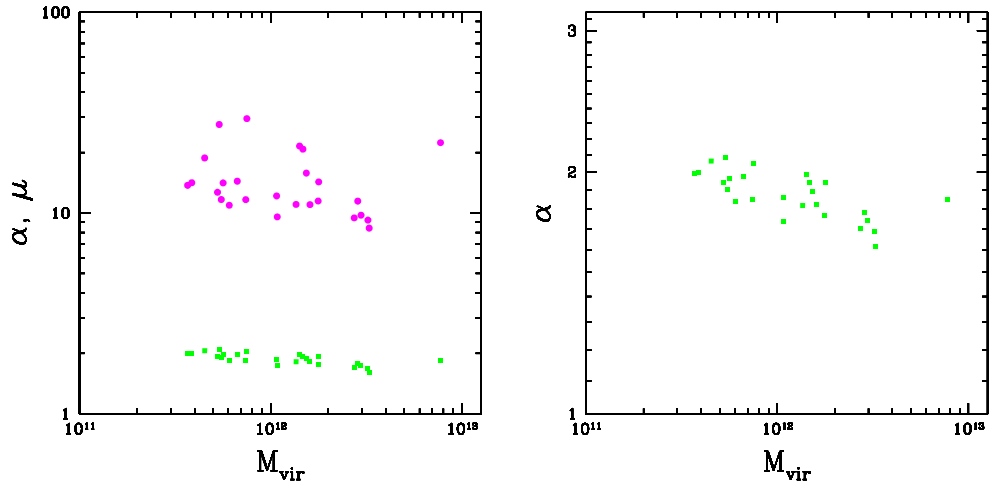

Figure 5.5: Left panel: the optimal inner slope α of the general Jing & Suto profile for the DM halos of ELOs (green filled squares) and the μ coefficient of the Einasto analytical profile (magenta filled circles), versus their virial mass for *EA*-Z0 sample ELOs. Right panel: zoom of the α versus virial mass plot to clarify the mass effect.

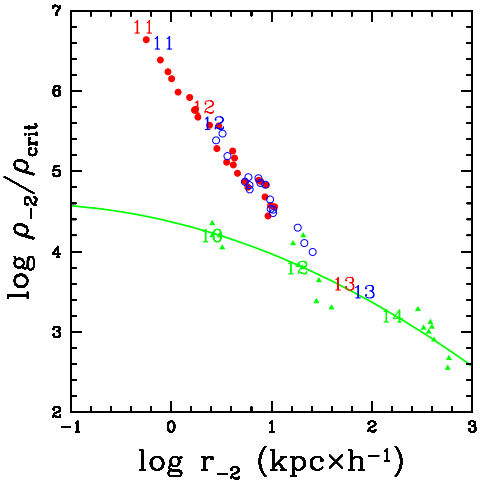

Figure 5.6: The ρ_{-2} density parameter versus the r_{-2} scale obtained from fits to the Einasto model, for ELOs in both the *EA*-Z0 sample (filled red circles) and the *EB*-Z0 sample (open blue circles). Green triangles are measurements by Navarro et al. (2004b), onto halos formed in N-body simulations, with its fit by (Mamon & Łokas, 2005a) (green line). Numbers correspond to the logarithms of the virial masses (in units of $M_\odot$) of halos formed in different simulations, according with their respective colors.

5.2.4 Baryonic Three-Dimensional Mass Density Profiles

We first analyze the baryon distribution at the ELO scale, where the main contribution to the mass density comes from stars. We lack of any observational input on how the three-dimensional stellar-mass density profiles $\rho^{\rm star}(r)$ can be, except for a deprojection of the Sérsic profiles (Prugniel & Simien, 1997; Lima Neto et al., 1999). In Figure 5.7 we plot $\rho^{\rm star}(r)$ for ELOs in the *EA*-Z0 sample. Different colors have been used for ELOs in different mass intervals and a clear mass effect can be appreciated in this Figure, and particularly so at the inner regions, where at fixed $r/r_{\rm vir}$ the stellar-mass density of less massive ELOs can be a factor of two or so higher than that of more massive ones. This means that the mass homology is broken in the three-dimensional stellar mass distribution.

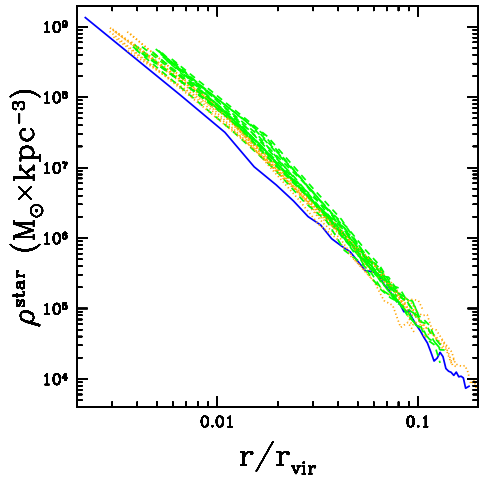

Figure 5.7: Three-dimensional stellar mass density profiles for ELOs in the *EA*-Z0 sample: green dashed lines, ELOs with $M_{\rm vir} < 1.5 \times 10^{12}$ $M_\odot$; orange point lines, ELOs with 1.5×10^{12} $M_\odot \leq M_{\rm vir} < 5 \times 10^{12}$ $M_\odot$; blue full lines: ELOs with $M_{\rm vir} \geq 5 \times 10^{12}$ $M_\odot$. The stellar mass density profiles show homology breaking.

Following the method described in Section 4.5, we fit the stellar three-dimensional mass density profiles of ELOs to JS and Einasto analytical formulas. The quality of the fits is illustrated in Figure 5.8, and in Figure 5.9 the values of the χ^2 p.d.o.f. statistics are given, normalized to $\log M_{\rm bo}^{\rm star}$. Both Figures show that these profiles describe adequately well the spherically-averaged stellar mass distribution in three dimensions, even if with very small r_{-2} values.

To study the possibility that the homology in the dark- versus bright-mass distribution is also broken, the stellar-to-dark density ratio profiles

$$f^{\rm star}(r) = \rho^{\rm star}(r)/\rho^{\rm dark}(r) \tag{5.1}$$

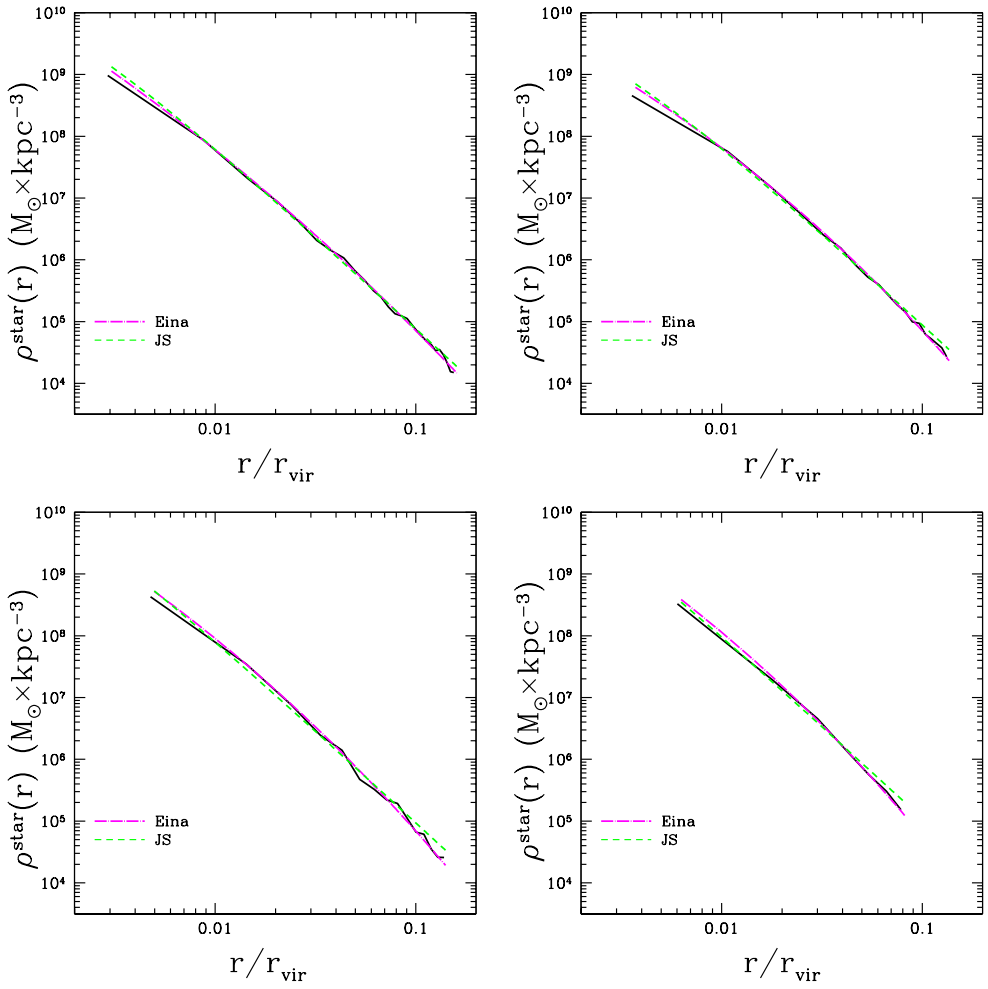

Figure 5.8: The stellar mass profiles for 4 typical ELOs in *EA*-Z0 sample (black continuous lines) and their optimal fits to Einasto profiles (magenta point-dashed lines) and JS profiles (green dashed lines).

are plot versus the radii normalized to virial radii (Figure 5.10). We see that there is a clear mass effect at the inner regions, with the stellar mass distribution relative to the dark mass one less concentrated with increasing ELO mass. For example, in Figure 5.10 we see that the fraction of the ELO virial volume where $f^{\rm star}(r) > 1$, is smaller as the ELO mass grows; also, at fixed $r/r_{\rm vir}$, $f^{\rm star}(r)$ increases with decreasing ELO mass. So, the homology is broken in the three-dimensional stellar-to-dark mass distribution, a fact that could be important to explain the tilt of the observed FP (see Section 6.2.

To further analyze this point and make the comparison with observational results easier, the dark-to-stellar mass ratio profiles, $M^{\rm dark}(r)/M^{\rm tot}(r)$, are drawn in Figure 5.11 for the same ELOs, with the radii in units of the three dimensional stellar half-mass radii, $r^{\rm star}_{\rm e,bo}$. We see that there is, in any case, a positive gradient, and again a clear mass effect, with a tendency of the dark matter fraction at fixed values of $r/r^{\rm star}_{\rm e,bo}$ to be higher

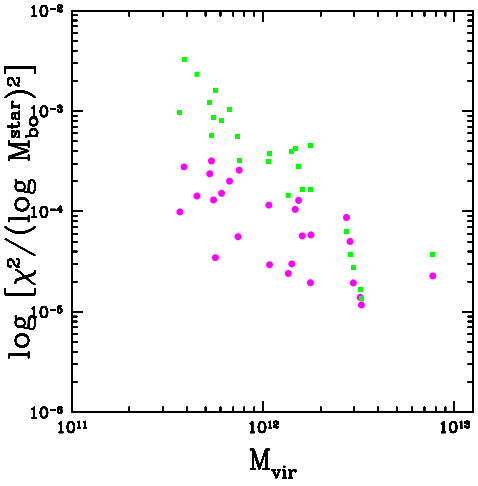

Figure 5.9: The χ^2 statistics (Eq. 4.12) corresponding to the fits of the stellar mass profiles for ELOs in the *EA*-Z0 sample Einasto profiles (magenta filled circles) and JS profiles (green filled squares).

as the mass scale increases. To be more quantitative and compare with observational data, we plot in Figure 5.12, left panel, the mean fraction of dark-to-total projected masses at $R/R^{\rm star}_{\rm e,bo} = 1$ for ELOs in the *EA*-Z0 and *EB*-Z0 samples, versus their stellar masses. We have computed this value for one hundred random projections. The error bars in the plot represent the dispersion over all these values. The differences among results for both samples come from the smaller $R^{\rm star}_{\rm e,bo}$ values of *EB*-Z0 sample ELOs as compared with their *EA*-Z0 counterparts (see discussion in Section 5.4). Green triangles with error bars are results from integral field SAURON data and models by Cappellari et al. (2006). We see that these empirical determinations of the dark matter fraction at the center of ellipticals are consistent with the values found in ELOs of both samples, including its growth with the mass scale.

In the right panel of Figure 5.12 we give the gradients of the $M^{\rm dark}_{\rm cyl}(R)/M^{\rm star}_{\rm cyl}(R)$ profiles $\nabla_{\rm l}\Upsilon$:

$$\nabla_{\rm l}\Upsilon = \frac{R^{\rm star}_{\rm e,bo}}{(R^{\rm out} - R^{\rm in})} \left(\frac{M^{\rm dark}_{\rm cyl}(R^{\rm out})}{M^{\rm star}_{\rm cyl}(R^{\rm out})} - \frac{M^{\rm dark}_{\rm cyl}(R^{\rm in})}{M^{\rm star}_{\rm cyl}(R^{\rm in})} \right) \tag{5.2}$$

as a function of their stellar masses. Green triangles with error bars are the empirical mass-to-light gradients as determined by Napolitano et al. (2005) for EGs with isophotal shape $a_4 \times 100 < 0.1$, that is, boxy ellipticals. We have used as inner and outer radii $R^{\rm in}/R^{\rm star}_{\rm e,bo} = 0.5$ and $R^{\rm out}/R^{\rm star}_{\rm e,bo} = 4$, roughly the average values of the inner and outer radii these authors give in their Table 1.

We see that there is a mass effect and that our results are consistent with those found by these authors in the range of stellar mass values our samples span, especially when

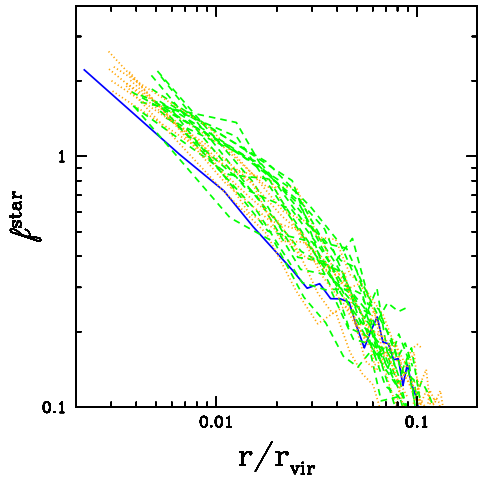

Figure 5.10: The stellar-to-dark mass density profiles for ELOs in the *EA*-Z0 sample: green dashed lines, ELOs with $M_{\rm vir} < 1.5 \times 10^{12}$ M$_\odot$; orange point lines, ELOs with 1.5×10^{12} M$_\odot \leq M_{\rm vir} < 5 \times 10^{12}$ M$_\odot$; blue full lines: ELOs with $M_{\rm vir} \geq 5 \times 10^{12}$ M$_\odot$.

we consider that ELOs in our *EA*-Z0 and *EB*-Z0 samples are boxy (see Section 5.3.2). A SF effect in the stellar mass distribution also appears in Figure 5.12, again due to the compactness of the *EB*-Z0 sample ELOs relative to their *EA*-Z0 sample counterparts.

We now turn to analyze the baryon space distribution at halo scales. To have an insight on how baryons of any kind are distributed relative to the dark matter at the halo scale and beyond, the baryon fraction profile

$$f^{\rm bar}(r) = \rho^{\rm bar}(r)/\rho^{\rm tot}(r), \tag{5.3}$$

where "bar" stands for baryons of any kind (i.e., stars, cold gas and hot gas) and "tot" stands for matter of any kind (i.e., dark plus baryons of any kind), is drawn in Figure 5.13 for ELOs in the *EA*-Z0 sample (red full lines) and in the *EB*-Z0 sample (blue dashed lines) in the same range of virial mass, 1.5×10^{12}M$_\odot \leq M_{\rm vir} < 5 \times 10^{12}M_\odot$. Despite individual characteristics, the $f^{\rm bar}(r)$ curves show a typical pattern in which their values are high at the center, then they decrease and have a minimum lower than the global value, $f^{\rm bar}_{\rm cosmo} \equiv \Omega_b/\Omega_m = 0.171$, at a radius $r^{\rm bar}_{\rm min}$, then they increase again, reach a maximum value and then they decrease and fall to the $f^{\rm bar}_{\rm cosmo}$ value at a rather large r value, larger than the corresponding virial radii. This result, i.e., that EGs are not baryonically closed, is also indicated by recent X-ray observations (Humphrey et al., 2006). Notice (Figure 5.14) that the increase of $f^{\rm bar}(r)$ at $r > r^{\rm bar}_{\rm min}$ is mainly contributed by hot gas, almost absent at $r < r^{\rm bar}_{\rm min}$, indicating that $r^{\rm bar}_{\rm min}$ separates the (inner) region where gas cooling has been possible from the (outer) region where gas has not had time enough to cool in the ELO lifetime. Note also in Figure 5.14 that an

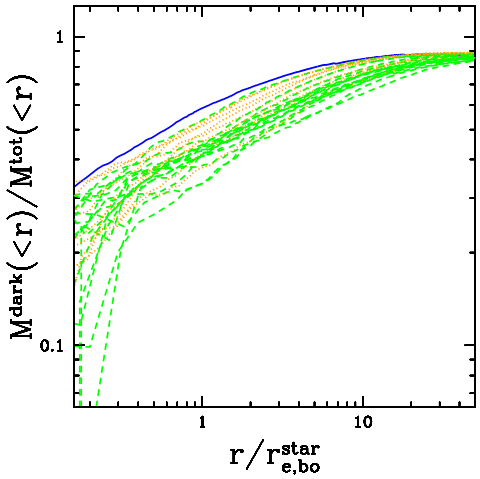

Figure 5.11: The fraction of dark-to-total mass profiles, $M^{\rm dark}(<r)/M^{\rm tot}(<r)$ for ELOs in the *EA*-Z0 sample; green dashed lines, ELOs with $M_{\rm vir} < 1.5\times10^{12}$ $M_\odot$; orange point lines, ELOs with 1.5×10^{12} $M_\odot \leq M_{\rm vir} < 5\times10^{12}$ $M_\odot$; blue full lines: ELOs with $M_{\rm vir} \geq 5\times10^{12}$ $M_\odot$. Radii are normalized to the 3D stellar half-mass radii.

important amount of hot gas is outside the spheres of radii $r_{\rm vir}$, that is, it is not bound to the self-gravitating configuration defined by the ELO halo. In fact, the mass of hot gas increases monotonically up to $r \simeq 4r_{\rm vir}$, and maybe also beyond this value, but it is difficult at these large radii to properly elucidate whether or not a given hot gas mass element belongs to a given ELO or to another close one (to alleviate this difficulty, only those ELOs not having massive neighbors within radii of $6\times r_{\rm vir}$ have been considered to draw this Figure). Another important result is that the hot gas mass fraction, relative to the cold mass fraction at the ELO scale, increases with $M_{\rm vir}$ at given $r/r_{\rm vir}$, and the differences between massive and less massive ELOs can be as high as a factor of ~ 2 at $r/r_{\rm vir} < 4$. We see that, in massive ELOs, this excess of baryons in the form of hot gas at the outer parts of their configurations, compensates for the lack of baryons in the form of stars at the ELO scales.

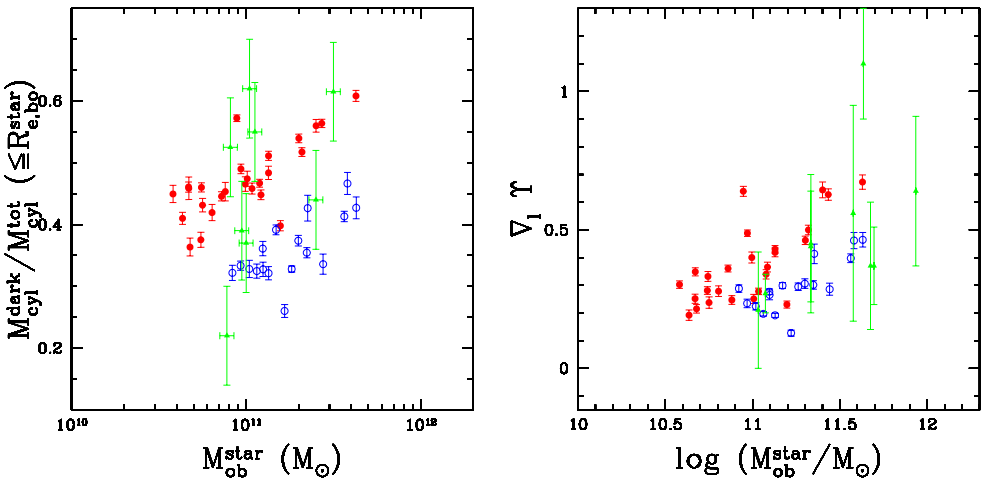

Figure 5.12: Left: the fraction of dark-to-total mass at $R/R^{\rm star}_{\rm e,bo} = 1$ versus the ELO stellar masses. Red filled (blue open) symbols: ELOs in *EA*-Z0 (*EB*-Z0) sample. Error bars account for projection effects. Green filled triangles are the values corresponding to the SAURON sample of ellipticals. Right: the gradients of the $M^{\rm dark}_{\rm cyl}(R)/M^{\rm star}_{\rm cyl}(R)$ profiles as a function of their stellar masses; green triangles with error bars are the empirical mass-to-light gradients as determined by Napolitano et al. (2005) for galaxies with the $a_4 \times 100$ shape parameter lower than 0.1 (that is, for boxy ellipticals).

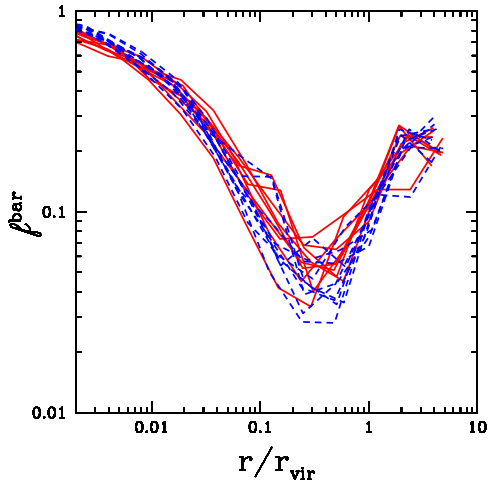

Figure 5.13: Baryon fraction profiles for ELOs in *EA*-Z0 sample (red full lines) and *EB*-Z0 sample (blue dashed lines), in the same range of virial mass, $1.5 \times 10^{12}{\rm M}_\odot \leq M_{\rm vir} < 5 \times 10^{12}{\rm M}_\odot$.

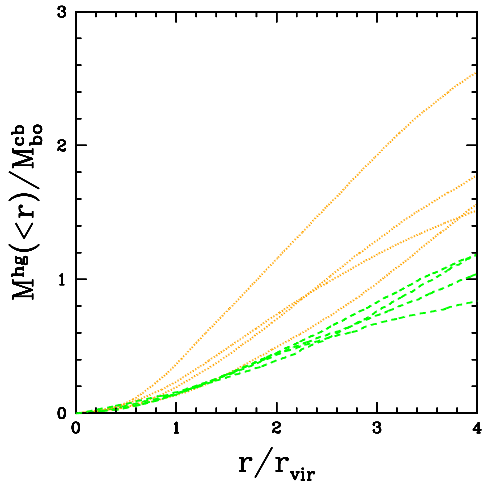

Figure 5.14: The $M^{\rm hg}(< r)/M^{\rm cb}_{\rm bo}$ profiles for typical ELOs. $M^{\rm hg}(< r)$ is the mass of hot gas within a sphere of radius r. Orange point lines: ELOs with $1.5 \times 10^{12} \leq M_{\rm vir} < 5 \times 10^{12}{\rm M}_{\odot}$; green dashed lines: ELOs with $M_{\rm vir} < 1.5 \times 10^{12}{\rm M}_{\odot}$. Only isolated ELOs have been considered.

5.2.5 Total Three-Dimensional Mass Density Profiles

We now address the issue of the total mass (i.e., baryonic plus dark) density profiles. In Figure 5.15 they are drawn for ELOs in the *EA*-Z0 sample (upper panel) as well as for those in the *EB*-Z0 sample (lower panel). In both cases, the profiles corresponding to ELOs in different mass intervals have been drawn with different line and color codes. Some important results are that i), they are well fit by power-law expressions $\rho^{\rm tot}(r) \propto r^{-\gamma}$ in a range of $r/r_{\rm vir}$ values larger than two decades, ii), the slope of the power-law increases with decreasing ELO mass, and, iii) a slight SF effects appears, but only at the very inner regions, with *EB*-Z0 sample ELOs showing a worse fit to a power law than their *EA*-Z0 counterparts. Koopmans et al. (2006) have also found that the total mass density profiles of their massive ($< \sigma_{\rm ap} >= 263$ km s^{-1}) lens EGs can be fit by power-law expressions within their Einstein radii ($< R_{\rm Einst} >= 4.2 \pm 0.4$ kpc, with $< R_{\rm Einst}/R_{\rm e}^{\rm light} >= 0.52 \pm 0.04$, i.e., the inner region), whose average slope is $< \gamma >= 2.01^{+0.02}_{-0.03} \pm 0.05$ (68 percent C.L.), with an intrinsic scatter of 0.12. These results, i.e., that all the components combine to make almost an isothermal profile, have been confirmed for early-type galaxies up to $r \leq 100$ kpc by Gavazzi et al. (2007). To elucidate how well the total mass density profiles of ELOs compare with these results, in Figure 5.16 we plot the slopes γ for ELOs, as well as for SLACS lens ellipticals (Table 1, Koopmans et al., 2006), versus their central L.O.S. stellar velocity dispersions. The fitting range for ELOs used to draw this Figure is $r < r^{\rm star}_{\rm 90,bo}$. Same trends are obtained using $r^{\rm star}_{\rm e,bo}$ or $r_{\rm vir}$ but for slightly higher or lower values of γ respectively. We see that results for ELO and SLACS lens galaxy samples are consistent in the range of velocity dispersion values where they coincide.

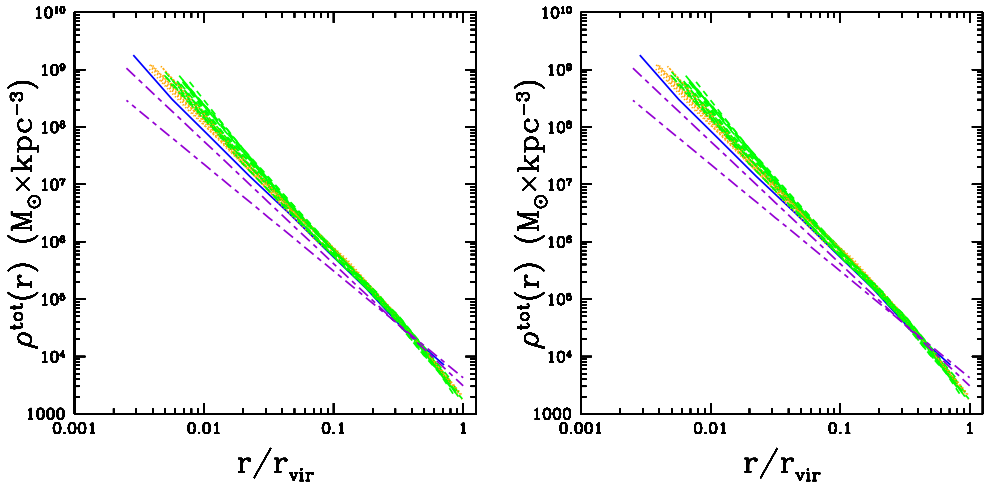

Figure 5.15: The total mass density profiles for ELOs in the *EA*-Z0 sample (up) and in the *EB*-Z0 sample (down). Green dashed lines: ELOs with $M_{\rm vir} < 1.5 \times 10^{12} {\rm M}_\odot$; orange point-dashed lines: ELOs with $1.5 \times 10^{12} {\rm M}_\odot \leq M_{\rm vir} < 5 \times 10^{12}$ ${\rm M}_\odot$; blue full lines: ELOs with $5 \times 10^{12} {\rm M}_\odot \leq M_{\rm vir}$. The violet long-dashed lines are the one sigma interval for the slope resulting from fits to power-law profiles of lens ellipticals from Koopmans et al. (2006).

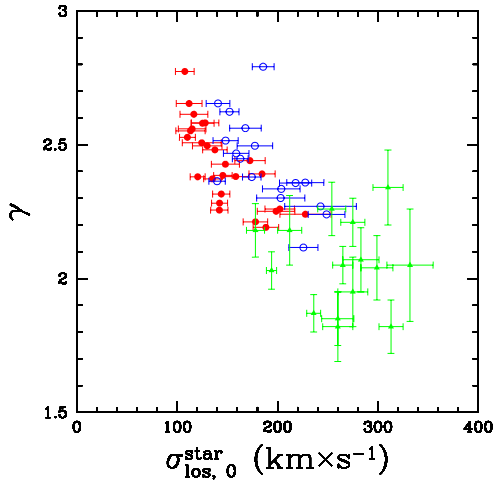

Figure 5.16: The logarithmic slopes corresponding to the total mass density profiles for ELOs in the *EA*-Z0 (red filled circles) and the *EB*-Z0 samples (blue open circles), versus their central L.O.S. stellar velocity dispersions. Green triangles with error bars correspond to data on SLACS lens ellipticals, as given in Table 1 of Koopmans et al. (2006).

5.2.6 Projected Stellar Mass Density Profiles

There has been a recent consensus on the applicability to virtually all elliptical galaxies of the Sérsic law to characterize their photometric properties (see Section 3.2). We have built a fitting method trying to mimic as much as possible the observational techniques (see Section 4.5) and we want to check if $\Sigma^{\rm star}(R)$ can be fitted by a Sérsic-like law comparing our results with observational data. This is in fact the case as shown in Figure 5.17 for several typical ELOs drawn from both *EA*-Z0 and *EB*-Z0 samples (see Kawata & Gibson, 2005, for a similar result concerning one virtual elliptical galaxy). We would deepen into the different relations between all these fundamental parameters in the next Chapter 6.3.

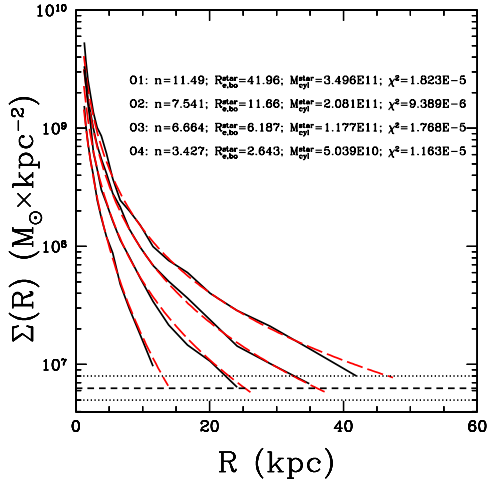

Figure 5.17: Projected stellar mass density profiles for different ELOs (black full line) along with their best fit by a Sérsic law (red long dashed). The corresponding shape parameter best values and minimal χ^2 per-degree-of freedom are also shown. The short dashed line stands for the geometric mean $\gamma_B^{\rm star} = 6.3$ used to calculate the outer boundary R_{27}. Dotted lines stand for the lower and higher limits of $\gamma_B^{\rm star}$.

As a test to check the consistency of the fits, we have compared the projected effective radii, $R_{\rm e,bo}^{\rm star}$, and the stellar mass, $M_{\rm cyl,bo}^{\rm star}$, obtained from the different fits versus the ones obtained directly from the profiles and find very similar results. We also checked that fixing the mass by boundary conditions and leaving just two free parameters (n and $R_{\rm e,bo}^{\rm star}$) gave us very similar results and trends. On the other side, using a de Vaucouleurs (1948) analytical profile (fixing $n = 4$) produced much poorer fits. In addition, we have checked the robustness of our method testing how all the different input variables that are used affect to the final fit. These tests have confirmed all our results and that all the different trends we found do not disappear. However, in order to compare with observational data we found that the outer and inner boundaries $R_{\rm max}$ and $R_{\rm min}$ are the most important parameters for the fit. As $R_{\rm max}$ increases, the shape parameter n

also shows a softly increase. However as long as the object is well defined up to the $R_{\rm max}$ (no satellites, bumps, etc.) increasing this radius in a $\sim 150\%$ produces just a $\sim 4\%$ increase in the different parameters of the fit. Moreover, concerning the comparison with observations, we can see in Figure 5.17 that the particular $\gamma_B^{\rm star}$ value used within its range of best values (dotted lines in Figure 5.17) produce very similar R_{27} results. Therefore these three different fits produce very similar results with a lower dispersion than the one produced just from projection effects.

5.3 Kinematic Profiles

Shapes and mass density profiles (i.e., positions) are related to the 3D velocity distributions of relaxed E galaxies through the Jeans equation (see Binney & Tremaine, 1987). Observationally, the information on such 3D distributions is not available for external galaxies, only the line-of-sight velocity distributions (LOSVD) can be inferred from their spectra. They have been found to be close to gaussian (Binney & Tremaine, 1987; van der Marel & Franx, 1993), so that simple equilibrium models can be expected to adequately describe their dynamical state (de Zeeuw & Franx, 1991). The complete six dimensional phase space information for each of the particles sampling the ELOs provided by numerical simulations, allow us to calculate the velocity profiles, $V_{\rm cir}(r)$, the 3D profiles for the velocity dispersion, $\sigma_{\rm 3D}(r)$, and their corresponding anisotropy profiles. These profiles, as well as the LOS velocity $V_{\rm los}(R)$ and LOS velocity dispersion $\sigma_{\rm los}(R)$ profiles, are analyzed in detail in this section. All the main algorithms used to compute each of these quantities are described in Section 4.5

5.3.1 Three-Dimensional Velocity Distributions

The complete six dimensional phase space information for each of the particles sampling the ELOs provided by numerical simulations, allow us to calculate the 3D profiles for the velocity dispersion, $\sigma_{\rm 3D}(r)$, as well as the circular velocity profiles, $V_{\rm cir}(r)$. In Figure 5.18 we draw the $V_{\rm cir}(r)$ profiles (full line), as well as their dark matter (short-dashed line) and baryonic contributions (stars, long-dashed line; stars plus cold gas, point line).

The $V_{\rm cir}(r)$ profiles provide another measure of ELO mass distribution. We note in Figure 5.18 that the baryon mass distribution is more concentrated than the dark matter one due to energy losses by the gaseous component before being transformed into stars. This is a general property of the circular velocity profiles of the ELO samples. Moreover, objects in *EB*-Z0 sample are more concentrated than their *EA*-Z0 sample counterparts, because of the SF implementation: the amount of baryons at their central volumes relative to dark matter is always lower in *EA*-Z0 than in *EB*-Z0 objects; this is a small scale effect as $r \sim 30$ kpc or $r \sim 40$ kpc radii enclose roughly similar amounts of baryons or dark matter in any cases.

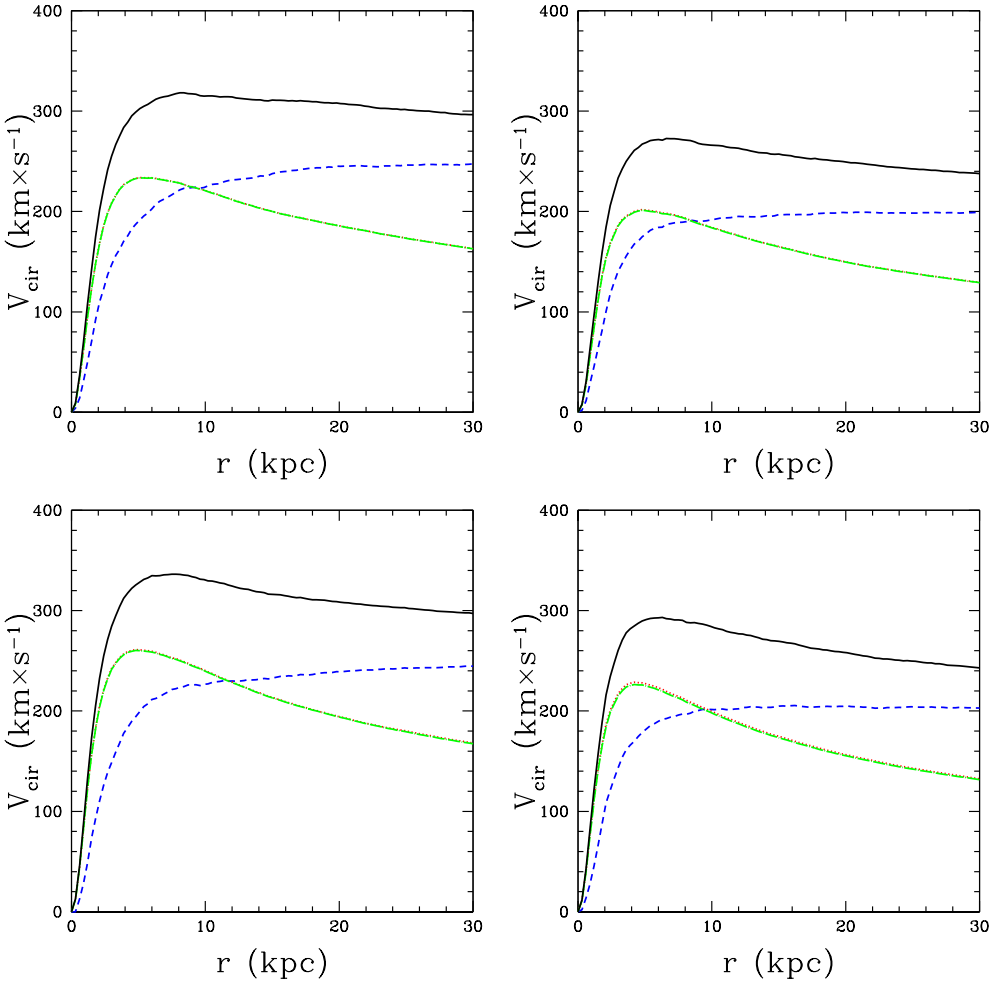

Figure 5.18: The circular velocities profiles of two typical ELOs in the *EA*-Z0 sample (upper panels) and their *EB*-Z0 sample counterparts (lower panels). Black full line: total mass; blue short-dashed line: dark matter contribution; green long-dashed line: stellar mass contribution; red point line: cold baryon contribution.

In Figure 5.19 we draw, for the same ELOs, the $\sigma_{3D}(r)$ profiles as measured by stars, ($\sigma_{3D}^{star}(r)$, starred symbols and short-dashed lines), and by dark matter, ($\sigma_{3D}^{dark}(r)$, open circles and long-dashed lines) as proof particles in the overall potential well. These profiles are in any case decreasing outwards, both for the dark matter and for the stellar components. An outstanding result illustrated by Figure 5.19 is that $\sigma_{3D}^{dark}(r)$ is always higher than $\sigma_{3D}^{star}(r)$ (because stars are made out of cooled gas), with $\sigma_{3D}^{star}(r)/\sigma_{3D}^{dark}(r) \sim 0.8$, in consistency with the values found by Loewenstein (2000) on theoretical grounds and by Dekel et al. (2005) from pre-prepared simulations of mergers of disc galaxies. This is the so-called kinematical segregation (Sáiz et al., 2003, 2004).

This is so because stars are formed from gas that had lost energy by cooling. This result on kinematical segregation is very interesting because it has the implication that

the use of stellar kinematics to measure the total mass of ellipticals could result into inaccurate values

To further analyze this issue, in Figure 5.20 we plot the $\sigma_{3D}^{\rm star}(r)/\sigma_{3D}^{\rm dark}(r)$ ratios for the ELOS in both the *EA*-Z0 sample and in the *EB*-Z0 sample, with different color and line codes depending on the ELO mass range. We see that the kinematical segregation does not show either a clear mass dependence, or a radial dependence. Moreover, the SF parameterization effect is only mild.

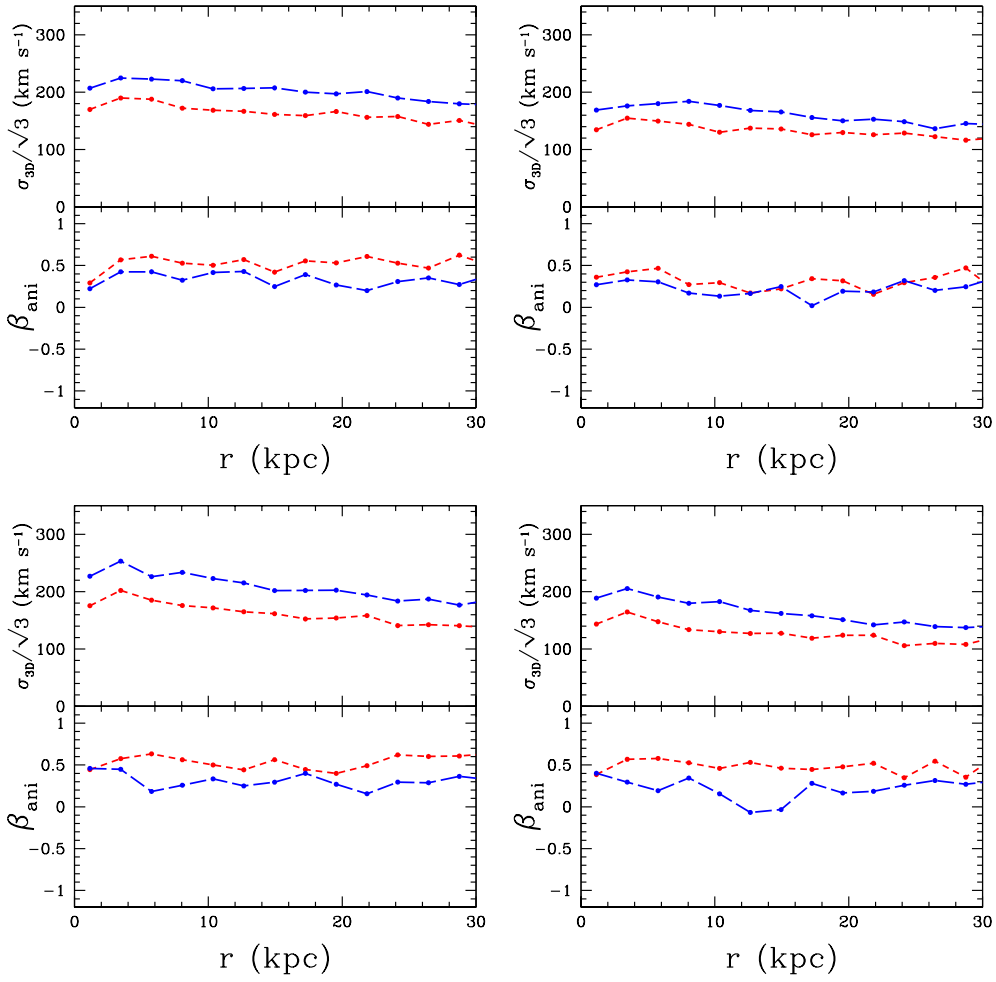

Figure 5.19: The $\sigma_{3D}(r)$ profiles of two typical ELOs in the *EA*-Z0 sample (upper panels) and their *EB*-Z0 sample counterparts (lower panels). Also shown are the anisotropy profiles $\beta_{\rm ani}(r)$. Blue long-dashed lines: dark matter; red short-dashed lines: stars.

The anisotropy profile, $\beta_{\rm ani}(r)$, is also represented in Figure 5.19 for typical ELOs in the sample, for their dark matter and stellar particle components. The anisotropy is always positive (i.e., an excess of dispersion in radial motions), the profiles are almost constant, except at the innermost regions, and the stellar component is always more anisotropic than the dark matter one, presumably as a consequence of the mergers

involved in the ELO mass assembly (see Section 9.2). In fact, the characteristics of the stellar anisotropy profiles (roughly constant and $\beta_{\rm ani}^{\rm star}(r) \simeq 0.5$ in most cases) are consistent with those found by Dekel et al. (2005), where they conclude that large radial anisotropy is generic to the stellar component of merger remnants of any kind.

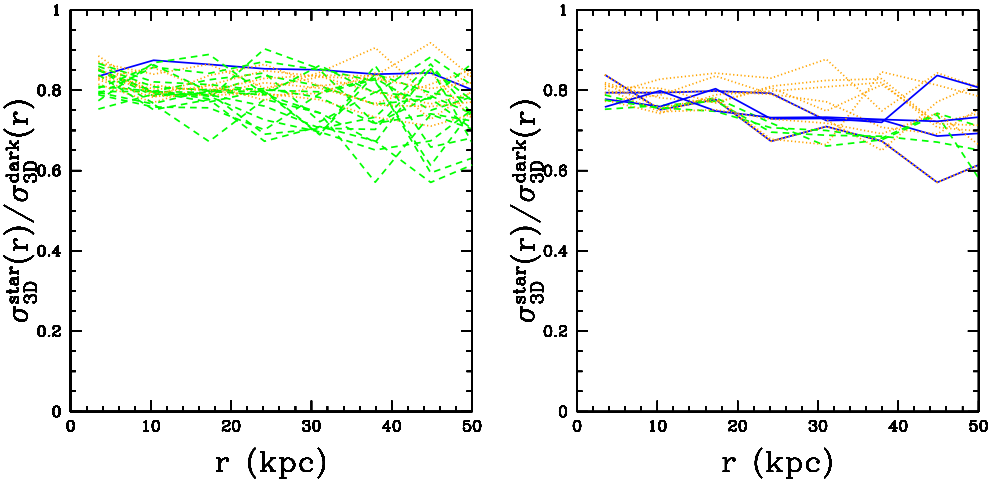

Figure 5.20: The $\sigma_{3D}^{\rm star}(r)/\sigma_{3D}^{\rm dark}(r)$ ratio profiles for ELOs in *EA*-Z0 (upper panel) and *EB*-Z0 (lower panel) samples. Different color and line codes stand for ELO mass intervals, as in Figure 9.

5.3.2 Stellar LOS Velocity and Velocity Dispersion Profiles

Figure 5.19 provide an illustration of the general characteristics of the lower-order moments of the 3D velocity distribution. The profiles plot in these Figures are not observationally available, but only the lower-order moments of the LOSVD are. We have measured the stellar line-of-sight velocity and the stellar velocity dispersion profiles, $V_{\rm los}^{\rm star}(R)$ and $\sigma_{\rm los}^{\rm star}(R)$, along one hundred random projections for all ELOs (see details in 4.5). Studying these stellar line-of-sight velocity profiles we have found that in some cases ELOs do indeed show a clear rotation curve, while in most cases the rotation is only modest or even very low, as illustrated in Figure 5.21.

We now comment on the major axis LOS stellar velocity dispersion profiles of ELOs (Figure 5.21). Their most outstanding feature is the decrease of the $\sigma_{\rm los}^{\rm star}(R)$ profiles in some cases and particularly so along some LOS directions at large R. These profiles are suited to compare with stellar kinematics data. In other cases, for example to compare with planetary nebulae data, the LOS velocity dispersion profiles must be calculated by averaging over the LOS velocities of stars placed within cylindrical shells, with their axes in the LOS direction. Figure 5.22 is a plot of such profiles normalized to $\sigma_{\rm los}^{\rm star}(R_{\rm e,bo}^{\rm star})$ for the *EA*-Z0 sample ELOs; each panel corresponds to a different orthogonal projection.

To make clearer the decline of the $\sigma_{\rm los}^{\rm star}(R)$ profiles, in Figure 5.23 we plot, at different

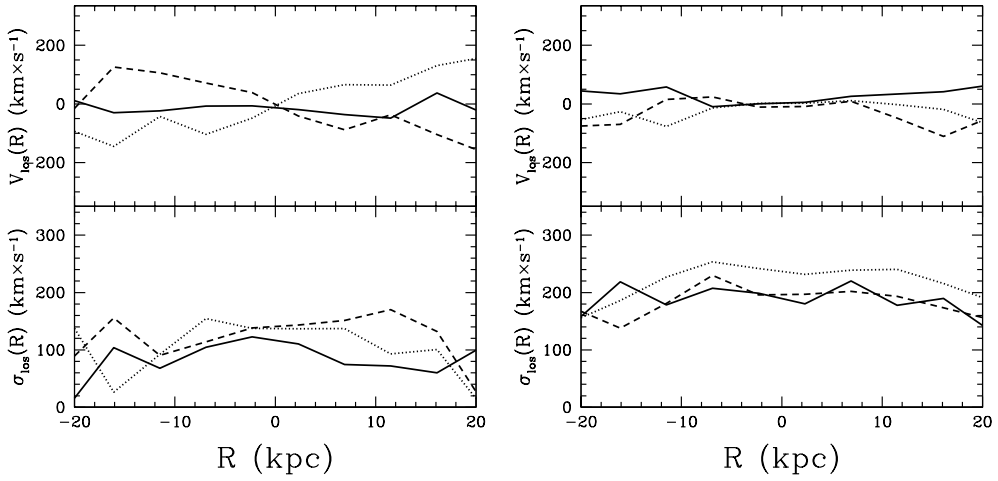

Figure 5.21: Left panel: Full line: the major axis stellar LOS velocity profile along the spin direction for an ELO in *EA*-Z0 sample. Point and dashed lines: same as the continuous line taking the LOS direction normal to the ELO spin vector. This particular ELO rotates. Right panel: Same as the left panel for another ELO. In this case, the rotation is only mild.

R values, the averages of the stacked profiles shown in Figure 5.22 with their dispersions (green points and error bars), as well as the averages of the profiles corresponding to young stars (age ≤ 3 Gyears, orange squares and error bars), normalized for each ELO to their corresponding $\sigma_{\rm los}^{\rm star}(R_{\rm e,bo}^{\rm star})$. The decline of these velocity dispersion profiles can be clearly appreciated, as well as the slightly larger decline of the profiles corresponding to the younger stellar populations. These results are consistent, within their dispersions, with that shown by Dekel et al. (2005) in their figure 2 (lower panel). They are also marginally consistent with the decline shown by PN data in the NGC 821, NGC 3379, NGC 4494 and NGC 4697 galaxies (Romanowsky et al., 2003; Romanowsky, 2006). Note, however, that our ELOs are boxy, while the $a_4 \times 100/a$ shape parameters for these galaxies are 2.5, 0.2, 0.3 and 1.4, respectively, that is, they are rather disky ellipticals.

5.3.2.1 Some Details About the Rotation of ELOs

To quantify the amount of rotation in ELOs and its possible dependence on the mass scale, in Figure 5.24 we plot the ratios $c_{\rm rot} = V_{\rm min}/(V_{\rm maj}^2 + V_{\rm min}^2)^{1/2}$ as a function of the ELO virial masses, for ELOs in both the *EA*-Z0 and the *EB*-Z0 samples ($V_{\rm maj}$ and $V_{\rm min}$ are the maximum values of the $V_{\rm los}^{\rm star}(R)$ profile when measured along the major and the minor axes, respectively). When the ELO shows a clear rotation curve, $V_{\rm min}$ is much lower than $V_{\rm maj}$, and the $c_{\rm rot}$ ratio is low; by contrast, when the rotation is unimportant, then $V_{\rm min} \simeq V_{\rm maj}$ and $c_{\rm rot} \sim 0.7$. For a given ELO, the $c_{\rm rot}$ value depends

on the direction taken as LOS direction, in such a way that it is maximum when the ELO spin is taken as LOS direction, and minimum when the LOS direction is normal to the ELO spin vector, that is, when rotation stands out. This is the LOS direction taken to draw this Figure, where we see that there is not a clear mass dependence, that most ELOs are in between the two situations described above and that the values of the $c_{\rm rot}$ ratio of ELOs are typical of boxy ellipticals (see, for example, Binney & Tremaine, 1987, figure 4.39). A detailed study of the rotation of different sample ELOs at $z = 0$ and its relation with shape can be found in Chapter 7.

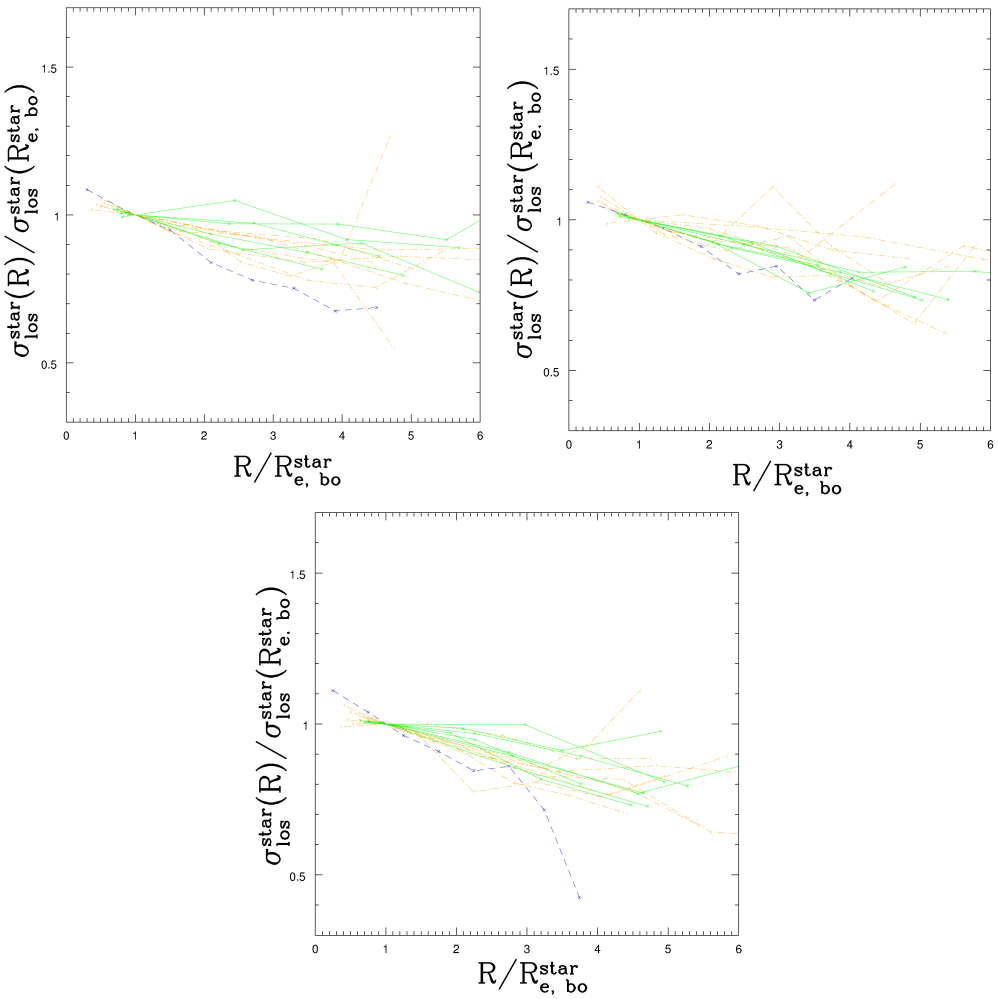

Figure 5.22: LOS velocity dispersion velocity profiles along three different orthogonal projections for ELOs in *EA*-Z0 sample up to 6 effective radii. The profiles are normalized to their value at $R^{\rm star}_{\rm e,bo}$ for each ELO. Green full lines: ELOs with $M_{\rm vir} < 1.5 \times 10^{12} {\rm M}_{\odot}$; orange point-dashed lines: ELOs with $1.5 \times 10^{12} {\rm M}_{\odot} \leq M_{\rm vir} < 5 \times 10^{12}$ ${\rm M}_{\odot}$; blue dashed lines: ELOs with $5 \times 10^{12} {\rm M}_{\odot} \leq M_{\rm vir}$.

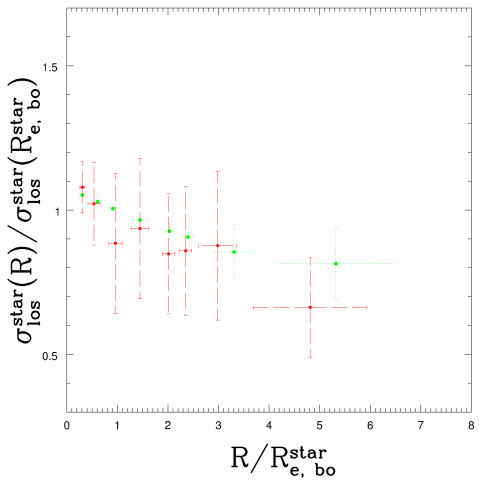

Figure 5.23: The *EA*-Z0 sample average LOS velocity dispersion profiles normalized to their values at $R^{\rm star}_{\rm e,bo}$ for each ELO (green points) along with their 1 σ dispersions. Orange points and error bars: the same for the young stellar particles, with the same normalization.

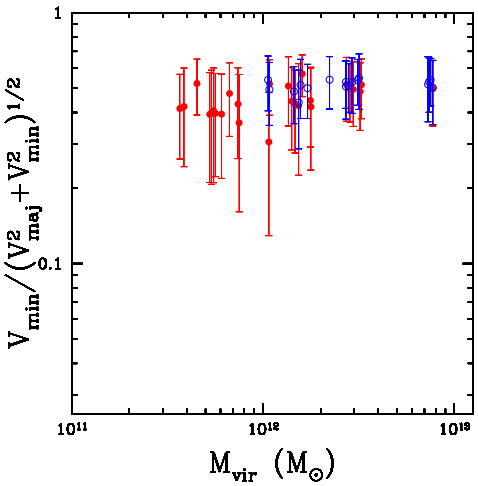

Figure 5.24: The $c_{\rm rot}$ ratios as a function of the virial mass for ELOs in the samples

5.4 Conclusions

In this Chapter we have presented an analysis of a set of samples of ELOs at $z = 0$, formed in different cosmological simulations. The information about position and velocity distributions of the ELO particles of different kinds (dark matter, stars, cold gas, hot gas) provided by the simulations, allows a detailed study of their intrinsic three dimensional mass and velocity distributions. We have reported on the three dimensional mass density, circular velocity and velocity dispersion profiles, as well as the projected stellar mass density profiles and the LOS velocity dispersion profiles.

The first step in the program of studying the origins of elliptical galaxies through self-consistent simulations, is to make sure that they produce ELO samples that have counterparts in the real local Universe. To answer to this question, we have compared along this chapter our virtual results with new observational data, obtaining a very satisfactory agreement. To be specific:

- The projected stellar *mass* profile, $\Sigma^{\rm star}(R)$, can be adequately fitted by a Sérsic-like law.
- The fraction of dark-to-total mass inside the projected half-mass radii are consistent with the observational ones obtained by Cappellari et al. (2006) from SAURON data.
- The gradients of the dark-to-stellar $M^{\rm dark}(< r)/M^{\rm star}(< r)$ profiles as a function of their stellar masses, are consistent with those observationally found by Napolitano et al. (2005) for boxy ellipticals.
- The total mass (i.e., baryonic plus dark) density profiles can be well fit by a power-law expression in a large range of $r/r_{\rm vir}$ values, with power-law slopes that are consistent with, within the dispersion, or slightly higher than those observationally found by Koopmans et al. (2006) for massive lens ellipticals within their Einstein radii.
- The line-of-sight velocity profiles along the major axis show, in some cases, a clear rotation, even if in most cases the rotation is modest or low. The values of the rotation ratio along the major and minor axis (a measure of the rotation in ELOs) does not depend on the mass scale
- The values spanned by the rotation ratios of ELOs are typical of boxy ellipticals.
- The line-of-sight velocity dispersion profiles, $\sigma_{\rm los}(R)$, decline outwards at large R, and the slope slightly increases when only the younger stellar populations are considered. These profiles are only marginally consistent with data on PNs at large radii; but these correspond to disky ellipticals while our virtual ellipticals are rather boxy.

These agreements with observational data strongly suggest that the intrinsic three-dimensional dark and bright matter mass and velocity distributions we get in our simulations might also adequately describe real ellipticals. We now summarize our most important findings on the study of the mass and velocity profiles of ELOs:

- ELOs are embedded in extended massive dark matter halos.
- The best fits of their spherically-averaged dark matter density profiles to usual analytical formulas (Hern90, NFW, TD, JS, Eina) are generally provided by the two last formulas. The quality of the fits is good, so that ELO halos form a two-parameter family where the two parameters are correlated. This is consistent with those produced in purely N-body simulations. The JS inner slope parameter, α, is always higher than the NFW value (α =1).
- The slope parameters grow as the ELO mass scale decreases, indicating that the halo concentration grows when the mass decreases.
- Halos have suffered from adiabatic contraction. This can be made quantitative by comparing the plot of the density at the Einasto scale, ρ_{-2}, versus the scale $r_{-2} = a_h$, with the plot provided by Navarro et al. (2004b, results of purely N-body simulations).
- At the ELO scale, most baryons have turned into stars. The three dimensional stellar-mass density profiles can be fit by Einasto or JS profiles, but with small r_{-2} values.
- The mass distribution homology is broken in the stellar mass as well as in the dark- versus bright-mass distributions, with the stellar mass distribution relative to dark mass one less concentrated with increasing ELO mass. That is, massive ELOs miss baryons at short scales as compared with less massive ones, when we normalize to the dark matter content. This result is consistent with the observational ones by Cappellari et al. (2006) from SAURON data, as well as by Napolitano et al. (2005) we quoted above.
- At the halo scale, the baryon fraction profiles have been found to show a typical pattern, where their values are high at the center, then they decrease and have a minimum roughly at $0.3 < r_{\rm min}^{\rm ab}/r_{\rm vir} < 0.7$, well below the global value, $\Omega_b/\Omega_m = 0.171$, then they increase again, reach a maximum value and then they decrease and fall to the global Ω_b/Ω_m value well beyond the virial radii $r_{\rm vir}$. This suggests that the baryons that massive ELOs miss at short scales (stars) are found at the outskirts of the configuration as diffuse hot gas. This result could reflect the presence of a stable virial shock that prevents gas infall more efficiently as mass increases (Dekel & Birnboim, 2006).

- Concerning kinematics, stellar and dark matter particles constitute a dynamically hot component with an important velocity dispersion. In addition, ELO velocity dispersion profiles in three dimensions are slightly decreasing for increasing r, both for dark matter and stellar particles, $\sigma_{3D}^{\rm dark}(r)$ and $\sigma_{3D}^{\rm star}(r)$.

- The dark and bright matter components of ELOs are cinematically segregated, as we have found that $(\sigma_{3D}^{\rm dark}(r))^2 \sim (1.4 - 2)\ (\sigma_{3D}^{\rm star}(r))^2$, confirming previous results (Sáiz et al., 2003; Loewenstein, 2000; Dekel et al., 2005). This is so because stars are formed from gas that had lost energy by cooling.

- This kinematical segregation does not show any clear mass or radial dependence.

- The anisotropy is always positive (i.e., an excess of radial motions) and almost non-varying with r inside the ELOs. Recall, however, that ELOs have been identified as dynamically relaxed objects: there are not recent mergers in the samples analyzed in this Chapter.

- The stellar component generally shows more anisotropy than the dark component, maybe derived from the radial motion of the gas particles that gave rise to the stars.

As we can see some of conclusions pointed above are really interesting and require further investigation. To this end, once we have analyzed the different structural and kinematical profiles of our ELOs, our next logical step has been to study the fundamental parameters that characterize them, their correlations and to try to make further comparisons with observations. In this Chapter we have already analyzed some of them, but in the next one we have delved deeper into this issue and tried to confirm some of the results pointed here.

Therefore, our final conclusions concerning the structure and kinematics of our simulated elliptical galaxies and detailed discussion on the robustness of the results presented here for a different cosmological model, resolution, box size, etc. can be found at the end of the next Chapter (Section 6.6).

Chapter 6

Ellipticals at z = 0: Fundamental Parameters[1]

6.1 Introduction

In the previous chapter we have studied the structural and kinematical profiles of our virtual ellipticals. We have analyzed these profiles and have given a qualitative description of their properties. In this Chapter we will use the different fundamental parameters that characterize the structural and kinematical properties of the simulated ellipticals at different scales, to give a more quantitative description of them, compare with real observations and to deepen into the origin of their observable relations.

This study has been done for all the different simulations discussed in 4.2. However for the sake of clarity, in this chapter, as well as in the previous one, we would first center our analysis on the *EA*-Z0 and *EB*-Z0 elliptical-like object (ELO) main samples. We discuss deeply the robustness of results and possible caveats between all the samples at the end of this chapter.

First, Section 6.2 is focused on the Fundamental Plane relation. Thereafter, in section 6.3 we examine the Photometric plane relation and their connection with the previous one. Section 6.4 describes the stellar age properties of our simulated ellipticals and their relation with the different structural and kinematical fundamental parameters. Section 6.5 includes different tests concerning the robustness of our main results. Summary and final conclusions can be found in the last Section (6.6).

[1]Based on Oñorbe, Domínguez-Tenreiro, Sáiz, Serna, & Artal (2005); Oñorbe, Domínguez-Tenreiro, Sáiz, Artal, & Serna (2006); Oñorbe, Domínguez-Tenreiro, & Sáiz (2006); González-García, Oñorbe, Domínguez-Tenreiro, & Gómez-Flechoso (2009)

6.2 Fundamental Parameters: The Fundamental Plane

In this Section we introduce most of the structural and kinematical fundamental parameters of our ELOs, and we deepen into the tightest observed relation among these parameters for elliptical galaxies: the Fundamental Plane (see Section 3.2 for a theoretical introduction to this issue).To help the reader, we remind that in Table 4.4 and Table 4.5 a list of the parameter names and symbols used in this thesis can be found.

6.2.1 Fundamental Parameters: Halo Scale

We have already seen in Section 4.4 that from a definition of a characteristic overdensity, we can obtain a characteristic radius, named the virial radius, $r_{\rm vir}$, which define the halo scale for each ELO. From this radius we can build characteristic masses, as the virial mass, $M_{\rm vir}$, for the total mass. We can also describe more mass scales associated to the different constituents considered here: dark matter, $M_{\rm h}^{\rm dark}$, baryons of any kind, $M_{\rm h}^{\rm dark}$, cold baryons (that is, cold gas particles with $T < 3 \times 10^4$ K and stellar particles), $M_{\rm h}^{\rm cb}$, stars, $M_{\rm h}^{\rm star}$, and hot gas (that is, gaseous particles with $T > 3 \times 10^4$ K), $M_{\rm h}^{\rm hg}$. Also, a measure of the compactness of the mass distribution for the different ELO constituents, at the halo scale, is given by their respective half-mass radii, or radii enclosing half the mass of these constituents within $r_{\rm vir}$; for example, the overall half-mass radii, $r_{\rm e,h}^{\rm tot}$, are the radii of the sphere enclosing $M_{\rm vir}/2$, the stellar half-mass radii $r_{\rm e,h}^{\rm star}$ enclose $M_{\rm h}^{\rm star}/2$ and so on. Concerning kinematics, the most significant velocity dispersion parameter for ELOs at the halo scale is $\sigma_{\rm 3,h}^{\rm tot}$, the average 3-dimensional velocity dispersion of the whole elliptical up to the virial radius, including both dark and baryonic matter.

In Figure 6.1 we plot the different correlations between the structural and kinematical fundamental parameters at the halo scale: $M_{\rm vir}$, $r_{\rm e,h}^{\rm tot}$ and $\sigma_{\rm 3,h}^{\rm tot}$. As expected from the virial theorem all of them show a very good correlation. We can see also that at the halo scale *EA* and *EB* samples do not present significant differences, indicating that at this scale the star formation algorithm is not really important. Note that the virial masses of ELOs have a lower limit of 3.7×10^{11} $\rm M_\odot$.

We now comment on length scales. As we have seen in Figure 6.1 the overall half-mass radius $r_{\rm e,h}^{\rm tot}$ are closely correlated to $M_{\rm vir}$. Concerning baryonic mass distributions, dissipation in shocks and gas cooling play now important roles to determine them. And so, the $r_{\rm e,h}^{\rm star}$ radii depend on how much energy was radiated before gaseous particles became dense enough to be turned into stars. This, in turn, depends on the mass scale, on the one hand, and, in a given mass range, on the values of SF parameters, on the other hand. And so, more massive ELOs tend to have larger $r_{\rm e,h}^{\rm star}$ radii and, in a given mass range, *EA*-Z0 sample ELOs tend to have larger $r_{\rm e,h}^{\rm star}$ radii than their *EB*-Z0 sample counterparts, because the SF implementation in the code demands denser gas to form stars in the later than in the former. This effect is more remarkable for sizes at the scale

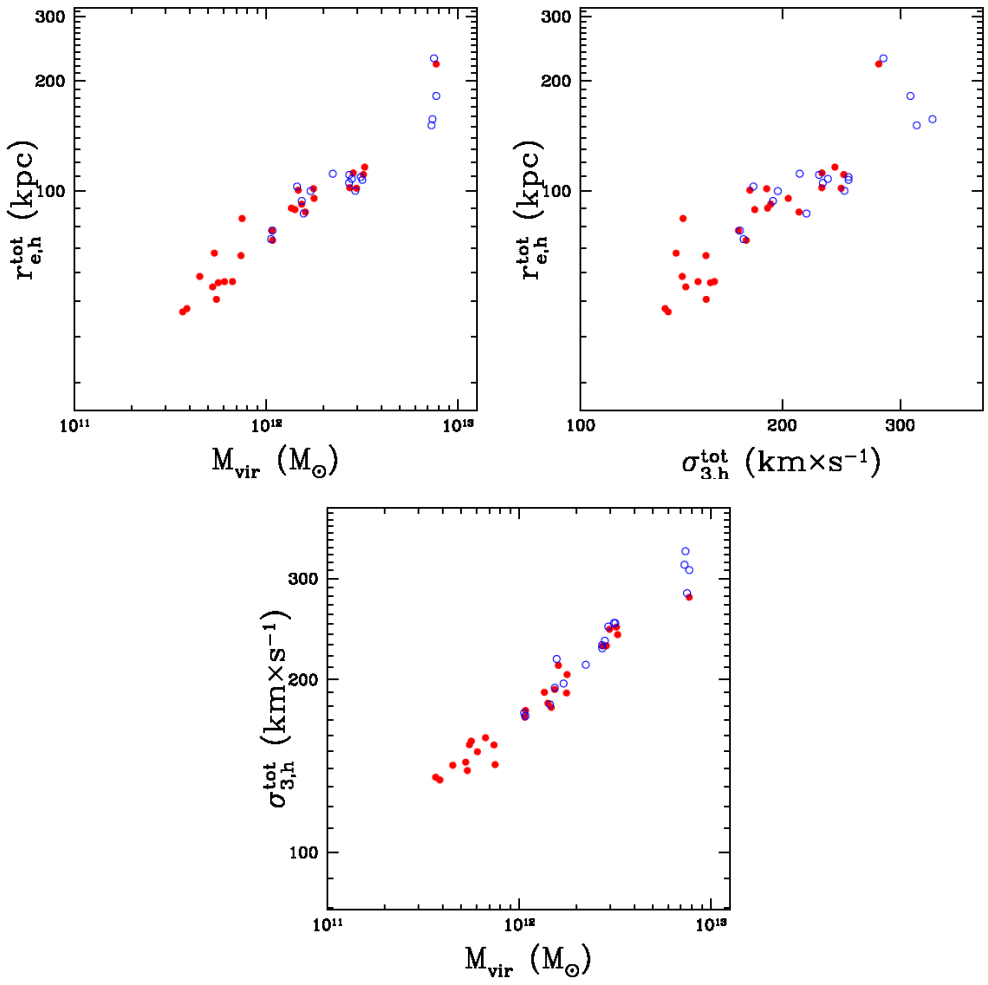

Figure 6.1: The different correlations between the structural and kinematical fundamental parameters at the halo scale: the virial mass, $M_{\rm vir}$, the overall half-mass radius, $r^{\rm tot}_{\rm e,h}$ and the total velocity dispersion, $\sigma^{\rm tot}_{\rm 3,h}$. Filled red symbols: *EA*-Z0 sample ELOs; open blue symbols: *EB*-Z0 sample ELOs.

of the baryonic object, as we shall see in the next subsection.

Concerning the different mass scales, all of them are strongly correlated with $M_{\rm vir}$ as shown in Figure 6.2(a) for $M^{\rm star}_{\rm h}$.

An important point is the amount of gas infall *relative* to the halo mass scale. As illustrated in Figure 6.2(b) for $M^{\rm cb}_{\rm h}/M_{\rm vir}$, any of the ratios $M^{\rm ab}_{\rm h}/M_{\rm vir}$, $M^{\rm cb}_{\rm h}/M_{\rm vir}$ or $M^{\rm star}_{\rm h}/M_{\rm vir}$ decreases as $M_{\rm vir}$ increases, as observationally found at smaller scales (see Chapter 3). Note that we have in any case $M^{\rm bar}_{\rm h}/M_{\rm vir} < \Omega_b/\Omega_m = 0.171$, the average cosmic fraction, so that there is a lack of baryons within $r_{\rm vir}$ relative to the dark mass content that becomes more important as $M_{\rm vir}$ increases. Otherwise, heating processes along ELO assembly give rise to a hot gas halo around the objects, partially beyond the virial radii. The amount of hot gas mass outside the virial radii, normalized to the ELO

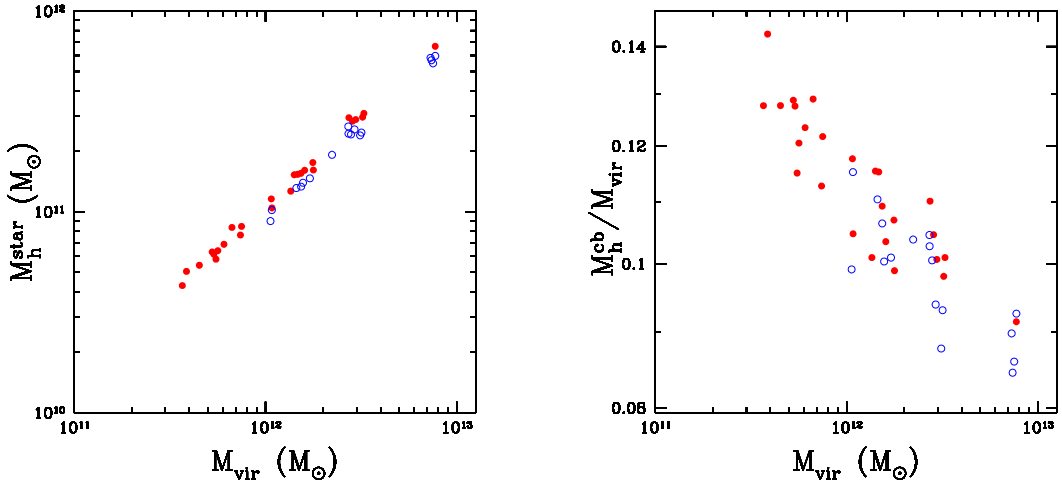

(a) (b)

Figure 6.2: a) Masses at the halo scale of stars versus their corresponding virial masses. b) Masses of cold baryons inside the virial radii in units of the corresponding virial mass for the ELO sample. Filled red symbols: *EA*-Z0 sample ELOs; open blue symbols: *EB*-Z0 sample ELOs.

stellar mass, $M_{\rm bo}^{\rm star}$ (see Section 6.2.2), increases with the mass scale. It also increases relative to the cold gas content at the halo scale.

We now turn again to the relation among the three main parameters that described the halo scale: the virial mass, $M_{\rm vir}$, the overall half-mass radius, $r_{\rm e,h}^{\rm tot}$ and the total velocity dispersion, $\sigma_{\rm 3,h}^{\rm tot}$. In Section 3.2 we have introduced the virial theorem (Eq. 3.4), that relates the characteristic mass, total velocity dispersion and a characteristic gravitational radius. We have chosen $r_{\rm e,h}^{\rm tot}$ as this characteristic gravitational radius.

To test that this is in fact the case, in Figure 6.3 we plot the $c_{\rm f} \equiv GM_{\rm vir}/(\sigma_{\rm 3,h}^{\rm tot})^2 r_{\rm e,h}^{\rm tot}$ form factors as a function of $M_{\rm bo}^{\rm star}$. The lack of any significant mass or SF parameterization effects in this Figure are quantitatively confirmed through a fit to power laws of the form $c_{\rm f} = A_{\rm f}(M_{\rm bo}^{\rm star})^{\beta_{\rm f}}$, whose results in Table 6.3 are consistent with $c_{\rm f}$ being independent of the ELO mass scale or SF parameter values. Note also that the $c_{\rm f}$ values are as expected (Binney & Tremaine, 1987) confirming the selection of $r_{\rm e,h}^{\rm tot}$ as the characteristic gravitational radius and that these three parameters define a plane: *The Virial Plane*.

6.2.2 Fundamental Parameters: Baryonic Object Scale

Let us now turn to the study of ELOs at the scale of the baryonic objects themselves, that is, at scales of some tens of kpcs (see Section 4.4). Physically, the mass parameter at the ELO scale is $M_{\rm bo}^{\rm cb}$, the total amount of cold baryons that have reached the central

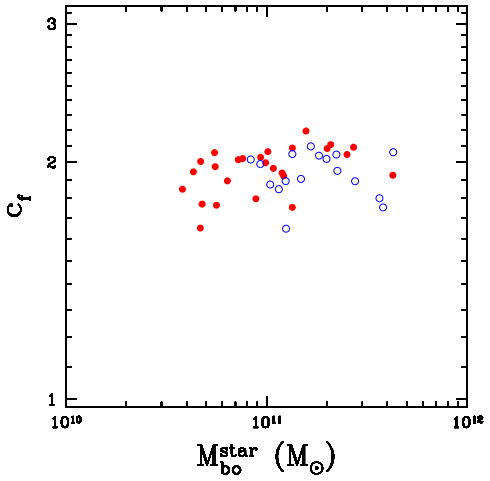

Figure 6.3: The $c_f \equiv GM_{vir}/(\sigma_{3,h}^{tot})^2 r_{e,h}^{tot}$ form factors (see Equation 3.4) versus the ELO mass scale. Symbols are as in previous Figures. This Figure confirms that $r_{e,h}^{tot}$ and $\sigma_{3,h}^{tot}$ are the size and velocity dispersion ELO parameters that must be used in the virial theorem.

volume of the halos, forming an ELO. Most of these cold baryons have turned into stars, depending on the strength of the dynamical activity in the volume surrounding the proto-ELO at high z, and, also, on the values of the SF parameters. Therefore the stellar mass, M_{bo}^{star}, can be used as a good characteristic mass scale for the baryonic object and have the great advantage of being a parameter largely obtained from luminosity data trough modeling (see, for example, Kauffmann et al., 2003b). Effective or half-mass radii at the baryonic object scale, $r_{e,bo}^{cb}$ and $r_{e,bo}^{star}$, can be defined as those radii enclosing half the M_{bo}^{cb} or M_{bo}^{star} masses, respectively.

To illustrate how the halo total mass, M_{vir}, determines the ELO structure at kpc scales, in Figures 6.4(a) and 6.4(b) we draw M_{bo}^{star} and $r_{e,bo}^{star}$ versus M_{vir}, respectively, for the ELO sample. A good correlation is apparent in Figure 6.4(a), where it is shown that ELO stellar masses are mainly determined by the halo mass scale, M_{vir}, with only a very slight dependence on the SF parameterization (*EA*-Z0 type ELOs have a slightly higher stellar content than their *EB*-Z0 counterparts, as expected). Figure 6.4(b) shows also a good correlation between the length scales for the stellar masses and M_{vir}, but now the sizes depend also on the SF parameters. The physical foundations of this behavior are the same as discussed in the previous section. Note that ELOs have a lower limit in their stellar mass content of 3.8×10^{10} $M_\odot$ (see Kauffmann et al., 2003a, for a similar result in SDSS early-type galaxies). Exactly the same trends with the virial mass are found for the cold baryon fundamental parametersM_{bo}^{cb} and r_{bo}^{cb}.

We now address the correlations of normalized mass and size scales. The increasing behavior of the M_{vir}/M_{bo}^{cb} and M_{vir}/M_{bo}^{star} ratios with increasing mass scale are very

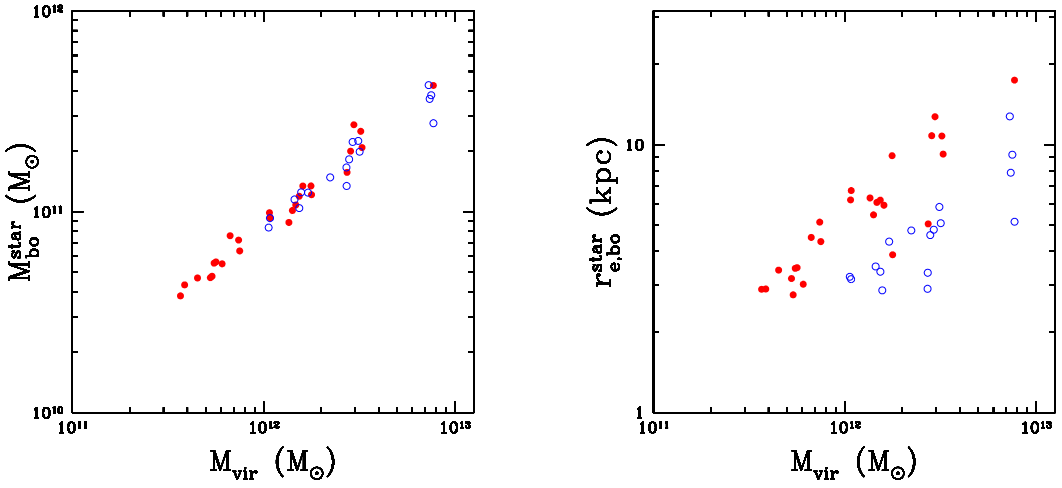

(a) (b)

Figure 6.4: a) Stellar masses at the baryonic object scale versus halo mass for the ELO sample. b) The 3D half-mass radii for stellar masses at the baryonic object scale versus halo mass for the ELO sample. Symbols are as in previous Figures.

interesting. In particular, the last ratio (Figure 6.5) follows the same trends as the empirical M_*/L versus L relation, see Bernardi et al. (2003b). The results of a fit to a power law of the form $M_{\rm vir}/M^{\rm star}_{\rm bo} = A_{\rm vir}(M^{\rm star}_{\rm bo})^{\beta_{\rm vir}}$ are given in Table 6.3, where we see that they do not depend on the SF parameterization. We would discuss more on this issue downwards.

To have an idea on how important cold baryon infall has been at the baryonic object scale relative to that at the halo scale, in Figure 6.6 the $M^{\rm cb}_{\rm h}/M^{\rm cb}_{\rm bo}$ ratios are drawn as a function of the ELO mass scale. We see that in any case more than half the mass of cold baryons inside the virial radii are concentrated in the central baryonic object, and that there is a mass effect in the sense that this fraction grows with decreasing ELO mass scale, and no appreciable SF effect.

Concerning kinematics, physically, a measure of the average dynamical state of stars in the ELO itself is provided by their mean square velocity relative to the ELO center of mass, or average three-dimensional velocity dispersion $\sigma^{\rm star}_{\rm 3,bo}$. All the significant parameters at the baryonic object scale are listed in Table 4.4.

In the last section it has been shown that the structural and kinematical parameters at the halo scale satisfy the virial relation. In the last section it has been shown that the mass, size and velocity dispersion parameters at the halo scale satisfy virial relations. This result is, however, at odds with the tilt of the observed FP of ellipticals discussed in 3.2, that involves the L, $R^{\rm light}_{\rm e}$ and σ_0 observed variables, whose virtual counterparts describe the ELO at the scale of the baryonic object. So, we have first to analyze whether or not the mass, size and velocity dispersion of ELOs at this scale define planes

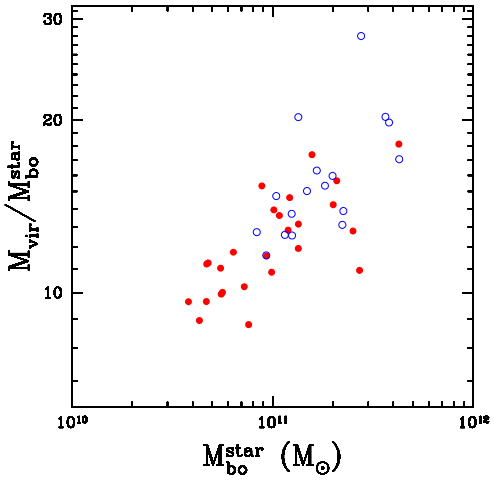

Figure 6.5: The $M_{\rm vir}/M^{\rm star}_{\rm bo}$ ratios as a function of the ELO mass scale. Symbols are as in previous Figures.

tilted relative to the virial one.

To this end, we have carried out a principal component analysis (PCA) of the *EA*-Z0 and *EB*-Z0 samples in the three dimensional variables $E \equiv \log_{10} M^{\rm star}_{\rm bo}$, $r \equiv \log_{10} r^{\rm star}_{\rm e,bo}$ and $v \equiv \log_{10} \sigma^{\rm star}_{\rm 3,bo}$ through their 3×3 correlation matrix **C**. PCA is a technique that can be used to simplify a dataset; more formally it is a linear transformation that chooses a new coordinate system for the data set such that the greatest variance by any projection of the data set comes to lie on the first axis (then called the first principal component), the second greatest variance on the second axis, and so on. Therefore, by finding the eigenvalues and eigenvectors of the covariance matrix, we find that the eigenvectors with the largest eigenvalues correspond to the dimensions that have the strongest correlation in the dataset (Saglia et al., 2001). By this, in a three-dimension space as we are using, if one eigenvalue is much lower than the other two we say that our data populates a plane. The square root of this lowest eigenvalue is the scatter of the plane.

We have found that, irrespective of the SF parameterization, one of the eigenvalues of **C** is considerably smaller than the others (see Table 6.1), so that ELOs populate in any case a flattened ellipsoid close to a two-dimensional plane in the (E, r, v) space that we call the *intrinsic dynamical plane* (IDP); the FP is the observed manifestation of this IDP. The eigenvectors of **C** indicate that the projection

$$E - \tilde{E} = \alpha^{\rm 3D}(r - \tilde{r}) + \gamma^{\rm 3D}(v - \tilde{v}), \tag{6.1}$$

where $\tilde{E}, \tilde{r}$ and $\tilde{v}$ are the mean values of the E, r and v variables, shows the IDP viewed edge-on. Table 6.1 gives the eigenvalues of the correlation matrix **C** (λ_1, λ_2, λ_3), the planes Eq. (6.1), as well as their corresponding thicknesses σ_{Erv}, both for the *EA*-Z0 and

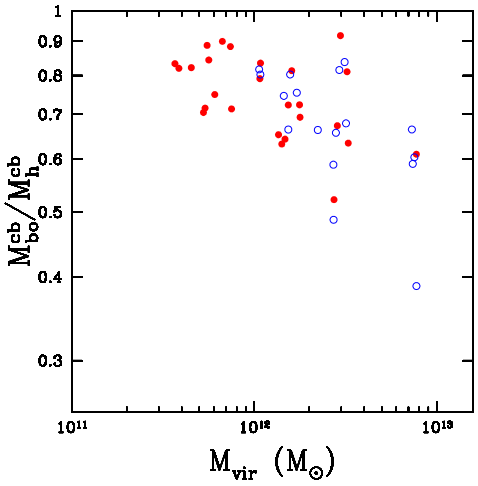

Figure 6.6: The $M_{\rm h}^{\rm cb}/M_{\rm bo}^{\rm cb}$ ratios as a function of the ELO mass scale. Symbols are as in previous Figures.

Sample	No.	$\tilde{\rm E}$	$\tilde{\rm r}$	$\tilde{\rm v}$	λ_1	λ_2	λ_3	$\alpha^{\rm 3D}$	$\gamma^{\rm 3D}$	$\sigma_{\rm Erv}$
EA-Z0	26	10.987	0.735	2.312	0.12930	0.00462	0.00020	0.459	1.928	0.014
EB-Z0	17	11.245	0.667	2.420	0.14509	0.00968	0.00014	0.392	1.776	0.012
EA-STAR-Z0	56	10.854	0.598	2.279	0.16664	0.00699	0.00077	0.586	1.529	0.028

Table 6.1: Results of PCA at $z = 0$. Column 2: ELO number in the sample. Columns 3, 4 and 5: sample mean values of the E, r and v variables. Columns 6, 7 and 8: eigenvalues of the correlation matrix. Columns 9 and 10: coefficients of the plane (Eq. 6.1). Column 11: IDP scatter in the E, r and v variables.

EB-Z0 samples. The IDPs are in fact tilted relative to the virial plane (characterized by $\alpha = 1, \gamma = 2$), and their scatter is very low as measured by their thicknesses σ_{Erv}. Note that the values of the eigenvalues of the PCA analysis are not dependent on the SF parameterization. In Table 6.1 we also present the IDP for the *EA*-STAR-Z0 sample. This sample includes ELOs that are not isolated up to the halo scale, therefore is a larger sample and more representative of a real one (see Section 4.4.1). We have confirmed that these ELOs also populate the IDP although slightly increasing the scatter of the plane.

In Figure 6.7 we plot the (E, v), (E, r) and (r, v) projections of the IDPs corresponding both to the *EA*-Z0 sample and the *EB*-Z0 sample. We see that the three plots show correlations and that these are very tight for the first of them. It is important to note that this correlation between $\sigma_{\rm 3,bo}^{\rm star}$ and $M_{\rm bo}^{\rm star}$ has the same zero-point both for the *EA*-Z0 sample and the *EB*-Z0 sample. Moreover, in these plots we clearly see again that the main difference between the *EA* and *EB* ELO samples are in their characteristic radii due to their differences in the star formation parameters of the simulations (see the discussion above).

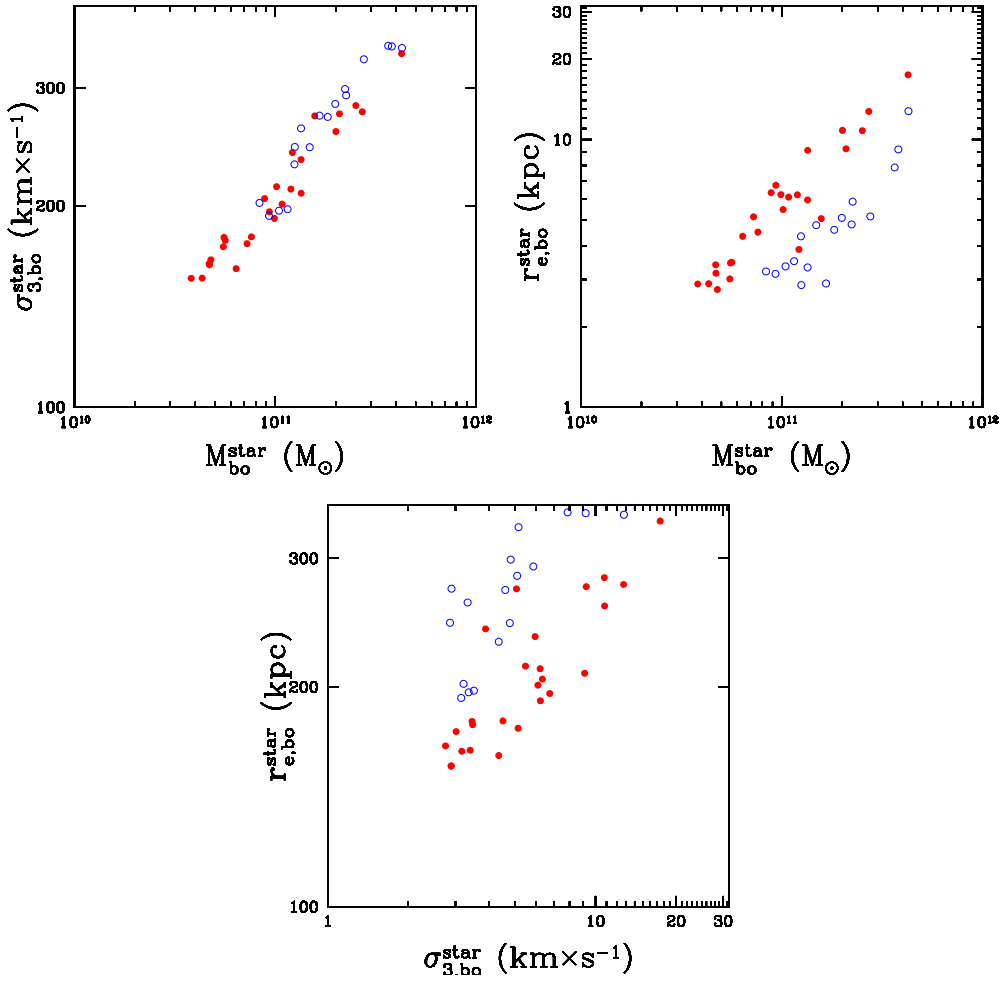

Figure 6.7: The IDPs for the *EA*-Z0 and *EB*-Z0 samples. Projections on the (E, v), (E, r) and (r, v) coordinate planes are shown.

6.2.3 Fundamental Parameters: Projected Baryonic Object Scale

In the previous section we have studied the fundamental parameters of the intrinsic baryonic object and discovered that they define a flattened ellipsoid close to a plane (the intrinsic dynamical plane, IDP). This plane is tilted relative to the virial one, and its observational projected counterparts (the luminosity L, effective projected size R_e^{light}, and the stellar central l.o.s. velocity dispersion, σ_0) enter the definition of the observed FP (see Section 3.2.2). Therefore the next step is to check how the IDP is related with the observed Fundamental Plane.

To make this analysis as clear as possible, Bender et al. (1992) introduced an orthogonal coordinate system, κ_i system, i=1,2,3 in order to improve the study of the Fundamental Plane. The κ coordinate system was obtained by a simple orthogonal coordinate transformation (i.e. rotation), applied to the observed parameters. The par-

ticular choice of orthogonal coordinate transformation was made so that κ_1 is a simple measure of galaxy mass, κ_3 is proportional to the mass-to-light ratio, the projection $\kappa_1 - \kappa_2$ correspond to a face-on view of the Fundamental Plane and the projection $\kappa_3 - \kappa_1$ shows the Fundamental Plane edge-on:

$$\kappa_1 \equiv (2\log(\sigma_0) + \log R_{\rm e}^{\rm light})/\sqrt{2} \tag{6.2}$$

$$\kappa_2 \equiv (2\log\sigma_0 + 2\log < I^{\rm light} >_{\rm e} - log R_{\rm e}^{\rm light})/\sqrt{6} \tag{6.3}$$

$$\kappa_3 \equiv (2\log\sigma_0 - \log < I^{\rm light} >_{\rm e} - \log R_{\rm e}^{\rm light})/\sqrt{3} \tag{6.4}$$

Assuming that the projected stellar *mass* density profile, $\Sigma^{\rm star}(R)$, can be taken as a measure of the surface *brightness* profile, then $< \Sigma^{\rm star} >_{\rm e} = c < I^{\rm light} >_{\rm e}$, with c a constant, and $R_{\rm e,bo}^{\rm star} \simeq R_{\rm e}^{\rm light}$ and we can look for a fundamental plane (hereafter, the dynamical FP) in the 3-space of the structural and dynamical parameters $R_{\rm e,bo}^{\rm star}$, $< \Sigma^{\rm star} >_{\rm e}$ and $\sigma_{\rm los,0}^{\rm star}$, directly provided by the hydrodynamical simulations. Therefore, the dynamical $\kappa_i^{\rm D}$ variables, free of age, metallicity or IMF effects, can be written as (Sáiz et al., 2003):

$$\kappa_1^{\rm D} \equiv (2\log\left(\sigma_{\rm los,0}^{\rm star}\right) + \log R_{\rm e,bo}^{\rm star}/\sqrt{2} \tag{6.5}$$

$$\kappa_2^{\rm D} \equiv (2\log\left(\sigma_{\rm los,0}^{\rm star}\right) + 2\log\langle\sum^{\rm star}\rangle_e - \log R_{\rm e,bo}^{\rm star})/\sqrt{6} \tag{6.6}$$

$$\kappa_3^{\rm D} \equiv (2\log\left(\sigma_{\rm los,0}^{\rm star}\right) - \log\langle\sum^{\rm star}\rangle_e - \log R_{\rm e,bo}^{\rm star})/\sqrt{3} \tag{6.7}$$

and they are related to the original κ coordinates through the expressions:

$$\kappa_1 = \kappa_1^{\rm D} \tag{6.8}$$

$$\kappa_2 = \kappa_2^{\rm D} - \frac{\sqrt{6}}{3}\log(\frac{M_{\rm bo}^{\rm star}}{L}) \tag{6.9}$$

$$\kappa_3 = \kappa_3^{\rm D} + \frac{\sqrt{3}}{3}\log(\frac{M_{\rm bo}^{\rm star}}{L}) \tag{6.10}$$

In Section 3.2 we have discussed how to obtain the observational fundamental parameters from the projected structural and kinematical profiles. We just recall that we have computed the characteristic mass, $M_{\rm cyl,bo}^{\rm star}$, radius, $R_{\rm e,bo}^{\rm star}$, and velocity dispersion, $\sigma_{\rm los,0}^{\rm star}$, for each ELO in one-hundred random projections. The $\kappa_{\rm i}^{\rm D}$ coordinates are also

computed in this form. Unless stated, we use the mean value over all these projections and its dispersion. We remind the reader that all the values for the different fundamental parameters of the ELO samples can be found in Appendix D.

In order to compare our results with observational data, we decided to use the SDSS catalog (York et al., 2000). We utilized a sample of 9000 early-type objects from SDSS studied by Bernardi et al. (2003a,b,c,d). A maximum likelihood estimation of the correlations among observables (Luminosity, effective radius, surface brightness, color and velocity dispersion) is made by these authors. We have also, from Kauffmann et al. (2003b), a median likelihood estimates of stellar burst fraction, dust attenuation strengths stellar masses and stellar mass-to-light ratios for a complete sample of 80000 galaxies drawn from SDSS. The most interesting thing of this last job concerning our work is that they obtain a constant stellar mass-to-light ratio for early-type galaxies in the range of masses of our samples. The values of the logarithm of this ratio are $\log \gamma_r^{\rm star} \simeq 0.53$ and $\log \gamma_z^{\rm star} \simeq 0.25$, with dispersions $\sigma_S < 0.15$ and 0.1, in the r and z SDSS bands, respectively. The constant stellar-mass-to-light ratios allow us to write the covariance matrix using the $E \equiv \log M_{\rm bo}^{\rm star}$ variable instead of absolute magnitude or the logarithm of the luminosity L.

We used the data of the z band to minimize stellar effects, since it is the redder available in SDSS. Also we present in this work test analyses in the r band for which we have obtained very close results. Defining $E = \log M_{\rm bo}^{\rm star}$ we have that mass is related with magnitudes as follows (Kauffmann et al., 2003b):

$$E = S_* - \frac{M_* - Qz - M_\odot}{2.5} \tag{6.11}$$

where $S_* = log\frac{M}{L}$ and Qz is a redshift correction. Q and S_* is taken from Kauffmann et al. (2003b). $M_\odot$ is the solar magnitude for the specific band, needed because S_* is normalized in solar units. We took it from Blanton et al. (2003). Once we get the median mass for SDSS ellipticals in z and r band, we also derived the correspondent covariance matrix for the new three parameter space for SDSS data: stellar mass, effective radius and velocity dispersion. Means, dispersions and correlations are given in table 6.2, where $R = logR_e$, $V = log\sigma_0$ and E is the logarithm of stellar mass calculated above. The last step before comparing the ELO samples with the SDSS data is to take into account that they have been calculated using a different Hubble constant. Radii and masses of our virtual ellipticals are in $h = 0.65$ and early-types of SDSS are in $h = 0.70$. We choose to move masses and distances of ELOs to $h = 0.70$ better than SDSS data because mass-to-light ratios were also obtained with the assumption of $h = 0.70$.

Figure 6.8 plots the $\kappa_3^{\rm D}$ versus $\kappa_1^{\rm D}$ (top) and $\kappa_2^{\rm D}$ versus $\kappa_1^{\rm D}$ (bottom) diagrams for ELOs in both the *EA*-Z0 and *EB*-Z0 samples. We also drew the 2σ concentration ellipses in the respective variables, as well as its major and minor axes, for the SDSS early-type galaxy sample in the SDSS z band (solid lines) and in the r band (point

Band used	$\bar{E}$	$\bar{R}$	$\bar{V}$	σ_E	σ_R	σ_V	ρ_{ER}	ρ_{EV}	ρ_{VR}
r	10.9	0.49	2.2	0.3509	0.241	0.111	0.8454	0.7419	0.543
z	10.81	0.45	2.2	0.3525	0.241	0.11	0.8486	0.7499	0.543

Table 6.2: Maximum likelihood estimates of the joint distribution of masses, sizes and velocity dispersions for SDSS early-type sample (Bernardi et al., 2003a,b,c,d). Masses are given in $\log M_{\odot}$, distances in $\log kpc$, velocity dispersions in $\log km \times s^{-1}$. The Hubble constant used in the SDSS is $h = 70$.

lines) as analyzed by Bernardi et al. (2003b,c). The most outstanding feature of this Figure (upper panel) is the good scaling behavior of $\kappa_3^{\rm D}$ versus $\kappa_1^{\rm D}$, with a very low scatter (see the slopes M_1 in Table 6.3). Note that the slopes for the *EA*-Z0 and *EB*-Z0 samples are consistent within their errors, while the zero-points depend on the SF parameterization through the ELO sizes. The values of the slopes in Table 6.3 mean that systematic variations of the structural and dynamical properties of ELOs with the mass scale cause, by themselves, a tilt of the dynamical FP relative to the virial relation. This confirms that the Fundamental Plane is the observed manifestation of the Intrinsic Dynamical Plane introduced in previous Section. In Table 6.3 we also present the value of this slope for the *EA*-STAR-Z0 sample showing that it is very similar as the *EA*-ZO slope. *EA*-STAR-Z0 sample is a larger sample and more representative of a real one because it includes ELOs that are not isolated up to the halo scale (see Section 4.4.1). The *EA*-STAR-ZO sample in κ space can be seen in Figure 6.27. We would deepen into the tilt and the scatter of the dynamical FP below (see 6.2.4 and 6.2.5 respectively).

Another interesting feature of Figure 6.8 is that it shows that most of the values of the $\kappa_i^{\rm D}$ coefficients are within the 2σ concentration ellipses in both plots for ELOs formed in *EA*-Z0 type simulations, with a slightly worse agreement for ELOs in the *EB*-Z0 sample. This means that ELOs have counterparts in the real world (Sáiz et al., 2004). Finally, we note that either the dynamical or the observed FPs are not homogeneously populated: both SDSS ellipticals and ELOs occupy only a region within these planes (see Figure 6.8 lower panel, see also, Guzman et al., 1993; Márquez et al., 2000). This means that, from the point of view of their structure and dynamics, ELOs are a two-parameter family where the two parameters are not fully independent. Moreover, concerning ELOs, the occupied region changes when the SF parameters change. The reason of this change is that the ELO sizes decrease as SF becomes more difficult, because the amount of dissipation experienced by the stellar component along ELO assembly increases (see discussion in Section 9.2).

In figure 6.9 ELO samples and SDSS (z and r band) are shown in a mass, radius and velocity dispersion coordinate system (Sáiz et al., 2004). These are more familiar variables, and it is maybe better for a first comparison with SDSS data. Error bars in ELOs variables account for the dispersion between the 100 projection values we are

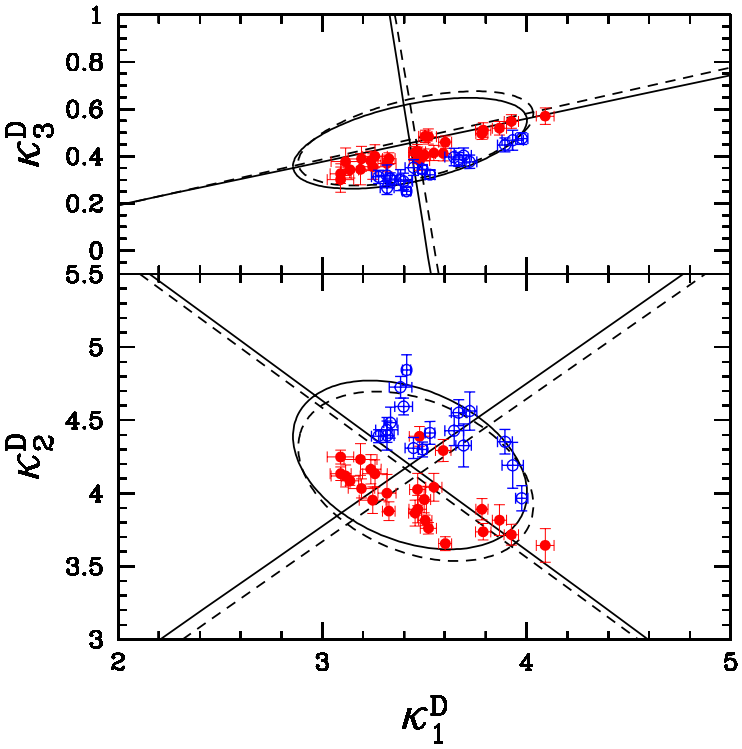

Figure 6.8: Dynamical Fundamental Plane in κ^D system. Edge-on projection (top panel) and nearly face-on projection (bottom panel) of the dynamical FP of ELOs in the κ^D variables (red filled symbols: *EA*-Z0 sample; blue open symbols: *EB*-Z0 sample). We also draw the respective concentration ellipses (with their major and minor axes) for the SDSS early-type galaxy sample from Bernardi et al. (2003b) in the z band (solid line) and the r band (dashed line). Error bars account for projection effects. See text for more details.

using (see Section 4.5.3). From these figures, we can see the advantages of using a *kappa* space, in which from projections of two coordinates we can obtain much more information. Finally in Figure 6.10 we show that the central l.o.s. velocity dispersion, $\sigma^{\rm star}_{\rm los,0}$, is a fair empirical estimator of the virial mass, $M_{\rm vir}$. This is a very important result because relates very strongly two quantities of very different scales and it does not depend on the star formation parameters. The *EA*-STAR-ZO sample in mass, radius and velocity dispersion space can be seen in Figure 6.28

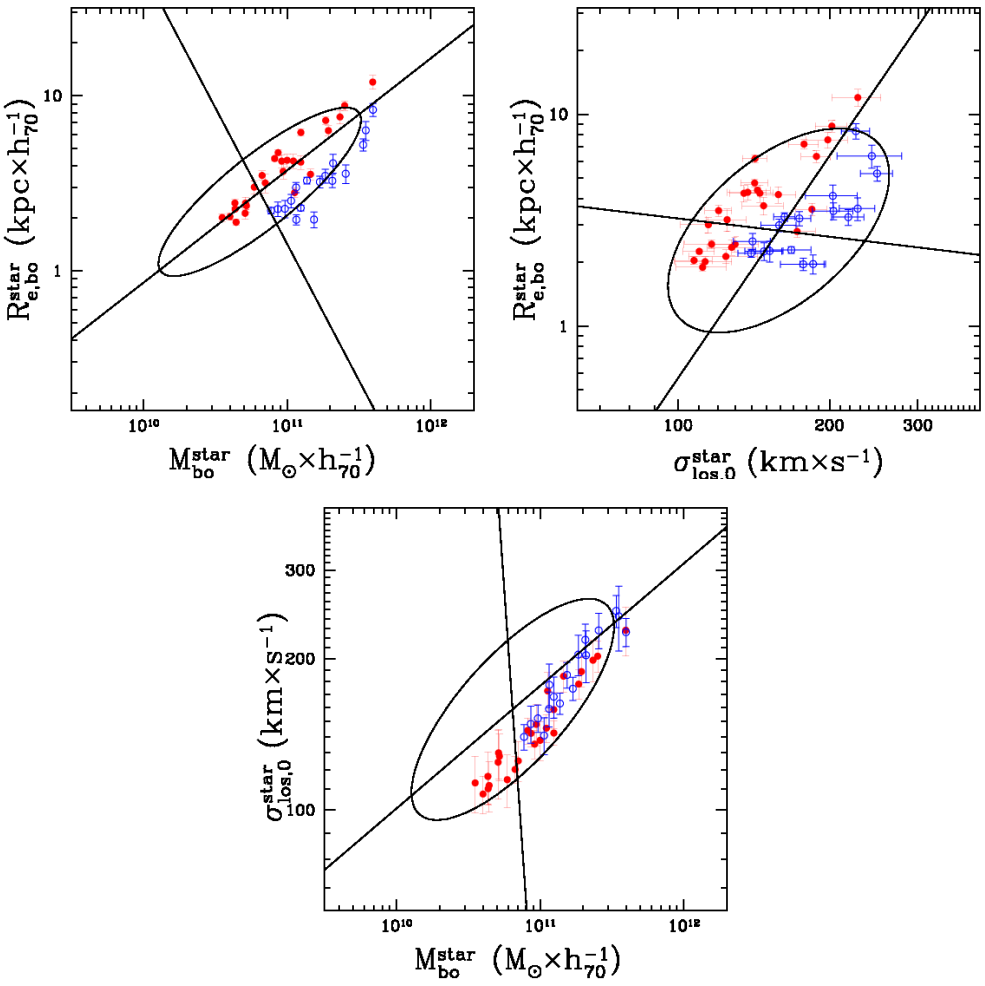

Figure 6.9: The Dynamical Plane: $R^{\rm star}_{\rm e,bo}$,$M^{\rm star}_{\rm bo}$ and $\sigma^{\rm star}_{\rm los,0}$ space. Symbols are as in previous Figures. Error bars account for projection effects.

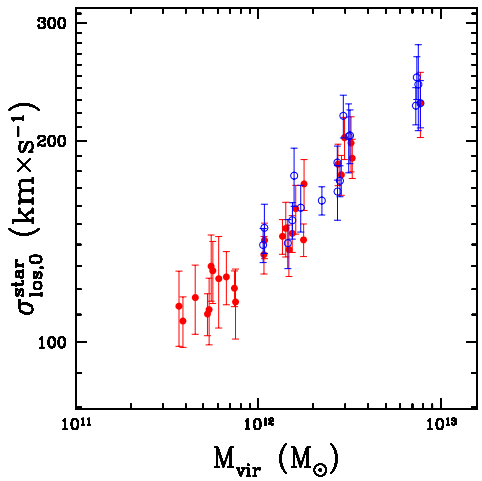

Figure 6.10: The correlation between the central l.o.s. velocity dispersion and the virial mass for the ELO samples. Symbols are as in previous Figures. Error bars account for projection effects.

6.2.4 The Origin of the Tilt of the Fundamental Plane

We now address the issue of the physical origin of the tilt of ELO IDPs relative to the virial relation. As discussed in Section 3.2, a non-zero tilt can be caused by a mass dependence of the mass-to-light ratio $M_{\rm vir}/L$, of the mass structure coefficients $c_{\rm M}^{\rm vir} \equiv \frac{GM_{\rm vir}}{3(\sigma_{\rm los,0}^{\rm star})^2 R_{\rm e,bo}^{\rm star}}$, or of both of them. We examine briefly these possibilities in turn.

i) We first note that the mass-to-light ratio can be written as:

$$M_{\rm vir}/L = A_{\rm vir}(M_{\rm bo}^{\rm star})^{\beta_{\rm vir}} \times \gamma^{\rm star}, \tag{6.12}$$

where $\gamma^{\rm star} \equiv M_{\rm bo}^{\rm star}/L$ is the stellar mass-to-light ratio, that, as already explained, can be considered to be independent of the E galaxy luminosity or ELO mass scale. Figure 6.5 and the values of the $\beta_{\rm vir}$ slopes given in Table 6.3, indicate that the dark to bright mass content of ELOs increases with their mass, contributing a tilt to their IDPs. Similar results have also been found in pre-prepared simulations of dissipative mergers (Robertson et al., 2006). Note that we have already seen that $M_{\rm cyl,bo}^{\rm star} \backsimeq M_{\rm bo}^{\rm star}$ (see Section 4.5).

ii) Writing the $c_{\rm M}^{\rm vir}$ mass structure coefficients as power laws $c_{\rm M}^{\rm vir} = A_{\rm M}(M_{\rm bo}^{\rm star})^{\beta_{\rm M}}$, ELO homology would imply $\beta_{\rm M} = 0$. To elucidate whether or not this is the case, the $\beta_{\rm M}$ slopes have been measured on the ELO samples through direct fits in log-log scales. The results are given in Table 6.3, where we see that the homology is in fact broken both for *EA*-Z0 or *EB*-Z0 samples. To deepen into the causes of this behavior, we remember here Equation 3.8:

$$c_{\rm M}^{\rm vir} \equiv c_{\rm f} \times c_{\rm r} \times c_{\rm v}, \tag{6.13}$$

Furthermore, from the definitions of the $c_{\rm v}$ and $c_{\rm r}$ coefficients (Equations 3.6 and 3.7), we note that both coefficients can be split into two terms, making our analysis clearer. First, one addressing the dissipation and gas cooling effect, this is, the change from the halo scale parameters that take into account the total matter, to the baryonic object scale parameters that includes only stars. The second one takes into account the projection, geometrical and concentration effects, indicating the change from the 3D baryonic scale parameters to the projected baryonic scale parameters which are the ones observed. So, we rewrite the velocity term as:

$$c_{\rm v} \equiv c_{\rm vd} \times c_{\rm vpc} \tag{6.14}$$

with

$$c_{\rm vd} \equiv (\sigma_{\rm 3,h}^{\rm tot})^2/(\sigma_{\rm 3,bo}^{\rm star})^2 \tag{6.15}$$

and

$$c_{\rm vpc} \equiv (\sigma_{\rm 3,bo}^{\rm star})^2/3(\sigma_{\rm los,0}^{\rm star})^2 \tag{6.16}$$

And for the size coefficient, we can write

$$c_{\rm r} \equiv c_{\rm rd} \times c_{\rm rp} \tag{6.17}$$

where

$$c_{\rm rd} \equiv r_{\rm e,h}^{\rm tot}/r_{\rm e,bo}^{\rm star} \tag{6.18}$$

and

$$c_{\rm rp} \equiv r_{\rm e,bo}^{\rm star}/R_{\rm e,bo}^{\rm star} \tag{6.19}$$

Finally, using these new definitions we have that,

$$c_{\rm M}^{\rm vir} = c_{\rm f} \times c_{\rm rd} \times c_{\rm rp} \times c_{\rm vd} \times c_{\rm vpc}, \tag{6.20}$$

So these parameters have to explain the slope ($\beta_{\rm M} \neq 0$) observed for the homology coefficient, $c_{\rm vir}^{\rm M}$. Taking into account the power-law forms of these coefficients, we have:

$$\beta_{\rm M} = \beta_{\rm F} + \beta_{\rm rd} + \beta_{\rm rp} + \beta_{\rm vd} + \beta_{\rm vpc}, \tag{6.21}$$

when the $\beta_{\rm i}$ slopes are calculated through direct fits.

First of all, we have already seen in Section 6.2.1 (Figure 6.3 and Table 6.3) that the $c_{\rm f}$ coefficient is independent of the ELO mass scale or SF parameter values and that ELOs satisfy the virial theorem at the halo scale. Consequently we have to study the two other coefficients and dilucidate which of them are relevant to explain the tilt of the Fundamental Plane.

Concerning sizes, in Figure 6.11 we plot the $c_{\rm rd} \equiv r_{\rm e,h}^{\rm tot}/r_{\rm e,bo}^{\rm star}$ ratios versus the $M_{\rm bo}^{\rm star}$ mass scale for ELOs in both the *EA*-Z0 and the *EB*-Z0 samples. In this Figure the effects of SF parameterization are clear: *EA*-Z0 type ELOs have larger sizes relative to the halo size than *EB*-Z0 type ELOs. There is also a clear mass effect, with more massive ELOs less concentrated relative to the total mass distribution than less massive ones (i.e., spatial homology breaking; note, however that the scatter is important). Moreover, Figure 6.11 suggests that this trend does not significantly depend on the SF parameterization. These indications are quantitatively confirmed through a fit to a power law $c_{\rm rd} = A_{\rm rd}(M_{\rm bo}^{\rm star})^{\beta_{\rm rd}}$ (see Table 6.3) and have interesting implications to explain the tilt of the observed FP.

Now, let us move to the observationally relevant scale lengths, the projected half-mass radii $R_{\rm e,bo}^{\rm star}$. Their correlations with their intrinsic three dimensional counterparts $r_{\rm e,bo}^{\rm star}$ are very good, as illustrated in Figure 6.12, where the very low dispersion in the plots of the $c_{\rm rp} \equiv r_{\rm e,bo}^{\rm star}/R_{\rm e,bo}^{\rm star}$ ratios versus the stellar mass $M_{\rm bo}^{\rm star}$ can be appreciated. The results of a fit to a power law of the form $c_{\rm rp} = A_{\rm rp}(M_{\rm bo}^{\rm star})^{\beta_{\rm rp}}$, are given in Table 6.3 where we see that the $c_{\rm rp}$ ratios show a very mild mass dependence in the *EA*-Z0 sample and none in the *EB*-Z0 sample. In Table 6.3 we also present the value of this

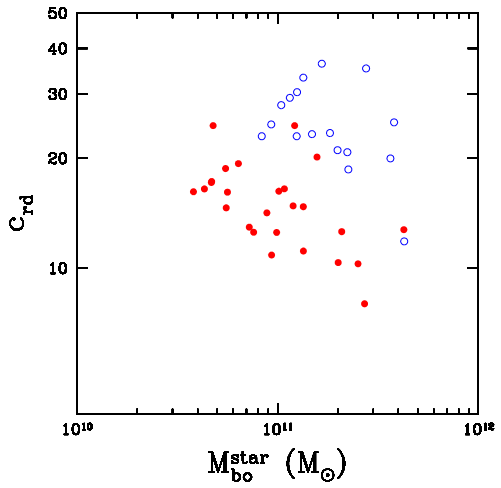

Figure 6.11: The $c_{\rm rd} \equiv r_{\rm e,h}^{\rm tot}/r_{\rm e,bo}^{\rm star}$ ratios as a function of the ELO mass scale. Symbols are as in previous Figures. Spatial homology breaking is clear in this Figure.

slope for the *EA*-STAR-Z0 sample[2] obtaining same conclusions as with the *EA*-Z0 and *EB*-Z0 samples. This result is important because it indicates that the observationally available *projected* radii $R_{\rm e,bo}^{\rm star}$ are robust estimators of the physically meaningful size scales $r_{\rm e,bo}^{\rm star}$.

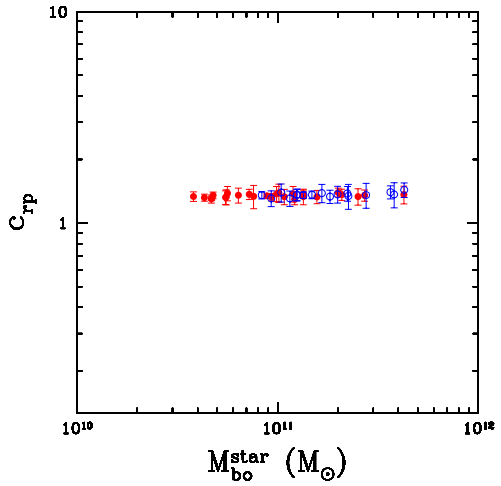

Figure 6.12: The $c_{\rm rp} \equiv r_{\rm e,bo}^{\rm star}/R_{\rm e,bo}^{\rm star}$ ratios versus the stellar masses at the baryonic object scale. Symbols are as in previous Figures. Error bars account for projection effects.

Next we study the velocity coefficients. In Figure 6.13 we plot the $c_{\rm vd} \equiv (\sigma_{\rm 3,h}^{\rm tot}/\sigma_{\rm 3,bo}^{\rm star})^2$ ratios, that measure how dissipation and concentration affect, on average, to the relative values of the dispersion at the halo scale (involving also dark matter) and at the

[2] *EA*-STAR-Z0 sample is a larger sample and more representative of a real one because it includes ELOs that are not isolated up to the halo scale (see Section 4.4.1).

baryonic object scale. No mass effects are apparent in this Figure, but an average kinematical segregation is clear, (see Table 6.3 for the results of a fit to the expression $c_{\rm vd} = A_{\rm vd}(M_{\rm bo}^{\rm star})^{\beta_{\rm vd}}$). These are important results, which could have interesting observational implications.

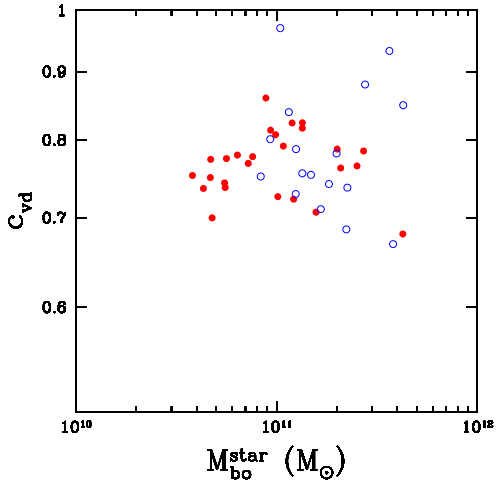

Figure 6.13: The $c_{\rm vd} \equiv (\sigma_{\rm 3,h}^{\rm tot}/\sigma_{\rm 3,bo}^{\rm star})^2$ ratios (average kinematical segregation) as a function of the ELO mass scale. Symbols are as in previous Figures. No dynamically broken homology can be seen in this Figure, but the kinematical segregation between dark matter and stars is clear.

In Figure 6.14 we plot the $c_{\rm vpc} \equiv (\sigma_{\rm 3,bo}^{\rm star})^2/3(\sigma_{\rm los,0}^{\rm star})^2$ ratios versus the ELO mass scale. We see that a significant mass effect is not apparent, and this is quantitatively confirmed in Table 6.3, where the results of a fit of the form $c_{\rm vpc} = A_{\rm vpc}(M_{\rm bo}^{\rm star})^{\beta_{\rm vpc}}$ are given. We also see that due to radial anisotropy, $c_{\rm vpc} < 1$, with no SF parameterization effect. In Table 6.3 we also present the value of this slope for the *EA*-STAR-Z0 sample[3] obtaining same conclusions as with the *EA*-Z0 and *EB*-Z0 samples. So, there is not mass bias when using $\sigma_{\rm los,0}^{\rm star}$ as an estimator for $\sigma_{\rm 3,bo}^{\rm star}$, but some warnings are in order concerning anisotropy effects.

To sum up, we see that, irrespective of the SF parameterization, the main contribution to the homology breaking comes from the $c_{\rm rd}$ coefficients (Guzman et al., 1993, i.e., spatial homology breaking, see), while $\beta_{\rm vd}$ have values consistent with $c_{\rm f}$ and $c_{\rm vd}$ being independent of the ELO mass scale, i.e., no dynamical homology breaking. $c_{\rm rp}$ and $c_{\rm vpc}$ show a very mild mass dependence in the *EA*-Z0 sample and none in the *EB*-Z0 sample, indicating that projection effects are not important in our ELO samples.

To estimate the contributions of projection effects, we built 40 new samples from *EA*-Z0 (*EA*-TEST1) and other 40 from *EB*-Z0 (*EB*-TEST1), taking the same number

[3] *EA*-STAR-Z0 sample is a larger sample and more representative of a real one because it includes ELOs that are not isolated up to the halo scale (see Section 4.4.1).

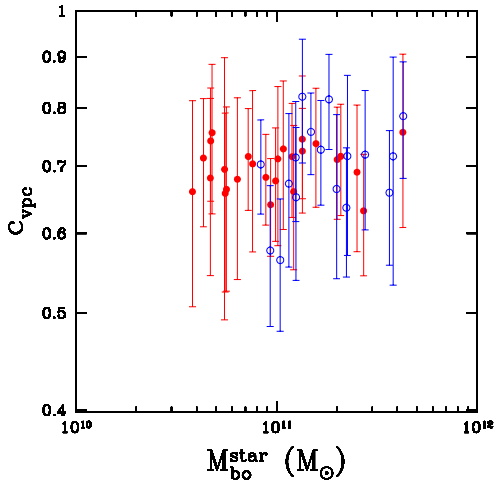

Figure 6.14: $c_{\rm vpc} \equiv (\sigma^{\rm star}_{\rm 3,bo})^2/3(\sigma^{\rm star}_{\rm los,0})^2$ ratios versus the ELO mass scale. Symbols are as in previous Figures. Error bars account for projection effects.

of objects but randomly choosing for each object one of the one hundred projections. For all the samples the same analysis made for *EA*-Z0 and *EB*-Z0 has been repeated, obtaining the same results as before. In column 2 of Table 6.4 two of these analyses are presented. As we can see the differences do not change the conclusions obtained before, although the errors clearly increase. A larger sample is built taking the whole one hundred projections for each ELO. Columns 3 and 4 of Table 6.4 show results for *EA*-Z0 sample (*EA*-TEST2) and for *EB*-Z0 (*EB*-TEST2), respectively. Results of these tests confirm our previous conclusions. These are that at least half of the tilt of the fundamental plane has its physical origin in that mass fraction of stars bound to the ELOs (similar results when using cold baryons) relative to the virial mass, decrease with the mass scale. The physical origin of the other part can be explained in terms of homology breaking, particularly from characteristics lengths between halo scale and ELO scale. The characteristic length at ELO scale, $r^{\rm star}_{\rm e,bo}$, relative to the characteristic distance at halo scale, $r_{\rm vir}$ is not constant for all ELOs, it increases for more massive ELOs. These trends are due to a systematic decrease with increasing ELO mass, of the relative amount of dissipation experienced by the baryonic mass component along ELO formation.

6.2.5 The Scatter of the Fundamental Plane

We now turn to consider the scatter of the dynamical FP for the ELO samples and compare it with the scatter of the FP for the SDSS elliptical sample, calculated as the square root of the smallest eigenvalue of the 3×3 covariance matrix in the E (or $\log L$), $V \equiv \log \sigma^{\rm star}_{\rm los,0}$ and $R \equiv \log R^{\rm star}_{\rm e,bo}$ variables (Saglia et al., 2001). As Figure 6.8 suggests, when projection effects are circumvented by taking averages over different

	EA-Z0	*EB*-Z0	*EA*-STAR-Z0
M_1	0.238 ± 0.039	0.277 ± 0.059	0.264 ± 0.024
$\beta_{\rm vir}$	0.221 ± 0.083	0.237 ± 0.158	–
$\beta_{\rm M}$	-0.162 ± 0.140	-0.167 ± 0.288	–
$\beta_{\rm f}$	0.048 ± 0.040	-0.007 ± 0.072	–
$\beta_{\rm vd}$	0.000 ± 0.037	0.000 ± 0.113	–
$\beta_{\rm vpc}$	0.012 ± 0.033	0.069 ± 0.109	0.006 ± 0.038
$\beta_{\rm rd}$	-0.231 ± 0.146	-0.247 ± 0.266	–
$\beta_{\rm rp}$	0.011 ± 0.012	0.026 ± 0.021	0.022 ± 0.014

Table 6.3: Slopes for Linear Fits. Column 2: the slopes of the $\kappa_3^{\rm D} = M_1\kappa_1^{\rm D} + M_0$ relation (direct fits); the slopes of the $M_{\rm vir}/M_{\rm bo}^{\rm star} \propto (M_{\rm bo}^{\rm star})^{\beta_{rmvir}}$ and $c_{\rm i} \propto (M_{\rm bo}^{\rm star})^{\beta_{\rm i}}$ scaling relations for the *EA*-Z0 sample, calculated in $\log - \log$ plots through direct fits. Errors stand for their respective 95% confidence intervals obtained using Student distribution. Columns 3: same as columns 2 for the *EB*-Z0 sample. Columns 3: same as columns 2 for the *EA*-STAR-Z0 sample. In this case only slopes at the baryonic object scale can be calculated.

Parameter	*EA*-TEST1	*EB*-TEST1	*EA*-TEST2	*EB*-TEST2
M_1	0.286 ± 0.054	0.297 ± 0.071	0.256 ± 0.005	0.293 ± 0.007
$\beta_{\rm M}$	-0.267 ± 0.186	-0.184 ± 0.305	-0.155 ± 0.016	-0.166 ± 0.028
$\beta_{\rm vpc}$	-0.013 ± 0.090	0.032 ± 0.092	0.017 ± 0.015	0.064 ± 0.019
$\beta_{\rm rp}$	0.023 ± 0.053	0.007 ± 0.089	0.010 ± 0.004	0.023 ± 0.009

Table 6.4: Slopes for linear fits *EA*-Z0 and *EB*-Z0 test samples relating projection effects. Column 2: the slopes of the $\kappa_3^{\rm D} = M_1\kappa_1^{\rm D} + M_0$ relation (direct fits); the slopes of the $c_{\rm i} \propto (M_{\rm bo}^{\rm star})^{\beta_{\rm i}}$ scaling relations for the *EA*-Z0 sample, calculated in $\log - \log$ plots through direct fits. Errors stand for their respective 95% confidence intervals. Column 3: the same slopes as column 2 for a random projection of *EB*-Z0 sample. Column 4: the same slopes as column 2 for a sample built with all the projections for each ELO of the *EA*-Z0 sample. Column 5: same as column 4 for *EB*-Z0. See text for details.

Parameter	*EA*-Z0	*EB*-Z0	*EA*-STAR-Z0	
σ_{EVR}	0.0183	0.0178	0.0224	
	EA-TEST1	*EB*-TEST1	*EA*-TEST2	*EB*-TEST2
σ_{EVR}	0.0361	0.0288	0.0339	0.0297
SDSS	z band	r band		
σ_{LVR}	0.0489	0.052		

Table 6.5: Scatter of the Fundamental Plane for the different samples and for different bands of the SDSS early-type sample (Bernardi et al., 2003c).

directions, the resulting three dimensional orthogonal scatter for ELOs is smaller than for SDSS ellipticals: $\sigma_{EVR} = 0.0164$ and $\sigma_{EVR} = 0.0167$ for the *EA*-Z0 and *EB*-Z0 samples, respectively, to be compared with $\sigma_{LVR} = 0.0489$ for the SDSS z band in the $\log L, V \equiv \log \sigma_0$ and $R \equiv \log R_{\rm e}^{\rm light}$ variables (see Table 6.5). We also present in this table the scatter of the dynamical FP for the *EA*-STAR-Z0 sample showing that it is also smaller than for the SDSS ellipticals. This is a larger sample and more representative of a real one because it includes ELOs that are not isolated up to the halo scale (see Section 4.4.1).

To estimate the contribution of projection effects to the observed scatter, we have used the TEST1 and TEST2 samples mentioned above. First we have calculated the scatter for *EA*-Z0 and *EB*-Z0 ELOs building a sample using just one random projection for each virtual elliptical (TEST1). We have also calculated the orthogonal scatter for ELOs when no averages over projection directions for the $R_{\rm e,bo}^{\rm star}$ and $\sigma_{\rm los,0}^{\rm star}$ variables are made (TEST2). In both cases, and for both SF parameterizations, the scatter increases (see Table 6.5), but it is still lower than observed. This indicates that a contribution from stellar population effects is needed to explain the scatter of the observed FP, as suggested by different authors (see, for example, Pahre et al., 1998; Trujillo et al., 2004; Hyde & Bernardi, 2008b).

6.3 The Photometric Plane

In the last years a great interest has arisen for the good correlations between the shape parameter, n, obtained from the surface brightness profiles of galaxies and all the other structural and kinematic fundamental parameters (see discussion in Section 3.2.2). We have already seen in section 5.2.6 that our ELOs are also well described by a Sérsic law. Now we will focus on the different relations between these fundamental parameters.

First of all we want to notice that the values obtained are in good agreement with observation (Caon et al., 1993; Prugniel & Simien, 1997; Graham, 1998; Márquez et al., 2000; D'Onofrio, 2001; Trujillo et al., 2001; Vazdekis et al., 2004; Graham et al., 2006), including their correlations with the effective radii $R_{\rm e}^{\rm light}$ and velocity dispersion, as illustrated in Figures 6.15(a) and 6.15(b). In Figure 6.15(a) we plot the shape parameter n versus the ELO projected stellar half-mass radii, $R_{\rm e,bo}^{\rm star}$, defined by the condition that $M_{\rm cyl}^{\rm star}(R_{\rm e,bo}^{\rm star})$ encloses half the total stellar mass of the system; assuming that $\gamma_B^{\rm star}$ does not depend on R, we will have $R_{\rm e,bo}^{\rm star} \simeq R_{\rm e}^{\rm light}$. Green triangles are data on n and $R_{\rm e}^{\rm light}$ from D'Onofrio (2001). Note that a slight effect resulting from the different SF parameterization in *EA*-Z0 and *EB*-Z0 samples is apparent in this plot, mainly due to the smaller sizes of *EB*-Z0 sample ELOs as compared with their *EA*-Z0 sample counterparts. Figure 6.15(b) shows the central l.o.s. velocity dispersion, $\sigma_{\rm los,0}^{\rm star}$, versus the shape parameter, n obtained from the Sérsic fits. Filled red circles stand for the *EA*-Z0 ELO sample and empty blue circles for the *EB*-Z0 sample. Green triangles stand for Vazdekis et al. (2004). The good correlation between the shape parameter n and other structural or kinematic parameters indicate a break of the structural homology of ELOs, that is, mass density profiles of ELOs varies according with their mass: more massive galaxies are more centrally concentrated that less massive ones. This consolidates similar conclusions obtained in previous section.

The Photometric Plane relation relates the $R_{\rm e}^{\rm light}$, $\mu_{\rm e}$ and n observational parameters (see Section 3.2.2.2). Following the same idea that we used when we studied the projected stellar mass density profiles (see section 4.5.3), we define an analogous relation for our elliptical-like objects, the Structural Photometric Plane (SPhoP) as: $\log R_{\rm e,bo}^{\rm star} = A \log n + B \log M_{\rm bo}^{\rm star} + C$, i.e., replacing the surface brightness with the stellar mass. We have calculated the orthogonal least square fit of this equation for the *EA*-Z0 sample obtaining: $A_{Z0}^{EA} = -0.30186$; $B_{Z0}^{EA} = 0.87653$; $C_{Z0}^{EA} = -9.86211$ and an orthogonal dispersion, $\sigma_{nRM,z0}^{EA} = 0.0556$. For the *EB*-Z0 sample we obtained: $A_{z0}^{EB} = 0.25221$; $B_{z0}^{EB} = 0.724734$; $C_{z0}^{EB} = -7.807486$ and $\sigma_{nRM,z0}^{EB} = 0.0633$. In Figure 6.16, we plot the edge-on projection of this plane for the *EA*-Z0 and *EB*-Z0 samples. In Table 6.6 we present the different parameters that define the SPhoP for the *EA*-Z0, *EB*-Z0 and *EA*-STAR-Z0 samples. As expected the SPhoP obtained for the *EA*-STAR-Z0 sample [4] is very similar as the one obtained for the *EA*-Z0. Present results show

[4] *EA*-STAR-Z0 sample is a larger sample and more representative of a real one because it includes

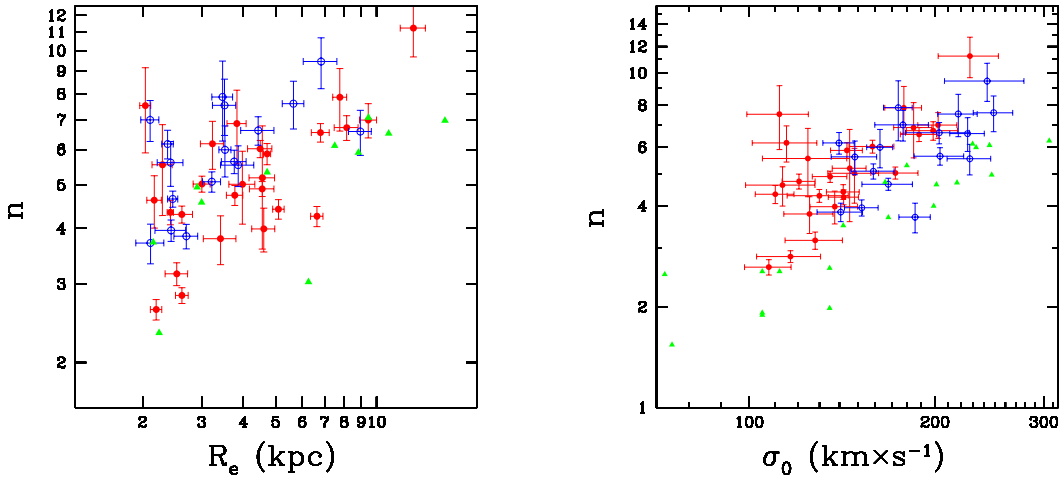

Figure 6.15: Fig. 6.15(a): The Sérsic shape parameter, n, versus the projected stellar half-mass radii, Re, for *EA*-Z0 sample (red filled circles) and *EB*-Z0 sample (blue open circles). For each ELO, the mean of projections along one hundred random directions are shown. Error bars stand for the dispersion generated just by projection effects. Green filled triangles are data on n and $R_{\rm e}^{\rm light}$ from D'Onofrio (2001). Fig. 6.15(b): The central l.o.s. velocity dispersion, $\sigma_{\rm los,0}^{\rm star}$, versus the shape parameter obtained from the Sérsic fits. Filled red circles stand for the *EA*-Z0 ELO sample and empty blue circles for the *EB*-Z0 sample. Green triangles stand for Vazdekis et al. (2004) local galaxies data.

that the Photometric Plane could be an interesting alternative tool for the study of elliptical galaxies at high redshifts instead of the Fundamental Plane, which requires a heavy amount of time for measuring velocity dispersions.

We have confirmed observational results (Khosroshahi et al., 2000; Graham, 2002) that indicate that the logarithms of n, $R_{\rm e,bo}^{\rm star}$ and $M_{\rm cyl,bo}^{\rm star}$ populate, at $z = 0$ a flattened ellipsoid close to a two-dimensional plane (the SPhoP). We have checked that we obtain the same results either when we use the $R_{\rm e,bo}^{\rm star}$ and $M_{\rm cyl,bo}^{\rm star}$ terms obtained from the Sérsic fits or those obtained directly from the projected mass profiles.

6.3.1 The Hyperplane in 4D

To explain this tight correlation among three parameters some authors have suggested that the observational parameters n, $R_{\rm e}^{\rm light}$, $< I^{\rm light} >_{\rm e}$ and σ_0 form a Hyperplane in 4D (Graham, 2002; Capozziello et al., 2007, see Section 3.2.2 for more details). In this scenario the Photometric Plane and the Fundamental Plane would be just two projections of this hyperplane. Since we have already confirmed that our samples of elliptical-like objects satisfy the Fundamental and Photometric Plane relations, we want

ELOs that are not isolated up to the halo scale (see Section 4.4.1).

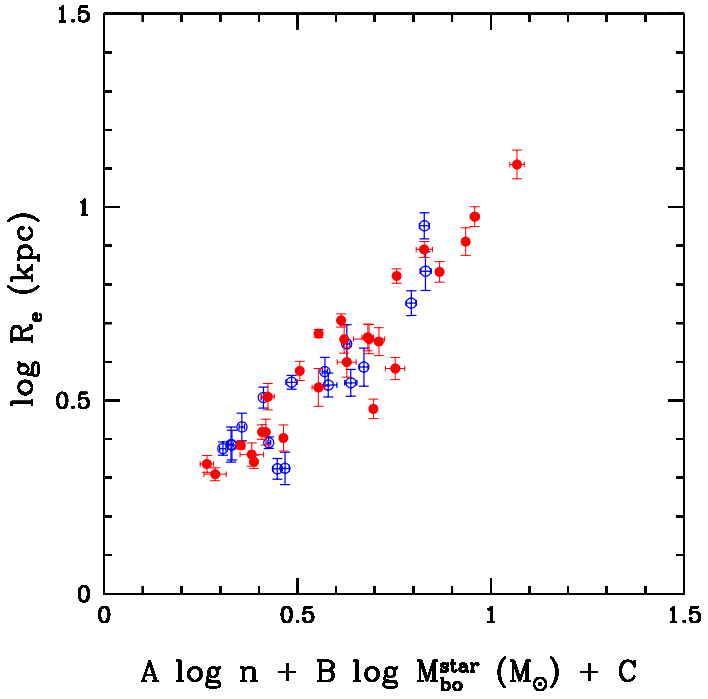

Figure 6.16: The Structural Photometric Plane at $z = 0$. Filled red circles stand for the *EA*-Z0 ELO sample and empty blue circles for the *EB*-Z0 sample. Error bars account for projection effects.

to explore this possibility.

We have made a Principal Component Analysis (PCA) between the different parameters involved in these relations and compared the orthogonal dispersion obtained for each one. We have done this for the $R_{\rm e,bo}^{\rm star}$-$M_{\rm cyl,bo}^{\rm star}$ relation, the Dynamical Plane, the Structural Plane and the Hyperplane in 4D. Also in order to check for the importance of projection effects we have done two things. First, we have built random samples of elliptical-like objects, this is, using just one random line-of-sight projection for each object instead of the mean value over one hundred. Second, we have extended this study to the 3D counterparts of all these relations. In the case of the Fundamental Plane we have used the 3D quantities already discussed in Section 6.2, $r_{\rm e,bo}^{\rm star}$, $\sigma_{\rm 3,bo}^{\rm star}$ and $M_{\rm bo}^{\rm star}$ that form the Intrinsic Dynamical Plane (IDP). Our analogous of the Photometric Plane in 3D, the Intrinsic Structural Plane (ISP), have been built using the μ term obtained from the fits of the Einasto equation (see Equation 4.11) to the 3D star mass density profiles of our simulated ellipticals presented in Section 5.2. As well as for the Structural Photometric Plane, we have found similar results using the characteristic radius and mass obtained from the fits or those obtained directly from the mass profiles. The orthogonal dispersion for each relation can be seen in Table 6.7.

From these numbers we can obtain several interesting remarks. First of all, we

Sample	#	A_z^{EA}	B_z^{EA}	C_z^{EA}	λ_1	λ_2	λ_3	$\sigma_z^{\rm nRE}$
EA-Z0	26	-0.30186	0.87653	-9.86211	0.12992	0.010797	0.003091	0.0556
EB-Z0	17	0.25221	0.72473	-7.80749	0.08067	0.008392	0.004006	0.0633
EA-STAR-Z0	56	-0.20651	0.84024	-8.51504	0.16439	0.014430	0.004547	0.0674

Table 6.6: Principal component analysis of mass, radius and dispersion velocity for *EA*-Z0, *EB*-Z0 and *EA*-STAR-Z0 samples. Column 2: number of objects in the sample. Columns 3, 4 and 5: coefficients of Equation 8.2 at each z. Columns 6, 7 and 8: eigenvalues of the correlation matrix. Columns 9: rms orthogonal scatter of the photometric plane at each z.

	Mass-Radius	Fundamental Plane	Photometric Plane	Hyperplane in 4D
	2D			
	$R_{\rm e,bo}^{\rm star}$, $M_{\rm cyl,bo}^{\rm star}$	$R_{\rm e,bo}^{\rm star}$, $M_{\rm cyl,bo}^{\rm star}$, $\sigma_{\rm los,0}^{\rm star}$	$R_{\rm e,bo}^{\rm star}$, $M_{\rm cyl,bo}^{\rm star}$, n	$R_{\rm e,bo}^{\rm star}$, $M_{\rm cyl,bo}^{\rm star}$, $\sigma_{\rm los,0}^{\rm star}$, n
$\sigma_{random}^{\rm ort}$	0.0625	0.0276	0.0580	0.0292
$\sigma_{mean}^{\rm ort}$	0.0592	0.0194	0.0556	0.0193
	3D			
	$r_{\rm e,bo}^{\rm star}$, $M_{\rm bo}^{\rm star}$	$r_{\rm e,bo}^{\rm star}$, $M_{\rm bo}^{\rm star}$, $\sigma_{\rm 3,bo}^{\rm star}$	$r_{\rm e,bo}^{\rm star}$, $M_{\rm bo}^{\rm star}$, μ	$r_{\rm e,bo}^{\rm star}$, $M_{\rm bo}^{\rm star}$, $\sigma_{\rm 3,bo}^{\rm star}$, μ
$\sigma^{\rm ort}$	0.0617	0.0145	0.0533	0.0144

Table 6.7: r.m.s. orthogonal scatter for the different relations between structural and kinematic parameters studied in our samples.

confirm that the Photometric Plane shows a slightly tighter correlation that the one obtained from the mass-radius relation. This is especially true for the random sample that is supposed to be closer to a real observational sample. We can also see that for all the possible combinations the Fundamental Plane shows a stronger correlation than the Photometric Plane and a great improvement relative to the radius-mass relation. Finally the Hyperplane in 4D presents the same dispersion as the Fundamental Plane. This indicates that we are not adding more information to this relation when we introduce the shape parameter n. However it is clear that we are not introducing a random variable either because this would make the orthogonal dispersion to increase. So, these results seem to indicate that although the shape parameter, n (or μ for the 3D profile), is very tightly correlated with all the parameters involved in the Fundamental Plane, it may not add any physical information to this relation.

In this sense, we have found that the Fundamental Plane and the Photometric Plane are not projections of a Hyperplane in 4D. It would be interesting to see what happens when the projection effects are circumvented in observations. Either because the statistical number of ellipticals in the Photometric Plane studies increase, or because the deprojection techniques evolve enough to get reliable predictions of the 3D structure of the galaxies. In both cases our results give a prediction of what could be found. Anyway, up to that moment the Photometric Plane seems to be a very powerful tool both for theoreticians and observers. This is especially true taking into account the

observational *low cost* of obtaining the shape parameter, n comparing with obtaining σ_0.

6.4 Stellar Population Properties

The final step in the analysis of virtual elliptical samples at redshift $z = 0$ is presented in this section. We have studied the stellar population properties of our ELOs and compare them with observational results. We have already discussed that elliptical galaxies present age effects with mass and that these effects link elliptical dynamical properties with the characteristics of their stellar population (see Section 3.3). To quantify these effects in our ELO samples, the global mean age, $\bar{t}$ of their stellar mass, $M_{\rm bo}^{\rm star}$, have been calculated. In addition, we have measured the percentiles of ELO stellar age distributions, $t_{\rm f}$, at which the fraction $f\%$ of the stellar mass at $z = 0$, $M_{\rm bo}^{\rm star}$, was already formed. We have done it for $f = 10, 50, 75, 90$. We have considered the difference $\Delta t = t_{75} - t_{10}$ as an estimation of the global width or timescale for ELO star formation.

We have found that for any f a trend exists with $M_{\rm vir}$. The observational age effects with $\sigma_{\rm los,0}^{\rm star}$ arise because, as we have already seen above (Section 6.2.3), $M_{\rm vir}$ and $\sigma_{\rm los,0}^{\rm star}$ are on their turn tightly correlated, making $\sigma_{\rm los,0}^{\rm star}$ an empirical virial mass estimator. As an illustration of these trends, in Figure 6.17 (upper panel) we plot the mean age versus $\sigma_{\rm los,0}^{\rm star}$ for the *EA*-Z0 and *EB*-Z0 samples and verify that they compare adequately well with relative mean age determinations through population synthesis modeling for Es obtained by Thomas et al. (2005). Lower panel of Figure 6.17 shows that observational width determinations from synthesis models (Thomas et al., 2002, 2005) are consistent with ELO widths. Therefore we see that, as for observational data, more massive ELOs have older mean ages and narrower spreads in the distributions of their stellar populations (downsizing). Note that these trends are independent of the particular details of the SF implementation, although their zero-point seems to depend. This result points to a contribution of purely dynamical effect with a cosmological origin for these trends, and plays a very important role in the development of the elliptical galaxy formation and evolution scenario (see Chapter 9).

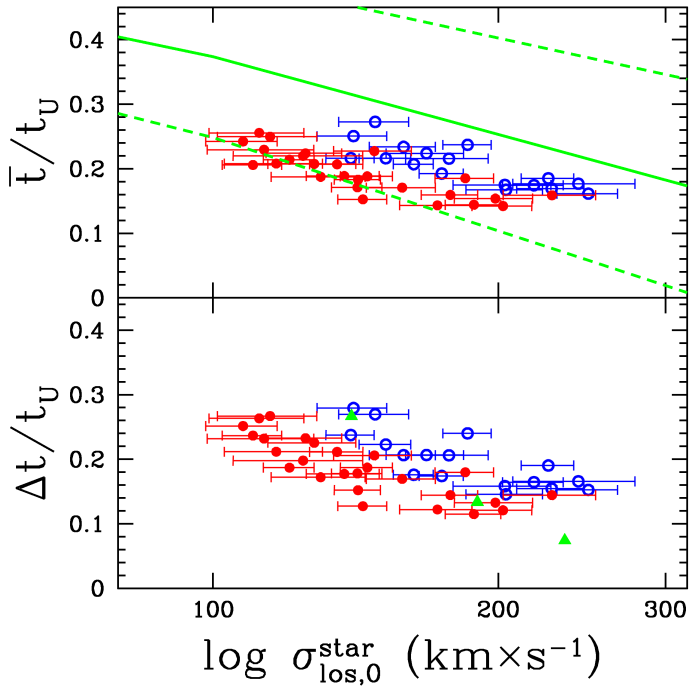

Figure 6.17: Upper panel: Mean age of the stellar population of our simulated ellipticals. Full green line is the observational fit obtained by Thomas et al. (2005) for high density environments. Dashed lines shows the error of this fit just taking into account errors in the age estimation. Lower panel: The width of the stellar population age distribution from our ELO samples compare with the one obtained from observations trough synthesis models (Thomas et al., 2005). In both panels, red filled circles stand for the *EA*-Z0 sample and blue open circles for the *EB*-Z0 sample. Error bars account for projection effects.

6.5 Robustness of Results and Beyond: Test Samples

In order to test the robustness of our results we have run a set of test simulations and built their corresponding ELO samples (see Section 4.2 and 4.4). In this Section we will discuss whether or not, slight changes in the cosmological model (*EC*-Z0 sample), a higher resolution (*ED*-Z0) and using a larger box size (*EF*1-Z0 and *EF*4-Z0), can affect the different results and conclusions presented in previous sections.

We have used these samples not only to test the robustness of all our results and conclusions but also to try to expand them. In this section we will focus on the virtual ellipticals at $z = 0$ of all these runs. In the next Chapters we will discuss on the formation and evolution scenario of these galaxies and how these test samples help to clarify it.

6.5.1 Changes in the Cosmological Model

We want to check if slight changes in the values of the Ω_Λ, $\Omega_{\rm baryon}$ or h parameters can affect the general trends found in our*EA* and *EB* samples. Specifically, we have run the (*EC*) simulation with the same parameters as in *EA* sample but for changing the cosmological parameters to their preferred WMAP values (Spergel et al., 2003). See Table 4.1 and Section 4.2 for more details.

We first check whether these ELOs satisfy the Fundamental Plane relation found in previous samples. In Figure 6.18 we plot the κ-space coordinates (left panel) and the $M_{\rm vir}/M_{\rm bo}^{\rm star}$ ratios. We have also performed the same analysis done in 6.2.4, to test not only the Fundamental Plane by itself but, also, the origin of their tilt, i.e., the relation between the Fundamental Parameters at different scales. To perform this test we replaced ELOs of one of the simulation of the *EA*-Z0 sample with ELOs identified in *EC*-Z0 simulation. Results of the fits are shown in Table 6.8 and 6.9 and indicate that there is no statistical difference between these two sets of ELOs. We can also see that these new ELOs seem to be less massive than the *EA*-Z0 sample. Although this could be true due to the change of the global cosmological parameters $\Omega_{\rm b}$ and $\Omega_{\rm m}$ to a lower value, in our case, this effect has more to do with the fact that the three more massive objects in the *EC*-Z0 sample are merging and cannot be included in the sample. This fact reduces the range of masses that can be studied with this simulation.

In Figure 6.19 we can appreciated other structural parameters that confirm that the ELOs of this simulation not only satisfy all the scaling relations found for the *EA* sample, but also that the zero-point of these trends do not really differ between both runs.

Finally, another important point is that stellar population properties and the trends found with the dynamical parameters, as $\sigma_{\rm los,0}^{\rm star}$, holds for the *EC*-Z0 sample. As expected, it shares the same zero point as the *EA*-Z0, as they both have the same star

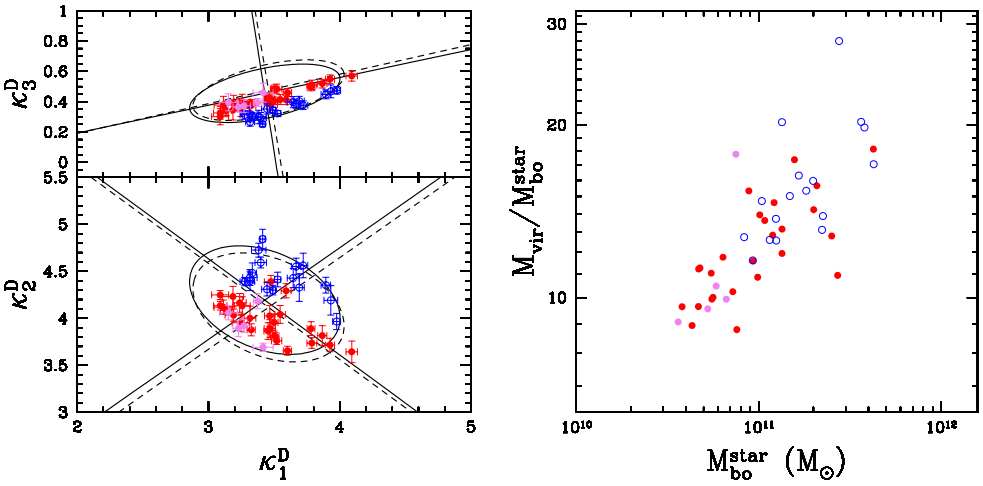

Figure 6.18: Robustness of results. Cosmology test I: The Fundamental Plane in kappa space (left) and the $M_{\rm vir}/M_{\rm bo}^{\rm star}$ ratio versus $M_{\rm bo}^{\rm star}$ (right) for the *EC*-Z0 sample (violet filled circles). To compare with previous results, *EA*-Z0 (red filled circles) and *EB*-Z0 (blue empty circles) samples are also shown. Error bars account for projection effects.

formation parameters (see Figure 6.20). This is a very important result because it indicates that the stellar age properties are linked with star formation parameters rather than with changes in the cosmological parameters: Ω_Λ, $\Omega_{\rm m}$, $\Omega_{\rm b}$ and h.

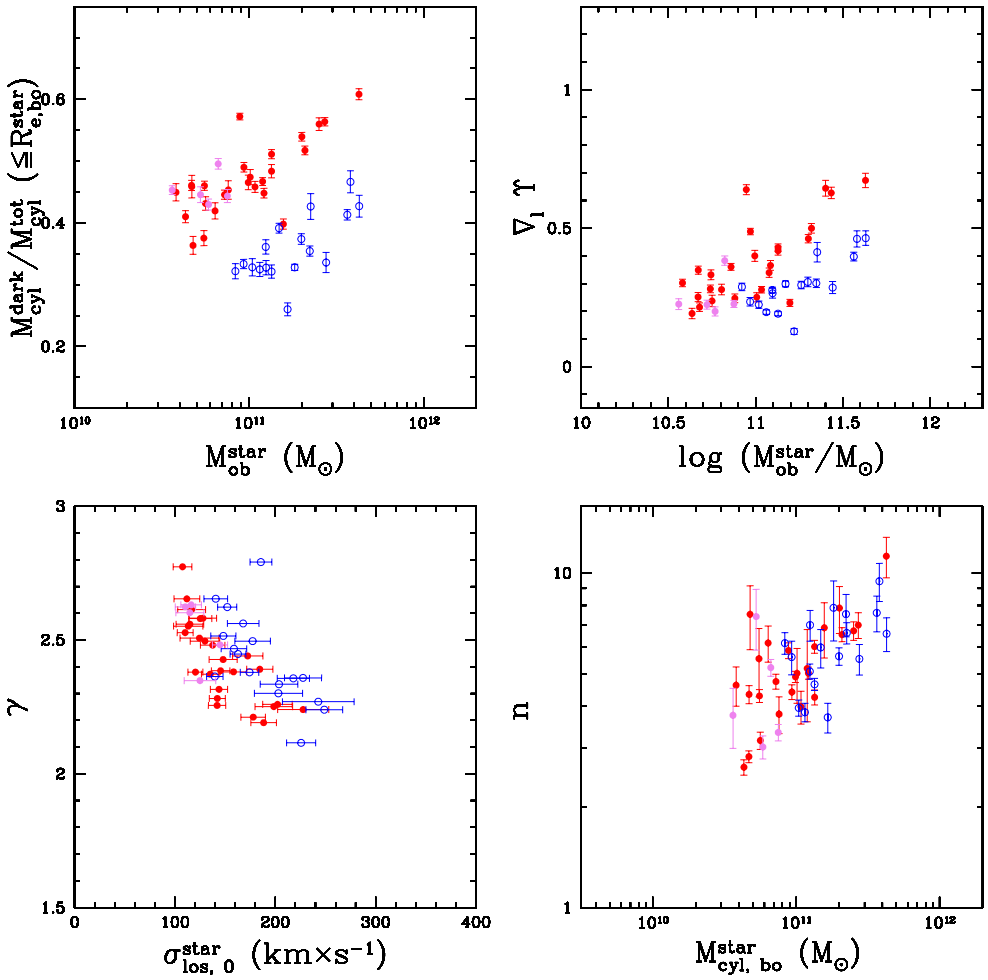

Figure 6.19: Robustness of results. Cosmology test II: Different structural parameters for the *EC*-Z0 sample (violet filled circles) that characterize their profiles. The dark-over-total mass ratio (upper left), gradients of the projected mass profiles (upper left), the total density profile slope obtained from fitting $\rho^{\rm tot}(r)\ r^{-\gamma}$ (lower left) and the shape parameter n versus $M^{\rm star}_{\rm bo}$. To compare with previous results, *EA*-Z0 (red filled circles) and *EB*-Z0 (blue empty circles) samples are also shown. Error bars account for projection effects.

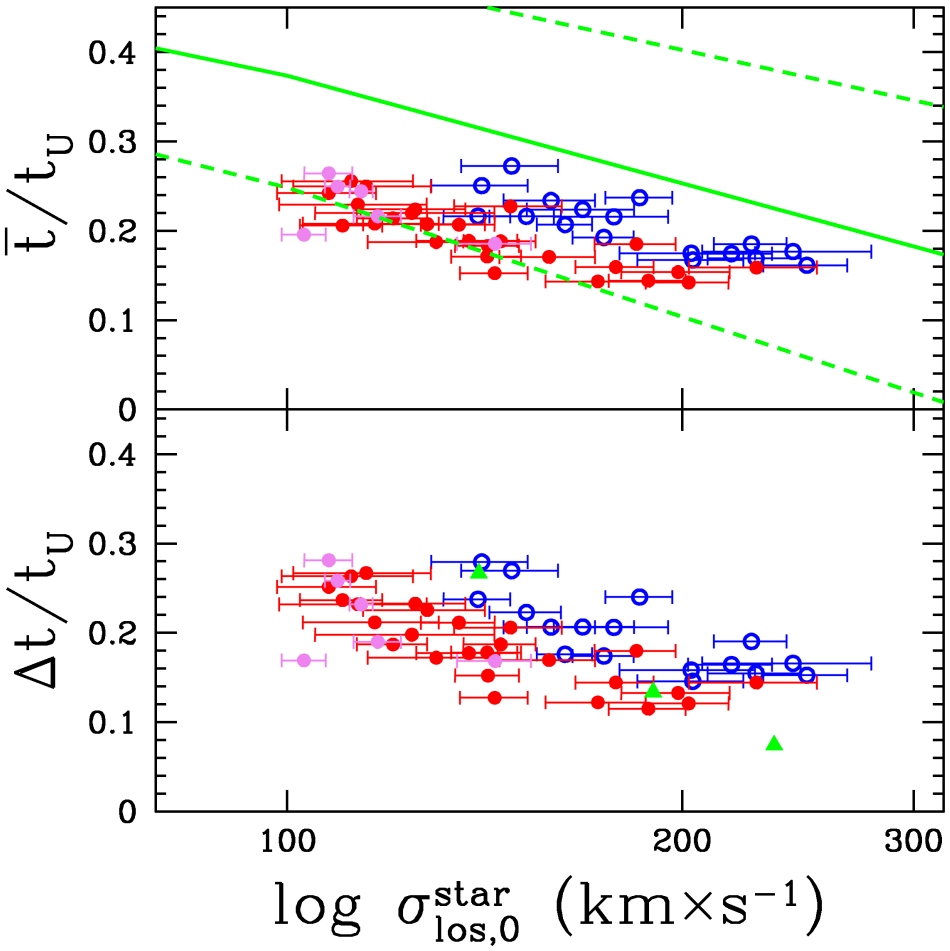

Figure 6.20: Robustness of results. Cosmology test III: Upper panel: Mean age of the stellar population of our simulated ellipticals. Full green line is the observational fit obtained by Thomas et al. (2005) for high density environments. Dashed lines shows the error of this fit just taking into account errors in the age estimation. Lower panel: The width of the stellar population age distribution from our ELO samples compare with the one obtained from observations trough synthesis models (Thomas et al., 2005). In both panels, red filled circles stand for the *EA*-Z0 sample, blue open circles for the *EB*-Z0 sample and violet filled circles for the *EC*-Z0 sample. Error bars account for projection effects.

6.5.2 Possible Resolution Effects

To test whether or not the resolution of our simulations can affect our conclusions, we have checked if the simulated ellipticals of a higher resolution simulation follow the same trends found for the *EA*-Z0 sample. We have used a *ED* simulation (S7714) with the same parameters as in the *EA* simulations but with more 2×128^3 particles and a higher softening length ($\epsilon = 0.00075$). See Table 4.1 and Section 4.2 for more details.

Figure 6.21 shows the FP in kappa coordinates (see Equations 6.5-6.7) and confirms that this relation holds for the new sample, with the same tilt and zero point those of the *EA*-Z0 sample. To check whether this is true for the different relations at halo and baryonic scale we have performed the same statistical study of the tilt and scatter of the Fundamental Plane, done in the cosmological test, for the *EC*-Z0 sample. Column two of Tables 6.8 and 6.9 present these results. Figure 6.22 shows also another set of structural parameters that define the dark matter, stellar and total mass distribution. In all of them we see no remarkable differences between the higher resolution sample and the *EA*-Z0 one.

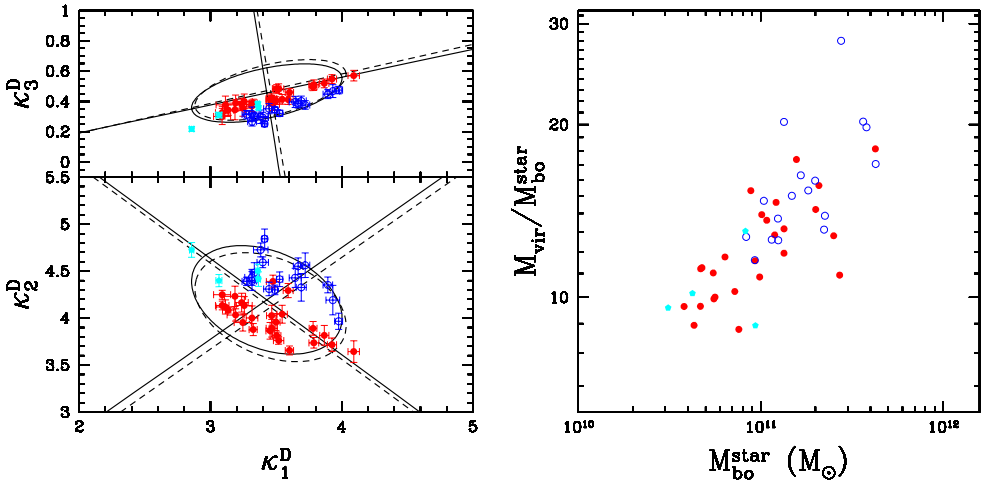

Figure 6.21: Robustness of results. Resolution test I: The Fundamental Plane in kappa space (left) and the $M_{\rm vir}/M_{\rm bo}^{\rm star}$ ratio versus $M_{\rm bo}^{\rm star}$ (right) for the *ED*-Z0 sample (cyan filled pentagons). To compare with previous results, *EA*-Z0 (red filled) and *EB*-Z0 (blue empty) samples are also shown. Error bars account for projection effects.

In these Figures we can see that the simulated ellipticals resulting from a higher resolution confirm all our previous conclusions. Moreover it seems that they also hold for ellipticals of masses lower than the ones we reached in the *EA* and *EB* samples.

Otherwise, Figures 5.19 and 5.20 show that two-body relaxation effects (typically the most stringent requirement for convergence) have not been important at least for r larger than ~ 1 kpc. In fact, two-body relaxation effects cause energy equipartition. But the values of the $\sigma_{3D}^{\rm star}(r)/\sigma_{3D}^{\rm dark}(r)$ ratios we have obtained ($\simeq 0.8$) exclude energy equiparti-

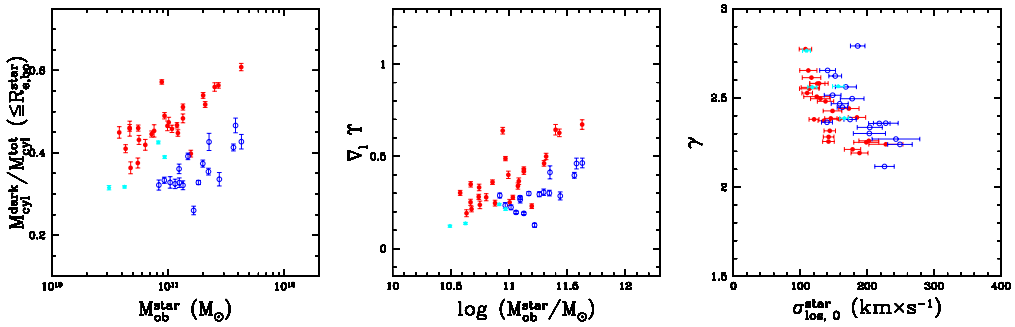

Figure 6.22: Robustness of results. Resolution test II: Different structural parameters for the *ED*-Z0 sample (cyan filled pentagons) that characterize their profiles. The dark-over-total mass ratio (left), gradients of the projected mass profiles (center) and the total density profile slope obtained from fitting $\rho^{\rm tot}(r)\ r^{-\gamma}$ (right). To compare with previous results, *EA*-Z0 (red filled circles) and *EB*-Z0 (blue empty circles) samples are also shown. Error bars account for projection effects.

tion among dark matter and stellar particles in ELOs, because such equipartition would demand $\sigma^{\rm star}_{3D}(r)/\sigma^{\rm dark}_{3D}(r) = \left[m^{\rm dark}/m^{\rm star}\right]^{0.5} = 2.194$, where $m^{\rm dark} = 1.29 \times 10^8 {\rm M}_\odot$ and $m^{\rm star} = 2.67 \times 10^7 {\rm M}_\odot$ are the mass of dark and stellar particles, respectively. This result is important because it shows that two-body relaxation effects have played no important role in the gravitational interaction.

Concerning age stellar population in Figure 6.23 we plot the mean and width of the stellar age distribution of the *ED*-Z0 sample. We found that this sample presents the same trends found in *EA*-Z0 y *EB*-Z0 and shares the zero-point with the first one.

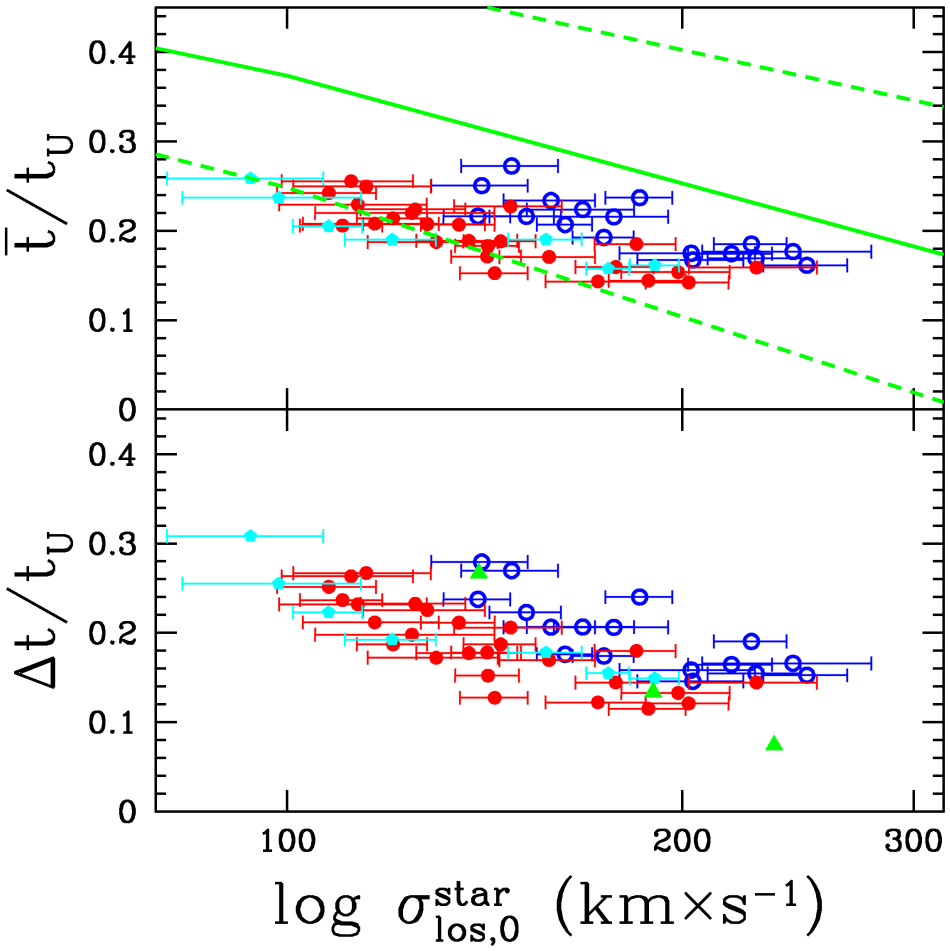

Figure 6.23: Robustness of results. Resolution test III: Upper panel: Mean age of the stellar population of our simulated ellipticals. Full green line is the observational fit obtained by Thomas et al. (2005) for high density environments. Dashed lines shows the error of this fit just taking into account errors in the age estimation. Lower panel: The width of the stellar population age distribution from our ELO samples compare with the one obtained from observations trough synthesis models (Thomas et al., 2005). In both panels, red filled circles stand for the *EA*-Z0 sample, blue open circles for the *EB*-Z0 sample and cyan filled pentagons for the *ED*-Z0 sample. Error bars account for projection effects.

6.5.3 Box Size Effects

To make sure that the results we report in this study are not unstable under changes in the box size of the simulations, we have run several new ones with 8 times and 512 times the volume of the *EA* and *EB* runs, i.e. $L_{box} = 20$ Mpc and $L_{box} = 80$ respectively (*EF*1-2 and *EF*3 runs). We have also increased the number of particles by the same factor to obtain identical physical resolution. See Table 4.1 and Section 4.2 for the details on their implementation. Again, have used different strong correlations found in *EA* samples to check our results.

6.5.3.1 $L_{\rm box} = 20$ Mpc

Figure 6.24 shows the Fundamental Plane projections in kappa coordinates and the $M_{\rm vir}/M_{\rm bo}^{\rm star}$ ratio for the virtual ellipticals of *EF*1-Z0 simulation (orange circles) and the *EA*-Z0 and *EB*-Z0 sample (red and blue respectively). We have performed a statistical analysis as the one made in Section 6.2.4 to study the origin of the tilt of the Fundamental Plane. Results of these statistical analyses can be found in Tables 6.8 and 6.9. From all this data it seems that the *EF*1-Z0 sample follows exactly the same trends found for the *EB*-Z0 sample rather than that found for the *EA*-Z0 sample, even if the star formation parameters of the *EF*1 run are the same as this last one. This can be due to the different gravitational softening parameter, ϵ, employed in this simulation, as it is a bit higher than the *EA* and *EB* runs.

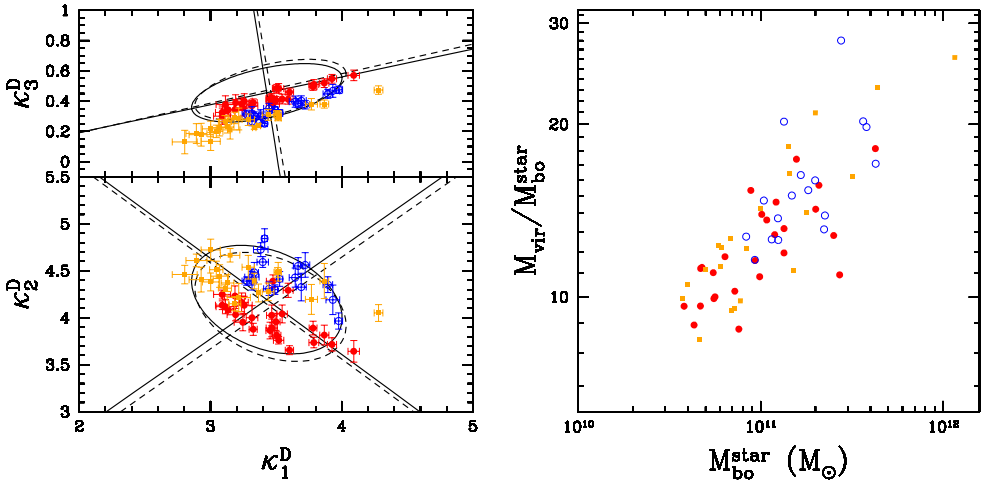

Figure 6.24: Robustness of results. Box size test I: $L_{\rm box} = 20$ Mpc. The Fundamental Plane in kappa space (left) and the $M_{\rm vir}/M_{\rm bo}^{\rm star}$ ratio versus $M_{\rm bo}^{\rm star}$ (right) for the *EF*1-Z0 sample (orange filled circles). To compare with previous results *EA*-Z0 (red filled symbols) and *EB*-Z0 (blue empty symbols) samples are also shown. Error bars account for projection effects.

In Figure 6.25 we plot a set of different parameters that define the dark matter,

stellar and total mass distribution of the *EF*1-Z0 sample. These plots confirm the idea that the *EF*1-Z0 sample is much more similar to the *EB*-Z0 than to *EA*-Z0, and that, in any case, all the conclusions discussed above hold for this new sample.

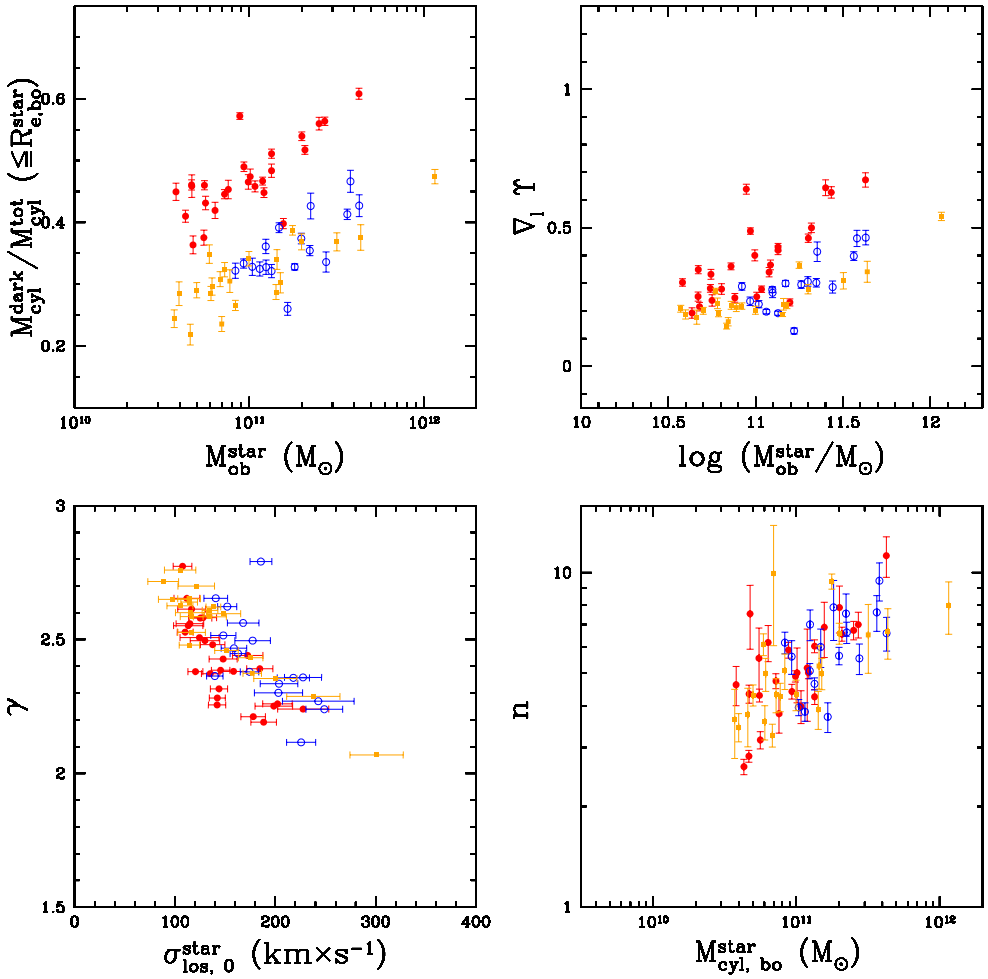

Figure 6.25: Robustness of results. Box size test II: $L_{box} = 20$ Mpc. Different structural parameters for the *EF*1-Z0 sample (orange filled squares) that characterize their profiles. The dark-over-total mass ratio (upper left), gradients of the projected mass profiles (upper left), the total density profile slope obtained from fitting $\rho^{tot}(r)\ r^{-\gamma}$ (lower left) and the shape parameter n versus M^{star}_{bo}. To compare with previous results, *EA*-Z0 (red filled symbols) and *EB*-Z0 (blue empty symbols) samples are also shown. Error bars account for projection effects.

Finally we have studied the stellar properties of this sample and compared them with the *EA*-Z0 and *EB*-Z0 samples. Figure 6.26 shows the results. Again we found that the trends with dynamical parameters are very similar to the *EB*-Z0. This is in agreement with the idea, discussed above, of the origin of trends between stellar and dynamical properties of ELOs being highly linked with a dynamical origin. The fact

that in the test sample, ELOs of similar $\sigma^{star}_{los,0}$ data present a higher dispersion both in the mean stellar age and in the width of the distribution is related with the larger box side. This would allow obtaining virtual ellipticals from a wider range of different environments and history (passive evolution, mergers, etc).

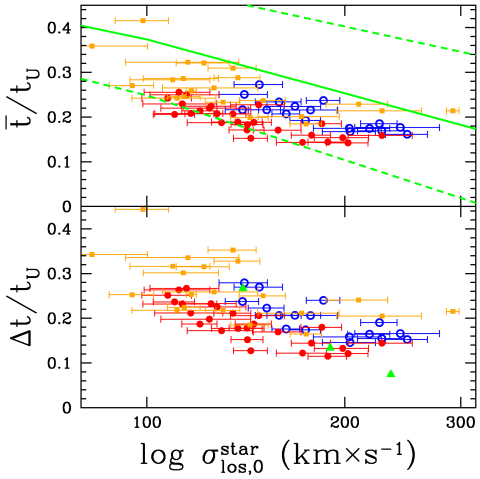

Figure 6.26: Robustness of results. Box size test III: $L_{box} = 20$ Mpc. Upper panel: Mean age of the stellar population of our simulated ellipticals. Full green line is the observational fit obtained by Thomas et al. (2005) for high density environments. Dashed lines shows the error of this fit just taking into account errors in the age estimation. Lower panel: The width of the stellar population age distribution from our ELO samples compare with the one obtained from observations trough synthesis models (Thomas et al., 2005). In both panels, red filled circles stand for the *EA*-Z0 sample, blue open circles for the *EB*-Z0 sample and orange filled squares for the *EF*1-Z0 sample. Error bars account for projection effects.

6.5.3.2 $L_{\rm box} = 80$ Mpc

Figure 6.27 shows the Fundamental Plane projections in kappa coordinates and the $M_{\rm vir}/M_{\rm bo}^{\rm star}$ ratio for the virtual ellipticals of *EF*1-Z0 simulation (orange circles) and the *EA*-Z0 and *EB*-Z0 sample (red and blue respectively). In figure 6.28 *EF*3 ELO sample and SDSS (z band) are shown in a mass, radius and velocity dispersion coordinate system. Although with just 11 ELOs in the *EF*3 sample, we have performed a statistical analysis as the one made in Section 6.2.4 to study the origin of the tilt of the Fundamental Plane. Results of these statistical analyses can be found in Tables 6.8 and 6.9. From all these data it seems that the *EF*3-Z0 sample follows the same trends found for the *EA*-Z0 sample. However, concerning the origin of the tilt of the Fundamental Plane, we obtain a clear signal from the relative content of the baryonic and the dark mass ELO components ($\beta_{\rm vir}$), but not for the relative distributions ($\beta_{\rm rd}$). Although this contribution is not statistically discarded either, this result must be taken into account at least until more statistics are available. Regarding the scatter of the Fundamental Plane, it is important to point out that the different *EF* samples show just a slightly higher scatter for the Dynamical Fundamental Plane than the smaller box samples, even for the -STAR samples, and still thinner than the observational one. This result indicates that stellar effects could have contributed to the scatter of the observed FP (see Hyde & Bernardi, 2008b, for similar conclusion from recent observational results).

Finally we have studied the stellar properties of this sample and compared them with the *EA*-Z0 and *EB*-Z0 samples. Figure 6.29 shows the results. We found that the trends with dynamical parameters are very similar to the previous samples, sharing its zero point with the *EA*-Z0 sample.

In this sense, our results concerning L_{box} point to the same conclusion of Power et al. (2003) in their convergence study of dark matter halos, i.e., the internal properties of virialized objects do not strongly depend on the L_{box} size. However simulations with higher box sizes produce virtual objects with higher dispersion in the different environments and history. Therefore these simulations are more realistic and very well suited in order to do statistical comparison with observations. On the other side, simulations with a smaller box size can be better to isolate and study the different fundamental physical processes that govern galaxy formation and evolution. In fact by combining both types of them, we can study the influence of environment and history on the different structural and kinematical properties of ellipticals. Here we have seen that the most important findings of our *EA* and *EB* simulations concerning the Fundamental Plane and other relations holds for the *EF* samples.

Differences between *EF* samples are tiny. However one interesting point is the different total number of elliptical-like galaxies for each sample (see Section 4.4). This fact seems to be related with two reasons. First one is related with the different environment and history issue. In simulations with a higher σ_8 everything occurs faster and therefore,

at redshift zero we have more elliptical-like objects well defined at the halo scale. The other important factor in the final number of ELOs is the specific cosmological model selected. The Ω_Λ, Ω_m and Ω_b parameters set the amount of baryonic matter that we will have in our simulation to form our galaxies. Therefore, although with slight changes in these values the main physical processes remain the same, these parameters determine the mass distribution of our galaxy-like objects and as we have a fixed cut in resolution we will have more objects as more baryonic matter is available in the simulation.

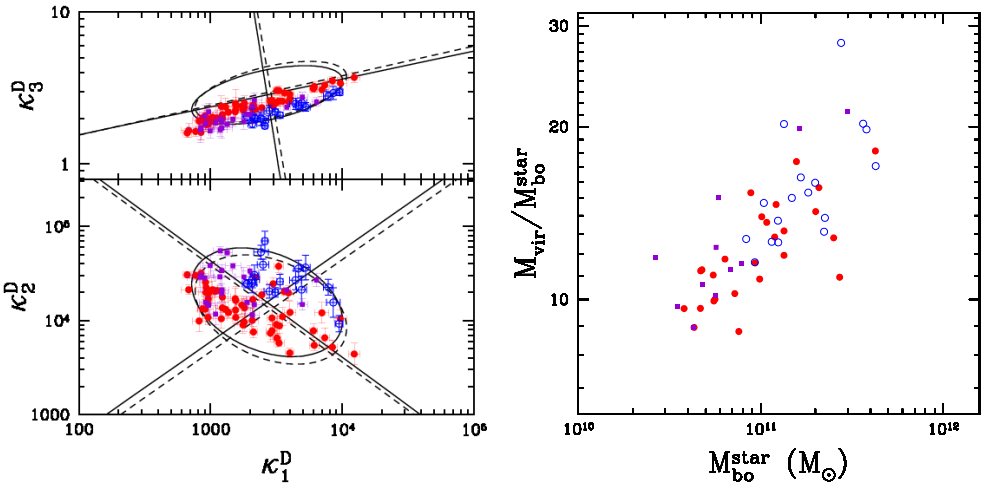

Figure 6.27: Robustness of results. Box size test Ia: $L_{\rm box}$ = 80 Mpc. Left: The Fundamental Plane in kappa space for the *EF*3-STAR-Z0 sample (dark violet filled squares). To compare with previous results *EA*-STAR-Z0 (red filled symbols) and *EB*-STAR-Z0 (blue empty symbols) samples are also shown. Right: The $M_{\rm vir}/M_{\rm bo}^{\rm star}$ ratio versus $M_{\rm bo}^{\rm star}$ (right) for the *EF*3-Z0 sample (dark violet filled squares). To compare with previous results *EA*-Z0 (red filled symbols) and *EB*-Z0 (blue empty symbols) samples are also shown. Error bars account for projection effects.

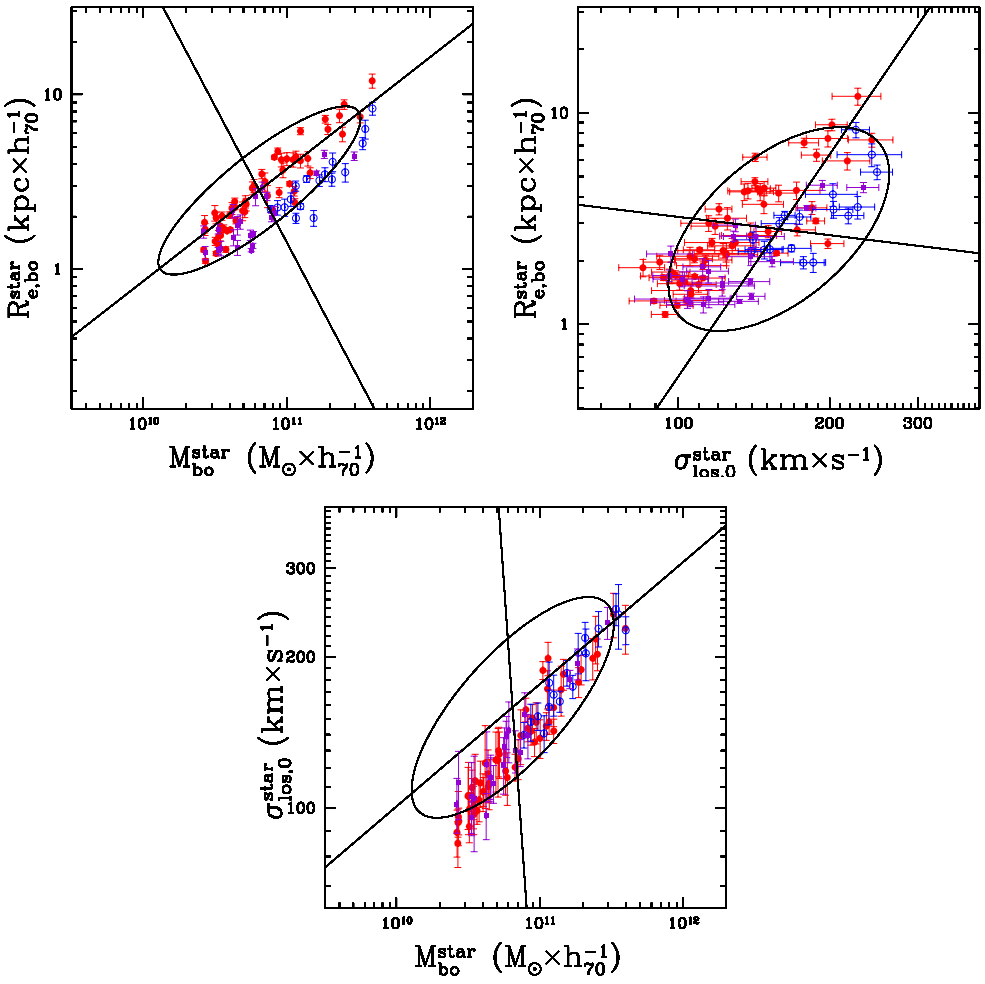

Figure 6.28: Box size test Ib: L_{box} = 80 Mpc: The Dynamical Plane: $R^{star}_{e,bo}$,M^{star}_{bo} and $\sigma^{star}_{los,0}$ space for the *EF*3-STAR-Z0 sample (dark violet filled squares). To compare with previous results *EA*-STAR-Z0 (red filled symbols) and *EB*-STAR-Z0 (blue empty symbols) samples are also shown. Error bars account for projection effects. We also draw the respective concentration ellipses (with their major and minor axes) for the SDSS early-type galaxy sample from Bernardi et al. (2003b) in the z band (solid line).

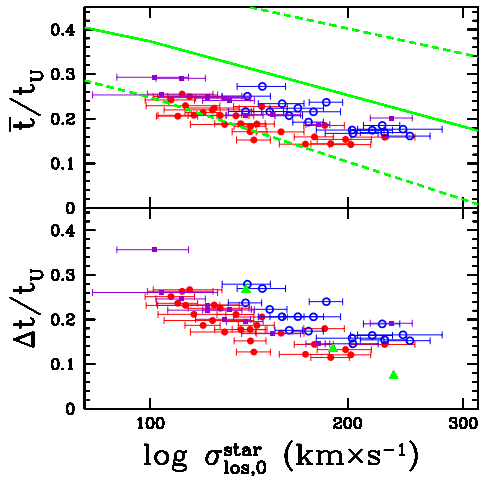

Figure 6.29: Robustness of results. Box size test III: L_{box} = 80 Mpc. Upper panel: Mean age of the stellar population of our simulated ellipticals. Full green line is the observational fit obtained by Thomas et al. (2005) for high density environments. Dashed lines shows the error of this fit just taking into account errors in the age estimation. Lower panel: The width of the stellar population age distribution from our ELO samples compare with the one obtained from observations trough synthesis models (Thomas et al., 2005). In both panels, red filled circles stand for the *EA*-Z0 sample, blue open circles for the *EB*-Z0 sample and dark violet filled squares for the *EF*3-Z0 sample. Error bars account for projection effects.

Parameter	*EC*-Z0	*ED*-Z0	*EF*1-Z0	*EF*3-Z0
M_1	0.237 ± 0.044	0.267 ± 0.040	0.225 ± 0.037	0.193 ± 0.111
$\beta_{\rm vir}$	0.217 ± 0.106	0.204 ± 0.096	0.280 ± 0.088	0.345 ± 0.166
$\beta_{\rm M}$	-0.142 ± 0.167	-0.243 ± 0.147	-0.087 ± 0.116	0.092 ± 0.249
$\beta_{\rm f}$	0.060 ± 0.048	0.066 ± 0.052	0.028 ± 0.035	0.056 ± 0.060
$\beta_{\rm vd}$	0.004 ± 0.040	0.046 ± 0.061	-0.002 ± 0.032	-0.035 ± 0.072
$\beta_{\rm vpc}$	0.012 ± 0.040	-0.005 ± 0.039	0.034 ± 0.040	0.086 ± 0.107
$\beta_{\rm rd}$	-0.228 ± 0.169	-0.356 ± 0.182	-0.167 ± 0.101	-0.045 ± 0.232
$\beta_{\rm rp}$	0.013 ± 0.013	0.008 ± 0.013	0.023 ± 0.013	0.026 ± 0.022

Table 6.8: Slopes for linear fits at $z = 0$ for the different test samples. Column 1: the slopes of the $\kappa_3^{\rm D} = M_1\kappa_1^{\rm D} + M_0$ relation (direct fits); the slopes of the $M_{\rm vir}/M_{\rm bo}^{\rm star}$ and $c_{\rm i} \propto (M_{\rm bo}^{\rm star})^{\beta_{\rm i}}$ scaling relations, calculated in $\log - \log$ plots through direct fits for the cosmological test sample (*EC* simulation). Errors stand for their respective 95% confidence intervals. Column 2: same as columns 1 for the higher resolution sample (*ED* simulation). Column 3 and 4: same as column 1 for the larger box size samples (*EF*1 and *EF*3 simulation). See text for details.

Parameter	*EC*-Z0	*ED*-Z0	*EF*1-Z0	*EF*1-STAR-Z0	*EF*3-Z0	*EF*3-STAR-Z0
σ_{EVR}	0.0197	0.0180	0.0215	0.0221	0.0188	0.0262
SDSS	z band	r band				
σ_{LVR}	0.0489	0.052				

Table 6.9: Scatter of the Fundamental Plane for the different test samples and for different bands of the SDSS early-type sample. See text for details.

Sample	No.	$\tilde{\rm E}$	$\tilde{\rm r}$	$\tilde{\rm v}$	λ_1	λ_2	λ_3	$\alpha^{\rm 3D}$	$\gamma^{\rm 3D}$	$\sigma_{\rm Erv}$
*EF*1	21	11.026	0.545	2.308	0.24067	0.00409	0.00050	0.331	2.129	0.022
*EF*1-STAR-Z0	31	10.991	0.518	2.299	0.17578	0.00458	0.00046	0.402	1.975	0.021
*EF*3-Z0	11	10.816	0.416	2.278	0.13238	0.00846	0.00034	0.352	1.969	0.018
*EF*3-STAR-Z0	22	10.774	0.418	2.259	0.10602	0.00787	0.00041	0.377	1.943	0.020

Table 6.10: Results of PCA at $z = 0$. Column 2: ELO number in the sample. Columns 3, 4 and 5: sample mean values of the E, r and v variables. Columns 6, 7 and 8: eigenvalues of the correlation matrix. Columns 9 and 10: coefficients of the plane (Eq. 6.1). Column 11: IDP scatter in the E, r and v variables.

Sample	#	A_z^{EA}	B_z^{EA}	C_z^{EA}	λ_1	λ_2	λ_3	σ_z^{nRE}
*EF*1-Z0	21	-0.41220	0.79899	-8.22228	0.22673	0.014084	0.002462	0.0496
*EF*1-STAR-Z0	31	-0.31867	0.75837	-7.70990	0.16490	0.019999	0.002774	0.0527
*EF*3-Z0	11	-0.49447	0.80827	-8.03058	0.13885	0.027877	0.003712	0.0609
*EF*3-STAR-Z0	22	-0.25006	0.74982	-7.58819	0.11996	0.027059	0.005245	0.0724

Table 6.11: Principal component analysis of mass, radius and dispersion velocity for *EA*-Z0, *EB*-Z0 and *EF*3 simulations. Column 2: number of objects in the sample. Columns 3, 4 and 5: coefficients of Equation 8.2 at each z. Columns 6, 7 and 8: eigenvalues of the correlation matrix. Columns 9: rms orthogonal scatter of the photometric plane at each z.

6.6 Discussion and Conclusions

In this Chapter we have reported on the structural and kinematical characteristic parameters of a set of samples of ELOs at $z = 0$, formed in different cosmological simulations. In this sense we have followed with the analysis started in the previous chapter and deepen into the different relations that all these parameters show. Our first goal in this Section is to check the robustness of the main results presented in the two previous Chapters.

6.6.1 Main Results

The first step in the program of studying the origins of EGs through self-consistent simulations, we want to ensure that our ELO samples have counterparts in the real local Universe. Concerning this goal, in this chapter an analysis of the structural and dynamical ELO parameters that can be constrained from observations has shown that they are consistent with those measured in the SDSS elliptical sample (see also Sáiz et al., 2004), including the Fundamental Plane relation. We had already seen that the projected stellar *mass* profile, $\Sigma^{\rm star}(R)$, can be adequately fitted by a Sérsic-like law (see Section 5.2.6). In addition, we have confirmed that the shape parameter values n we have obtained are consistent with observations, including their correlations with the ELO luminosity (mass), size and velocity dispersion (Photometric Plane relation). Also, ELO stellar populations have age distributions with the same trends as those inferred from observations, i.e., most stars have formed at high z on short timescales, and, moreover more massive objects have older means and narrower spreads in their stellar age distributions than less massive ones (Domínguez-Tenreiro et al., 2004).

These agreements with observational data strongly suggest that the intrinsic three-dimensional dark and bright matter mass and velocity distributions we get in our simulations might also adequately describe real ellipticals. Let us now summarize the main results obtained from the study of the different characteristic parameters that describe the structural and kinematical properties of our virtual ellipticals.

Mass, size and velocity dispersion scales for their different components have been measured in the ELO samples, both at the scale of their halo and at the scale of the baryonic object (a few tens of kiloparsecs). At the *halo scale*, the masses of both cold gas and stars, $M_{\rm h}^{\rm cb}$ and $M_{\rm h}^{\rm star}$, respectively, have been found to be tightly correlated with the halo total mass, $M_{\rm vir}$, with the ratios $M_{\rm h}^{\rm cb}/M_{\rm vir}$ and $M_{\rm h}^{\rm star}/M_{\rm vir}$ decreasing as $M_{\rm vir}$ increases (that is, massive objects miss cold baryons within $r_{\rm vir}$ when compared with less massive ELOs), presumably because gas gets more difficulties to cool and fall as $M_{\rm vir}$ increases. The overall half-mass radii, $r_{\rm e,h}^{\rm tot}$ shows also a very tight correlation with $M_{\rm vir}$. Half-mass radii for the cold baryon or stellar mass distributions have a more complex behavior, as in these cases gas heating in shocks and energy losses due gas

cooling are in competition to determine these distributions.

Another interesting result we have found when analyzing ELOs at the *scale of the baryonic object*, is that $M_{\rm vir}$ plays an important role to determine the ELO structure also below a few tens of kiloparsecs scales. In fact, both the masses of cold baryons $M_{\rm bo}^{\rm cb}$ (i.e., those baryons that have reached the central regions of the configuration), and of stars $M_{\rm bo}^{\rm star}$, show a good correlation with $M_{\rm vir}$, and, moreover, the $M_{\rm bo}^{\rm cb}/M_{\rm vir}$ and $M_{\rm bo}^{\rm star}/M_{\rm vir}$ ratios (i.e., the relative content of cold baryons or stars versus total mass) decrease as $M_{\rm vir}$ increases. This is the same qualitative behavior shown by these ratios observationally in the SDSS data, and, also, by ELOs at the halo scale. The dependence of $M_{\rm bo}^{\rm cb}$ or $M_{\rm bo}^{\rm star}$ on the SF parameterization is only very slight, with *EA*-Z0 type ELOs having slightly more stars than their *EB*-Z0 type counterparts. The half-mass radii for cold baryon and stellar masses, $r_{\rm e,bo}^{\rm cb}$ and $r_{\rm e,bo}^{\rm star}$, show also a good correlation with $M_{\rm vir}$, but now the values of the SF parameters also play a role, because their change implies a change in the time interval during which gas cooling is turned on, and this changes the ELO stellar mass distribution, i.e., its length scale, so that ELO compactness increases from *EA*-Z0 to *EB*-Z0 type simulations. Another important result is that, regardless of the SF parameterizations used in this work, the relative distributions of the stellar and dark mass components in ELOs show a systematic trend measured through the $c_{\rm rd} \equiv r_{\rm e,h}^{\rm tot}/r_{\rm e,bo}^{\rm star}$ ratios, with stars relatively more concentrated as $M_{\rm vir}$ decreases (i.e., a quantification of the spatial homology breaking). However it is important to note that this trend is not statistically confirmed (nor discarded) in all samples (see discussion in Section 6.5.3). Note that to compare with observational data, the relevant parameters are the *projected* half-mass radii, $R_{\rm e,bo}^{\rm star}$. We have checked that they show an excellent correlation with the corresponding three dimensional half-mass radii, with the $c_{\rm rp} \equiv r_{\rm e,bo}^{\rm star}/R_{\rm e,bo}^{\rm star}$ ratios showing no significant dependence on the ELO mass scale.

Concerning kinematics, a useful characterization of the ELO velocity dispersion is the central stellar line-of-sight velocity dispersion, $\sigma_{\rm los,0}^{\rm star}$, whose observational counterpart can be measured from elliptical spectra. A very important outcome is the very tight correlation we have found between $M_{\rm vir}$ and $\sigma_{\rm los,0}^{\rm star}$, confirming that the observationally measurable σ_0 is a fair virial mass estimator. In addition, $\sigma_{\rm los,0}^{\rm star}$ is closely related to the mean square velocity of both, the whole elliptical at the halo scale (including the dark matter), $\sigma_{\rm 3,h}^{\rm tot}$, and the stellar component of the central object, $\sigma_{\rm 3,bo}^{\rm star}$. We have also found that the $c_{\rm vd} \equiv (\sigma_{\rm 3,h}^{\rm tot}/\sigma_{\rm 3,bo}^{\rm star})^2$ or the $c_{\rm vpc} \equiv (\sigma_{\rm 3,bo}^{\rm star})^2/3(\sigma_{\rm los,0}^{\rm star})^2$ ratios are roughly independent of the ELO mass scale. And so, ELOs do not show dynamically broken homology, even if their stellar and dark components are cinematically segregated (i.e., $c_{\rm vd} \neq 1$). This could lead to inaccurate determinations of the total mass of ellipticals when using stellar kinematics.

A very important result is that, irrespective of the SF parameterization, the (loga-

rithms of the) ELO stellar masses $M_{\rm bo}^{\rm star}$, stellar half-mass radii $r_{\rm e,bo}^{\rm star}$, and stellar mean square velocity of the central object $\sigma_{\rm 3,bo}^{\rm star}$, define *intrinsic dynamical* planes (IDPs). These planes are tilted relative to the virial plane and the tilt does not significantly depend on the SF parameterization, but the zero point does depend. Otherwise, the intrinsic dynamical plane is not homogeneously populated, but ELOs, as well as E galaxies in the FP (Guzman et al., 1993), occupy only a particular region defined by the range of their masses. The observational manifestation of this relation is the Fundamental Plane.

In addition, ELOs 3D structural parameters, $M_{\rm bo}^{\rm star}$, $r_{\rm e,bo}^{\rm star}$ and μ define *intrinsic structural* planes (ISPs). However these planes are not as tightly correlated as the IDPs ones. The Photometric Plane is the observational manifestation of this relation. We have also discarded the possibility that the Fundamental Plane and the Photometric Plane, are a projection of a four parameter law. We made the study for the 2D *observational* relations and their 3D counterparts. We found that the shape parameter n (or μ in 3D) does not add physical information to the Fundamental Plane relation (or intrinsic).

Stellar age properties of virtual ellipticals have shown a clear trend with their structural and dynamical characteristic parameters and seem to be linked with their formation and evolution processes in a cosmological scenario. Also, ELO stellar populations have age distributions with the same trends as those inferred from observations, i.e., most stars have formed at high z on short timescales, and, moreover more massive objects have older means and narrower spreads in their stellar age distributions than less massive ones (Domínguez-Tenreiro et al., 2004). This is equivalent to downsizing (see 3.3). We will discuss the implications of these results on the elliptical galaxy formation and evolution scenarios in Chapter 9.

6.6.1.1 The Dimensionality of ELO and Elliptical Samples in Parameter Space

The intrinsic dynamical planes and their occupations presented in this Chapter reflect the fact that dark matter halos are a two-parameter family (for example, the virial mass and the energy content or the concentration; see, for example, Hernquist, 1990; Navarro et al., 1995, 1996; Manrique et al., 2003; Navarro et al., 2004b) where the two parameters are correlated (see, for example, Bullock et al., 2001; Wechsler et al., 2002; Manrique et al., 2003). Adding gas implies that heating and cooling processes also play a role at determining the mass and velocity distributions, and, more particularly, the length scales. However, as explained above, we have found that, the relative content of the dark and baryonic mass components show systematic trends with the ELO mass scale, that can be written as power-laws of the form $M_{\rm vir}/M_{\rm bo}^{\rm star} = A_{\rm vir}(M_{\rm bo}^{\rm star})^{\beta_{\rm vir}}$. A similar trend as the first one, although not statistically confirmed (nor discarded) in all samples (see discussion in Section 6.5.3) is also observed in the relative distributions of

the dark and baryonic mass components, $r_{\rm e,h}^{\rm tot}/r_{\rm e,bo}^{\rm star} = A_{\rm rd}(M_{\rm bo}^{\rm star})^{\beta_{\rm rd}}$.

A first consequence of the regularity of the trends with the mass scale found in this Chapter is that no new parameters are added relative to the dark matter halo family, so that the baryonic objects are also a two-parameter family, and ELO structural and dynamical parameters define also a plane. A second consequence is that the plane is tilted relative to the halo plane (i.e., the virial plane) because $\beta_{\rm vir} - \beta_{\rm rd} \neq 0$. Finally, the plane is not homogeneously populated because of the mass-concentration halo correlation that at the scale of the baryonic objects appears for example as a mass—size correlation. This explains the role played by $M_{\rm vir}$ to determine the intrinsic three dimensional correlations. In this study we have also shown that $\sigma_{\rm los,0}^{\rm star}$ is a fair empirical estimator of $M_{\rm vir}$, and this explains the central role played by σ_0 at determining the observational correlations.

The fundamental plane shown by real elliptical samples is the observationally manifestation of the IDPs when using projected parameters $R_{\rm e,bo}^{\rm star}$, $\sigma_{\rm los,0}^{\rm star}$ and luminosity variables instead of stellar masses $M_{\rm bo}^{\rm star}$. We have taken advantage of the constancy of the stellar-mass-to-light ratios of ellipticals in the SDSS (Kauffmann et al., 2003b,a) to put the elliptical sample of Bernardi et al. (2003b,c) in the same projected variables we can measure in our virtual ellipticals. We have found that the FPs shown by the two ELO samples are consistent with that shown by the SDSS elliptical sample in the same variables, with no further need for any relevant contribution from stellar population effects to explain the observed tilt. These effects could, however, have contributed to the scatter of the observed FP, as the IDPs have been found to be thinner than the observed FP.

6.6.1.2 The Physical Processes Underlying Mass Homology Breaking and their Observational Implications

One of the most important findings in this study is the homology breaking ELO samples show in the relative content and, possibly although still not statistically clear, in the relative distribution of the baryonic and the dark mass components. As explained in Oñorbe et al. (2005, 2006), this has as a consequence the observed tilt of the Fundamental Plane relation relative to the virial one. Which are the physical processes underlying this breaking of homology? According with our simulations, they lie in the systematic decrease, with increasing ELO mass, of the relative amount of dissipation experienced by the baryonic mass component along ELO stellar mass assembly (Domínguez-Tenreiro et al., 2006; Oñorbe et al., 2006). This possibility, already suggested by Bender et al. (1992); Guzman et al. (1993); Ciotti et al. (1996), was first addressed through numerical methods by Bekki (1998). He studied elliptical formation through pre-prepared simulations of dissipative mergers of disc galaxies, where the rapidity of the SF in mergers is controlled by a free efficiency parameter $C_{\rm SF}$. He shows that the SF rate history of

galaxies determines the differences in dissipative dynamics, so that to explain the lack of homology in EGs he *needs to assume* that more luminous galaxies are formed by galaxy mergers with a shorter timescale for gas transformation into stars. Recently, Kobayashi (2005) and Robertson et al. (2006) have confirmed the importance of dissipation and the timescale for SF to explain mass homology breaking in ellipticals.

6.6.1.3 The Physical Origin of the Tilt in a Cosmological Context

We now turn to discuss the physical origin of the trends given by the power laws $M_{\rm vir}/M_{\rm bo}^{\rm star} = A_{\rm vir}(M_{\rm bo}^{\rm star})^{\beta_{\rm vir}}$ and $r_{\rm e,h}^{\rm tot}/r_{\rm e,bo}^{\rm star} = A_{\rm rd}(M_{\rm bo}^{\rm star})^{\beta_{\rm rd}}$. As explained in Chapter 2, the simulations provide us with clues on the physical processes involved in elliptical formation (see also Domínguez-Tenreiro et al., 2004, 2006). Our simulations show that the physical origin of the trends above lie in the systematic decrease, with increasing ELO mass, of the relative amount of dissipation experienced by the baryonic mass component along ELO stellar mass assembly (Domínguez-Tenreiro et al., 2006; Oñorbe et al., 2006). This possibility had been suggested by Bender et al. (1992); Guzman et al. (1993); Ciotti et al. (1996). Bekki (1998) first addressed it numerically in the framework of the merger hypothesis for elliptical formation through pre-prepared simulations of dissipative mergers of disk galaxies, where the rapidity of the star formation in mergers is controlled by a free efficiency parameter $C_{\rm SF}$. He shows that the star formation rate history of galaxies determine the differences in dissipative dynamics, so that to explain the slope of the FP he *needs to assume* that more luminous galaxies are formed by galaxy mergers with a shorter timescale for gas transformation into stars. Recently, Robertson et al. (2006) have confirmed these findings on the importance of dissipation to explain the FP tilt.

In this thesis we go one step further and analyze the FP of virtual ellipticals formed in a cosmological context, where individual galaxy-like objects naturally appear as an output of the simulations. Our results essentially include previous ones and add important new information. First, our results on the role of dissipation to produce the tilt of the FP essentially agree with those obtained through dissipative pre-prepared mergers and observational results, but it is important to note that, moreover, more massive objects produced in the simulations *do have* older means and narrower spreads in their stellar age distributions than less massive ones (see details Domínguez-Tenreiro et al., 2004); this naturally appears in the simulations and need not be considered as an additional assumption.

6.6.2 Summary

We conclude that the simulations provide a unified scenario where most current observations on ellipticals can be interrelated. In particular, this scenario proofs the importance of dark matter halos in relaxed virtual ellipticals, and suggests that real ellipticals must

also have extended, massive dark matter halos. Also, this scenario explains the homology breaking in the relative dark to bright mass content and distribution of ellipticals, which have important implications to explain the physical origin of the Fundamental Plane relation, indicating that the FP tilt is due dissipative dynamics. In fact, the ELO samples have been found to show systematic trends with the mass scale in both, the relative content and the relative distributions of the baryonic and the dark mass ELO components (see however, discussion in Section 6.5.3 on this last contribution). These trends cause a tilt of the virial plane in such a way that there is no further need of any relevant contribution from stellar population effects to explain the observed tilt. The scatter of the observed FP, however, probably requires a contribution from such stellar effects. All these trends are due to a systematic decrease, with increasing ELO mass, of the relative amount of dissipation experienced by the baryonic mass component along ELO formation, a possibility that Bender et al. (1992); Guzman et al. (1993); Ciotti et al. (1996) had suggested and in which we will deepen into the next Chapters.

Additionally, we have studied the Photometric Plane, another strong correlation between structural parameters which could be an interesting alternative tool for the study of elliptical galaxies at high redshifts instead of the Fundamental Plane that requires a heavy amount of time for measuring velocity dispersions. We have found a good agreement between our data and observations.

ELO stellar populations show age effects, that is, more massive objects produced in the simulations do have older means and narrower spreads in their stellar age distributions than less massive ones this is equivalent to downsizing (Cowie et al., 1996; Thomas et al., 2005) and naturally appears in the simulations, so that it need not be considered as an additional assumption.

We have also shown that all these results do not depend significantly on the star formation parameterization, cosmological values, resolution or box size. Concerning the box size of our simulations we have arisen to the conclusion that simulations with a larger box size are more realistic because they cover a wide range of possible environments and histories for our virtual ellipticals. However this also leads to a much richer variety of different physical processes and histories than in the smaller box simulations because they cover a wide range of environment possibilities. Therefore, our samples with $L_{box} =$ 10 Mpc have a great advantage which is that we are able to isolate the different physical processes which take part in the formation and evolution of elliptical galaxies. This allows us to study the main processes involved in elliptical formation.

We will investigate in the following chapters all the fundamental relations presented here at higher redshifts (Chapter 8) and the impact of these results concerning the different elliptical formation and evolution scenarios (Chapter 9).

Chapter 7

Ellipticals at z = 0: The Rotation versus Shape Relation[1]

7.1 Introduction

In this Chapter we continue the study of the properties of elliptical galaxies. We now turn to the observed relationships between the rotation support and the shape of elliptical galaxies. We have already discussed the relevance of this interdependence in understanding the origin and evolution of this type of galaxies (see Section 3.2.2). Here we present a formal study of this relation using our samples of simulated ellipticals at redshift zero.

In order to minimize possible bias in our samples, in this Chapter we extend our analysis to all the objects that are well defined just at the ELO scale increasing the number of elliptical-like objects in each sample: -STAR samples (see section 4.4 for more details). ELOs in these samples show the same correlations as previous ones for the stellar object scale, i.e., the Fundamental Plane, Photometric Plane and stellar age properties. However they are embedded in a dark matter halo that it is not relaxed, making the halo properties ill-defined. This happens because the halo is suffering a merger at this scale. In these cases there can be some other significant stellar objects around the main ELO. Therefore we consider that these ELOs are not relaxed (or in equilibrium) at the halo scale. This is a problem in order to study, for example, the origin of the Fundamental Plane, however for the analysis of this Chapter this is not an important issue and in fact, we want to obtain a bigger and more representative sample of elliptical galaxies. In general and for the sake of clarity, in this section we show results for the *EA*-STAR-Z0 sample. Nevertheless, at the end of this Chapter we will discuss all our conclusions for the different -STAR samples at $z = 0$ of our simulations (see Table 4.3).

[1]Based on González-García, Oñorbe, Domínguez-Tenreiro, & Gómez-Flechoso (2009)

This Chapter is organized as follows: In Section 7.2 we describe and discuss the shape of the ELO samples. Section 7.3 is focused on the rotational support of simulated ellipticals and the best parameters that describe it. Section 7.4 deals with the relation between both properties. In Section 7.6 we present our conclusions.

7.2 The Shape of ELOs

We first study the 3D shape of the simulated ellipticals assuming that they can be described by an ellipsoid of semiaxes a, b and c, with $a > b > c$. These parameters have been obtained from the mass within the stellar effective radius, $r^{\rm star}_{\rm e,bo}$, and within the stellar 90% mass radius, $r^{\rm star}_{\rm 90,bo}$ (see 4.5 for details on their calculation from the inertia tensor). From these quantities we have defined several parameters that describe the 3D shape at both radii. First, we have calculated the axis ratios, b/a, c/a and the triaxiality parameter, T, introduced by de Zeeuw & Franx (1991)

$$T = \frac{1-(b/a)^2}{1-(c/a)^2} \tag{7.1}$$

as a more complete descriptor of the 3D shape of the simulated elliptical. However as the T parameter does not distinguishes between a triaxial object with $c/a \sim 0.9$ (which is close to be a sphere) and a more flattened one with $c/a = 0.5$, we have defined a new shape parameter, $S = s + (1 - T)$, where

$$s = \begin{cases} 0 & if \quad c/a < 0.9 \ \& \ T > 0.7 & (prolate) \\ 1 & if \quad c/a < 0.9 \ \& \ 0.3 \leq T \leq 0.7 & (triaxial) \\ 2 & if \quad c/a < 0.9 \ \& \ T < 0.3 & (oblate) \\ 3 & if \quad c/a > 0.9 & (sphere) \end{cases} \tag{7.2}$$

so S takes values $\in (0,1)$ for prolate spheroids, $\in (1,2)$ for triaxial spheroids, $\in (2,3)$ for oblate objects and $\in (3,4)$ for sphere-like objects.

In Figure 7.1 we present the results for the axis ratios obtained within both radii for the *EA*-STAR-Z0 sample. Also, to deepen into the shape distribution of simulated ellipticals at redshift $z = 0$ in Figure 7.2 we present the histogram of the S parameter for the *EA*-STAR-Z0, *EB*-STAR-Z0 and *EF*1-STAR-Z0 samples. We will discuss about possible differences between these samples in Section 7.5.

The first conclusion that arises from these figures is that the shape of simulated ellipticals clearly depends on the radius where we calculate it. This is not surprising and was already notice in first calculations of the projected shape of ellipticals (Bender, 1988; Ryden et al., 2001). This is also found in our simulations, and as the observational data, our results indicate that in general as we deepen into the inner parts of an object, it tends to be rounder. So, statistically, just using smaller radius limits we obtain higher

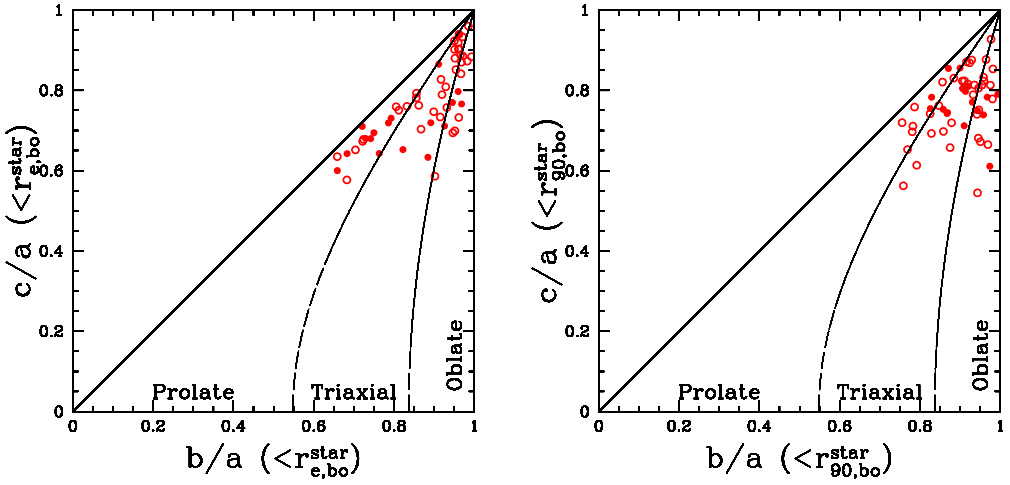

Figure 7.1: 3D axis ratios for the *EA*-STAR-Z0 sample calculated at different radii: $r^{\rm star}_{\rm e,bo}$ (left) and $r^{\rm star}_{\rm 90,bo}$ (right). Full red circles stand for ELOs with $M^{\rm star}_{\rm bo} > 1 \times 10^{11}\ M_{\odot}$ while empty red circles stand for ELOs with $M^{\rm star}_{\rm bo} \leq 1 \times 10^{11}\ M_{\odot}$.

axis ratios.

Concerning the shape distribution of nearby ellipticals, recently Kimm & Yi (2007) have calculated the intrinsic axis ratio distribution of nearby ($0.05 \leq z \leq 0.06$) early-type galaxies from the SDSS. From a total 3922 sample they have obtained that around $\sim 45\%$ are triaxial, $\sim 29\%$ oblate and $\sim 30\%$ prolate. Also they found that luminous early-types are mostly triaxial($\sim 68\%$), whereas the less luminous sample has a larger number of oblate types ($\sim 38\%$) than the complete sample. A clear comparison of our results with Kimm & Yi (2007) data is not straightforward because the authors have to make several assumptions in order to do the deprojection and this technique is highly model dependent. Moreover it is not clear what characteristic radii limit was used. However our results are interesting in two ways. First, we have confirmed that axis ratios are clearly greater than 0.2, one of the assumptions of these authors used to build their models. Second, concerning statistics, we obtain $\sim 2(14)\%$ spherical objects, $\sim 54(34)\%$ triaxial, $\sim 30(25)\%$ oblate and $\sim 14(27)\%$ prolate objects for the $r^{\rm star}_{\rm 90,bo}$ ($r^{\rm star}_{\rm e,bo}$) radius. In this context, it is also interesting to point out that taking into account the axis ratios seen in Figure 7.1, using the classical division between just triaxial, prolate and oblate objects, all the sphere-like objects in our sample would be classified as triaxial ones. Therefore our statistics seems to be in good agreement with that obtained from the deprojection of the SDSS early-type galaxies. In this sense, it is also worth noting that the shape distribution for a sample obtained from a simulation with different star formation parameters (*EB*-STAR) show very small differences at the effective radius, $r^{\rm star}_{\rm e,bo}$. At $r^{\rm star}_{\rm 90,bo}$ results are in agreement within the errors bars.

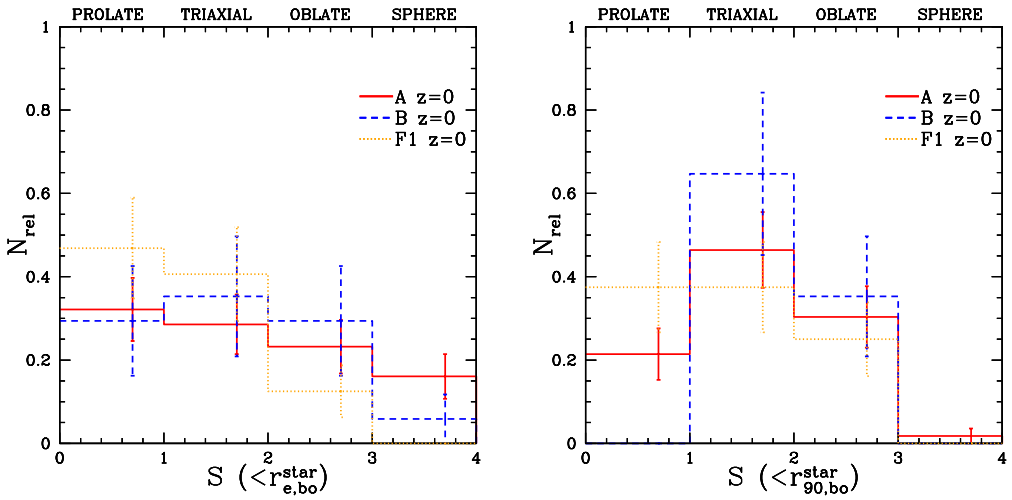

Figure 7.2: 3D Shape histogram, S, for the *EA*-STAR-Z0 (red line), *EB*-STAR-Z0 (blue dashed line) and *EF*1-STAR-Z0 (orange dotted line) samples calculated using Equation 7.2 at two different characteristic radii: $r^{\rm star}_{\rm e,bo}$ (left) and $r^{\rm star}_{\rm 90,bo}$ (right).

Another important parameter we have measured is the 3D ellipticity, $\epsilon_{\rm 3D} = 1 - c/a$. This is the quantity that appears in the Equation 3.15, relating the amount of rotation with the anisotropy of a virialized object (see Section 3.2). We have calculated it both at the $r^{\rm star}_{\rm e,bo}$ and the $r^{\rm star}_{\rm 90,bo}$ radii. Its observational counterpart is the projected ellipticity, ϵ, which is the quantity used to determine the shape of real galaxies. We have measured it using one hundred random projections, also for two radii, the projected equivalent of the 3D cut-off radii, $R^{\rm star}_{\rm e,bo}$, and $R^{\rm star}_{\rm 90,bo}$. See Section 4.5 for the details on how we measure these quantities.

In Figure 7.3 we can see a remarkably good correlation between the 3D shape parameters and their observational counterparts. It is important to mention that we found that the dispersion due to projection effects for the 2D quantities is high (up to $\sim 40\%$). Concerning the relation between $\epsilon_{\rm 3D}$ and other shape parameters, no tight correlation with T is found. This just indicates that the values of the three axis of the ellipsoid are not correlated and that for certain c/a we obtain some dispersion in the b/a axis ratio (see Figure 7.1). Although obviously, c/a puts the lower limit to this relation.

Finally we have studied the correlation between the different shape parameters described in this section S, T and $\epsilon_{\rm 3D}$ and the stellar mass, $M^{\rm star}_{\rm bo}$ (Figure 7.4). No clear trend has been found. Concerning observational results, the first ones suggested that more massive objects were rounder (see Section 3.2). Recent work with the SDSS data (Hao et al., 2006), also point towards this direction but with a very high dispersion. When we plot the 3D ellipticity versus the stellar mass (see Figure 7.4) we obtain very similar results as these authors, especially in the sense that for lower masses we obtain a higher dispersion in the ellipticity values.

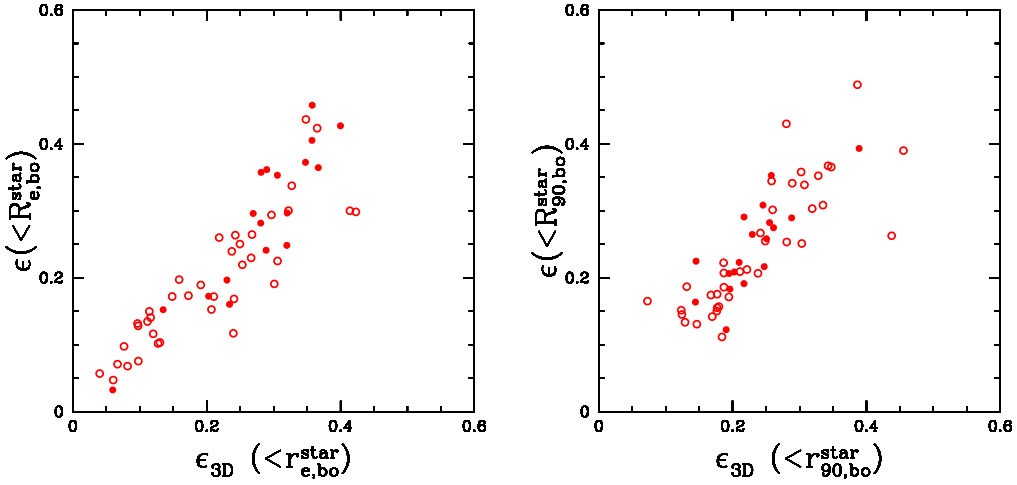

Figure 7.3: 3D shape parameters, ϵ_{3D}, calculated at two different characteristic radii: $r^{star}_{e,bo}$ (left) and $r^{star}_{90,bo}$ (right) versus their projected counterparts for the *EA*-STAR-Z0 sample. Full red circles stand for ELOs with $M^{star}_{bo} > 1 \times 10^{11}\ M_{\odot}$ while empty red circles stand for ELOs with $M^{star}_{bo} \leq 1 \times 10^{11}\ M_{\odot}$.

To sum up, concerning the 3D shape of simulated objects both scales, $r^{star}_{e,bo}$ and $r^{star}_{90,bo}$, can be used, both of them are convenient descriptors and correlate well between each other. Concerning the 2D shape descriptor, current observations of elliptical galaxies usually measure their ellipticity between 0.5 and 2 times the projected effective radius (Bender et al., 1994; Cappellari et al., 2007). In consequence we will use $\epsilon(< R^{star}_{e,bo})$ as the formal descriptor of the 2D shape of the simulated ellipticals and the one we would use whenever we want to compare with real data.

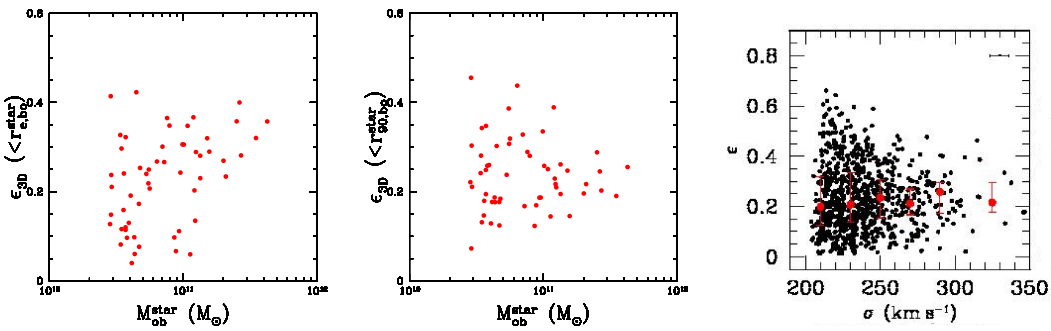

Figure 7.4: 3D shape parameters, ϵ_{3D}, calculated at two different characteristic radii: $r^{star}_{e,bo}$ (left) and $r^{star}_{90,bo}$ (middle) versus the stellar mass for the *EA*-STAR-Z0 sample. Right panel shows results for the SDSS data (Hao et al., 2006).

7.3 The Rotation of ELOs

The phase-space information available in our simulations allows us to calculate the amount of rotation in ELOs in several ways and using different descriptors. In fact, there are several different options in the literature to account for the 3D rotation of an object (Emsellem et al., 2007). Our method aims to two main objectives. First, we want to compare with observations. For this purpose the best option is obtaining $V_{\rm max}/\sigma^{\rm star}_{\rm los,0}$ which, as explained in Section 4.5.3, is the more often used parameter in real data measurements (see however van der Marel & van Dokkum, 2007; Emsellem et al., 2007, for new observational descriptors). Second, we want a robust descriptor of the real 3D amount of rotation for elliptical-like objects that can be also easily compared with the 2D descriptor. For this purpose we choose the tangential stellar velocity in units of the 3D dispersion, $V_\phi/\sigma^{\rm star}_3$. Basic details on their calculation can be found in Section 3.2 and here we would just discuss the results and the different options and paths. One of this subjects, as in the shape study, is how the amount of rotation depends on the radius where it is measured or, in the case of $V_{\rm max}$, the length of the slit. Therefore, as in the shape analysis, we have chosen $r^{\rm star}_{\rm e,bo}$ and $r^{\rm star}_{\rm 90,bo}$ for the 3D studies and their projected counterparts, $R^{\rm star}_{\rm e,bo}$ and $R^{\rm star}_{\rm 90,bo}$ for the 2D.

Concerning the guest for a suitable 3D rotation descriptor, two possible candidates are $V_\phi/\sigma^{\rm star}_3$ (see Section 4.5.3) and the specific angular momentum of each ELO, both of them at the two characteristic radii (i.e. 4 possibilities). Note that the intrinsic angular momentum is a cumulative quantity, while $V_\phi/\sigma^{\rm star}_3$ is measured at a given radius. Our results show that the two intrinsic angular momenta correlate well with the 3D rotation descriptor calculated at the effective radius, $V_\phi/\sigma^{\rm star}_3(r^{\rm star}_{\rm e,bo})$. On the other hand, we found that $V_\phi/\sigma^{\rm star}_3(r^{\rm star}_{\rm 90,bo})$ do not show any strong trend with the intrinsic angular momenta. This is not really surprising because it depends on the external layer of the simulated object which takes longer to relax to any perturbation of the object (for example, matter coming from a recent major merger) and it is very sensitive to different events, as small satellite mergers or gas infall, which do not account for the global properties of the object. We do not find this problem for the shape descriptors, nor the intrinsic angular momenta, because contrary to $V_\phi/\sigma^{\rm star}_3$, they are cumulative quantities. For these reasons, the best 3D rotation descriptor to account for the global properties of simulated ellipticals is $V_\phi/\sigma^{\rm star}_3(r^{\rm star}_{\rm e,bo})$, while $V_\phi/\sigma^{\rm star}_3(r^{\rm star}_{\rm 90,bo})$ describes rather rotation at the external layers.

Concerning the 2D descriptor, we have also measured $V_{\rm max}$ choosing the maximum length of the slit to be either $R^{\rm star}_{\rm e,bo}$ or $R^{\rm star}_{\rm 90,bo}$ (see Section 4.5 for details on this calculation). Results can be appreciated in Figure 7.5 where we plot $V_\phi/\sigma^{\rm star}_3(r^{\rm star}_{\rm e,bo})$ versus $V_{\rm max}/\sigma^{\rm star}_{\rm los,0}(R^{\rm star}_{\rm e,bo})$ and $V_{\rm max}/\sigma^{\rm star}_{\rm los,0}(R^{\rm star}_{\rm 90,bo})$ and we see for both limits we found a good correlation between the 2D and the 3D rotation parameter $V_\phi/\sigma^{\rm star}_3(r^{\rm star}_{\rm e,bo})$. We also found some interesting facts. First of all, the two projected quantities show a good cor-

relation between each other and secondly, for the same ELO, $V_{\rm max}$ shows a higher value for a larger length of the slit. The dependence of $V_{\rm max}$ on the slit length was already noticed in real ellipticals by Bender (1988) who pointed out that in order to obtain a good estimation of this parameter one should be able to measure, at least, up to the projected effective radius of the galaxies ($R^{\rm star}_{\rm e,bo}$). Taking into account Figure 5.21 the correct way of doing it would be obtaining the profiles, at least, up to a radius where they settle down. In this sense, $R^{\rm star}_{\rm 90,bo}$, seems to be a more suitable option than $R^{\rm star}_{\rm e,bo}$. Note, however, as it happens with the shape, current observations reach between 0.5 and 2 times the projected effective radius (Bender et al., 1994; Cappellari et al., 2007). So we will use both of them. Two comments are in order: i) the amount of rotation measured at $R^{\rm star}_{\rm e,bo}$ is a lower limit of that measured at $R^{\rm star}_{\rm 90,bo}$ (see Figure 7.5); ii) Both $V_{\rm max}/\sigma^{\rm star}_{\rm los,0}$ quantities have to be considered as lower limits of the intrinsic rotational support of the galaxy, just due to projection effects (see discussion on this topic in Rothberg & Joseph, 2006). It is also important to remark that, the $V_{\rm max}$ parameter presents a high dispersion due to projection effects ($\sim 35\%$) for both slit lengths.

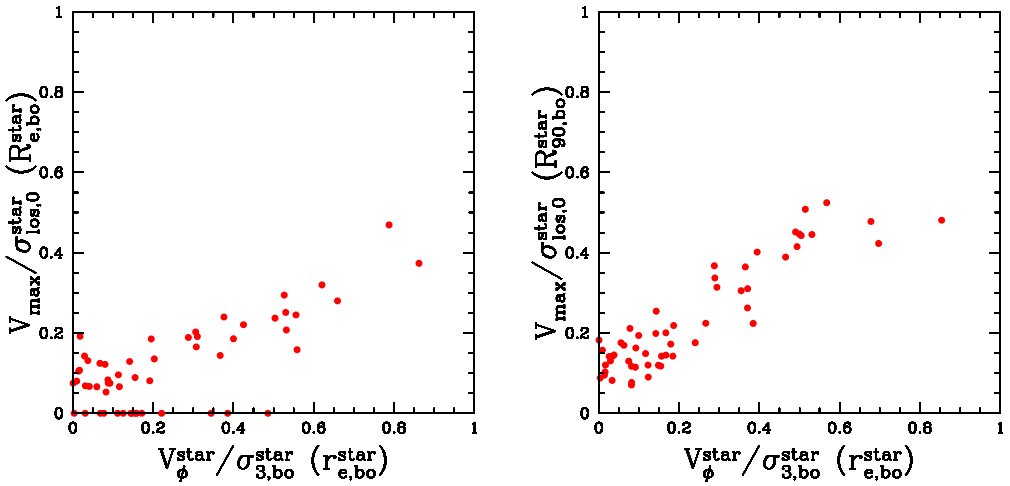

Figure 7.5: *EA*-STAR-Z0 3D rotational support parameter, $V_\phi/\sigma^{\rm star}_3$, calculated at the effective radius, $r^{\rm star}_{\rm e,bo}$, versus its projected counterparts, $V_{\rm max}/\sigma^{\rm star}_{\rm los,0}$, calculated at two different characteristic radii: $R^{\rm star}_{\rm e,bo}$ (left) and $R^{\rm star}_{\rm 90,bo}$ (right).

The only exceptions to all these trends are some small objects for which we obtain $V_{\rm max}(R^{\rm star}_{\rm e,bo}) = 0$. These results are related with the resolution limits. In these cases, the slit is too small to include enough particles to have a proper estimation of $V_{\rm max}$ up to $R^{\rm star}_{\rm e,bo}$.

We have also studied the relation between the amount of rotation of each simulated elliptical with their stellar mass. From Figure 7.6 we can see that, as the stellar mass increases, the mean and dispersion of the rotational support decreases. This is in good

agreement with recent observational results (Rothberg & Joseph, 2006; Emsellem et al., 2007) and seems to follow roughly the prediction of Davies et al. (1983) that luminosity (and therefore mass) increases as objects have a lower rotational support.

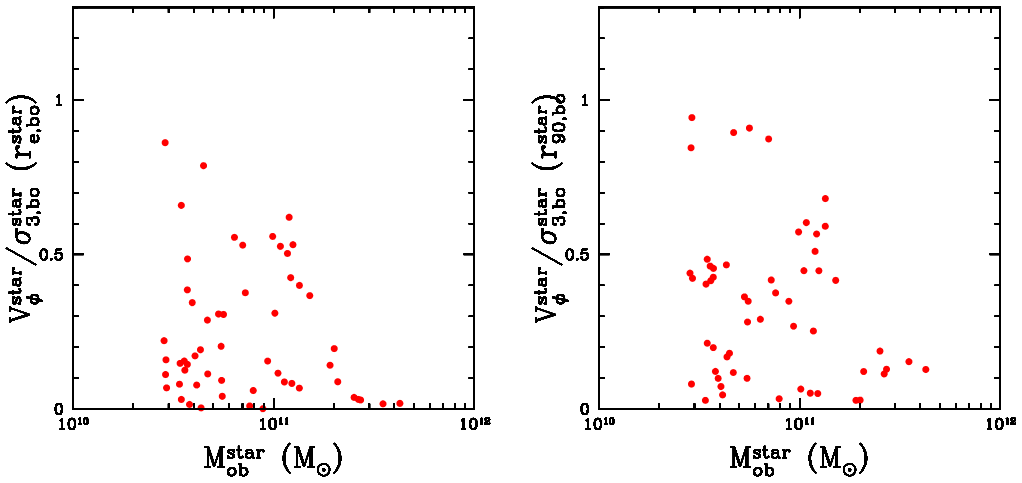

Figure 7.6: 3D rotational support parameters, $V_\phi/\sigma_3^{\rm star}$, calculated at two different characteristic radii: $r_{\rm e,bo}^{\rm star}$ (left) and $r_{\rm 90,bo}^{\rm star}$ (right) versus the stellar mass for the *EA-STAR-Z0* sample.

7.4 Rotation vs. Shape: 3D and 2D Results

Once we have robust descriptors of the shape and the rotational support of our simulated ellipticals, both for 3D and 2D analyzes, we have studied their possible relation. Figure 7.7 shows the classical diagram introduced by Davies et al. (1983) between the two observational parameters for our simulated ellipticals. In this Figure we also plot some recent observational results for elliptical galaxies. We find a very good agreement between observational data (Bender et al., 1994; Cappellari et al., 2007) and our simulated ellipticals. On one hand, fast rotators ($V_{\rm max}/\sigma_{\rm los,0}^{\rm star} > 0.2$) show a good correlation with the shape parameter, ϵ. On the other hand, slow rotators ($V_{\rm max}/\sigma_{\rm los,0}^{\rm star} < 0.2$) display misalignment between the structural and kinematical axes. These results are consistent independently of the length of the slit used to obtain $V_{\rm max}$, $R_{\rm e,bo}^{\rm star}$ or $R_{\rm 90,bo}^{\rm star}$, however we obtain a better comparison with the last one. In Figure 7.8 we present the 3D equivalent plot for these quantities and found that the relation observed between shape and kinematics not only holds for the 3D parameters data but moreover it is clearer.

In order to study the shape and kinematics misalignment, we plot in Figure 7.9 (upper panels) the same diagrams introduced in previous Figures but in this case showing the 3D shape parameter, S, for each object. Results are really interesting because

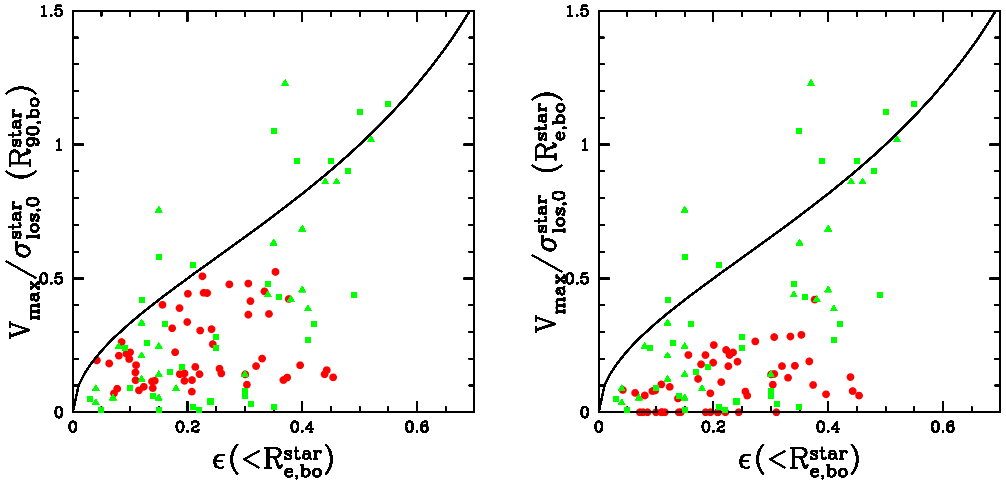

Figure 7.7: The projected shape parameter at $R^{\rm star}_{\rm e,bo}$ versus the projected rotational support parameter calculated at two different characteristic radii: $R^{\rm star}_{\rm e,bo}$ (left) and $R^{\rm star}_{\rm 90,bo}$ (right) for the *EA*-STAR-Z0 sample. Green triangles stand for Cappellari et al. (2007) data for ellipticals. Green squares stand for Bender et al. (1994) data for ellipticals. Black solid line indicates the locus for oblate rotators (Binney, 1978).

they point towards a possible clear segregation of elliptical galaxies in the 2D classical diagram depending on the 3D shape. This is not a surprise and it is in good agreement with the theoretical prediction made in Section 3.2 based on the virial theorem approximation. First, we can see that oblate objects show a clear correlation between shape and rotation which is exactly what we expect from our approximation. Second, prolate objects tend be in the lower part of the diagram. As expected, triaxial objects seem to be between the two previous types (see Binney, 1978). This result is found not only for the 3D values of shape and rotation but also for the mean projected values (lower panels of Figure 7.9).

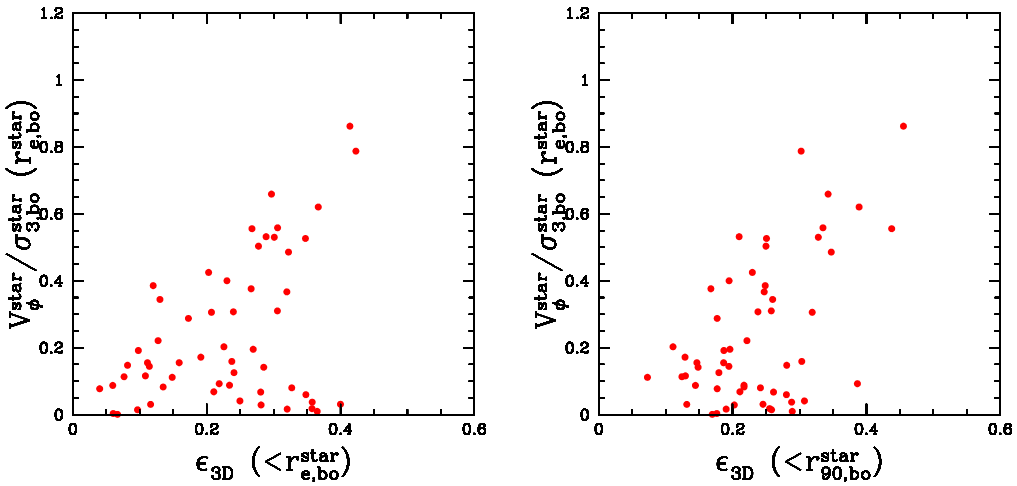

Figure 7.8: The 3D rotational support parameter at $r_{\rm e,bo}^{\rm star}$ versus the 3D shape parameter, $\epsilon_{\rm 3D}$, calculated at two different characteristic radii: $r_{\rm e,bo}^{\rm star}$ (left) and $r_{\rm 90,bo}^{\rm star}$ (right) for the *EA*-STAR-Z0 sample.

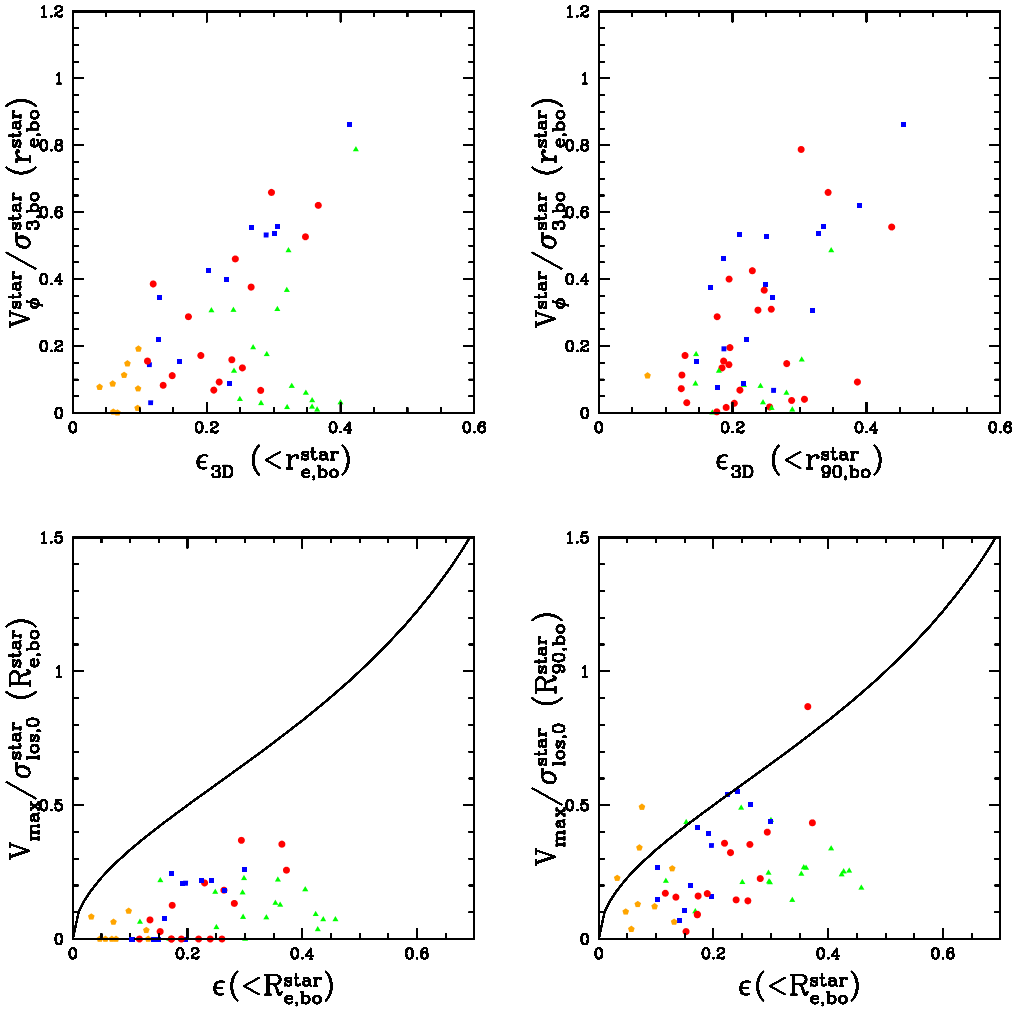

Figure 7.9: 3D (up) and 2D (down) rotational support ($V_\phi/\sigma_3^{\rm star}$ and $V_{\rm max}/\sigma_{\rm los,0}^{\rm star}$) versus shape descriptors ($\epsilon_{\rm 3D}$ and ϵ) for the *EA*-STAR-Z0 sample. Color and shapes of this figure stand for the 3D shape calculated using Equation 7.2 for the characteristic radius that corresponds in each case: Yellow pentagons for spheres, blue squares for oblate objects, red circles for triaxial objects and green triangles for oblate objects. Black solid line indicates the locus for oblate rotators (Binney, 1978).

7.5 Consistency Checks

Concerning resolution Figure 7.10 shows the results of two consistency checks performed using the 6705 and 7705 simulations (*ED* sample, see Section 4.2 for details). Figure 7.10 (left panel) shows the star-formation history of two objects, the most and least massive ELOs in these simulations (see Section 9.2 for more details on the star formation histories of our ELOs). The black dotted line and the solid green line depict the results of the simulations with 2×128^3 and 2×64^3 particles, respectively. We found small differences, especially at early times, although the two systems display general similar behavior, and at high cosmic times (low redshift) no significant differences are evident. A similar test was completed by Naab et al. (2007) and, although the numerical approaches differ, it is reassuring to also find convergence in this resolution test.

Figure 7.10 (right panel) presents comparative results of the same objects at $z = 0$ in the two simulations where we computed the observables introduced above on shape and kinematics. The systems appear to be stable and agreement between the simulations results is good, although one object does exhibit a significant difference. This system is not the least massive in these simulations and the difference is due to the peculiar way in which the $V_\phi/\sigma_3^{\rm star}$ parameter is measured, such that particles at different radii are considered.

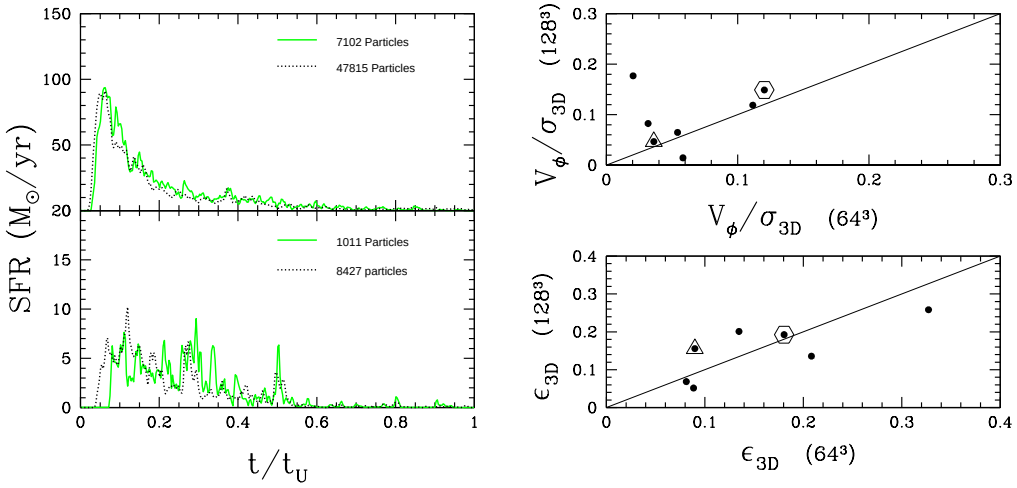

Figure 7.10: Left: Star formation history of the most (top) and least (bottom) massive ELOs for the *ED* test simulations with 2×64^3 particles (7705, solid green line) and 2×128^3 particles (6705, dotted black line). Right, comparison of the kinematic (top) and shape (bottom) observables. For details, see text.

We now comment on the box size and star formation systematics. First, the good agreement obtained between 2D and 3D parameters and their trends with mass for the EA-STAR-Z0 ELOs also hold for samples obtained from simulations with different box sizes and/or star formation parameters. In Figure 7.2 we have seen the shape

distribution for the *EB*-STAR-Z0 and *EF*1-STAR-Z0 samples. Results show a good agreement within the error bars. Figure 7.11 shows 3D and 2D rotation versus shape diagrams for *EB*-STAR-Z0, EF1-STAR-Z0 and *EF*3-STAR-Z0 samples, using the 3D global shape parameter, S, to determine the color and shape for each object. Segregation in the diagram depending on this parameter is also found for these samples.

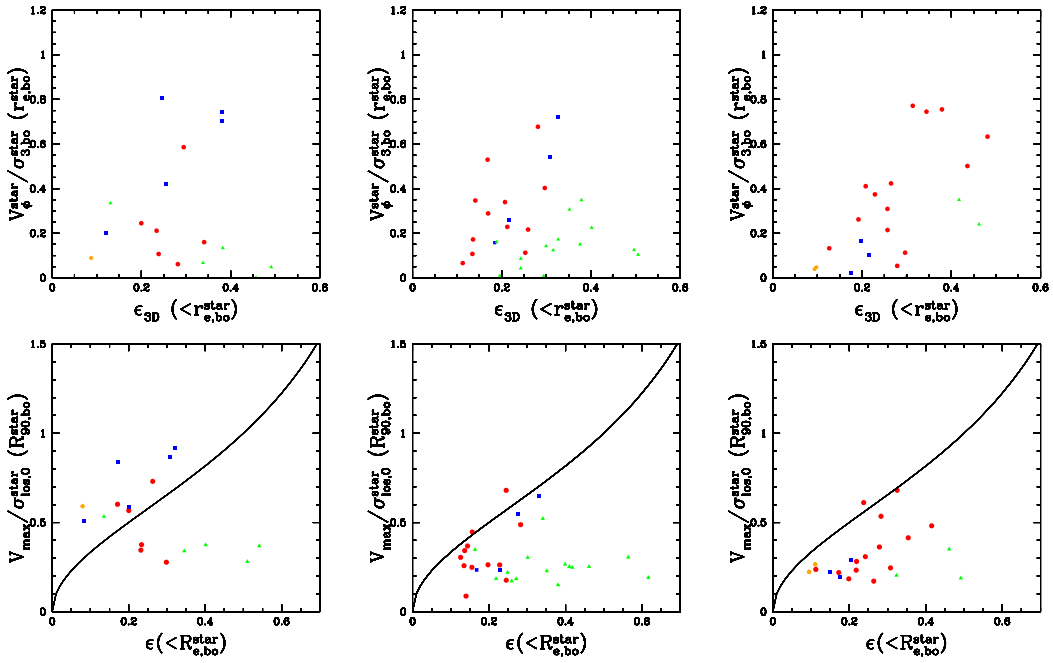

Figure 7.11: 3D (up) and 2D (down) rotational support versus projected shape descriptors for the *EB*-STAR-Z0 (left), *EF*1-STAR-Z0 (middle) and *EF*3-STAR-Z0 (right) samples. Color and shapes of this figure stand for the 3D shape parameter, S, calculated using Equation 7.2 for the characteristic radius that corresponds in each case: Yellow pentagons for spheres, blue squares for oblate objects, red circles for triaxial objects and green triangles for prolate objects.

7.6 Conclusions

To conclude, by studying the classical diagram introduced by Davies et al. (1983), we have shown that the shape distribution of our simulated galaxies and their kinematics are closely related and in good agreement with the observational data. Current observational results on this diagram still lack of reliable statistics when comparing with other known Fundamental Relations, mostly due to the high cost of measuring $V_{\rm max}$. The largest homogeneous set of long-slit $V_{\rm max}/\sigma^{\rm star}_{\rm los,0}$ and ellipticity values is currently constituted by the 94 measurements for elliptical galaxies by R. Bender (see Cappellari et al., 2007). In this context, we have been able to deepen into this relation through our simulations and we have reached several interesting new ideas on this topic. First,

this classical diagram holds when we use the 3D parameter counterparts. The clear segregation of elliptical galaxies in the ϵ vs. $V_{\rm max}/\sigma^{\rm star}_{\rm los,0}$ diagram depending on the 3D shape is a very interesting result, expected from theoretical considerations (see Section 3.2), but never confirmed in self-consistent cosmological simulations. It could explain some observational results for merger remnants (Rothberg & Joseph, 2006) that showed variations among expected correlations between shape and rotation. We think that our conclusions can be very useful to both, observers and theoreticians, in order to constrain and use different structural and kinematical models to describe elliptical galaxies. For example, concerning the shape distribution, we have put some clear limits on the intrinsic axis ratio values, useful for the deprojection techniques applied in observed galaxies (Kimm & Yi, 2007). Also the confirmation that, just because projection effects, the $V_{\rm max}/\sigma^{\rm star}_{\rm los,0}$ ratio measured in real ellipticals must be considered as a lower limit to the rotational support is an important issue in order to analyze observational data. The study of these projection effects has allowed us to show that both parameters, ϵ and $V_{\rm max}$, present a high dispersion from the mean, 40% and 35% respectively, taking one hundred random projections (see Section 4.5.3). This is much higher than any other quantities studied in this thesis, as $R^{\rm star}_{\rm e,bo}$ or $\sigma^{\rm star}_{\rm los,0}$, that present around 5% dispersion due to projection effects.

We have confirmed that more massive ELOs show a lower dispersion in rotational support and shape values than less massive ones, pointing to rounder shapes and less rotational support for the first ones. Finally we have seen that the 3D shape of a simulated elliptical could be constrained by the position that it occupies in the classical diagram that relates these two quantities. All these conclusions can be also corroborated in the 2D projected parameters, observationally available, that quantify these characteristics ϵ and $V_{\rm max}/\sigma^{\rm star}_{\rm los,0}$. Moreover we have seen that the 3D shape of an elliptical could be constrained by the position that it occupies in the classical diagram that relates these two quantities.

In fact, ELOs have shown a very good agreement with a different set of observations at $z = 0$. In following chapters we will study how they formed and their structure and kinematics at higher redshifts. In addition, we will discuss deeply the impact of all these results concerning the different elliptical formation and evolution scenarios.

Chapter 8

Evolution of Ellipticals out to z=1.5 [1]

8.1 Introduction

Once the simulated elliptical population at redshift $z = 0$ has been analyzed in detail, the next logical step is to extend this work to the population samples at higher redshifts: $z = 0.5$, $z = 1$ and $z = 1.5$. We have searched for ELOs in all the simulations and analyzed them at these three different redshifts. The process of building all these samples is explained in Section 4.4. Nevertheless, here we remember the reader that higher redshift samples have been built following the same criteria as the $z = 0$ samples. In addition, we have calculated all the different parameters studied in the $z = 0$ samples following the same methodology. We point to Section 4.5 for a complete description of the analysis method. The exact values of these parameters for the different ELO samples can be found in Appendix D.

This Chapter focuses on the study of possible indications of evolution for the different virtual elliptical samples. In order to obtain results easily to compare we have focused our work in studying the tightest correlations found at redshift $z = 0$. First Section is related with the most important of all these relations, the Fundamental Plane. Afterwards, in Section 8.3, we deepen into the Photometric Plane relation, closely related with the first one. In Section 8.4 we analyze other interesting structural and kinematical parameters discussed in the previous Chapter and their correlations. Finally Section 8.5 describes how the shape and rotational support relation behaves at different redshifts. Our conclusions are summarized and discussed in Section 8.6.

[1] Based on Domínguez-Tenreiro et al. (2006); Oñorbe et al. (2007, 2008); González-García et al. (2009)

8.2 The Fundamental Plane

In our study of virtual ellipticals at $z = 0$ we found that they populate a flattened ellipsoid close to a two-dimensional plane in the intrinsic (i.e., three-dimensional) characteristic mass ($M_{\rm bo}^{\rm star}$), radius ($r_{\rm e,bo}^{\rm star}$) and velocity dispersion ($\sigma_{\rm 3,bo}^{\rm star}$) space (the Intrinsic Dynamical Plane, IDP, see Section 6.2.2). Therefore to characterize and study possible evolution effects of the structural and dynamical properties of ELOs, we describe their three dimensional distributions of mass and velocity through these three intrinsic parameters the stellar mass at the baryonic object scale, $M_{\rm bo}^{\rm star}$, the stellar half-mass radius at the same scale, $r_{\rm e,bo}^{\rm star}$ and the mean square velocity for stars, $\sigma_{\rm 3,bo}^{\rm star}$, whose observational projected counterparts (the luminosity L, effective projected size $R_{\rm e}^{\rm light}$, and stellar central line of sight velocity dispersion, σ_0) enter the definition of the observed FP. We use firstly three dimensional variables rather than projected ones to avoid projection effects. As well as in our study at $z = 0$ we have used ELOs that are well defined both at the stellar and halo scales. See Section 4.4.1 for the details about how we built these samples.

To measure the structural and dynamical evolution of ELOs, we carry out a principal component analysis of the *EA*, *EB* (different star formation) parameters and *EF*3 (larger box size) samples at redshifts $z = 0.5$, $z = 1$ and $z = 1.5$ (defined in Section 4.4) in the three dimension variables $E \equiv \log M_{\rm bo}^{\rm star}$, $r \equiv \log r_{\rm e,bo}^{\rm star}$ and $v \equiv \log \sigma_{\rm 3,bo}^{\rm star}$ through their 3×3 correlation matrix $\mathbf{C}$. In Section 6.2.2 we presented an introduction on the PCA method and the results of this study for the different samples at $z = 0$. We have found that one of the eigenvalues of $\mathbf{C}$ is, for the three ELO samples analyzed, considerably smaller than the others (as we found for the *EA*-Z0 sample), so that ELOs populate at any z a flattened ellipsoid close to a two-dimensional plane in the (E, r, v) space; the observed FP is the observational manifestation of this dynamical plane. The eigenvectors of $\mathbf{C}$ indicate that the projection

$$E - \tilde{E_{\rm z}} = \alpha_{\rm z}^{\rm 3D}(r - \tilde{r_{\rm z}}) + \gamma_{\rm z}^{\rm 3D}(v - \tilde{v_{\rm z}}), \tag{8.1}$$

where $\tilde{\rm E}_{\rm z}, \tilde{\rm r}_{\rm z}$ and $\tilde{\rm v}_{\rm z}$ are the mean values of the E, r and v variables at redshift z, shows the plane viewed edge-on.

Table 8.1 gives the planes Eq. (8.1) for the *EA*, *EB* and *EF*3 samples at different zs, as well as their corresponding thicknesses $\sigma_{\rm Erv}(z)$, the distances $d(z)$ of the sample center of mass at z (i.e., the $[\tilde{\rm E}_{\rm z}, \tilde{\rm r}_{\rm z}, \tilde{\rm v}_{\rm z}]$ point) to the plane Eq. (8.1) at $z = 0$, and the fraction of ELOs in the $z = 0.5$, $z = 1$ and $z = 1.5$ samples whose distance to the $z = 0$ sample is larger than $2\sigma_{\rm Erv}(z = 0)$. In order to compare the *EB* and *EF*3 samples with *EA* we also show the distances $d(z)$ of the sample center of mass at z (i.e., the $[\tilde{\rm E}_{\rm z}, \tilde{\rm r}_{\rm z}, \tilde{\rm v}_{\rm z}]$ point) to the *EA*-Z0 plane and the fraction of ELOs of these samples whose distance to the *EA*-Z0 sample is larger than $2\sigma_{\rm Erv}^{EA-Z0}$.

We see that the sample averages $\tilde{E}_z, \tilde{r}_z$ and $\tilde{v}_z$ grow as z decreases, but in any case for the *EA* and *EF*3 samples $\mid d(z) \mid < \sigma_{\rm Erv}(z=0)$, so that they move roughly *on* the $z=0$ plane within its rms scatter. We have also plot this space of parameters in Figure 8.1 for the *EA*-Z0 sample. *EB* present very similar result but for the $z=1.5$ sample. However, we also checked that all ELOs of these samples are within 3 times the $\sigma_{\rm Erv}(z=0)$. These results indicate that ELO evolution preserves their dynamical plane and strongly suggest that the evolution shown by the Fundamental Plane of real ellipticals must be explained, basically, as due to the changes of luminosity of their passively evolving stellar populations, corroborating other observational findings on elliptical homogeneity (see section 3.3.1). In regard to the comparison between the *EB* and *EF*3 samples with the *EA*-Z0 intrinsic dynamical plane (columns 11 and 12 of Table 8.1), mean values of *EB* samples are displaced by a constant distance from the *EA*-Z0 plane. These results consolidate the idea, already discussed in Section 6.2, that *EB* dynamical plane is the same one as the *EA* one but with a different zero point. Results on the *EF*3 samples show a very good agreement with the *EA*-Z0 plane.

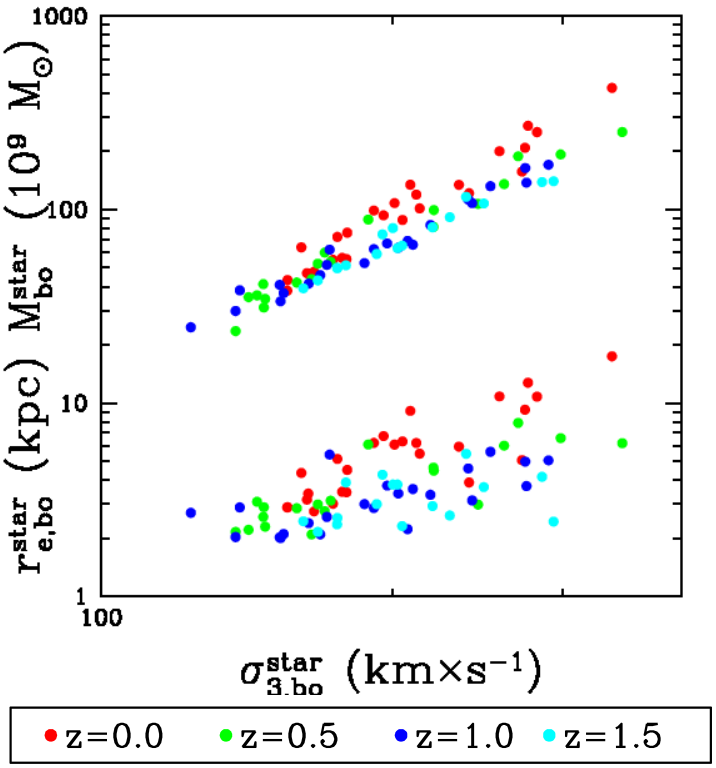

Figure 8.1: Evolution of the structural and kinematical fundamental parameters: $M^{\rm star}_{\rm bo}$, $r^{\rm star}_{\rm e,bo}$, $\sigma^{\rm star}_{\rm 3,bo}$ for *EA* runs at different redshifts.

We have also searched for the observational manifestation of this intrinsic relation in all these samples. As in Chapter 6 we have used the projected parameters $M^{\rm star}_{\rm cyl,bo}$,

Sample	#	$\tilde{E}_z$	$\tilde{r}_z$	$\tilde{v}_z$	α_z^{3D}	γ_z^{3D}	σ_z^{Erv}	d_z^{Z0}	% outside $2\sigma_{Erv}^{Z0}$	d_z^{EA-Z0}	% outside $2\sigma_{Erv}^{EA-Z0}$
EA-Z0	26	10.987	0.735	2.312	0.459	1.928	0.014	–	–	–	–
EA-Z0.5	19	10.821	0.550	2.278	0.230	2.166	0.021	0.007	30%	0.007	30%
EA-Z1	21	10.803	0.492	2.282	0.239	2.066	0.016	0.008	13%	0.008	13%
EA-Z1.5	16	10.860	0.495	2.317	0.239	2.120	0.013	0.009	18%	0.009	18%
EB-Z0	17	11.245	0.667	2.420	0.392	1.776	0.017	–	–	0.032	35%
EB-Z0.5	14	10.943	0.368	2.339	0.331	2.009	0.012	0.020	21%	0.031	50%
EB-Z1	16	10.999	0.399	2.360	0.380	2.248	0.018	0.017	25%	0.031	56%
EB-Z1.5	16	10.832	0.261	2.307	0.497	1.936	0.015	0.057	31%	0.032	63%
*EF*3-Z0	11	10.816	0.416	2.278	0.352	1.969	0.018	–	–	0.018	45%
*EF*3-Z1	8	10.686	0.378	2.236	1.259	1.278	0.019	0.015	13%	0.005	13%

Table 8.1: Principal component analysis of mass, radius and dispersion velocity for *EA* simulations. Column 2: number of objects in the sample. Columns 3, 4 and 5: mean values of the E, r and v variables at each z. Columns 6 and 7: coefficients of Eq. (8.1). Column 8: rms orthogonal scatter of the dynamical planes at each z. Column 9: for each z, distance of the $(\tilde{E}_z, \tilde{r}_z, \tilde{v}_z)$ point of the different samples to its Z0 plane. Column 10: % of objects of the different samples whose distance to its Z0 plane is larger than twice its scatter. Column 11: for each z, distance of the $(\tilde{E}_z, \tilde{r}_z, \tilde{v}_z)$ point to the *EA*-Z0 plane. Column 12: % of objects of the different samples whose distance to the *EA*-Z0 plane is larger than twice its scatter.

$R^{\rm star}_{\rm e,bo}$, $\sigma^{\rm star}_{\rm los,0}$ to build the Dynamical Plane and compare with observational data. We have moved these variables to the κ^D system (see Equations 6.5-6.7) so that we can plot easily the edge-on and face-on projections of this plane. As Figure 8.2 shows, we have found that *EA* ELOs at all these redshifts also lay on a fundamental plane with almost the same tilt as ELOs in $z = 0$. We have obtained the slopes, through direct fits, of the $\kappa^{\rm D}_3 = M_1\kappa^{\rm D}_1 + M_0$ relation that reflects the edge-on projection of the Fundamental Plane. Results of these fits can be found in Table 8.2 and confirm the lack of evolution of the tilt of the Dynamical Plane. We also show the kappa space projections for the *EB* and *EF*3 samples in Figure 8.3. M_1 coefficients for these samples can be found in Tables 8.3 and Tables 8.4, respectively.

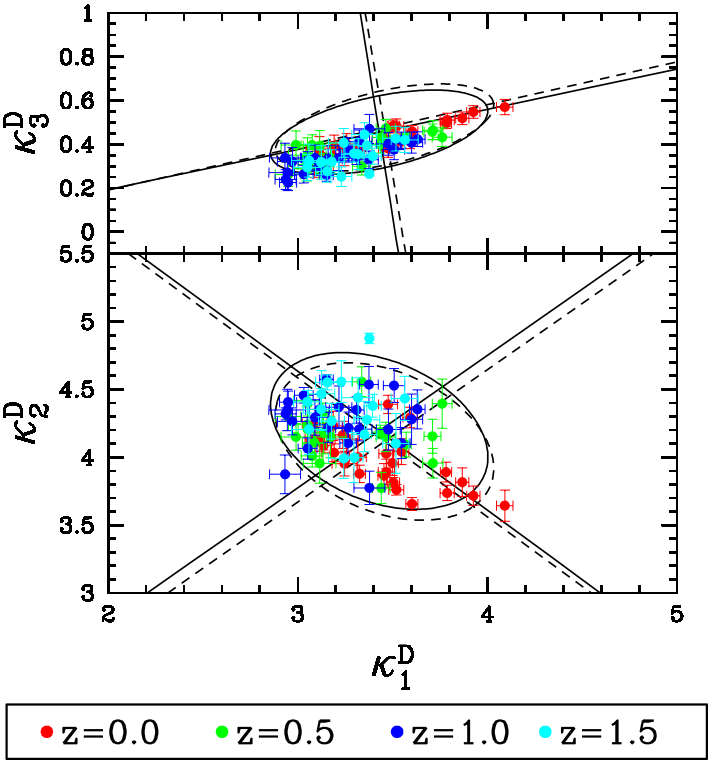

Figure 8.2: The Dynamical Plane viewed edge-on (top) and face-on (bottom) for *EA*-Z0 (red), *EA*-Z0.5 (green), *EA*-Z1 (blue) and *EA*-Z1.5 (cyan) in the kappa space. We also draw the respective concentration ellipses (with their major and minor axes) for the SDSS early-type galaxies sample from Bernardi et al. (2003c) in the z-band and r-band. See text for more details.

To deepen into the tilt issue and the origin of the Fundamental Plane, we have made the same statistical analysis as for the $z = 0$ samples. That is, we have studied the fundamental structure and kinematical parameters that characterize our virtual ellipticals at different scales: the halo scale, the baryonic object scale and the projected baryonic scale, verifying that higher redshift samples also satisfy the virial theorem

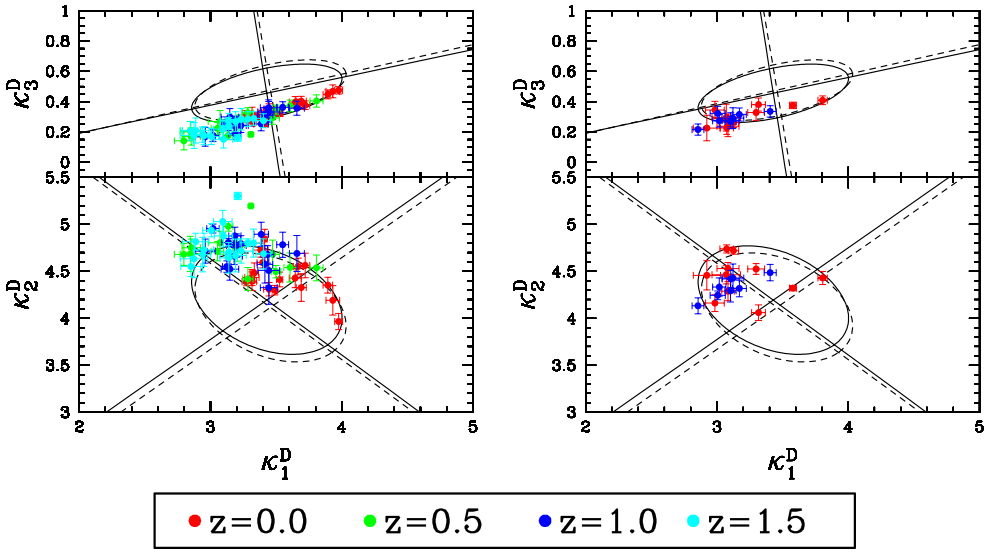

Figure 8.3: The Dynamical Plane viewed edge-on (top) and face-on (bottom) at different redshifts ($z = 0$ red; $z = 0.5$ green; $z = 1$ blue; $z = 1.5$ cyan) for *EB* (left) and *EF*3 (right) in the kappa space. We also draw the respective concentration ellipses (with their major and minor axes) for the SDSS early-type galaxies sample from Bernardi et al. (2003c) in the z-band and r-band. See text for more details.

relation and searching for the origin of the tilt of this relation at the projected baryonic scale (see more details in Section 6.2.4). Results of the log-log fits are in Tables 8.2, 8.3 and 8.4 for the *EA*, *EB* and *EF*3 samples. It is interesting to point out that higher redshifts samples (apart of having a lower number of virtual ellipticals) cover a bit lower mass range. In spite of these drawbacks the statistical analysis confirms robustly that $M_{\rm vir}/M_{\rm bo}^{\rm star}$ leads to a $\beta_{\rm vir} \neq 0$, thus contributing to the tilt at any z (see also Figure 8.6). The other factor involved in explaining the origin of tilt at $z = 0$ is the $c_{\rm rd} = r_{\rm vir}/r_{\rm e,bo}^{\rm star}$ relation. In this case, dispersion is too high at higher redshifts to allow us to reach a firmly statement however they do not discard our previous conclusions.

Finally we want to discuss some indications of mild evolution observed in our statistical analyzes (Tables 8.2, 8.3 and 8.4) and Figure 8.1, specially for the most massive objects in our samples. These trends for the massive galaxies point to a decrease of the effective radius and an increase of the velocity dispersion as redshift increases at a fixed mass. Both changes compensate one to each other so we do not see any changes in the edge-on view of the Fundamental Plane. This result is in agreement with the conclusions of Ciotti et al. (2007) and Robertson et al. (2006); Hopkins et al. (2008b,a). These authors showed, using an analytical approach and by simulating galaxy mergers respectively, the great importance of dissipation in the evolution of the fundamental scale relations. Recent observational results have shown a very strong evolution of the effective radius and velocity dispersion in this direction for the massive ellipticals (Tru-

Parameter	*EA*-Z0	*EA*-Z0.5	*EA*-Z1	*EA*-Z1.5
M_1	0.238 ± 0.039	0.191 ± 0.086	0.226 ± 0.077	0.235 ± 0.177
$\beta_{\rm vir}$	0.221 ± 0.083	0.355 ± 0.104	0.237 ± 0.193	0.398 ± 0.212
$\beta_{\rm M}$	-0.162 ± 0.140	0.129 ± 0.214	-0.048 ± 0.298	0.288 ± 0.415
$\beta_{\rm f}$	0.048 ± 0.040	0.030 ± 0.061	0.011 ± 0.099	-0.032 ± 0.089
$\beta_{\rm vd}$	0.000 ± 0.037	-0.046 ± 0.060	-0.139 ± 0.097	-0.074 ± 0.091
$\beta_{\rm vpc}$	0.012 ± 0.033	0.102 ±0.050	0.038 ± 0.075	0.086 ± 0.159
$\beta_{\rm rd}$	-0.231 ± 0.146	0.018± 0.198	0.035 ± 0.282	0.308 ± 0.398
$\beta_{\rm rp}$	0.011 ± 0.012	0.029 ± 0.020	0.014 ± 0.016	0.009 ± 0.044

Table 8.2: Slopes for linear fits at different redshifts for *EA* samples. Column 2: the slopes, for *EA*-Z0 sample, of the $\kappa_3^{\rm D} = M_1\kappa_1^{\rm D} + M_0$ relation (direct fits); the slopes of the $M_{\rm vir}/M_{\rm bo}^{\rm star}$ and $c_{\rm i} \propto (M_{\rm bo}^{\rm star})^{\beta_{\rm i}}$ scaling relations for the *EA*-Z0 sample, calculated in $\log - \log$ plots through direct fits. Errors stand for the respective 95% confidence intervals. Column 3, 4 and 5: same as columns 2 for *EA*-Z0.5, *EA*-Z1 and *EA*-Z1.5 samples respectively.

jillo et al., 2007; Buitrago et al., 2008; van der Wel et al., 2008; Cenarro & Trujillo, 2009) raising a considerable interest for this issue in all the astrophysical community.

Although still not clear, the interpretation of these trends could be linked with the amount of dissipation that each ELO has suffered along its mass assembly. Mergers that do not involve gas (also called dry mergers) will produce remnants with larger effective radius and lower velocity dispersion than those mergers which do involve it (wet). Available observations seem to indicate that mergers do happen in the life of elliptical galaxies, with wet mergers dominating at high redshift and dry merging mainly affecting massive elliptical galaxies at $z < 1.5$ (e.g., see Khochfar & Burkert, 2003; Bell et al., 2004, 2006; van Dokkum, 2005; Conselice, 2006; Faber et al., 2007). Therefore for a galaxy with a fixed mass, its effective radius will be higher as the assembly of its mass occurs at lower redshift because it has involved less dissipation.

We can also see this effect in Figures 8.2 and 8.3. Some mild evolution can be seen in the κ_1^D vs κ_2^D projection, while the edge-on view (κ_1^D vs κ_3^D) does not show significant changes. In general, ELOs at lower redshifts tend to have lower values of κ_2^D for a specific value of κ_1^D than higher redshift ones, specially as we go to higher values of κ_1^D. In this sense, the position of a simulated elliptical in this plot is linked with the amount of dissipation that it has suffered along it mass assembly. We will deepen into this picture in Section 9.2 of the next Chapter.

Parameter	*EB*-Z0	*EB*-Z0.5	*EB*-Z1	*EB*-Z1.5
M_1	0.277 ± 0.060	0.237 ± 0.086	0.288 ± 0.091	0.198 ± 0.124
$\beta_{\rm vir}$	0.290 ± 0.193	0.293 ± 0.153	0.313 ± 0.288	0.500 ± 0.203
$\beta_{\rm M}$	-0.167 ± 0.288	-0.095 ± 0.300	-0.104 ± 0.427	0.307 ± 0.254
$\beta_{\rm f}$	-0.007 ± 0.072	-0.003 ± 0.044	-0.076 ± 0.110	-0.089 ± 0.073
$\beta_{\rm vd}$	0.000 ± 0.113	-0.067 ± 0.102	0.053 ± 0.111	-0.010 ± 0.091
$\beta_{\rm vpc}$	0.069 ± 0.109	0.047 ± 0.081	-0.159 ± 0.106	0.021 ± 0.136
$\beta_{\rm rd}$	-0.247 ± 0.266	0.025 ± 0.277	0.029 ± 0.398	0.413 ± 0.279
$\beta_{\rm rp}$	0.026 ± 0.021	-0.001 ± 0.035	0.062 ± 0.047	-0.034 ± 0.028

Table 8.3: Slopes for linear fits at different redshifts for *EB* samples. Column 2: the slopes, for *EB*-Z0 sample, of the $\kappa_3^{\rm D} = M_1\kappa_1^{\rm D} + M_0$ relation (direct fits); the slopes of the $M_{\rm vir}/M_{\rm bo}^{\rm star}$ and $c_{\rm i} \propto (M_{\rm bo}^{\rm star})^{\beta_{\rm i}}$ scaling relations for the *EB*-Z0 sample, calculated in $\log-\log$ plots through direct fits. Errors stand for the respective 95% confidence intervals. Column 3, 4 and 5: same as columns 2 for *EB*-Z0.5, *EB*-Z1 and *EB*-Z1.5 samples respectively.

Parameter	*EF*3-Z0	*EF*3-Z1
M_1	0.193 ± 0.111	0.184 ± 0.156
$\beta_{\rm vir}$	0.345 ± 0.166	0.533 ± 0.544
$\beta_{\rm M}$	0.092 ± 0.249	0.317 ± 0.488
$\beta_{\rm f}$	0.056 ± 0.060	0.008 ± 0.117
$\beta_{\rm vd}$	-0.035 ± 0.072	0.038 ± 0.158
$\beta_{\rm vpc}$	0.086 ± 0.107	-0.020 ± 0.281
$\beta_{\rm rd}$	-0.045 ± 0.232	0.270 ± 0.408
$\beta_{\rm rp}$	0.026 ± 0.022	0.022 ± 0.056

Table 8.4: Slopes for linear fits at different redshifts for *EF*3 samples. Column 2: the slopes, for *EF*3-Z0 sample, of the $\kappa_3^{\rm D} = M_1\kappa_1^{\rm D} + M_0$ relation (direct fits); the slopes of the $M_{\rm vir}/M_{\rm bo}^{\rm star}$ and $c_{\rm i} \propto (M_{\rm bo}^{\rm star})^{\beta_{\rm i}}$ scaling relations for the *EF*3-Z0 sample, calculated in $\log-\log$ plots through direct fits. Errors stand for the respective 95% confidence intervals. Column 3: same as column 2 for *EF*3-Z1.

8.3 The Photometric Plane Evolution

Following the analysis of structural and kinematical fundamental parameters, we want to deepen into one that has earned a lot of interest in the last years, the shape parameter, n. We want to study the evolution of the different correlations, as the Photometric Plane, that we found at $z = 0$ in which this parameter is involved (see Section 6.3). Therefore, firstly we have analyzed how suitable the Sérsic law is to describe the stellar mass distribution of virtual ellipticals at higher redshifts. To make a proper comparison between them a special attention in the fitting method is needed (see Section 4.5). Specifically the outer boundary limit for the fit has proved to be a very important parameter. For this reason we have decided to use the same criterion for all samples. We have used the same projected stellar mass density limit $6.32\times10^{12}M_{\odot}/Mpc^2$ used at $z = 0$ which was obtained from an observational resolution limit in blue band $\mu_B = 27\ mag\times arcsec^{-2}$. Of course, at these redshifts this mass density limit translates into unavailable values of observational resolution threshold. However this is the same procedure used in recent studies that test the evolution of different fundamental parameters with redshift (see for example Trujillo et al., 2007; van der Wel et al., 2008), but for a higher resolution limit.

We have found that the projected mass density profiles of ELOs at redshifts $z = 0.5$, $z = 1$ and $z = 1.5$ can also be well fitted by a Sérsic law with similar χ^2 values. In Figure 8.4 we plot the mean shape parameter n versus the mean projected stellar half-mass radius $R^{\rm star}_{\rm e,bo}$ and l.o.s. velocity dispersion $\sigma^{\rm star}_{\rm los,0}$. In general, we can see that as we go to higher redshifts our ELO samples have lower values of n and that this parameter shows a higher dispersion for ELOs with a smaller $R^{\rm star}_{\rm e,bo}$ (and therefore less massive). It is important to remark the good correlation between n and $\sigma^{\rm star}_{\rm los,0}$ parameters at any redshift. We have carried out a direct fit of the form: $\log(n) = \beta\log(x_i) + \gamma$ for these parameters. The slopes of these fits and their respective 95% confidence intervals are given in Table 8.5. First conclusion from these results is that there can be a mild evolution of these parameters in the samples. In order to clarify this issue we have carried out same fits for the projected stellar mass, $M^{\rm star}_{\rm cyl,bo}$ along redshift. Results can be found in Table 8.5. From these results we can conclude that the possible evolution points out to more concentrated ELOs for a fixed mass as we go to higher redshifts. This is in good agreement with the mild evolution discussed in previous Section.

Additionally, we have analyzed if a similar relation to the Photometric Plane exists in our ELO samples involving the effective radius, the stellar mass and the Sérsic index. We define it as the Structural Photometric Plane (SPhoP):

$$\log R^{\rm star}_{\rm e,bo} = A\log n + B\log M^{\rm star}_{\rm cyl,bo} + C. \tag{8.2}$$

Orthogonal least square fits of Equation 8.2 for the *EA* and *EF*3-STAR samples at

	EA-Z0	*EA*-Z0.5	*EA*-Z1	*EA*-Z1.5
$n \propto (R^{\rm star}_{\rm e,bo})^{\beta}$	0.388 ± 0.134	0.462 ± 0.246	0.540 ± 0.319	0.361 ± 0.521
$n \propto (\sigma^{\rm star}_{\rm los,0})^{\beta}$	0.823 ± 0.106	0.682 ± 0.146	0.582 ± 0.182	0.377 ± 0.392
$n \propto (M^{\rm star}_{\rm cyl,bo})^{\beta}$	0.330 ± 0.114	0.344 ± 0.159	0.454 ± 0.155	0.556 ± 0.285

Table 8.5: Slopes from direct fits and their respective 95% confidence intervals of the shape parameter n and other Fundamental parameters up to $z = 1.5$.

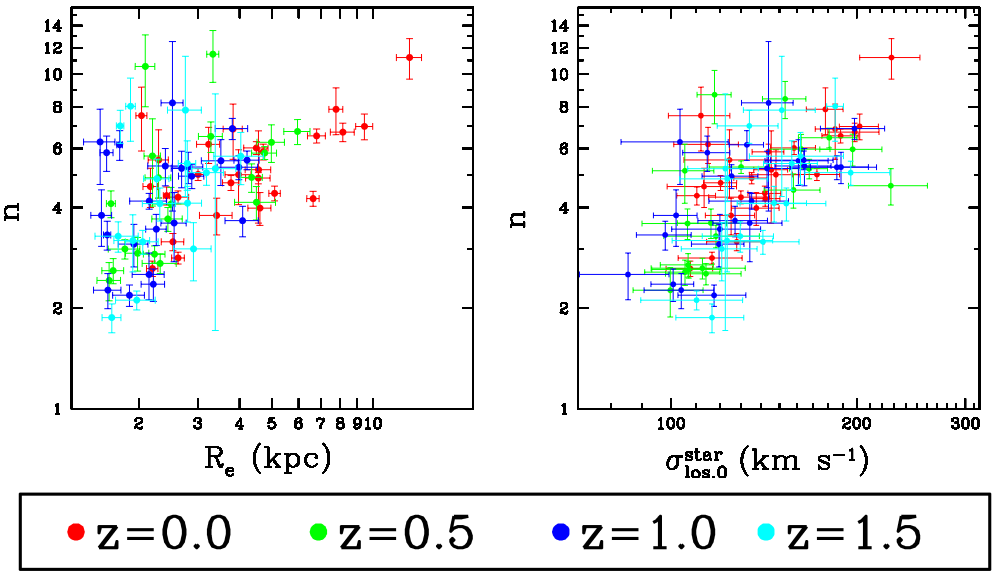

Figure 8.4: Shape parameter, n, versus different structural and kinematical Fundamental parameters since $z < 1.5$. Error bars account for projection effects.

different redshifts are shown in Table 8.6. *EA*-Z0 sample gives $A^{EA}_{Z0} = -0.30186$; $B^{EA}_{Z0} = 0.87653$; $C^{EA}_{Z0} = -9.86211$ $\sigma^{EA}_{\rm nRM,Z0} = 0.0556$. In Figure 8.5 we plot the edge-on projection of this plane (*EA*-Z0) for all the *EA* ELO samples at different redshifts. From these results we have confirmed that the logarithms of n, $R^{\rm star}_{\rm e,bo}$ and $M^{\rm star}_{\rm cyl,bo}$ populate a flattened ellipsoid close to a two-dimensional plane at any redshift up to $z = 1.5$. The deviation between these planes as we go to higher redshifts could be explained by a mild evolution of the $R^{\rm star}_{\rm e,bo} - M^{\rm star}_{\rm cyl,bo}$ relation already mentioned in the previous section. Table 8.6 also presents the orthogonal least square fits of the SPhoP for *EF*1 and *EF*3 samples. Although with slightly different slopes, we found that ELOs of these samples lie in a SPhoP at all redshifts.

Finally, what is clear is that the Structural Photometric Plane puts a limit on the values of the shape parameter, radius and mass at any redshift. Present results show that the Photometric Plane could be an interesting alternative tool for the study of elliptical galaxies at least up to $z \sim 1.5$ instead of the Fundamental Plane, that requires

a heavy amount of time for measuring velocity dispersions.

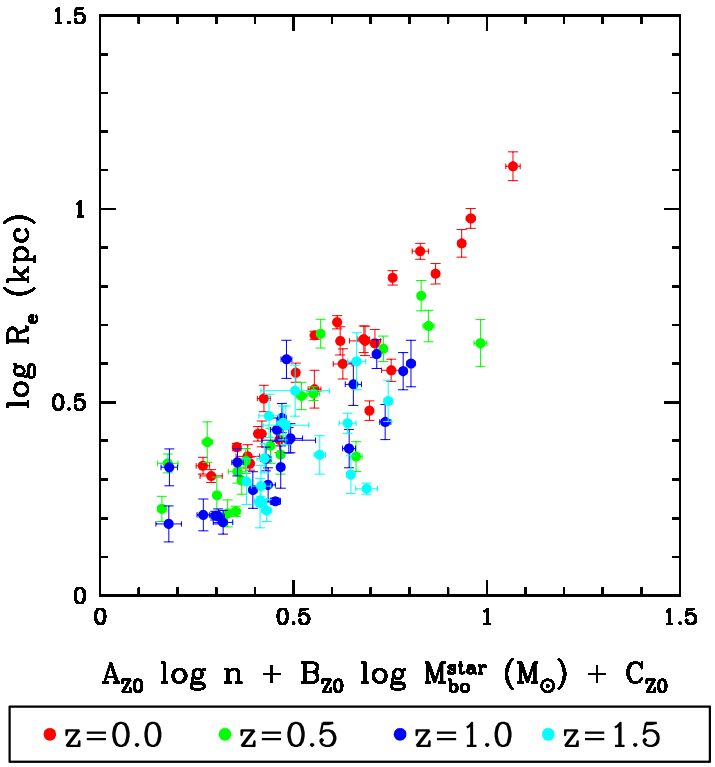

Figure 8.5: The Structural Photometric Plane for the *EA* sample at different redshifts. Error bars account for projection effects.

Sample	#	A_z^{EA}	B_z^{EA}	C_z^{EA}	λ_1	λ_2	λ_3	$\sigma_z^{\rm nRE}$
EA-Z0	26	-0.30186	0.87653	-9.86211	0.12992	0.010797	0.003091	0.0556
EA-Z0.5	19	0.08668	0.52395	-5.29105	0.13307	0.017580	0.005699	0.0755
EA-Z1	23	-0.52376	0.76243	-7.52951	0.08398	0.016350	0.004481	0.0669
EA-Z1.5	16	-0.69873	1.15367	-11.71195	0.05981	0.011577	0.007786	0.0882
*EF*1-Z0	21	-0.41220	0.79899	-8.22228	0.22673	0.014084	0.002462	0.0496
*EF*1-STAR-Z0	31	-0.31867	0.75837	-7.70990	0.16490	0.019999	0.002774	0.0527
*EF*1-STAR-Z0.5	25	0.07537	0.35217	-3.51303	0.08313	0.018030	0.002646	0.0514
*EF*1-STAR-Z1	22	-0.49517	0.67825	-6.73783	0.04681	0.008310	0.006083	0.0780
*EF*1-STAR-Z1.5	18	-0.50476	0.52369	-5.10680	0.12102	0.065926	0.002531	0.0503
*EF*3-Z0	11	-0.49447	0.80827	-8.03058	0.13885	0.027877	0.003712	0.0609
*EF*3-Z1	8	-0.10306	0.34100	-3.32734	0.03570	0.006471	0.000483	0.0220
*EF*3-STAR-Z0	22	-0.25006	0.74982	-7.58819	0.11996	0.027059	0.005245	0.0724
*EF*3-STAR-Z1	14	-0.18301	0.23100	-2.10632	0.03732	0.016548	0.002944	0.0543

Table 8.6: Principal component analysis of mass, radius and dispersion velocity for *EA*, *EF*1 and *EF*3 simulations. Column 2: number of objects in the sample. Columns 3, 4 and 5: coefficients of Equation 8.2 at each z. Columns 6, 7 and 8: eigenvalues of the correlation matrix. Columns 9: rms orthogonal scatter of the photometric plane at each z.

8.4 Other Structural and Kinematical Parameters

In this section we show some important results concerning the evolution of different relations between structural and kinematical parameters studied in Chapters 5 and 6. In the upper left panel of Figure 8.6 we plot, for the *EA* samples at $z = 0$, $z = 0.5$, $z = 1$ and $z = 1.5$, the slopes obtained from a power law fit of the total mass density profiles ($\rho(r) \propto r^{-\gamma}$, see Section 5.2.5 for more details on the method). We do not find any evolution trend for these slopes, confirming that all the mass components combine to make almost an isothermal profile at any redshift. Moreover, in the upper right panel of Figure 8.6 we present the ratio between the total virial mass, $M_{\rm vir}$, and the stellar mass, $M_{\rm bo}^{\rm star}$ for the same ELO samples. The dependence of this ratio with the stellar mass is one of the main factors that explains the tilt of the Fundamental Plane in ELO samples (see Sections 6.2 and 8.2). Slopes from log-log direct fits for this relation can be found in Tables 8.2, 8.3 and 8.4 ($\beta_{\rm vir}$ parameter) for *EA*, *EB* and *EF*3 samples respectively. Although we obtain a possible decrease of the slopes as we go to lower redshifts, the statistical errors (95% confidence level) still allow the non evolution possibility. Lower left panel of Figure 8.6 shows another interesting result regarding the structure of ELOs along redshift. In this plot we can see the $M_{\rm cyl}^{\rm dark}/M_{\rm cyl}^{\rm tot}(\leq R_{\rm e,bo}^{\rm star})$ ratios introduced in Section 5.2.4 for the *EA* samples at higher redshifts. We observe a small trend, especially for more massive ELOs, pointing towards an increase of the fraction of dark-to-total mass at the effective radius as we go to lower redshifts. This result indicates that for a fixed stellar mass, the stellar component at the ELO scale is less concentrated as we move to lower redshifts (see previous results in Section 8.2 and discussion in 8.6). Finally, the lower right panel confirms the extremely good correlation at any redshift between the virial mass, $M_{\rm vir}$, and the central stellar line-of-sight velocity dispersion, $\sigma_{\rm los,0}^{\rm star}$. However it is important to remark that the dispersion in this correlation increases if we include ELOs which are not really isolated up to the virial scale, i.e., they are suffering a merger at this scale and still have not reached an equilibrium state.

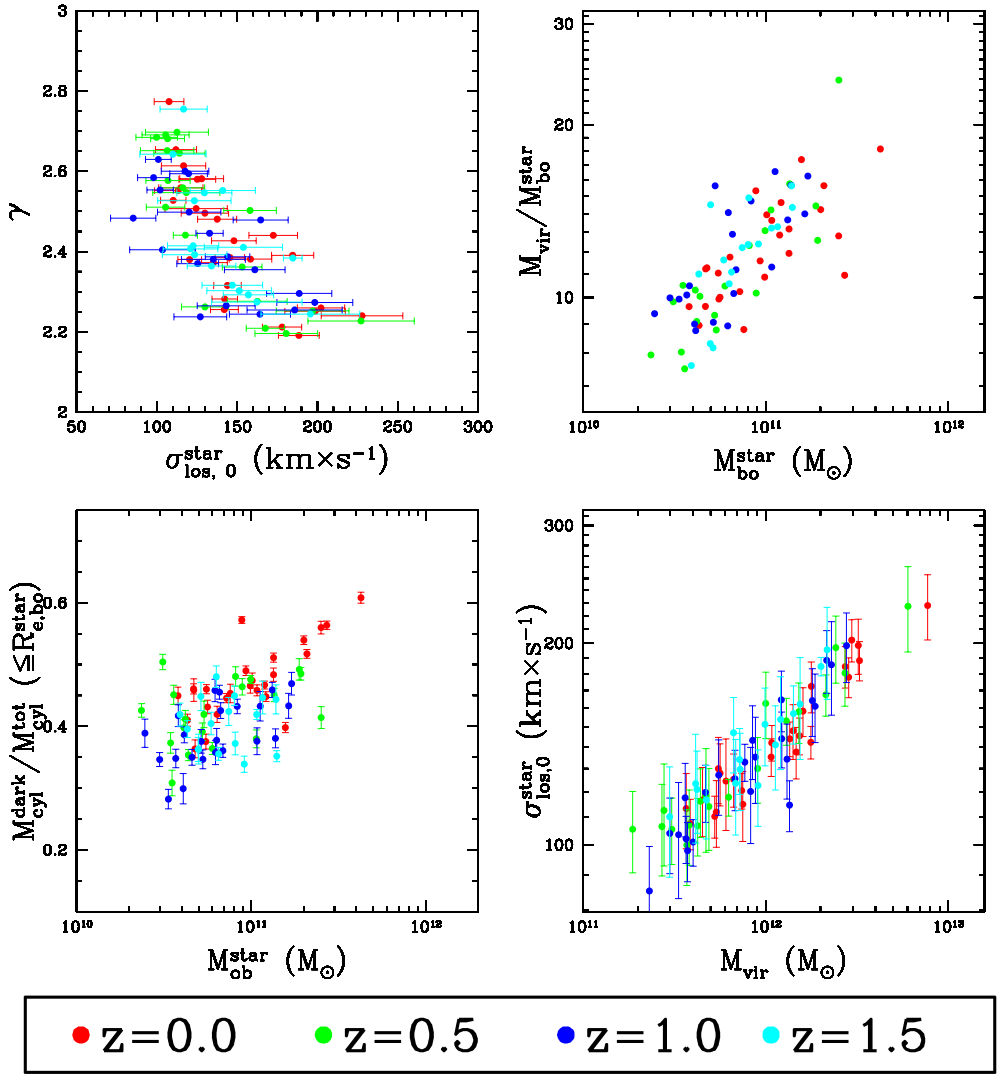

Figure 8.6: Structural and kinematical parameters evolution since $z < 1.5$ for the *EA* sample. Error bars account for projection effects. See text for details.

8.5 The Rotation versus Shape Diagram

In this section we continue with the analysis started in Chapter 7 of the relation between the shape and the rotational support of elliptical galaxies at $z = 0$ and study the evolution of this relation up to $z = 1.5$ for our different samples. We will show that all of them share some interesting general trends. In order to have better statistics we present in next section the results of a total sample formed by joining *EA*-STAR, *EF*1-STAR and *EF*2-STAR samples (see Section 4.4). A proper description on how the different parameters studied in this section are calculated can be found in Section 4.5.

8.5.1 Shape and Kinematics of Elliptical Galaxies: Evolution Due to Merging at z<1.5

Astronomy & Astrophysics manuscript no. aa'accepted'corr
March 9, 2009

Shape and kinematics of elliptical galaxies: evolution due to merging at $z < 1.5$

A. César González-García, José Oñorbe, Rosa Domínguez-Tenreiro, and M. Ángeles Gómez-Flechoso

Departamento de Física Teórica, Universidad Autónoma de Madrid, 28049, SPAIN; c.gonzalezgarcia@uam.es

Received 1 Dic 2008 / Accepted 14 January 2009

ABSTRACT

Aims. We investigate the evolution in the shape and kinematics of elliptical galaxies in a cosmological framework.
Methods. We identified relaxed, elliptical-like objects (ELOs) at redshifts $z = 0$, $z = 0.5$, $z = 1$ and $z = 1.5$ within a set of hydrodynamic, self-consistent simulations completed for a concordance cosmological model.
Results. The population of elliptical systems that we analysed evolve systematically with time becoming rounder in general by $z = 0$ and also more velocity dispersion supported. We found that this is due primarily to major dry mergers where only a modest amount of angular momentum is involved in the merger event. Despite the general trend, in a significant number of cases the merger event involves a relatively high amount of specific angular momentum, which causes the system in general to acquire higher rotational support and/or a more oblate shape. These evolutionary patterns persist when we study our systems in projection, in simulating true observations, and thus should be evident in future observations.

Key words. Galaxies: elliptical and lenticular, cD – Galaxies: fundamental parameters – Galaxies: interactions – Galaxies: Evolution – Galaxies: Formation – Galaxies: kinematics and dynamics

1. Introduction

Surveys of high-redshift galaxies suggest that some relaxed, massive elliptical galaxies may already be in place at $z \sim 2-1.5$ (Cimatti et al. 2004; Conselice et al. 2007), or even by $z \sim 5$ (Wiklind et al. 2008). These results notwithstanding, according to current formation scenarios, merging has played an important role in the mass assembly of most of the local massive elliptical galaxies. Observations and theory suggest that, first, violent mergers at high z have transformed most of the available gas into stars, and, later on, these systems might have evolved through gas-free (the so-called dry) mergers (Conselice 2006; see otherwise Scarlata et al. 2007).

Since the study by Bertola & Cappacioli (1975), we know that elliptical galaxies are supported against gravity by random motions as well as rotation. Davies et al. (1983) studied the now classical V_{max}/σ_o versus ϵ diagram for spheroids (Illingworth 1977; Binney 1978), where V_{max} is the maximum of the line-of-sight (l.o.s.) rotation curve, σ_o is the central l.o.s. velocity dispersion of the galaxy, and ϵ is the mean ellipticity inside a given radius. They found that luminous (and massive) elliptical galaxies were characterised by low V_{max}/σ_o and a fairly circular morphology (low ϵ), while ellipticals with intermediate luminosity tend to have higher values of both V_{max}/σ_o and ϵ. Several observations involving 1D spectroscopy of near by elliptical galaxies (Lauer 1985; Bender 1988; Nieto et al. 1989; Bender et al. 1994; Pellegrini 2005; Lauer et al. 2005), and 2D spectroscopy confirmed this characteristics for ellipticals (see Emsellem et al. 2007 and Cappellari et al. 2007, hereafter CAP07). Van der Marel & van Dokkum (2007) presented evidence of evolution in the rotation support of elliptical systems since z=0.5. Present formation schemes should be capable of explaining these observations of the kinematics and shapes of elliptical galaxies and their possible evolution.

A number of N-body simulations of isolated galaxy mergers have dealt with the population of the classical diagram and the formation of boxy and disky objects (Naab & Burkert 2003; González-García & Balcells 2005; González-García & van Albada 2005; Naab, Khochfar & Burkert et al. 2006; Bournaud et al. 2005; Robertson et al. 2006; Cox et al. 2006; González-García et al. 2006; Jesseit et al. 2007; Naab & Ostriker 2007). These studies indicate that mergers between disk galaxies tend to produce too high rotational support when compared with present-day massive elliptical galaxies. Mergers between elliptical galaxies have indeed been shown to reproduce the observed characteristics of massive ellipticals. Khochfar & Burkert (2003) and Kang et al. (2007) (and references therein) presented the first attempts by semi-analytical modelling to recreate the kinematics and shapes of early-type galaxies. Naab et al. (2007) studied the formation of three massive galaxies from cosmological initial conditions. However, a detailed, statistical analysis of the internal kinematics and shapes of objects formed in fully self-consistent cosmological simulations and their possible evolution is, to the best of our knowledge, still missing yet mandatory in providing a clear picture of the mechanisms at play in the formation and evolution of present day Ellipticals (E's).

In this paper, we present the results of self-consistent cosmological simulations that we developed to investigate the shape and kinematical evolution of elliptical-like objects (hereafter ELOs) at several redshifts. In the present analysis, we consider both three-dimensional (hereafter, 3D) and projected data on the sky. Other kinematic parameters proposed will be investigated in a forthcoming paper, and are omitted from the present study for the sake of simplicity.

Send offprint requests to: c.gonzalezgarcia@uam.es

2. Methods and numerical experiments

2.1. Simulations

We completed seven hydrodynamical simulations in the context of a concordance cosmological model (Spergel et al. 2006). For five of the simulations, we employed a 10 Mpc side periodic box with flat ΛCDM cosmological model, with $h = 0.65$, $\Omega_m = 0.35$ and $\Omega_b = 0.06$. To set the initial conditions, we employed the algorithm developed by Couchman (1991) with a slightly high normalisation parameter input $\sigma_8 = 1.18$, compared to the average fluctuations, to mimic an active region of the Universe (Evrard, Silk & Szalay 1990). These simulations represented the A-sample in Oñorbe et al. (2005, 2006, 2007) and they differ from each other in the seed used to generate the initial conditions.

To test whether the evolutionary trends found in these simulations are robust, we executed two simulations with a box side twice as long as in the first simulations and a factor of 8 higher number of particles, for the same cosmology as before, now using input values $\sigma_8 = 0.75$ and 0.95. The first of these values is such that the initial distribution of kinetic energy per unit volume is similar to that in the small box simulations (Gelb & Bertschinger 1994; Sirko 2005; Power & Knebe 2006). To execute the small and larger box simulations, we used respectively DEVA (Serna, Domínguez-Tenreiro & Sáiz, 2003) and P-DEVA (its OpenMP version, see Serna et al., in preparation), which are two Lagrangian SPH-AP3M codes. The mass resolution is $1.28 \times 10^8 M_\odot$ for dark-matter particles and $2.67 \times 10^7 M_\odot$ for baryon particles. Star-formation (SF) processes were includedin terms of a simple phenomenological parametrisation (Katz 1992, see also Serna et al. 2003 and Oñorbe et al. 2007 for details).

We applied a consistency test by executing two simulations with identical initial conditions in a 10Mpc side periodic box, one containing 2×64^3 particles and a second containing 2×128^3 particles, with masses as above for the 2×64^3 simulation and $1.6\times10^7 M_\odot$ for dark-matter particles and $3.3\times10^6 M_\odot$ for baryon particles in the 2×128^3 simulation.

Galaxy-like objects of different morphologies appear in the simulations. ELOs were identified as those having a prominent, relaxed spheroidal component, consisting of stars, with no extended discs. These baryonic objects are embedded in a dark matter extended halo, typically 10 times more massive. In Oñorbe et al. (2005, 2006), it was shown that these ELOs satisfy dynamical Fundamental Plane relations. In Oñorbe et al. (2007), the total, bright, and dark matter profiles of ELOs and their kinematics were analysed and found to be in satisfactory agreement with observational data.

2.2. Methods and analyses

We analysed the ELOs at four redshifts: $z = 1.5$, $z = 1.0$, $z = 0.5$, and $z = 0$. We selected undisturbed ELOs (i.e. within their limiting radius, we observe a quasi-equilibrium behaviour of the system) because we wanted to analyse their shapes, although their dark matter halos could be in the first stages of merging. We analysed those systems that at each redshift have more total stellar mass than $2.6 \times 10^{10} M_\odot$. This limit agrees with Kauffmann et al. (2003) for early-type galaxies, and the number of particles per ELO is sufficiently large to avoid resolution problems (see below). In total, we have 425 ELOs (225 from the small box simulations, and 200 from the large box simulations), 127 at $z = 0$, 107 at $z = 0.5$, 97 at $z = 1.0$, and 94 at $z = 1.5$.

To quantify the shape of the ELO, we measured the axis ratios (c/a versus b/a, with $a > b > c$) of the ellipsoidal figures defined by the particles inside r_{90} (the radius enclosing 90% of the stellar mass of the system), by computing the eigenvalues of their inertia tensor (see González-García & van Albada 2005). To classify the shape of our objects, we used the triaxiality parameter introduced by de Zeeuw & Franx (1991), $T = (1 - (b/a)^2)/(1 - (c/a)^2)$, in the following way: we introduce the parameter s as $s = 3$ if $c/a > 0.9$ (close to spherical objects), $s = 2$ if $c/a < 0.9$ and $T < 0.3$ (oblate objects), $s = 0$ if $c/a < 0.9$ and $T > 0.7$ (prolate objects), and $s = 1$ elsewhere (triaxial objects). Concerning kinematics, we studied the three dimensional velocity dispersion inside the effective radius r_e[1] (σ_{3D}), and considered the mean tangential velocity at $r = r_e$, (V_ϕ). We also studied these characteristics at r_{90}.

To compare with classical observations, we investigated the line-of-sight rotation and velocity dispersion measurements to one projected effective radius (R_e) for each object. We chose a point of view perpendicular to the spin angular momentum vector of the stellar matter because these particular points of view should maximise the effects of rotation when evident (see Binney 2005, and Burkert & Naab 2005). We first derived the ellipticity of each ELO by projecting the complete particle distribution onto a plane perpendicular to the line-of-sight. Local surface densities were then computed following a logarithmic binning of space. Ellipses were fitted to the ELO isophotes, as performed for observational data. The ellipticity computed in our analysis was taken to be the mean of the ellipticities inside one R_e. Although the number of particles may not be very high in some objects, the signal at half the mass radii in projection is sufficiently high to calculate these values. We performed consistency tests with methods based on a diagonalization of the moment-of-inertia tensors, and values were consistent with each other. To derive the line-of-sight rotation and velocity dispersion profiles, we placed a slit along the major axis of the projected system (as obtained in the previous step) and projected the velocities of each particle along the line of sight. From these curves, we finally derived the central l.o.s. velocity dispersion (σ_o) and the maximum of the velocity curve inside R_e (V_{max}).

To understand the physical processes underlying the shape and rotation-support changes, for each of the 127 ELOs at $z = 0$ we compiled its mass aggregation track (MAT) along the main branch of its merger tree, for both its baryonic (the mass inside fixed radii) and total mass (the virial mass). These MATs provide information about the mass assembly processes with time. Major mergers (MM; $M_{secondary}/M_{primary} > 0.25$), minor mergers (mM), and aggregation (i.e. smooth in-fall of mostly gaseous material) processes can be clearly identified. We can also compute the amount of dissipation involved in the different processes as well as estimate the amount of angular momentum involved. Complementary information about a merger is provided by the configurations shown, in a time interval around the merger event, by the baryonic particles destined to form the ELO later on, i.e. the type and number of objects involved, and the environment. This way we analysed 150 events of any type along the main branch of the merger tree at $z < 1.5$, and classified them into several categories: mM or MM; binary or multiple; or involving a high or a low amount of specific angular momentum (and their combinations).

[1] r_e is the radius enclosing half of the stellar mass of the system

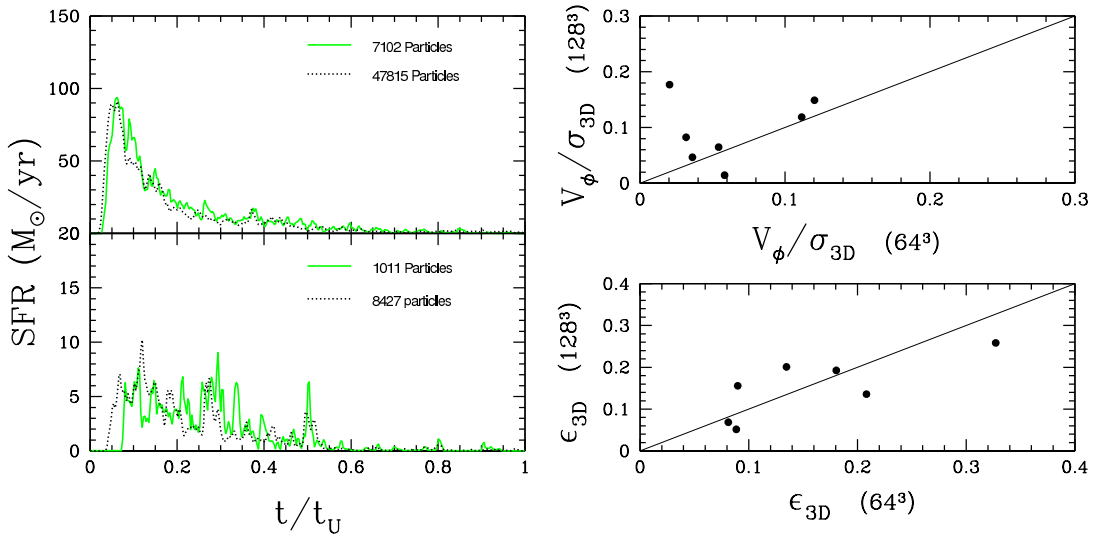

Fig. 1. Left: Star formation history of the most (top) and least (bottom) massive ELOs for the test simulations with 2×64^3 particles (solid green line) and 2×128^3 particles (dotted black line). Right, comparison of the kinematic (top) and shape (bottom) observables. The most massive system is the marked with a triangle and the least massive with an hexagon. For details, see text.

2.3. Consistency checks

Figure 1 shows the results of the consistency simulations. Figure 1 (left panel) shows the star-formation history of two objects, the most and least massive ELOs in the simulations. The black dotted line and the solid green line depict the results of the simulations with more and less particles, respectively. We found small differences, especially at early times, although the two systems display general similar behaviour, and at high cosmic times (low redshift) no significant differences are evident. A similar test was completed by Naab et al. (2007) and, although the numerical approaches differ, it is reassuring to also find convergence in this resolution test.

Figure 1 (right panel) presents comparative results of the same objects at $z = 0$ in the two simulations where we computed the observables introduced above on shape and kinematics. The systems appear to be stable and agreement between the simulations results is good, although one object does exhibit a significant difference. This system is not the least massive in these simulations and the difference is due to the peculiar way in which the V_ϕ parameter is measured, such that particles at different radii are considered. The overall consistency in these tests prompt us to use the 2×64^3 simulations for the sake of computing time.

3. Results

3.1. Shape and kinematic evolution

Figure 2, top row, shows the shape for the 4 redshifts, presented in different colours. Figure 2 (a) shows c/a versus b/a. Blue symbols ($z > 1$) appear mostly in the middle-left of the diagram, while red symbols ($z = 0$) appear in the top right, that is, the values of c/a and b/a tend to increase with decreasing redshift, or in summary, the population of ELOs become rounder on average with time. These results hold when we use r_e instead of r_{90} to calculate inertia tensors, although in this case ELOs tend to appear even rounder. Figure 2 (b) shows a histogram for the shape parameter s defined above. Results are given in relative numbers, and the error bars express the Poissonian noise. Most of our systems are triaxial objects at all redshifts, except at $z > 1$ when there is a fair amount of prolate systems. For all the simulations we consider here, the fraction of prolate objects decreases with decreasing redshift, and at all redshifts there is a small number of perfect spheres. The number of triaxial and oblate objects also increases with decreasing redshift. It is noteworthy that our results on ELO shapes at $z = 0$ compare reasonably well with those obtained from the Sloan survey for elliptical galaxies (Kimm & Yi 2007), where they show that the sample consists of about 45% triaxial objects and around 26 – 29% prolate and oblate objects.

Figure 2 (c), illustrates the rotational support of the ELOs. The histograms are normalised to their total number at each redshift, and the error bars represent the Poissonian noise. There is a trend towards increasing the number of systems with a lower value of V_ϕ/σ_{3D} as z decreases; this trend appears independently of the details of the simulation. Figure 2 (d) shows the diagram of V_ϕ/σ_{3D} versus ϵ_{3D}, where $\epsilon_{3D} = 1 - c/a$. Blue objects ($z > 1$) appear mostly again at high ϵ_{3D} values with a broad range of V_ϕ/σ_{3D} values, while at $z = 0$ (red symbols), ϵ_{3D} and V_ϕ/σ_{3D} are smaller on average. These trends persist if we use r_{90} instead of r_e (i.e., we measure external rotation instead of rotational support), although in this case there is a higher fraction of systems with higher values of V_ϕ/σ_{3D}.

We performed Kolmogorov-Smirnov tests to check whether the samples at different z's originate for the same distribution. Such null hypotheses can be ruled out in all cases, both for shapes and rotational support, at confidence levels of between 95 and 99.9 %. Given the consistency in the direction of the more frequent changes (i.e., towards becoming 'rounder' and more pressure-supported), we refer to these changes as an evo-

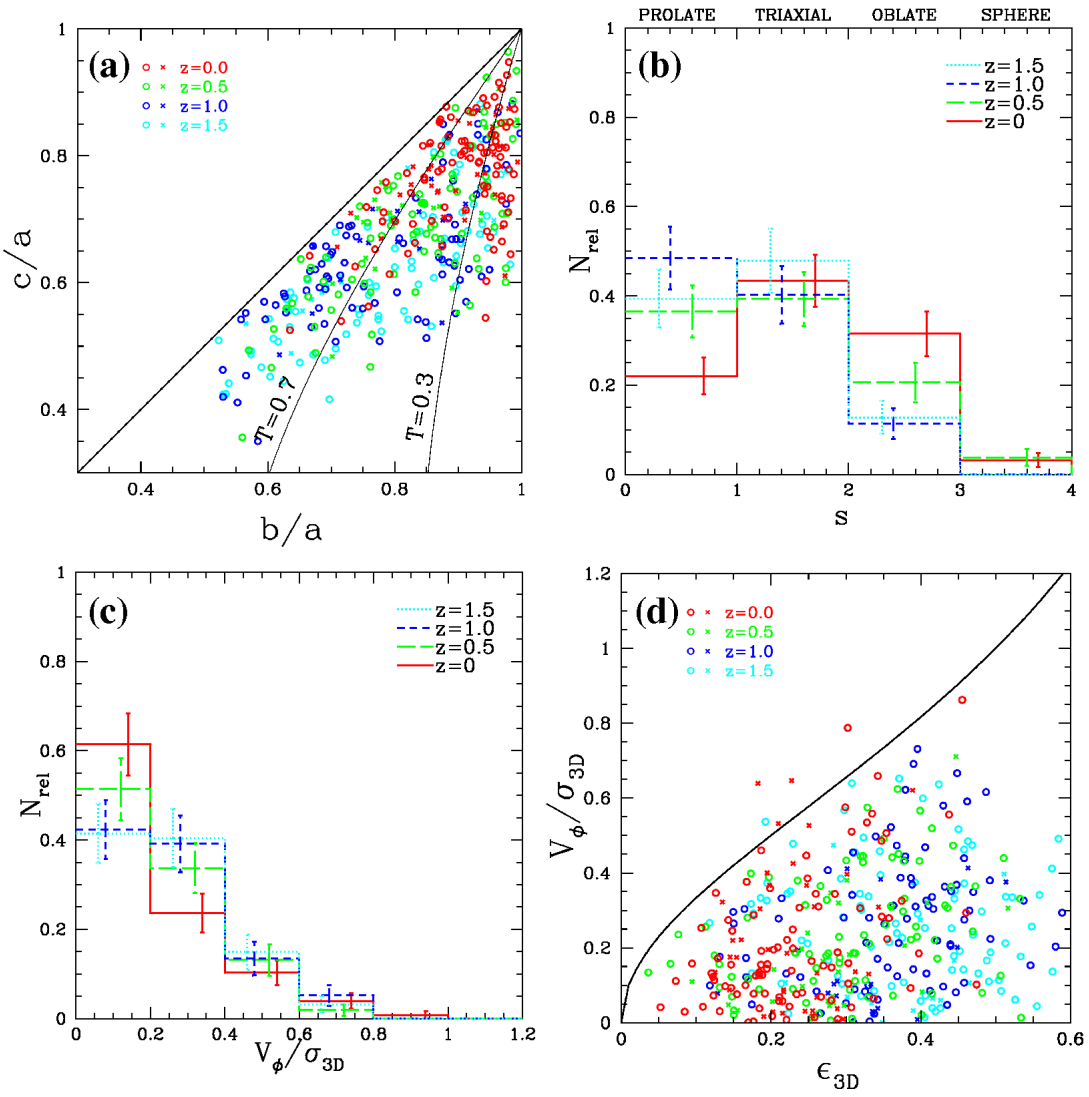

Fig. 2. (a) Axis ratios of the spheroids. Colours indicate the different redshits. Crosses are objects more massive than $M_* > 1{\times}10^{11}\mathrm{M}_\odot$, circles are objects of lower mass. (b) Histograms of the shape parameter S vs. relative number for all our systems. Different lines and colours indicate the histograms for the four redshift bins. (c) Histograms of the rotational support measured as $V_\phi/\sigma_{3\mathrm{D}}$ (at r_e) in relative number for our systems, colours and lines as in (b). (d) $V_\phi/\sigma_{3\mathrm{D}}$ vs. $\epsilon_{3\mathrm{D}}$ for the ELOs, colours and symbols as in (a) panel. Black solid line indicates the locus for oblate rotators. For details, see text.

lutionary track. We emphasise that this evolution concerns the global population of E's rather than individual ones.

We now consider the 2D analysis. First of all, there is reasonable agreement between the 3D and the projected kinematics, i.e. the rapidly rotating systems are in agreement in both samples. Also, objects with higher values of c/a ($\sim$ 1) tend to be those with the smaller ϵ, while the larger ellipticities are found among those objects with lower c/a. This correlation between 3D and 2D results for ELOs is noteworthy because it implies that the intrinsic evolution detected in virtual systems, should also be detected in observational (projected) data, if it occurs in true elliptical galaxies.

Figure 3 presents the results for the classical V_{max}/σ_o versus ϵ diagram (Davies et al. 1983). For the sake of clarity, we plot only the most massive objects $M_* > 1{\times}10^{11}\mathrm{M}_\odot$ of the small-sized simulations and the values are measured from a point of view perpendicular to the angular momentum vector. Each object is indicated by an open symbol, the colour representing the

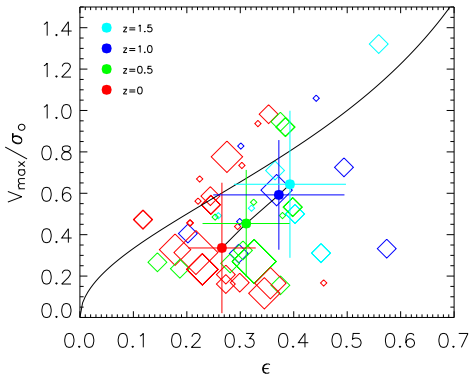

Fig. 3. V_{max}/σ_o vs. ϵ diagram. The black solid curve gives the locus of the oblate rotators (Binney 1978). Only models with $M_* > 1{\times}10^{11}M_\odot$ are plotted. Colours are as in Fig 2. Filled circles give a mean for the objects at each redshift. Finally the size of the symbol gives the accumulated number of major mergers that a system has undergone.

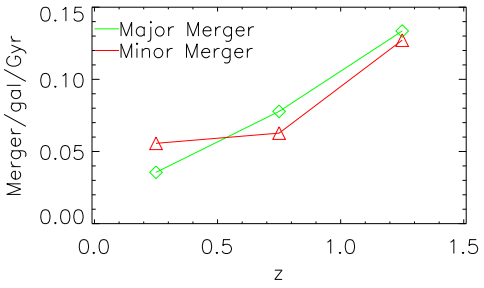

Fig. 4. Number of mergers per galaxy per Gyr as a function of redshift interval. Red line gives the rate for minor mergers. Green line gives the rate for major mergers. We observe a decline in the number of mergers, this decline is slightly steeper in the fraction of MM.

redshift of that object. At high z (light and dark blue), ELOs tend to appear as more flattened systems with a high relative rotation. However, at lower redshifts (green and red), we have more massive systems, which tend to appear rounder and more pressure-supported (except those few with high V_ϕ/σ_{3D}), in agreement with the 3D data (see Fig. 2(d)). The filled circles indicate the mean of the distribution at each redshift and the error bars are a measure of the standard deviation in the distribution. The systems evolve on average from being flat and relatively rotationally supported to being rounder/triaxial and pressure-supported systems. Finally, we note that if we include all systems in this plot, the evolution still holds. The size of the open symbols in Fig. 3 is a measure of the accumulated number of major mergers that the system has undergone since $z = 1.5$. Larger symbols are mostly located in the lower left part of the diagram. This indicates that merging is one of the key ingredients driving this evolution towards rounder and more pressure-supported ELOs. Although this is the general trend, we also note that there are some cases with high V_{max}/σ_o and a significant number of mergers, and this indicates that merging effects could be far more complex.

It has been argued (Binney 2005; Burkert & Naab 2005; CAP07) that the V_{max}/σ_o versus ϵ diagram is affected by projection effects. The results presented in Fig. 3 are obtained by looking at each object from a point of view perpendicular to the angular momentum vector. For oblate rotators, this vector should be close to the short principal axis, and the projected image would provide the maximum ellipticity and V_{max}/σ_o. However, many of our most massive systems are triaxial and the angular momentum vector has neither to coincide or be close to the short principal axis. In these cases, the V_{max}/σ_o diagram could be affected by projection effects. To test the effects of projection we have analysied the systems along 100 randomly chosen lines of sight, deriving the projected observables of the classical diagram. We obtained a distribution of points, which in the case of the most massive ELOs did not differ significantly from the points presented in Fig. 3. We tested the null hypothesis that the distributions of points at the different redshifts originate in the same distribution by completing a Kolmogorov-Smirnov test. The result is that we can exclude this hypothesis at the 99.9% confidence level. The same result is obtained by a Kuiper test. We conclude that the results presented are robust and that the evolution observed in the projected quantities in shape and kinematics is indeed real.

3.2. Merging rate

To understand how merging affects evolution, we carefully studied and classified all the merger events along the MATs of the 127 ELOs identified at $z = 0$.

We investigated the number of mergers in three redshift intervals $z \in (1.5, 1)$; $(1, 0.5)$ and $(0.5, 0)$. We were particularly interested in the mergers experienced by our ELOs. We investigated the main branch of the ELO merger tree and looked at the mass aggregation track to identify increments in mass. We identified major mergers (MM) and minor mergers (mM). For the three redshift intervals, we identified 21, 23, and 23 MMs, and 20, 22, and 36 mMs. Figure 4 shows the evolution in the merger rate since $z = 1.5$ for the three redshift bins. The merger rate is expressed in terms of the number of mergers per galaxy per gigayear. We measured a decrease in the number of mergers, which is more pronounced in the MM fraction than in mM.

We note that this result concerns the number of mergers experienced by the ELOs in our sample only along the main branch of their merger tree. Also, we analysed the high-mass end of the galaxy mass distribution, not taking into account mergers resulting in disk-like systems or systems of smaller mass. Despite these caveats, we compared these numbers with recent theoretical results. Naab et al. (2007) performed cosmological simulations including gas, cooling, and star formation to investigate the formation of three systems, two resembling true elliptical galaxies and a third resembling an S0 galaxy. They found that at $z < 1$, the systems have experienced few merger events, with one major merger in one case and a minor merger in another one. Scannapieco et al. (2008) used results from the Aquarius simulations (Springel et al. 2008) to investigate the survival of disks. The number of mergers is an important aspect in estimating the impact of merging in the survival of disks. They found that the disks have suffered a moderate number of mergers since $z = 2$. Finally, using the Millennium simulation Genel et al. (2008; 2009) found that since $z = 2.2$, the number of MM expe-

rienced by a halo of mass M in the redshift interval z_i and z_f can be approximated by $\bar{N}_{MM}(z_i, z_f, M) \approx 0.13\{\log[M/(10^{10}M_\odot)] + 1\}(z_i - z_f)$. Our simulations predict slightly higher values of this parameter, perhaps related to the active environment conditions modelled in our runs. However, we found that the results are in agreement with Fig. 8 of Genel et al. (2009) and our numbers are consistent with these theoretical works. Finally, Conselice et al. (2009) studied the merger history of a large number of galaxies for $z < 1.2$. Our results here are again in good agreement with those presented in their Fig.7 for observational results.

3.3. Trends of merger characteristics with time

At high z ($z > 1.5$), dissipative, multiple MMs are more frequent than other merger types. At $z < 1.5$, most mergers are rather dry (ELOs are mostly devoid of gas, with percentages of less than a few percent), with a higher frequency of low angular-momentum MM compared to high angular-momentum MMs (a frequency of $\sim 2:1$). Most mergers involving a fair amount of specific angular momentum are multiple events. However, the opposite is not true, since there are multiple events where only a small amount of angular momentum is involved, and particularly so at $z > 1.5$.

4. Discussion

We have compared the merger characteristics with the changes measured in shape and rotational support. We have found that there is a close correlation between the shape and the amount of rotational support of a given ELO at a given time and the characteristics of the last merger event it has suffered. Specifically, MMs always produce changes in both shape and rotational support in the outer and the inner parts. MMs with little angular momentum most often decrease the rotational support inside r_e, producing mostly rounder (i.e., a larger value of c/a) prolate spheroids, while MMs with a high (intermediate) amount of angular momentum increase rotational support, producing oblate or triaxial systems. This picture of the role of angular momentum is consistent with the transformation found in binary mergers of spheroidal systems by González-García & van Albada (2005). mMs most often produce triaxial or oblate spheroids and increase the rotational support, although the effect is most likely to affect the outer parts of the ELO (see Balcells & Quinn 1990, Eliche-Moral et al. 2006), except for penetrating mMs. Finally, aggregation processes are also important and may affect the shape and kinematics of the final object. We have found that around 85% of the changes in both shape and rotational support are associated with merging (in contrast to aggregation).

Combining these findings on the trends of merger characteristics with time and the different effects a merger causes according to these characteristics, we can understand that prolate ELOs are the most frequent at high z, and they are then transformed most often into rounder triaxial objects with less rotational support. An interesting conclusion from this study is that, due to dry merging, the most luminous (i.e. massive) ellipticals must be rounder and in general less rotationally supported. Indeed, this is what is found in observational data (see e.g., Davies et al. 1983).

The results presented here are not intended to represent fully at a quantitative level the characteristics of the shape and kinematic evolution of elliptical galaxies, but rather to unveil some qualitative trends in dense environments and the mechanisms causing them in a cosmological context. It is reassuring to find that all the simulations analysed here show in general an evolution in the population of E's towards roundish and less rotationally supported systems, mostly driven by dry merging, and that the mechanisms at play described above, which cause either the general trend or the exceptions, are consistent in all kind of simulations, of different box size, particle number, input σ_8, and code.

Van der Marel & van Dokkum (2007) reported a similar evolution for two samples of ~ 40 galaxies at $z = 0.5$ and $z = 0$. Although the evolution that we observe in our simulations seems milder than the one reported by their study, the amount of evolution remains unclear to higher redshifts. Thus, it would be highly desirable to perform larger statistical studies of the shape and kinematics of true elliptical galaxies at low z, and acquire observations of galaxy kinematics at higher redshifts to confirm the evolutionary trend of ellipticals predicted here.

Acknowledgements. We would like to thank the anonymous referee for stimulating comments that improved the quality of the paper. We thank A. Serna and F. Martínez-Serrano for making available the new P-DEVA code for us. This work was partially supported by the MCyT (Spain) grants: AYA-07468-C03-03 and AYA2006-15492-C03-01 from the PNAyA, and the regional government of Madrid through the ASTROCAM Astrophysics network (S0505/ESP0237). We thank the Centro de Computación Científica (UAM, Spain) for computing facilities.

References

Balcells, M., & Quinn, P. J. 1990, ApJ, 361, 381
Bender, R. 1988, A&A, 193,L7
Bender, R., Saglia, R. P., Gerhard, O. E. 1994, MNRAS, 269, 785
Bertola, F., Capaccioli, M. 1975, ApJ, 200, 439
Binney, J. 1978, MNRAS, 183, 501
Binney, J. 2005, MNRAS, 363, 937
Bournaud, F., Jog, C. J., Combes, F. 2005, A&A, 437, 69
Burkert, A., Naab, T. 2005, MNRAS, 363, 597
Cappellari, M., et al. 2007, MNRAS,379,418 (CAP07)
Cimatti, A., et al. 2004, Nature, 430, 184
Conselice, C. J. 2006, ApJ, 638, 686
Conselice, C. J., et al. 2007, MNRAS, 381, 962
Conselice, C. J., Yang, C., Bluck, F. L. 2009, MNRAS, submitted, astro-ph/0812.3237v1
Couchman, H. M. P. 1991, ApJ, 368, L23
Cox, T. J., Dutta, S. N., Di Matteo, T., Hernquist, L., Hopkins, P. F., Robertson, B., & Springel, V. 2006, ApJ, 650, 791
Davies, R. L., Efstathiou, G., Fall, S. M., Illinwort, G., Schechter, P. L. 1983, ApJ, 266, 41
de Zeeuw, T., Franx, M. 1991, ARA&A, 29, 239
Eliche-Moral, M. C., Balcells, M., Aguerri, J. A. L., & González-García, A. C. 2006, A&A, 457, 91
Emsellem, E, et al. 2007, MNRAS, 379, 401
Evrard, A., Silk, J., Szalay, A. S. 1990, ApJ, 365, 13
Genel, S., et al. 2008, ApJ, 688, 789
Genel, S., Genzel, R., Bouché, N., Naab, T., Sternberg, A. 2009, ApJ, submitted, astro-ph/0812.3154v1
Gelb, J. M., Bertschinger, E. 1994, ApJ, 436, 467
González-García, A. C. & Balcells, M. 2005, MNRAS, 357, 753
González-García, A. C. & van Albada, T. S. 2005, MNRAS, 361, 1030
González-García, A. C., Balcells, M., Olshevsky, V. S. 2006, MNRAS, 372, L78
Illingworth, G. 1977, ApJL, 218, L43
Jesseit, R., Naab, T., Peletier, R. F., Burkert, A. 2007, MNRAS, 376, 997
Kang, X., van den Bosch, F. C., Pasquali, A. 2007, MNRAS, 381, 389
Katz, N. 1992, ApJ, 391, 502
Kauffmann, G., et. al 2003, MNRAS, 341, 33
Khochfar, S., Burkert, A. 2003, ApJ, 597, 117
Kimm, T, Yi, T. S. 2007, ApJ, 670, 1048
Lauer, T. R. 1985, MNRAS, 216, 429
Lauer, T. R., et al. 2005, AJ, 129, 2138
Naab, T., Burkert, A. 2003, ApJ, 597, 893
Naab, T., Khochfar, S. and Burkert, A. 2006, ApJ, 636, L81
Naab, T., Johansson, P. H., Ostriker, J. P., Efstathiou, G. 2007, ApJ, 658, 710
Naab, T., Ostriker, J.P. 2007, preprint (astro.ph/0702535)
Nieto, J.-L., Bender, R. 1989, A&A, 215, 266

Oñorbe, J., Domínguez-Tenreir,o R., Sáiz, A., Serna, A., Artal, H. 2005, ApJ, 632, L57
Oñorbe, J., Domínguez-Tenreiro, R., Sáiz, A., Artal, H., Serna, A. 2006, MNRAS, 373, 503
Oñorbe, J., Domínguez-Tenreiro, R., Sáiz, A., Serna, A. 2007, MNRAS, 376, 39
Power, C., Knebe, A. 2006, MNRAS, 370, 691
Pellegrini, S. 2005, MNRAS, 364, 169
Robertson, B., Cox, T.J., Hernquist, L., Franx, M., Hopkins, P. F., Martini, P., Springel, V. 2006, ApJ, 641, 21
Scannapieco, S., White, S. D. M., Springel, V., Tissera, P. B. 2008, MNRAS, submitted, astro-ph/0812.0976v1
Scarlata, C., et al. 2007, ApJS, 172, 494
Serna, A., Domínguez-Tenreiro, R., Sáiz, A. 2003, ApJ, 597, 878
Sirko, E. 2005, ApJ, 634, 728
Spergel, D. N. 2006, IAUJD, 7, 6
Springel, V., et al. 2008, MNRAS, 391, 1685
van der Marel, R.P., van Dokkum, P.G. 2007, ApJ, 668, 738
Wiklind, T., Dickinson, M., Ferguson, H. C., Giavalisco, M., Mobasher, B., Gorgin, N. A., Panagia, N. 2008, ApJ, 676, 781

8.5.1.1 Consistency Checks

In this Section we present results from the different samples studied in this work regarding the evolution of shape and rotational support of ELO samples. Figure 8.7 present the evolution of the Shape parameter, S, inside the radius enclosing 90% of the stellar mass, $r^{\rm star}_{\rm 90,bo}$, for *EA*-STAR, *EB*-STAR, *EF*1-STAR and *EF*3-STAR samples. All these samples show the same general trends pointed out in the previous section. For all simulations, the fraction of prolate objects decreases with decreasing redshift, and at all redshifts there is a small number of perfect spheres. The number of triaxial and oblate objects also increases with decreasing redshift. Same conclusions arise if we use the Shape parameter calculated at $r^{\rm star}_{\rm e,bo}$. Figure 8.8 illustrates the rotational support of the ELOs for *EA*-STAR, *EB*-STAR, *EF*1-STAR and *EF*3-STAR samples. The general trend discussed in previous section towards the increase of the number of systems with a lower rotational support as we go to lower redshifts is confirmed for all these samples.

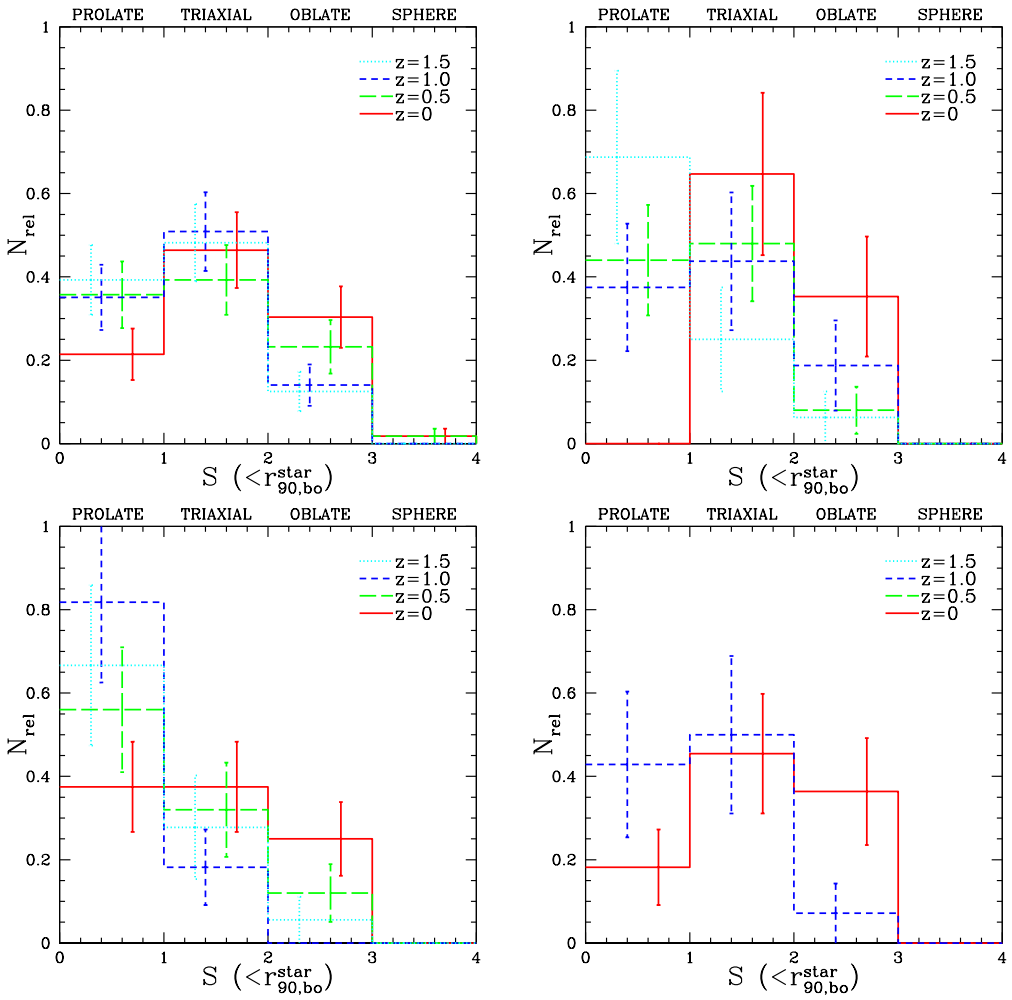

Figure 8.7: 3D Shape histogram, S, of the *EA*-STAR (upper left), *EB*-STAR (upper right), *EF*1-STAR (lower left) and *EF*3-STAR (lower right) samples at different redshifts calculated for the $r^{\rm star}_{\rm 90,bo}$ using Equation 7.2. The histograms are normalized to their total number at each redshift, and the error bars represent the Poissonian noise.

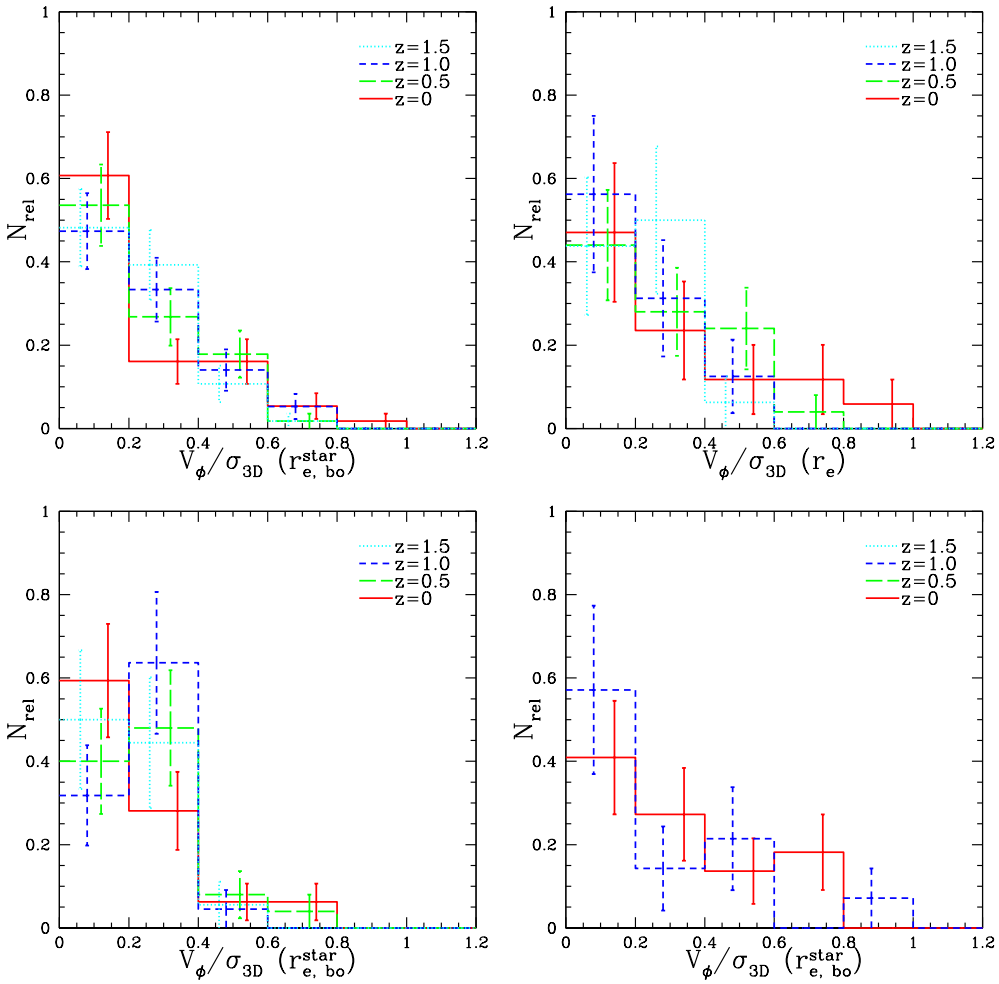

Figure 8.8: 3D Rotational support histogram, $V_\phi/\sigma_3^{\rm star}$, of the *EA*-STAR (upper left), *EB*-STAR (upper right), *EF*1-STAR (lower left) and *EF*3-STAR (lower right) samples at different redshifts calculated for the effective radius $r_{\rm e,bo}^{\rm star}$. The histograms are normalized to their total number at each redshift, and the error bars represent the Poissonian noise.

8.6 Conclusions

In this Chapter we have studied up to $z = 1.5$ the different fundamental relations presented in previous Chapters at $z = 0$: The Fundamental Plane, The Photometric Plane and the relation between shape and rotational support.

The Fundamental Plane

The results we report on the evolution of the Fundamental Plane indicate that ELOs conform a homogeneous population at any redshift. The preservation of the dynamical plane in these redshifts for our simulations also agrees with previous work based on dissipationless simulations of pre-prepared mergers (Capelato et al., 1995; Dantas et al., 2003; González-García & van Albada, 2003; Nipoti et al., 2003; Boylan-Kolchin et al., 2005). This result explains the preservation of the Fundamental Plane with z when seen in the edge-on projection. A mild evolution is also found indicating that high z ELOs could be, more compact and have a higher velocity dispersion, than their lower z counterparts. The interpretation of these trends could be linked with the amount of dissipation that each ELO has suffered along its mass assembly.

Concerning the tilt of the Fundamental Plane relative to the virial relation at higher redshifts, it has shown a similar origin as we found at $z = 0$: $\beta_{\rm vir} \neq 0$ $\beta_{\rm rd} \neq 0$ (Chapter 6). Our simulations point out that the physical origin of the trends above lie in the systematic decrease, with increasing ELO mass, of the relative amount of dissipation experienced by the baryonic mass component along ELO stellar mass assembly. We observed an evolution trend of $\beta_{\rm vir}$ parameter towards an increase of the contribution of the $M_{\rm vir}/M^{\rm star}_{\rm bo}$ ratio in the tilt of the Fundamental Plane as we go to higher redshifts. On the other side, $\beta_{\rm rd}$ contribution is not statistically confirmed (nor discarded) in all samples.

The Photometric Plane

We have found that the projected mass density profiles of ELOs at different redshifts can be well fitted by a Sérsic law. We also obtain a good comparison with observational scaling relations up to $z \sim 1.5$: n vs $R^{\rm star}_{\rm e,bo}$; n vs $M^{\rm star}_{\rm cyl,bo}$; n vs $\sigma^{\rm star}_{\rm los,0}$; $R^{\rm star}_{\rm e,bo}$ vs $M^{\rm star}_{\rm cyl,bo}$; $M^{\rm star}_{\rm cyl,bo}$ vs $\sigma^{\rm star}_{\rm los,0}$. This last correlation shows that ELOs of a given stellar mass become less compact as z decreases, and that the higher the ELO mass and the more important the difference. The Structural Photometric Plane, namely the relation between $R^{\rm star}_{\rm e,bo}$, $M^{\rm star}_{\rm cyl,bo}$ and n parameters, is found up to $z = 1.5$ in all the samples analyzed and puts some strong limits on the structural values at any redshift. These results confirm observational studies of La Barbera et al. (2005) for early-type galaxies at intermediate redshifts.

From these results, one can arises with the wrong conclusion that individual objects

do not evolve. The answer is that individual objects do evolve and that they do it onto the Intrinsic Dynamical Plane. We have seen that some of the ancestors of the *EA*-Z0 sample are found up to $z = 1.5$ in the Intrinsic Dynamical Plane and Structural Photometric Plane that we found at $z = 0$. This implies that mergers between these two redshifts keep the ELOs in the Fundamental Plane. These mergers are mostly gas-free. Figure 8.9 shows an example of the evolution of an ELO in the shape parameter, n, effective radius, $r_{\rm e,bo}^{\rm star}$ and stellar mass, $M_{\rm bo}^{\rm star}$. This is an important conclusion that put some light in the question about if it is possible to obtain massive early-type galaxies from (dissipative or gas-free) mergers of galaxies (Aceves et al., 2006; Ciotti et al., 2007).

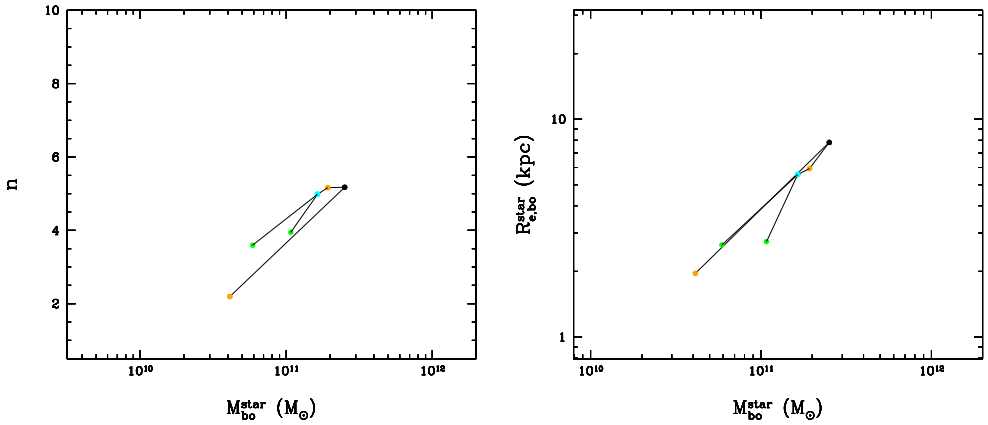

Figure 8.9: Parameter evolution for an ELO analyzed at four different redshifts: $z = 1.5$ (green), $z = 1.0$ (cyan), $z = 0.5$ (orange) and $z = 0$ (black).

Rotation versus Shape

On the other hand, studying the rotational support and shape of a bigger sample of ELOs, we found that a systematic change through time, i.e. evolution, by becoming rounder in general at $z = 0$ and, at the same time more velocity dispersion supported. This is found to be primarily due to major dry mergers where only a modest amount of angular momentum is involved into the merger event. Despite the general trend, in a significant amount of cases the merger event involves a higher specific angular momentum, which in general causes the system to acquire a higher rotational support and/or a more oblate shape. These evolutionary patterns are still present when we study our systems in projection, mimicking real observations, and thus they should become apparent in future observations.

We have seen that relaxed ELO samples show a mild evolution in their structural and kinematical parameters that describe their 3D ($M_{\rm bo}^{\rm star}$,$r_{\rm e,bo}^{\rm star}$,$\sigma_{\rm 3,bo}^{\rm star}$ and μ) and 2D ($M_{\rm cyl,bo}^{\rm star}$,$R_{\rm e,bo}^{\rm star}$,$\sigma_{\rm los,0}^{\rm star}$ and n) mass and velocity distributions. On the other hand, shape

(ϵ) and rotational support ($V_{\rm max}/\sigma^{\rm star}_{\rm los,0}$) show clear signs of evolution. These results are not in disagreement between each other because these parameters characterize different properties of ELOs. In the case of shape and rotation for elliptical galaxies, the specific value of these parameters is more related with the particular history of the ELO as they are heavily linked with the dynamical events in which the ELO has been involved along its mass assembly and especially by the last one of these events. In the first case, this assembly process seems to be erased from the structural and kinematical properties of the ELO, but for a mild evolution observed for the more massive ELOs. Therefore we conclude that these parameters provide a more detailed description for relaxed ELOs. This is not very surprising because equilibrium states do not depend on how the paths leading to them. Manrique et al. (2003) have analytically probed a similar result for dark matter halos. In their model, the density profile of relaxed halos permanently adapts to the profile currently building up through accretion and does not depend on their past aggregation history. Therefore the typical density profile of halos of a given mass at a given epoch is set by their time-evolving cosmology-dependent typical accretion rates. As a consequence this model predicts the existence of time-invariant relations among the structural parameters that describe these halos (See discussion in Salvador-Solé et al., 2005, 2007). To try to put all these results under a common framework, we have to study ELO assembly and its effect on ELO mass and velocity distributions, as well as on the stellar age distributions. This is the subject of our next chapter.

Chapter 9

Galaxy Formation and Evolution from DEVA Simulations[1]

9.1 Introduction

In the previous Chapters we have studied the fundamental structural and kinematical properties of elliptical-like objects (ELOs) at redshift zero and their evolution since $z = 1.5$. We have obtained some clues about how they are settled and we have seen that they show a very good agreement with several *classical* observational relations. However as discussed in Section 3.3 different observational results point to apparently paradoxical results concerning the formation of elliptical galaxies. None of the formation scenarios proposed (monolithical collapse or hierarchical mass assembly), can so far recover all the observational information we have at our disposal on local ellipticals (downsizing or age effects in their stellar populations; the tilt of the Fundamental Plane relation; the presence blue cores), as well as at intermediate or high redshifts (the near-lack of evolution of the FP in dynamical terms, among others).

The aim of this chapter is to describe a scenario arising from the simulations providing an explanation of the different results discussed in previous sections. To this end, we have made use of the opportunity that brings us self-consistent simulations. This is, to follow different physical processes relevant to elliptical formation along cosmic time with a high enough time resolution: mass assembly, star formation and dissipation rates, gas accretion history and their relation with different properties of galaxies.

The following section is devoted to the mass assembly history of simulated ellipticals and its relation with the star formation and dissipation rates. It introduces a massive galaxy formation model. Section 9.3 presents the results of a study on the links among the gas infall rate history and the star formation rate history along mass assembly,

[1]Based on Domínguez-Tenreiro, Oñorbe, Sáiz, Artal, & Serna (2006); Domínguez-Tenreiro, Oñorbe, Serna, & González-García (2008); González-García, Oñorbe, Domínguez-Tenreiro, & Gómez-Flechoso (2009)

giving some important hints on how galaxies obtained its gas. Section 9.4 presents our conclusions.

9.2 Insights into ELO Assembly

To try to decipher the physical processes underlying the formation and evolution of simulated ellipticals, we have drawn their mass aggregation track (MAT) along the main branch of the corresponding tree, both for baryonic (the mass inside fixed radii) and for total mass (the virial mass).

For each ELO in the different samples analyzed, we have identified its constituent particles (gaseous or stellar) at $z = 0$. Among them, the most tightly bound particle has also been identified and used, altogether with a sigma-clipping algorithm (see Section 4.3) to search for the center-of mass of the object in the previous timestep available for the simulation. This process is repeated at different z's, so that we can determine the trajectory of the virtual elliptical center-of-mass across the time. Once we have the virtual elliptical center at different z's, the mass aggregation track (MAT) along the main branch of the merger tree can be drawn. So, for each ELO in the samples, its MAT has been drawn, both for its baryonic component (the mass inside fixed radii) and for its dark matter halo mass (the mass inside the virial radii). Figure 9.1 shows some examples.

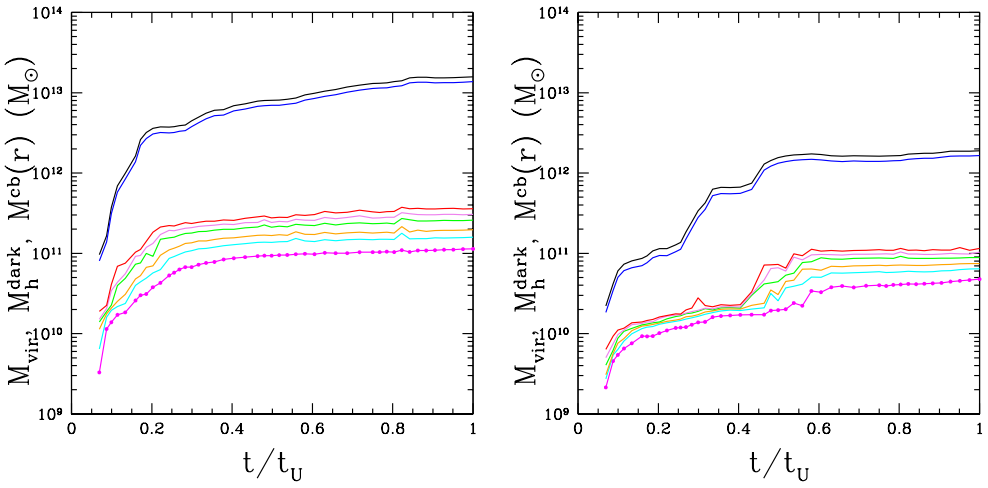

Figure 9.1: The mass-aggregation track along the main branches of the merger tree, for two typical ELOs. Left: a massive ELO. Right: a less massive ELO. Both panels give the total mass of the halo (black) and dark matter (blue) at $r_{\rm vir}$. Color lines stand for the baryonic mass of the ELO at different fixed radii (3, 6, 9, 15, 21, 30 kpc). Discontinuities represent merger events. In each of them we can differentiate fast ($t/t_u \lesssim 0.3$) and slow ($t/t_u \gtrsim 0.3$) mass aggregation rates, corresponding to the fast and slow phase.

These MATs inform us on the mass assembly process through time. Major merger

can be clearly observed through a sudden increase of the stellar mass of a factor $M_{secondary}/M_{primary} < 0.25$ while minor mergers imply a lower mass gain. Aggregation (i.e. smooth in-fall of mostly gaseous material) processes can also be clearly identified.

The relative angular momentum involved in a given merger event can also be estimated through the MAT at a qualitative level in the following way: Any merger process begins with the halo fusion, then the virtual galaxies they host begin to orbit around each other, until their final coalescence. The higher the relative angular momentum involved in the merger, and the higher the time interval elapsed since the first halo contact and the coalescence of the virtual galaxies (i.e., the baryonic components). This time interval can be directly measured in the MATs. Indeed, any mass entering into the final virtual elliptical is first noticed in the halo mass as an increase in the virial mass. Later on if the systems merge, such increase will be noticed as an increase in the stellar mass. The difference in time between both moments may give us a qualitative estimate of the orbital momentum involved in the merger (see for example the papers by González-García & van Albada, 2003; González-García & Balcells, 2005).

We have also computed the star formation history of these objects taking into account all the stellar particles inside $r_{\rm bo}$. Figure 9.2 shows two examples. The different trends between stellar age properties observed in these Figures and the structural and kinematical parameters have been discussed in Section 6.4 for ELOs.

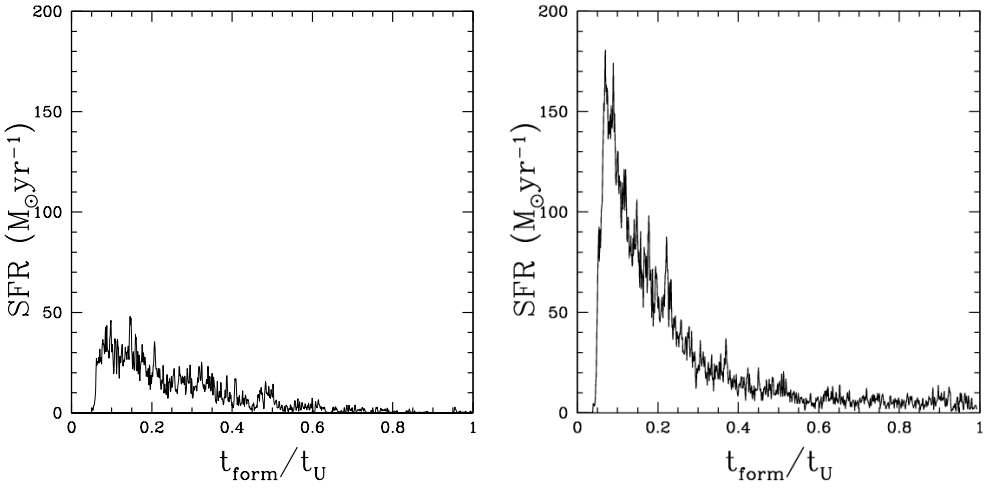

Figure 9.2: The star formation rate histories of two typical ELOs versus the Universe age. Left: a massive ELO. Right: a less massive ELO. Note that most stars are formed at high z, and the age effects according with the ELO mass.

All these analyses indicate that two different phases operate along ELO mass assembly: first, a violent fast one, where the mass aggregation rates are high, and then, a slower one, with lower mass aggregation rates. Results from analytical models, as well as N-body simulations, have already pointed out this result (Wechsler et al., 2002; Zhao

et al., 2003; Salvador-Solé et al., 2005). Here we have confirmed that this conclusion holds also for the baryonic component (see De Lucia et al., 2006, for same results using semi-analytical models).

9.2.1 The *Two Phase* Scenario

The simulations unveil the physical patterns of ELO mass assembly, energy dissipation and star formation. These simulations indicate that ELOs are assembled out of the mass elements that at high z are enclosed by those overdense regions R whose local coalescence length $L_c(t, R)$ (Vergassola et al., 1994) grows much faster than average, and whose mass scale (total mass enclosed by R, M_R), is of the order of an E galaxy virial mass.

These overdense regions act as flow convergence regions (FCRs hereafter), whose baryon content defines the particles that will end up in a bound configuration forming an ELO. FCRs contain a hierarchy of attraction basins toward which a fraction of the matter flows feeding the clumps they host. Another fraction of the matter keeps diffuse (Figures 9.3 and 9.4).

9.2.1.1 Physics of the Fast Phase

At a given scale, overdense regions first expand slower than average, then they turn around and collapse through fast global compressions, involving the cellular structure elements they enclose (Figure 9.4) and in particular nodes connected by filaments, that experience fast head-on fusions (i.e., multiclump collapse, see Thomas et al., 1999). Figures 9.3 and 9.1 . Our hydrodynamical simulations indicate that these fast head-on mergers (that is, with very low relative orbital angular momentum) result in strong shocks and high cooling rates of their gaseous component (i.e., dissipation), and, consequently, in strong and very fast SF bursts (Figure 9.2) that transform most of the available cold gas at the FCR into stars (Figures 9.3 and 9.4).

For the massive ELO in the Figures, this happens between $z = 6$ and $z = 2.5$ (Figures 9.1 and 9.2) and mainly corresponds to a cold mode of gas aggregation, as in Kereš et al. (2005, see next section for a detailed discussion on this issue). Consequently, most of the dissipation involved in the mass assembly of a given ELO occurs in this violent early phase at high z; moreover, its rate history[2] is reflected by the SF rate history (Figure 9.5).

The age distribution of the stellar populations of ELOs shows age effects: their means are lower and their widths are narrower for more massive ELOs than for less massive ones (see section 6.4), as inferred from observations. At the end of this phase, most stars are already formed, the ELOs are virialized and the Fundamental Plane is in

[2]That is, the amount of cooling per time unit experienced by those gas particles that at $z = 0$ form the ELO stellar component

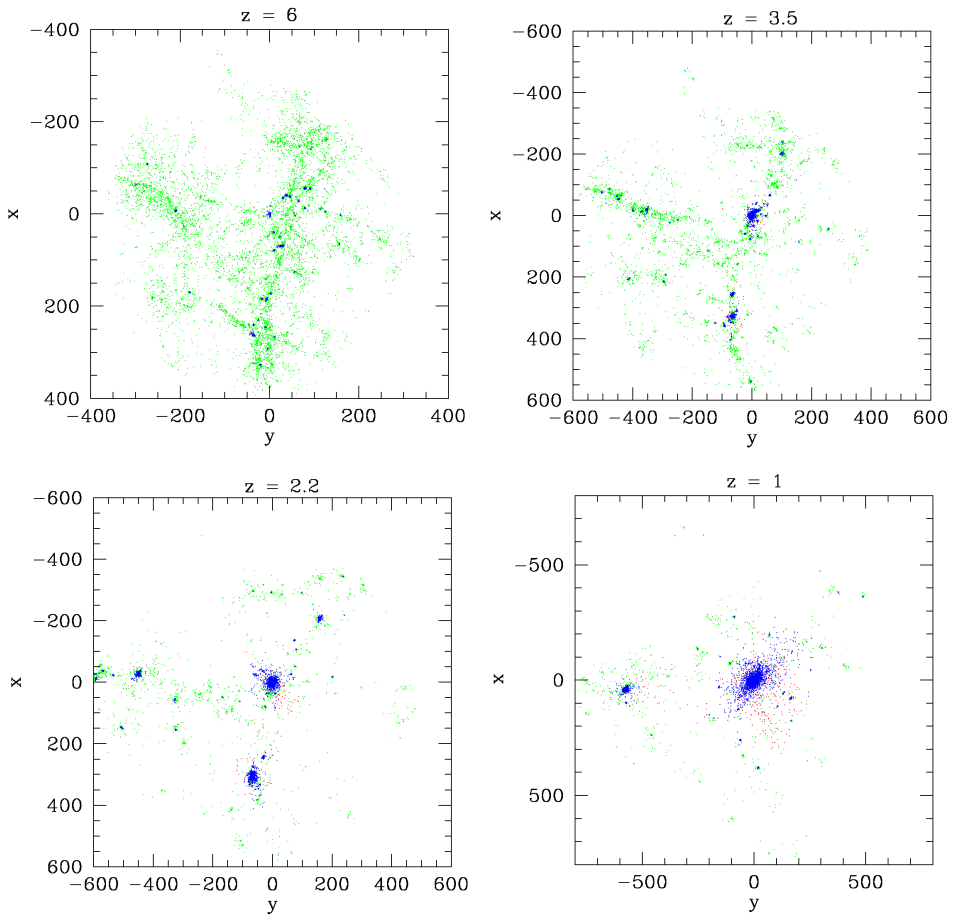

Figure 9.3: This Figure shows projections, at different redshifts, of the baryonic particles that at $z = 0$ form the stars of a typical massive ELO. Green: cold gas particles. Blue: stellar particles. The redshift decreases from left to right and from top to bottom ($z = 6$, $z = 3.5$, $z = 2.2$, $z = 1$). Note the clumpy collapse of two different FCRs between $z = 3.5$ and $z = 2.2$ (fast phase) with ELO formation, and their merging between $z = 2.2$ and $z = 1$ to give massive ELOs (slow phase).

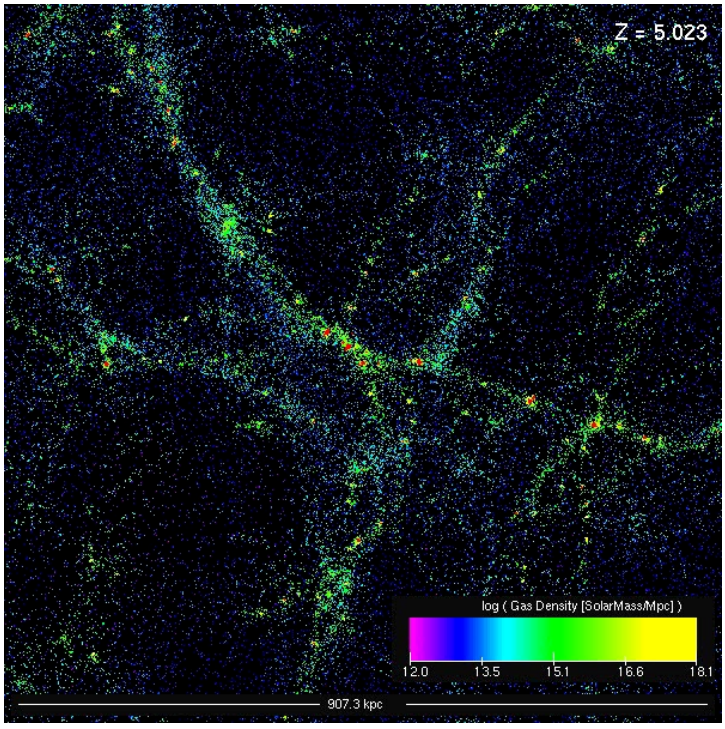

Figure 9.4: A projection of a 900 side box at $z = 5.02$. Red: stars. The other colors mean gas density according with the code in the bar. This region will transform later on into a virtual elliptical. At this high redshift we can appreciate the cellular structure, the denser regions already turned into stars, and dense (cold) gas flowing towards the node at the center of the FCR through filaments. Note also the presence of CHAIN galaxies.

place as a consequence of dissipation and homology breaking in the mass distribution (see Chapters 6 and 8).

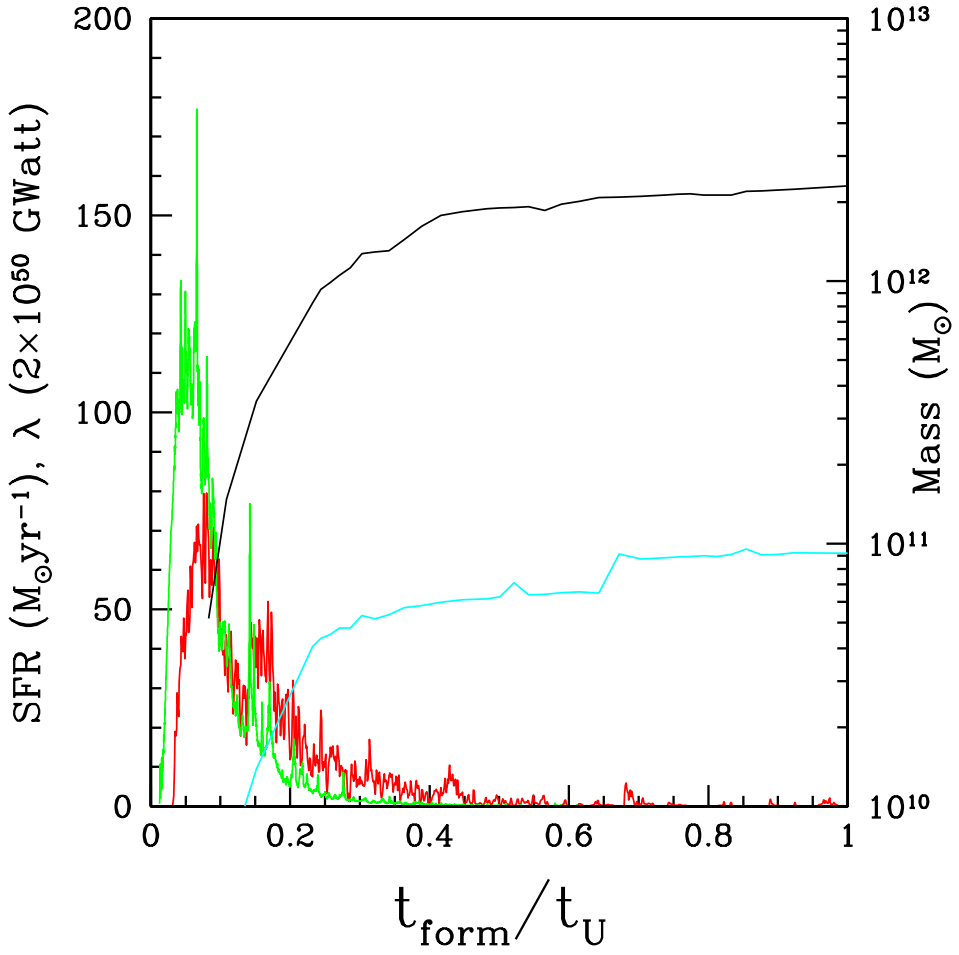

Figure 9.5: The cooling rate history (green line) and the star formation rate history (red line) of a typical ELO in the simulations. Its mass-aggregation tracks are also shown, both for total mass (dash line) and for cold baryon mass (i.e., stars and cold gas, point-dashed line). The fast (left) and slow (right) phases of mass aggregation are clearly shown. Note that most dissipation and SF corresponds to the fast aggregation phase and that the last major merger results in a rather modest SFB at $t/t_U = 0.72$.

9.2.1.2 Physics of the Slow Phase

The slow phase comes after the multiclump collapse or fast phase. In this phase, the halo mass aggregation rate is low and the $M_{\rm vir}$ increment results from major mergers, minor mergers or continuous accretion. Our simulations show that the fusion rates are generally low (see previous Chapter) and that these mergers generally imply only a modest amount of energy dissipation or SF. In fact, a strong SF burst and dissipation

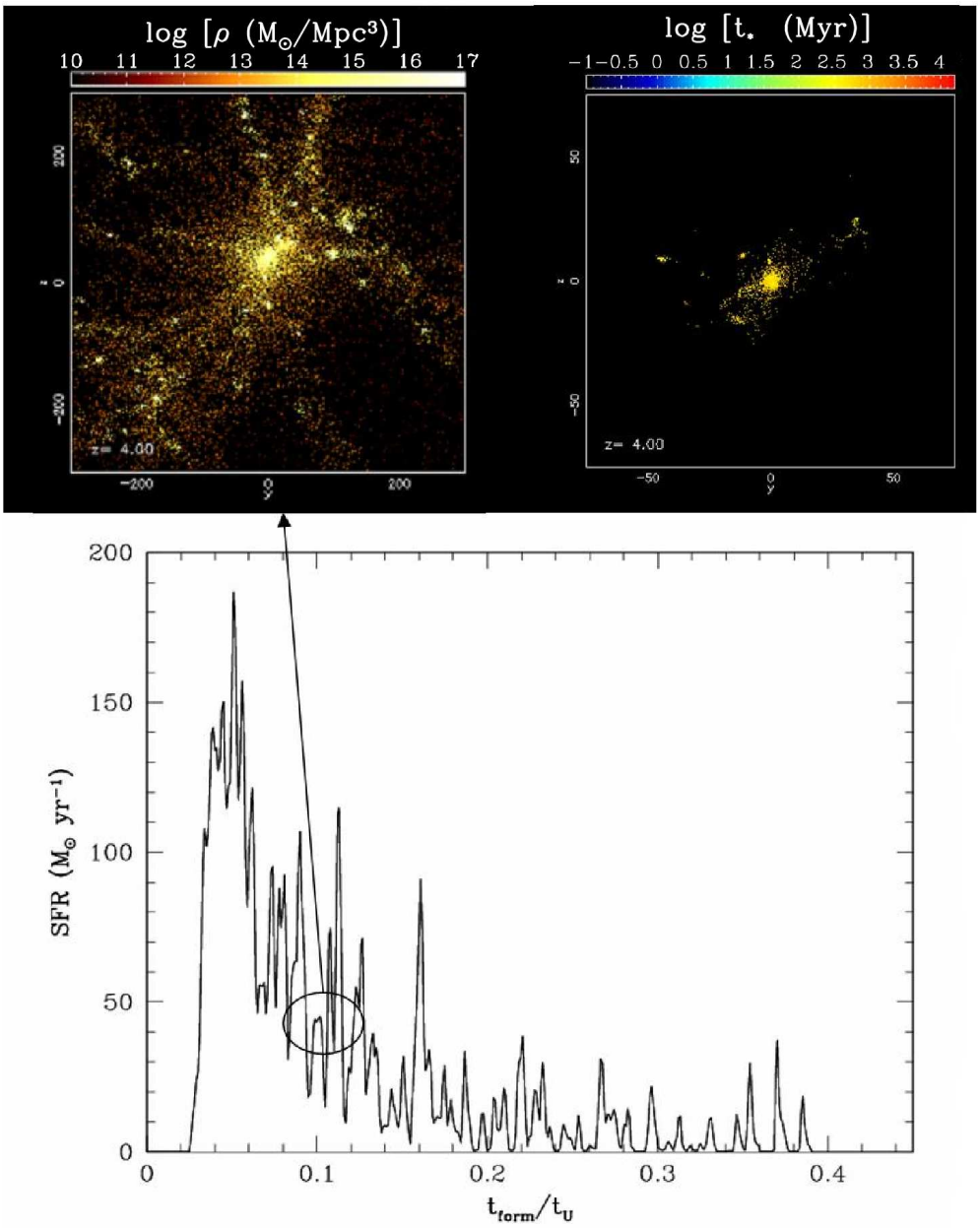

Figure 9.6: $z \sim 4$: Fast phase is over. Gas flows still feed the center. Stellar system concentrated at the center, low SFR dominated by minor mergers, and passive ageing of older stars. Gas density and stellar age are shown in the upper left panel and upper right panel respectively.

follow a major merger only if enough gas is still available after the early violent phase. This is unlikely in any case, and it becomes more and more unlikely as $M_{\rm vir}$ increases. And so, these mergers imply only a modest amount of energy dissipation or SF. A consequence of this behavior is that the dynamical plane is preserved at the slow phase. In fact, we have found in our cosmological simulations that *dissipationless* merger events increase the ELO mass content, the size and the stellar mean square velocity, but roughly preserve the dynamical FP[3]. A second consequence of this behavior is the trend of the means and the spreads of the ELO stellar age distributions with $M_{\rm vir}$, that are consistent with observations (see Domínguez-Tenreiro et al., 2004).

Apart from ELO stellar mass growth following dry mergers, our simulations indicate that $M_{\rm bo}^{\rm star}$ can also increase due to newborn stars, either (1), formed within the ELO itself from accreted gas or gas coming in satellites, that falls to the central regions before being turned into stars, or (2), more unlikely, formed through dissipative mergers. While the first implies quiescent modes of star formation (see Papovich et al., 2005), and could explain the blue cores observed in some relaxed spheroids, both of them could explain the need for a young stellar population to fit some of their spectra, see references above. Major merger events become less frequent as time elapses, allowing for a higher fraction of relaxed spheroids. Both, on-going stellar mass assembly (either accreting stellar mass fragments or forming newborn stars) and the decrease of the major merger rate, imply an increase of the stellar mass density contributed by relaxed ELOs. In fact, we find that it has changed by a factor of 2.1 between $z = 1$ and $z = 0$, in consistency with empirical estimations (see Section 3.3.1).

Our simulations indicate that the halo mass aggregation rate is low and that its increment results from major mergers, minor mergers or continuous mass accretion.

So, our simulations suggest that most of the stars of today ellipticals, could have formed at high redshifts while they are assembled later on (see De Lucia et al., 2006, for similar results from a semi-analytic model of galaxy formation grafted to the *Millennium Simulation*). This formation scenario shares some aspects of both, the hierarchical merging and the monolithic collapse scenarios, but it has also significant differences, mainly that most stars belonging to EGs form out of cold gas that had never been shock heated at the halo virial temperature and then formed a disc, as the conventional recipe for galaxy formation propounds (see discussion in Kereš et al., 2005, and references therein). An important point is that our simulations indicate that this formation scenario follows from simple physical principles in the context of the current ΛCDM scenario.

[3]The preservation of the FP in pre-prepared dissipationless mergers had already been studied by Capelato et al. (1995); González-García & van Albada (2003); Nipoti et al. (2003); Boylan-Kolchin et al. (2005) through N-body simulations.

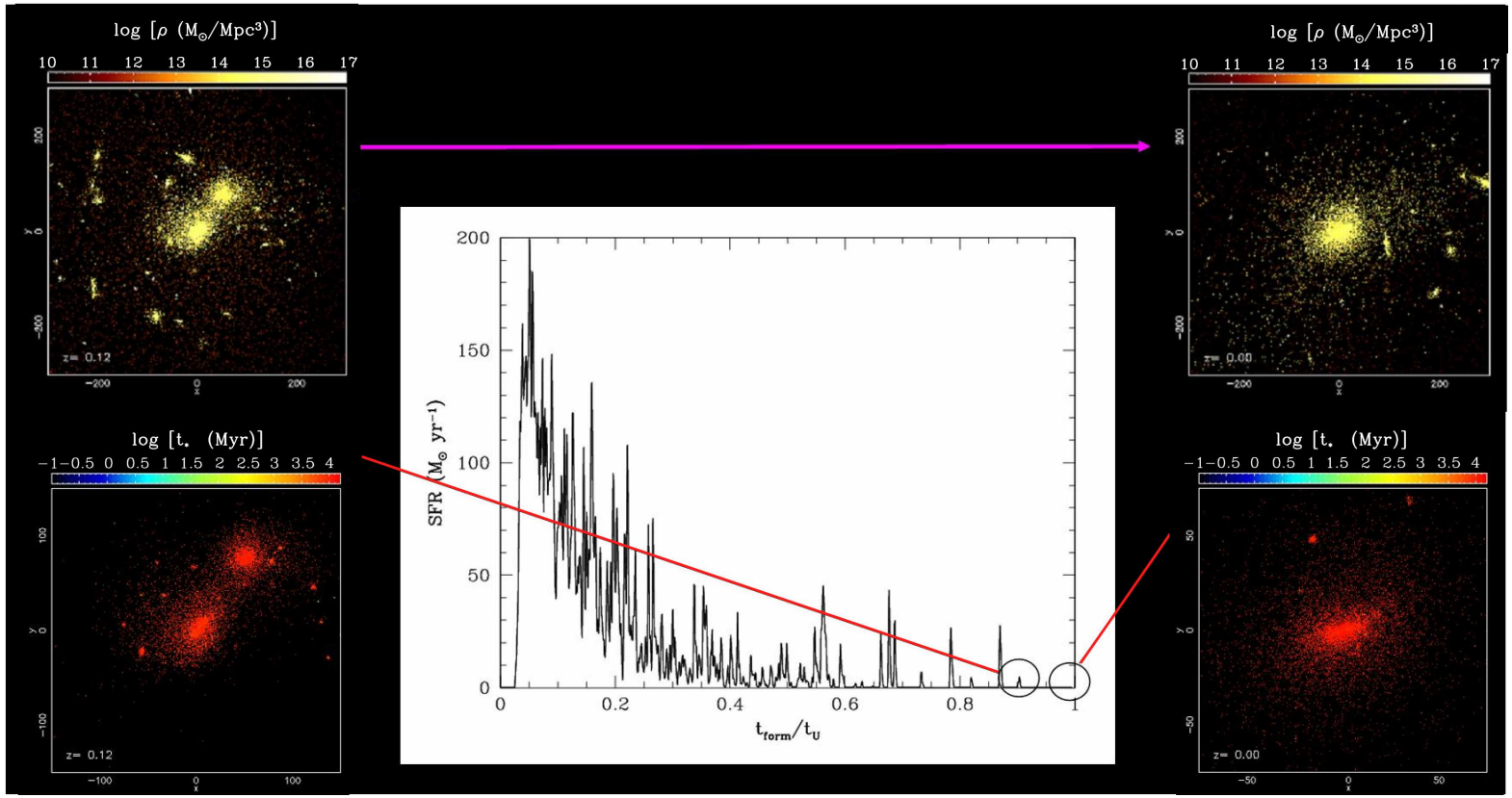

Figure 9.7: A merger begins around $z = 0.1$ between two objects which are very gas-poor (left). Although the merger is dynamically very violent, it produces only a very modest SFB. By $z = 0$ the merger is over and the ELO is almost relaxed (right). Upper panels show the gas density and lower panels the stellar age according with the scales on the top of each image.

9.3 Accreting and Expelling Gas in ELOs

Galaxy formation scenarios generally predict that galaxies are embedded into halos of hot diffuse gas, extending well beyond the distribution of stars. These halos are thought to consist of gravitationally trapped gas with a temperature of millions of Kelvin. It is important to remark the difficulty of studying the structure of hot gas halos around elliptical galaxies because it requires that they are as isolated as possible and this type of galaxies (specially the most luminous) are usually in dense environments.

The new generation of X-ray instruments (Chandra, XMM) confirms and extends previous findings in ellipticals. Recent Chandra measurements (Humphrey et al., 2006) have determined their total baryon fractions inside their virial radii. These fractions indicate that these systems, despite having masses $\geq 5 \times 10^{12}\ M_{\odot}$, are not baryonically closed at virial radius, i.e., their baryon fraction is lower than the average cosmological one (Spergel et al., 2007). Put in other words, ellipticals miss baryons inside their virial radii. In this sense elliptical formation scenarios must answer the following questions: How did hot gas halos form? Where and when is the gas heated? Why are ellipticals not baryonically closed? Where the missing baryons are? In this Section we have deepen into these questions using the results of hydrodynamical simulations and tested the model presented above.

9.3.1 Hot Gas in ELOS

Irrespective of their mass, ELOs identified in the simulations have an X-ray emitting hot gas halo. The X-ray surface brightness profiles and total X-Ray luminosities of ELOs have been studied by Sáiz et al. (2003) and they found an overall agreement with observational data. We have already seen in Section 5.2.4 that these halos extend well beyond their virial radii. Figure 9.8 shows these halos for 3 ELOs with different virial masses. We can see that the temperature of the gas is linked with the mass and that there are clear signs of substructure.

9.3.2 Baryon Fraction

An important point is the amount of gas infall relative to the halo mass scale. In Section 5.2.4, we have studied the baryon space distribution at halo scales for ELOs at $z = 0$ and obtained that the $f^{\rm bar}(r) = \rho^{\rm bar}(r)/\rho^{\rm tot}(r)$ profiles show a typical pattern in which their values are high at the center, then they decrease and have a minimum lower than the global value (see Figure 5.13). We have measured the amount of baryonic mass that it is inside the virial radii out of the total mass, $M_h^{\rm bar}/M_{\rm vir}$ at redshifts $z = 0$, $z = 0.5$, $z = 1$, $z = 1.5$ for ELOs of the *EA* sample. Figure 9.9 shows the results. We found that in any case this quantity is lower than the average cosmic fraction (0.171 for the *EA* sample cosmological model), i.e., ELOs are not baryonically closed. This means

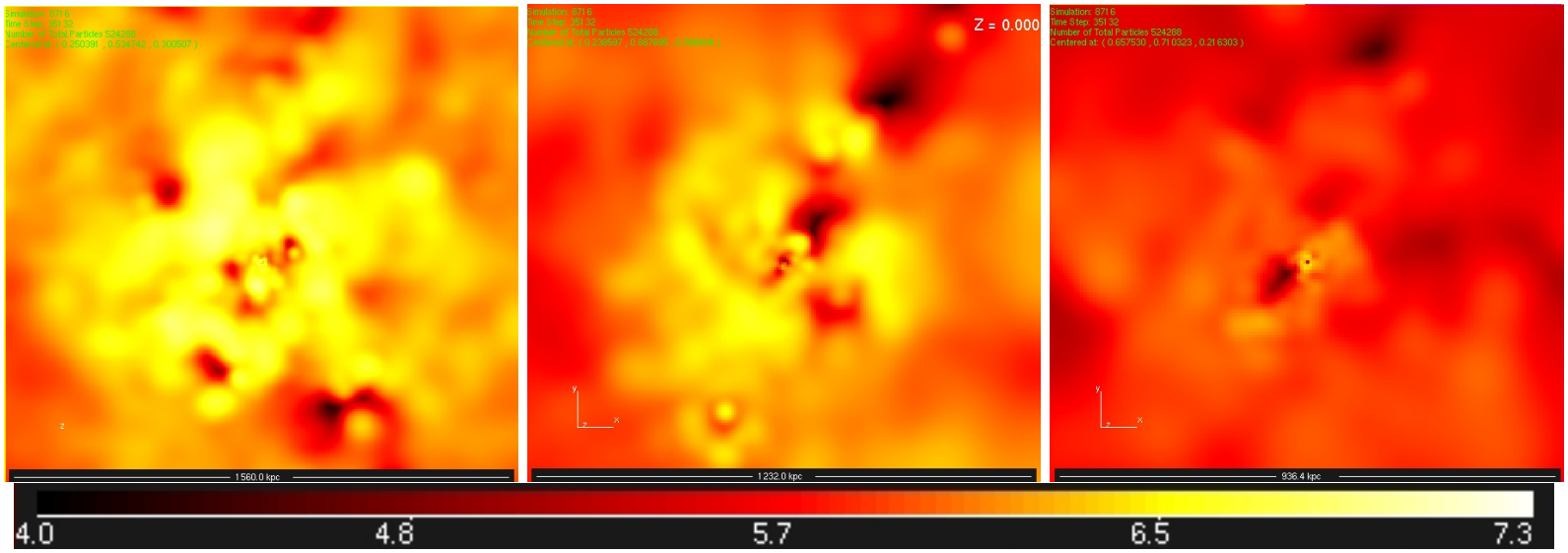

Figure 9.8: Slice of $4 \times r_{\rm vir}$ side showing the gas temperature (in $\log K$) for ELOs whose virial mass is, from left to right, $3 \times 10^{12} M_{\odot}$,$1 \times 10^{12} M_{\odot}$, $5 \times 10^{11} M_{\odot}$.

that there is a lack of baryons within $r_{\rm vir}$ relative to the dark mass content that becomes more important as $M_{\rm vir}$ increases and time elapses. By studying the hot gas profiles in Section 5.2.4 we encountered that the baryons that ELOs miss inside the virial radius are found at the outskirts of the configuration as diffuse hot gas (see Figure 5.14). In the following section we will deepen into this issue and try to disentangle how these baryons are heated.

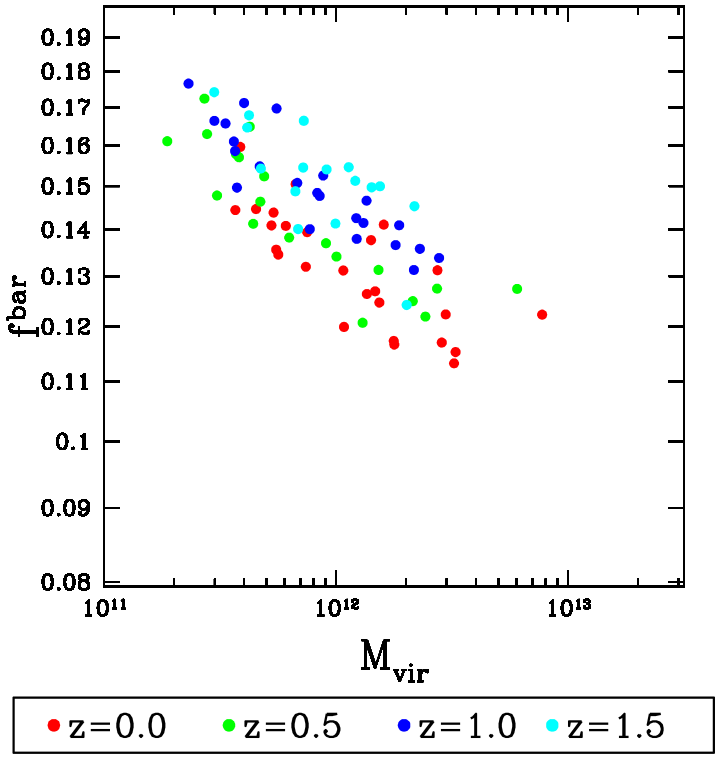

Figure 9.9: Baryon fraction at different redshifts for the *EA* samples

9.3.3 When and Where is the Hot Gas Heated?

Therefore heating processes along ELO assembly give rise to a hot gas halo around the objects, partially beyond the virial radii. Figure 5.14 shows that the amount of hot gas mass, normalized to the cold baryonic content inside the virial radii, increase with mass. The mass of hot gas increases monotonically up to $r \sim 4 \times r_{\rm vir}$. This suggest that the cold baryons massive ELOs miss inside $r_{\rm vir}$ relative to less massive ones, appear as diffuse warm component at the outskirts of their configurations.

According to the classical scenario, gas falling into a dark matter potential is shock heated to the virial temperature at the virial radius, and forms a quasi-hydrostatic equilibrium configuration with the dark matter. Shocked hot gas slowly cools and travels inwards, forming the central cooled component (the galaxy) (White & Rees, 1978).

However this scenario has recently been challenged by (Katz et al., 2003; Birnboim & Dekel, 2003). These authors have found that only a fraction of the gas accreted onto galaxies is shocked at virial radius (hot mode). The other fraction (cold mode) is accreted onto a galaxy without ever being heated to high temperatures. This cold accretion would owe its existence to the short cooling times present in low mass halos near the virial radius, which prevents the development of a stable accretion shock. They show that the cooling time condition corresponds approximately to a threshold in the galaxy's halo mass, with little dependence on redshift (see Kereš et al., 2008; Dekel et al., 2009, for last results on this topic).

To deepen into all these issues we have studied the evolution of the gas component of ELOs. To this end we have used a simulation (8716, see Section 4.2 for more details) for which we have a lot of timesteps saved, that allow us to perform high time resolution analyses ($\Delta t = 6.9 \times 10^6$ yr) . We have followed the density and temperature evolution of each baryonic particle that form ELOs at $z = 0$ by splitting them into several categories depending on their radii ($r < r_{\rm bo}$, $r_{\rm bo} < r < r_{\rm vir}$ and $r_{\rm vir} < r < 2 \times r_{\rm vir}$) and types (stars, cold and hot gas). The temperature limit for cold and hot gas particles has been set at $T = 2.5 \times 10^5$ Kelvin (see Kereš et al., 2005).

Figure 9.10 illustrates the typical path that particles from the different categories follow in a temperature-density plot. Colors represent the redshift: red for $20 < z < 3$, blue for $3 < z < 2$ and green for $z < 2$. In general, hot gas particles at $r < r_{\rm vir}$ fall deeper into the potential well before they are heated than particles at $r > r_{\rm vir}$. Otherwise, the underlying physical process is the same: gas shocks.

In Figure 9.11 we plot a histogram of the maximum temperature reached by all the cold baryonic particles that at $z = 0$ are inside $r_{\rm bo}$ for the most and least massive ELOs in the 8716 simulation ($M_{\rm bo}^{\rm star} \sim 3 \times 10^{11} M_\odot$ and $M_{\rm bo}^{\rm star} \sim 5 \times 10^{10} M_\odot$ respectively). Two different populations can be clearly observed, one that has never been heated (cold mode) and another one that has (hot mode). Moreover, Figure 9.12 shows a histogram of the cooling time for the hot mode particles, that is, the time interval elapsed from the moment when the particle reaches its maximum temperature until it is cold again. From this Figure we infer that the hot mode population does not remain in the halo and slowly cools, but it cools faster than expected in the classical scenario. The typical path for particles of the hot mode along time is shown in the upper panels of Figure 9.10. Another important piece of information is provided by Figure 9.13. The histogram shows the SFRHs for the same ELOs as above. Moreover, the red histogram shows for each bin [t, t + Delta t], the mass of that particles (among the previous ones) that reach their maximum temperature just in this time interval. Note the maxima of these two histograms are correlated, as the read maxima do not appear while important bursts of SF are turned on, but just after. That is, SF and gas heating are correlated, but with a time delay. We have seen in the previous section that these star formation bursts

are heavily linked with dynamical processes as mergers and/or aggregation. Therefore, heating processes giving rise to the hot gas halos take place in regions of mass assembly following violent dynamical events. Shocks heat the gas as it is accreted and, as a consequence, it is partially expelled to the outskirts of the configuration. Another interesting result from Figure 9.13 is that, for both ELOs, the ratio between hot mode and cold mode is higher as we go to lower redshifts. Moreover, the hot over cold mode mass ratio seems to be higher in the more massive objects. In order to deepen into this issue Figure 9.14 shows the baryonic mass inside $r_{\rm bo}$ at $z = 0$ that has never turned into hot gas over the total baryonic mass inside $r_{\rm bo}$ (i.e. the cold mode) for all ELOs in the simulation. This Figure shows that the more massive ELOs have a more important hot accretion mode population than the less massive ones. In fact, we have found in our simulations (and can also be seen in Figure 9.14) that hot mode is delayed as we go to lower mass objects indicating a strong relation between the mass of the object and gas heating.

All these results presented here confirm the conclusions concerning the gas accretion in galaxies obtained by Katz et al. (2003); Kereš et al. (2005, 2008) from cosmological simulation, using a different code (`DEVA`) and a time resolution two orders of magnitude higher than the one used by these authors.

Finally, we remark that the hot gas halos we show in this study are the result of a continuous mass assembly process in the ΛCDM model. They are strongly linked with shocks generated in accretion and merging processes. The cold gas in a flow convergence region follows a fast cosmological collapse, described in previous section and at some moment it is shocked, heated and expelled out of the densest regions. Our results show that gas heating processes are more effective as the mass of the halo increases.

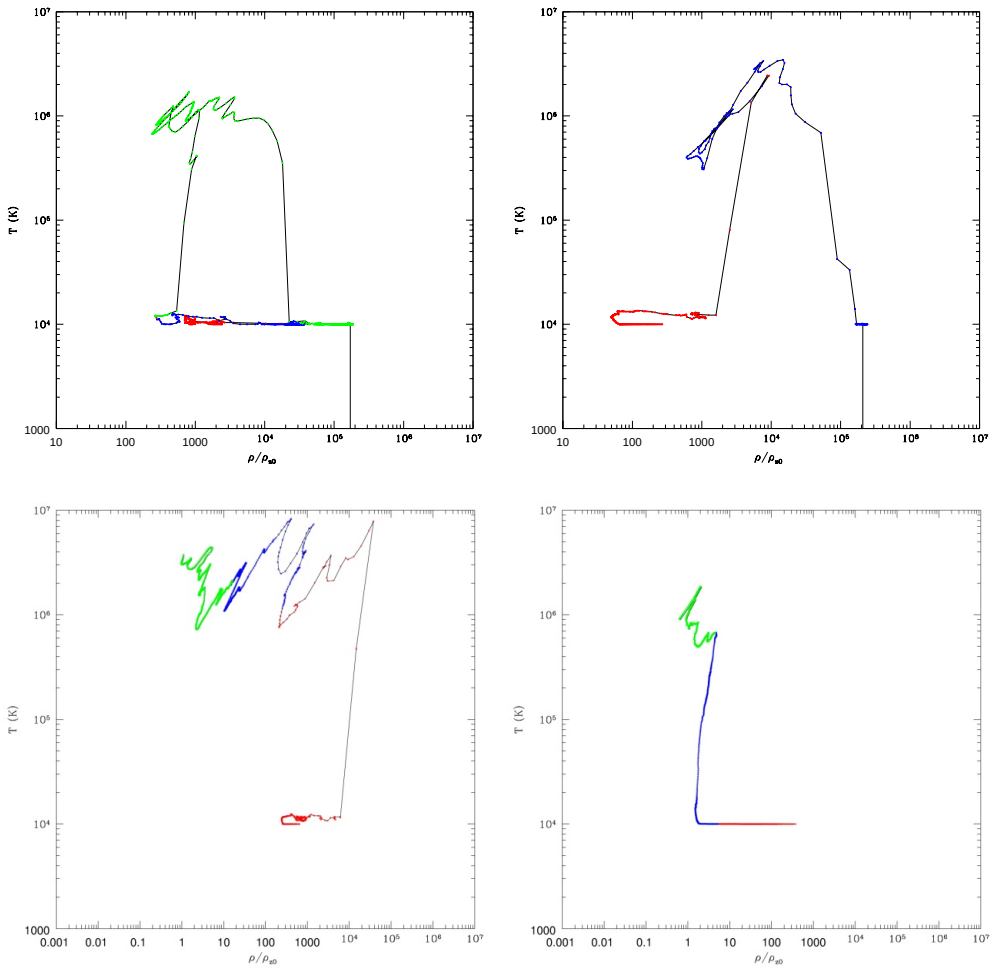

Figure 9.10: Density-temperature paths for different particles along z. Colors represent the redshift: red for $20 < z < 3$, blue for $3 < z < 2$ and green for $z < 2$. Up left and right: two gas particles heated before falling into the galaxy and then transformed into stars. Lower left panel: Hot gas particle inside $r_{\rm vir}$ at $z = 0$. Lower right panel: Hot gas particle outside $r_{\rm vir}$ at $z = 0$.

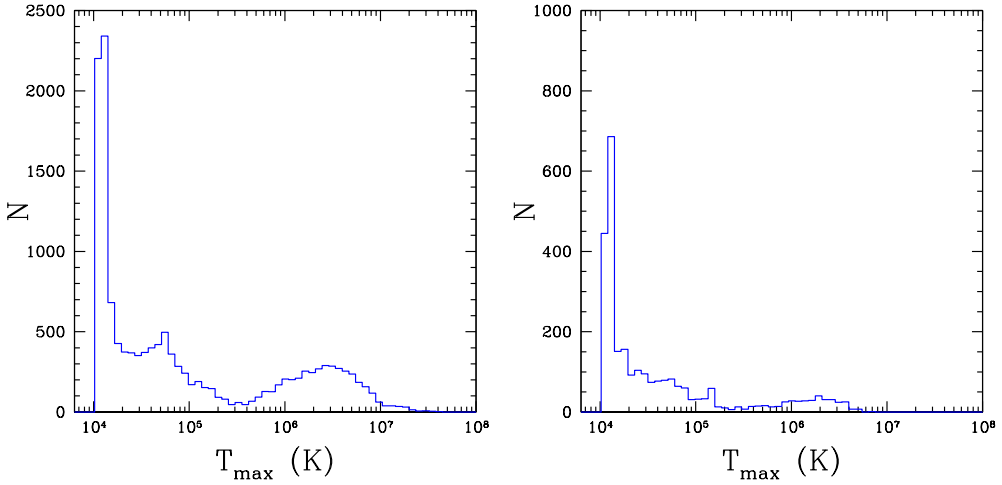

Figure 9.11: Histogram of the maximum temperature reached by all the baryonic particles inside $r_{\rm bo}$ of two ELOs. Left: $M_{\rm bo}^{\rm star} \sim 3 \times 10^{11} M_{\odot}$. Right: $M_{\rm bo}^{\rm star} \sim 5 \times 10^{10} M_{\odot}$.

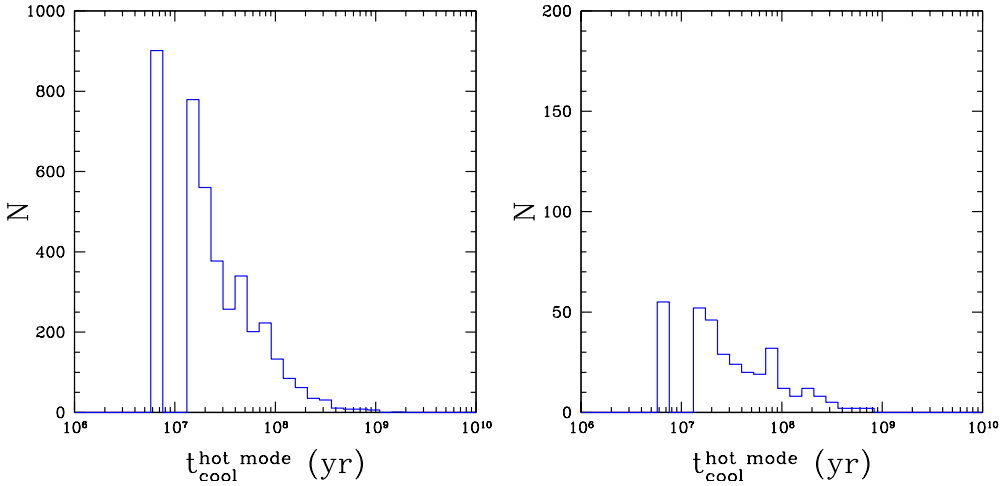

Figure 9.12: Histogram of the cooling time for all the baryonic particles inside $r_{\rm bo}$ that were accreted through the hot mode. Left: $M_{\rm bo}^{\rm star} \sim 3 \times 10^{11} M_{\odot}$. Right: $M_{\rm bo}^{\rm star} \sim 5 \times 10^{10} M_{\odot}$.

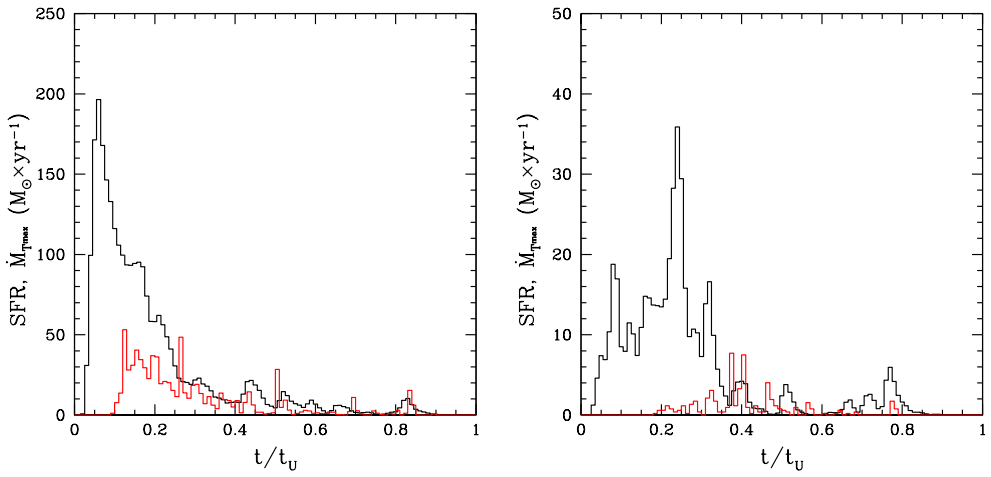

Figure 9.13: Star formation rate and the maximum temperature mass rate of the hot mode particles. Left: $M_{\rm bo}^{\rm star} \sim 3 \times 10^{11} M_{\odot}$. Right: $M_{\rm bo}^{\rm star} \sim 5 \times 10^{10} M_{\odot}$.

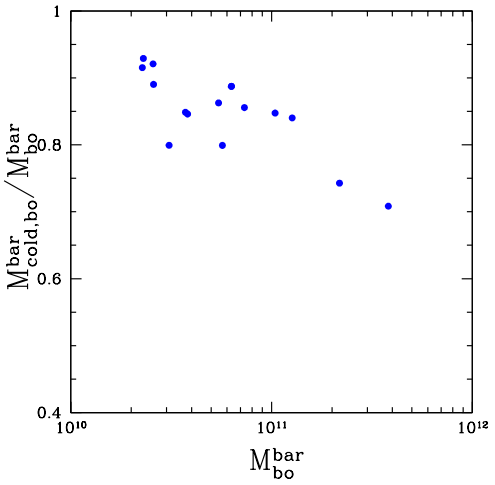

Figure 9.14: Baryonic mass accreted in cold mode over the total mass for ELOs of the 8716 simulation.

9.4 Conclusions

In this thesis we have studied mass and velocity distributions of several samples of virtual ellipticals formed in self-consistent cosmological simulations. The simulations provide us with clues on the physical processes involved in elliptical formation. They indicate that most of the dissipation involved in the mass assembly of a given ELO occurs in the violent early phase at high z and on very short timescales (and earlier on and on shorter timescales as the ELO mass grows, see details in Domínguez-Tenreiro et al. 2004, 2006), as a consequence of ELO assembly out of gaseous material and its transformation into stars. Moreover, the dissipation rate history is reflected by the star formation rate history. During the later slower phase of mass assembly, ELO stellar mass growth essentially occurs without any dissipation and the SF rate substantially decreases. So, the mass homology breaking appears in the early, violent phase of mass assembly and it is essentially preserved during the later, slower phase. A consequence is that the dynamical plane appears in the violent phase and is roughly preserved along the slower phase, see discussion in Chapter 8.

We see that our results on the role of dissipative dynamics essentially include previous ones, but they also add important new information. First, our results on the role of dissipative dynamics to break mass homology agree with the previous ones, but it is important to note that, moreover, ELO stellar populations show age effects, that is, more massive objects produced in the simulations *do have* older means and narrower spreads in their stellar age distributions than less massive ones (see details in Section 6.4); this is equivalent to downsizing (Cowie et al., 1996; Thomas et al., 2005) and naturally appears in the simulations, so that it need not be considered as an additional assumption.

Second, the preservation of the FP in the slow phase of mass aggregation in our simulations also agrees with previous work based on dissipationless simulations of pre-prepared mergers (Capelato et al., 1995; Dantas et al., 2003; González-García & van Albada, 2003; Nipoti et al., 2003; Boylan-Kolchin et al., 2005). But, again, it is important to note that the considerable decrease of the dissipation rate in the slow phase of evolution naturally appears in the simulations and we do not have to assume this decrease. Also, the decrease of the merger rate in the later phase of mass assembly results from the global behavior of the merger rate history in the particular cosmological context we have considered. Third, it turns out that the physical processes involved in ELO formation unveiled by our simulations, not only explain mass homology breaking (and its implications in the formation and preservation of the dynamical plane), and stellar age effects or downsizing in ellipticals, but they might also explain other elliptical properties recently inferred from observations. For example, the appearance of blue cores, Menanteau et al. (2004); Lee et al. (2006); the increase of the stellar mass contributed by the elliptical population since higher z, Bell et al. (2004); Conselice et al. (2005); Faber et al. (2007) (see more details in Domínguez-Tenreiro et al., 2006).

All our results on the structural and kinematical properties of elliptical galaxies indicate that baryonic matter (specifically dissipation and gravitational shocking) plays an important role in the origin of the observed fundamental relations. For this reason we have tried to deepen into the history of gas particles and how they were accreted in the ELO. In the classical scenario gas particles are first heated by gravitational shocks and then cool and fall into the galaxy. However, we have found that there are two different modes of gas accretion by galaxies: a cold mode and a hot mode, confirming previous results (Kereš et al., 2005, 2008). The cold mode includes gas particles that had never been heated before being accreted by the galaxy. Simulations also show that heated gas particles (hot mode) cool faster than expected in the classical scenario (White & Rees, 1978). We found that the importance of both modes are related with the mass of the galaxy and more massive galaxies are more efficient in heating the gas by gravitational shocks. This is also related with the fact that these galaxies have a lower baryonic content inside its virial radius than the less massive ones. However more detailed simulations would be needed in order to obtain the real ratio of each one.

It is worth mentioning that the scenario presented in this Chapter shares some characteristics of previously proposed scenarios, but it has also significant differences, mainly that most stars in elliptical galaxies form out of cold gas that had never been shock heated at the halo virial temperature and then formed a disk, as the conventional recipe for galaxy formation propounds (see discussion in Kereš et al., 2005, and references therein). The scenario for elliptical formation emerging from our simulations has the advantage that it results from simple physical laws acting on initial conditions that are realizations of power spectra consistent with observations of CMB anisotropies.

Part IV

Conclusions and Outlook

Chapter 10

Conclusions and Outlook

10.1 Summary and Conclusions

In this work, we have presented results from self-consistent cosmological hydrodynamical simulations, run with the DEVA code (Serna et al., 2003), both in its sequential and parallelized (OPENMP) versions. DEVA is a multistep AP3M-like SPH code particularly designed to study galaxy formation and evolution in connection with the global cosmological model. This code uses a formulation of SPH equations that ensures both energy and entropy conservation by including the so-called ∇h terms. Particular attention has also been paid to hold angular momentum conservation as accurately as possible. Cooling processes have been included for the baryonic component. Star formation (SF) has been implemented in the code in the framework of the turbulent sequential scenario (Elmegreen, 2002) through a phenomenological parameterization that transforms cold locally collapsing gas, denser than a threshold density, ρ_{thres}, into stars with a timescale given by the empirical Kennicutt-Schmidt law (Kennicutt, 1998).

Galaxy-like objects of different morphologies are formed in the simulations. We have been extremely careful in designing a solid method for the classification of galaxies so that the fulfillment of some specific requirements is guaranteed. Using this method and with the aim of studying structure and kinematics of elliptical galaxies we have built samples of elliptical-like objects for each simulation. Within this process, special emphasis is made on the features that differentiate this work from previous studies: obtaining a statistically reliable sample of elliptical-like objects from cosmological initial conditions with enough spatial resolution. In order to do so, we have developed visualization software, –for a first approximation to the simulations– and an important pipeline for numerical analysis of the simulations that allowed us to characterize and to study elliptical-like-objects at two different scales: halo scale and baryon object scale.

The proposed approach covers the whole analysis process, from running the simulation to its final comparison with observational results. We have focused on different fundamental relations between kinematic and structural parameters, first trying to char-

acterize them at $z = 0$ and then studying their evolution. At the end of each Chapter partial conclusions on the different subjects studied in this work can be found. Here we summarize them and give a global vision of this thesis:

We have first analyzed the structural and kinematical profiles of ELOs, finding a good agreement with observations in the projected stellar profiles (Sérsic law) and the dark-to-stellar gradients and dark-over-total ratios. These agreements with observational data strongly suggest that the intrinsic three-dimensional dark and bright matter mass and velocity distributions we get in the simulations might also adequately describe real ellipticals. We can summarize that ELOs are embedded in extended massive dark matter halos which have suffer from adiabatic contraction. At the halo scale, ELOs are not baryonically closed at this scale, i.e., ELOs miss baryons inside the virial radius ($r_{\rm vir}$) compared with the average baryon-to-dark fraction. Moreover, massive ELOs miss baryons as compared with less massive ones, when we normalize to the dark matter. This trend extends up to the short scales of ELOs. Baryon fraction profiles have been found to show a typical pattern such that, the baryons that ELOs miss are found at the outskirts of the configuration as diffuse hot gas. Concerning kinematics, stellar and dark matter particles constitute two dynamically hot components with important velocity dispersions. These dark and bright matter components of ELOs are kinematically segregated and do not show any clear mass or radial dependence. (Chapter 5).

As a second step, we have defined the different characteristic parameters which describe these profiles at different scales (from the halo scale to the projected stellar object). We have found that the (logarithms of the) ELO stellar masses, projected stellar half-mass radii, and stellar central line-of-sight (LOS) velocity dispersions define a dynamical fundamental planes (dynamical FPs) for all the different ELO samples. Zero points depend on the particular values that the star formation parameters take, while slopes do not change significantly when we change the size of the box simulated, cosmological parameters (within the ΛCDM framework), resolution or star formation. These planes are the observational manifestation of the intrinsic dynamical plane (IDPs) which relates the 3D parameter counterparts: stellar masses $M_{\rm bo}^{\rm star}$, stellar half-mass radii $r_{\rm e,bo}^{\rm star}$, and stellar mean square velocity of the central object $\sigma_{\rm 3,bo}^{\rm star}$. All the ELO samples have been found to show systematic trends with the mass scale in in the relative content of the dark and baryonic mass components that can be written as power-laws of the form $M_{\rm vir}/M_{\rm bo}^{\rm star} = A_{\rm vir}(M_{\rm bo}^{\rm star})^{\beta_{\rm vir}}$. A similar trend as the first one, although not statistically confirmed (nor discarded) in all samples, is also observed in the relative distributions of the dark and baryonic mass components, $r_{\rm e,h}^{\rm tot}/r_{\rm e,bo}^{\rm star} = A_{\rm rd}(M_{\rm bo}^{\rm star})^{\beta_{\rm rd}}$ (See discussion in Section 6.5.3). We have found that the dynamical FPs established by the ELO samples are consistent with that shown by the SDSS elliptical sample in the same variables, with no further need for any relevant contribution from stellar

population effects to explain the tilt of the observed Fundamental Plane from the virial relation. These effects could, however, have contributed to the scatter of the observed FP, as the dynamical FPs have been found to be thinner than the observed one. The results we report on hint, for the first time, at a possible way to understand the tilt of the observed FP in a cosmological context. Our simulations suggest that the physical origin of these trends lies in the systematic decrease, with increasing ELO mass, of the relative dissipation experienced by the baryonic mass component along ELO mass assembly. (Chapter 6).

In addition, ELOs 3D structural parameters, $M_{\rm bo}^{\rm star}$, $r_{\rm e,bo}^{\rm star}$ and μ (the 3D shape parameter equivalent to the 2D Sérsic shape parameter n) define *intrinsic structural* planes (ISPs). However these planes are not as tightly correlated as the IDPs are. The Photometric Plane is the observational manifestation of this relation. An interesting result is that we have discarded the possibility that the Fundamental Plane and the Photometric Plane are two projections of a four parameter law. We made the study for the 2D *observational* relations and their 3D counterparts. We found that the shape parameter n (or μ in 3D) does not add significant physical information to the Fundamental Plane relation (or intrinsic). (Chapter 6).

Stellar age properties of virtual ellipticals have shown a clear trend with their structural and dynamical characteristic parameters and seem to be linked with their formation and evolution processes in a cosmological scenario. Also, ELO stellar populations have age distributions with the same trends as those inferred from observations, i.e., most stars have formed at high z on short timescales, and, moreover more massive objects have older means and narrower spreads in their stellar age distributions than less massive ones (Domínguez-Tenreiro et al., 2004). This is equivalent to downsizing (see 3.3). (Chapter 6).

By studying the classical diagram introduced by Davies et al. (1983), we have shown that the shape distribution of our simulated galaxies and their kinematics are closely related and in good agreement with the observational data. We have confirmed that more massive ELOs show a lower dispersion in rotational support and ϵ shape values than less massive ones, pointing to rounder shapes and lower rotational support for the first ones. Finally we have seen that the 3D shape of a simulated elliptical could be constrained by the position that it occupies in the classical diagram that relates these two quantities. (Chapter 7).

From the analysis of ELOs at different redshifts, the main result we report on is the quasi-homogeneity of the relaxed ELO population with respect to z, as measured through the dynamical plane defined by their stellar masses, three-dimensional sizes and mean square stellar velocities at different zs, and, at the same time, the increase of the average values of these parameters as time elapses. The simulations also provide us with clues on how these evolutionary patterns arise from the physical processes

involved in galaxy assembly, namely, the plane appearance at an early violent phase as a consequence of dissipation (i.e., gas cooling and its subsequent transformation into stars), and the plane preservation during a later, quiescent phase, where dissipationless merging plays an important role in stellar mass assembly. This early gas consumption of proto-ellipticals also explains why most of the stars of today ellipticals formed at high redshifts. Simulations give also clues on why the homogeneity is consistent with the appearance of blue cores as well as with the increase of the stellar mass contributed by the elliptical population since higher z. (Chapters 8 and 9)

However, studying the rotational support and shape of ELOs we found a systematic change through time, i.e. evolution, by becoming rounder as we move to lower redshifts and at the same time more velocity dispersion supported. This is found to be primarily due to major dry mergers where only a modest amount of angular momentum is involved into the merger event. Despite the general trend, in a significant amount of cases the merger event involves a higher specific angular momentum, which in general causes the system to acquire a higher rotational support and/or a more oblate shape. These evolutionary patterns are still present when we study our systems in projection, mimicking real observations, and thus they should become apparent in future observations. (Chapter 8).

All our results on the structural and kinematical properties of elliptical galaxies indicate that baryonic matter (specifically dissipation and gravitational shocking) plays an important role in the origin of the observed fundamental relations. For this reason we have tried to deepen into the history of gas particles and how they were accreted in the ELO. In the classical scenario gas particles are first heated by gravitational shocks and then they slowly cool and fall forming the galaxy. However, we have found that there are two different modes of gas accretion by galaxies: a cold mode and a hot mode, confirming previous results (Kereš et al., 2005, 2008). The cold mode includes gas particles that had never been heated before being accreted by the galaxy. Simulations also show that heated gas particles (hot mode) cool faster than expected in the classical scenario (White & Rees, 1978). We found that the importance of both modes is related with the mass of the galaxy and more massive galaxies are more efficient in heating the gas by gravitational shocks. This is also related with the fact that these galaxies have a lower baryonic content inside its virial radius than the less massive ones. However more detailed simulations would be needed in order to obtain the real ratio of each one. (Chapter 9)

Finally, we conclude that the simulations studied in this work provide a unified scenario where most current observations on ellipticals can be interrelated, and that this scenario has the advantage that it results from simple physical laws acting on initial conditions that are realizations of power spectra consistent with the observations of CMB anisotropies. The scenario presented in this work should be considered as a

first order approximation to the real process in which elliptical galaxies are formed. In this scenario subresolution processes of energy injection have been implicit included through the values of ρ_{thres} and c_*. In a near future we will add to our codes these physical processes in an explicit way.

10.2 Discussion

We have been extremely careful in studying the impact of different systematics in our conclusions. We have checked how the star formation parameters, the resolution, the cosmological model parameters or the size of the box simulated can affect our results. We have presented and discussed them and found that:

- Changes in the star formation parameters have a great impact in the ELO properties and settle the zero point of several fundamental relations for elliptical galaxies studied in this work, as the Fundamental Plane or the relation between stellar age properties and kinematical descriptors. However, we have found that the star formation algorithm affect in different directions these relations in terms of obtaining a good agreement with observational data. Therefore for a given simulation, the star formation parameters have just a narrow specific range in which they can produce realistic objects.

- We have run several resolution tests using simulations in which the space resolution was increased by a factor of two and the mass resolution by a factor of eight. All these analyzes have shown a good agreement for the structural, kinematic and stellar properties between elliptical-like objects of different resolutions.

- Changes in the cosmological parameters (Ω_Λ, Ω_m, Ω_b, h) within the ΛCDM framework have not produced any significant change in the trends and results found for simulated ellipticals. Nevertheless, we can mention that the amount of baryonic matter available is one of the parameters that determine the final number of elliptical-like objects and the range in mass of the sample that we will obtain from a simulation. The other parameter that has an important effect in the final number of ELOs in a simulation is the normalization parameter, σ_8. Simulations with a higher σ_8 have higher energy input. These simulations mimic an active region of the Universe (Bryan & Norman, 1998). In these regions all the evolution from primordial inhomogeneities occurs faster and early-type objects are more frequent.

- Concerning the size of the box, we have obtained ELO samples for simulations with $L_{box} = 10$, 20 and 80 Mpc. As discussed in Section 4.2, L_{box} affects the results in a simulation because decreasing L_{box} is equivalent to putting a large-scale

cut-off to the power spectrum of perturbations. Simulations with a large box size are required to correctly get convergence on the results for the two-point correlation, mass functions, etc. However, this does not imply that the modification of these global properties of the large scale structure has necessarily an impact on the inner properties of the small scale systems (galaxies and their halos). We have found that box sizes changes imply that the clustering properties change and consequently, the statistics of ELO mass assembly paths change: i.e. the fraction of ELOs assembled through mergers of different characteristics, or at different times, changes. However this has no significant consequences on average on the 3D mass profiles, velocity distribution. That is, relaxed mass and velocity distributions forget the details on how mass is assembled or the velocity is acquired. This is not very surprising because equilibrium states do not depend on the path leading to them. Manrique et al. (2003) have analytically probed a similar result for dark matter halos. In their model, the density profile of relaxed halos permanently adapts to the profile currently building up through accretion and does not depend on their past aggregation history. Therefore the typical density profile of halos of a given mass at a given epoch is set by their time-evolving cosmology-dependent typical accretion rates. As a consequence this model predicts the existence of time-invariant relations among the structural parameters that describe these halos (See discussion in Salvador-Solé et al., 2005, 2007).

Finally we discuss briefly on some of the different sub-scale physic which have not been explicitly considered in our simulations: metal enrichment and stellar evolution (supernovae and black holes). Concerning chemical evolution, Martínez-Serrano et al. (2008) have recently included it in `DEVA` code. Preliminary results on the structural and kinematical properties of the elliptical-like objects of cosmological simulations have showed a good agreement with the results presented in this thesis. Feedback effects from supernovae, active galactic nuclei (AGN) or energy inputs other than gravitational have not been explicitly included in these simulations. We note that the role of discrete stellar energy sources at the scales resolved in this work is not yet clear. Theoretical arguments (Efstathiou, 2000) suggest that supernova feedback rapidly becomes ineffective in systems with velocity dispersions greater than 100 $km \times s^{-1}$. Indeed, MHD simulations also indicate that supernova effects in the star formation of galaxies are more important for low massive galaxies (Scannapieco et al., 2008). On the other hand, AGN feedback may be important in galaxies with high velocity dispersions (Silk & Rees, 1998; Ciotti & Ostriker, 2001) such as those studied in this work. However the nature, and indeed the direction, of the triggering is unclear (Silk, 2005), and it is worth mentioning that until now, only models which incorporate negative (namely which quenches SF) feedback have been simulated (see however Pipino et al., 2009, for a first approach into the opposite direction). Our point of view, therefore, is to keep

the physics of the simulations as simple as possible and to get an understanding on the behavior of a simplified problem before investigating additional complexities such as supernova and AGN feedback.

10.3 Outlook

It is said that in a work such as this one, development is never truly finished, it is only halted. This is certainly true in this case; there are just too many things to test, to polish, to add. But at some moment the line must be drawn. In the case of this work, it has been drawn at the point in which the approach is beginning to prove effective: we have a cosmological based framework that is able to reproduce and explain some of the tightest structural and kinematical correlations observed for ellipticals and it is robust against changes in the cosmological parameters, the space and mass resolution and the size of the box simulated.

Concerning our tools, the development of a parallelized version of the code has had an incredible impact, increasing the number of particles that can be simulated and opening the door to the `DEVA` code of high performance facilities as the Leibniz Supercomputing Center. Also, Martínez-Serrano et al. (2008) have just introduced chemical evolution in `DEVA` code. This will bring us the possibility of obtaining variables that are directly observable through the use of stellar population synthesis models. This issue, together with the advantage of having a parallelized version of the code will certainly open an incredible amount of possibilities for the future. In this sense, the analysis pipeline developed in this thesis is a solid instrument that could be used as the main branch for the expected development of algorithms and functions to analyze these forthcoming simulations.

Part V

Appendix

Apéndice A

Introducción

Este trabajo describe una propuesta para el estudio de la formación y evolución de galaxias elípticas en un contexto cosmológico.

La introducción comienza con una descripción de la motivación inicial y los objetivos buscados. En el siguiente apartado, se procede a enumerar y describir una serie de áreas de conocimiento relacionadas con la propuesta, y, a continuación, se presenta la propuesta en sí. En la última sección se describe, a grandes rasgos, la organización del resto del trabajo.

A.1 Motivación y objetivos

Desde 1930, cuando las galaxias se confirmaron como los elementos de construcción fundamentales del universo, su origen y evolución se ha mantenido como uno de los más importantes retos para la astronomía y la cosmología. Sin embargo, también resultó evidente que era uno de los más difíciles de discernir fundamentalmente por dos razones:

Primero porque las galaxias evolucionan en un tiempo muy prolongado, lo que hace imposible estudiar una galaxia desde su nacimiento a su muerte. Así pues, los astrónomos se han enfrentado al reto de estudiar las galaxias a través de fotos instantáneas aisladas. Recientemente una nueva generación de telescopios y espectrógrafos ha hecho posible coleccionar un inmenso número de estas instantáneas e incluso lo que es aun más importante, ver galaxias muy lejanas.

La segunda razón fue que, como en cualquier problema físico, el estudio de la formación de galaxias necesita unas condiciones iniciales sólidas. La cosmología ha estudiado este tema durante las últimas siete décadas y en los últimos años ha surgido un modelo cosmológico basado en firmes ideas físicas y observacionalmente consistente. El modelo del Big Bang ó de la gran explosión para describir el Universo en expansión, cuya estructura y dinámica puede ser descrita en el marco de la relatividad general, tiene un numero de parámetros cosmológicos que actualmente están bien acotados por numerosas

observaciones: Las medidas del satélite WMAP del fondo de radiación de microondas (FRM, Dunkley et al., 2009), los datos de supernovas (Riess et al., 2007) las mediciones de estructura a gran escala (Massey et al., 2007; Percival et al., 2007) entre otras, han establecido un modelo concordante de Universo espacialmente plano con una densidad de materia de aproximadamente el 30 % de la crítica.

Este modelo predice que la estructura a gran escala de la distribución de galaxias que observamos en los catálogos de galaxias tiene que haberse formado a través del colapso gravitacional de pequeñas fluctuaciones primordiales. Las propiedades de estas densidades a gran escala pueden predecirse desde las condiciones iniciales observadas en el FRM combinadas con nuestro conocimiento de la gravedad descrita por la relatividad general. Los distintos catálogos que incluyen estudios a gran escala como SDSS (York et al., 2000) o 2dF (Folkes et al., 1999) confirman esta idea. Mientras que la teoría del origen de las estructuras a gran escala es más que prometedor, existen sin embargo, preguntas abiertas a menor escala que el modelo estándar tiene todavía que contestar. Una de ellas es la formación de las galaxias para la que el modelo tiene que poder explicar un inmenso número de datos observacionales ya disponibles.

De hecho, actualmente el número de datos observacionales disponibles es tan inmenso que el estudio detallado del origen y evolución de las galaxias exige centrarse en algún caso específico. El termino galaxia comprende una amplia variedad de tipos de galaxias con diferentes propiedades. Una forma de profundizar en este tema durante las últimas décadas ha sido intentar conocer como se ha formado cada uno de estos tipos de galaxias, ya que compartiendo las mismas propiedades físicas su proceso de formación debería compartir también algunos aspectos comunes.

De todas las clases o tipos de galaxias, las galaxias elípticas son las más fáciles de estudiar ya que muestran las regularidades empíricas más precisas, a veces en forma de correlaciones muy fuertes entre sus parámetros observacionales (Djorgovski & Davis, 1987; Faber et al., 1987; Caon et al., 1993; Bernardi et al., 2003a). El interés de estas regularidades reside en que pueden tener codificada mucha información relevante acerca del proceso físico que subyace en la formación y evolución de las elípticas.

Todos los nuevos avances hacen posible por vez primera preguntarse cuestiones clave, significativas sobre el modo en que las galaxias elípticas se formaron y como evolucionaron a través de los 10 billones de años de historia del Universo. ¿Cuándo aparecieron? ¿Qué provocó el proceso de su formación? ¿Se forman todas en una única época bien definida ó su formación se extiende en el tiempo? ¿Cuál es la conexión entre esta población y la física del inicio del universo? Y quizá lo más interesante de todo, ¿Cual es el proceso que establece las relaciones observadas entre varias propiedades estructurales y cinemáticas?

Las simulaciones hidrodinámicas autoconsistentes son una poderosa herramienta para investigar estas preguntas, ya que permiten seguir de forma precisa la evolución

de las propiedades dinámicas y termodinámicas de la materia en el universo. La idea general es resolver simultáneamente las ecuaciones gravitacionales e hidrodinámicas. La clave está en conectar las condiciones iniciales ofrecidas por la cosmología y todos los datos disponibles de las observaciones. Por ello, en cierto sentido juegan el papel de los experimentos para los astrofísicos.

La mayor ventaja de este tipo de simulaciones es que la física se introduce al nivel más general, y los procesos dinámicos relativos al ensamblaje de las galaxias, tales como el colapso, la caída de gas, interacciones, fusiones, etc., surgen de forma natural, en vez de postulados a priori, y pueden ser seguidos en detalle. Sólo la escala física subresolución necesita ser modelada. Estas consideraciones enfatizan el interés en las simulaciones hidrodinámicas como una herramienta conveniente para entender la formación y evolución de galaxias desde el campo de las fluctuaciones primordiales.

Así, la motivación para el presente trabajo ha sido usar simulaciones hidrodinámicas autoconsistentes para construir un armazón teórico con el que interpretar y estudiar las diferentes observaciones de galaxias elípticas.

A.2 Aspectos teóricos

La propuesta que se esboza en la sección anterior tiene relación con varias áreas de conocimiento. Los primeros Capítulos de este trabajo se incluyen en la Parte I, Marco Teórico, donde se describen las principales áreas de conocimiento asociadas a la propuesta. A continuación se presentan brevemente los campos que se tratarán en esta Parte I, así como las razones que han sugerido incluirlos en dichos Capítulos.

Desde el momento que los modelos teóricos proporcionaron algunas condiciones iniciales era una cuestión de tiempo que los científicos comenzaran a estudiar su evolución y a compararlos con las observaciones. La compleja evolución de las perturbaciones iniciales hace de las simulaciones cosmológicas de N-cuerpos, en las que se calcula solo la fuerza gravitatoria, una poderosa herramienta para estudiarlos en el régimen no lineal. Los primeros intentos de usar esta técnica en el estudio de la formación de estructuras a gran escala comenzaron en los 70 (Peebles, 1974; Press & Schechter, 1974; Miyoshi & Kihara, 1975; Aarseth et al., 1979), obteniendo un gran éxito y motivando varias simulaciones cosmológicas de N-cuerpos en todo el mundo.

Desde estas primeras aproximaciones hasta nuestros días, los diferentes algoritmos e ideas que engloba esta técnica han ido refinándose continuamente. En este sentido, y en primer lugar habría que decir que los simuladores están en deuda con todos los increíbles avances en tecnología de computadores producidos en las últimas décadas.

La incorporación de la hidrodinámica a las simulaciones cosmológicas ha hecho posible estudiar no solo la formación gravitacional de los halos de materia oscura, sino también las propiedades de la materia bariónica, y por tanto la formación de galaxias

asociada con esos halos. Las primeras simulaciones hidrodinámicas autoconsistentes se realizaron a finales de los 80 (Evrard, 1988; Hernquist & Katz, 1989; Navarro & White, 1994).

Hasta la fecha, ningún código tiene el suficiente rango dinámico para considerar a la vez la evolución cosmológica a gran escala en cientos de megapársecs y la formación de estrellas de bariones. Pero la heurística física ha incorporado con éxito algunos algoritmos para a partir de modelos realizar la conversión de bariones en estrellas (Cen, 1992; Tissera et al., 1997; Thacker & Couchman, 2000). Desde el comienzo de este nuevo milenio varios grupos han obtenido gran éxito en modelar la formación de galaxias utilizando simulaciones autoconsistentes que tienen en cuenta la dinámica de la materia oscura y el gas, el enfriamiento radiactivo, la formación de estrellas y algunos otros aspectos físicos a escalas subresolución (Sommer-Larsen et al., 2002; Murali et al., 2002; Meza et al., 2003; Sáiz et al., 2003; Kawata & Gibson, 2003; Sáiz et al., 2004).

En cualquier caso para hacer un estudio adecuado tenemos que entender no solo la forma en que estas simulaciones funcionan, sus limitaciones y sus ventajas, sino también conocer como comparar correctamente sus resultados con la teoría y las observaciones. En este punto necesitamos profundizar en los datos disponibles para las galaxias elípticas y descubrir que es lo que realmente sabemos sobre ellas. Es muy importante entender como se ha obtenido toda esta información, para ser capaz de mimetizar en lo posible los mismos métodos y facilitar la comparación.

Por último, también tenemos que estudiar los diferentes modelos que se han propuesto para la formación y evolución de las galaxias elípticas. Por una parte, un grupo de primeras observaciones sugería que las galaxias elípticas se formaron en épocas tempranas y en escalas de tiempo muy cortas, en lo que se ha llamado escenario de colapso monolítico (Eggen et al., 1962; Larson, 1974; Matteucci, 2003). Por otra parte, otro grupo de observaciones recientes sugiere que las fusiones de galaxias a *redshift* intermedios e incluso bajos pueden haber jugado un papel importante en la formación de las elípticas, señalando hacia lo que se conoce como escenario jerárquico (White & Rees, 1978; Cole et al., 1994; Bundy et al., 2005). Estos resultados observacionales, que resultan a la vez paradójicos y desafiantes, indican que el estudio de este problema en conexión con el modelo cosmológico es una clara necesidad y un método muy prometedor.

A.3 Método

Inspirado por todo el trabajo previo en simulaciones autoconsistentes ya mencionado, y especialmente por el trabajo de Sáiz et al. (2004) hemos intentado avanzar un paso más en el estudio de las galaxias elípticas usando este método. Para ello hemos trabajado en obtener de las simulaciones estudiadas una amplia muestra de sistemas que permita a la vez tener suficiente estadística, y que la resolución de estos sistemas sea lo

suficientemente alta para permitir un análisis cinemático y estructural apropiado.

Un aspecto crítico en relación con el código utilizado para realizar las simulaciones es que las leyes de conservación se verifiquen exactamente. Particularmente, un código numérico apropiado debe satisfacer todas las leyes de conservación para cantidades físicas como el momento, energía, o entropía. En esta tesis hemos usado el código `DEVA` (Serna et al., 2003) y su versión paralela `P-DEVA` que cumplen todos estos requisitos.

Ya que intentamos utilizar estas simulaciones como un método para entender mejor el Universo real, es esencial tener una vía más o menos directa de comparación entre los resultados de la simulación y las observaciones. Para realizar esta comparación debemos basarnos en las propiedades de las galaxias que se miden tanto en los resultados de las simulaciones como en las observaciones.

En este trabajo, hemos estudiado la fuerte correlación observada entre diferentes parámetros estructurales y dinámicos de las elípticas. Utilizando las simulaciones hidrodinámicas hemos estudiado, además del equivalente a diversas medidas observacionales, los parámetros fundamentales en 3D a escala estelar y los parámetros a escala del halo para todos nuestros objetos virtuales de tipo elíptico. Con la información obtenida en este trabajo, queremos profundizar en el origen de estas correlaciones, señalar su evolución con redshift y sus implicaciones en la formación de galaxias elípticas.

Para poder realizar esta tarea primero debemos lidiar con el diseño de las simulaciones que necesitamos para conseguir el objetivo estadístico y de resolución en nuestras muestras. Hemos de tener en cuenta que los recursos disponibles son limitados, en el sentido no solo de la potencia de cálculo de las maquinas, sino también de tiempo real.

Una vez que configurados todos los detalles de las simulaciones, hemos construido un grupo de herramientas de análisis dirigidas a una comparación apropiada entre los datos observacionales y los resultados teóricos (analíticos y simulaciones). Tal y como puede verse a lo largo de este trabajo, estamos interesados en muchos parámetros y propiedades diferentes de nuestras elípticas virtuales, así que necesitamos desarrollar una cantidad significativa de programas de computación y algoritmos. Sin embargo, la idea general que preside nuestra implementación ha sido crear un proyecto sólido de análisis que pueda ser útil no solo para analizar estas simulaciones sino también las del futuro. Hemos hecho su arquitectura muy modular, para facilitar la inclusión de más funciones y/o la mejora de las antiguas. Para facilitar la utilización de nuevos usuarios se han definido diferentes parámetros globales que pueden ser ajustados rápidamente.

A.4 Estructura de la tesis

La tesis se organiza en cuatro partes:

Parte I – Marco teórico: Proporciona la base del trabajo para los resultados de la Parte III con una introducción para cada campo de conocimiento utilizado en

el presente trabajo. Los términos y conceptos utilizados en los resultados son introducidos y descritos. El Capítulo 2 Introduce las simulaciones hidrodinámicas autoconsistentes. En particular presentamos el código utilizado en nuestras simulaciones, `DEVA`. El Capítulo 3 proporciona una visión general de la teoría actual de formación de galaxias, los modelos y las cotas observacionales.

Parte II – Simulaciones y herramientas: Incluye el Capítulo 4 en el que se presenta una descripción detallada de las diferentes simulaciones estudiadas, como se han analizado, y los diferentes aspectos técnicos relativos al análisis de las propiedades de los objetos virtuales tipo elíptica.

Parte III – Resultados: Presentamos los resultados de nuestro estudio de la formación de galaxias utilizando simulaciones hidrodinámicas en dos bloques separados. El primero, que incluye los Capítulos 5, 6 y 7, profundizan en diversas propiedades cinemáticas y estructurales de las elípticas virtuales. El segundo bloque versa sobre las características de las galaxias elípticas en épocas más tempranas. En particular, el Capítulo 8 presenta un estudio de evolución de las diferentes relaciones fundamentales para este tipo de galaxias a partir de un corrimiento al rojo (z) por debajo de 1,5. Finalmente, el capitulo 9, profundiza en los diferentes escenarios de formación y evolución de galaxias elípticas.

Parte IV – Conclusiones y trabajo futuro: Contiene las conclusiones, una breve discusión y un esbozo general de futuras líneas de trabajo.

El Apéndice A contiene la presente traducción al español del primer Capítulo. En el Apéndice B se puede encontrar la traducción al español de la parte IV: Conclusiones y trabajo futuro. Adicionalmente, como marco general de este trabajo, el Apéndice C presenta el Modelo Cosmológico Estándar a grandes rasgos, introduciendo varios conceptos utilizados en esta tesis. El Apéndice D incluye varias tablas de datos a las que nos referiremos a lo largo de esta tesis.

Finalmente, hay que indicar que parte del trabajo que se presenta en este manuscrito ha aparecido publicado en diferentes revistas (Oñorbe et al., 2005; Domínguez-Tenreiro et al., 2006; Oñorbe et al., 2006; Oñorbe et al., 2007; González-García et al., 2009)[1] y resúmenes de conferencias (Oñorbe et al., 2006; Oñorbe et al., 2006, 2007; Domínguez-Tenreiro et al., 2008; Oñorbe et al., 2008) en los que he participado durante el desarrollo de esta tesis, tal y como se indicará en cada Capítulo cuando corresponda.

[1]Los primeros cuatro artículos pueden encontrarse en el Apéndice E. El último artículo ha sido incluido en la Sección 8.5

Apéndice B

Conclusiones y trabajo futuro

B.1 Conclusiones

En este trabajo hemos presentado resultados de simulaciones cosmológicas hidrodinámicas autoconsistentes realizadas con el código DEVA (Serna et al., 2003), en sus versiones secuencial y paralelizada (OPENMP). DEVA es un código tipo SPH-AP3M multipaso diseñado específicamente para estudiar la formación y evolución de las galaxias en conexión con el modelo cosmológico. Este código usa una formulación para las ecuaciones SPH que asegura la conservación tanto de la energía como de la entropía incluyendo los llamados términos ∇h. En este sentido se ha prestado una particular atención a que la conservación del momento angular sea lo más precisa posible. El proceso de enfriamiento se ha incluido para la componente bariónica. La formación de estrellas (FE) ha sido implementada en el código en el marco del escenario secuencial turbulento (Elmegreen, 2002) a través de un algoritmo de parametrizacion fenomenológica que transforma el gas frió con una densidad superior a una densidad umbral y en colapso local, en estrellas con una escala de tiempo dada por la ley empírica Kennicutt-Schmidt (Kennicutt, 1998).

En las simulaciones realizadas se han formado objetos tipo galaxia de diferentes morfologías. Hemos sido extraordinariamente cuidadosos en diseñar un método sólido para la clasificación de las galaxias en el que el cumplimiento de ciertos requerimientos específicos esté garantizado. Usando este método, y con el fin de estudiar la estructura y la cinemática de las galaxias elípticas hemos construido muestras de objetos tipo-elíptica (OTEs) para cada simulación. Durante este proceso se ha hecho un especial énfasis en los aspectos que lo hacen diferente de otros estudios previos: la obtención de una muestra estadísticamente significativa de objetos tipo-elíptica obtenidos a partir de condiciones cosmológicas iniciales y con suficiente resolución espacial. Para ello hemos desarrollado un software de visualización, –para una primera aproximación a las simulaciones–, y un importante grupo de herramientas para el análisis numérico de las simulaciones que nos permite caracterizar y estudiar los objetos tipo-elíptica a dos escalas diferentes: a escala del halo y a escala del objeto bariónico.

La aproximación propuesta en este trabajo cubre el análisis del proceso completo, desde la realización de las simulaciones, hasta su comparación final con los resultados observacionales. Nos hemos centrado en diferentes relaciones fundamentales entre los parámetros estructurales y cinemáticos, primero intentado caracterizarlos a $z = 0$, y después estudiando su evolución. Al final de cada capítulo se pueden encontrar conclusiones parciales de los diferentes aspectos estudiados en este trabajo. Aquí los resumimos y damos una visión general de esta tesis:

Primero hemos analizado los perfiles estructurales y cinemáticos de los OTEs encontrando un buen acuerdo con las observaciones en los perfiles estelares proyectados (ley de Sérsic) y los gradientes de masa de materia oscura sobre la estelar y los cocientes entre masa de materia oscura sobre la total. Este buen acuerdo con los datos observacionales sugiere que las distribuciones intrínsecas tridimensionales de masa y velocidad de la materia oscura y las estrellas que obtenemos en las simulaciones pueden también describir adecuadamente las elípticas reales. En resumen podemos decir que los OTEs están embebidos en extensos halos masivos de materia oscura que ha sufrido contracción adiabática. A la escala del halo, los OTEs no están cerrados barionicamente, esto es, los OTEs pierde bariones dentro del radio virial ($r_{\rm vir}$) comparado con el promedio cosmológico de fracción de masa bariónica sobre materia oscura. Es más, los OTEs más masivos pierden bariones comparados con los menos masivos, cuando normalizamos sobre el contenido de materia oscura. Esta tendencia se extiende a escalas más pequeñas de los OTEs. Los perfiles de fracción bariónica muestran un perfil típico, de forma que los bariones que los OTEs pierden se encuentran en los alrededores de la configuración como gas caliente difuso. En relación a la cinemática las partículas estelares y la materia oscura constituyen una componente caliente con una importante dispersión de velocidades. Las componentes de materia oscura y materia estelar de los OTEs están cinemáticamente segregados y no muestran ninguna dependencia radial o en masa clara. (Capítulo 5).

En un segundo paso, hemos definido los diferentes parámetros característicos que describen esos perfiles a diferentes escalas (desde la escala del halo al objeto estelar proyectado). Hemos encontrado que (el logaritmo de) las masas estelares de los OTEs, el radio efectivo proyectado y las dispersión de velocidades estelar central en la línea-de-visión definen el Plano Fundamental Dinámico (PFD). El punto cero depende de los valores particulares que toman los parámetros de formación estelar, mientras que la pendiente no cambia significativamente cuando cambiamos el tamaño de caja simulado, los parámetros cosmológicos (dentro del marco ΛCDM), la resolución o la formación estelar. Estos planos son la manifestación observacional del plano dinámico intrínseco (PDI) que relaciona los parámetros 3D homólogos: la masa estelar $M_{\rm bo}^{\rm star}$, el radio efectivo estelar $r_{\rm e,bo}^{\rm star}$, y la dispersión de velocidades estelar en 3D $\sigma_{\rm 3,bo}^{\rm star}$. Todas las muestras

de OTEs han mostrado una clara correlación entre la masa estelar y el contenido relativo de las componentes bariónica y de materia oscura que puede describirse como una ley de potencias $M_{\rm vir}/M_{\rm bo}^{\rm star} = A_{\rm vir}(M_{\rm bo}^{\rm star})^{\beta_{\rm vir}}$. También se ha encontrado una correlación similar a la anterior entre la masa estelar y la distribución relativa de estas dos componentes, $r_{\rm e,h}^{\rm tot}/r_{\rm e,bo}^{\rm star} = A_{\rm rd}(M_{\rm bo}^{\rm star})^{\beta_{\rm rd}}$, aunque en este caso no ha sido confirmada (ni descartada) estadísticamente para todos las muestras (ver discusión en la Sección 6.5.3). Hemos encontrado que los Planos Fundamentales Dinámicos de las distintas muestras de OTE son consistentes con el obtenido de la muestra de elípticas SDSS en las mismas variables, sin necesidad de ninguna contribución relevante del efecto de la población estelar para explicar la inclinación observada. Sin embargo estos efectos podrían contribuir a la dispersión del PF observado, ya que los PFDs han resultado ser más finos que este. Los resultados que se presentan en este trabajo sugieren, por primera vez, una posible explicación del origen de la inclinación del Plano Fundamental en un contexto cosmológico. Nuestras simulaciones sugieren que el origen físico de estas tendencias reside en la disminución sistemática, con el aumento de la masa del OTE, de la disipación relativa experimentada por la componente bariónica a lo largo del ensamblaje del objeto. (Capítulo 6).

Además, los parámetros estructurales en 3D de los OTEs, $M_{\rm bo}^{\rm star}$, $r_{\rm e,bo}^{\rm star}$, y μ (el parámetro de forma en 3D equivalente al parámetro de forma de Sérsic en 2D, n) definen planos intrínsecos estructurales (PIEs). Sin embargo estos parámetros no están tan correlacionados como los que conforman el PDI. El Plano Fotométrico es la manifestación observacional de esta relación. Un resultado interesante es que hemos descartado la posibilidad de que el Plano Fundamental y el Plano Fotométrico sean dos proyecciones de una relación aún más fuerte entre los cuatro parámetros que intervienen en ellas. Este estudio se ha hecho para las relaciones observacionales en 2D y de sus equivalencias en 3D. Encontramos que la forma del parámetro n (ó μ en 3D) no añade información física significativa a la relación del Plano Fundamental Dinámico. (Capítulo 6).

Las propiedades de la edad estelar de las elípticas virtuales han mostrado una clara correlación con sus parámetros estructurales y dinámicos característicos que parece ligada a su proceso de formación y evolución en un escenario cosmológico. Las poblaciones estelares de OTE tienen distribuciones de edad con las mismas características que las inferidas de las observaciones, esto es, la mayoría de las estrellas se ha formado a alto z en escalas de tiempo cortas, y, además, los objetos más masivos muestran medias más viejas y una dispersión más estrecha en la distribución estelar que los menos masivos (Domínguez-Tenreiro et al., 2004). Esto es equivalente al *dowsizing* (Ver 3.3). (Capítulo 6).

Estudiando el diagrama clásico introducido por Davies et al. (1983), hemos demostrado que la forma de nuestras galaxias simuladas y su cinemática se encuentran relacionadas y en buena concordancia con los datos observacionales. Hemos confirmado

que los OTEs mas masivos muestran una dispersión más baja en su soporte rotacional y los valores de forma ϵ, que las menos masivas, apuntando a formas más redondas y a un soporte rotacional menor en las primeras. Finalmente hemos visto que la forma en 3D de una elíptica simulada puede obtenerse a través de la posición que ocupa en el diagrama clásico que relaciona estas dos cantidades en 2D (Capítulo 7).

Del análisis de los OTEs a diferentes épocas, el principal resultado es la cuasi-homogeneidad de la población de OTEs relajados con respecto a z, medida a través del plano dinámico definido por sus masa estelares, tamaños tridimensionales y dispersión de velocidades a diferentes zs, y, al mismo tiempo, el aumento de los valores medios de estos parámetros según pasa el tiempo. La simulación también nos da claves de cómo estas pautas de evolución surgen de los procesos físicos involucrados en el ensamblaje de galaxias, esto es, la aparición del Plano Fundamental en una fase violenta inicial como consecuencia de la disipación (esto es enfriamiento del gas y su subsiguiente transformación en estrellas). La conservación del plano durante una fase posterior, quiescente, donde las fusiones sin disipación juegan un papel importante en el ensamblaje de la masa estelar. Este consumo precoz del gas en las proto-elípticas también explica porque la mayoría de las estrellas de las elípticas de hoy en día se formaron a altos redshifts. Las simulaciones también nos dan ciertas pistas en cómo esta homogeneidad puede ser consistente con la aparición de núcleos azules y con el aumento de la contribución de las galaxias elípticas a la masa estelar desde alto z. (Capítulos 8 y 9).

Sin embargo, por otra parte, estudiando el soporte rotacional de la forma OTEs encontramos que existe un cambio sistemático a través del tiempo, esto es, evolución, que indica que los objetos son más redondos conforme el tiempo avanza y, al mismo tiempo, el soporte por la dispersión de velocidades aumenta. Esto se debe principalmente a las fusiones mayores secas donde solo una modesta cantidad del momento angular está implicada en el evento de fusión. A pesar de la pauta general, en un grupo significativo de casos el evento de fusión implica un momento angular específico más alto que en general, hace al sistema adquirir un soporte rotacional más alto y/ó una forma más achatada. Estas pautas de evolución están aún presentes cuando estudiamos nuestros sistemas en proyección, mimetizan las observaciones reales, y así podrían aparecer en futuras observaciones. (Capítulo 8).

Todos nuestros resultados sobre las propiedades estructurales y cinemáticas de las galaxias elípticas indican que la física ligada a la materia bariónica (disipación específica y calentamiento gravitacional) juega un papel importante en el origen de las relaciones fundamentales observadas. Por esta razón hemos intentado profundizar en la historia de las partículas de gas y en cómo fue acretada por los OTE. Encontramos dos modelos diferentes de acreción de gas por las galaxias: un modo frío y un modo caliente confirmando resultados previos (Kereš et al., 2005, 2008). El modo frió incluye partículas de gas que no han sido nunca calentadas antes de ser acretadas por la galaxia. En el

escenario clásico se sugiere que en el modo caliente las partículas de gas son primero calentadas por choques gravitacionales y después se enfrían lentamente formando la galaxia (White & Rees, 1978). Hemos encontrado que la importancia de los dos modos esta fuertemente relacionada con la masa de la galaxia ya que las galaxias más masivas son más eficientes al calentar el gas mediante choques gravitacionales. Esto se relaciona también con el hecho de que estas galaxias tienen un fracción de masa bariónica sobre masa total dentro del radio virial menor que las menos masivas. (Capítulo 9).

Finalmente, concluimos que las simulaciones estudiadas en este trabajo proporcionan un escenario unificado donde muchas de las actuales observaciones para galaxias elípticas pueden ser interrelacionadas, y que este escenario tiene la ventaja de que resulta de leyes físicas *simples* actuando sobre unas condiciones iniciales que son realizaciones del espectro de potencias consistente con las observaciones de anisotropías de la Radiación de Fondo de Microondas. El escenario presentado en este trabajo debe ser considerado una aproximación a *primer orden* del complejo proceso en el que se forman las galaxias elípticas. En este escenario los procesos físicos subresolución que implican inyección de energía han sido incluidos de forma implícita a través de los parámetros del algoritmo de formación estelar: ρ_{thres} y c_*. En un futuro próximo estos procesos físicos serán incluidos en el código de forma explícita.

B.2 Discusión

El estudio del impacto de las diferentes sistemáticas en nuestras conclusiones se ha realizado de forma muy cuidadosa. Hemos revisado como los parámetros de formación estelar, la resolución, los parámetros de modelo cosmológico o el tamaño de la caja de la simulación pueden afectar nuestros resultados. Tras discutirlos hemos encontrado que:

- Los cambios en los parámetros de formación estelar tienen un gran impacto en las propiedades de los OTE y sitúan el punto cero de varias relaciones fundamentales de las galaxias elípticas estudiadas en este trabajo, como el Plano Fundamental o la relación entre la edad estelar y los descriptores cinemáticos. Sin embargo hemos encontrado que el algoritmo de formación estelar afecta en diferentes direcciones estas relaciones en términos de obtener una buena concordancia con los datos observacionales. Así, para una simulación dada, los parámetros de formación estelar tienen un rango específico estrecho en el que pueden producir objetos reales.

- Hemos realizado varios test de resolución usando simulaciones en las que la resolución espacial fue aumentada en un factor dos y la resolución en masa en un factor ocho. Todos estos análisis han mostrado buena concordancia para las propiedades estructurales, cinemáticas y estelares entre los objetos de tipo elíptica de diferentes resoluciones.

- Los cambios de los parámetros cosmológicos (Ω_Λ, Ω_m, Ω_b, h) en el marco del ΛCDM no han producido cambios significativos en las tendencias y resultados encontrados en las simulaciones elípticas. Sin embargo podemos mencionar que la cantidad de materia bariónica disponible es uno de los parámetros que determina el número final de objetos de tipo elíptica y el rango en masa de la muestra, que obtendremos en una simulación. El otro parámetro que tiene un efecto importante en el número final de OTEs en una simulación es el parámetro de normalización σ_8 ya que las simulaciones con un σ_8 más alto tienen una entrada de energía más alta. Estas simulaciones mimetizan una región activa del Universo (Bryan & Norman, 1998). En estas regiones la evolución a partir de las perturbaciones primordiales ocurre más rápido y los objetos de tipo temprano son más frecuentes.

- En relación al tamaño de la caja, hemos obtenido muestras de OTE para simulación con L_{box} = 10, 20 y 80 Mpc. Como se discute en la Sección 4.2, el tamaño de L_{box} puede afectar los resultados de una simulación porque disminuir L_{box} es equivalente a poner un corte a gran escala en el espectro de potencias. Las simulaciones con un tamaño de caja grande son necesarias para conseguir una correcta convergencia de los resultados para la función de correlación, la función de masa, etc. Sin embargo esto no implica que las modificaciones de estas propiedades globales de la estructura a gran escala tenga necesariamente un impacto en las propiedades internas de los sistemas a pequeña escala (las galaxias y sus halos). Hemos encontrado que los cambios del tamaño de caja implican que las propiedades de agrupamiento cambian y consecuentemente, hay cambios a nivel estadístico en los distintos caminos de ensamblaje de masa para los OTEs: esto es, la fracción de OTE ensamblada a través de fusiones de diferentes características y diferentes tipos, cambia. Sin embargo, esto no tiene consecuencias significativas en promedio de los perfiles de masa o la distribución de velocidades en 3D. Es decir, la relajación de las distribuciones de masa y velocidad olvida los detalles sobre cómo se ha ensamblado la masa o se adquiere la velocidad. Esto no es muy sorprendente porque el equilibrio de los estados no depende de los caminos que han conducido a ellos. Manrique et al. (2003) han demostrado analíticamente un resultado similar en halos de materia oscura. En su modelo el perfil de densidad de los halos relajados se adapta permanentemente al perfil que se formaría a través de simple acreción y no depende de su historia pasada de agregación. Como consecuencia el perfil típico de densidad de los halos a una masa determinada y a una época dada es determinado por la tasa típica de acreción que evoluciona en el tiempo y depende del modelo cosmológico. Como consecuencia, este modelo predice la existencia de relaciones invariables en el tiempo entre los parámetros estructurales que describen estos halos (ver discusión en Salvador-Solé et al., 2005, 2007)

Finalmente discutiremos brevemente sobre algunos procesos físicos sub-escala que no han sido considerados explícitamente en nuestras simulaciones: el enriquecimiento metálico y la evolución estelar (supernovas y agujeros negros). En relación a lo primero, Martínez-Serrano et al. (2008) han incluido recientemente en el código DEVA la evolución química. Los resultados preliminares de las propiedades estructurales y cinemáticas de los objetos de tipo elíptica de las simulaciones cosmológicas han mostrado una buena concordancia con los resultados presentados en esta tesis. Los efectos de las supernovas y de núcleos galácticos activos (NGA) u otros inputs de energía diferente a la gravitacional no han sido incluidos explícitamente en estas simulaciones. Hay que destacar que el papel de las fuentes de energía discreta de origen estelar en las escalas resueltas por este trabajo no está aun clara. Argumentos teóricos (Efstathiou, 2000) sugieren que el efecto de las supernova se hace poco efectivo rápidamente en sistemas con velocidad de dispersión mayor de $100km \times s^{-1}$. De hecho, resultados obtenidos mediante simulaciones magneto-hidrodinámicas también indican que los efectos de la supernovas en la formación de galaxias son más importantes para galaxias de baja masa (Scannapieco et al., 2008). Por otra parte el efecto de los NGA puede ser importante en galaxias con una alta dispersión de velocidades (Silk & Rees, 1998; Ciotti & Ostriker, 2001) como las estudiadas en este trabajo. Sin embargo la naturaleza y la dirección en las que este fenómeno afecta a la formación estelar es poco clara (Silk, 2005) y merece la pena mencionar que hasta ahora los modelos solo incorporan el efecto negativo (inhibición la formación estelar) (ver Pipino et al., 2009, para una primera aproximación en la dirección contraria). Nuestro punto de vista es dejar la física de las simulaciones lo más simple posible y avanzar en la comprensión de la conducta del problema simplificado antes de investigar complejidades adicionales como la supernovas y los agujeros negros.

B.3 Trabajo Futuro

Se dice que en un trabajo como este, el desarrollo nunca termina definitivamente, solo se detiene momentáneamente. Esto es realmente cierto en este caso; existen un gran número de temas que pueden verificarse, pulirse, y añadirse. Pero en algún momento la línea debe detenerse. En el caso de este trabajo, nos hemos parado en el punto en que la aproximación está comenzando a demostrarse efectiva: tenemos un escenario cosmológico que es capaz de reproducir y explicar algunas de las correlaciones estructurales y cinemáticas mas fuertes observadas para las galaxias elípticas y que es robusto frente a cambios en los parámetros cosmológicos, la resolución espacial y en masa y el tamaño de la caja simulado.

En relación a nuestras herramientas, el desarrollo de una versión paralelizada del código ha tenido un impacto increíble, aumentando el número de partículas que pueden ser simuladas y abriendo la puerta del código DEVA a centros de computación de alto

rendimiento como el Leibniz Supercomputing Center. También Martínez-Serrano et al. (2008) acaba de introducir la evolución química en el código DEVA. Esto proporcionará la posibilidad de obtener variables directamente comparables con las observaciones a través del uso de modelos de síntesis de población estelar. Este hecho, junto con la ventaja de tener una versión paralelizada del código, ofrece sin duda una increíble cantidad de posibilidades para el futuro. En este sentido las herramientas de análisis desarrolladas en esta tesis son un instrumento sólido que puede ser utilizado como el tronco principal para el desarrollo de algoritmos y funciones que analicen las futuras simulaciones.

Appendix C

The Standard Cosmological Model

C.1 Introduction

Nowadays all our knowledge about the Universe as a whole is joined to form what it is called the standard cosmological model. The *Hot Big Bang* Model defines its general framework and, generally speaking, it could be said that it explains with incredibly accuracy the thermodynamical homogeneous evolution of the Universe. The theoretical background of the theory has suffered very little changes since its introduction in the beginning of the XXth century. However the observational side of cosmology has suffered a very different evolution. New technologies have made it possible a dramatic development and we are currently able of discussing a Standard Model of Cosmology with a fixed set of parameters bounded to at least a few percent accuracy in their values.

This Chapter will cover briefly the theoretical basics of the Hot Big Bang theory, describing the key observational facts that have corroborated it. Firstly in Section C.2 we set the basis and notation of the theory. In the following Sections we would briefly introduce the different observational great successes of the model: the Hubble law (Section C.3), Nucleosynthesis (Section C.4), the Cosmic Microwave Background (Section C.5) and the Formation of Large Scale Structure (Section C.6).

C.2 The Hot Big Bang Model

The Hot Big Bang Model is a broadly accepted description for the origin and evolution of our Universe. The model is based in two theoretical pillars: the theory of General Relativity (GR) and the Cosmological Principle.

To the extent of our present knowledge, the gravitation at large scales is correctly described by Einstein's GR. It is the mathematical structure for cosmology and provides the geometrical framework for cosmological models. Einstein demonstrated that

gravitation can be explained by the inertial motion in a curved space-time.

Since then, there have been some theoretical proposals to modify GR, however observations so far have not been able to discriminate between models. Many theoretical and experimental progresses are studying the problem; for the time being, the simplest, original GR remains in force.

Now, we can make use of all the old and new knowledge to describe the background evolution of the universe, or Hot Big Bang Cosmology. This section will only cover the basis about the Hot Big Bang model that it is needed as a theoretical context of this thesis. We refer to Weinberg (1972) for a complete description of General Relativity.

Working inside a general relativistic framework, we need to define a metric tensor, $g_{\mu\nu}$, in order to characterize the evolution and properties of space-time. Once specified, the space-time interval between two points is given by:

$$ds^2 = g_{\mu\nu} dx^\mu dx^\nu \tag{C.1}$$

In general $g_{\mu\nu}$ is coordinate dependent and ds^2 must be invariant under a change of coordinates.

Once one is provided with the gravity theory, one should introduce symmetries that restrict the large variety of possible cosmological models. For this, Einstein introduced the *Cosmological Principle*. It states that, on large scales, the universe is spatially homogeneous and isotropic. So far, its strongest support comes from the observed isotropy of the cosmic microwave background radiation (CMB). Homogeneity remains as a hypothesis, however if we assume that we do not occupy a privileged location in the Universe (Copernican principle), then isotropy leads to homogeneity.

The formulation of the Cosmological Principle applied to what we know of the metric lead us to the *Robertson-Walker metric*. The most general metric form describing this family of cosmological models can be written as follows:

$$ds^2 = c^2 dt^2 - R^2(t) \left[\frac{dr^2}{1 - kr^2} + r^2 (d\theta^2 + sin^2\theta d\phi^2) \right] \tag{C.2}$$

where t is the physical cosmic time and the constant k specifies the sign of the spatial curvature of the universe. The spatial terms have been decomposed into a product of a time-dependent scale factor $R(t)$ and comoving, time-independent, spherical coordinates r, θ, ϕ. A comoving observer is an observer who measures zero momentum at its own location or who sees an isotropic universe. Therefore, the cosmic time t, is the time measured by the comoving observers which are at rest with respect to the expansion. Using comoving coordinates allow distances, locations, etc. in an expanding homogeneous and isotropic cosmology to be related solely in terms of the scale factor.

One can make the scale factor dimensionless, defining:

$$a(t) \equiv \frac{R(t)}{R(t_0)} \tag{C.3}$$

where t_0 is the age of the universe today so that $a = 1$ at the present. It is useful to keep in mind the relationship between physical, $\vec{r}(t)$, and comoving coordinates $\vec{x}$, which applies to any cosmic distance:

$$\vec{r}(t) = a(t)\vec{x} \tag{C.4}$$

In cosmology it is useful to define time and distances in terms of the redshift, z. It is defined by:

$$z \equiv \frac{R(t_0)}{R(t)} - 1 = \frac{1 - a(t)}{a(t)} \tag{C.5}$$

The historical origin of its name comes from the analogy with the Doppler effect. Taking into account that $t < t_0$, if $R(t_0) > R(t)$, the universe is expanding and gives a red shift ($z > 0$) while if the universe is contracting, then $R(t_0) < R(t)$, and gives a blue shift. As we will see in the following section, observational data points to the first case.

The Cosmological Principle also restricts the form of the material content of the Universe. Since a perfect fluid can be characterized by its isotropy around observers comoving with the fluid, the energy-momentum tensor for the material content of Universe must have the perfect fluid form

$$T_{\mu\nu} = p g_{\mu\nu} + (\rho + \frac{p}{c^2}) u_\mu u_\nu \tag{C.6}$$

where p and ρ are respectively the pressure and the energy density measured by a comoving observer, and u_μ is the four velocity of the fluid, $u_\mu = dx_\mu/ds$.

Provided with the energy-momentum tensor, we can now move to the search for the relativistic field equations. However these equations cannot be derived in any rigorous sense; all that can be done is to follow Einstein and start by thinking about the simplest form such an equation might take. To obtain some insight into how this can be achieved, it is helpful to consider first the weak-field limit (for $v << c$ we have to recover Newton's theory) and the analogy with electromagnetism. Here we would just point that in a similar spirit to Maxwell's equation for the electromagnetic field Einstein derived the Einstein's Field equations (see Peacock, 1999, for the complete argumentation):

$$G_{\mu\nu} = \frac{8\pi G}{c^4} T_{\mu\nu} \tag{C.7}$$

Here $T_{\mu\nu}$ is the energy-momentum tensor, G is the Newton constant, c the light velocity and $G_{\mu\nu}$ is known as the Einstein field. He identified the gravitational field with the metric tensor $g_{\mu\nu}$. Once this relation is made, the Einstein field is characterized with

what we know about it at weak scale and with what is known of the energy-momentum tensor. We get,

$$G_{\mu\nu} = R_{\mu\nu} - \frac{1}{2}g_{\mu\nu}R = \frac{8\pi G}{c^4}T_{\mu\nu} \tag{C.8}$$

where $R_{\mu\nu}$ is the Ricci tensor, a contraction of the Riemann tensor, $R_{\mu\nu} = R^{\alpha}_{\mu\alpha\nu}$, with components:

$$\begin{aligned} R_{00} &= 3\frac{\ddot{R}}{R};\ R_{0i} = 0; \\ R_{ij} &= (\ddot{R}R + 2\dot{R}^2 + 2k)g_{ij} \end{aligned} \tag{C.9}$$

and R the Ricci, or curvature, scalar, $R = g^{\alpha\beta}R_{\alpha\beta}$.

In 1917 Einstein, in an attempt to balance the forces and preserve the previously accepted picture of a static universe, modified his equation introducing a term, the cosmological constant Λ, playing the role of a repulsive force (when $\Lambda > 0$), allowing the construction of a static universe.

$$G_{\mu\nu} + \Lambda g_{\mu\nu} = \frac{8\pi G}{c^4}T_{\mu\nu} \tag{C.10}$$

This term can be introduced in Einstein's equations if we consider also terms of zero order in second derivatives of the metric. The physical meaning of the cosmological constant can be seen as the curvature of empty space or, if we move the term to the right-hand side of the field equations, as the energy-momentum tensor of the vacuum. Therefore the existence of a cosmological constant dark energy different from zero, is equivalent to the existence of a non-zero vacuum energy.

Inserting Equations (C.2) and (C.6) into (C.10) lead to the Friedmann equations, that govern the expansion of space in homogeneous and isotropic models of the universe within the context of GR.

$$H^2 \equiv \left(\frac{\dot{R}}{R}\right)^2 = \frac{8\pi G}{3}\rho - \frac{kc^2}{R^2} + \frac{\Lambda c^2}{3} \tag{C.11}$$

and

$$2\frac{\ddot{R}}{R} + \left(\frac{\dot{R}}{R}\right)^2 = -8\pi G p + \Lambda c^2 - \frac{kc^2}{R^2} \tag{C.12}$$

where H is called the *Hubble parameter*. Its present value H_0 is the Hubble constant, usually expressed in terms of the dimensionless number h in the form $H_0 = 100 \times h \times km \times s^{-1} \times Mpc^{-1}$. From these two equations and the Bianchi identities[1] we can obtain

[1] These identities are obtained from the symmetries of the Riemann tensor and its covariant derivative.

a cosmological energy conservation law:

$$\frac{d}{dt}\left(\rho c^2 R^3\right) + p\frac{d}{dt}\left(R^3\right) = 0 \tag{C.13}$$

This equation is easily solvable if the equation of state of the fluid is specified. The various species entering the cosmological models are assumed to satisfy barotropic linear equations of state of the form $p = \omega\rho$ and $\omega = cons.$ All the cosmological models that use Friedmann equations and the equation of state are known as Friedmann-Robertson-Walker models.

In addition, it is useful to define the critical density of the universe as

$$\rho_c(t) = \frac{3H^2(t)}{8\pi G} \tag{C.14}$$

This is the energy density, obtained from Equation C.11, corresponding to a flat Universe ($k = 0$) and including the cosmological constant as a part of the total energy density ($\rho_\Lambda = \Lambda c^2/8\pi G$). Using this critical density we can redefine the density parameters as:

$$\Omega_i(t) = \rho_i(t)/\rho_c(t) \tag{C.15}$$

for each species, i, that could be present in the universe at different epochs: baryons (b), dark matter (DM), photons (γ), energy vacuum (Λ) and so on. With the density parameters we can rewrite Friedmann equations in the following form,

$$\Omega(t) = \sum_i \Omega_i(t) = 1 - \frac{kc^2}{a^2(t)H^2(t)} \tag{C.16}$$

that relates the density parameters to spatial curvature. The parameter $\Omega(t)$ is the value of the total energy density. When we refer to its value at the present epoch, we write Ω_0.

Using the last definition we can rewrite energy conservation (Equation (C.13) as

$$\frac{d(\Omega_i(t)H^2(t)a^{3+3\omega_i})}{dt} = 0 \tag{C.17}$$

allowing us to derive how each of the energy densities evolve with time

$$\Omega_i(t)H^2(t)a^{3+3\omega_i} = cons. = \Omega_{i,0}H_0^2 \tag{C.18}$$

We can also obtain how the scale factor $a(t)$ evolve with time in case one specie dominates the universe:

$$a(t) = \left(\frac{t}{t_0}\right)^{2/3(\omega+1)}. \tag{C.19}$$

Hence we can now calculate how all the different densities have evolved, and which

one has been more important over time. In Table C.1 we present energy density evolution for different contents of the universe.

type of content	ω	$n_i \equiv 3 + 3\omega_i$
stiff fluid	1	6
radiation and/or ultra-relativistic matter	$\frac{1}{3}$	4
cold non relativistic matter	0	3
vacuum energy	-1	0
"curvature"	$-\frac{1}{3}$	2

Table C.1: Energy density evolution for different contents of the Universe

Consequently, with all these findings we not only know that the evolution of the Universe depends on what it contents, we also know how each content will affect its evolution. From C.18 one can immediately see that at the beginning of times, when $a = 0$, $\rho = \infty$. That is, the solution has a singularity at that time, presumably at the Universe's beginning. This initial cosmological singularity is also called Big Bang singularity, and why Hot Big Bang theory has its name. Plugging in (C.18) in (C.16) we arrive at

$$H^2(t) = H_0^2 \left[\sum_i \Omega_{i,0} a^{-n_i(t)} - \frac{kc^2}{a^2(t)H^2(t)} \right] \tag{C.20}$$

and considering a Universe composed by radiation, no relativistic matter and with vacuum energy we get

$$H^2(t) = H_0^2 \left[\Omega_{\Lambda,0} - \frac{kc^2}{a^2(t)H^2(t)} + \Omega_{m,0} a^{-3}(t) + \Omega_{\gamma,0} a^{-4}(t) \right] \tag{C.21}$$

From the last equation we observe that in the general model, relativistic matter and/or radiation domain the expansion during the primitive Universe, follow by the non-relativistic matter and the curvature, finally expanding as the cosmological constant dictates. So one way to characterize a specific Friedmann-Robertson-Walker model is by just fixing actual values, H_0 and all the $\Omega_{i,0}$.

Equation (C.20) is the one usually used to describe the Big Bang Model Universe. In fact, a set of very different Universes, depending on the values that H_0 and all the $\Omega_{i,0}$ take. Here rather than going to all these possibilities we just resume what all these models have in common. In the Big bang model, the Universe has been evolving, starting from an initial, extremely dense, small and hot state, when the size of the universe was zero and the temperature was infinite. During the first fraction of a second, the initial temperature was so high as to allow equilibrium between matter and radiation. During the subsequent expansion the density and temperature fall and particles were moving with non-relativistic energies. The processes of formation of particle pairs gradually gave their way to those of nucleosynthesis and the formation of the first light element

abundances. Finally, the temperature was lowered to a point to permit the formation of structures through the action of gravity, responsible for the great concentrations of mass that would later form the stars and the galaxies. The spatial geometry of these models can either be positively curved, $k > 0$ (like the surface of a sphere), flat, $k = 0$ (like Euclid's space) or negatively curved, $k < 0$ (like a saddle). In the first case the volume of the Universe is finite, in the other two it can be infinitive.

Up to now we have seen all the theoretical development of the *Hot Big Bang Model*. But, why it has become our *Standard Cosmological Model*? Simply because it gives very good answers to a variety of independent observational facts. The four key observational successes of the standard Hot Big Bang model are the following: The Expansion of the Universe, Nucleosynthesis of the light elements, Existence of Cosmic Background Radiation and the Formation of Large Scale Structure. The Big Bang model makes accurate and scientifically testable hypotheses in each of these areas and the remarkable agreement with the observational data gives us considerable confidence in it.

C.3 The Expansion of the Universe: The Hubble Law

In 1929 E. Hubble found the *empirical Hubble law*

$$z = H_0 d_L \tag{C.22}$$

linearly relating the redshift of galaxies to their luminosity distance. The luminosity distance is defined as $d_L = \sqrt{L/4\pi F}$, where L is the absolute luminosity of the source and F its apparent luminosity, i. e. the flux of energy received in the collecting surface of the telescope. So, luminosity distance d_L is defined as such that a source of absolute luminosity L, located in a static Euclidean space, would produce a flux F at distance d_L.

In the approximation in which galaxies are comoving, the proper distance to a given galaxy scales with $a(t)$, and consequently its recession velocity V is related to its physical distance d at a given time by

$$V = Hd \tag{C.23}$$

So the Big Bang model gives as straightly the empirical Hubble Law! We can even go one step further, using instead of Euclidean metric the Robertson-Walker metric, which we know is the one that rules at large scales. It follows that the relation between d_L and the redshift parameter z is nonlinear. To second order this relation takes the form

$$H_0\, d_{\rm L}(z) = z + \frac{1}{2}(1 - q_0)z^2 + \cdots \tag{C.24}$$

where $q = -R\ddot{R}/\dot{R}^2$ is the *deceleration parameter* of the Universe and q_0 its present value. We can also write it, from Friedmann Equations (C.11-C.12), as a function of

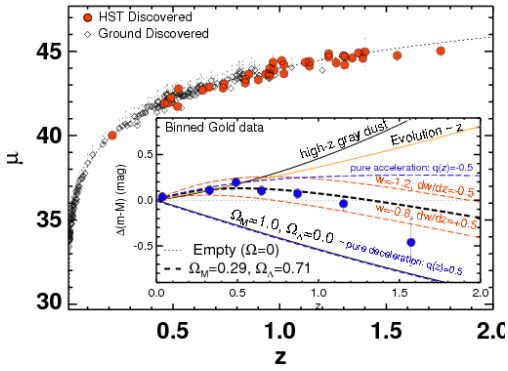

Figure C.1: Hubble law for SNe Ia: MLCS2k2 SN Ia Hubble diagram. SNe Ia from ground-based discoveries in the gold sample are shown as diamonds, *HST*-discovered SNe Ia are shown as filled symbols. Overplotted is the best fit for a flat cosmology. $\Omega_m = 0.29$, $\Omega_\Lambda = 0.71$. Inset: Residual Hubble diagram and models after subtracting empty universe model. Figure taken from Riess et al. (2007)

density parameters, $q = \Omega_m/2 + \Omega_\gamma - \Omega_k$. It follows then from RW metric, i. e. from Cosmological Principle, that the empirical Hubble law can be expected to be true only for $z \ll 1$. On the other hand for $z \ll 1$, the approximate equalities $d \approx d_L(z)$ and $V \approx z$ hold. Thus empirical and theoretical Hubble laws coincide in this regime. In this weak sense checking Hubble's law is also a check of the RW metric.

The accurately check of Hubble's law, measuring H_0 and eventually going deeper in redshift to determine q_0, has been a central research program in cosmology since 1929. The key observational tools for this endeavor are *standard candles*: luminous sources whose absolute luminosity has been properly calibrated. The most important ones, for being the most accurate are: Cepheids (local distance scale, Freedman et al., 2001), global properties of galaxies as The Fundamental Plane, the Faber-Jackson relation or the Tully-Fisher relation (up to 300 Mpc, Sakai et al., 2000; Bernardi et al., 2002) & Supernovas (large and very large scale, ∼400 Mpc or more, Riess et al., 2007; Kowalski et al., 2008). Also Sunyaev-Zel'dovich effect in clusters (Reese et al., 2002) and gravitationally lensed images of distant quasars (Outram et al., 2004) are starting to give some constrains on cosmological models. As observational methods improved we are capable of reaching higher redshifts, mainly thanks to Supernova data, constraining H_0 and specially q_0 with lower errors. Last results can be seen in Kowalski et al. (2008). From this work, here we show first a Hubble diagram C.1 and the cosmological constraints on Ω_m, Ω_Λ obtained just from Supernova data.

Relating with the Hubble parameter, it is possible to learn a good deal about the

past and future expansion of universe by simple inspecting Friedmann equations, even without specifying a definite equation of state. Since at present $R > 0$ by definition, $\frac{\dot{R}}{R} > 0$ because what we see are redshifts and no blueshifts and as long as $\rho + 3p$ remains positive, the acceleration $\ddot{R}/R$ is negative. Therefore it follows that the curve of $R(t)$ versus t must be concave, and must have reached $R(t) = 0$ at some finite time in the past. If we take $\ddot{R} = 0$ between this moment and now, we get that $R(t) = R(t_0)t/t_0$ and so the age of the universe would be just equal the Hubble time, H_0^{-1}. If we take the more realistic assumption of $\ddot{R} < 0$, we get a lower limit to the age of the Universe. t_0 must be less than the Hubble time $t_0 < H_0^{-1}$. So, in all Friedmann-Robertson-Walker models, measuring the current value of Hubble parameter, H_0, also give us an idea of what is the age of the universe. Therefore, for example, with $H_0 = 72 \pm 8 km \times sec^{-1} \times Mpc^{-1}$ (Freedman et al., 2001), we get a minimum age for our Universe of $t_0 = 13,97 Gyr$.

C.4 Nucleosynthesis

Another important point which Big Bang model has to give some answer is the origin of chemical elements and the abundances that we observe nowadays. G. Gamow was the first to propose a Big Bang nucleosynthesis in the early 50's, proposing some theoretical abundances of light elements that fit incredibly well with observations and that have suffered little variations since then. He also used the observed helium abundance to predict the existence of relic radiation in the microwave band. However these predictions require that, in order to match the observational data, the ratio of the number of baryons per photon, η, in the early Universe have a very low value. Since the discovery of the $3K$ background radiation (see next section) and the subsequent measure of this ratio, Gamow's ideas have been elaborated into one of the key ingredients of the big bang.

The very early Universe in the Big Bang Model is too hostile environment for nuclei. When the temperature stays above a few MeV (typical nucleon binding energy) photons will destroy any existing nuclei. Because of this reason, nucleosynthesis has to wait until the Universe has cooled down enough, approximately below $0.1 MeV$. At this temperature deuterons are able to survive transforming into helium. Finally some ^7Li is also formed. Why not higher nuclei? The reason is that the Universe is cooling down very fast and Coulomb barriers are higher for heavier nuclei, making cross-sections decline rapidly as temperature decreases. The heavier elements, of which we are partly made, were created later in the interiors of stars and spread widely in supernova explosions. The major interest of this theory is that it only needs one cosmological number, η, the number of baryons per photon

$$\eta \equiv \frac{n_b}{n_\gamma} = 2.68 x 10^{-8} (\Omega_b h^2) \tag{C.25}$$

where n_b is the density of baryons and n_γ is the density of photons. Ω_b is the contribution

of baryonic particles to total non-relativistic matter, $\Omega_b = \Omega_m f_b$. In this sense Big Bang Nucleosynthesis (BBN) gives us independent constrains on Ω_b, therefore on Ω_m. As we will see, the exact value of f_b is not yet clear but it seems quite confirmed that is not one (see below C.6). It is important to note that given η, all the abundance predictions are based in standard particle physic. Therefore, one feature of BBN is that the physical laws and constants that govern the behavior of matter at these energies are very well understood, and hence BBN lacks some of the speculative uncertainties that characterize earlier periods in the life of the universe. Another feature is that the process of nucleosynthesis is determined by conditions at the beginning of this period of the life of the universe, making what happens before irrelevant. Theoretical calculations for these nuclear processes predict abundances for: H, ^2D, ^3He, ^4He of ^4Li. One of

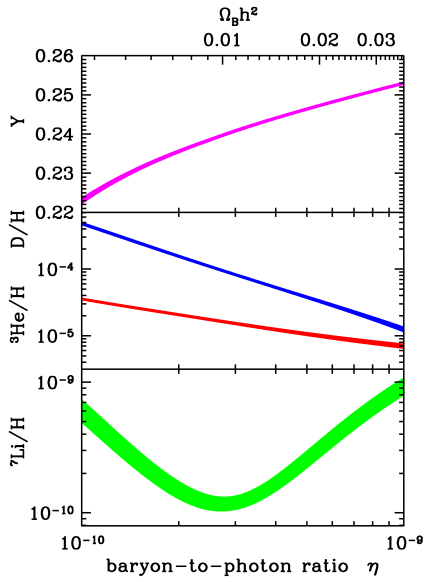

Figure C.2: Nucleosynthesis abundance predictions. Abundance predictions in function of τ, from Cyburt et al. (2003).

the most important, in terms of confirming Big Bang Model, is the abundance for ^4He. Nucleosynthesis predicts that about a quarter of the Universe consists of ^4He, a result which is in great agreement with current stellar observations. We remit the reader to Iocco et al. (2008) for a complete revision of the area and the last observational results.

C.5 Existence of a Cosmic Microwave Background

Another important prediction of the Big Bang model, first addressed by Gamov (1946), is the existence of a Cosmic Microwave Background (CMB). If the universe was once very hot and dense, the photons and baryons would have formed a plasma, i.e., a gas of ionized matter coupled to the radiation through the constant scattering of photons off ions and electrons. As the universe expanded and cooled it comes a point when the radiation (photons) decoupled from the matter. From this time onwards, radiation was effectively unable to interact with the background gas; it has propagated freely ever since, while constantly losing energy because its wavelength is stretched by the expansion of the Universe. We can model the time last scattering by a visibility function, which measures the probability that a particular photon last scattered in a redshift interval dz. Conveniently, this proves to be well approximated by a Gaussian at mean redshift $z \approx 1100$ with width $\Delta z \approx 80$, pretty much independent of all cosmological parameters (Jones & Wyse, 1985). Originally, the radiation temperature was about 3000 degrees Kelvin, whereas today it should has fallen to only 3K.

The CMB radiation was discovered in 1965, by Penzias and Wilson. Currently the best information on the spectrum of the CMB comes from the FIRAS instrument on the COBE satellite (Fixsen et al., 1996): CMB spectrum is that of a nearly perfect blackbody with a temperature of 2.725 ± 0.002 K (See C.3).

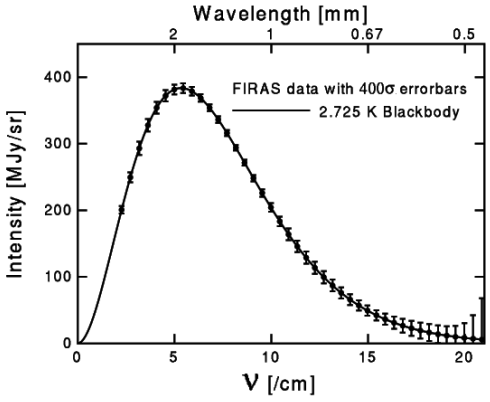

Figure C.3: CMB: Black Body radiation. Measurements of the spectrum of CMB from COBE satellite Fixsen et al. (1996).

This result shows that the temperature of the CMB is almost the same all over the sky. Thus the microwave sky is extremely isotropic. But there is also a great deal to be learned from this "almost" and the distribution of microwave background in angle. As we will see in the following section these *anisotropies* can be related with the formation of galaxies and clusters. The origin of anisotropies can be due to a various set of physical processes that: gravitational (Sachs Wolfe) perturbations, intrinsic (adia-

batic) perturbations, velocity (Doppler) perturbations and scattering along line-of sight (Rees-Sciama effect, Sunyaev-Zeldovich effect). For a further insight see e.g. Bond et al. (1997). All these dependencies make the CMB fluctuations very dependent of the cosmological model. The study of CMB fluctuations has subsequently blossomed into a critical tool for pinning down cosmological models. As the CMB temperature distribution in the sky, being a function defined on a sphere is most naturally analyzed through a spherical harmonics expansion

$$T(\theta,\phi) = \sum_{lm} a_{lm} Y_{lm}(\theta,\phi) \tag{C.26}$$

The monopole component gives the mean temperature of CMB, 2.725 ± 0.002. The largest anisotropy is the $\ell = 1$ dipole term interpreted as the result of the Doppler shift caused by the Solar system motion relative to the CMB. Once the monopole and the dipole have been removed from the expansion, we are left with the CMB intrinsic anisotropies which are of the order of 10^{-5}, or below in all angular scales, and contain the imprints of the early Universe physics at radiation-matter decoupling. Most of the cosmological information is contained in the two point temperature-temperature (TT) correlation function. This quantity is defined by averaging the product of the fractional temperature deviations in directions $\vec{n}$ and $\vec{n'}$ over the sky, and expanding the result in Legendre polynomials

$$C(\theta) \equiv \langle \frac{\Delta T(\vec{n})}{T} \frac{\Delta T(\vec{n'})}{T} \rangle = \sum_{\ell=0}^{\infty} \frac{2\ell+1}{4\pi} C_l P_l(\cos\theta) \tag{C.27}$$

The expansion coefficients C_l, when represented as function of ℓ (more suitably $\log \ell$) give the so-called *angular power spectrum* which is the key function in comparing theory with observations. Distinct physical processes (some at very different scales) are linked with a specific range of C_l coefficients. In this sense, a set of hypotheses on physical processes lead to predictions on the values of C_l coefficients, therefore predictions on the power spectrum function. On the other hand we have that these processes are intrinsically related with cosmological parameters so, hypotheses just mentioned before are hypotheses on the values of cosmological parameters. Therefore studying the power spectrum is the way in which cosmological model can be deduced from CMB observations. A more complete description of physics contained in C_l can be found in Peacock (1999).

Electron-photon Thomson scattering at the last scattering surface transforms anisotropies into CMB photons polarization. The analysis of polarization leads to four new non-vanishing two sky points correlation, with its corresponding angular spectra (TE power spectrum). Inclusion of polarization measurements help to better constrain some of the cosmological parameters, by probing the ionization history of the universe, therefore

better constraining the optical depth at reionization and breaking degeneracies of this with other parameters. The theoretical and observational analysis of these spectra lies at the present frontier of CMB research (Komatsu et al., 2009).

The first map of CMB anisotropies was obtained with COBE satellite. After COBE a series of ground and balloon based measurements: ARCHEOPS, BOOMERANG, DASI, MAXIMA, VSA, CBI, ACBAR, have been carried out to improve the quality of temperature anisotropies data. The most recent advance has been the five years of operation results from NASA's WMAP (Wilkinson Microwave Anisotropy Probe, Dunkley et al., 2009; Komatsu et al., 2009). This work corresponds to a twofold full coverage of sky and provides a much more precise anisotropies map and by itself it definitely make some strong constrains on several cosmological parameters.

Parameter		Mean (68% confidence range)
Total density	Ω_{tot}	$1.09^{+0.01}_{-0.085}$
Dark energy density	Ω_Λ	0.742 ± 0.030
Baryon density	$\Omega_b h^2$	0.0441 ± 0.0030
Hubble constant	h	$0.719^{-0.026}_{+0.027}$
Galaxy fluctuation amplitude	σ_8	0.796 ± 0.036

Table C.2: Cosmology from CMB anisotropies measured by WMAP. Recommended parameters values derived from WMAP data only (Dunkley et al., 2009).

C.6 Formation of Large Scale Structure

Although the isotropic microwave background indicates that the universe in the past was extraordinarily homogeneous, we know that the universe today is far from homogeneous: there are regions in which matter is strongly clumped forming galaxies, clusters and even larger structures, whereas at the same time, we can also find almost empty regions with very low densities.

So, the standard Hot Big Bang model also provides a framework in which to understand the collapse of matter to form galaxies and other large-scale structures observed in the Universe today. These structures are expected to arise from very small primordial inhomogeneities. When the temperature had fallen to such an extent that the energy density of the Universe began to be dominated by massive particles, rather than the light and other radiation which had predominated earlier, gravitational forces between the massive particles could begin to take effects, so that any small perturbations in their density would grow. These inhomogeneities can be characterized as

$$\delta(\vec{x}) \equiv \frac{\delta\rho(\vec{x})}{\bar{\rho}} = \frac{\rho(\vec{x}) - \bar{\rho}}{\bar{\rho}} \tag{C.28}$$

where $\bar{\rho}$ is the average density of the Universe, and $\rho(\vec{x})$ is the density of the Universe at the point $\vec{x}$, and they must have left some trace as temperature anisotropies in the microwave background.

In the search of these traces a popular statistical characterization of inhomogeneities in the distribution of cosmic structures is provided by a two-point correlation function, ξ, which describes the expected excess fluctuations with respect to a uniform distribution:

$$\xi(r) = \langle \delta_{\vec{x}} \delta_{\vec{x}+\vec{r}} \rangle \tag{C.29}$$

where the symbol $\langle\rangle$ indicates the average over all the pairs of points at separation r.

It is often convenient to consider building up a general field by superposition of many modes. So density contrast is commonly expanded into a Fourier expansion

$$\delta(x) = \frac{V}{(2\pi)^3} \int_{vol} \delta_k e^{-ik\cdot x} d^3k \tag{C.30}$$

$$\delta(k) = \frac{1}{(V)} \int_{vol} \delta_x e^{-ik\cdot x} d^3x \tag{C.31}$$

In this context we define the Fourier transform of ξ as the power spectrum $P(k)$

$$P(k) \equiv \langle |\delta_k|^2 \rangle \tag{C.32}$$

In earlier literature, attention normally was focused on determining the two point correlation function, $\xi(r)$. We have seen the definition of this for a continuous field such as the matter-density distribution Equation (C.29), for a discrete field, such as a collection of galaxy locations, the definition must be phrased more carefully. The galaxy two-point correlation function ξ_{gal} can be defined in terms of the probability of finding two galaxies within small volumes dV_1 dV_2 a distance r apart:

$$Prob = n^2 \left(1 + \xi_{gal}(r)\right) dV_1 dV_2 \tag{C.33}$$

where n is the mean galaxy number density. Notice that for a random distribution $\xi_{gal}(r)$ is 0. One thing we have to keep in mind is that while we are measuring *observable* matter what we really would like to know is about the distribution of all matter. There is no a priori reason why galaxy distribution should be a good tracer of mass distribution in the Universe. Indeed, observations show that it definitely cannot be; the correlation functions for, to give an example, galaxies selected optically and galaxies selected in the infrared are different and hence clearly cannot both trace the mass distribution accurately. This effect is known as *bias* in the galaxy distribution, and it seriously impairs our abilities to use it to constrain the matter spectrum. The statistical analysis of galaxy bias is based on the key idea of peak biasing. In this scenario, galaxies are

fairly rare objects forming from peaks in the matter distribution. The rarer the peaks, probability of a peak being near another peak is enhanced (Bardeen et al., 1986).

Measuring the current Power Spectrum is one of the most challenging features in modern cosmology. It tells us all that there is to know about statistical properties of the density field. During last years scientist have done a great effort in improving the accuracy of power spectrum measurements. Nowadays, for the power spectrum we have a complete set of independent measurements that shows a general good agreement with this scenario (Seljak et al., 2005; Massey et al., 2007; Komatsu et al., 2009).

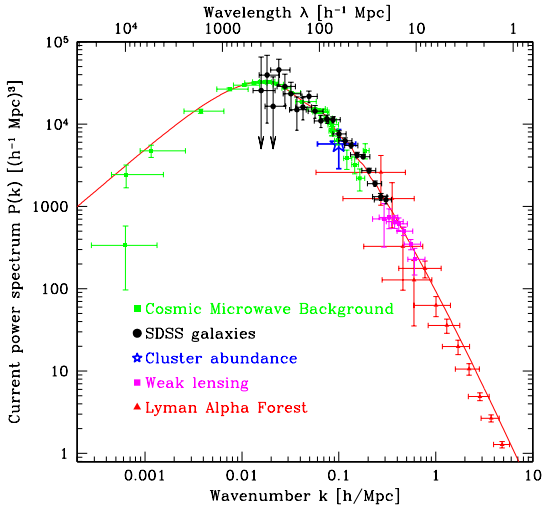

Figure C.4: Power Spectrum measurements. Measurement of the Power Spectrum from a set of different observables: CMB, SDSS, Weak lensing and Lα Forest (Tegmark et al., 2004). Solid line correspond to a $\Omega_m = 0.28$ $h = 0.72$ $\Omega_b/\Omega_m = 0.16$ Universe.

The Dark Matter

CMB anisotropies not only confirm that in the total amount of matter that encloses the Universe ($\sim$ 25% of the total energy), just $\sim$ 20% is baryonic matter (see Table C.2). The Ω_b value obtained from CMB is also in concordance with the nucleosynthesis theory (see Section C.4). Therefore everything point to a non baryonic dark matter to make

the total of matter that observations require. Moreover we have more cosmological probes. We know from measurements of the cosmic microwave background that the Universe was extraordinarily homogeneous in the past. At the present epoch, however, the Universe is no longer particularly homogeneous: it contains galaxies, clusters of galaxies, superclusters etc. This large scale structure is believed to arise from small primordial inhomogeneities that grow via gravitational instability. However ordinary baryonic density perturbations cannot begin to grow because of radiation pressure until photon decoupling occurs at a temperature of around $T_{dec} \sim 3000K$, corresponding to a redshift of $z_{dec} \sim 1100$. But this is too late, perturbations which have amplitude of order $\delta \sim 10^{-5}$ (as inferred from the anisotropies of the cosmic microwave background) do not have enough time to grow into galaxies, where $\delta \sim 10^{3-4}$. This suggests that inhomogeneities begin to grow prior to photon decoupling. This is one role that non-baryonic dark matter is expected to fill, it should be weakly coupled to the ordinary particles in the plasma so that density perturbation growth can begin prior to photon decoupling. In the context of the Big Bang Model is easy to think in a weekly interacting relic particle to make the role of dark matter.

On the other hand, in addition of all these *cosmological* evidences, we have also some solid *astrophysical* evidences. As dark matter consist in matter particles that cannot be detected by their emitted radiation, its presence should be inferred from gravitational effects on visible matter such as galaxies, groups and clusters. The first of all these indirect proofs was made by Zwicky (1933) studying the velocity dispersions of Coma Cluster and obtaining higher Mass-to-light ratios than expected if this object was just formed by baryonic matter. This kind of study in clusters has been improved since then, showing basically the same conclusions. Masses of clusters have been also calculated from X-Ray Hot gas (Arnaud, 2005) and from gravitational lensing (Squires et al., 1996) confirming this result. Also just analyzing total luminosity density values, and taking into account a minimum limit for ω_m (from nucleosynthesis, for example) leads us to mass-to-light ratios that suggest the existence of some more matter than normal stellar populations (Efstathiou & Rees, 1988). Another important evidence is the existence of flat rotation curves in galaxies rather than the Keplerian fall-off rotation curve. An example is showed in Figure C.5. More details can be found in (Corbelli & Salucci, 2000; Jimenez et al., 2003). See also (Romanowsky et al., 2003) for some surprising results on this subject. There is also ample evidence for dark matter in dwarf galaxies (Colín et al., 2004).

By all this, the existence of dark matter is a very solid state in modern cosmology. However what particle, or particles, forms dark matter and which are their properties is not a closed question. Although we can make some interesting constraints. As we just mention dark matter has enormous implications in the formation of structures because it determines the final density distribution at different scales. Taking into account this fact,

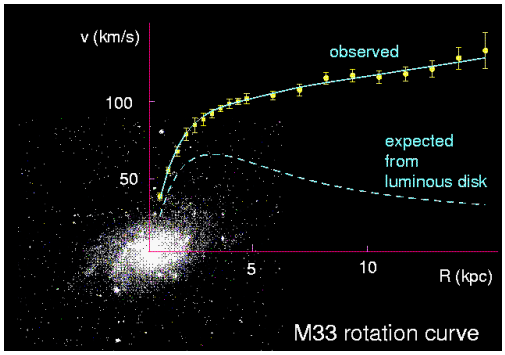

Figure C.5: Rotation curve: Dark matter. This rotation curve implies that near 90% of the galaxy mass cannot be seen. Figure from Foot (2004).

usually all particle candidates classify in three generic types: Hot Dark Matter (HDM), Warm Dark Matter (WDM) and Cold Dark Matter (CDM). Hot dark matter would be particles with very small mass ($\sim eV$) that travel with relativistic velocities because they would have decoupled from radiation when relativistic. Fast moving particles, however, cannot clump together on small scales and, in fact, they can escape from overdense regions into underdense ones, erasing the density fluctuations on scales smaller than the free-streaming scale λ_{fs}. Typical values are $\lambda_{fs} \sim 40Mpc$. In the hot dark matter paradigm, popular in the early eighties, structure forms by fragmentation (top-down), with the largest superclusters forming first in flat pancake-like sheets and subsequently fragmenting into smaller pieces like our galaxy. On the opposite side, if the relic particles decouple when they are nonrelativistic, mass can apparently be as large as desired. If decoupling occurs at very high redshift, the horizon scale at that time is very small and so negligible damping occurs through free streaming. Structure formation in a CDM universe is then a hierarchical process in which nonlinear structures grow via the merger of very small initial units. There is also a middle point approach known as warm dark matter model originally introduced to solve some apparent problems of the CDM model. To reduce the present-day velocity while retaining particles that decouple when relativistic, or in other words, to retain low-mass particles ($1 - 10keV$) while still allowing a short of hierarchical scenario. However latest observations go in the direction of CDM model predictions (Bullock et al., 2000; Kochanek & Dalal, 2003; Primack, 2004; Tegmark et al., 2004; Pratt & Arnaud, 2005; Pointecouteau et al., 2005). Here we present Figure C.6.

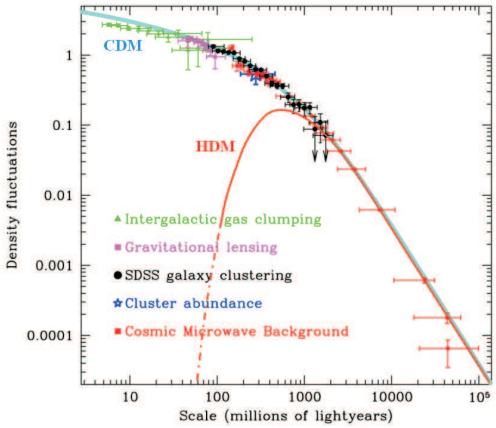

Figure C.6: Cold Dark Matter vs Hot Dark Matter

C.7 Conclusions

Through this Chapter we have presented a general view of the Big Bang Model and its observational pillars. The union of these ideas conform what is known as *the standard cosmological model* which, during last decades all observational data have consolidated. But, although consolidated, we had a wide set of possible Universes very different one from each other. In the past few years, with the advent of new generation of observational projects (WMAP, SN projects, Hubble telescope, SDSS, 2dF) we have entered in what has been called "precision cosmology". In this new era we are being able of ruling out false Universes by constraining all cosmological parameters. We have seen that all these experiments, one by one and independently, offer results that consolidate the standard model and reduce the number of possible Universes. The fact that all these experiments agree in the most probable model is fascinating and has lead us to what is call the *concordance model*. This model corresponds with a flat Universe, with cosmological constant and formed by baryonic matter and cold dark matter. Combining results from the different experiments we can even achieve more precision in the cosmological parameters (Dunkley et al., 2009; Komatsu et al., 2009). Table C.3 shows best fit cosmological parameters using CMB (WMAP and small scale measurements), SDSS and SNIa data:

Parameter		Mean ± 68% confidence range
Total density	Ω	1.0052 ± 0.0064
Dark energy density	Ω_{Lambda}	0.721 ± 0.015
Baryon density	Ω_b	0.0462 ± 0.0015
Optical depth	τ	0.084 ± 0.016
Spectral index	n_s	$0.960^{+0.014}_{-0.013}$
Galaxy fluctuation amplitude	σ_8	0.817 ± 0.026
Hubble constant	h	0.701 ± 0.013
Age of the Universe	t_0	$(13.73 \pm 0.12)x10^9$ years

Table C.3: Some of the derived cosmological parameters using WMAP+SN+BAO data, see Dunkley et al. (2009).

So we are living in a Lambda-Cold Dark Matter ΛCDM Universe. This model is able to explain a huge amount of precise and independent observational data as cosmic microwave background observations (WMAP), as well as large scale structure observations (2dF,SDSS) and supernovae observations of the accelerating expansion of the universe (SN). However, although ΛCDM model has been consolidated with unexpected robustness and precision, there are still major open questions that need to be answered and are far beyond the scope of this thesis. Some examples are, the origin of the cosmological constant, the dark matter particle and the formation of the Hubble sequence.

Appendix D

Data Tables

This Appendix presents all the fundamental structural and kinematical parameters of the different ELO samples studied in this thesis. In Table D.1 parameters discussed in Chapter 6 can be found. Table D.2 includes the shape and rotational parameters considered in Chapter 7. Values for these variables at higher redshifts, examined in Chapter 8, can be found in Tables D.3, D.4 ($z = 0.5$ ELO samples), D.5, D.6 ($z = 1$ ELO samples) and D.7, D.8 ($z = 1.5$ ELO samples).

Table D.1: Masses, sizes and mean square velocities at the halo and baryonic object scale, as well as their projected counterparts ($z = 0$). Masses are given in 10^{10} $M_\odot$, distances in kpc, velocity dispersions in $km \times s^{-1}$.

$z = 0$		Halo scale					Stellar scale					Projected stellar scale				
sim	ELO	$M_{\rm vir}$	$M_{\rm h}^{\rm bar}$	$r_{\rm vir}$	$r_{\rm e,h}^{\rm tot}$	$\sigma_{3,\rm h}^{\rm tot}$	$M_{\rm bo}^{\rm star}$	$M_{\rm bo}^{\rm cb}$	$r_{\rm e,bo}^{\rm star}$	$r_{90,\rm bo}^{\rm star}$	$\sigma_{3,\rm bo}^{\rm star}$	$M_{\rm cyl,bo}^{\rm star}$	$R_{\rm e,bo}^{\rm star}$	$R_{90,\rm bo}^{\rm star}$	$\sigma_{\rm los,0}^{\rm star}$	n
A sample																
8714	#173	772.82	70.65	527.00	222.53	278.46	42.59	43.12	17.45	96.12	337.54	42.57	12.89	74.12	227.74	11.23
8714	#353	322.18	31.60	394.00	110.99	246.99	25.17	25.62	10.79	63.11	282.37	25.17	8.15	50.61	198.53	6.72
8714	#581	177.03	18.94	322.00	101.54	189.58	13.45	13.70	9.11	44.06	208.84	13.45	6.64	34.67	142.26	4.25
8714	#296	153.52	16.79	308.00	92.12	192.28	11.95	12.14	6.22	49.40	211.85	11.94	4.56	38.02	145.47	5.19
8714	#399	–	–	–	–	–	7.02	7.28	5.12	32.95	174.26	6.21	3.13	14.19	118.34	3.22
8714	#373	74.00	8.35	241.00	66.65	153.91	7.23	7.38	5.14	34.12	175.57	7.23	3.77	26.31	120.45	4.74
8714	#772	60.71	7.50	226.00	56.57	149.76	5.51	5.62	3.02	22.44	173.73	5.51	2.29	16.80	124.48	5.55
8714	#284	53.76	6.86	217.00	67.69	138.90	4.77	4.91	2.75	13.80	166.06	4.77	2.04	10.77	111.91	7.53
8714	#398	–	–	–	–	–	4.48	4.77	3.08	27.21	204.91	4.48	2.40	20.97	122.74	4.22
8714	#156	–	–	–	–	–	3.72	3.82	2.15	13.42	142.23	3.72	1.68	10.60	100.57	2.92
8714	#173	–	–	–	–	–	3.59	3.76	1.92	9.84	158.44	3.59	1.49	7.63	105.95	3.59
8747	#317	–	–	–	–	–	35.07	35.17	11.31	43.98	345.09	35.06	8.02	34.97	242.87	7.21
8747	#288	285.17	29.83	378.00	112.14	229.15	20.04	20.08	10.82	41.20	258.21	20.04	7.77	33.24	177.99	7.86
8747	#348	–	–	–	–	–	9.56	9.65	3.84	14.61	236.58	9.55	2.95	11.64	150.95	7.40
8747	#115	178.07	17.62	323.00	95.55	204.18	12.17	12.21	3.89	32.04	240.20	12.17	3.01	24.77	172.48	5.02
8747	#100	–	–	–	–	–	5.32	5.52	3.24	17.84	172.49	5.31	2.32	13.71	124.55	4.48
8747	#189	45.15	5.77	205.00	58.45	141.87	4.68	4.74	3.40	16.46	163.82	4.68	2.62	13.14	116.64	2.83
8747	#114	–	–	–	–	–	4.14	4.48	2.37	16.30	164.90	4.14	1.78	12.51	112.03	3.36
8747	#915	38.63	5.51	194.00	47.74	133.76	4.32	4.52	2.89	13.27	155.92	4.32	2.20	10.04	107.60	2.63
8747	#317	–	–	–	–	–	4.06	4.11	1.82	11.03	153.44	4.06	1.39	8.60	103.63	3.83
8747	#200	–	–	–	–	–	3.73	3.95	2.51	11.57	153.40	3.72	1.90	8.86	96.92	2.28
8747	#216	–	–	–	–	–	3.72	3.84	2.23	13.71	153.23	3.72	1.70	10.63	103.02	3.27
8747	#102	–	–	–	–	–	3.61	3.67	2.20	12.57	151.75	3.61	1.66	9.59	109.66	3.83

$z = 0$		Halo scale					Stellar scale					Projected stellar scale				
sim	ELO	$M_{\rm vir}$	$M_{\rm h}^{\rm bar}$	$r_{\rm vir}$	$r_{\rm e,h}^{\rm tot}$	$\sigma_{3,\rm h}^{\rm tot}$	$M_{\rm bo}^{\rm star}$	$M_{\rm bo}^{\rm cb}$	$r_{\rm e,bo}^{\rm star}$	$r_{90,\rm bo}^{\rm star}$	$\sigma_{3,\rm bo}^{\rm star}$	$M_{\rm cyl,bo}^{\rm star}$	$R_{\rm e,bo}^{\rm star}$	$R_{90,\rm bo}^{\rm star}$	$\sigma_{\rm los,0}^{\rm star}$	n
8741	#617	–	–	–	–	–	8.61	8.67	3.09	17.81	245.01	8.60	2.33	14.01	156.82	10.35
8741	#011	273.34	30.12	373.00	102.20	229.07	15.72	15.72	5.07	18.43	272.52	15.71	3.83	15.02	184.57	6.86
8741	#218	–	–	–	–	–	11.32	11.37	4.63	12.11	309.96	11.31	3.32	10.18	187.84	4.65
8741	#218	–	–	–	–	–	12.49	12.67	6.34	27.95	220.18	12.49	4.74	22.23	148.22	4.54
8741	#017	141.44	16.33	299.00	89.04	181.96	10.15	10.32	5.48	28.71	213.59	10.15	3.97	21.34	148.01	5.02
8741	#930	135.71	13.70	295.00	89.82	190.12	8.85	8.95	6.33	38.83	205.01	8.85	4.71	30.26	143.96	5.87
8741	#945	107.34	12.63	273.00	78.06	172.06	9.89	10.00	6.23	37.65	191.49	9.89	4.55	29.60	135.21	4.90
8741	#097	108.18	11.33	274.00	73.36	176.73	9.34	9.46	6.75	37.61	195.93	9.34	5.09	29.23	142.03	4.41
8741	#907	55.15	6.35	219.00	50.61	154.04	5.55	5.63	3.46	19.66	179.41	5.55	2.62	15.86	129.92	4.29
8741	#015	–	–	–	–	–	4.35	4.52	2.39	19.22	164.43	4.35	1.81	14.15	107.78	3.88
8741	#907	–	–	–	–	–	3.47	4.02	1.72	15.45	149.46	3.47	1.32	12.02	99.44	2.99
8741	#617	–	–	–	–	–	7.92	7.99	3.81	21.94	202.20	7.92	2.83	17.35	139.33	5.76
8742	#293	–	–	–	–	–	12.33	12.36	3.52	7.89	321.62	12.28	2.59	6.56	198.52	2.33
8742	#234	296.59	29.86	383.00	101.79	244.83	27.13	27.41	12.74	76.04	276.34	27.13	9.45	59.68	202.21	6.99
8742	#283	160.41	16.60	312.00	87.69	211.82	13.44	13.51	5.95	35.49	234.44	13.44	4.49	28.29	158.35	6.03
8742	#254	147.26	16.98	303.00	100.62	178.97	10.81	10.91	6.10	29.11	201.15	10.81	4.60	22.95	137.59	3.99
8742	#092	75.03	9.14	242.00	84.18	142.24	6.38	6.52	4.35	23.09	161.11	6.38	3.23	18.78	114.91	6.18
8742	#896	–	–	–	–	–	3.93	4.04	2.48	11.49	151.36	3.93	1.83	8.55	98.67	3.49
8742	#316	–	–	–	–	–	3.47	3.71	2.75	14.86	125.02	3.47	2.12	11.32	91.78	2.35
8742	#898	–	–	–	–	–	2.90	3.07	2.42	12.75	142.19	2.89	1.79	10.23	93.41	5.54
8742	#893	–	–	–	–	–	2.91	3.06	2.40	13.14	135.19	2.91	1.82	10.19	95.93	2.97
8743	#647	–	–	–	–	–	26.40	26.47	8.73	33.07	313.38	26.40	6.38	26.68	217.02	5.60
8743	#563	–	–	–	–	–	15.15	15.18	6.59	22.59	255.24	15.14	4.63	18.13	171.90	4.64
8743	#238	327.12	33.03	396.00	116.33	239.60	20.88	20.95	9.24	35.72	274.42	20.89	6.80	28.82	188.43	6.55
8743	#328	66.83	8.62	233.00	56.61	158.46	7.60	7.76	4.51	25.65	179.72	7.60	3.42	20.33	125.22	3.79
8743	#515	56.33	6.79	220.00	56.20	156.30	5.63	5.73	3.48	17.93	177.56	5.63	2.53	13.80	127.91	3.16
8743	#437	52.65	6.78	215.00	54.73	143.64	4.70	4.78	3.17	21.88	163.29	4.70	2.42	16.92	110.22	4.34
8743	#421	36.75	4.69	191.00	46.77	135.19	3.81	3.91	2.89	15.69	155.82	3.81	2.17	12.14	113.23	4.62
8743	#555	–	–	–	–	–	3.42	3.63	2.02	10.99	139.81	3.42	1.55	8.58	105.79	3.87

$z = 0$		Halo scale					Stellar scale					Projected stellar scale				
sim	ELO	$M_{\rm vir}$	$M_{\rm h}^{\rm bar}$	$r_{\rm vir}$	$r_{\rm e,h}^{\rm tot}$	$\sigma_{3,\rm h}^{\rm tot}$	$M_{\rm bo}^{\rm star}$	$M_{\rm bo}^{\rm cb}$	$r_{\rm e,bo}^{\rm star}$	$r_{90,\rm bo}^{\rm star}$	$\sigma_{3,\rm bo}^{\rm star}$	$M_{\rm cyl,bo}^{\rm star}$	$R_{\rm e,bo}^{\rm star}$	$R_{90,\rm bo}^{\rm star}$	$\sigma_{\rm los,0}^{\rm star}$	n
8743	#637	–	–	–	–	–	3.40	3.51	3.02	13.54	141.83	3.40	2.26	10.68	105.47	2.92
8743	#239	–	–	–	–	–	2.93	3.21	1.50	12.94	142.79	2.93	1.20	9.82	94.08	3.87
8743	#626	–	–	–	–	–	2.88	3.13	2.52	15.77	108.65	2.88	1.99	12.43	84.98	1.82
8743	#437	–	–	–	–	–	2.85	3.10	1.78	11.94	129.76	2.85	1.39	8.75	89.37	3.37
B sample																
8716	#173	753.34	64.75	523.00	230.70	283.01	38.07	39.11	9.19	53.39	346.06	38.07	6.83	42.33	242.82	9.46
8716	#253	312.64	27.42	390.00	109.32	251.09	22.54	22.98	5.86	35.85	292.47	22.54	4.43	28.89	203.14	6.62
8716	#581	170.89	17.25	319.00	100.06	196.95	12.46	13.01	4.35	25.33	230.67	12.46	3.22	19.96	158.88	5.08
8716	#296	153.65	16.36	308.00	93.98	193.67	10.43	10.87	3.36	18.66	196.67	10.43	2.43	13.94	152.17	3.95
8717	#317	739.03	62.44	519.00	157.32	334.98	36.51	36.87	7.87	37.14	346.89	36.51	5.65	29.36	248.82	7.61
8717	#288	280.20	28.17	376.00	108.00	233.88	18.25	18.51	4.60	28.36	271.59	18.24	3.47	21.90	174.32	7.87
8717	#348	222.99	23.15	348.00	111.59	212.37	14.84	15.36	4.79	27.15	244.67	14.83	3.53	21.22	162.86	5.99
8721	#011	271.20	28.36	372.00	105.34	229.84	16.62	16.70	2.90	12.37	272.72	16.61	2.11	9.64	185.62	3.71
8721	#945	107.97	12.45	274.00	78.03	172.92	9.30	9.99	3.15	23.01	193.20	9.30	2.42	17.82	148.29	5.61
8721	#097	106.32	10.54	272.00	73.94	175.11	8.34	8.61	3.21	18.75	202.01	8.34	2.37	14.86	139.77	6.17
8722	#293	729.97	65.54	516.00	151.34	317.31	42.75	43.56	12.77	44.49	344.31	42.74	8.95	35.36	225.74	6.59
8722	#234	292.30	27.44	381.00	100.25	247.54	22.28	22.38	4.82	29.53	298.88	22.28	3.51	22.50	218.03	7.54
8722	#283	157.20	15.78	310.00	86.87	217.34	12.51	12.67	2.86	18.77	244.91	12.50	2.11	14.64	177.41	7.00
8722	#254	145.18	16.04	302.00	102.95	181.11	11.52	11.97	3.51	24.58	197.69	11.52	2.70	19.43	140.69	3.84
8723	#647	773.24	71.59	527.00	182.08	310.61	27.62	27.76	5.16	24.67	331.10	27.61	3.86	19.57	227.64	5.54
8723	#238	318.02	29.60	392.00	107.38	251.09	19.91	20.09	5.10	25.06	283.99	19.91	3.76	19.82	203.72	5.64
8723	#563	271.83	27.93	372.00	110.79	226.91	13.44	13.61	3.33	14.75	261.07	13.44	2.46	11.58	167.99	4.65
C sample																
5714	#296	133.51	14.52	284.00	88.66	179.15	7.51	7.57	3.77	13.78	207.67	7.51	2.76	10.56	144.92	3.34
5714	#399	61.38	8.24	219.00	71.34	145.72	5.86	5.97	4.03	19.63	171.07	5.86	3.06	15.36	116.25	3.02
5714	#373	66.10	7.54	225.00	61.80	151.66	6.65	6.79	5.71	32.01	171.10	6.65	4.28	25.47	124.97	5.22
5714	#772	–	–	–	–	–	3.57	3.67	1.99	11.13	157.90	3.57	1.52	8.41	102.18	3.33
5714	#284	50.33	6.33	205.00	68.42	140.71	5.27	5.49	4.00	28.74	166.88	5.26	2.97	21.35	110.41	7.41

$z = 0$		Halo scale					Stellar scale					Projected stellar scale				
sim	ELO	$M_{\rm vir}$	$M_{\rm h}^{\rm bar}$	$r_{\rm vir}$	$r_{\rm e,h}^{\rm tot}$	$\sigma_{\rm 3,h}^{\rm tot}$	$M_{\rm bo}^{\rm star}$	$M_{\rm bo}^{\rm cb}$	$r_{\rm e,bo}^{\rm star}$	$r_{\rm 90,bo}^{\rm star}$	$\sigma_{\rm 3,bo}^{\rm star}$	$M_{\rm cyl,bo}^{\rm star}$	$R_{\rm e,bo}^{\rm star}$	$R_{\rm 90,bo}^{\rm star}$	$\sigma_{\rm los,0}^{\rm star}$	n
5714	#156	32.88	4.04	178.00	41.10	137.46	3.63	3.89	2.77	22.42	153.92	3.63	2.15	17.28	114.85	3.76
D sample																
7714	#527	–	–	–	–	–	14.09	14.15	4.87	24.15	272.85	14.09	3.46	19.34	193.74	16.05
7714	#705	107.65	13.20	273.00	80.55	181.38	8.26	8.59	3.06	23.23	227.05	8.25	2.23	18.68	165.68	19.98
7714	#724	83.57	11.64	251.00	68.85	181.98	9.36	9.54	3.45	27.62	230.34	9.36	2.54	21.03	156.67	11.35
7714	#645	–	–	–	–	–	2.14	2.15	0.78	8.24	147.30	2.14	0.60	6.33	101.45	18.79
7714	#917	43.05	5.92	201.00	49.33	143.43	4.24	4.25	2.22	11.52	181.26	4.24	1.68	9.22	117.99	8.10
7714	#027	29.86	4.58	178.00	51.92	124.51	3.11	3.13	1.36	13.36	159.05	3.11	1.00	10.13	109.16	9.19
7714	#735	–	–	–	–	–	1.61	1.64	0.86	8.58	121.39	1.61	0.65	6.64	86.54	9.78
F1 sample																
8935	#351	3032.07	263.26	832.00	300.19	437.64	135.97	137.78	25.86	90.54	485.00	135.97	18.51	72.74	301.19	9.79
8935	#028	1012.29	90.57	577.00	194.82	327.10	43.62	44.02	8.19	35.77	354.44	43.61	5.75	28.33	237.89	6.66
8935	#122	517.29	50.08	461.00	159.37	265.16	31.83	32.23	7.73	38.63	295.99	31.83	5.88	31.22	200.12	6.52
8935	#239	418.21	38.81	430.00	138.95	243.49	19.97	20.27	4.52	24.09	267.75	19.97	3.31	19.18	175.50	6.58
8935	#543	260.93	27.29	367.00	136.53	208.63	14.25	14.59	3.96	17.93	213.53	14.25	2.93	14.02	138.33	3.91
8935	#437	–	–	–	–	–	14.76	15.17	3.48	17.02	257.99	14.75	2.52	13.42	159.95	6.01
8935	#202	248.73	23.29	361.00	102.25	229.86	17.74	18.25	4.42	30.89	266.10	17.74	3.18	24.01	177.04	9.41
8935	#040	–	–	–	–	–	11.44	11.59	2.83	15.83	225.27	11.43	2.17	12.76	140.17	6.95
8935	#222	237.16	25.52	356.00	120.25	201.56	14.44	14.58	4.92	21.01	226.95	14.43	3.48	16.71	151.33	5.26
8935	#734	168.07	18.99	317.00	109.40	194.20	15.11	15.65	4.67	32.72	215.75	15.10	3.43	25.25	134.97	5.01
8935	#334	–	–	–	–	–	10.73	11.01	3.67	18.18	203.44	10.73	2.71	14.62	141.37	6.60
8935	#139	142.38	15.33	300.00	95.82	186.66	9.98	10.19	3.06	14.59	213.47	9.97	2.22	11.33	148.59	4.32
8935	#436	–	–	–	–	–	10.34	10.51	4.16	24.92	213.31	10.34	3.06	19.15	145.70	5.66
8935	#335	–	–	–	–	–	9.04	9.26	2.72	20.22	195.12	9.04	2.08	15.92	127.20	6.75
8935	#221	86.40	11.67	254.00	82.23	152.19	6.83	7.06	3.63	13.17	168.68	6.82	2.66	10.58	114.19	3.27
8935	#351	–	–	–	–	–	8.45	8.74	2.94	24.42	188.40	8.44	2.22	18.72	130.13	11.95
8935	#361	–	–	–	–	–	8.15	8.36	2.90	20.20	188.70	8.15	2.18	15.53	119.63	7.21
8935	#003	101.34	9.41	268.00	72.72	169.86	8.35	8.51	2.19	17.16	190.53	8.35	1.72	13.36	134.83	5.09
8935	#734	76.33	9.24	244.00	83.53	145.83	7.75	8.05	3.44	19.83	163.77	7.75	2.67	15.93	121.25	4.25

$z=0$		Halo scale					Stellar scale					Projected stellar scale				
sim	ELO	$M_{\rm vir}$	$M_{\rm h}^{\rm bar}$	$r_{\rm vir}$	$r_{\rm e,h}^{\rm tot}$	$\sigma_{3,\rm h}^{\rm tot}$	$M_{\rm bo}^{\rm star}$	$M_{\rm bo}^{\rm cb}$	$r_{\rm e,bo}^{\rm star}$	$r_{90,\rm bo}^{\rm star}$	$\sigma_{3,\rm bo}^{\rm star}$	$M_{\rm cyl,bo}^{\rm star}$	$R_{\rm e,bo}^{\rm star}$	$R_{90,\rm bo}^{\rm star}$	$\sigma_{\rm los,0}^{\rm star}$	n
8935	#231	74.76	8.31	242.00	65.75	161.02	6.14	6.38	2.23	11.12	177.26	6.14	1.69	8.90	114.11	4.98
8935	#026	69.08	8.08	236.00	60.87	156.57	7.24	7.54	2.87	15.22	175.87	7.24	2.14	12.08	116.70	4.31
8935	#239	65.89	7.86	232.00	60.40	146.58	6.97	7.17	1.90	20.59	166.44	6.97	1.42	15.24	116.59	9.94
8935	#380	72.75	8.19	240.00	59.39	160.32	5.92	6.06	2.83	13.61	175.81	5.91	2.08	10.69	114.46	6.10
8935	#534	–	–	–	–	–	6.17	6.34	2.13	13.87	187.28	6.17	1.66	11.03	121.74	7.80
8935	#243	68.21	7.25	235.00	61.69	154.69	6.04	6.18	2.39	11.38	173.66	6.04	1.82	8.92	114.99	3.58
8935	#198	55.90	7.44	220.00	61.68	140.52	5.01	5.11	2.35	11.08	159.72	5.01	1.74	8.63	105.03	4.30
8935	#008	–	–	–	–	–	4.84	5.00	2.01	14.80	143.96	4.84	1.60	10.97	92.96	3.41
8935	#093	38.90	5.24	195.00	58.82	127.61	4.60	4.81	2.10	12.24	134.78	4.60	1.60	9.65	97.88	3.76
8935	#232	–	–	–	–	–	4.51	4.70	2.84	11.11	137.33	4.51	2.17	8.99	88.88	2.65
8935	#176	37.01	4.99	192.00	49.10	125.05	3.73	3.94	1.69	7.93	131.75	3.72	1.32	6.23	88.29	3.63
8935	#713	41.76	4.77	199.00	47.59	134.93	3.97	4.15	1.62	7.09	151.97	3.97	1.23	5.76	105.22	3.45
F3 sample																
2100	#975	634.16	58.79	450.00	148.71	294.30	29.86	30.08	6.28	29.64	347.79	29.84	4.47	23.70	233.64	11.11
2100	#610	324.52	30.10	360.00	118.39	239.13	16.35	16.58	4.93	28.05	273.96	16.34	3.58	22.66	180.30	13.61
2100	#198	–	–	–	–	–	18.47	18.84	6.51	37.31	272.78	18.47	4.58	29.39	193.50	19.81
2100	#835	–	–	–	–	–	8.31	8.44	2.83	15.63	204.33	8.31	2.11	11.96	139.35	4.75
2100	#663	–	–	–	–	–	6.13	6.17	3.76	18.08	189.60	6.12	2.62	14.32	142.72	7.28
2100	#408	91.27	9.19	236.00	67.62	175.34	7.91	8.15	2.62	23.25	207.36	7.91	2.00	18.79	153.70	13.93
2100	#557	–	–	–	–	–	7.36	7.46	3.58	19.39	191.10	7.36	2.63	15.20	128.79	4.35
2100	#396	76.64	8.81	223.00	66.37	155.78	6.81	6.89	3.90	20.66	181.13	6.80	2.97	15.98	129.85	5.11
2100	#528	88.16	8.87	233.00	63.66	173.09	5.86	6.06	1.86	11.63	211.86	5.86	1.37	9.07	139.67	7.46
2100	#972	57.33	7.05	202.00	60.17	154.06	5.64	5.89	2.01	13.29	170.69	5.64	1.58	10.59	122.22	5.31
2100	#072	–	–	–	–	–	4.58	4.68	1.75	11.33	172.75	4.58	1.34	8.63	115.03	7.51
2100	#873	70.33	7.39	216.00	65.46	153.73	5.71	5.84	1.72	19.07	188.19	5.71	1.29	14.96	132.27	11.60
2100	#669	–	–	–	–	–	5.92	6.08	2.12	11.87	191.42	5.92	1.60	9.31	138.93	4.35
2100	#678	50.85	6.05	194.00	61.79	138.65	4.79	4.95	2.43	12.90	158.73	4.79	1.88	10.08	111.76	3.38
2100	#601	–	–	–	–	–	4.58	4.65	2.41	16.41	163.46	4.58	1.80	12.76	114.81	4.52
2100	#791	38.40	5.00	177.00	51.80	131.87	4.30	4.37	2.01	13.42	153.64	4.30	1.53	10.88	122.23	6.10

$z = 0$		Halo scale					Stellar scale					Projected stellar scale				
sim	ELO	$M_{\rm vir}$	$M_{\rm h}^{\rm bar}$	$r_{\rm vir}$	$r_{\rm e,h}^{\rm tot}$	$\sigma_{3,\rm h}^{\rm tot}$	$M_{\rm bo}^{\rm star}$	$M_{\rm bo}^{\rm cb}$	$r_{\rm e,bo}^{\rm star}$	$r_{90,\rm bo}^{\rm star}$	$\sigma_{3,\rm bo}^{\rm star}$	$M_{\rm cyl,bo}^{\rm star}$	$R_{\rm e,bo}^{\rm star}$	$R_{90,\rm bo}^{\rm star}$	$\sigma_{\rm los,0}^{\rm star}$	n
2100	#545	–	–	–	–	–	4.26	4.41	2.76	13.25	135.36	4.26	2.17	10.53	96.58	2.49
2100	#080	31.48	4.31	166.00	47.90	118.46	2.66	2.87	2.21	12.89	130.20	2.66	1.65	10.45	101.74	3.97
2100	#207	34.01	4.27	170.00	48.26	131.03	3.51	3.63	1.72	9.87	148.06	3.51	1.33	8.10	104.24	5.17
2100	#969	–	–	–	–	–	3.37	3.52	1.67	9.98	145.10	3.37	1.28	7.74	105.52	4.03
2100	#339	–	–	–	–	–	3.36	3.53	2.36	15.99	132.45	3.36	1.71	12.83	95.80	9.28
2100	#521	–	–	–	–	–	2.73	2.91	1.68	9.46	145.36	2.73	1.25	6.97	112.12	4.05

Table D.2: 3D and 2D Rotation and Shape parameters for ELO samples ($z = 0$).

$z = 0$		Rotation and Shape									
		3D						2D			
sim	ELO	$V_\phi/\sigma_3^{\rm star}(r_{\rm e,bo}^{\rm star})$	$\epsilon_{\rm 3D}(r_{\rm e,bo}^{\rm star})$	$S(r_{\rm e,bo}^{\rm star})$	$V_\phi/\sigma_3^{\rm star}(r_{\rm 90,bo}^{\rm star})$	$\epsilon_{\rm 3D}(r_{\rm 90,bo}^{\rm star})$	$S(r_{\rm 90,bo}^{\rm star})$	$V_{\rm max}/\sigma_{\rm los,0}^{\rm star}(R_{\rm e,bo}^{\rm star})$	$\epsilon(R_{\rm e,bo}^{\rm star})$	$V_{\rm max}/\sigma_{\rm los,0}^{\rm star}(R_{\rm 90,bo}^{\rm star})$	$\epsilon(R_{\rm 90,bo}^{\rm star})$
A sample											
8714	#173	0.0165	0.3575	0.2888	0.1274	0.3575	0.2888	0.1900	0.3671	0.1202	0.2881
8714	#353	0.0339	0.3577	0.0919	0.1824	0.3577	0.0919	0.1315	0.4388	0.1420	0.2536
8714	#581	0.3708	0.2303	2.7401	0.6684	0.2303	2.7401	0.1889	0.2418	0.3103	0.1949
8714	#296	0.5677	0.3668	1.6360	0.5008	0.3668	1.6360	0.2893	0.3533	0.5245	0.4160
8714	#399	0.5043	0.3011	2.8151	0.0000	0.3011	2.8151	0.2511	0.2005	0.4427	0.3449
8714	#373	0.3545	0.2665	1.6481	0.4031	0.2665	1.6481	0.2327	0.2221	0.3052	0.2006
8714	#772	0.0924	0.2188	1.3121	0.2859	0.2188	1.3121	0.0773	0.2557	0.1627	0.3967
8714	#284	0.1432	0.2533	1.5658	0.0283	0.2533	1.5658	0.0000	0.2440	0.2544	0.1834
8714	#398	0.6971	0.4230	0.1991	0.1740	0.4230	0.1991	0.4208	0.3764	0.4230	0.3053
8714	#156	0.3847	0.1201	1.5836	0.4160	0.1201	1.5836	0.0000	0.0998	0.2239	0.2130
8714	#173	0.1673	0.1589	2.7770	0.4504	0.1589	2.7770	0.0000	0.1947	0.1450	0.1488
8747	#317	0.0158	0.3203	0.1641	0.1523	0.3203	0.1641	0.1029	0.3035	0.1029	0.1805
8747	#288	0.1793	0.2695	0.2029	0.0280	0.2695	0.2029	0.1724	0.3194	0.1724	0.2171
8747	#348	0.4653	0.2428	1.6900	0.4308	0.2428	1.6900	0.2136	0.1860	0.3891	0.1719
8747	#115	0.3946	0.2029	2.7833	0.5508	0.2029	2.7833	0.2140	0.1563	0.4015	0.2452
8747	#100	0.2943	0.2399	0.2724	0.3610	0.2399	0.2724	0.1247	0.1732	0.3138	0.2405
8747	#189	0.2664	0.1728	1.4955	0.1142	0.1728	1.4955	0.1792	0.1783	0.2243	0.1881
8747	#114	0.0816	0.0401	3.6270	0.0444	0.0401	1.6270	0.0000	0.0716	0.0704	0.1758
8747	#915	0.1866	0.0979	3.4830	0.4543	0.0979	1.4830	0.0792	0.0935	0.2187	0.1822
8747	#317	0.1846	0.1912	1.6031	0.0710	0.1912	1.6031	0.0000	0.1864	0.1424	0.1373
8747	#200	0.4939	0.3222	0.1201	0.4429	0.3222	0.1201	0.0000	0.3097	0.4152	0.3446
8747	#216	0.1546	0.1144	2.7391	0.1925	0.1144	2.7391	0.0000	0.1428	0.1176	0.1471
8747	#102	0.1226	0.2408	0.1699	0.4011	0.2408	0.1699	0.0000	0.2078	0.1201	0.1980

$z = 0$		Rotation and Shape									
		3D						2D			
sim	ELO	$V_\phi/\sigma_3^{\rm star}(r_{\rm e,bo}^{\rm star})$	$\epsilon_{\rm 3D}(r_{\rm e,bo}^{\rm star})$	$S(r_{\rm e,bo}^{\rm star})$	$V_\phi/\sigma_3^{\rm star}(r_{\rm 90,bo}^{\rm star})$	$\epsilon_{\rm 3D}(r_{\rm 90,bo}^{\rm star})$	$S(r_{\rm 90,bo}^{\rm star})$	$V_{\rm max}/\sigma_{\rm los,0}^{\rm star}(R_{\rm e,bo}^{\rm star})$	$\epsilon(R_{\rm e,bo}^{\rm star})$	$V_{\rm max}/\sigma_{\rm los,0}^{\rm star}(R_{\rm 90,bo}^{\rm star})$	$\epsilon(R_{\rm 90,bo}^{\rm star})$
8741	#617	0.0778	0.0975	3.5796	0.0385	0.0975	1.5796	0.0628	0.0802	0.2113	0.1055
8741	#011	0.1671	0.2898	0.0306	0.1451	0.2898	0.0306	0.1289	0.3300	0.2004	0.1902
8741	#218	0.0994	0.0596	3.3355	0.0518	0.0596	1.3355	0.0831	0.0419	0.1938	0.1665
8741	#218	0.4997	0.2888	2.7109	0.4420	0.2888	2.7109	0.2141	0.2280	0.4464	0.2510
8741	#017	0.2879	0.3057	0.1549	0.0630	0.3057	0.1549	0.1736	0.3420	0.3673	0.3544
8741	#930	0.0008	0.0668	3.5491	0.3370	0.0668	1.5491	0.0724	0.0634	0.1823	0.1447
8741	#945	0.5145	0.3060	2.7989	0.5544	0.3060	2.7989	0.1722	0.2259	0.5080	0.3254
8741	#097	0.1421	0.1116	1.6795	0.2585	0.1116	1.6795	0.0811	0.0983	0.1988	0.1831
8741	#907	0.0381	0.2497	0.2195	0.3356	0.2497	0.2195	0.0622	0.2588	0.1452	0.3210
8741	#015	0.0036	0.0604	3.3588	0.1640	0.0604	1.3588	0.0000	0.0773	0.0879	0.1642
8741	#907	0.0332	0.1163	2.9378	0.2047	0.1163	2.9378	0.0000	0.1152	0.0818	0.1280
8741	#617	0.0553	0.3482	0.1232	0.0318	0.3482	0.1232	0.0671	0.3963	0.1756	0.3534
8742	#293	0.0912	0.1350	1.3250	0.0509	0.1350	1.3250	0.0514	0.1380	0.1148	0.2643
8742	#234	0.0259	0.2813	0.2094	0.1244	0.2813	0.2094	0.1415	0.3005	0.1415	0.1853
8742	#283	0.0627	0.2807	1.5747	0.5751	0.2807	1.5747	0.1129	0.2135	0.1694	0.2143
8742	#254	0.4902	0.3476	1.4358	0.5926	0.3476	1.4358	0.2829	0.3341	0.4515	0.2296
8742	#092	0.5308	0.2677	2.8359	0.2831	0.2677	2.8359	0.2235	0.2341	0.4453	0.4054
8742	#896	0.3704	0.1301	2.7406	0.0968	0.1301	2.7406	0.0000	0.0850	0.2624	0.2878
8742	#316	0.6778	0.2968	1.5095	0.4720	0.2968	1.5095	0.2646	0.2729	0.4777	0.3454
8742	#898	0.1232	0.1485	1.6750	0.0785	0.1485	3.6750	0.0000	0.1394	0.0902	0.0926
8742	#893	0.1563	0.2375	1.3853	0.9138	0.2375	1.3853	0.0000	0.2208	0.1423	0.2906
8743	#647	0.0292	0.4000	0.1157	0.1116	0.4000	0.1157	0.0623	0.4539	0.1305	0.2715
8743	#563	0.3651	0.3198	0.1277	0.4133	0.3198	0.1277	0.1432	0.3059	0.3646	0.2378
8743	#238	0.0816	0.2340	2.8482	0.1186	0.2340	2.8482	0.0709	0.1945	0.1173	0.2165
8743	#328	0.0092	0.3651	0.0514	0.3645	0.3651	0.0514	0.0791	0.4427	0.1572	0.3280
8743	#515	0.2892	0.2071	0.2799	0.8882	0.2071	0.2799	0.1853	0.1994	0.3371	0.2798
8743	#437	0.1166	0.0766	3.3431	0.8676	0.0766	1.3431	0.1040	0.1091	0.1488	0.1552
8743	#421	0.0142	0.0967	3.5981	0.1174	0.0967	1.5981	0.0948	0.1237	0.0952	0.3189

$z = 0$		Rotation and Shape									
		3D						2D			
sim	ELO	$V_\phi/\sigma_3^{\rm star}(r_{\rm e,bo}^{\rm star})$	$\epsilon_{\rm 3D}(r_{\rm e,bo}^{\rm star})$	$S(r_{\rm e,bo}^{\rm star})$	$V_\phi/\sigma_3^{\rm star}(r_{\rm 90,bo}^{\rm star})$	$\epsilon_{\rm 3D}(r_{\rm 90,bo}^{\rm star})$	$S(r_{\rm 90,bo}^{\rm star})$	$V_{\rm max}/\sigma_{\rm los,0}^{\rm star}(R_{\rm e,bo}^{\rm star})$	$\epsilon(R_{\rm e,bo}^{\rm star})$	$V_{\rm max}/\sigma_{\rm los,0}^{\rm star}(R_{\rm 90,bo}^{\rm star})$	$\epsilon(R_{\rm 90,bo}^{\rm star})$
8743	#555	0.1485	0.0817	3.4972	0.3896	0.0817	1.4972	0.0000	0.1093	0.1196	0.2775
8743	#637	0.0745	0.3271	0.1245	0.0269	0.3271	0.1245	0.1019	0.3738	0.1299	0.2822
8743	#239	0.0817	0.2107	1.5897	0.4066	0.2107	1.5897	0.0000	0.2074	0.0769	0.1874
8743	#626	0.8540	0.4140	2.7159	0.8165	0.4140	2.7159	0.2809	0.3059	0.4808	0.3955
8743	#437	0.2402	0.1274	2.8539	0.4257	0.1274	2.8539	0.0000	0.1102	0.1758	0.2236
B sample											
8716	#173	0.0482	0.4910	0.1652	0.3064	0.4910	0.1652	0.2400	0.5413	0.3685	0.3483
8716	#253	0.1335	0.3824	0.1584	0.2562	0.3824	0.1584	0.1105	0.4012	0.3745	0.3129
8716	#581	0.2110	0.2340	1.5551	0.1987	0.2340	1.5551	0.1720	0.2002	0.5670	0.2395
8716	#296	0.7454	0.3799	2.8001	0.8441	0.3799	2.8001	0.2816	0.3219	0.9155	0.4386
8717	#317	0.1599	0.3407	1.3836	0.0127	0.3407	1.3836	0.2023	0.2985	0.2774	0.1979
8717	#288	0.4187	0.2549	2.7517	0.3752	0.2549	2.7517	0.2617	0.2002	0.5892	0.2109
8717	#348	0.3348	0.1307	0.1439	0.0206	0.1307	0.1439	0.2213	0.1355	0.5332	0.2193
8721	#011	0.5858	0.2948	1.4666	0.4608	0.2948	1.4666	0.5466	0.2629	0.7305	0.3104
8721	#945	0.7033	0.3816	2.8316	0.3495	0.3816	2.8316	0.2776	0.3084	0.8674	0.3101
8721	#097	0.2028	0.1197	2.8159	0.2583	0.1197	2.8159	0.1579	0.0831	0.5057	0.1307
8722	#293	0.1068	0.2386	1.6560	0.0576	0.2386	1.6560	0.2271	0.2336	0.3757	0.2132
8722	#234	0.0669	0.3381	0.2696	0.1047	0.3381	0.2696	0.0726	0.3456	0.3397	0.2000
8722	#283	0.2446	0.1997	1.4538	0.2661	0.1997	1.4538	0.0117	0.1707	0.6019	0.2505
8722	#254	0.8060	0.2452	2.8498	0.6270	0.2452	2.8498	0.4135	0.1710	0.8399	0.2589
8723	#647	0.0008	0.4570	0.1012	0.0770	0.4570	0.1012	0.0676	0.5098	0.2804	0.3111
8723	#238	0.0612	0.2817	1.4873	0.0712	0.2817	1.4873	0.0686	0.2318	0.3449	0.2343
8723	#563	0.0892	0.0872	3.5130	0.1849	0.0872	1.5130	0.1053	0.0794	0.5909	0.1961
C sample											
5714	#296	0.4523	0.2298	2.7188	0.7257	0.2298	2.7188	0.2049	0.1684	0.5075	0.3788
5714	#399	0.4517	0.2733	1.6577	0.7157	0.2733	1.6577	0.2353	0.1924	0.5230	0.2413
5714	#373	0.3940	0.2077	2.9585	0.1064	0.2077	2.9585	0.1668	0.1739	0.2897	0.1672
5714	#772	0.3735	0.2224	1.4546	0.2761	0.2224	1.4546	0.0000	0.1473	0.2466	0.2569

$z = 0$		Rotation and Shape									
		3D						2D			
sim	ELO	$V_\phi/\sigma_3^{\rm star}(r_{\rm e,bo}^{\rm star})$	$\epsilon_{\rm 3D}(r_{\rm e,bo}^{\rm star})$	$S(r_{\rm e,bo}^{\rm star})$	$V_\phi/\sigma_3^{\rm star}(r_{\rm 90,bo}^{\rm star})$	$\epsilon_{\rm 3D}(r_{\rm 90,bo}^{\rm star})$	$S(r_{\rm 90,bo}^{\rm star})$	$V_{\rm max}/\sigma_{\rm los,0}^{\rm star}(R_{\rm e,bo}^{\rm star})$	$\epsilon(R_{\rm e,bo}^{\rm star})$	$V_{\rm max}/\sigma_{\rm los,0}^{\rm star}(R_{\rm 90,bo}^{\rm star})$	$\epsilon(R_{\rm 90,bo}^{\rm star})$
5714	#284	0.2133	0.1624	1.6629	0.2298	0.1624	1.6629	0.1114	0.0923	0.2698	0.2830
5714	#156	0.1090	0.1934	0.0935	0.4193	0.1934	0.0935	0.0916	0.2046	0.1641	0.2138
D sample											
6705	#823	0.0466	0.1558	0.1282	0.0373	0.1558	0.1282	0.0622	0.1775	0.2198	0.1830
6705	#814	0.1188	0.1358	0.0743	0.1049	0.1358	0.0743	0.1849	0.1540	0.3143	0.1956
6705	#712	0.0648	0.0516	3.8455	0.0489	0.0516	2.8455	0.0862	0.0353	0.2533	0.1993
6705	#622	0.0145	0.2010	2.8358	0.0855	0.2010	2.8358	0.0906	0.1670	0.2185	0.2383
6705	#203	0.1769	0.0687	3.5020	0.1065	0.0687	1.5020	0.1630	0.0653	0.3210	0.1390
6705	#689	0.0825	0.2584	0.1969	0.0435	0.2584	0.1969	0.2334	0.2306	0.2819	0.4552
6705	#622	0.1489	0.1926	1.6343	0.0245	0.1926	1.6343	0.1528	0.2105	0.2787	0.1762
7705	#823	0.0361	0.0899	3.3733	0.0309	0.0899	1.3733	0.0332	0.0970	0.1877	0.1700
7705	#814	0.1115	0.2082	0.2144	0.0640	0.2082	0.2144	0.0770	0.2090	0.2227	0.1430
7705	#622	0.0584	0.1347	1.5069	0.1148	0.1347	1.5069	0.0810	0.1407	0.1703	0.2114
7705	#711	0.0542	0.0886	3.3472	0.0015	0.0886	1.3472	0.0952	0.0887	0.1765	0.1076
7705	#203	0.0204	0.0812	3.6331	0.2250	0.0812	3.6331	0.0000	0.1017	0.0748	0.1135
7705	#689	0.0318	0.3272	0.2547	0.2259	0.3272	0.2547	0.1019	0.2800	0.1303	0.3412
7705	#622	0.1203	0.1805	1.5965	0.0441	0.1805	1.5965	0.1136	0.1039	0.1107	0.1728
F1 sample											
8935	#351	0.0083	0.2939	0.1945	0.0569	0.2939	0.1945	0.1761	0.3407	0.5215	0.3100
8935	#028	0.0027	0.4468	0.0063	0.0888	0.4468	0.0063	0.0590	0.4617	0.2527	0.3022
8935	#122	0.1249	0.4967	0.0935	0.1689	0.4967	0.0935	0.0630	0.5641	0.3052	0.3022
8935	#239	0.4027	0.2965	1.4105	0.5060	0.2965	1.4105	0.2407	0.2826	0.4878	0.2755
8935	#543	0.7201	0.3261	2.7698	0.4886	0.3261	2.7698	0.3300	0.3309	0.6489	0.2131
8935	#437	0.1574	0.1842	2.8851	0.2008	0.1842	2.8851	0.0521	0.1675	0.2340	0.3097
8935	#202	0.1721	0.1356	1.4013	0.4270	0.1356	1.4013	0.1047	0.1258	0.3044	0.1451
8935	#040	0.3468	0.1407	1.3729	0.4269	0.1407	1.3729	0.0920	0.1439	0.3682	0.3981
8935	#222	0.1234	0.3153	0.0994	0.3757	0.3153	0.0994	0.0821	0.3013	0.3037	0.1786
8935	#734	0.6774	0.2811	1.4526	0.5409	0.2811	1.4526	0.3708	0.2449	0.6800	0.1923

$z = 0$		Rotation and Shape									
		3D						2D			
sim	ELO	$V_\phi/\sigma_3^{\rm star}(r_{\rm e,bo}^{\rm star})$	$\epsilon_{\rm 3D}(r_{\rm e,bo}^{\rm star})$	$S(r_{\rm e,bo}^{\rm star})$	$V_\phi/\sigma_3^{\rm star}(r_{\rm 90,bo}^{\rm star})$	$\epsilon_{\rm 3D}(r_{\rm 90,bo}^{\rm star})$	$S(r_{\rm 90,bo}^{\rm star})$	$V_{\rm max}/\sigma_{\rm los,0}^{\rm star}(R_{\rm e,bo}^{\rm star})$	$\epsilon(R_{\rm e,bo}^{\rm star})$	$V_{\rm max}/\sigma_{\rm los,0}^{\rm star}(R_{\rm 90,bo}^{\rm star})$	$\epsilon(R_{\rm 90,bo}^{\rm star})$
8935	#334	0.2245	0.4016	0.2641	0.1744	0.4016	0.2641	0.1290	0.4179	0.2474	0.1792
8935	#139	0.1421	0.2995	0.1453	0.2687	0.2995	0.1453	0.0789	0.2489	0.2199	0.2401
8935	#436	0.0093	0.1958	0.1056	0.0712	0.1958	0.1056	0.0740	0.2184	0.1849	0.3243
8935	#335	0.0856	0.2427	0.2837	0.1302	0.2427	0.2837	0.0000	0.2713	0.1838	0.2120
8935	#221	0.5417	0.3089	2.7888	0.4984	0.3089	2.7888	0.3093	0.2751	0.5459	0.3533
8935	#351	0.2591	0.2168	2.7253	0.5417	0.2168	2.7253	0.0920	0.2283	0.2357	0.2512
8935	#361	0.0660	0.1126	1.3791	0.2521	0.1126	1.3791	0.0983	0.1346	0.2578	0.2070
8935	#003	0.0423	0.2425	0.1295	0.3848	0.2425	0.1295	0.0000	0.2593	0.1713	0.2137
8935	#734	0.1037	0.5056	0.0790	0.2825	0.5056	0.0790	0.1085	0.6166	0.1910	0.5617
8935	#231	0.2164	0.2589	1.4735	0.2985	0.2589	1.4735	0.0000	0.2279	0.2621	0.2484
8935	#026	0.1609	0.1886	0.2649	0.5881	0.1886	0.2649	0.0592	0.1637	0.3476	0.2566
8935	#239	0.1500	0.3754	0.0646	0.2003	0.3754	0.0646	0.0000	0.3807	0.1498	0.1804
8935	#380	0.2888	0.1694	1.6029	0.2192	0.1694	1.6029	0.0000	0.1364	0.3423	0.1082
8935	#534	0.2284	0.2125	1.5042	0.3928	0.2125	1.5042	0.0000	0.1552	0.2485	0.1932
8935	#243	0.1719	0.3266	0.2250	0.3491	0.3266	0.2250	0.0000	0.3512	0.2280	0.3508
8935	#198	0.1124	0.2527	1.3644	0.4602	0.2527	1.3644	0.0000	0.2452	0.1763	0.3599
8935	#008	0.3063	0.3518	0.1791	0.3268	0.3518	0.1791	0.0000	0.4101	0.2524	0.4622
8935	#093	0.3485	0.3787	0.0711	0.2899	0.3787	0.0711	0.0000	0.3989	0.2656	0.4336
8935	#232	0.5296	0.1683	1.3336	0.6079	0.1683	1.3336	0.2393	0.1562	0.4466	0.3255
8935	#176	0.3396	0.2073	1.4361	0.2890	0.2073	1.4361	0.0000	0.1974	0.2628	0.4802
8935	#713	0.1071	0.1341	1.6510	0.0436	0.1341	1.6510	0.0000	0.1399	0.0873	0.1893
F2 sample											
8914	#351	0.0255	0.3137	0.0994	0.0534	0.3137	0.0994	0.0811	0.3244	0.3038	0.2361
8914	#371	0.1988	0.1277	2.7409	0.0119	0.1277	2.7409	0.0973	0.0918	0.3113	0.2506
8914	#022	0.1405	0.3304	0.1197	0.1887	0.3304	0.1197	0.1020	0.3613	0.3426	0.3900
8914	#028	0.2273	0.0200	3.7151	0.3717	0.0200	2.7151	0.2035	0.0263	0.3159	0.1477
8914	#928	0.2980	0.1559	1.6139	0.3759	0.1559	1.6139	0.2287	0.1280	0.3726	0.1900
8914	#113	0.0493	0.1885	0.2517	0.4982	0.1885	0.2517	0.1030	0.2262	0.3223	0.2301

$z = 0$		Rotation and Shape									
		3D						2D			
sim	ELO	$V_\phi/\sigma_3^{\rm star}(r_{\rm e,bo}^{\rm star})$	$\epsilon_{\rm 3D}(r_{\rm e,bo}^{\rm star})$	$S(r_{\rm e,bo}^{\rm star})$	$V_\phi/\sigma_3^{\rm star}(r_{\rm 90,bo}^{\rm star})$	$\epsilon_{\rm 3D}(r_{\rm 90,bo}^{\rm star})$	$S(r_{\rm 90,bo}^{\rm star})$	$V_{\rm max}/\sigma_{\rm los,0}^{\rm star}(R_{\rm e,bo}^{\rm star})$	$\epsilon(R_{\rm e,bo}^{\rm star})$	$V_{\rm max}/\sigma_{\rm los,0}^{\rm star}(R_{\rm 90,bo}^{\rm star})$	$\epsilon(R_{\rm 90,bo}^{\rm star})$
8914	#202	0.2986	0.2026	1.4027	0.2178	0.2026	1.4027	0.1081	0.1711	0.3422	0.1596
8914	#212	0.1204	0.2443	1.5699	0.2025	0.2443	1.5699	0.1159	0.1949	0.2530	0.1570
8914	#535	0.1261	0.1094	2.7124	0.6053	0.1094	2.7124	0.2373	0.0950	0.2406	0.1758
8914	#543	0.2626	0.0741	3.6180	0.5538	0.0741	1.6180	0.1429	0.0868	0.2508	0.1618
8914	#334	0.0941	0.1077	0.2434	0.2918	0.1077	0.2434	0.1494	0.1156	0.2390	0.1457
8914	#232	0.0425	0.0357	3.3622	0.0056	0.0357	1.3622	0.0405	0.0528	0.1715	0.1128
8914	#129	0.1479	0.0760	3.5612	0.4798	0.0760	3.5612	0.0818	0.0522	0.2069	0.0926
8914	#536	0.1257	0.1548	1.6486	0.3004	0.1548	1.6486	0.2148	0.1285	0.2668	0.1961
8914	#361	0.0732	0.0640	3.1514	0.2857	0.0640	0.1514	0.1132	0.0801	0.2102	0.1700
8914	#335	0.0282	0.0780	3.4851	0.0211	0.0780	3.4851	0.0697	0.0681	0.1525	0.0753
8914	#351	0.3354	0.3167	1.4595	0.3104	0.3167	1.4595	0.2084	0.3313	0.2887	0.3056
8914	#094	0.0074	0.1882	1.6737	0.0015	0.1882	1.6737	0.1172	0.1551	0.1631	0.2038
8914	#135	0.1300	0.0715	3.1542	0.2433	0.0715	0.1542	0.1199	0.1059	0.2129	0.1461
8914	#578	0.2670	0.1648	2.9895	0.6026	0.1648	2.9895	0.2784	0.1677	0.2833	0.3668
8914	#282	0.1894	0.1132	2.8329	0.0036	0.1132	2.8329	0.1249	0.1262	0.2781	0.1834
8914	#244	0.2340	0.0949	3.3542	0.2295	0.0949	1.3542	0.1267	0.0819	0.2580	0.1388
8914	#198	0.0170	0.1019	1.5479	0.7910	0.1019	1.5479	0.0832	0.1012	0.1745	0.2120
8914	#151	0.0565	0.2485	1.6156	0.1018	0.2485	1.6156	0.1005	0.2168	0.1808	0.2234
8914	#050	0.4230	0.2781	1.6382	0.3821	0.2781	1.6382	0.1589	0.2476	0.3426	0.2501
8914	#361	0.0655	0.1874	2.7518	0.0349	0.1874	2.7518	0.1139	0.1418	0.1921	0.2164
8914	#198	0.1755	0.2594	1.5246	0.2807	0.2594	1.5246	0.2266	0.2604	0.2483	0.3346
8914	#028	0.0973	0.0365	3.1269	0.2852	0.0365	0.1269	0.2420	0.0787	0.2430	0.1633
8914	#361	0.1158	0.0658	3.5124	0.0093	0.0658	1.5124	0.0784	0.0979	0.1851	0.1400
8914	#908	0.0599	0.2208	0.2192	0.3122	0.2208	0.2192	0.1870	0.1969	0.2078	0.3210
8914	#039	0.1467	0.1326	1.5763	0.5707	0.1326	1.5763	0.1963	0.1382	0.1963	0.1846
8914	#637	0.1706	0.2497	1.5943	0.1657	0.2497	1.5943	0.2022	0.2114	0.2081	0.4261
8914	#734	0.0694	0.1603	1.3616	0.0174	0.1603	1.3616	0.1646	0.1563	0.2064	0.2482
8914	#232	0.3234	0.1122	2.7508	0.1767	0.1122	2.7508	0.2043	0.1229	0.2973	0.1566

$z = 0$		Rotation and Shape									
		3D						2D			
sim	ELO	$V_\phi/\sigma_3^{\rm star}(r_{\rm e,bo}^{\rm star})$	$\epsilon_{\rm 3D}(r_{\rm e,bo}^{\rm star})$	$S(r_{\rm e,bo}^{\rm star})$	$V_\phi/\sigma_3^{\rm star}(r_{\rm 90,bo}^{\rm star})$	$\epsilon_{\rm 3D}(r_{\rm 90,bo}^{\rm star})$	$S(r_{\rm 90,bo}^{\rm star})$	$V_{\rm max}/\sigma_{\rm los,0}^{\rm star}(R_{\rm e,bo}^{\rm star})$	$\epsilon(R_{\rm e,bo}^{\rm star})$	$V_{\rm max}/\sigma_{\rm los,0}^{\rm star}(R_{\rm 90,bo}^{\rm star})$	$\epsilon(R_{\rm 90,bo}^{\rm star})$
8914	#239	0.2071	0.3987	1.6129	0.2825	0.3987	1.6129	0.1056	0.3599	0.1561	0.4120
8914	#141	0.0428	0.1645	1.6402	0.2444	0.1645	3.6402	0.0000	0.1485	0.0953	0.1198
8914	#335	0.2955	0.1291	1.4313	0.2830	0.1291	1.4313	0.1828	0.1433	0.2686	0.2623
8914	#361	0.3339	0.1347	1.6401	0.1257	0.1347	1.6401	0.1690	0.1442	0.2838	0.2151
F3 sample											
2100	#975	0.0537	0.2789	1.3097	0.0190	0.2789	1.3097	0.0397	0.3077	0.2454	0.2072
2100	#610	0.0474	0.0975	3.8275	0.1130	0.0975	2.8275	0.0676	0.0948	0.2229	0.1130
2100	#198	0.2142	0.2570	1.6503	0.2246	0.2570	1.6503	0.1535	0.2419	0.3084	0.1607
2100	#835	0.3497	0.4174	0.1473	0.5210	0.4174	0.1473	0.1840	0.4615	0.3498	0.3509
2100	#663	0.1126	0.2965	1.3231	0.0209	0.2965	1.3231	0.1089	0.2638	0.1713	0.2484
2100	#408	0.1652	0.1968	2.8038	0.1689	0.1968	2.8038	0.0000	0.1757	0.1965	0.1527
2100	#557	0.1019	0.2151	2.9382	0.2443	0.2151	2.9382	0.1295	0.2052	0.2922	0.1670
2100	#396	0.0017	0.2977	0.0975	0.1593	0.2977	0.0975	0.0840	0.3234	0.2031	0.1880
2100	#528	0.0224	0.1746	2.7889	0.3191	0.1746	2.7889	0.0000	0.1496	0.2236	0.1980
2100	#972	0.7713	0.3136	1.6173	0.6825	0.3136	1.6173	0.0000	0.2829	0.5346	0.2395
2100	#072	0.6330	0.4812	1.6308	0.5534	0.4812	1.6308	0.0000	0.4153	0.4813	0.4195
2100	#873	0.0391	0.0938	3.5569	0.4301	0.0938	1.5569	0.0000	0.1108	0.2656	0.1483
2100	#669	0.1324	0.1264	1.4836	0.2925	0.1264	1.4836	0.0000	0.1124	0.2369	0.1454
2100	#678	0.7549	0.3790	1.6832	0.5981	0.3790	1.6832	0.0000	0.3249	0.6805	0.4381
2100	#601	0.5011	0.4362	1.4624	0.6376	0.4362	1.4624	0.0000	0.3541	0.4142	0.3608
2100	#791	0.2398	0.4622	0.1775	0.4949	0.4622	0.1775	0.0000	0.4917	0.1883	0.3044
2100	#545	0.7448	0.3443	1.6303	0.8359	0.3443	1.6303	0.4021	0.2375	0.6112	0.3637
2100	#080	0.3090	0.2570	1.6101	0.4603	0.2570	1.6101	0.0000	0.1986	0.1841	0.3102
2100	#207	0.2619	0.1920	1.3470	0.4770	0.1920	1.3470	0.0000	0.1723	0.2193	0.6161
2100	#969	0.4108	0.2081	1.4546	0.4819	0.2081	1.4546	0.0000	0.2179	0.2327	0.1878
2100	#339	0.4232	0.2649	1.5746	0.5863	0.2649	1.5746	0.0000	0.2786	0.3627	0.4284
2100	#521	0.3741	0.2288	1.5281	0.4709	0.2288	1.5281	0.0000	0.2187	0.2816	0.5054

Table D.3: Masses, sizes and mean square velocities at the halo and baryonic object scale, as well as their projected counterparts ($z = 0.5$). Masses are given in 10^{10} $M_\odot$, distances in kpc, velocity dispersions in $km \times s^{-1}$.

$z = 0.5$		Halo scale					Stellar scale					Projected stellar scale				
sim	ELO	$M_{\rm vir}$	$M_{\rm h}^{\rm bar}$	$r_{\rm vir}$	$r_{\rm e,h}^{\rm tot}$	$\sigma_{\rm 3,h}^{\rm tot}$	$M_{\rm bo}^{\rm star}$	$M_{\rm bo}^{\rm cb}$	$r_{\rm e,bo}^{\rm star}$	$r_{\rm 90,bo}^{\rm star}$	$\sigma_{\rm 3,bo}^{\rm star}$	$M_{\rm cyl,bo}^{\rm star}$	$R_{\rm e,bo}^{\rm star}$	$R_{\rm 90,bo}^{\rm star}$	$\sigma_{\rm los,0}^{\rm star}$	n
A sample																
8714	#073	–	–	–	–	–	11.49	11.58	1.80	6.71	309.97	11.47	1.39	5.28	190.28	3.08
8714	#173	–	–	–	–	–	12.61	12.79	6.83	24.78	233.32	12.61	4.91	20.13	157.18	5.74
8714	#353	242.58	23.91	266.00	81.98	260.64	19.29	19.55	6.59	34.62	298.73	19.29	4.98	27.62	197.02	6.26
8714	#581	–	–	–	–	–	5.25	5.32	2.58	8.03	194.06	5.24	1.90	6.50	128.14	2.72
8714	#296	–	–	–	–	–	7.43	7.60	2.97	13.85	197.04	7.43	2.24	10.71	136.56	4.17
8714	#473	–	–	–	–	–	4.41	4.61	2.96	11.51	179.00	4.40	2.14	9.36	112.03	5.63
8714	#309	–	–	–	–	–	4.84	4.99	3.18	7.84	179.12	4.83	2.42	6.42	110.41	6.69
8714	#285	–	–	–	–	–	3.79	3.91	1.94	9.46	157.39	3.78	1.51	7.04	96.55	3.44
8714	#343	42.43	5.96	149.00	51.44	153.26	4.12	4.57	2.58	14.73	147.18	4.12	1.98	11.28	106.71	2.92
8714	#157	–	–	–	–	–	3.55	3.64	1.84	10.51	142.68	3.55	1.43	8.01	100.24	2.82
8714	#208	30.65	3.79	134.00	34.69	133.28	3.12	3.25	2.89	17.93	147.37	3.12	2.20	14.50	105.43	5.70
8747	#317	602.91	59.43	361.00	132.50	308.42	25.20	25.34	6.20	20.08	345.93	25.18	4.49	15.90	227.16	4.15
8747	#288	–	–	–	–	–	8.18	8.26	2.54	7.78	255.19	8.17	1.97	6.35	164.24	2.73
8747	#348	–	–	–	–	–	6.41	6.49	2.37	8.60	214.10	6.40	1.85	7.03	138.03	3.35
8747	#015	152.21	15.39	228.00	74.76	212.48	10.71	10.77	2.98	16.68	245.40	10.71	2.29	13.22	158.04	4.91
8747	#179	38.12	5.13	144.00	40.87	146.07	4.20	4.35	2.86	11.19	159.37	4.19	2.23	8.94	106.95	2.90
8747	#815	–	–	–	–	–	3.06	3.24	2.09	6.70	140.81	3.05	1.61	5.32	95.85	2.23
8747	#319	–	–	–	–	–	4.37	4.49	1.96	14.94	151.36	4.37	1.50	11.45	100.43	5.75
8747	#114	–	–	–	–	–	3.97	4.48	2.09	15.80	160.55	3.97	1.61	11.91	108.90	4.26
8747	#100	–	–	–	–	–	3.47	3.98	2.19	13.26	140.56	3.47	1.68	10.71	96.68	4.50
8747	#206	–	–	–	–	–	3.28	3.57	2.02	9.19	146.90	3.28	1.60	7.49	100.91	3.51
8747	#102	27.77	3.90	129.00	33.80	136.38	3.46	3.67	2.30	12.49	147.82	3.46	1.82	9.92	112.52	3.01
8747	#100	–	–	–	–	–	1.90	2.22	2.06	6.10	121.89	1.90	1.56	4.96	86.42	1.99

$z = 0.5$		Halo scale					Stellar scale					Projected stellar scale				
sim	ELO	$M_{\rm vir}$	$M_{\rm h}^{\rm bar}$	$r_{\rm vir}$	$r_{\rm e,h}^{\rm tot}$	$\sigma_{\rm 3,h}^{\rm tot}$	$M_{\rm bo}^{\rm star}$	$M_{\rm bo}^{\rm cb}$	$r_{\rm e,bo}^{\rm star}$	$r_{\rm 90,bo}^{\rm star}$	$\sigma_{\rm 3,bo}^{\rm star}$	$M_{\rm cyl,bo}^{\rm star}$	$R_{\rm e,bo}^{\rm star}$	$R_{\rm 90,bo}^{\rm star}$	$\sigma_{\rm los,0}^{\rm star}$	n
8741	#011	–	–	–	–	–	8.59	8.71	3.45	17.01	215.34	8.58	2.52	13.54	147.72	5.07
8741	#217	213.94	22.60	255.00	80.71	226.23	13.56	13.77	6.02	21.34	261.10	13.55	4.35	17.18	167.55	4.92
8741	#229	–	–	–	–	–	5.63	5.66	2.26	6.25	212.53	5.61	1.68	4.96	138.04	2.60
8741	#607	130.01	12.96	216.00	70.58	198.91	9.94	10.61	4.47	33.23	220.88	9.94	3.33	26.43	153.18	11.49
8741	#097	90.45	10.56	192.00	58.59	175.55	8.89	8.95	6.11	30.79	188.95	8.89	4.75	24.92	129.97	5.82
8741	#940	100.29	10.72	198.00	57.95	193.11	8.14	8.22	4.63	24.14	220.66	8.14	3.28	18.77	162.57	6.53
8741	#026	–	–	–	–	–	5.59	5.80	2.94	14.59	177.21	5.59	2.32	11.79	130.34	1.76
8741	#945	–	–	–	–	–	7.72	8.04	4.02	26.32	192.94	7.72	3.01	20.69	136.15	7.11
8741	#507	62.76	7.16	170.00	48.41	166.19	6.00	6.26	2.76	24.88	170.38	5.99	2.09	19.07	117.77	10.56
8741	#917	47.13	5.87	154.00	38.71	156.47	5.37	5.50	3.13	18.95	172.76	5.37	2.44	15.29	118.32	3.70
8741	#014	43.91	5.07	151.00	41.17	146.57	4.37	4.57	2.09	21.13	165.13	4.37	1.65	15.92	116.16	4.11
8741	#997	–	–	–	–	–	2.92	3.49	1.50	7.18	151.02	2.92	1.17	5.36	94.14	1.80
8742	#293	–	–	–	–	–	14.73	14.80	3.71	11.72	293.46	14.71	2.63	9.32	197.13	3.24
8742	#234	–	–	–	–	–	11.19	11.27	3.06	11.69	282.31	11.18	2.42	9.68	168.08	4.91
8742	#383	–	–	–	–	–	6.51	6.66	2.05	12.18	224.34	6.51	1.61	9.63	138.08	5.80
8742	#992	–	–	–	–	–	4.03	4.17	2.20	6.97	154.43	4.02	1.74	5.64	102.30	2.33
8742	#706	37.03	5.17	142.00	47.62	128.67	3.53	3.71	2.21	8.88	142.11	3.53	1.63	6.80	99.87	2.42
8742	#898	–	–	–	–	–	2.57	2.86	1.99	10.10	138.33	2.57	1.46	8.09	91.47	4.56
8742	#666	18.70	2.68	114.00	25.76	125.50	2.35	2.54	2.16	8.64	137.80	2.35	1.68	6.95	105.46	2.59
8742	#316	–	–	–	–	–	1.74	1.89	1.71	7.34	113.57	1.74	1.35	5.66	86.74	2.92
8742	#894	–	–	–	–	–	1.29	1.48	1.74	4.53	94.46	1.29	1.38	3.81	74.27	1.52
8743	#647	–	–	–	–	–	11.04	11.11	2.52	8.97	281.47	11.02	1.92	7.17	177.62	3.60
8743	#238	272.44	28.28	277.00	89.57	243.97	18.87	18.96	7.90	33.49	270.02	18.86	5.96	26.71	180.56	6.75
8743	#563	–	–	–	–	–	10.92	11.00	3.82	19.04	242.96	10.92	2.97	15.60	158.49	6.42
8743	#318	–	–	–	–	–	3.58	3.79	2.28	6.55	186.44	3.57	1.69	5.17	113.55	2.03
8743	#438	–	–	–	–	–	4.06	4.28	2.58	12.52	174.86	4.06	1.93	9.58	112.04	4.63
8743	#615	48.93	6.51	156.00	47.45	149.01	5.26	5.37	2.99	12.49	167.59	5.25	2.32	9.79	114.04	2.72
8743	#649	27.05	4.13	128.00	34.25	130.57	3.60	3.80	3.09	16.50	145.00	3.60	2.50	13.26	106.47	4.10
8743	#565	–	–	–	–	–	1.83	2.02	1.30	3.64	113.10	1.82	1.02	2.94	75.13	1.88

$z = 0.5$		Halo scale					Stellar scale					Projected stellar scale				
sim	ELO	$M_{\rm vir}$	$M_{\rm h}^{\rm bar}$	$r_{\rm vir}$	$r_{\rm e,h}^{\rm tot}$	$\sigma_{\rm 3,h}^{\rm tot}$	$M_{\rm bo}^{\rm star}$	$M_{\rm bo}^{\rm cb}$	$r_{\rm e,bo}^{\rm star}$	$r_{\rm 90,bo}^{\rm star}$	$\sigma_{\rm 3,bo}^{\rm star}$	$M_{\rm cyl,bo}^{\rm star}$	$R_{\rm e,bo}^{\rm star}$	$R_{\rm 90,bo}^{\rm star}$	$\sigma_{\rm los,0}^{\rm star}$	n
8743	#411	–	–	–	–	–	3.11	3.27	2.13	12.42	149.41	3.11	1.61	9.57	112.42	4.91
8743	#129	–	–	–	–	–	2.59	3.07	1.48	8.83	135.77	2.59	1.15	6.89	88.48	4.16
8743	#438	–	–	–	–	–	2.59	2.82	1.61	8.64	119.49	2.59	1.25	6.79	83.86	3.34
8743	#625	–	–	–	–	–	1.52	1.66	1.38	4.71	100.52	1.51	1.06	3.96	71.23	3.01
B sample																
8716	#173	–	–	–	–	–	11.35	11.56	3.37	12.65	251.52	11.34	2.48	10.12	170.67	–
8716	#073	280.40	23.69	279.00	77.87	265.27	15.53	15.67	1.76	18.50	307.49	15.52	1.39	14.62	192.13	–
8716	#353	240.97	22.37	266.00	79.68	255.80	17.23	17.49	3.30	19.84	289.08	17.22	2.58	15.90	187.08	–
8716	#296	–	–	–	–	–	8.38	8.66	2.52	11.14	193.12	8.37	1.84	8.43	144.91	–
8716	#173	–	–	–	–	–	5.81	6.11	1.61	10.88	180.93	5.81	1.26	8.38	122.73	–
8716	#309	–	–	–	–	–	4.04	4.24	1.55	6.23	149.97	4.04	1.18	4.83	106.73	–
8716	#157	29.88	4.34	133.00	33.74	140.98	3.48	3.62	1.35	4.58	149.33	3.48	1.05	3.78	97.63	–
8717	#317	586.95	55.27	357.00	134.44	316.87	32.74	33.39	6.08	26.73	356.04	32.73	4.38	21.33	246.80	–
8717	#815	–	–	–	–	–	3.31	3.52	1.31	5.37	141.61	3.31	1.06	4.18	109.84	–
8721	#011	–	–	–	–	–	9.21	9.62	2.18	12.29	219.04	9.20	1.66	9.60	155.77	–
8721	#217	210.84	20.97	254.00	82.08	228.79	15.03	15.38	4.09	21.22	261.73	15.03	2.95	17.09	180.54	–
8721	#229	142.61	17.04	223.00	91.46	182.05	8.72	9.11	2.26	13.26	215.17	8.72	1.67	10.18	149.48	–
8721	#945	97.39	12.18	196.00	53.87	198.22	5.78	6.26	1.87	6.99	182.45	5.77	1.38	5.43	128.29	–
8721	#607	127.54	11.78	215.00	68.67	201.69	9.10	9.54	1.68	18.68	223.74	9.10	1.30	14.91	150.39	–
8721	#097	87.72	9.97	190.00	54.64	186.50	8.12	8.65	3.26	18.31	199.30	8.12	2.32	14.06	144.24	–
8721	#940	99.84	10.08	198.00	55.28	194.80	7.92	8.16	2.07	14.77	224.73	7.91	1.57	11.34	157.26	–
8721	#917	47.76	5.63	155.00	37.09	163.33	5.15	5.37	1.63	9.51	187.32	5.15	1.23	7.50	141.68	–
8721	#707	–	–	–	–	–	3.41	3.78	1.25	6.30	159.08	3.42	0.94	5.03	119.74	–
8722	#254	–	–	–	–	–	6.03	6.42	2.21	11.18	186.34	6.03	1.58	8.46	133.09	–
8722	#706	37.81	5.18	144.00	49.18	132.53	3.73	4.09	1.39	7.73	148.26	3.74	1.03	5.86	107.29	–
8722	#293	–	–	–	–	–	2.78	2.92	1.26	4.70	131.07	2.78	0.97	3.78	97.68	–
8723	#647	–	–	–	–	–	15.01	15.44	2.39	15.46	303.73	15.00	1.89	12.24	187.74	–
8723	#238	267.05	27.15	275.00	87.54	254.44	19.31	19.49	4.50	21.12	286.91	19.31	3.29	17.04	205.56	–
8723	#563	–	–	–	–	–	9.03	9.27	1.95	9.37	230.05	9.03	1.52	7.44	148.15	–

$z = 0.5$		Halo scale					Stellar scale					Projected stellar scale				
sim	ELO	$M_{\rm vir}$	$M_{\rm h}^{\rm bar}$	$r_{\rm vir}$	$r_{\rm e,h}^{\rm tot}$	$\sigma_{\rm 3,h}^{\rm tot}$	$M_{\rm bo}^{\rm star}$	$M_{\rm bo}^{\rm cb}$	$r_{\rm e,bo}^{\rm star}$	$r_{\rm 90,bo}^{\rm star}$	$\sigma_{\rm 3,bo}^{\rm star}$	$M_{\rm cyl,bo}^{\rm star}$	$R_{\rm e,bo}^{\rm star}$	$R_{\rm 90,bo}^{\rm star}$	$\sigma_{\rm los,0}^{\rm star}$	n
8723	#411	25.69	3.41	126.00	27.85	134.45	3.15	3.39	1.46	5.30	143.37	3.15	1.04	3.94	106.66	–

Table D.4: 3D and 2D Rotation and Shape parameters for ELO samples ($z = 0.5$).

$z = 0.5$		Rotation and Shape									
		3D						2D			
sim	ELO	$V_\phi/\sigma_3^{\rm star}(r_{\rm e,bo}^{\rm star})$	$\epsilon_{\rm 3D}(r_{\rm e,bo}^{\rm star})$	$S(r_{\rm e,bo}^{\rm star})$	$V_\phi/\sigma_3^{\rm star}(r_{\rm 90,bo}^{\rm star})$	$\epsilon_{\rm 3D}(r_{\rm 90,bo}^{\rm star})$	$S(r_{\rm 90,bo}^{\rm star})$	$V_{\rm max}/\sigma_{\rm los,0}^{\rm star}(R_{\rm e,bo}^{\rm star})$	$\epsilon(R_{\rm e,bo}^{\rm star})$	$V_{\rm max}/\sigma_{\rm los,0}^{\rm star}(R_{\rm 90,bo}^{\rm star})$	$\epsilon(R_{\rm 90,bo}^{\rm star})$
A sample											
8714	#073	0.1335	0.0660	3.6482	0.1513	0.0660	3.6482	0.0000	0.0682	0.2239	0.0845
8714	#173	0.3108	0.3486	2.7481	0.3845	0.3486	2.7481	0.1271	0.2599	0.3407	0.2737
8714	#353	0.0688	0.3706	0.0640	0.1013	0.3706	0.0640	0.0874	0.4388	0.3323	0.3195
8714	#581	0.1194	0.2852	2.9040	0.2108	0.2852	2.9040	0.0000	0.2280	0.2160	0.3262
8714	#296	0.4886	0.3665	1.4648	0.6969	0.3665	1.4648	0.2757	0.3521	0.5316	0.3977
8714	#473	0.0374	0.2104	1.6006	0.0989	0.2104	1.6006	0.0708	0.1486	0.1587	0.1892
8714	#309	0.3015	0.4150	0.1361	0.9986	0.4150	0.1361	0.2317	0.4619	0.4288	0.6525
8714	#285	0.5964	0.3280	1.5652	0.3851	0.3280	1.5652	0.0000	0.3419	0.4036	0.4191
8714	#343	0.5345	0.3379	1.5063	0.6510	0.3379	1.5063	0.1914	0.3067	0.4443	0.3961
8714	#157	0.3746	0.1756	1.6567	0.4124	0.1756	1.6567	0.0000	0.1678	0.2664	0.5369
8714	#208	0.0055	0.1444	1.4839	0.0177	0.1444	1.4839	0.1135	0.1451	0.0934	0.3606
8747	#317	0.0812	0.4757	0.1017	0.0918	0.4757	0.1017	0.0701	0.5201	0.2926	0.4392
8747	#288	0.0754	0.3276	0.1479	0.0443	0.3276	0.1479	0.0000	0.3408	0.1981	0.4742
8747	#348	0.2038	0.1793	0.2194	0.2688	0.1793	0.2194	0.0000	0.1901	0.2801	0.2790
8747	#015	0.3254	0.3308	0.2385	0.5305	0.3308	0.2385	0.1946	0.3270	0.5058	0.3379
8747	#179	0.3071	0.2840	0.2290	0.4778	0.2840	0.2290	0.2132	0.3197	0.3918	0.4439
8747	#815	0.1887	0.2678	0.2397	0.0407	0.2678	0.2397	0.0000	0.2945	0.2159	0.2907
8747	#319	0.2859	0.2233	0.1574	0.8074	0.2233	0.1574	0.0000	0.1894	0.2275	0.3128
8747	#114	0.0736	0.0713	3.5544	0.3660	0.0713	1.5544	0.0000	0.1146	0.1236	0.1449
8747	#100	0.3894	0.1544	0.2438	0.4951	0.1544	0.2438	0.0000	0.1617	0.2373	0.2503
8747	#206	0.1723	0.2241	1.6716	0.3429	0.2241	1.6716	0.0000	0.1754	0.1328	0.2034
8747	#102	0.1205	0.3977	0.0287	0.3319	0.3977	0.0287	0.0000	0.4978	0.1532	0.5833
8747	#100	0.4268	0.2295	1.5312	0.5942	0.2295	1.5312	0.0000	0.2224	0.3158	0.3240

$z = 0.5$		Rotation and Shape									
		3D						2D			
sim	ELO	$V_\phi/\sigma_3^{\rm star}(r_{\rm e,bo}^{\rm star})$	$\epsilon_{\rm 3D}(r_{\rm e,bo}^{\rm star})$	$S(r_{\rm e,bo}^{\rm star})$	$V_\phi/\sigma_3^{\rm star}(r_{\rm 90,bo}^{\rm star})$	$\epsilon_{\rm 3D}(r_{\rm 90,bo}^{\rm star})$	$S(r_{\rm 90,bo}^{\rm star})$	$V_{\rm max}/\sigma_{\rm los,0}^{\rm star}(R_{\rm e,bo}^{\rm star})$	$\epsilon(R_{\rm e,bo}^{\rm star})$	$V_{\rm max}/\sigma_{\rm los,0}^{\rm star}(R_{\rm 90,bo}^{\rm star})$	$\epsilon(R_{\rm 90,bo}^{\rm star})$
8741	#011	0.0884	0.2441	0.1903	0.2206	0.2441	0.1903	0.0788	0.2499	0.2204	0.1669
8741	#217	0.0549	0.2177	0.1287	0.0672	0.2177	0.1287	0.0887	0.1938	0.2602	0.2667
8741	#229	0.3430	0.2211	2.7002	0.3194	0.2211	2.7002	0.0000	0.2136	0.2678	0.5186
8741	#607	0.0874	0.2037	0.2560	0.1260	0.2037	0.2560	0.0824	0.1964	0.2354	0.2168
8741	#097	0.1342	0.3350	0.2717	0.4019	0.3350	0.2717	0.0976	0.3039	0.2025	0.2823
8741	#940	0.0104	0.1838	0.1826	0.0256	0.1838	0.1826	0.0702	0.1541	0.2025	0.3036
8741	#026	0.6123	0.5559	0.2252	0.1941	0.5559	0.2252	0.2858	0.5729	0.4147	0.3448
8741	#945	0.2182	0.1912	1.6498	0.3808	0.1912	1.6498	0.1414	0.1947	0.3120	0.4836
8741	#507	0.4382	0.2265	2.9060	0.5344	0.2265	2.9060	0.0865	0.2246	0.5323	0.3952
8741	#917	0.0127	0.3231	0.0410	0.0393	0.3231	0.0410	0.0774	0.3873	0.1203	0.5588
8741	#014	0.1035	0.1249	1.3617	0.0363	0.1249	1.3617	0.0000	0.1211	0.0924	0.1660
8741	#997	0.1314	0.1060	0.1372	0.2756	0.1060	0.1372	0.0000	0.1038	0.1532	0.1251
8742	#293	0.1011	0.3037	0.1622	0.0256	0.3037	0.1622	0.0720	0.2788	0.1670	0.2580
8742	#234	0.4354	0.2916	1.4536	0.3988	0.2916	1.4536	0.1907	0.2477	0.4043	0.2335
8742	#383	0.1359	0.0392	3.8794	0.1066	0.0392	2.8794	0.0000	0.0471	0.1773	0.1221
8742	#992	0.4841	0.3804	0.2272	0.5600	0.3804	0.2272	0.0000	0.4254	0.3073	0.4958
8742	#706	0.4812	0.1251	1.4806	0.4628	0.1251	1.4806	0.0000	0.2039	0.3664	0.4214
8742	#898	0.3131	0.3419	2.7039	0.0192	0.3419	2.7039	0.0000	0.3315	0.2095	0.1899
8742	#666	0.1572	0.2787	1.6076	0.1770	0.2787	1.6076	0.0000	0.2048	0.1140	0.3093
8742	#316	0.4237	0.3411	1.4577	0.4221	0.3411	1.4577	0.0000	0.2822	0.2282	0.2003
8742	#894	0.6782	0.3798	2.7181	0.8949	0.3798	2.7181	0.0000	0.2601	0.3317	0.3033
8743	#647	0.0515	0.2636	0.0731	0.0561	0.2636	0.0731	0.0000	0.2965	0.1905	0.3809
8743	#238	0.0546	0.3960	1.3451	0.1257	0.3960	1.3451	0.0684	0.3784	0.3279	0.3024
8743	#563	0.1930	0.2948	0.2479	0.1223	0.2948	0.2479	0.1262	0.2969	0.2946	0.2573
8743	#318	0.5018	0.1284	0.1368	0.6137	0.1284	0.1368	0.0000	0.1402	0.2850	0.3224
8743	#438	0.2090	0.1247	1.6175	0.8142	0.1247	1.6175	0.0000	0.1159	0.3250	0.3044
8743	#615	0.3467	0.3386	0.1899	0.5061	0.3386	0.1899	0.1890	0.3770	0.3032	0.5763
8743	#649	0.1623	0.4244	0.1609	0.2303	0.4244	0.1609	0.1159	0.4804	0.1469	0.5062

$z = 0.5$		Rotation and Shape									
		3D						2D			
sim	ELO	$V_\phi/\sigma_3^{\rm star}(r_{\rm e,bo}^{\rm star})$	$\epsilon_{\rm 3D}(r_{\rm e,bo}^{\rm star})$	$S(r_{\rm e,bo}^{\rm star})$	$V_\phi/\sigma_3^{\rm star}(r_{\rm 90,bo}^{\rm star})$	$\epsilon_{\rm 3D}(r_{\rm 90,bo}^{\rm star})$	$S(r_{\rm 90,bo}^{\rm star})$	$V_{\rm max}/\sigma_{\rm los,0}^{\rm star}(R_{\rm e,bo}^{\rm star})$	$\epsilon(R_{\rm e,bo}^{\rm star})$	$V_{\rm max}/\sigma_{\rm los,0}^{\rm star}(R_{\rm 90,bo}^{\rm star})$	$\epsilon(R_{\rm 90,bo}^{\rm star})$
8743	#565	0.2078	0.1392	1.3260	0.2323	0.1392	1.3260	0.0000	0.1657	0.1538	0.1951
8743	#411	0.0209	0.1874	1.3813	0.0652	0.1874	1.3813	0.0000	0.1270	0.0993	0.5031
8743	#129	0.3053	0.2258	1.3558	0.4065	0.2258	1.3558	0.0000	0.1665	0.2077	0.2916
8743	#438	0.3334	0.2100	0.0711	0.3213	0.2100	0.0711	0.0000	0.1829	0.2719	0.3234
8743	#625	0.4420	0.2724	2.7997	0.7471	0.2724	2.7997	0.0000	0.2297	0.3482	0.5303
B sample											
8716	#173	0.0286	0.2646	0.0247	0.1188	0.2646	0.0247	0.0757	0.2859	0.1894	0.3808
8716	#073	0.0254	0.0697	3.4092	0.0865	0.0697	1.4092	0.0000	0.0839	0.2379	0.1298
8716	#353	0.0142	0.3828	0.1506	0.1025	0.3828	0.1506	0.0490	0.4315	0.2074	0.4053
8716	#296	0.6892	0.3570	2.7639	0.6800	0.3570	2.7639	0.0000	0.3387	0.6301	0.4639
8716	#173	0.4088	0.2840	1.5676	0.0234	0.2840	1.5676	0.0000	0.2445	0.2818	0.1802
8716	#309	0.3374	0.3921	0.0834	0.2465	0.3921	0.0834	0.0000	0.4442	0.2396	0.5280
8716	#157	0.6459	0.2984	2.7832	0.6564	0.2984	2.7832	0.0000	0.1992	0.4270	0.4993
8717	#317	0.2040	0.4763	1.3809	0.2156	0.4763	1.3809	0.0807	0.4225	0.3030	0.2690
8717	#815	0.1219	0.4008	1.3240	0.2640	0.4008	1.3240	0.0000	0.3646	0.0885	0.4960
8721	#011	0.4411	0.3770	1.4343	0.3392	0.3770	1.4343	0.0000	0.3691	0.4303	0.3158
8721	#217	0.1252	0.0996	3.1615	0.2633	0.0996	0.1615	0.0836	0.0829	0.2085	0.2822
8721	#229	0.4892	0.3660	1.4928	0.4097	0.3660	1.4928	0.0000	0.2999	0.4224	0.4326
8721	#945	0.5397	0.2591	1.5804	0.7818	0.2591	1.5804	0.0000	0.2126	0.3923	0.4518
8721	#607	0.3324	0.1818	2.8158	0.3090	0.1818	2.8158	0.0000	0.1882	0.3333	0.2104
8721	#097	0.2024	0.3263	0.0408	0.0539	0.3263	0.0408	0.1500	0.3275	0.2635	0.2042
8721	#940	0.0019	0.0914	3.5811	0.1186	0.0914	1.5811	0.0000	0.1127	0.1695	0.1880
8721	#917	0.0633	0.2335	1.4666	0.0689	0.2335	1.4666	0.0000	0.2151	0.1013	0.5292
8721	#707	0.0079	0.1701	0.1869	0.1690	0.1701	0.1869	0.0000	0.1646	0.0780	0.1843
8722	#254	0.5928	0.5085	0.1880	0.3175	0.5085	0.1880	0.0000	0.4677	0.4665	0.4500
8722	#706	0.5480	0.1863	1.5754	0.5006	0.1863	1.5754	0.0000	0.1706	0.3626	0.4680
8722	#293	0.3747	0.3009	1.6332	0.3837	0.3009	1.6332	0.0000	0.2517	0.2302	0.5929
8723	#647	0.0257	0.3041	0.0619	0.0918	0.3041	0.0619	0.0000	0.3795	0.2963	0.3545

$z = 0.5$		Rotation and Shape									
		3D						2D			
sim	ELO	$V_\phi/\sigma_3^{\rm star}(r_{\rm e,bo}^{\rm star})$	$\epsilon_{\rm 3D}(r_{\rm e,bo}^{\rm star})$	$S(r_{\rm e,bo}^{\rm star})$	$V_\phi/\sigma_3^{\rm star}(r_{\rm 90,bo}^{\rm star})$	$\epsilon_{\rm 3D}(r_{\rm 90,bo}^{\rm star})$	$S(r_{\rm 90,bo}^{\rm star})$	$V_{\rm max}/\sigma_{\rm los,0}^{\rm star}(R_{\rm e,bo}^{\rm star})$	$\epsilon(R_{\rm e,bo}^{\rm star})$	$V_{\rm max}/\sigma_{\rm los,0}^{\rm star}(R_{\rm 90,bo}^{\rm star})$	$\epsilon(R_{\rm 90,bo}^{\rm star})$
8723	#238	0.1291	0.3876	1.3263	0.1389	0.3876	1.3263	0.0534	0.3631	0.2162	0.3889
8723	#563	0.0954	0.2028	0.0281	0.3827	0.2028	0.0281	0.0000	0.2638	0.2753	0.2236
8723	#411	0.3230	0.3452	0.1096	0.3729	0.3452	0.1096	0.0000	0.3466	0.2572	0.5547
8935	#132	0.1457	0.1927	0.1639	0.1614	0.1927	0.1639	0.0417	0.1899	0.3035	0.2129
F1 sample											
8935	#028	0.0519	0.1317	0.2007	0.1500	0.1317	0.2007	0.0000	0.1324	0.1739	0.2817
8935	#022	0.2286	0.3648	1.3066	0.0667	0.3648	1.3066	0.3180	0.3406	0.3836	0.3108
8935	#928	0.3068	0.3053	0.0557	0.3427	0.3053	0.0557	0.1524	0.3227	0.3550	0.4363
8935	#238	0.3286	0.4134	0.1527	0.4374	0.4134	0.1527	0.1543	0.4590	0.3917	0.5375
8935	#202	0.1877	0.1498	0.1663	0.0783	0.1498	0.1663	0.0858	0.1627	0.3309	0.3856
8935	#212	0.2169	0.3942	1.3097	0.3761	0.3942	1.3097	0.1108	0.3775	0.3140	0.3944
8935	#371	0.7591	0.4275	1.5329	0.6713	0.4275	1.5329	0.3525	0.3487	0.6288	0.3647
8935	#232	0.1418	0.2025	1.4912	0.1925	0.2025	1.4912	0.0718	0.1729	0.1986	0.3005
8935	#334	0.0554	0.4557	0.0582	0.3002	0.4557	0.0582	0.1138	0.5115	0.2029	0.3227
8935	#129	0.1689	0.3222	0.0780	0.0947	0.3222	0.0780	0.1708	0.3258	0.2636	0.3268
8935	#336	0.0975	0.2975	0.0214	0.2257	0.2975	0.0214	0.0000	0.3394	0.2123	0.3652
8935	#536	0.2222	0.2000	1.4288	0.4032	0.2000	1.4288	0.1323	0.1735	0.3446	0.3913
8935	#094	0.2775	0.3057	0.2168	0.2582	0.3057	0.2168	0.0000	0.3076	0.1886	0.4534
8935	#042	0.4174	0.2898	1.5106	0.1470	0.2898	1.5106	0.1203	0.3059	0.3299	0.3091
8935	#239	0.1292	0.3546	0.0533	0.3553	0.3546	0.0533	0.0000	0.4204	0.1748	0.3907
8935	#534	0.2359	0.3000	0.1388	0.4881	0.3000	0.1388	0.1125	0.3402	0.2568	0.3703
8935	#280	0.3988	0.1976	2.7663	0.2835	0.1976	2.7663	0.1627	0.1614	0.3306	0.2098
8935	#135	0.0261	0.2275	1.6991	0.0650	0.2275	1.6991	0.0000	0.2387	0.1654	0.2947
8935	#244	0.3034	0.3157	0.0737	0.3322	0.3157	0.0737	0.1567	0.3774	0.2330	0.4745
8935	#371	0.5158	0.3623	1.5058	0.6236	0.3623	1.5058	0.0000	0.3470	0.3921	0.4342
8935	#637	0.4688	0.2636	2.8027	0.3108	0.2636	2.8027	0.0000	0.1884	0.2614	0.3726
8935	#734	0.3596	0.5277	1.3129	0.5427	0.5277	1.3129	0.2087	0.5046	0.2847	0.5779
8935	#351	0.2517	0.3272	0.2895	0.2937	0.3272	0.2895	0.1342	0.2938	0.2155	0.4541

$z = 0.5$		Rotation and Shape									
		3D						2D			
sim	ELO	$V_\phi/\sigma_3^{\rm star}(r_{\rm e,bo}^{\rm star})$	$\epsilon_{\rm 3D}(r_{\rm e,bo}^{\rm star})$	$S(r_{\rm e,bo}^{\rm star})$	$V_\phi/\sigma_3^{\rm star}(r_{\rm 90,bo}^{\rm star})$	$\epsilon_{\rm 3D}(r_{\rm 90,bo}^{\rm star})$	$S(r_{\rm 90,bo}^{\rm star})$	$V_{\rm max}/\sigma_{\rm los,0}^{\rm star}(R_{\rm e,bo}^{\rm star})$	$\epsilon(R_{\rm e,bo}^{\rm star})$	$V_{\rm max}/\sigma_{\rm los,0}^{\rm star}(R_{\rm 90,bo}^{\rm star})$	$\epsilon(R_{\rm 90,bo}^{\rm star})$
8935	#039	0.0830	0.3441	0.2079	0.0560	0.3441	0.2079	0.1218	0.3427	0.1677	0.4523
F2 sample											
8914	#371	0.0502	0.1481	2.7552	0.1310	0.1481	2.7552	0.0550	0.1348	0.3246	0.1682
8914	#132	0.0528	0.2131	0.1958	0.2387	0.2131	0.1958	0.0469	0.1988	0.2156	0.3340
8914	#928	0.3363	0.3323	0.2346	0.4079	0.3323	0.2346	0.1115	0.3278	0.4405	0.2814
8914	#928	0.0339	0.1460	2.8071	0.5554	0.1460	2.8071	0.0829	0.1049	0.2446	0.1605
8914	#202	0.1658	0.1986	2.8196	0.0650	0.1986	3.8196	0.1269	0.1502	0.2263	0.0920
8914	#381	0.4357	0.3769	1.3851	0.6146	0.3769	1.3851	0.2019	0.3457	0.4573	0.2997
8914	#243	0.1080	0.1870	0.0816	0.1499	0.1870	0.0816	0.0641	0.2022	0.2166	0.3153
8914	#434	0.4618	0.2731	0.1909	0.5781	0.2731	0.1909	0.2589	0.2329	0.3549	0.3223
8914	#129	0.1705	0.1718	0.2464	0.2369	0.1718	0.2464	0.1169	0.1940	0.2835	0.2797
8914	#336	0.1492	0.1323	0.0505	0.2764	0.1323	0.0505	0.1219	0.1393	0.2465	0.1795
8914	#536	0.1822	0.1202	1.6771	0.0885	0.1202	1.6771	0.1178	0.1383	0.2966	0.2461
8914	#094	0.0130	0.1862	0.2022	0.0522	0.1862	0.2022	0.0516	0.1712	0.1570	0.2954
8914	#022	0.1789	0.2102	0.1390	0.2130	0.2102	0.1390	0.1235	0.2149	0.1727	0.2953
8914	#289	0.1295	0.1294	1.6282	0.4185	0.1294	3.6282	0.0957	0.1265	0.1838	0.0691
8914	#371	0.3561	0.2823	2.7949	0.1565	0.2823	2.7949	0.1960	0.2230	0.3039	0.3963
8914	#036	0.2249	0.2184	1.5518	0.0937	0.2184	1.5518	0.1607	0.1920	0.2152	0.3258
8914	#254	0.3186	0.3065	0.1342	0.4360	0.3065	0.1342	0.1732	0.3450	0.2640	0.3015
8914	#042	0.2705	0.0839	3.5255	0.3717	0.0839	1.5255	0.0903	0.0792	0.3103	0.1401
8914	#051	0.0762	0.1823	1.6555	0.1535	0.1823	1.6555	0.0878	0.1428	0.1625	0.3389
8914	#282	0.3698	0.3050	0.2549	0.4784	0.3050	0.2549	0.2039	0.2995	0.3125	0.1941
8914	#198	0.2410	0.1231	1.3332	0.0154	0.1231	3.3332	0.0000	0.1401	0.1413	0.0795
8914	#038	0.0220	0.1024	1.4815	0.0904	0.1024	1.4815	0.0741	0.1189	0.1301	0.1310
8914	#341	0.1917	0.1589	1.5046	0.1201	0.1589	1.5046	0.1119	0.1501	0.1791	0.3777
8914	#109	0.2320	0.2554	1.6399	0.4317	0.2554	1.6399	0.1207	0.2485	0.2162	0.3323
8914	#238	0.3245	0.2776	2.9198	0.6343	0.2776	2.9198	0.1062	0.2693	0.3947	0.4377

$z = 0.5$		Rotation and Shape									
		3D						2D			
sim	ELO	$V_\phi/\sigma_3^{\rm star}(r_{\rm e,bo}^{\rm star})$	$\epsilon_{\rm 3D}(r_{\rm e,bo}^{\rm star})$	$S(r_{\rm e,bo}^{\rm star})$	$V_\phi/\sigma_3^{\rm star}(r_{\rm 90,bo}^{\rm star})$	$\epsilon_{\rm 3D}(r_{\rm 90,bo}^{\rm star})$	$S(r_{\rm 90,bo}^{\rm star})$	$V_{\rm max}/\sigma_{\rm los,0}^{\rm star}(R_{\rm e,bo}^{\rm star})$	$\epsilon(R_{\rm e,bo}^{\rm star})$	$V_{\rm max}/\sigma_{\rm los,0}^{\rm star}(R_{\rm 90,bo}^{\rm star})$	$\epsilon(R_{\rm 90,bo}^{\rm star})$
8914	#114	0.0689	0.2177	1.4594	0.0492	0.2177	1.4594	0.0000	0.1882	0.1008	0.3161

Table D.5: Masses, sizes and mean square velocities at the halo and baryonic object scale, as well as their projected counterparts ($z = 1$). Masses are given in 10^{10} $M_\odot$, distances in kpc, velocity dispersions in $km \times s^{-1}$.

$z = 1$		Halo scale					Stellar scale					Projected stellar scale				
sim	ELO	$M_{\rm vir}$	$M_{\rm h}^{\rm bar}$	$r_{\rm vir}$	$r_{\rm e,h}^{\rm tot}$	$\sigma_{3,\rm h}^{\rm tot}$	$M_{\rm bo}^{\rm star}$	$M_{\rm bo}^{\rm cb}$	$r_{\rm e,bo}^{\rm star}$	$r_{\rm 90,bo}^{\rm star}$	$\sigma_{3,\rm bo}^{\rm star}$	$M_{\rm cyl,bo}^{\rm star}$	$R_{\rm e,bo}^{\rm star}$	$R_{\rm 90,bo}^{\rm star}$	$\sigma_{\rm los,0}^{\rm star}$	n
A sample																
8714	#353	229.51	23.26	204.00	78.19	245.44	16.41	16.55	4.98	22.48	274.59	16.41	3.98	18.27	185.79	5.28
8714	#073	–	–	–	–	–	12.75	12.86	2.02	11.72	313.72	12.74	1.55	8.68	195.78	6.04
8714	#680	131.11	15.41	169.00	84.68	208.44	6.35	6.64	3.41	16.05	202.92	6.34	2.55	12.50	134.24	3.60
8714	#473	–	–	–	–	–	5.42	5.81	4.92	24.72	167.26	5.42	3.61	19.75	122.17	5.51
8714	#206	–	–	–	–	–	4.58	4.95	2.10	16.34	168.55	4.58	1.60	12.17	114.61	5.83
8714	#772	–	–	–	–	–	3.94	4.17	1.98	13.02	140.53	3.94	1.58	10.04	97.34	3.05
8714	#285	–	–	–	–	–	2.71	3.13	1.87	7.24	118.37	2.71	1.47	5.55	83.27	1.77
8714	#309	–	–	–	–	–	3.82	4.12	3.36	12.95	181.63	3.82	2.54	9.77	128.20	1.65
8714	#282	–	–	–	–	–	3.19	3.77	1.93	9.99	148.51	3.19	1.45	7.51	96.15	4.58
8714	#208	–	–	–	–	–	2.79	2.96	2.82	14.34	140.82	2.79	2.07	10.80	107.07	5.11
8714	#147	–	–	–	–	–	1.83	2.02	1.22	3.23	112.55	1.83	0.95	2.65	73.58	1.38
8747	#417	277.63	26.18	217.00	87.87	276.98	17.06	17.26	5.06	26.65	290.23	17.05	3.81	20.85	198.34	6.89
8747	#278	186.84	21.05	190.00	71.20	232.37	11.27	11.44	4.59	20.71	239.77	11.27	3.52	16.84	161.01	5.52
8747	#015	122.04	13.18	165.00	55.70	215.40	10.80	11.05	3.14	21.03	241.99	10.80	2.40	16.13	164.63	5.32
8747	#347	–	–	–	–	–	7.84	8.09	3.46	19.10	207.64	7.84	2.67	15.30	136.65	5.50
8747	#319	36.69	4.77	111.00	29.94	152.03	4.08	4.36	2.02	12.44	153.06	4.08	1.55	9.46	102.03	3.79
8747	#288	40.10	5.93	114.00	47.57	141.58	3.83	4.25	2.89	13.15	139.16	3.82	2.21	9.94	100.94	2.36
8747	#103	37.37	4.89	111.00	31.12	147.80	3.70	4.15	2.10	12.02	154.49	3.70	1.61	9.44	97.97	3.31
8747	#826	29.88	4.42	103.00	29.90	153.56	2.99	3.26	2.03	8.19	137.77	2.99	1.62	6.60	103.99	2.27
8747	#190	–	–	–	–	–	2.99	3.53	2.26	6.41	186.46	2.99	1.72	5.55	122.31	3.79
8747	#070	–	–	–	–	–	3.12	3.41	2.65	10.34	135.23	3.13	2.05	8.26	106.74	2.29
8747	#337	23.09	3.45	95.00	30.65	128.15	2.46	2.60	2.71	9.88	123.85	2.46	2.15	7.89	85.29	2.52
8747	#102	–	–	–	–	–	1.61	1.79	1.32	6.29	113.39	1.61	1.03	5.01	86.10	3.19

$z = 1$		Halo scale					Stellar scale					Projected stellar scale				
sim	ELO	$M_{\rm vir}$	$M_{\rm h}^{\rm bar}$	$r_{\rm vir}$	$r_{\rm e,h}^{\rm tot}$	$\sigma_{\rm 3,h}^{\rm tot}$	$M_{\rm bo}^{\rm star}$	$M_{\rm bo}^{\rm cb}$	$r_{\rm e,bo}^{\rm star}$	$r_{\rm 90,bo}^{\rm star}$	$\sigma_{\rm 3,bo}^{\rm star}$	$M_{\rm cyl,bo}^{\rm star}$	$R_{\rm e,bo}^{\rm star}$	$R_{\rm 90,bo}^{\rm star}$	$\sigma_{\rm los,0}^{\rm star}$	n
8741	#217	180.49	20.21	188.00	63.40	238.95	13.22	13.48	5.60	25.20	252.75	13.22	4.21	19.86	164.19	5.54
8741	#607	122.68	13.36	165.00	66.19	204.92	8.33	8.75	3.35	27.77	219.11	8.33	2.52	22.00	144.02	8.22
8741	#940	84.88	9.78	146.00	43.93	196.36	6.59	6.79	3.59	17.48	210.13	6.59	2.68	13.55	143.19	5.24
8741	#087	82.84	10.37	145.00	54.54	176.82	5.29	5.36	3.00	11.49	187.26	5.29	2.26	9.44	120.11	3.45
8741	#229	87.92	10.98	148.00	65.95	181.26	6.25	6.46	2.87	14.30	191.49	6.25	2.15	11.31	135.19	4.18
8741	#012	–	–	–	–	–	5.77	6.09	2.20	14.65	177.09	5.77	1.73	11.44	120.14	3.86
8741	#507	–	–	–	–	–	5.19	5.66	2.38	17.56	174.28	5.19	1.84	12.87	130.14	5.41
8741	#955	–	–	–	–	–	4.83	4.91	2.06	11.21	173.37	4.83	1.56	8.46	119.09	2.50
8741	#027	46.86	5.82	120.00	35.51	161.39	5.18	5.47	2.58	11.86	171.22	5.18	1.93	9.67	119.72	3.11
8741	#917	36.26	4.91	110.00	27.26	159.83	4.14	4.45	2.39	10.48	163.96	4.14	1.88	8.50	117.54	2.19
8741	#014	–	–	–	–	–	3.71	4.01	1.97	10.94	170.45	3.70	1.48	8.08	119.47	6.49
8741	#707	33.36	4.70	107.00	35.07	148.01	3.36	3.63	2.00	13.82	153.33	3.36	1.53	10.52	103.51	6.28
8741	#897	–	–	–	–	–	2.78	3.35	1.64	7.82	135.80	2.78	1.27	5.82	85.86	1.58
8742	#293	–	–	–	–	–	12.95	13.12	3.59	11.97	280.20	12.94	2.68	9.63	185.38	3.17
8742	#234	–	–	–	–	–	7.59	7.87	2.08	10.52	231.82	7.59	1.63	8.25	145.17	5.39
8742	#254	–	–	–	–	–	2.14	2.36	1.47	5.32	133.71	2.14	1.16	4.25	88.42	2.86
8742	#234	67.99	8.49	136.00	39.06	183.50	6.69	6.97	3.74	18.73	197.63	6.69	2.88	14.92	125.41	4.96
8742	#482	77.00	7.94	142.00	37.66	190.63	6.89	7.02	2.23	18.24	207.47	6.89	1.75	14.23	132.86	6.16
8742	#991	–	–	–	–	–	2.56	2.92	2.03	8.66	129.81	2.56	1.55	6.72	88.33	2.58
8742	#898	–	–	–	–	–	2.30	2.64	1.93	8.55	134.31	2.30	1.45	6.58	94.25	3.18
8742	#706	–	–	–	–	–	2.14	2.41	1.87	7.60	124.73	2.14	1.43	6.28	81.52	2.87
8742	#317	–	–	–	–	–	1.50	1.74	2.12	6.74	101.92	1.50	1.57	5.22	77.84	1.91
8743	#238	–	–	–	–	–	8.93	9.01	2.48	6.64	277.75	8.94	1.85	5.42	170.55	2.82
8743	#648	216.28	22.40	200.00	67.59	255.63	13.79	13.88	3.72	17.52	275.36	13.79	2.81	14.05	188.64	5.28
8743	#663	–	–	–	–	–	8.73	8.85	2.97	14.33	233.31	8.72	2.31	11.48	152.81	5.16
8743	#737	55.38	8.12	127.00	38.05	164.77	6.21	6.37	5.41	21.92	172.36	6.21	4.08	17.82	127.07	3.65
8743	#614	–	–	–	–	–	3.77	4.13	2.49	9.78	154.80	3.77	1.88	7.49	106.05	2.24
8743	#438	–	–	–	–	–	3.67	4.03	2.25	7.42	201.16	3.67	1.71	5.81	131.36	2.18
8743	#411	–	–	–	–	–	1.92	2.08	1.43	3.98	126.59	1.92	1.09	3.18	79.67	1.68

$z = 1$		Halo scale					Stellar scale					Projected stellar scale				
sim	ELO	$M_{\rm vir}$	$M_{\rm h}^{\rm bar}$	$r_{\rm vir}$	$r_{\rm e,h}^{\rm tot}$	$\sigma_{3,\rm h}^{\rm tot}$	$M_{\rm bo}^{\rm star}$	$M_{\rm bo}^{\rm cb}$	$r_{\rm e,bo}^{\rm star}$	$r_{\rm 90,bo}^{\rm star}$	$\sigma_{3,\rm bo}^{\rm star}$	$M_{\rm cyl,bo}^{\rm star}$	$R_{\rm e,bo}^{\rm star}$	$R_{\rm 90,bo}^{\rm star}$	$\sigma_{\rm los,0}^{\rm star}$	n
8743	#317	–	–	–	–	–	2.26	2.84	1.86	6.80	123.47	2.26	1.43	5.26	84.51	1.52
8743	#120	–	–	–	–	–	2.44	2.92	1.51	8.27	135.44	2.44	1.20	6.45	92.60	3.11
8743	#438	–	–	–	–	–	2.37	2.66	1.81	6.98	120.81	2.37	1.31	5.60	84.52	4.44
8743	#665	–	–	–	–	–	1.67	2.01	1.35	4.04	105.54	1.67	1.05	3.27	72.43	1.73
8743	#659	–	–	–	–	–	1.64	1.84	1.62	6.66	108.95	1.64	1.23	5.41	75.54	3.71
B sample																
8716	#173	133.03	16.14	170.00	55.25	217.30	12.00	12.62	4.00	20.17	227.54	11.98	3.15	16.47	161.75	3.71
8716	#172	58.52	7.48	129.00	43.65	166.48	5.31	5.58	1.62	7.67	179.04	5.31	1.27	6.12	115.61	3.71
8717	#417	269.80	23.05	215.00	85.49	282.30	16.72	17.25	3.10	20.35	295.75	16.72	2.42	16.26	218.14	3.71
8717	#278	189.90	21.24	191.00	71.00	239.97	13.23	13.69	3.33	29.05	239.80	13.22	2.56	22.86	171.38	3.71
8717	#015	121.33	12.70	165.00	55.43	209.62	10.25	10.91	1.98	10.96	225.48	10.24	1.53	8.70	150.77	3.71
8717	#347	–	–	–	–	–	8.18	8.74	2.19	15.41	209.38	8.18	1.74	11.84	140.66	3.71
8721	#217	182.31	19.48	189.00	68.64	238.81	13.03	13.42	3.19	13.89	265.07	13.03	2.29	11.84	185.09	3.71
8721	#011	101.70	12.01	155.00	57.04	191.50	8.53	9.03	2.16	10.25	202.30	8.53	1.61	8.01	150.64	3.71
8721	#940	84.68	9.28	146.00	42.17	203.46	6.75	7.06	1.82	11.40	215.81	6.75	1.39	8.55	146.07	3.71
8722	#293	511.72	53.94	266.00	116.69	304.33	24.37	25.54	4.65	33.87	299.64	24.37	3.21	25.60	227.20	3.71
8722	#234	66.83	8.22	135.00	36.04	191.45	6.38	7.41	2.28	14.02	202.59	6.38	1.72	11.26	128.40	3.71
8722	#482	77.48	7.98	142.00	35.60	197.73	6.25	7.05	1.40	10.03	209.78	6.25	1.10	7.68	135.35	3.71
8723	#648	214.93	21.18	199.00	66.99	262.93	15.18	15.75	2.46	19.65	275.52	15.18	1.93	15.17	186.85	3.71
8723	#547	169.28	19.94	184.00	70.19	222.99	13.35	13.78	3.72	19.49	239.52	13.35	2.75	15.58	173.14	3.71
8723	#663	202.12	22.70	195.00	81.00	244.68	9.54	9.93	2.11	13.77	232.33	9.54	1.66	10.52	156.20	3.71
8723	#737	54.60	7.24	126.00	37.24	170.46	5.82	6.21	2.28	13.38	184.23	5.82	1.75	10.66	133.47	3.71
F3 sample																
2100	#629	225.17	24.04	203.00	74.89	250.62	10.89	11.14	3.25	12.50	255.28	10.88	2.44	9.94	165.30	3.54
2100	#470	–	–	–	–	–	8.50	8.70	2.29	8.99	232.97	8.50	1.78	6.99	153.97	2.91
2100	#638	72.01	9.10	139.00	49.32	171.92	5.21	5.35	2.20	10.41	189.44	5.21	1.73	8.24	120.79	4.45
2100	#740	–	–	–	–	–	3.96	4.26	3.38	14.55	149.12	3.96	2.51	11.54	93.41	3.23
2100	#562	47.13	6.40	121.00	33.23	166.91	5.16	5.31	2.24	8.64	178.02	5.16	1.73	6.85	125.16	2.76
2100	#953	–	–	–	–	–	4.23	4.32	2.29	8.18	157.36	4.22	1.72	6.51	108.89	2.06

$z = 1$		Halo scale					Stellar scale					Projected stellar scale				
sim	ELO	$M_{\rm vir}$	$M_{\rm h}^{\rm bar}$	$r_{\rm vir}$	$r_{\rm e,h}^{\rm tot}$	$\sigma_{\rm 3,h}^{\rm tot}$	$M_{\rm bo}^{\rm star}$	$M_{\rm bo}^{\rm cb}$	$r_{\rm e,bo}^{\rm star}$	$r_{\rm 90,bo}^{\rm star}$	$\sigma_{\rm 3,bo}^{\rm star}$	$M_{\rm cyl,bo}^{\rm star}$	$R_{\rm e,bo}^{\rm star}$	$R_{\rm 90,bo}^{\rm star}$	$\sigma_{\rm los,0}^{\rm star}$	n
2100	#517	47.92	6.04	121.00	38.13	155.51	5.32	5.49	2.61	12.76	156.05	5.32	1.96	9.92	112.95	3.83
2100	#233	51.92	6.14	125.00	40.83	160.80	5.50	5.60	2.63	11.74	176.58	5.50	2.00	9.32	124.66	3.29
2100	#087	–	–	–	–	–	2.70	2.88	1.96	9.35	136.73	2.70	1.52	7.39	94.39	3.62
2100	#129	–	–	–	–	–	3.93	4.06	2.18	11.55	149.87	3.93	1.69	9.22	102.13	3.90
2100	#444	38.31	4.69	113.00	30.61	152.77	3.95	4.19	2.16	11.72	158.04	3.95	1.63	9.04	107.72	3.91
2100	#452	–	–	–	–	–	2.57	2.75	2.59	8.40	122.17	2.57	2.05	6.74	79.43	1.28
2100	#292	37.96	4.23	112.00	39.66	143.27	3.13	3.31	2.18	9.95	152.09	3.13	1.62	7.61	105.72	3.57
2100	#538	23.16	3.53	95.00	29.64	128.40	2.93	3.17	2.04	9.82	135.34	2.93	1.63	7.67	82.71	2.45

Table D.6: 3D and 2D Rotation and Shape parameters for ELO samples ($z = 1$).

$z = 1$		Rotation and Shape									
		3D						2D			
sim	ELO	$V_\phi/\sigma_3^{\rm star}(r_{\rm e,bo}^{\rm star})$	$\epsilon_{\rm 3D}(r_{\rm e,bo}^{\rm star})$	$S(r_{\rm e,bo}^{\rm star})$	$V_\phi/\sigma_3^{\rm star}(r_{\rm 90,bo}^{\rm star})$	$\epsilon_{\rm 3D}(r_{\rm 90,bo}^{\rm star})$	$S(r_{\rm 90,bo}^{\rm star})$	$V_{\rm max}/\sigma_{\rm los,0}^{\rm star}(R_{\rm e,bo}^{\rm star})$	$\epsilon(R_{\rm e,bo}^{\rm star})$	$V_{\rm max}/\sigma_{\rm los,0}^{\rm star}(R_{\rm 90,bo}^{\rm star})$	$\epsilon(R_{\rm 90,bo}^{\rm star})$
A sample											
8714	#353	0.0367	0.4273	0.0204	0.0397	0.4273	0.0204	0.0966	0.4969	0.2135	0.4539
8714	#073	0.0962	0.0513	3.5784	0.0088	0.0513	1.5784	0.0000	0.0581	0.3948	0.1946
8714	#680	0.1006	0.4581	2.7814	0.1502	0.4581	2.7814	0.1308	0.3947	0.4312	0.3826
8714	#473	0.2524	0.1488	1.6923	0.3615	0.1488	1.6923	0.2320	0.1681	0.3630	0.3425
8714	#206	0.0038	0.1880	2.9682	0.0948	0.1880	2.9682	0.0000	0.2229	0.1575	0.3404
8714	#772	0.6782	0.3009	2.8604	0.5212	0.3009	2.8604	0.0000	0.2248	0.4273	0.3166
8714	#285	0.8216	0.2751	1.5139	0.9862	0.2751	1.5139	0.0000	0.2483	0.4840	0.3845
8714	#309	0.2742	0.4335	0.2200	0.2454	0.4335	0.2200	0.2500	0.4895	0.3112	0.6478
8714	#282	0.3965	0.2225	1.4492	0.2170	0.2225	1.4492	0.0000	0.2199	0.2763	0.2670
8714	#208	0.2001	0.2124	1.5437	0.2248	0.2124	1.5437	0.1626	0.2197	0.1820	0.4442
8714	#147	0.2191	0.1653	0.1940	0.0076	0.1653	0.1940	0.0000	0.1372	0.2107	0.2026
8747	#417	0.0958	0.3386	0.0764	0.2350	0.3386	0.0764	0.0872	0.3507	0.2760	0.3955
8747	#278	0.0218	0.4281	0.1141	0.3612	0.4281	0.1141	0.0847	0.5025	0.2569	0.4020
8747	#015	0.4074	0.3941	0.2575	0.4153	0.3941	0.2575	0.2213	0.3781	0.4712	0.4078
8747	#347	0.2865	0.3118	0.1964	0.4328	0.3118	0.1964	0.1843	0.3244	0.3078	0.2900
8747	#319	0.3186	0.2889	0.2881	0.2367	0.2889	0.2881	0.0000	0.2774	0.2321	0.3380
8747	#288	0.5894	0.3508	1.6962	0.9000	0.3508	1.6962	0.3081	0.3446	0.5389	0.4678
8747	#103	0.0561	0.0972	3.5391	0.0449	0.0972	1.5391	0.0000	0.1083	0.0922	0.1919
8747	#826	0.0841	0.3527	0.1118	0.2641	0.3527	0.1118	0.0000	0.4194	0.1431	0.4925
8747	#190	0.3237	0.2841	1.3131	1.1976	0.2841	1.3131	0.0000	0.2663	0.4005	0.4919
8747	#070	0.6280	0.3832	2.7385	0.6501	0.3832	2.7385	0.2551	0.3017	0.4552	0.4735
8747	#337	0.3278	0.3091	0.1179	0.2343	0.3091	0.1179	0.3881	0.3705	0.3312	0.6344
8747	#102	0.1583	0.2631	2.7610	0.0642	0.2631	2.7610	0.0000	0.1649	0.1807	0.4429

$z = 1$		Rotation and Shape									
		3D						2D			
sim	ELO	$V_\phi/\sigma_3^{\rm star}(r_{\rm e,bo}^{\rm star})$	$\epsilon_{\rm 3D}(r_{\rm e,bo}^{\rm star})$	$S(r_{\rm e,bo}^{\rm star})$	$V_\phi/\sigma_3^{\rm star}(r_{\rm 90,bo}^{\rm star})$	$\epsilon_{\rm 3D}(r_{\rm 90,bo}^{\rm star})$	$S(r_{\rm 90,bo}^{\rm star})$	$V_{\rm max}/\sigma_{\rm los,0}^{\rm star}(R_{\rm e,bo}^{\rm star})$	$\epsilon(R_{\rm e,bo}^{\rm star})$	$V_{\rm max}/\sigma_{\rm los,0}^{\rm star}(R_{\rm 90,bo}^{\rm star})$	$\epsilon(R_{\rm 90,bo}^{\rm star})$
8741	#217	0.1867	0.3369	0.2237	0.1311	0.3369	0.2237	0.0837	0.3155	0.2933	0.2597
8741	#607	0.0726	0.2003	0.1158	0.0319	0.2003	0.1158	0.0483	0.1955	0.2215	0.3365
8741	#940	0.0514	0.1502	1.3534	0.2516	0.1502	1.3534	0.0811	0.1497	0.2115	0.2951
8741	#087	0.1501	0.1637	1.5397	0.1978	0.1637	1.5397	0.2208	0.1755	0.2117	0.4478
8741	#229	0.0474	0.4037	0.1460	0.0061	0.4037	0.1460	0.1001	0.4236	0.1346	0.5174
8741	#012	0.4466	0.2191	2.8155	0.8617	0.2191	2.8155	0.0000	0.1572	0.4335	0.4181
8741	#507	0.6439	0.1870	1.6607	0.3190	0.1870	1.6607	0.0000	0.1855	0.5326	0.4857
8741	#955	0.1213	0.2158	2.7918	0.1134	0.2158	2.7918	0.0000	0.1926	0.1097	0.2451
8741	#027	0.3338	0.4154	1.4279	0.0564	0.4154	1.4279	0.1477	0.3820	0.3629	0.4618
8741	#917	0.0829	0.3367	0.1410	0.0146	0.3367	0.1410	0.0000	0.3937	0.1452	0.5261
8741	#014	0.1454	0.0766	3.1326	0.2666	0.0766	0.1326	0.0000	0.0792	0.2506	0.3339
8741	#707	0.0913	0.2930	0.0915	0.1687	0.2930	0.0915	0.0000	0.3155	0.1866	0.4043
8741	#897	0.2066	0.0697	3.3238	0.0161	0.0697	1.3238	0.0000	0.1026	0.1890	0.1233
8742	#293	0.1110	0.3259	1.4790	0.0034	0.3259	1.4790	0.1062	0.2994	0.2426	0.3097
8742	#234	0.1160	0.1002	1.5135	0.0106	0.1002	1.5135	0.0000	0.0888	0.2021	0.1190
8742	#254	0.4409	0.2925	1.5559	0.6770	0.2925	1.5559	0.0000	0.2778	0.3386	0.4933
8742	#234	0.4014	0.1972	1.4472	0.2636	0.1972	1.4472	0.1416	0.1566	0.3448	0.2093
8742	#482	0.0934	0.0705	3.3443	0.1361	0.0705	1.3443	0.0000	0.0698	0.1752	0.2104
8742	#991	0.4641	0.2053	1.6401	0.5784	0.2053	1.6401	0.0000	0.1863	0.2427	0.3425
8742	#898	0.3837	0.2889	2.7678	0.3467	0.2889	2.7678	0.0000	0.2572	0.2724	0.3375
8742	#706	0.3671	0.2941	1.4167	0.2096	0.2941	1.4167	0.0000	0.2412	0.2496	0.2301
8742	#317	0.5597	0.4095	0.2625	0.7865	0.4095	0.2625	0.0000	0.3267	0.3063	0.3243
8743	#238	0.2383	0.3072	0.1878	0.2423	0.3072	0.1878	0.0000	0.3014	0.2499	0.4643
8743	#648	0.0306	0.3942	0.0435	0.0288	0.3942	0.0435	0.0783	0.4988	0.2000	0.3571
8743	#663	0.0262	0.2931	0.0875	0.0262	0.2931	0.0875	0.1184	0.3155	0.1938	0.3040
8743	#737	0.0845	0.4434	0.2513	0.1003	0.4434	0.2513	0.1019	0.4834	0.1926	0.4259
8743	#614	0.3216	0.1477	1.3061	0.4809	0.1477	1.3061	0.0000	0.1397	0.2890	0.3782
8743	#438	0.6170	0.1489	1.4570	0.6610	0.1489	1.4570	0.0000	0.1768	0.4025	0.4773

$z = 1$		Rotation and Shape									
		3D						2D			
sim	ELO	$V_\phi/\sigma_3^{\rm star}(r_{\rm e,bo}^{\rm star})$	$\epsilon_{\rm 3D}(r_{\rm e,bo}^{\rm star})$	$S(r_{\rm e,bo}^{\rm star})$	$V_\phi/\sigma_3^{\rm star}(r_{\rm 90,bo}^{\rm star})$	$\epsilon_{\rm 3D}(r_{\rm 90,bo}^{\rm star})$	$S(r_{\rm 90,bo}^{\rm star})$	$V_{\rm max}/\sigma_{\rm los,0}^{\rm star}(R_{\rm e,bo}^{\rm star})$	$\epsilon(R_{\rm e,bo}^{\rm star})$	$V_{\rm max}/\sigma_{\rm los,0}^{\rm star}(R_{\rm 90,bo}^{\rm star})$	$\epsilon(R_{\rm 90,bo}^{\rm star})$
8743	#411	0.3234	0.1069	0.1948	0.3206	0.1069	0.1948	0.0000	0.1355	0.2153	0.1967
8743	#317	0.5287	0.2563	1.6978	0.5958	0.2563	1.6978	0.0000	0.2329	0.3509	0.3552
8743	#120	0.3814	0.2954	1.4404	0.5253	0.2954	1.4404	0.0000	0.2438	0.2445	0.2646
8743	#438	0.3430	0.1509	1.5858	0.5918	0.1509	1.5858	0.0000	0.1180	0.2984	0.4269
8743	#665	0.1480	0.1730	1.5286	0.1822	0.1730	1.5286	0.0000	0.1870	0.1435	0.1956
8743	#659	0.4716	0.2084	1.3617	0.6634	0.2084	1.3617	0.0000	0.1640	0.2788	0.2987
B sample											
8716	#173	0.0663	0.4915	0.0355	0.4889	0.4915	0.0355	0.1270	0.5941	0.5957	0.4629
8716	#172	0.3393	0.3011	1.3199	0.4721	0.3011	1.3199	0.0000	0.3454	0.6886	0.5459
8717	#417	0.0970	0.3188	0.0436	0.1893	0.3188	0.0436	0.0799	0.3803	0.3741	0.3497
8717	#278	0.2174	0.5161	0.1151	0.2332	0.5161	0.1151	0.2534	0.5574	0.6429	0.4215
8717	#015	0.5950	0.1916	1.4112	0.3518	0.1916	1.4112	0.0000	0.1794	0.8000	0.4308
8717	#347	0.4483	0.2785	0.2734	0.2339	0.2785	0.2734	0.0000	0.2879	0.7112	0.3275
8721	#217	0.0587	0.2175	0.1049	0.1615	0.2175	0.1049	0.0475	0.2155	0.4732	0.2413
8721	#011	0.3955	0.4498	0.1158	0.6599	0.4498	0.1158	0.0000	0.4892	0.9387	0.3736
8721	#940	0.0643	0.1969	2.7086	0.0014	0.1969	2.7086	0.0000	0.2014	0.6562	0.2676
8722	#293	0.0182	0.5274	0.2614	0.0132	0.5274	0.2614	0.2003	0.4831	0.4294	0.3193
8722	#234	0.3685	0.0973	3.6720	0.3201	0.0973	1.6720	0.0000	0.0787	0.8754	0.3325
8722	#482	0.1270	0.1726	1.3313	0.2088	0.1726	1.3313	0.0000	0.1472	0.6935	0.2236
8723	#648	0.0788	0.3631	0.0323	0.2951	0.3631	0.0323	0.0000	0.4472	0.5251	0.3801
8723	#547	0.1599	0.5534	1.3666	0.3003	0.5534	1.3666	0.2058	0.4632	0.6137	0.3763
8723	#663	0.0003	0.3057	0.1297	0.2992	0.3057	0.1297	0.0000	0.3450	0.8014	0.2593
8723	#737	0.2942	0.4091	0.2652	0.3122	0.4091	0.2652	0.0000	0.3889	0.7088	0.3052
F1 sample											
8935	#928	0.1965	0.3402	0.0169	0.2372	0.3402	0.0169	0.1176	0.4193	0.2873	0.5125
8935	#022	0.4365	0.3574	1.4079	0.3600	0.3574	1.4079	0.2120	0.3264	0.3489	0.4420
8935	#238	0.4179	0.3649	1.3188	0.4529	0.3649	1.3188	0.2448	0.3226	0.4125	0.4880
8935	#202	0.3580	0.1196	1.4835	0.0751	0.1196	1.4835	0.0000	0.1234	0.2691	0.1403

$z = 1$		Rotation and Shape									
		3D						2D			
sim	ELO	$V_\phi/\sigma_3^{\rm star}(r_{\rm e,bo}^{\rm star})$	$\epsilon_{\rm 3D}(r_{\rm e,bo}^{\rm star})$	$S(r_{\rm e,bo}^{\rm star})$	$V_\phi/\sigma_3^{\rm star}(r_{\rm 90,bo}^{\rm star})$	$\epsilon_{\rm 3D}(r_{\rm 90,bo}^{\rm star})$	$S(r_{\rm 90,bo}^{\rm star})$	$V_{\rm max}/\sigma_{\rm los,0}^{\rm star}(R_{\rm e,bo}^{\rm star})$	$\epsilon(R_{\rm e,bo}^{\rm star})$	$V_{\rm max}/\sigma_{\rm los,0}^{\rm star}(R_{\rm 90,bo}^{\rm star})$	$\epsilon(R_{\rm 90,bo}^{\rm star})$
8935	#243	0.2289	0.2583	0.2275	0.1894	0.2583	0.2275	0.1673	0.2441	0.2727	0.4030
8935	#129	0.2751	0.4159	0.0678	0.2846	0.4159	0.0678	0.1392	0.4497	0.2496	0.4529
8935	#535	0.0082	0.4236	0.0720	0.1737	0.4236	0.0720	0.0722	0.4689	0.2172	0.4568
8935	#949	0.1188	0.0936	3.5425	0.2751	0.0936	1.5425	0.0000	0.1112	0.2034	0.5430
8935	#336	0.0013	0.3099	0.1545	0.1206	0.3099	0.1545	0.2461	0.3690	0.2658	0.3993
8935	#942	0.5004	0.2522	1.5184	0.5046	0.2522	1.5184	0.2539	0.2630	0.5041	0.3723
8935	#022	0.2305	0.2158	0.2782	0.2717	0.2158	0.2782	0.0000	0.2209	0.1870	0.4748
8935	#239	0.1642	0.4184	0.0038	0.2102	0.4184	0.0038	0.1069	0.5114	0.1576	0.6103
8935	#230	0.2892	0.3269	0.2889	0.0485	0.3269	0.2889	0.0000	0.3411	0.2956	0.5962
8935	#462	0.4384	0.2616	2.7947	0.4327	0.2616	2.7947	0.0000	0.1872	0.3120	0.4136
8935	#534	0.2146	0.2802	0.0718	0.2691	0.2802	0.0718	0.1528	0.3527	0.3231	0.4843
8935	#289	0.3397	0.2792	1.6409	0.3180	0.2792	1.6409	0.0942	0.2226	0.2248	0.4405
8935	#135	0.0266	0.2705	1.6789	0.0059	0.2705	1.6789	0.0974	0.2680	0.1900	0.3659
8935	#254	0.3825	0.3353	0.1459	0.3375	0.3353	0.1459	0.2230	0.3631	0.3058	0.5828
8935	#371	0.2413	0.3908	0.1780	0.3903	0.3908	0.1780	0.0000	0.3993	0.1710	0.6348
8935	#282	0.1376	0.2637	1.4582	0.2763	0.2637	1.4582	0.1137	0.3097	0.1983	0.4353
8935	#198	0.3110	0.2787	1.5059	0.4822	0.2787	1.5059	0.0000	0.2279	0.1905	0.5079
8935	#114	0.1096	0.4424	1.4290	0.1898	0.4424	1.4290	0.0000	0.3358	0.1134	0.5922
F2 sample											
8914	#341	0.4165	0.3353	0.1841	0.3858	0.3353	0.1841	0.2383	0.3778	0.4460	0.3200
8914	#471	0.0795	0.2344	1.4222	0.0819	0.2344	1.4222	0.0512	0.2124	0.2555	0.2596
8914	#828	0.0689	0.2909	0.0659	0.1589	0.2909	0.0659	0.0370	0.2919	0.2384	0.2764
8914	#928	0.1099	0.1998	1.4152	0.0127	0.1998	1.4152	0.0842	0.1837	0.1996	0.2968
8914	#238	0.3724	0.4268	0.1720	0.5567	0.4268	0.1720	0.2408	0.4805	0.4804	0.3642
8914	#350	0.1706	0.3571	0.1029	0.2533	0.3571	0.1029	0.1640	0.4169	0.2312	0.4660
8914	#202	0.1308	0.0992	3.6794	0.1091	0.0992	1.6794	0.0000	0.0652	0.2451	0.1728
8914	#243	0.0985	0.1326	0.0330	0.0135	0.1326	0.0330	0.0000	0.1551	0.1192	0.5045
8914	#022	0.5461	0.3676	1.4253	0.3808	0.3676	1.4253	0.2708	0.3480	0.4335	0.3443

$z = 1$		Rotation and Shape									
		3D						2D			
sim	ELO	$V_\phi/\sigma_3^{\rm star}(r_{\rm e,bo}^{\rm star})$	$\epsilon_{\rm 3D}(r_{\rm e,bo}^{\rm star})$	$S(r_{\rm e,bo}^{\rm star})$	$V_\phi/\sigma_3^{\rm star}(r_{\rm 90,bo}^{\rm star})$	$\epsilon_{\rm 3D}(r_{\rm 90,bo}^{\rm star})$	$S(r_{\rm 90,bo}^{\rm star})$	$V_{\rm max}/\sigma_{\rm los,0}^{\rm star}(R_{\rm e,bo}^{\rm star})$	$\epsilon(R_{\rm e,bo}^{\rm star})$	$V_{\rm max}/\sigma_{\rm los,0}^{\rm star}(R_{\rm 90,bo}^{\rm star})$	$\epsilon(R_{\rm 90,bo}^{\rm star})$
8914	#451	0.7670	0.3200	2.9028	0.3038	0.3200	2.9028	0.0000	0.2933	0.6160	0.4049
8914	#222	0.6978	0.2925	2.7795	0.9732	0.2925	2.7795	0.2084	0.1774	0.6055	0.3664
8914	#326	0.4416	0.2719	0.2733	0.5128	0.2719	0.2733	0.3144	0.2744	0.3123	0.4653
8914	#471	0.3591	0.3587	0.2458	0.4841	0.3587	0.2458	0.0000	0.3786	0.2160	0.4972
8914	#536	0.2741	0.1539	1.4021	0.0272	0.1539	1.4021	0.0918	0.1839	0.1944	0.1675
8914	#994	0.0600	0.3102	1.3592	0.1500	0.3102	1.3592	0.0560	0.2756	0.1369	0.4421
8914	#022	0.3072	0.3273	0.1283	0.2498	0.3273	0.1283	0.1878	0.2871	0.1764	0.3855
8914	#643	0.4815	0.3059	1.5821	0.3953	0.3059	1.5821	0.0000	0.2584	0.2735	0.3141
8914	#283	0.3647	0.3745	0.2706	0.3223	0.3745	0.2706	0.2125	0.3412	0.3051	0.4300
F3 sample											
2100	#629	0.0620	0.2066	1.4029	0.0464	0.2066	1.4029	0.0511	0.1599	0.1897	0.2984
2100	#470	0.0969	0.3928	0.2404	0.3086	0.3928	0.2404	0.0000	0.4483	0.2172	0.4241
2100	#638	0.1864	0.2963	1.6515	0.2394	0.2963	1.6515	0.0000	0.2645	0.2290	0.2637
2100	#740	0.4214	0.1913	2.8392	0.6518	0.1913	2.8392	0.1755	0.2054	0.2712	0.3769
2100	#562	0.0251	0.3008	0.0532	0.0067	0.3008	0.0532	0.0000	0.3604	0.0928	0.5584
2100	#953	0.0633	0.4223	0.1160	0.4365	0.4223	0.1160	0.0000	0.4744	0.1421	0.5702
2100	#517	0.5232	0.4041	0.2836	0.6943	0.4041	0.2836	0.2038	0.4098	0.4820	0.5045
2100	#233	0.1695	0.1874	1.4507	0.2960	0.1874	1.4507	0.0000	0.1558	0.2524	0.3345
2100	#087	0.3037	0.3175	1.4166	0.1517	0.3175	1.4166	0.0000	0.2789	0.2028	0.2898
2100	#129	0.0906	0.1618	0.2691	0.1741	0.1618	0.2691	0.0000	0.1632	0.1011	0.4071
2100	#444	0.3240	0.3676	1.6029	0.2266	0.3676	1.6029	0.0000	0.4063	0.2684	0.4266
2100	#452	0.8686	0.6066	0.1457	0.9754	0.6066	0.1457	0.2452	0.6889	0.3776	0.6143
2100	#292	0.1095	0.1452	1.3466	0.0391	0.1452	1.3466	0.0000	0.1566	0.1643	0.1839
2100	#538	0.5646	0.2325	2.8773	0.5246	0.2325	2.8773	0.0000	0.1934	0.3061	0.3898

Table D.7: Masses, sizes and mean square velocities at the halo and baryonic object scale, as well as their projected counterparts ($z = 1.5$). Masses are given in 10^{10} $M_\odot$, distances in kpc, velocity dispersions in $km \times s^{-1}$.

$z = 1.5$		Halo scale					Stellar scale					Projected stellar scale				
sim	ELO	$M_{\rm vir}$	$M_{\rm h}^{\rm bar}$	$r_{\rm vir}$	$r_{\rm e,h}^{\rm tot}$	$\sigma_{\rm 3,h}^{\rm tot}$	$M_{\rm bo}^{\rm star}$	$M_{\rm bo}^{\rm cb}$	$r_{\rm e,bo}^{\rm star}$	$r_{\rm 90,bo}^{\rm star}$	$\sigma_{\rm 3,bo}^{\rm star}$	$M_{\rm cyl,bo}^{\rm star}$	$R_{\rm e,bo}^{\rm star}$	$R_{\rm 90,bo}^{\rm star}$	$\sigma_{\rm los,0}^{\rm star}$	n
8714	#973	201.35	18.84	159.00	55.84	269.82	14.03	14.45	2.44	24.68	293.76	14.03	1.89	18.77	184.64	8.03
8714	#353	142.25	15.81	141.00	52.31	238.42	10.77	11.68	3.67	27.43	248.78	10.77	2.79	21.84	157.04	5.42
8714	#343	68.55	7.32	111.00	39.64	198.06	5.90	6.30	3.00	14.89	192.79	5.90	2.26	11.65	123.51	4.88
8714	#580	–	–	–	–	–	4.62	4.82	2.88	11.44	166.13	4.62	2.21	9.07	116.95	2.84
8714	#473	–	–	–	–	–	2.79	3.08	2.07	10.21	134.77	2.78	1.63	7.83	87.04	3.06
8714	#172	42.12	5.73	94.00	28.68	175.60	5.15	5.30	3.89	16.96	179.17	5.15	2.91	13.62	120.98	3.01
8714	#206	–	–	–	–	–	4.35	4.57	1.97	13.59	168.96	4.36	1.50	9.87	124.07	5.16
8714	#771	–	–	–	–	–	3.34	3.52	1.97	7.25	136.51	3.35	1.54	5.75	88.47	1.93
8714	#282	–	–	–	–	–	3.00	3.53	2.05	11.14	143.34	3.00	1.59	8.33	96.43	4.01
8714	#209	–	–	–	–	–	2.22	2.35	2.02	8.36	142.07	2.22	1.60	6.75	106.33	3.61
8714	#285	–	–	–	–	–	0.88	1.29	1.37	3.03	81.16	0.88	1.02	2.52	55.71	1.11
8714	#409	–	–	–	–	–	1.59	1.82	1.56	5.24	111.28	1.59	1.24	4.03	79.21	1.75
8714	#147	–	–	–	–	–	1.51	1.84	1.23	2.99	104.73	1.51	0.95	2.49	65.44	1.17
8747	#416	217.44	23.45	163.00	62.08	268.43	13.89	14.16	4.15	18.95	285.77	13.88	3.19	14.89	195.59	5.08
8747	#178	154.61	18.21	145.00	62.53	237.34	11.64	12.19	5.46	30.06	238.56	11.64	4.03	23.59	162.25	5.69
8747	#015	113.26	12.78	131.00	48.42	221.21	9.14	9.38	2.62	17.03	229.43	9.14	2.05	13.16	141.04	3.16
8747	#357	–	–	–	–	–	7.45	7.80	3.53	17.38	207.78	7.45	2.73	13.83	134.27	3.82
8747	#310	–	–	–	–	–	3.92	4.15	1.96	12.69	143.34	3.92	1.48	9.59	100.76	5.66
8747	#103	–	–	–	–	–	3.59	3.85	1.95	13.13	151.15	3.59	1.54	10.29	104.62	3.51
8747	#070	–	–	–	–	–	1.84	2.23	2.08	6.15	125.15	1.84	1.55	5.01	83.72	1.80
8747	#205	–	–	–	–	–	2.86	3.19	2.35	9.65	135.56	2.86	1.89	7.74	89.04	2.50
8747	#190	–	–	–	–	–	2.51	2.87	1.90	6.95	153.90	2.51	1.46	5.80	93.20	3.74
8747	#200	–	–	–	–	–	1.78	2.11	2.19	7.30	105.15	1.78	1.71	5.67	74.01	1.53
8747	#826	–	–	–	–	–	1.47	1.69	1.75	5.39	95.46	1.47	1.37	4.55	70.80	2.07

$z = 1.5$		Halo scale					Stellar scale					Projected stellar scale				
sim	ELO	$M_{\rm vir}$	$M_{\rm h}^{\rm bar}$	$r_{\rm vir}$	$r_{\rm e,h}^{\rm tot}$	$\sigma_{\rm 3,h}^{\rm tot}$	$M_{\rm bo}^{\rm star}$	$M_{\rm bo}^{\rm cb}$	$r_{\rm e,bo}^{\rm star}$	$r_{\rm 90,bo}^{\rm star}$	$\sigma_{\rm 3,bo}^{\rm star}$	$M_{\rm cyl,bo}^{\rm star}$	$R_{\rm e,bo}^{\rm star}$	$R_{\rm 90,bo}^{\rm star}$	$\sigma_{\rm los,0}^{\rm star}$	n
8747	#102	–	–	–	–	–	1.55	1.67	1.45	6.73	108.82	1.55	1.09	4.84	75.87	2.32
8741	#217	–	–	–	–	–	8.51	8.78	3.38	9.44	283.82	8.50	2.44	7.99	176.13	5.09
8741	#607	99.29	11.19	125.00	50.78	199.70	8.03	8.56	3.79	35.38	200.34	8.03	2.76	28.69	151.29	7.82
8741	#011	90.95	11.23	122.00	53.18	186.83	7.45	7.88	4.26	15.97	195.47	7.45	3.39	12.93	122.60	5.23
8741	#940	66.77	7.67	110.00	35.53	191.39	6.32	6.54	3.79	17.62	202.58	6.32	2.80	14.03	147.00	4.12
8741	#002	–	–	–	–	–	3.94	4.20	1.60	6.28	175.75	3.94	1.21	4.72	108.05	2.44
8741	#087	–	–	–	–	–	4.81	5.44	2.97	18.38	183.74	4.81	2.33	14.57	111.01	6.95
8741	#220	72.53	10.24	113.00	51.84	175.72	5.00	5.32	2.36	11.93	175.46	5.00	1.74	9.15	129.62	3.28
8741	#027	41.37	5.46	94.00	29.99	164.08	4.98	5.25	2.55	12.87	175.55	4.98	1.92	10.22	123.38	3.19
8741	#507	–	–	–	–	–	4.01	4.44	1.96	14.31	164.63	4.01	1.49	10.72	115.39	6.44
8741	#955	47.34	5.88	98.00	33.09	172.28	4.31	4.56	2.16	8.49	167.56	4.31	1.66	6.84	116.65	1.88
8741	#917	29.81	4.42	84.00	22.18	159.60	3.92	4.12	2.45	10.47	161.88	3.92	1.97	8.35	110.10	2.11
8741	#014	–	–	–	–	–	2.79	2.95	1.54	4.72	141.89	2.79	1.17	3.70	93.39	1.71
8741	#897	–	–	–	–	–	2.68	3.07	1.59	9.57	129.93	2.68	1.22	7.32	85.34	1.45
8742	#293	–	–	–	–	–	13.60	14.33	6.28	21.43	257.30	13.60	4.45	17.20	165.31	3.97
8742	#334	–	–	–	–	–	6.39	6.64	1.75	6.69	234.84	6.37	1.35	5.18	149.46	3.05
8742	#472	72.09	8.40	113.00	34.60	192.27	6.51	6.69	2.31	18.27	204.82	6.51	1.76	14.52	134.05	7.01
8742	#991	–	–	–	–	–	1.84	2.13	1.51	4.98	117.26	1.83	1.14	3.90	74.36	1.94
8742	#898	–	–	–	–	–	1.81	2.13	1.63	6.62	130.22	1.81	1.25	5.04	91.30	3.23
8742	#254	–	–	–	–	–	2.24	2.61	1.79	12.96	113.32	2.23	1.41	9.64	80.30	2.62
8742	#706	–	–	–	–	–	1.83	2.11	1.75	6.56	112.84	1.83	1.30	5.07	82.62	7.43
8742	#317	–	–	–	–	–	1.31	1.57	2.64	7.19	96.33	1.31	2.02	5.67	70.03	1.24
8743	#758	–	–	–	–	–	13.63	13.88	4.27	19.12	280.07	13.63	3.30	15.47	181.54	4.95
8743	#238	–	–	–	–	–	8.57	8.67	2.57	10.60	251.04	8.57	2.01	8.38	161.95	3.76
8743	#663	120.89	13.69	134.00	49.13	223.17	8.11	8.29	2.93	15.21	220.17	8.10	2.31	11.79	153.86	4.11
8743	#439	–	–	–	–	–	2.89	3.22	1.99	9.16	146.91	2.89	1.51	7.03	99.74	3.15
8743	#120	–	–	–	–	–	2.04	2.44	1.42	4.69	122.99	2.04	1.12	3.73	79.46	1.85
8743	#208	–	–	–	–	–	1.95	2.21	1.63	6.73	121.12	1.95	1.26	5.16	87.23	2.57
8743	#437	–	–	–	–	–	1.81	2.13	1.67	5.42	106.30	1.81	1.27	4.21	78.13	2.03

$z = 1.5$		Halo scale					Stellar scale					Projected stellar scale				
sim	ELO	$M_{\rm vir}$	$M_{\rm h}^{\rm bar}$	$r_{\rm vir}$	$r_{\rm e,h}^{\rm tot}$	$\sigma_{\rm 3,h}^{\rm tot}$	$M_{\rm bo}^{\rm star}$	$M_{\rm bo}^{\rm cb}$	$r_{\rm e,bo}^{\rm star}$	$r_{\rm 90,bo}^{\rm star}$	$\sigma_{\rm 3,bo}^{\rm star}$	$M_{\rm cyl,bo}^{\rm star}$	$R_{\rm e,bo}^{\rm star}$	$R_{\rm 90,bo}^{\rm star}$	$\sigma_{\rm los,0}^{\rm star}$	n
8743	#411	–	–	–	–	–	1.84	2.03	1.47	3.86	122.91	1.85	1.12	3.17	90.57	1.39
8743	#659	–	–	–	–	–	1.57	1.75	1.52	6.84	110.92	1.57	1.19	5.50	79.22	6.69
8743	#675	–	–	–	–	–	1.29	1.71	1.36	3.30	88.73	1.29	1.02	2.84	64.67	1.43
B sample																
8716	#973	199.56	17.74	158.00	54.85	275.70	12.22	13.16	1.45	11.14	286.63	12.22	1.10	8.45	183.36	1.43
8716	#172	42.27	5.65	94.00	26.97	172.75	5.00	5.26	1.61	6.73	174.38	5.00	1.23	5.24	116.23	1.43
8717	#015	112.70	12.63	131.00	47.39	226.13	8.96	10.06	1.79	8.64	225.85	8.96	1.40	6.96	137.89	1.43
8717	#417	127.44	16.34	136.00	57.20	219.46	7.59	7.95	2.26	9.71	204.80	7.59	1.72	7.51	145.04	1.43
8717	#310	31.76	4.34	86.00	23.82	156.24	3.57	4.03	1.33	4.77	161.86	3.57	0.98	3.79	117.19	1.43
8721	#217	176.38	19.80	152.00	61.98	239.56	9.62	10.06	2.17	10.46	237.78	9.62	1.70	8.28	168.27	1.43
8721	#011	90.71	11.34	122.00	52.78	187.81	7.15	7.59	2.13	8.60	194.09	7.13	1.67	6.90	135.02	1.43
8721	#607	99.97	11.12	126.00	51.37	205.31	6.70	7.25	1.44	9.91	223.61	6.70	1.10	7.39	153.90	1.43
8721	#940	65.57	7.41	109.00	31.70	197.22	6.30	6.89	1.94	11.28	202.09	6.30	1.50	8.74	141.94	1.43
8721	#027	41.60	5.58	94.00	30.58	161.84	4.71	5.27	1.71	5.76	157.81	4.71	1.26	4.36	112.67	1.43
8721	#917	30.21	4.35	84.00	21.52	155.64	3.89	4.18	1.51	6.06	154.05	3.89	1.19	4.94	105.56	1.43
8722	#472	71.36	7.87	112.00	35.07	195.25	6.14	6.73	1.44	10.97	204.65	6.15	1.11	8.57	132.67	1.43
8723	#758	205.83	19.61	160.00	60.32	267.53	14.77	15.96	2.97	24.48	267.01	14.76	2.35	18.69	174.70	1.43
8723	#238	153.33	17.38	145.00	58.63	230.90	10.86	11.57	2.38	13.84	235.43	10.86	1.83	10.83	174.66	1.43
8723	#663	118.96	13.45	133.00	48.35	230.07	8.18	8.55	2.18	9.44	229.63	8.18	1.71	7.37	155.81	1.43
8723	#604	29.09	4.30	83.00	26.84	150.42	3.18	3.94	1.59	4.97	148.04	3.18	1.18	3.84	100.26	1.43

Table D.8: 3D and 2D Rotation and Shape parameters for ELO samples ($z = 1.5$).

$z = 1.5$		Rotation and Shape									
		3D						2D			
sim	ELO	$V_\phi/\sigma_3^{\rm star}(r_{\rm e,bo}^{\rm star})$	$\epsilon_{\rm 3D}(r_{\rm e,bo}^{\rm star})$	$S(r_{\rm e,bo}^{\rm star})$	$V_\phi/\sigma_3^{\rm star}(r_{\rm 90,bo}^{\rm star})$	$\epsilon_{\rm 3D}(r_{\rm 90,bo}^{\rm star})$	$S(r_{\rm 90,bo}^{\rm star})$	$V_{\rm max}/\sigma_{\rm los,0}^{\rm star}(R_{\rm e,bo}^{\rm star})$	$\epsilon(R_{\rm e,bo}^{\rm star})$	$V_{\rm max}/\sigma_{\rm los,0}^{\rm star}(R_{\rm 90,bo}^{\rm star})$	$\epsilon(R_{\rm 90,bo}^{\rm star})$
A sample											
8714	#973	0.0772	0.0666	3.6378	0.0137	0.0666	1.6378	0.0000	0.0558	0.2650	0.2918
8714	#353	0.1089	0.2262	1.5318	0.1577	0.2262	1.5318	0.0770	0.2348	0.2949	0.2879
8714	#343	0.1001	0.1687	0.2376	0.4303	0.1687	0.2376	0.0904	0.1920	0.1823	0.4396
8714	#580	0.0308	0.4494	2.8182	0.2442	0.4494	2.8182	0.0807	0.3517	0.1040	0.4882
8714	#473	0.4982	0.2507	2.7261	0.4331	0.2507	2.7261	0.0000	0.2111	0.3516	0.3838
8714	#172	0.0712	0.4886	1.4717	0.0377	0.4886	1.4717	0.2006	0.3604	0.2719	0.4467
8714	#206	0.0151	0.2077	1.4969	0.0665	0.2077	1.4969	0.0000	0.1782	0.1565	0.4025
8714	#771	0.6644	0.3283	1.5399	0.7844	0.3283	1.5399	0.0000	0.2464	0.4131	0.3813
8714	#282	0.3869	0.2979	0.2338	0.7235	0.2979	0.2338	0.0000	0.3082	0.2804	0.2455
8714	#209	0.2114	0.3207	1.3304	0.1887	0.3207	1.3304	0.0000	0.3134	0.1896	0.5876
8714	#285	0.4240	0.3312	2.9197	0.3588	0.3312	2.9197	0.0000	0.2765	0.3005	0.4231
8714	#409	0.2833	0.3421	1.3901	0.4606	0.3421	1.3901	0.0000	0.3474	0.3019	0.3539
8714	#147	0.1386	0.2237	0.1269	0.0088	0.2237	0.1269	0.0000	0.1992	0.1249	0.2469
8747	#416	0.0316	0.3665	0.1050	0.2570	0.3665	0.1050	0.0716	0.4117	0.2709	0.4688
8747	#178	0.1587	0.5387	0.0977	0.1690	0.5387	0.0977	0.2238	0.5857	0.3523	0.4775
8747	#015	0.5214	0.3729	1.5084	0.4152	0.3729	1.5084	0.1884	0.2793	0.5839	0.4638
8747	#357	0.2135	0.3407	0.2151	0.4542	0.3407	0.2151	0.1878	0.3883	0.3797	0.3505
8747	#310	0.2391	0.3142	0.0203	0.6410	0.3142	0.0203	0.0000	0.3325	0.2131	0.3327
8747	#103	0.1303	0.1259	1.3876	0.1969	0.1259	1.3876	0.0000	0.1393	0.1233	0.2844
8747	#070	0.1073	0.2619	0.1165	0.3351	0.2619	0.1165	0.0000	0.2063	0.0973	0.3183
8747	#205	0.1178	0.3181	2.7364	0.1482	0.3181	2.7364	0.0000	0.2464	0.1809	0.5011
8747	#190	0.3400	0.3786	0.2504	0.8031	0.3786	0.2504	0.0000	0.3264	0.3941	0.5090
8747	#200	0.5912	0.3211	1.4570	0.8409	0.3211	1.4570	0.0000	0.2832	0.3495	0.3430

$z = 1.5$		Rotation and Shape									
		3D						2D			
sim	ELO	$V_\phi/\sigma_3^{\rm star}(r_{\rm e,bo}^{\rm star})$	$\epsilon_{\rm 3D}(r_{\rm e,bo}^{\rm star})$	$S(r_{\rm e,bo}^{\rm star})$	$V_\phi/\sigma_3^{\rm star}(r_{\rm 90,bo}^{\rm star})$	$\epsilon_{\rm 3D}(r_{\rm 90,bo}^{\rm star})$	$S(r_{\rm 90,bo}^{\rm star})$	$V_{\rm max}/\sigma_{\rm los,0}^{\rm star}(R_{\rm e,bo}^{\rm star})$	$\epsilon(R_{\rm e,bo}^{\rm star})$	$V_{\rm max}/\sigma_{\rm los,0}^{\rm star}(R_{\rm 90,bo}^{\rm star})$	$\epsilon(R_{\rm 90,bo}^{\rm star})$
8747	#826	0.1893	0.3614	1.4674	0.3930	0.3614	1.4674	0.0000	0.3516	0.2143	0.6452
8747	#102	0.1199	0.2766	1.3149	0.0671	0.2766	1.3149	0.0000	0.2987	0.1965	0.4781
8741	#217	0.1052	0.2462	0.1675	0.0799	0.2462	0.1675	0.0994	0.2455	0.3617	0.2619
8741	#607	0.1254	0.3098	0.1320	0.0012	0.3098	0.1320	0.1429	0.2681	0.2537	0.3959
8741	#011	0.3401	0.4720	0.0825	0.2354	0.4720	0.0825	0.1680	0.5458	0.4672	0.3837
8741	#940	0.0373	0.2334	0.2066	0.1287	0.2334	0.2066	0.0836	0.2403	0.1511	0.4606
8741	#002	0.2576	0.2554	1.5138	0.3687	0.2554	1.5138	0.0000	0.1567	0.2199	0.2557
8741	#087	0.3715	0.2847	0.2032	0.1991	0.2847	0.2032	0.2566	0.3074	0.4217	0.1610
8741	#220	0.0614	0.4507	1.3130	0.1823	0.4507	1.3130	0.0000	0.3919	0.1258	0.5025
8741	#027	0.3196	0.4671	0.2440	0.1883	0.4671	0.2440	0.1923	0.4636	0.3312	0.5741
8741	#507	0.3716	0.0855	3.7552	0.4612	0.0855	2.7552	0.0000	0.1025	0.2900	0.3692
8741	#955	0.0570	0.2758	1.6546	0.2087	0.2758	1.6546	0.0000	0.2348	0.1361	0.4065
8741	#917	0.0869	0.4310	0.1619	0.1011	0.4310	0.1619	0.0000	0.4352	0.1796	0.5687
8741	#014	0.3517	0.1487	1.5918	0.4191	0.1487	1.5918	0.0000	0.1413	0.2563	0.1907
8741	#897	0.2834	0.1563	0.2551	0.2713	0.1563	0.2551	0.0000	0.1445	0.2541	0.1146
8742	#293	0.4899	0.3709	2.7360	0.6071	0.3709	2.7360	0.2819	0.3121	0.5158	0.3334
8742	#334	0.0275	0.1142	0.2848	0.1376	0.1142	0.2848	0.0000	0.1265	0.4478	0.1892
8742	#472	0.1197	0.0507	3.3912	0.0877	0.0507	1.3912	0.0000	0.0714	0.5811	0.3400
8742	#991	0.1452	0.0342	3.1406	0.1620	0.0342	0.1406	0.0000	0.1207	0.9006	0.2340
8742	#898	0.3279	0.2668	0.1707	0.3229	0.2668	0.1707	0.0000	0.2506	0.8920	0.3628
8742	#254	0.5205	0.3419	1.5533	0.1642	0.3419	1.5533	0.0000	0.3486	0.9884	0.3911
8742	#706	0.4837	0.2405	1.6925	0.4103	0.2405	1.6925	0.0000	0.1887	0.8432	0.3295
8742	#317	0.6373	0.5453	0.1049	0.6581	0.5453	0.1049	0.4682	0.5505	0.3444	0.5137
8743	#758	0.0618	0.4731	0.0533	0.0840	0.4731	0.0533	0.1010	0.5536	0.3095	0.4965
8743	#238	0.0417	0.3417	0.0651	0.3638	0.3417	0.0651	0.0000	0.4233	0.2848	0.5244
8743	#663	0.0735	0.3675	0.2451	0.0269	0.3675	0.2451	0.1053	0.3490	0.2029	0.4322
8743	#439	0.2702	0.2128	0.1798	0.2855	0.2128	0.1798	0.0000	0.2211	0.2112	0.4019
8743	#120	0.3457	0.1749	0.2548	0.3692	0.1749	0.2548	0.0000	0.1668	0.2359	0.2874

$z = 1.5$		Rotation and Shape									
		3D						2D			
sim	ELO	$V_\phi/\sigma_3^{\rm star}(r_{\rm e,bo}^{\rm star})$	$\epsilon_{\rm 3D}(r_{\rm e,bo}^{\rm star})$	$S(r_{\rm e,bo}^{\rm star})$	$V_\phi/\sigma_3^{\rm star}(r_{\rm 90,bo}^{\rm star})$	$\epsilon_{\rm 3D}(r_{\rm 90,bo}^{\rm star})$	$S(r_{\rm 90,bo}^{\rm star})$	$V_{\rm max}/\sigma_{\rm los,0}^{\rm star}(R_{\rm e,bo}^{\rm star})$	$\epsilon(R_{\rm e,bo}^{\rm star})$	$V_{\rm max}/\sigma_{\rm los,0}^{\rm star}(R_{\rm 90,bo}^{\rm star})$	$\epsilon(R_{\rm 90,bo}^{\rm star})$
8743	#208	0.1759	0.0888	3.3749	0.4481	0.0888	1.3749	0.0000	0.1432	0.1446	0.4907
8743	#437	0.3769	0.2557	0.2024	0.5955	0.2557	0.2024	0.0000	0.2747	0.3269	0.5647
8743	#411	0.4048	0.1521	0.2505	0.3556	0.1521	0.2505	0.0000	0.1636	0.2337	0.2322
8743	#659	0.2822	0.2876	1.5633	0.4972	0.2876	1.5633	0.0000	0.2953	0.2438	0.5763
8743	#675	0.3290	0.1481	1.4201	0.4455	0.1481	1.4201	0.0000	0.1750	0.2458	0.2426
B sample											
8716	#973	0.0805	0.1552	2.7753	0.1276	0.1552	2.7753	0.0000	0.1729	0.5989	0.2262
8716	#172	0.3380	0.3263	0.1044	0.3576	0.3263	0.1044	0.0000	0.3544	0.6932	0.5787
8717	#015	0.5771	0.2002	0.1769	0.7640	0.2002	0.1769	0.0000	0.1761	1.0855	0.5135
8717	#417	0.2979	0.5164	0.1424	0.5389	0.5164	0.1424	0.0000	0.5561	0.9021	0.5539
8717	#310	0.2524	0.2597	1.3708	0.4718	0.2597	1.3708	0.0000	0.2306	0.7201	0.3956
8721	#217	0.1138	0.2186	0.0453	0.1539	0.2186	0.0453	0.0000	0.2770	0.6035	0.1799
8721	#011	0.4092	0.4860	0.1463	0.4150	0.4860	0.1463	0.0000	0.5128	0.9439	0.6221
8721	#607	0.2372	0.3181	0.1517	0.4543	0.3181	0.1517	0.0000	0.3457	0.7786	0.5723
8721	#940	0.1569	0.1474	2.7019	0.2205	0.1474	2.7019	0.0000	0.1712	0.5119	0.4982
8721	#027	0.4018	0.4339	0.2880	0.5214	0.4339	0.2880	0.0000	0.3789	0.7478	0.5700
8721	#917	0.0331	0.3621	0.0367	0.0627	0.3621	0.0367	0.0000	0.4349	0.3933	0.6645
8722	#472	0.1492	0.3027	0.2313	0.0743	0.3027	0.2313	0.0000	0.3102	0.5810	0.2556
8723	#758	0.0368	0.4529	0.0538	0.2444	0.4529	0.0538	0.1078	0.5633	0.6700	0.5319
8723	#238	0.0457	0.4820	0.1850	0.0408	0.4820	0.1850	0.0000	0.5168	0.8031	0.5333
8723	#663	0.3145	0.3983	0.0676	0.1095	0.3983	0.0676	0.0000	0.4640	0.8748	0.5269
8723	#604	0.4310	0.3897	0.1499	0.8066	0.3897	0.1499	0.0000	0.4212	0.9225	0.4634
F1 sample											
8935	#471	0.0008	0.2876	1.3382	0.0131	0.2876	1.3382	0.0740	0.2504	0.2744	0.3294
8935	#828	0.1152	0.2240	0.0656	0.1000	0.2240	0.0656	0.1330	0.2550	0.2672	0.5770
8935	#928	0.2970	0.2930	0.2231	0.3674	0.2930	0.2231	0.1926	0.3031	0.3067	0.4145
8935	#351	0.0663	0.3640	0.1890	0.3889	0.3640	0.1890	0.0883	0.3913	0.1996	0.4709
8935	#238	0.4180	0.4344	0.1833	0.5134	0.4344	0.1833	0.2615	0.4332	0.4792	0.5276

$z = 1.5$		Rotation and Shape									
		3D						2D			
sim	ELO	$V_\phi/\sigma_3^{\rm star}(r_{\rm e,bo}^{\rm star})$	$\epsilon_{\rm 3D}(r_{\rm e,bo}^{\rm star})$	$S(r_{\rm e,bo}^{\rm star})$	$V_\phi/\sigma_3^{\rm star}(r_{\rm 90,bo}^{\rm star})$	$\epsilon_{\rm 3D}(r_{\rm 90,bo}^{\rm star})$	$S(r_{\rm 90,bo}^{\rm star})$	$V_{\rm max}/\sigma_{\rm los,0}^{\rm star}(R_{\rm e,bo}^{\rm star})$	$\epsilon(R_{\rm e,bo}^{\rm star})$	$V_{\rm max}/\sigma_{\rm los,0}^{\rm star}(R_{\rm 90,bo}^{\rm star})$	$\epsilon(R_{\rm 90,bo}^{\rm star})$
8935	#202	0.3793	0.1847	2.9502	0.0134	0.1847	2.9502	0.0000	0.1352	0.3019	0.1855
8935	#537	0.5597	0.2141	1.6774	0.8826	0.2141	1.6774	0.0000	0.1878	0.4761	0.1558
8935	#022	0.0478	0.3911	0.0598	0.0476	0.3911	0.0598	0.2592	0.4895	0.2436	0.5866
8935	#243	0.3162	0.2691	0.2697	0.2890	0.2691	0.2697	0.1447	0.2685	0.2852	0.4633
8935	#129	0.2165	0.4029	0.2300	0.1962	0.4029	0.2300	0.2971	0.3859	0.3906	0.5474
8935	#326	0.2694	0.4047	1.3473	0.1195	0.4047	1.3473	0.2632	0.4079	0.3005	0.5362
8935	#381	0.1408	0.3354	0.0390	0.1593	0.3354	0.0390	0.0000	0.4170	0.1542	0.6729
8935	#212	0.2073	0.2462	1.4333	0.0691	0.2462	1.4333	0.0000	0.2786	0.1630	0.3093
8935	#634	0.1961	0.3463	0.2262	0.2865	0.3463	0.2262	0.1389	0.3558	0.2584	0.5520
8935	#036	0.4035	0.1623	1.5582	0.0194	0.1623	1.5582	0.2152	0.1534	0.3108	0.5547
8935	#643	0.1961	0.2358	1.4826	0.4759	0.2358	1.4826	0.0000	0.2145	0.2472	0.4451
8935	#361	0.2048	0.2080	1.5835	0.0275	0.2080	1.5835	0.0000	0.1838	0.1477	0.5079
8935	#140	0.2886	0.2105	0.0851	0.2164	0.2105	0.0851	0.0000	0.2409	0.2385	0.3338
F2 sample											
8914	#471	0.0546	0.3095	0.2275	0.0586	0.3095	0.2275	0.0576	0.2468	0.2415	0.3100
8914	#341	0.3156	0.2007	0.2884	0.5080	0.2007	0.2884	0.1825	0.1931	0.3838	0.3844
8914	#928	0.3777	0.1608	0.2855	0.0099	0.1608	0.2855	0.1907	0.1819	0.2342	0.4362
8914	#828	0.3949	0.1058	1.4560	0.3315	0.1058	1.4560	0.1909	0.1165	0.4319	0.3846
8914	#537	0.5675	0.1734	1.5020	0.1920	0.1734	1.5020	0.0000	0.1489	0.4268	0.1821
8914	#203	0.2343	0.1452	0.2565	0.3463	0.1452	0.2565	0.0000	0.1880	0.3055	0.2870
8914	#461	0.7230	0.3099	1.6828	0.3797	0.3099	1.6828	0.0000	0.2368	0.4802	0.3278
8914	#243	0.1367	0.2897	0.0932	0.1492	0.2897	0.0932	0.1053	0.3188	0.2127	0.5296
8914	#450	0.5346	0.2637	2.7476	0.5240	0.2637	2.7476	0.0000	0.2468	0.3619	0.3775
8914	#928	0.2442	0.2973	2.8735	0.3719	0.2973	2.8735	0.0000	0.2692	0.1956	0.4240
8914	#912	0.4010	0.1861	2.7708	0.4758	0.1861	2.7708	0.0000	0.1812	0.2874	0.1843
8914	#326	0.5273	0.4003	1.4449	0.4019	0.4003	1.4449	0.0000	0.3641	0.3341	0.4623
8914	#440	0.4917	0.1489	2.9451	0.9603	0.1489	2.9451	0.1662	0.1197	0.4856	0.3534
8914	#913	0.6837	0.2131	2.8262	0.7115	0.2131	2.8262	0.0000	0.2130	0.4615	0.3298

$z = 1.5$		Rotation and Shape									
		3D						2D			
sim	ELO	$V_\phi/\sigma_3^{\rm star}(r_{\rm e,bo}^{\rm star})$	$\epsilon_{\rm 3D}(r_{\rm e,bo}^{\rm star})$	$S(r_{\rm e,bo}^{\rm star})$	$V_\phi/\sigma_3^{\rm star}(r_{\rm 90,bo}^{\rm star})$	$\epsilon_{\rm 3D}(r_{\rm 90,bo}^{\rm star})$	$S(r_{\rm 90,bo}^{\rm star})$	$V_{\rm max}/\sigma_{\rm los,0}^{\rm star}(R_{\rm e,bo}^{\rm star})$	$\epsilon(R_{\rm e,bo}^{\rm star})$	$V_{\rm max}/\sigma_{\rm los,0}^{\rm star}(R_{\rm 90,bo}^{\rm star})$	$\epsilon(R_{\rm 90,bo}^{\rm star})$
8914	#562	0.4975	0.1999	1.4530	0.4632	0.1999	1.4530	0.0000	0.1861	0.3185	0.4149
8914	#481	0.4354	0.4745	0.0920	0.4441	0.4745	0.0920	0.2008	0.5518	0.2339	0.6583
8914	#283	0.5067	0.4285	1.3057	0.3196	0.4285	1.3057	0.0000	0.4135	0.3558	0.6200
8914	#643	0.3801	0.3310	0.2351	0.5272	0.3310	0.2351	0.0000	0.3466	0.2424	0.4286
8914	#038	0.1535	0.1384	0.2833	0.0518	0.1384	0.2833	0.0000	0.1702	0.1532	0.4511
8914	#140	0.3641	0.2416	2.7202	0.2826	0.2416	2.7202	0.0000	0.1827	0.2026	0.2984

Appendix E

Published Articles

THE ASTROPHYSICAL JOURNAL, 632:L57–L60, 2005 October 20

CLUES ON THE PHYSICAL ORIGIN OF THE FUNDAMENTAL PLANE FROM SELF-CONSISTENT HYDRODYNAMICAL SIMULATIONS

J. OÑORBE,[1] R. DOMÍNGUEZ-TENREIRO,[1] A. SÁIZ,[1,2] A. SERNA,[3] AND H. ARTAL[1]
Received 2005 May 16; accepted 2005 September 6; published 2005 October 10

ABSTRACT

We report on a study of the parameters characterizing the mass and velocity distributions of two samples of relaxed elliptical-like objects (ELOs) identified, at $z = 0$, in a set of self-consistent hydrodynamical simulations operating in the context of a concordance cosmological model. Star formation (SF) has been implemented in the simulations in the framework of the turbulent sequential scenario through a phenomenological parameterization that takes into account stellar physics processes implicitly through the values of a threshold gas density and an efficiency parameter. Each ELO sample is characterized by the values these parameters take. We have found that the (logarithms of the) ELO stellar masses, projected stellar half-mass radii, and stellar central line-of-sight (LOS) velocity dispersions define *dynamical* fundamental planes (FPs). Zero points depend on the particular values that the SF parameters take, while slopes do not change. The ELO samples have been found to show systematic trends with the mass scale in both the relative content and the relative distributions of the baryonic and the dark mass ELO components. The physical origin of these trends lies in the systematic decrease, with increasing ELO mass, of the relative dissipation experienced by the baryonic mass component along ELO mass assembly, resulting in a tilt of the dynamical FP relative to the virial plane. ELOs also show kinematical segregation, but it does not appreciably change with the mass scale. We have found that the dynamical FPs shown by the two ELO samples are consistent with that shown by the SDSS elliptical sample in the same variables, with no further need for any relevant contribution from stellar population effects to explain the observed tilt. These effects could, however, have contributed to the scatter of the observed FP, as the dynamical FPs have been found to be thinner than the observed one. The results we report on hint, for the first time, at a possible way to understand the tilt of the observed FP in a cosmological context.

Subject headings: dark matter — galaxies: elliptical and lenticular, cD — galaxies: evolution — galaxies: formation — galaxies: fundamental parameters — hydrodynamics — methods: *n*-body simulations

1. INTRODUCTION

The three-parameter space of the observed effective radius, $R_e^{\rm light}$, the mean surface brightness within that radius, $\langle I^{\rm light}\rangle_e$, and the central line-of-sight (LOS) velocity dispersion, $\sigma_{\rm LOS,0}$, of early-type galaxies is not homogeneously populated. These galaxies define a plane on this space, known as the fundamental plane (FP; Djorgovski & Davis 1987; Dressler et al. 1987; Faber et al. 1987; Kormendy & Djorgovski 1989), defined by

$$\log_{10} R_e^{\rm light} = a \log_{10} \sigma_{\rm LOS,0} + b \log_{10} \langle I^{\rm light}\rangle_e + c. \qquad (1)$$

A new standard of reference for nearby elliptical galaxies is provided by the Sloan Digital Sky Survey (SDSS; see York et al. 2000) sample of early-type galaxies (for the Early Data Release, see Bernardi et al. 2003a, 2003b, 2003c), containing to date 9000 morphologically selected elliptical galaxies from different environments, a number larger than the number of elliptical galaxies in all of the previously analyzed samples. The values of the FP coefficients from this sample are $a \simeq 1.5$, similar in the four SDSS bands, $b \simeq -0.77$, and $c \simeq -8.7$ (see their exact values in Table 2 of Bernardi et al. 2003c) with a small scatter. These SDSS results confirm previous ones, either in the optical (Lucey et al. 1991; de Carvalho & Djorgovski 1992; Bender et al. 1992; Jorgensen et al. 1993, 1996; Prugniel & Simien 1996) or in the near-IR wavelengths (Recillas-Cruz et al. 1990, 1991; Pahre et al. 1995; Mobasher et al. 1999), even if the published values of a show larger values in the K band than at shorter wavelengths (see, e.g., Pahre et al. 1998).

The existence of the FP and its small scatter has the important implication that it provides us with a strong constraint when studying elliptical galaxy formation and evolution (Bender et al. 1993; Guzmán et al. 1993; Renzini & Ciotti 1993). The physical origin of the FP is not yet clear, but it must be a consequence of the physical processes responsible for galaxy assembly. These processes built up early-type galaxies as dynamically hot systems whose configuration in phase space is close to equilibrium. Taking an elliptical galaxy as a system in equilibrium, a mass scale $M_{\rm FP}$ can be estimated from the observable $R_e^{\rm light}$, $\langle I^{\rm light}\rangle_e$, and $\sigma_{\rm LOS,0}$ parameters through the expression

$$M_{\rm FP} = 3 c_M \sigma^2_{\rm LOS,0} R_e^{\rm light}/G, \qquad (2)$$

where G is the gravitational constant and c_M is a mass structure coefficient. The total luminosity of the galaxy is given by the expression $L = 2\pi \langle I^{\rm light}\rangle_e (R_e^{\rm light})^2$. As Faber et al. (1987) first pointed out, the virial theorem $M_{\rm vir} = c_F (\sigma_3^{\rm tot})^2 r_e^{\rm tot}/G$, with $\sigma_3^{\rm tot}$ the average three-dimensional velocity dispersion of the whole elliptical, including both dark and baryonic matter, $r_e^{\rm tot}$ the dynamical half-radius or radius enclosing half the total mass of the system, and c_F a form factor of order unity, would imply

$$R_e^{\rm light} = \frac{3 c_M^{\rm vir} L \sigma^2_{\rm LOS,0} \langle I^{\rm light}\rangle_e^{-1}}{2\pi G M_{\rm vir}}, \qquad (3)$$

[1] Departamento Física Teórica C-XI, Universidad Autónoma de Madrid, E-28049 Cantoblanco, Madrid, Spain; jose.onorbe@uam.es, rosa.dominguez@uam.es, hector.artal@uam.es.
[2] Current address: Department of Physics, Mahidol University, Rama 6 Road, Rajthewee, Bangkok 10400, Thailand; alex@astro.phys.sc.chula.ac.th.
[3] Departamento Física y A.C., Universidad Miguel Hernández, E-03206 Elche, Alicante, Spain; arturo.serna@umh.es.

where $c_M^{\rm vir}$ is defined by equation (2) when $M_{\rm FP} = M_{\rm vir}$; that is,

$$c_M^{\rm vir} = \frac{GM_{\rm vir}}{3\sigma^2_{\rm LOS,0} R_e^{\rm light}}, \quad (4)$$

or

$$c_M^{\rm vir} = c_F c_V c_r, \quad (5)$$

with $c_V = (\sigma_3^{\rm tot})^2/3\sigma^2_{\rm LOS,0}$ and $c_r = r_e^{\rm tot}/R_e^{\rm light}$. Assuming that both the quantities $c_M^{\rm vir}$ and the dynamical mass-to-light ratios, $M_{\rm vir}/L$, are independent of mass, the scaling relation $R_e^{\rm light} \propto \sigma^2_{\rm LOS,0}\langle I^{\rm light}\rangle_e^{-1}$ would then hold. However, this predicted scaling law is inconsistent with those found observationally ($a \neq 2$, $b \neq -1$); i.e., the FP is tilted relative to the virial relation, implying that at least some of the assumptions made to derive it are incorrect.

Different authors interpret the tilt of the FP relative to the virial relation as caused by different misassumptions, on which we comment briefly as follows [note that we can write $M_{\rm vir}/L = (M^{\rm star}/L)(M_{\rm vir}/M^{\rm star})$, where $M^{\rm star}$ is the stellar mass of the elliptical galaxy]: (1) A first possibility is that the tilt is due to systematic changes of stellar age and metallicity with galaxy mass or, even, to changes of the slope of the stellar initial mass function (IMF) with galaxy mass, resulting in systematic changes in the *stellar* mass-to-light ratios, $M^{\rm star}/L$, with mass or luminosity (Zepf & Silk 1996; Pahre et al. 1998; Mobasher et al. 1999). But these effects could explain at most only about one-third of the $\beta \neq 0$ value in the *B* band (Tinsley 1978; Dressler et al. 1987; Prugniel & Simien 1996; see also Renzini & Ciotti 1993; Trujillo et al. 2004). Futhermore, early-type galaxies in the SDSS have been found to have roughly constant stellar mass-to-light ratios (Kauffmann et al. 2003a, 2003b). Anyhow, the presence of a tilt in the *K*-band FP, where population effects are not important, indicates that it is very difficult for the tilt to be caused by stellar physics processes alone, as Bender et al. (1992), Renzini & Ciotti (1993), Guzmán et al. (1993), and Pahre et al. (1998), among others, have suggested. (2) A second possibility is that $M_{\rm vir}/L$ changes systematically with the mass scale because the total dark-to-visible mass ratio, $M_{\rm vir}/M^{\rm star}$, changes (see, e.g., Renzini & Ciotti 1993; Pahre et al. 1998; Ciotti et al. 1996; Padmanabhan et al. 2004). Otherwise, a dependence of $c_M^{\rm vir}$ on the mass scale could be caused by systematic differences in (3) the dark versus bright matter spatial distribution, which could be measured through systematic variations of the c_r coefficients with mass; (4) the kinematical segregation, the rotational support, and/or velocity dispersion anisotropy in the stellar component (dynamical nonhomology), measurable through the c_V coefficients; and (5) systematic geometrical effects, measurable through the c_F, c_r, or c_V coefficients. Taking into account these effects in the FP tilt demands modelizing the galaxy mass and velocity three-dimensional distributions and comparing the outputs with high-quality data. Bender et al. (1992) considered effects 3 and 4; Ciotti et al. (1996) explore effects 2–4 and conclude that a systematic increase in the dark matter content with mass, or differences in its distribution, and a dependence of the Sérsic (1968) shape parameter for the luminosity profiles on mass may by themselves formally produce the tilt; Padmanabhan et al. (2004) find evidence of effect 2 in SDSS data. Other authors have also shown that allowing for broken homology, either dynamical (Busarello et al. 1997), in the luminosity profiles (Trujillo et al. 2004), or both (Prugniel & Simien 1997; Graham & Colless 1997; Pahre et al. 1998), brings the observed FP closer to the virial plane.

One important source of ambiguity in observational data analysis comes from the impossibility of getting accurate measurements of the elliptical three-dimensional mass distributions (either dark, stellar, or gaseous) and velocity distributions. Analytical models give very interesting insights into these distributions, as well as the physical processes causing them, but are somewhat limited by symmetry considerations and other necessary simplifying hypotheses. Self-consistent gravo-hydrodynamical simulations are a very convenient tool to work out this problem, as they *directly* provide with complete six-dimensional phase-space information on each constituent particle sampling a given galaxy-like object formed in the simulation; that is, they give directly the mass and velocity distributions of dark matter, gas, and stars of each object. This phase-space information allows us to test whether or not the $c_M^{\rm vir}$ (that is, the c_F, c_V, and c_r) coefficients, as well as the $M_{\rm vir}/M^{\rm star}$ ratios, do or do not systematically depend on the mass scale. This is the issue addressed in this letter, where we analyze whether the dependence is such that the tilt and the scatter of the observed FP can be explained in terms of the regularities in the structural and dynamical properties of ELOs formed in self-consistent hydrodynamical simulations.

2. THE DYNAMICAL FUNDAMENTAL PLANE OF SIMULATED OBJECTS

In a self-consistent numerical approach initial conditions are set at high z as a Monte Carlo realization of the field of primordial fluctuations in a given cosmological model; then the evolution of these fluctuations is numerically followed up to $z = 0$ by means of a computing code that solves the *N*-body plus hydrodynamical evolution equations. We have run 10 simulations in the framework of a flat ΛCDM cosmological model, with $\Omega_\Lambda = 0.65$, $\Omega_{\rm baryon} = 0.06$, $\sigma_8 = 1.18$, and $h = 0.65$. The code used in our simulations is DEVA (Serna et al. 2003). In this code, particular attention has been paid to the implementation of conservation laws (energy; entropy, taking into account the ∇h terms; and angular momentum). Star formation (SF) has been implemented in the code in the framework of the turbulent sequential scenario (Elmegreen 2002) through a phenomenological parameterization that transforms cold locally collapsing gas, denser than a threshold density, $\rho_{\rm thres}$, into stars with a timescale given by the empirical Kennicutt-Schmidt law (Kennicutt 1998), with an average star formation efficiency at the scales resolved by the code c_*; possible feedback effects are implicitly taken into account through the values of the SF parameters. In any run, 64^3 dark matter and 64^3 baryon particles, with a mass of 1.29×10^8 and $2.67 \times 10^7\ M_\odot$, respectively, have been used to homogeneously sample the density field in a periodic box of 10 Mpc on each side. We refer the reader to Serna et al. (2003) and Sáiz et al. (2004) for further details on the simulation technique and SF implementation in the code. Five out of the 10 simulations (the SF-A–type simulations) share the SF parameters ($\rho_{\rm thres} = 6 \times 10^{-25}$ g cm^{-3}, $c_* = 0.3$) and differ in the seed used to build up the initial conditions. To test the role of SF parameterization, the same initial conditions have been run with different SF parameters ($\rho_{\rm thres} = 1.8 \times 10^{-24}$ g cm^{-3}, $c_* = 0.1$), making SF more difficult, contributing another set of five simulations (hereafter the SF-B–type simulations). Galaxy-like objects of different morphologies appear in the simulations. ELOs have been identified as those objects having a prominent dynamically

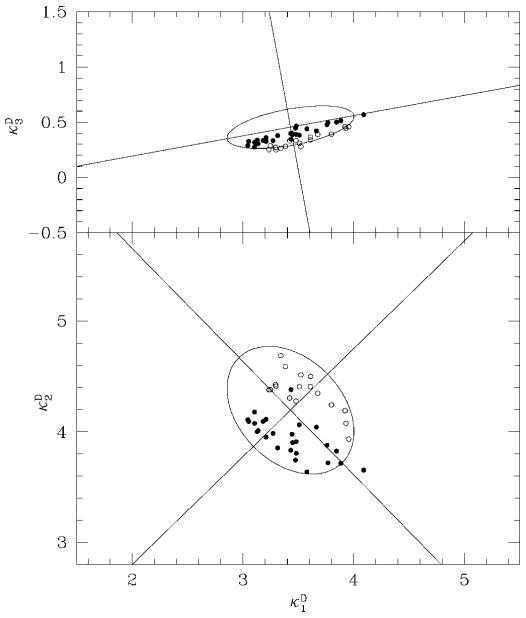

FIG. 1.—Edge-on projection (*top*) and nearly face-on projection (*bottom*) of the dynamical FP of ELOs in the κ^D variables (*filled circles*: SF-A sample; *open circles*: SF-B sample). We also draw the respective concentration ellipses (with their major and minor axes) for the SDSS early-type galaxy sample from Bernardi et al. (2003b) in the z band. See text for more details.

relaxed stellar spheroidal component, with no disks and very low cold gas content. This stellar component has typical sizes of no more than ~10–40 kpc and is embedded in a halo of dark matter typically 10 times larger in size. ELOs also have an extended corona of hot diffuse gas. It turns out that 26 (17) of the more massive objects formed in SF-A (SF-B)–type simulations fulfil this condition, giving the hereafter termed SF-A and SF-B ELO samples. Note that due to their respective SF implementations, galaxy-like objects formed in SF-A–type simulations tend to be of earlier type than their counterparts formed in SF-B–type simulations; this is why the ELO number in the SF-A sample is higher than in the SF-B sample. Moreover, gas has had more time to lose energy along SF-B–type ELO assembly than in their SF-A–type counterparts, and, consequently, the former have smaller sizes than the latter.

Following the discussion in § 1, two mass scales have been measured on ELOs: the virial mass $M_{\rm vir}$, or total mass of the ELO at its halo scale (we adopt the fitting formula of Bryan & Norman [1998] for the spherical overdensity at virialization), and the stellar mass of the baryonic object at the ELO scale, $M_{\rm bo}^{\rm star}$. Concerning length scales, the relevant ones are (1) at the halo scale: the virial radii, $r_{\rm vir}$, and the total half-mass radii, $r_{e,h}^{\rm tot}$, enclosing $M_{\rm vir}/2$; and (2), at the ELO scale, the stellar half-mass radii, $r_{e,\rm bo}^{\rm star}$, defined as those radii enclosing half the $M_{\rm bo}^{\rm star}$ mass, and the projected stellar half-mass radii, $R_{e,\rm bo}^{\rm star}$, measured onto the projected mass distribution. The total (including baryons and dark matter) mean square velocity within $r_{\rm vir}$, $\sigma_{3,h}^{\rm tot}$, as well as the mean square stellar and central stellar[4] LOS velocity dispersions, $\sigma_{3,\rm bo}^{\rm star}$ and $\sigma_{\rm LOS,0}^{\rm star}$, respectively, have also been measured on ELOs. Note that the scales entering the virial relation are $r_{e,h}^{\rm tot}$ and $\sigma_{3,h}^{\rm tot}$ and that they are not observationally available. Assuming that the projected stellar *mass* distribution, $\Sigma_{\rm star}(R)$, can be taken as a measure of the surface *brightness* profile, then $\langle\Sigma_{\rm star}\rangle_e = c\langle I^{\rm light}\rangle_e$, with c a constant, and $R_{e,\rm bo}^{\rm star} \simeq R_e^{\rm light}$, and we can look for an FP (hereafter the dynamical FP) in the three-space of the structural and dynamical parameters $R_{e,\rm bo}^{\rm star}$, $\langle\Sigma_{\rm star}\rangle_e$, and $\sigma_{\rm LOS,0}^{\rm star}$, directly provided by the hydrodynamical simulations. To make this analysis as clear as possible, we transform to a κ-like orthogonal coordinate system, the dynamical κ_i^D system, $i = 1, 2, 3$, similar to that introduced by Bender et al. (1992), but using $R_{e,\rm bo}^{\rm star}$ instead of $R_e^{\rm light}$ and $\langle\Sigma_{\rm star}\rangle_e$ instead of $\langle I^{\rm light}\rangle_e$, and, consequently, free of age, metallicity, or IMF effects. The κ^D and κ coordinates are related by the expressions $\kappa_1 \simeq \kappa_1^D$, $\kappa_2 \simeq \kappa_2^D - \sqrt{6}/3 \log (M_{\rm bo}^{\rm star}/L)$, and $\kappa_3 \simeq \kappa_3^D + \sqrt{3}/3 \log (M_{\rm bo}^{\rm star}/L)$. We discuss the tilt and the scatter of the dynamical FP separately. We first address the tilt issue. We use at this stage for the $R_{e,\rm bo}^{\rm star}$ and $\sigma_{\rm LOS,0}^{\rm star}$ variables the averages over three orthogonal LOS projections, to minimize the scatter in the plots caused by projection effects.

Figure 1 plots the κ_3^D versus κ_1^D (*top panel*) and κ_2^D versus κ_1^D (*bottom panel*) diagrams for ELOs in the SF-A (*filled symbols*) and SF-B (*open symbols*) samples. We also drew the 2 σ concentration ellipses in the respective variables, as well as its major and minor axes, for the SDSS early-type galaxy sample in the z band as analyzed by Bernardi et al. (2003b, 2003c).[5] We recall that the ellipse major axis corresponds to the orthogonal mean square regression line for the two variables in the figure (for further details see Sáiz et al. 2004). The most outstanding feature of Figure 1 (*top panel*) is the good scaling behavior of κ_3^D versus κ_1^D, with a very low scatter (see the slopes M_1 in Table 1; note that the slopes for the SF-A and SF-B samples are consistent within their errors while the zero points depend on the SF parameterization through the ELO sizes). The values of the slopes in Table 1 mean that systematic variations of the structural and dynamical properties of ELOs with the mass scale cause, by themselves, a tilt of the dynamical FP relative to the virial relation. Another interesting feature of Figure 1 is that it shows that most of the values of the κ_i^D coefficients are within the 2 σ concentration ellipses in both plots for ELOs formed in SF-A–type simulations, with a

TABLE 1
SLOPES FOR LINEAR FITS

Parameter (1)	SF-A (2)	SF-B (3)
M_1	0.256 ± 0.035	0.281 ± 0.048
$\beta_{\rm vir}$	0.221 ± 0.083	0.237 ± 0.158
β_M	−0.204 ± 0.116	−0.247 ± 0.189
β_F	0.025 ± 0.048	0.022 ± 0.081
$\beta_{V,D}$	0.021 ± 0.041	0.076 ± 0.075
$\beta_{V,P,C}$	−0.044 ± 0.029	−0.044 ± 0.093
$\beta_{r,D}$	−0.225 ± 0.127	−0.316 ± 0.199
$\beta_{r,P}$	0.019 ± 0.009	0.016 ± 0.017

NOTES.—Col. (2): Slopes of the $\kappa_3^D = M_1\kappa_1^D + M_0$ relation (direct fits) and the slopes of the $M_{\rm vir}/M_{\rm bo}^{\rm star}$ and $c_i \propto (M_{\rm bo}^{\rm star})^{\beta_i}$ scaling relations for the SF-A sample, calculated in log-log plots through direct fits, as well as their respective 95% confidence intervals. Col. (3): Same as col. (2), but for the SF-B sample.

[4] Recall that the empirical LOS velocity dispersion, $\sigma_{\rm LOS,0}$, is measured through *stellar spectra*.

[5] The constant stellar mass-to-light ratios allow us to write the covariance matrix using the $E \equiv \log M_{\rm bo}^{\rm star}$ variable instead of absolute magnitude or the logarithm of the luminosity L.

slightly worse agreement for ELOs in the SF-B sample. This means that ELOs have counterparts in the real world (Sáiz et al. 2004). It is also worth mentioning that these results are stable against slight changes in the values of the Ω_Λ, $\Omega_{\rm baryon}$, or h parameters; for example, we have tested that using their preferred *WMAP* values shows results negligibly different from those plotted in Figure 1.

To examine in more depth the causes of the tilt, we have calculated the slope $\beta_{\rm vir}$ of the $M_{\rm vir}/M_{\rm bo}^{\rm star} \propto (M_{\rm bo}^{\rm star})^{\beta_{\rm vir}}$ scaling relation for ELOs in the SF-A and SF-B samples (Table 1). We got $\beta_{\rm vir} > 0$, indicating that the mass fraction of stars bound to the ELOs (or, more generically, cold baryons) relative to total mass within $r_{\rm vir}$ decreases with the mass scale (as suggested by Renzini & Ciotti 1993; Pahre et al. 1998). We have also found that the $c_M^{\rm vir}$ coefficients show a mass dependence that can be parameterized as a scaling relation $c_M^{\rm vir} \propto (M_{\rm bo}^{\rm star})^{\beta_M}$ (broken homology; see Table 1). As discussed in § 1, different possible sources for homology breaking exist. To elucidate which of them are relevant, we first note that the c_V and c_r coefficients can be written as $c_V = c_{V,D} \times c_{V,P,C}$, with $c_{V,D} \equiv (\sigma_{3,h}^{\rm tot}/\sigma_{3,\rm bo}^{\rm star})^2$ and $c_{V,P,C} \equiv (\sigma_{3,\rm bo}^{\rm star})^2/3(\sigma_{\rm LOS,0}^{\rm star})^2$, and $c_r = c_{r,D} \times c_{r,P}$, with $c_{r,D} \equiv r_{e,h}^{\rm tot}/r_{e,\rm bo}^{\rm star}$ and $c_{r,P} \equiv r_{e,h}^{\rm star}/R_{e,\rm bo}^{\rm star}$. This gives $c_M^{\rm vir} = c_F c_{V,D} c_{V,P,C} c_{r,D} c_{r,P}$, where the $c_{V,D}$ and $c_{r,D}$ factors measure the kinematical and spatial segregations between dark and stellar matter, respectively, while $c_{V,P,C}$ and $c_{r,P}$ measure projection and other geometrical effects in the stellar mass and velocity distributions. Writing $c_i \propto (M_{\rm bo}^{\rm star})^{\beta_i}$ (with $i = F; V, D; V, P, C; r, D$; and r, P), we get $\beta_M = \beta_F + \beta_{V,D} + \beta_{V,P,C} + \beta_{r,D} + \beta_{r,P}$ when the β_i slopes are calculated through direct fits. These β_i slopes are given in Table 1, as well as their 95% confidence intervals for both the SF-A and SF-B samples. We see that, irrespective of the SF parameterization, the main contribution to the homology breaking comes from the $c_{r,D}$ coefficients. We also see that β_F and $\beta_{V,D}$ have values consistent with c_F and $c_{V,D}$ being independent of the ELO mass scale, and $c_{r,P}$ and $c_{V,P,C}$ show a very mild mass dependence in the SF-A sample and none in the SF-B sample.

We now consider the scatter of the dynamical FP for the ELO samples and compare it with the scatter of the FP for the SDSS elliptical sample, calculated as the square root of the smallest eigenvalue of the 3 × 3 covariance matrix in the E (or log L), V, and R variables (Saglia et al. 2001). As the top panel of Figure 1 suggests, when projection effects are circumvented by taking averages over different directions, the resulting three-dimensional orthogonal scatter for ELOs is smaller than for SDSS elliptical galaxies ($\sigma_{E,V,R} = 0.0164$ and 0.0167 for the SF-A and SF-B samples, respectively, to be compared with $\sigma_{L,V,R} = 0.0489$ for the SDSS in the log L, V, and R variables). To estimate the contribution of projection effects to the observed scatter, we have calculated the orthogonal scatter for ELOs when no averages over projection directions for the $R_{e,\rm bo}^{\rm star}$ and $\sigma_{\rm LOS,0}^{\rm star}$ variables are made. The scatter ($\sigma_{E,V,R} = 0.0238$ and 0.0214 for the SF-A and SF-B samples, respectively) increases, but it is still lower than observed. This indicates that a contribution from stellar population effects is needed to explain the scatter of the observed FP, as suggested by different authors (see, e.g., Pahre et al. 1998; Trujillo et al. 2004).

To sum up, the ELO samples have been found to show systematic trends with the mass scale in both the relative content and the relative distributions of the baryonic and the dark mass ELO components. These trends do not significantly depend on the star formation parameterization and are due to a systematic decrease, with increasing ELO mass, of the relative amount of dissipation experienced by the baryonic mass component along ELO formation, a possibility that Bender et al. (1992), Guzmán et al. (1993), and Ciotti et al. (1996) had suggested. These trends cause a tilt of the virial plane in such a way that there is no further need of any relevant contribution from stellar population effects to explain the observed tilt. The scatter of the observed FP, however, probably requires a contribution from such stellar effects.

This work was partially supported by the MCyT and MEyD (Spain) through grants AYA-0973, AYA-07468-C03-02, and AYA-07468-C03-03 from the PNAyA. We thank the Centro de Computación Científica (UAM, Spain) for computing facilities. A. S. acknowledges FEDER financial support from UE.

REFERENCES

Bender, R., Burstein, D., & Faber, S. M. 1992, ApJ, 399, 462
———. 1993, ApJ, 411, 153
Bernardi, M., et al. 2003a, AJ, 125, 1817
———. 2003b, AJ, 125, 1849
———. 2003c, AJ, 125, 1866
Bryan, G. L., & Norman, M. L. 1998, ApJ, 495, 80
Busarello, G., Capaccioli, M., Capozziello, S., Longo, G., & Puddu, E. 1997, A&A, 320, 415
Ciotti, L., Lanzoni, B., & Renzini, A. 1996, MNRAS, 282, 1
de Carvalho, R. R., & Djorgovski, S. 1992, ApJ, 389, L49
Djorgovski, S., & Davis, M. 1987, ApJ, 313, 59
Dressler, A., Lynden-Bell, D., Burstein, D., Davies, R. L., Faber, S. M., Terlevich, R., & Wegner, G. 1987, ApJ, 313, 42
Elmegreen, B. G. 2002, ApJ, 577, 206
Faber, S. F., Dressler, A., Davies, R. L., Burstein, D., Lynden-Bell, D., Terlevich, R., & Wegner, G. 1987, in Nearly Normal Galaxies: From the Planck Time to the Present, ed. S. M. Faber (New York: Springer), 175
Graham, A., & Colless, M. 1997, MNRAS, 287, 221
Guzmán, R., Lucey, J., & Bower, R. G. 1993, MNRAS, 265, 731
Jorgensen, I., Franx, M., & Kjærgaard, P. 1993, ApJ, 411, 34
———. 1996, MNRAS, 280, 167
Kauffmann, G., et al. 2003a, MNRAS, 341, 33
———. 2003b, MNRAS, 341, 54
Kennicutt, R. C., Jr. 1998, ApJ, 498, 541
Kormendy, J., & Djorgovski, S. 1989, ARA&A, 27, 235
Lucey, J. R., Bower, R. J., & Ellis, R. S. 1991, MNRAS, 249, 755
Mobasher, B., Guzmán, R., Aragón-Salamanca, A., & Zepf, S. 1999, MNRAS, 304, 225
Padmanabhan, N., et al. 2004, NewA, 9, 329
Pahre, M. A., de Carvalho, R. R., & Djorgovski, S. G. 1998, AJ, 116, 1606
Pahre, M. A., Djorgovski, S. G., & de Carvalho, R. R. 1995, ApJ, 453, L17
Prugniel, Ph., & Simien, F. 1996, A&A, 309, 749
———. 1997, A&A, 321, 111
Recillas-Cruz, E., et al. 1990, A&A, 229, 64
———. 1991, A&A, 249, 312
Renzini, A., & Ciotti, L. 1993, ApJ, 416, L49
Saglia, R. P., Colless, M., Burstein, D., Davies, R. L., McMahan, R. K., & Wegner, G. 2001, MNRAS, 324, 389
Sáiz, A., Domínguez-Tenreiro, R., & Serna, A. 2004, ApJ, 601, L131
Serna, A., Domínguez-Tenreiro, R., & Sáiz, A. 2003, ApJ, 597, 878
Sérsic, J. L. 1968, Atlas de Galaxias Australes (Córdoba: Obs. Astron.)
Tinsley, B. M. 1978, ApJ, 222, 14
Trujillo, I., Burkert, A., & Bell, E. F. 2004, ApJ, 600, L39
York, D. G., et al. 2000, AJ, 120, 1579
Zepf, S., & Silk, J. 1996, ApJ, 466, 114

THE ASTROPHYSICAL JOURNAL, 636:L77–L80, 2006 January 10

THE LACK OF STRUCTURAL AND DYNAMICAL EVOLUTION OF ELLIPTICAL GALAXIES SINCE $z \sim 1.5$: CLUES FROM SELF-CONSISTENT HYDRODYNAMIC SIMULATIONS

R. DOMÍNGUEZ-TENREIRO,[1] J. OÑORBE,[1] A. SÁIZ,[1,2] H. ARTAL,[1] AND A. SERNA[3]
Received 2005 January 26; accepted 2005 November 23; published 2005 December 16

ABSTRACT

We present the results of a study of the evolution of the parameters that characterize the structure and dynamics of the relaxed elliptical-like objects (ELOs) identified at redshifts $z = 0$, $z = 1$, and $z = 1.5$ in a set of hydrodynamic, self-consistent simulations operating in the context of a concordance cosmological model. The values of the stellar mass $M_{\rm bo}^{\rm star}$, the stellar half-mass radius $r_{e,\rm bo}^{\rm star}$, and the mean square velocity for stars $\sigma_{3,\rm bo}^{\rm star}$ have been measured in each ELO and found to populate, at any z, a flattened ellipsoid close to a plane (the dynamical plane, DP). Our simulations indicate that at the intermediate z's considered, individual ELOs evolve, increasing their $M_{\rm bo}^{\rm star}$, $r_{e,\rm bo}^{\rm star}$, and $\sigma_{3,\rm bo}^{\rm star}$ parameters as a consequence of ongoing mass assembly, but nevertheless, their DP is roughly preserved within its scatter, in agreement with observations of the fundamental plane at different z's. We briefly discuss how this lack of significant dynamical and structural evolution in ELO *samples* arises, in terms of the two different phases operating in the mass aggregation history of their dark matter halos. According to our simulations, most dissipation involved in ELO formation takes place at the early violent phase, causing the $M_{\rm bo}^{\rm star}$, $r_{e,\rm bo}^{\rm star}$, and $\sigma_{3,\rm bo}^{\rm star}$ parameters to settle down to the DP and, moreover, the transformation of most of the available gas into stars. In the subsequent slow phase, ELO stellar mass growth preferentially occurs through nondissipative processes, so that the DP is preserved and the ELO star formation rate considerably decreases. These results hint, for the first time, at a possible way of explaining, in the context of cosmological simulations, different and apparently paradoxical observational results for elliptical galaxies.

Subject headings: dark matter — galaxies: elliptical and lenticular, cD — galaxies: evolution — galaxies: formation — galaxies: fundamental parameters — hydrodynamics

1. INTRODUCTION

Among all galaxy families, elliptical galaxies (E's) are the simplest ones and those that show the most precise regularities in the form of relations among some of their observable parameters. One of the most meaningful is the so-called fundamental plane (FP) relation (Djorgovski & Davis 1987; Dressler et al. 1987; Faber et al. 1987), defined by their observed effective radius, $R_e^{\rm light}$, mean surface brightness within that radius, $\langle I^{\rm light}\rangle_e$, and central line-of-sight velocity dispersion, $\sigma_{\rm los,0}$. Analyses of the Sloan Digital Sky Survey (SDSS) sample of local elliptical galaxies confirm previous results on the FP (see Bernardi et al. 2003a and references therein). Studies of the FP of early-type galaxies up to $z \sim 1$ (van Dokkum et al. 2001; van de Ven et al. 2003; Wuyts et al. 2004; Treu et al. 2005) show that changes in the FP with z can be described in terms of the evolution of their average stellar mass-to-light ratio, $M^{\rm star}/L_B$, as predicted by a scenario of pure luminosity evolution of their stellar populations, and with no further need for any significant structural or dynamical evolution of the sample (see, however, di Serego Alighieri et al. 2005).

Different authors interpret the tilt of the FP relative to the virial relation as being caused by different assumptions concerning the dependence of the dynamical mass-to-light ratios, $M_{\rm vir}/L$, or the mass structure coefficients, $c_M^{\rm vir} = GM_{\rm vir}/(3\sigma_{\rm los,0}^2 R_e^{\rm light})$, on the mass scale (see discussion in Oñorbe et al. 2005). A possibility is that $M_{\rm vir}/L$ grows systematically with increasing mass scale because the total dark-to-visible mass ratio, $M_{\rm vir}/M^{\rm star}$, grows (as suggested, e.g., by Ciotti et al. 1996; Pahre et al. 1998; Cappellari et al. 2006). Otherwise, a dependence of $c_M^{\rm vir}$ on the mass scale could be caused by, among other possibilities, systematic differences in the relative spatial distribution of the baryonic and dark mass components of elliptical galaxies (Ciotti et al. 1996). Recently, we have confirmed these possibilities (Oñorbe et al. 2005), finding that the samples of elliptical-like objects (ELOs) identified, at $z = 0$, in our fully consistent cosmological hydrodynamic simulations exhibit just such trends, giving rise to *dynamical* planes. We also found that the physical origin of these trends presumably lies in the systematic decrease, with increasing ELO mass, of the relative amount of dissipation experienced by the baryonic mass component along ELO mass assembly. So, these results suggest that the dissipative processes involved in the mass assembly of elliptical galaxies result in the tilt of the FP relative to the virial plane. A consequence would be that the tilt of the FP must be preserved during those time intervals when no significant amounts of dissipation occur along E assembly.

Concerning the epochs of dissipation along E assembly, because star formation (SF) requires gas cooling, the age distribution of the stellar populations of a given elliptical galaxy should reflect the time structure of the dissipative processes involved in its formation and assembly (i.e., when the dissipation rate was high, its timescale, and so on). These age distributions indicate that, in elliptical galaxies, most SF occurred (1) at high z, (2) on short timescales, and, moreover, (3) at higher z's and on shorter timescales for increasing E mass (they show age effects; see, e.g., Caldwell et al. 2003; Bernardi et al. 2003b; Thomas et al. 2005). This would be the generic behavior of the dissipation rate history for elliptical galaxies, should the assumption of its connection with their SF rate history be correct.

Points 1 and 2 above are the basic ingredients of the so-called monolithic collapse scenario (see details and discussion

[1] Departamento de Física Teórica, Módulo C-XI, Universidad Autónoma de Madrid, E-28049 Cantoblanco, Madrid, Spain; rosa.dominguez@uam.es.
[2] Current address: Department of Physics, Mahidol University, Rama 6 Road, Ratchathewi, Bangkok 10400, Thailand.
[3] Departamento de Física y Arquitectura de Computadores, Universidad Miguel Hernández, E-03206 Elche, Alicante, Spain.

in Peebles 2002; Matteucci 2003; Somerville et al. 2004). This scenario also explains another set of observational results on E homogeneity, such as, for example, (1) the lack of significant structural and dynamical evolution of lens ellipical galaxies, at least out to $z \sim 1$ (Treu & Koopmans 2004), (2) the lack of any strong structural evolution in the stellar mass-size relation since $z \sim 3$ (Trujillo et al. 2004; McIntosh et al. 2005), and (3) the confirmed existence of a population of old, relaxed, massive ($M^{\rm star} > 10^{11}\ M_{\odot}$) spheroidal galaxies at intermediate redshifts ($z \sim 1$–2; Cimatti et al. 2002, 2004; Stanford et al. 2004) or even earlier (Mobasher et al. 2005). However, the monolithic scenario does not recover all the currently available observations on E's either. Important examples, suggesting that mergers at $z \lesssim 1.5$–2 could have played an important role in E assembly, are (1) the growth of the total stellar mass bound up in bright red galaxies by a factor of ~2 since $z = 1$ (Bell et al. 2004; Conselice et al. 2005; Fontana et al. 2004; Drory et al. 2004; Bundy et al. 2005; Faber et al. 2005), implying that the mass assembly of most E's continues below $z = 1$; (2) the signatures of merging observed by the moment out to intermediate z (Le Fèvre et al. 2000; Patton et al. 2002; Conselice 2003; Cassata et al. 2005), in particular of major dissipationless mergers between spheroidal galaxies (Bell et al. 2006), which translate into a relatively high merger rate for massive galaxies even below $z = 1$; and (3) the need for a young stellar component in some elliptical galaxies (van Dokkum & Ellis 2003; van der Wel et al. 2004) or, more particularly, the finding of blue cores (i.e., recent SF at the central regions) and inverse color gradients in 30%–40% of the spheroidal galaxies in some samples out to $z \sim 1.2$ (see Menanteau et al. 2004 and references therein).

The observational results above are paradoxical because they demand, on the one hand, that spheroids have passively evolving stellar populations and an FP that preserves its tilt below $z \sim 1$ or higher and, on the other hand, that mass assembly is an ongoing process for most of them and they still form some stars below these redshifts. In fact, one could think that in principle, the tilt of the FP could be modified by these last processes and, so, the preservation of the FP tilt (or its evolution) is a very important issue because it could encode a lot of relevant information on the dissipation rate history of elliptical samples and, consequently, on the physical processes underlying E formation and evolution. In order to reconcile all these physical assumptions and observational background within a formation scenario, it is useful to study E assembly from simple physical principles and in the context of the global cosmological model. Fully consistent gravohydrodynamic simulations are a very convenient tool for working out this problem (Navarro & White 1994; Sommer-Larsen et al. 2003; Meza et al. 2003; Kobayashi 2005; Romeo et al. 2005). In fact, individual galaxy-like objects naturally appear as an output of the simulations, so that the parameters characterizing them can be measured and compared with observations. Concerning E assembly, the method has already proved to be useful. Apart from the physical origin of their FP (Oñorbe et al. 2005), the issue of age effects of their stellar populations has been addressed in Domínguez-Tenreiro et al. (2004, hereafter DSS04), where clues on how these age effects arise are given. Moreover, the structural and dynamical properties of these ELOs have been found to be consistent with observations (Sáiz et al. 2004; Oñorbe et al. 2005). The next step is to study whether the dynamical FP of ELO samples does not evolve below $z \sim 1.5$ or so, and whether this is or is not consistent with ongoing mass assembly as detected in real E samples and, if it is, to try to understand how this arises with regard to the cooling rate, the SF rate, and the mass assembly histories of ELOs. These are the issues addressed in this Letter.

2. THE HOMOGENEITY OF THE ELLIPTICAL POPULATION: CLUES FROM THEIR ASSEMBLY HISTORY

We have run five hydrodynamic simulations in the context of a concordance cosmological model (Spergel et al. 2003), in which the normalization parameter has been taken slightly high, $\sigma_8 = 1.18$, as compared with the average fluctuations of galaxies from the Two Degree Field Galaxy Redshift Survey or SDSS (Lahav et al. 2002; Tegmark et al. 2003) to mimic an active region of the universe (Evrard et al. 1990). Galaxy-like objects of different morphologies form in these simulations. ELOs have been identified as those objects having a prominent, dynamically relaxed stellar spherical component, with no disks and a very low cold-gas content. This stellar component has typical sizes of no more than ~10–40 kpc (hereafter the *baryonic object* or "bo" scale), and it is embedded in a halo of dark matter typically 10 times larger in size. ELOs also have an extended corona of hot diffuse gas. We consider the whole sample of ELOs identified in each of the five simulations at $z = 0$, $z = 1$, and $z = 1.5$ (samples E-Z0, E-Z1, and E-Z1.5, with 26, 24, and 16 ELOs, respectively) and analyze the evolution of their mass and velocity distributions between $z = 0$ and $z = 1.5$ by comparing the ELOs in these three samples. To run the simulations, we have used DEVA, a Lagrangian SPH-AP3M code using particles to sample dark matter or baryonic (i.e., gaseous and stellar) mass elements. We refer the reader to Serna et al. (2003) for details on the simulation technique and to Sáiz et al. (2004) for details on its implementation in the runs we analyze here and on the general sample properties at $z = 0$. All simulations started at a redshift $z_{\rm in} = 20$. SF processes have been implemented, in the framework of the turbulent sequential SF scenario (Elmegreen 2002), through a simple parameterization that transforms cold, locally collapsing gas denser than a threshold density $\rho_{\rm thres}$ into stars at a rate $d\rho_{\rm star}/dt = c_*\rho_{\rm gas}/t_g$, where t_g is a characteristic timescale chosen to be equal to the maximum of the local gasdynamical time and the local cooling time and c_* is the average SF efficiency at the scales resolved by the code. This is the empirical Kennicutt-Schmidt law (Kennicutt 1998). The five simulations share the same values for the SF parameters ($c_* = 0.3$ and $\rho_{\rm thres} = 6.0 \times 10^{-25}$ g cm^{-3}) and differ in the seed used to build up the initial conditions.

To characterize the structural and dynamical properties of ELOs, we will describe their three-dimensional distributions of mass and velocity through the three intrinsic (i.e., three-dimensional) parameters (the stellar mass at the baryonic object scale, $M_{\rm bo}^{\rm star}$, the stellar half-mass radius at the same scale, $r_{e,{\rm bo}}^{\rm star}$, defined as that radius enclosing half the $M_{\rm bo}^{\rm star}$ mass, and the mean square velocity for stars, $\sigma_{3,{\rm bo}}^{\rm star}$) whose observational projected counterparts (the luminosity L, effective projected size $R_e^{\rm light}$, and stellar central line-of-sight velocity dispersion, $\sigma_{{\rm los},0}$) enter the definition of the observed FP. We use three-dimensional variables rather than projected ones to avoid projection effects. To measure the structural and dynamical evolution of ELOs, we carry out a principal component analysis of the E-Z0, E-Z1, and E-Z1.5 samples in the three-dimensional variables $E \equiv \log M_{\rm bo}^{\rm star}$, $r \equiv \log r_{e,{\rm bo}}^{\rm star}$, and $v \equiv \log \sigma_{3,{\rm bo}}^{\rm star}$ through their 3×3 correlation matrix $\mathbf{C}$. We have found that one of the eigenvalues of $\mathbf{C}$ is, for the three ELO samples analyzed, considerably smaller than the others, so that at any z ELOs populate a flattened ellipsoid close to a two-dimensional plane

TABLE 1
DYNAMICAL PLANE PARAMETERS

Sample	$\tilde{E}_z$	$\tilde{r}_z$	$\tilde{v}_z$	α_z^{3D}	β_z^{3D}	$\sigma_{z,\mathrm{Erv}}$	d_z
E-Z0	11.0	0.75	2.34	0.43	2.07	0.011	...
E-Z1	10.8	0.52	2.30	0.25	2.10	0.011	0.008
E-Z1.5	10.9	0.49	2.33	0.31	2.01	0.013	0.009

in (E, r, v)-space; the observed FP is the observational manifestation of this dynamical plane (DP). The eigenvectors of **C** indicate that the projection

$$E - \tilde{E}_z = \alpha_z^{3D}(r - \tilde{r}_z) + \beta_z^{3D}(v - \tilde{v}_z), \quad (1)$$

where $\tilde{E}_z$, $\tilde{r}_z$, and $\tilde{v}_z$ are the mean values of the variables E, r, and v at redshift z, shows the DP viewed edge-on. Table 1 gives the planes equation for samples E-Z0, E-Z1, and E-Z1.5, as well as their corresponding thicknesses, $\sigma_{z,\mathrm{Erv}}$, and the distances d_z of the point $(\tilde{E}_z, \tilde{r}_z, \tilde{v}_z)$ to the E-Z0 plane. We see that the sample averages $\tilde{E}_z$, $\tilde{r}_z$, and $\tilde{v}_z$ grow as z decreases, but in any case $|d_z| < \sigma_{z,\mathrm{Erv}}$, so that they move *on* the E-Z0 plane within its rms scatter. Moreover, only 8.4% and 0% of ELOs in the E-Z1 and E-Z1.5 samples, respectively, are at distances greater than $\sigma_{z=0,\mathrm{Erv}}$ from the E-Z0 plane. These results indicate that ELO evolution roughly preserves their DP. The results in Table 1 strongly suggest that the evolution shown by the FP of real elliptical galaxies is not the result of a dynamical or structural evolution of elliptical samples, corroborating other observational findings on E homogeneity (see § 1). To try to understand these results, we report on ELO assembly and its effect on the DP preservation at intermediate and low redshift.

Our simulations indicate that ELOs are assembled out of mass elements that at high z are enclosed by those overdense regions R whose local coalescence length $L_c(t, R)$ (Vergassola et al. 1994) grows much faster than average, and whose mass scale M_R (total mass enclosed by R) is on the order of an E total (i.e., including its halo) mass (see DSS04 and references therein). The virial mass of the ELO at low z, M_{vir}, is the sum of the masses of the particles that belong to R and are involved into the ELO merger tree. Analytical models, as well as N-body simulations, indicate that two different phases operate along halo mass assembly: first, a violent, fast one, in which the mass aggregation rates are high, and then a slower one, with lower mass aggregation rates (Wechsler et al. 2002; Zhao et al. 2003; Salvador-Solé et al. 2005). Our hydrodynamic simulations give us, for each ELO, its mass aggregation track (i.e., its mass aggregation history along the main branch of the corresponding merger tree) and, moreover, its dissipation rate[4] and SF rate histories, among others; these three histories are plotted in Figure 1 for a typical ELO. We have found that the fast phase occurs through a multiclump collapse following turnaround of the overdense regions and is characterized by fast head-on fusions experienced by the nodes of the cellular structure these regions enclose, resulting in strong shocks and high cooling rates for their gaseous component and, at the same time, in strong and very fast star formation bursts (SFBs) that transform most of the available cold gas in R. For the massive ELOs in this work, this happens between $z \sim 6$ and $z \sim 2.5$ and corresponds to a cold mode of gas aggregation, as in Keres et al. (2005). Consequently, most of the dissipation involved in the mass assembly of a given ELO occurs in this violent early phase at high z; moreover, its rate history is reflected by the SF rate history, as illustrated in Figure 1. This implies that the dynamical variables settle down to the ELO DP at this early phase. This plane is tilted relative to the virial plane, as discussed in § 1 (see Oñorbe et al. [2005] and also Robertson et al. [2005] for preprepared mergers).

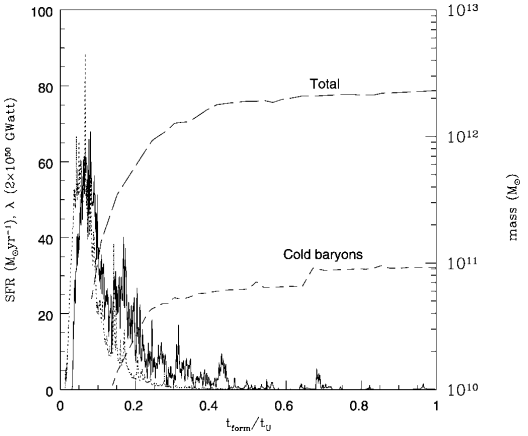

FIG. 1.—Cooling rate history λ (*dotted line*) and SF rate history (*solid line*) of a typical ELO in the simulations. We also plot its mass aggregation tracks, both for cold baryons (i.e., stars and cold gas) and total mass. The fast (*left*) and slow (*right*) phases of mass aggregation are clearly shown.

The slow phase comes after the multiclump collapse. In this phase, the halo mass aggregation rate is low and the M_{vir} increment results from major mergers, minor mergers, or continuous accretion. Our cosmological simulations show that the fusion rates are generally low and that a strong SFB follows a major merger only if enough gas is still available after the early, violent phase. This is very unlikely in any case, and it becomes more and more unlikely as M_{vir} increases (see DSS04). And so, these mergers imply only a modest amount of energy dissipation or SF, as the major merger in Figure 1 at $t/t_U \sim 0.66$ (where t_U is the age of the universe) illustrates. Note, however, that mergers play an important role in this slow phase: ~50% of ELOs in the sample have experienced a major merger event at $2 < z < 0$, which results in the increase of the ELO mass content (see Fig. 1), size r, and stellar mean square velocity v. A consequence of the lack of dissipation could be that the DP is preserved at the slow phase, and in fact, we have found in our cosmological simulations that *dissipationless* merger events roughly preserve it (see Table 1).[5]

Apart from ELO stellar mass growth following dissipationless mergers in the slow phase, our simulations indicate that $M_{\mathrm{bo}}^{\mathrm{star}}$ can also increase as a consequence of newborn stars, formed either (1) within the ELO itself from accreted gas or gas coming in satellites that falls to the central regions before being turned into stars (see the weak SFBs in Fig. 1 at $0.45 < t/t_U < 0.68$) or (2) through mergers, as the SFB at $t/t_U \sim 0.68$ in Figure 1. While the first implies quiescent modes of star formation (see Papovich et al. 2005) and could explain the blue cores observed in some relaxed spheroids, both could explain the need for a young stellar population to fit some E spectra

[4] That is, the amount of cooling per time unit experienced by those gas particles that at $z = 0$ form the ELO stellar component.

[5] The preservation of the FP in preprepared dissipationless mergers has already been studied by Capelato et al. (1995), González-García & van Albada (2003), Nipoti et al. (2003), and Boylan-Kolchin et al. (2005).

(see references above). Major merger events become less frequent as time elapses, allowing for a higher fraction of relaxed spheroids. Both ongoing stellar mass assembly (either through stellar mass aggregation or forming newborn stars) and the decrease of the major merger rate imply an increase of the stellar mass density contributed by relaxed ELOs. In fact, we find that it has changed by a factor of 2.1 between $z = 1$ and $z = 0$, consistent with empirical estimates (see § 1).

To sum up, the main result we report on is the homogeneity of the relaxed ELO population with respect to z, as measured through the dynamical plane defined by their stellar masses, three-dimensional sizes, and mean square stellar velocities at different z's, and, at the same time, the increase of the average values of these parameters as time elapses. The simulations also provide us with clues to how these evolutionary patterns arise from the physical processes involved in E formation, namely, the plane's appearance at an early violent phase as a consequence of E assembly out of gaseous material, with cooling and on short timescales (as in the monolithic collapse scenario), and the plane's preservation during a later, slower phase, where dissipationless merging plays an important role in stellar mass assembly (as in the hierarchical scenario of E formation). This early gas consumption of proto-E's also explains why most of the stars of today's elliptical galaxies formed at high redshifts, while they are assembled later on (see De Lucia et al. [2006] for similar conclusions from a semianalytic model of galaxy formation grafted to the Millennium Simulation [Springel et al. 2005]). Simulations also provide clues to why E homogeneity is consistent with the appearance of blue cores, as well as with the increase of the stellar mass contributed by the E population as z decreases. We conclude that the simulations provide a unified scenario within which most current observations on elliptical galaxies can be interrelated. This scenario shares some characteristics with previously proposed scenarios, but it also has significant differences, mainly that stars form out of cold gas that had never been shock-heated at the halo virial temperature and then formed a disk, as the conventional recipe for galaxy formation propounds (see discussion in Binney 2004; Keres et al. 2005; references therein). To finish, let us note that the scenario for elliptical galaxy formation emerging from our simulations has the advantage that their dark mass and gas aggregation histories result from simple physical laws acting on generic initial conditions (i.e., realizations of power spectra consistent with CMB anisotropy data).

This work was partially supported by the MECD (Spain) through grants AYA-07468-C03-02 and AYA-07468-C03-03 from the Plan Nacional de Astronomía y Astrofísica. We thank E. Salvador-Solé for discussions, and the Centro de Computación Científica (UAM) for computing facilities. A. S. thanks the European Union for Fonds Européens de Développement Regional (FEDER) financial support.

REFERENCES

Bell, E. F., et al. 2004, ApJ, 608, 752
———. 2006, ApJ, in press (astro-ph/0506425)
Bernardi, M., et al. 2003a, AJ, 125, 1866
———. 2003b, AJ, 125, 1882
Binney, J. 2004, MNRAS, 347, 1093
Boylan-Kolchin, M., Ma, C.-P., & Quataert, E. 2005, MNRAS, 362, 184
Bundy, K., Ellis, R. S., & Conselice, C. J. 2005, ApJ, 625, 621
Caldwell, N., Rose, J. A., & Concannon, K. D. 2003, AJ, 125, 2891
Capelato, H. V., de Carvalho, R. R., & Carlberg, R. G. 1995, ApJ, 451, 525
Cappellari, M., et al. 2006, MNRAS, in press (astro-ph/0505042)
Cassata, P., et al. 2005, MNRAS, 357, 903
Cimatti, A., et al. 2002, A&A, 381, L68
———. 2004, Nature, 430, 184
Ciotti, L., Lanzoni, B., & Renzini, A. 1996, MNRAS, 282, 1
Conselice, C. J. 2003, ApJS, 147, 1
Conselice, C. J., Blackburne, J. A., & Papovich, C. 2005, ApJ, 620, 564
De Lucia, G., Springel, V., White, S. D. M., Croton, D., & Kauffmann, G. 2006, MNRAS, in press (astro-ph/0509725)
di Serego Alighieri et al. 2005, A&A, 442, 125
Djorgovski, S., & Davis, M. 1987, ApJ, 313, 59
Domínguez-Tenreiro, R., Sáiz, A., & Serna, A. 2004, ApJ, 611, L5 (DSS04)
Dressler, A., Lynden-Bell, D., Burstein, D., Davies, R. L., Faber, S. M., Terlevich, R. J., & Wegner, G. 1987, ApJ, 313, 42
Drory, N., Bender, R., Feulner, G., Hopp, U., Maraston, C., Snigula, J., & Hill, G. J. 2004, ApJ, 608, 742
Elmegreen, B. G. 2002, ApJ, 577, 206
Evrard, A. E., Silk, J., & Szalay, A. S. 1990, ApJ, 365, 13
Faber, S. F., Dressler, A., Davies, R. L., Burstein, D., Lynden-Bell, D., Terlevich, R., & Wegner, G. 1987, in Nearly Normal Galaxies: From the Planck Time to the Present, ed. S. M. Faber (New York: Springer), 175
Faber, S. M., et al. 2005, ApJ, submitted (astro-ph/0506044)
Fontana, A., et al. 2004, A&A, 424, 23
González-García, A. C., & van Albada, T. S. 2003, MNRAS, 342, L36
Kennicutt, R. C., Jr. 1998, ApJ, 498, 541
Keres, D., Katz, N., Weinberg, D. H., & Davé, R. 2005, MNRAS, 363, 2
Kobayashi, C. 2005, MNRAS, 361, 1216
Lahav, O., et al. 2002, MNRAS, 333, 961
Le Fèvre, O., et al. 2000, MNRAS, 311, 565
Matteucci, F. 2003, Ap&SS, 284, 539
McIntosh, D. H., et al. 2005, ApJ, 632, 191
Menanteau, F., et al. 2004, ApJ, 612, 202
Meza, A., Navarro, J. F., Steinmetz, M., & Eke, V. R. 2003, ApJ, 590, 619
Mobasher, B., et al. 2005, ApJ, 635, 832
Navarro, J. F., & White, S. D. M. 1994, MNRAS, 267, 401
Nipoti, C., Londrillo, P., & Ciotti, L. 2003, MNRAS, 342, 501
Oñorbe, J., Domínguez-Tenreiro, R., Sáiz, A., Serna, A., & Artal, H. 2005, ApJ, 632, L57
Pahre, M. A., de Carvalho, R. R., & Djorgovski, S. G. 1998, AJ, 116, 1606
Papovich, C., Dickinson, M., Giavalisco, M., Conselice, C. J., & Ferguson, H. C. 2005, 631, 101
Patton, D. R., et al. 2002, ApJ, 565, 208
Peebles, P. J. E. 2002, in ASP Conf. Ser. 283, A New Era in Cosmology, ed. N. Metcalf & T. Shanks (San Francisco: ASP), 351
Robertson, B., Cox, T. J., Hernquist, L., Franx, M., Hopkins, P. F., Martini, P., & Springel, V. 2005, ApJ, submitted (astro-ph/0511053)
Romeo, A. D., Portinari, L., & Sommer-Larsen, J. 2005, MNRAS, 361, 983
Sáiz, A., Domínguez-Tenreiro, R., & Serna, A. 2004, ApJ, 601, L131
Salvador-Solé, E., Manrique, A., & Solanes, J. Mª. 2005, MNRAS, 358, 901
Serna, A., Domínguez-Tenreiro, R., & Sáiz, A. 2003, ApJ, 597, 878
Somerville, R. S., Lee, K., Ferguson, H. C., Gardner, J. P., Moustakas, L. A., & Giavalisco, M. 2004, ApJ, 600, L135
Sommer-Larsen, J., Götz, M., & Portinari, L. 2003, ApJ, 596, 47
Spergel, D. N., et al. 2003, ApJS, 148, 175
Springel, V., et al. 2005, Nature, 435, 629
Stanford, S. A., Dickinson, M., Postman, M., Ferguson, H. C., Lucas, R. A., Conselice, C. J., Budavári, T., & Somerville, R. 2004, AJ, 127, 131
Tegmark, M., et al. 2003, Phys. Rev. D, 69, 103501
Thomas, D., Maraston, C., Bender, R. & Mendes de Oliveira, C. 2005, ApJ, 621, 673
Treu, T., & Koopmans, L. V. E. 2004, ApJ, 611, 739
Treu, T., et al. 2005, ApJ, 633, 174
Trujillo, I., et al. 2004, ApJ, 604, 521
van de Ven, G., van Dokkum, P. G., & Franx, M. 2003, MNRAS, 344, 924
van der Wel, A., Franx, M., van Dokkum, P. G., & Rix, H.-W. 2004, ApJ, 601, L5
van Dokkum, P. G., & Ellis, R. S. 2003, ApJ, 592, L53
van Dokkum, P. G., Franx, M., Kelson, D. D., & Illingworth, G. D. 2001, ApJ, 553, L39
Vergassola, M., Dubrulle, B., Frisch, U., & Noullez, A. 1994, A&A, 289, 325
Wechsler, R. H., Bullock, J. S., Primack, J. R., Kravtsov, A. V., & Dekel, A. 2002, ApJ, 568, 52
Wuyts, S., van Dokkum, P. G., Kelson, D. D., Franx, M., & Illingworth, G. D. 2004, ApJ, 605, 677
Zhao, D. H., Mo, H. J., Jing, Y. P., & Börner, G. 2003, MNRAS, 339, 12

Mon. Not. R. Astron. Soc. **376,** 39–60 (2007) doi:10.1111/j.1365-2966.2006.11411.x

Bright and dark matter in elliptical galaxies: mass and velocity distributions from self-consistent hydrodynamical simulations

J. Oñorbe,[1]★ R. Domínguez-Tenreiro,[1] A. Sáiz[1]† and A. Serna[2]
[1]*Departamento de Física Teórica, C-XI. Universidad Autónoma de Madrid, Madrid, E-28049, Spain*
[2]*Departamento de Física y A.C., Universidad Miguel Hernández, Elche, Spain*

Accepted 2006 December 8. Received 2006 November 2; in original form 2006 May 16

ABSTRACT

We have analysed the mass and velocity distributions of two samples of relaxed elliptical-like objects (ELOs) identified, at $z = 0$, in a set of self-consistent hydrodynamical simulations operating in the context of a concordance cosmological model. ELOs have been identified as those virtual galaxies having a prominent, dynamically relaxed stellar spheroidal component, with no extended discs and very low gas content. Our analysis shows that they are embedded in extended, massive dark matter haloes, and they also have an extended corona of hot diffuse gas. Dark matter haloes have experienced adiabatic contraction along their assembly process. The relative ELO dark- to bright-mass content and space distributions show broken homology, and they are consistent with observational results on the dark matter fraction at the central regions, as well as on the gradients of the mass-to-light ratio profiles for boxy ellipticals, as a function of their stellar masses. These results indicate that massive ellipticals miss stars (i.e. baryons) at their central regions, as compared to less massive ones. Our simulations indicate that these missing baryons could be found beyond the virial radii as a hot, diffuse plasma. This mass homology breaking could have important implications to explain the physical origin of the Fundamental Plane relation. The projected stellar mass profiles of our virtual ellipticals can be well fitted by the Sérsic formula, with shape parameters n that agree, once a stellar mass-to-light ratio independent of position is assumed, with those obtained from surface brightness profiles of ellipticals. The agreement includes the empirical correlations of n with size, luminosity and velocity dispersion. The total mass density profiles show a power-law behaviour over a large $r/r_{\rm vir}$ interval, consistent with data on massive lens ellipticals at shorter radii. The velocity dispersion profiles show kinematical segregation, with no systematic mass dependence (i.e. no dynamical homology breaking) and a positive anisotropy (i.e. radial orbits), roughly independent of the radial distance outside the central regions. The line-of-sight (LOS) velocity dispersion profiles are declining. These results give, for the first time from cosmological simulations, a rather detailed insight into the intrinsic mass and velocity distributions of the dark, stellar and gaseous components of virtual ellipticals. The consistency with observations strongly suggests that they could also describe important intrinsic characteristics of real ellipticals, as well as some of their properties recently inferred from observational data (e.g. downsizing, the appearance of blue cores, the increase of the stellar mass contributed by the elliptical population as z decreases).

Key words: hydrodynamics – galaxies: elliptical and lenticular, cD – galaxies: haloes – galaxies: kinematics and dynamics – galaxies: structure – dark matter.

1 INTRODUCTION

Among all galaxy families, elliptical galaxies (EGs) are the simplest ones and those that show the most precise empirical regularities, such as, the very similar shapes their surface brightness profiles show (i.e. the Sérsic law; Sérsic 1968), the power-law form of their

★E-mail: jose.onnorbe@uam.es
†Present address: Department of Physics, Mahidol University, Bangkok 10400, Thailand.

three-dimensional mass density profiles emerging from strong lensing analyses (Koopmans et al. 2006) and the relations among some of their observable parameters. The importance of these regularities lies in that they very likely encode a lot of relevant information on the physical processes underlying the histories of the mass assembly, the rates of dissipation and the rates of star formation (SF) of EGs.

Despite of their interest, little is known, from both the theoretical and observational points of view, about the mass or velocity distributions of the different elliptical mass components (stars, hot and cold gas and dark matter). There has been, nevertheless, important recent progress on the photometric characterization of EGs, and, in fact, authors now agree that the Sérsic law adequately describes the optical surface brightness profiles of most of them (Caon, Capaccioli & D'Onofrio 1993; Trujillo, Graham & Caon 2001; Bertin, Ciotti & Del Principe 2002). The Sérsic law can be written as

$$I^{\rm light}(R) = I_0^{\rm light} \exp\left[-b_n\left(R/R_{\rm e}^{\rm light}\right)^{1/n}\right], \qquad (1)$$

where $I^{\rm light}(R)$ is the surface brightness at projected distance R from the elliptical centre, $R_{\rm e}^{\rm light}$ is the effective half-light radius, encompassing half the total galaxy luminosity, $b_n \simeq 2n - 1/3 + 0.009876/n$, and n is the Sérsic shape parameter. Putting $n = 4$, the largely used de Vaucouleurs $R^{1/4}$ law (de Vaucouleurs 1948) is recovered.

It is generally assumed that galaxies of any type are embedded in massive haloes of dark matter. However, from the observational point of view, the importance and the distribution of dark matter in EGs are still a matter of debate. Data on stellar kinematics from integrated-light spectra are very scarce beyond $2R_{\rm e}^{\rm light}$, making it difficult even to establish the presence of a dark matter halo (Kronawitter et al. 2000; Magorrian & Ballantyne 2001) through this method. Otherwise, the lack of mass tracers at larger distances that can be interpreted without any ambiguity has historically hampered the proper mapping of the mass distribution at the outer regions of EGs. The situation is changing and a dramatic improvement is expected in the near future. In fact, several ongoing projects have already produced high-quality data on samples of ellipticals through different methods, for example: stellar kinematics from integral-field spectroscopic measurements (SAURON; de Zeeuw et al. 2002; Cappellari et al. 2006); strong gravitational lensing (Cosmic Lens All Sky Survey, CLASS; Myers et al. 1995; Lenses Structure and Dynamics Survey, LSD; Koopmans & Treu 2003; Treu & Koopmans 2004; Sloan Lens Advanced Camera for Surveys, SLACS; Koopmans et al. 2006); stellar kinematics from planetary nebulae (PNs; Douglas et al. 2002) or globular cluster (Bergond et al. 2006) observations and X-rays (O'Sullivan & Ponman 2004a,b). In particular, the combination of high-quality stellar spectroscopy and strong lensing analyses breaks the so-called mass-anisotropy degeneracy, giving strong indications that constant mass-to-light ratios can be ruled out at >99 per cent confidence level (CL), consistent with the presence of massive and extended dark matter haloes around, at least, the massive lens ellipticals analysed so far (Treu & Koopmans 2004; Koopmans et al. 2006). Moreover, these authors have also found that the dark matter and the baryons mass density profiles combine in such a way that the total mass density profiles can be fit by power-law expressions within their Einstein radii, whose slopes are consistent with isothermality. Similar conclusions on the important amounts of dark matter inside the virial radii of ellipticals have been reached from weak lensing of L_* galaxies (Guzik & Seljak 2002; Hoekstra, Yee & Gladders 2004), dynamical satellite studies (van den Bosch et al. 2004) and X-ray analyses (Humphrey et al. 2006). Other observational results or some of their interpretations, however, could suggest that the amounts of dark matter in the haloes of some ellipticals are not that important. For example, Napolitano et al. (2005) have analysed the mass-to-light gradients of a sample of elliptical + SO galaxies, and found that these are positive and important in massive, boxy EGs, but not very important for faint, discy EGs. These results have been confirmed by Ferreras, Saha & Williams (2005) using lensing analyses. This result is similar to what Romanowsky et al. (2003; see also Romanowsky 2006) have propounded from the study of random velocities at the outskirts of EGs through PN, found to be low, and first interpreted by these authors as proving a dearth of dark matter in EGs, while Dekel et al. (2005) explain these large-radii low-velocity dispersions as an effect of anisotropy and triaxiality of the halo stellar populations of these galaxies.

Assuming that ellipticals are embedded in massive haloes of dark matter, a second important concern is the possibility that their profiles have near-universal shapes. Here, most inputs come from numerical simulations because observational inputs are scarce. When no dissipative processes are taken into account, spherically averaged dark matter density profiles of relaxed haloes produced in N-body simulations have been found to be well fitted by analytical expressions such that, once rescaled, they give essentially a unique mass density profile, determined by two parameters. These two parameters are usually taken to be the total mass, $M_{\rm vir}$, and the concentration, c, or the energy content, E. These two parameters are, on their turn, correlated (i.e. the mass–concentration relation; see e.g. Bullock et al. 2001; Wechsler et al. 2002; Manrique et al. 2003). When hydrodynamical forces and cooling processes enter the assembly of these haloes and the baryonic objects they host, the dark matter profiles could be modified in the regions where baryons are dynamically dominant, due to the so-called adiabatic contraction [see e.g. Blumenthal et al. 1986; Dalcanton, Spergel & Summers 1997; Tissera & Domínguez-Tenreiro 1998 (hereafter TD); Gnedin et al. 2004; Gustafsson, Fairbairn & Sommer-Larsen 2006]. So, the shapes of dark matter haloes in ellipticals could deviate from the near-universal behaviour of dark matter haloes produced in purely N-body simulations.

Another important issue concerns the 3D cold baryon mass (i.e. stellar mass) distribution, and, more particularly, its distribution relative to the dark matter haloes: are ellipticals homologous systems or is the homology broken in their stellar mass distribution or in their *relative* dark- versus bright-mass distribution?

Concerning the 3D velocity distributions of the different elliptical components, little is known either. In particular, the anisotropy of the stellar 3D velocity dispersion tensor is hard to be observationally characterized. This is an important issue, however, because anisotropy not only plays an important role in the analyses of the elliptical dark matter content at several effective radii, but also could keep fossil information about the physical processes involved in mass assembly and stellar formation in EGs. The relative behaviour of the 3D velocity dispersion tensors for the stellar and the dark mass components (i.e. the so-called kinematical segregation) is still more uncertain. There is not an unambiguous observational input about its presence in ellipticals, or about its possible systematic dependence with the elliptical mass scale. This is an important point because of its possible connection with the physical origin of the so-called Fundamental Plane (FP) relation, as different authors have suggested (Busarello et al. 1997; Graham & Colless 1997; Pahre, de Carvalho & Djorgovski 1998).

Understanding the FP relation (Djorgovski & Davis 1987; Dressler et al. 1987; Faber et al. 1987; Bernardi et al. 2003, and references therein) is in fact a milestone in the physics of elliptical

formation. The FP is defined by the three observational parameters characterizing the mass and velocity distributions of the stellar component: luminosity L, radius at half projected light $R_{\rm e}^{\rm light}$ and central LOS velocity dispersion $\sigma_{\rm LOS,0}$. The FP is tilted relative to the virial plane. Different authors interpret this tilt as caused by different misassumptions relative to the constancy of the dynamical mass-to-light ratios, $M_{\rm vir}/L$, or the mass structure coefficients, $c_{\rm M}^{\rm vir} = \frac{GM_{\rm vir}}{3\sigma_{\rm LOS,0}^2 R_{\rm e}^{\rm light}}$, with the mass scale [see discussion in Oñorbe et al. (2005, 2006), and references cited therein]. Recently, Oñorbe et al. (2005, 2006) have found that the samples of elliptical-like objects (ELOs) identified at $z = 0$ in their fully consistent cosmological hydrodynamical simulations show systematic trends with the mass scale in both the relative global dark- to bright-mass content and the relative sizes of the stellar and the dark mass components, giving rise to *dynamical* FPs.

We see that the mass or velocity distributions of the different elliptical mass components encode a lot of information about the physical origin of the FP, and, consequently, on the physics of elliptical formation. We also see that, unfortunately, observational methods, by themselves, suffer from some drawbacks to deepen into these issues. A major drawback is that the information on the intrinsical mass distribution is not directly available: we see the projections of luminosity (not 3D mass) distributions. Another major drawback is that the intrinsic 3D velocity distribution of galaxies is severely limited by projection, only the LOS velocity distributions can be inferred from galaxy spectra. And, so, the interpretation of observational data is not always straightforward. To complement the information provided by data and circumvent these drawbacks, analytical modelling is largely used in the literature (Kronawitter et al. 2000; Gerhard et al. 2001; Romanowsky & Kochanek 2001; Borriello, Salucci & Danese 2003; Padmanabhan et al. 2004; Mamon & Łokas 2005a,b). They give very interesting insights into mass and velocity distributions, as well as the physical processes causing them, but are somewhat limited by symmetry considerations and other necessary simplifying hypotheses. These difficulties and limitations could be circumvented should we have at our disposal complete information on the phase space of the galaxy constituents. This is not possible through observations, but can be attained, at least in a virtual sense, through numerical simulations.

The first authors who studied the formation and properties of EGs by means of numerical methods used purely gravitatory pre-prepared simulations. The origin of the FP was addressed, among others, by Capelato, de Carvalho & Carlberg (1995), González-García & van Albada (2003), Dantas et al. (2003), Nipoti, Londrillo & Ciotti (2003, 2006) and Boylan-Kolchin, Ma & Quataert (2005). Some of these authors (Dantas et al. 2003; Nipoti et al. 2003) conclude that dissipation must be a basic ingredient in elliptical formation. Bekki (1998) first considered the role of dissipation in elliptical formation through pre-prepared simulations. He adopts the merger hypothesis (i.e. ellipticals form by the mergers of two equal-mass gas-rich spirals) and focuses on the role of the time-scale for SF in determining the structural and kinematical properties of the merger remnants. He concludes that the slope of the FP reflects the difference in the amount of dissipation the merger end products have experienced in accordance with their luminosity (or mass). Recently, Robertson et al. (2006) have confirmed this conclusion on the role of dissipative dynamics to shape the FP, again through pre-prepared mergers of disc galaxies.

Apart from the FP relation origin, other aspects of the formation and evolution of EGs have been analysed through pre-prepared simulations. For example, the different isophotal shapes of ellipticals and their kinematical support (either intrinsic rotation or anisotropic dispersion) have been addressed by A. Burkert and co-workers, who analysed in detail binary mergers of virtual galaxies with different morphologies and initial conditions (Naab & Burkert 2003; Naab & Trujillo 2006; Naab, Khochfar & Burkert 2006). Otherwise, González-García, Balcells & Olshevsky (2006) analysed the velocity distribution of dissipationless binary merger remnants involving galaxies with different morphologies.

We see that pre-prepared simulations of merger events provide a very useful tool to work out the mass and velocity distributions of EGs. They also allow to find out their links with the processes involved in galaxy assembly, but they are somewhat limited, for example, by the fact that the probability of a particular initial setup at a given z is not known a priori, and that mergers involving more than two objects also occur and are frequent at high zs, so that some complementary information must be provided, for example, through semi-analytical models (Khochfar & Burkert 2005; Naab et al. 2006).

To overcome these limitations, a convenient method is to study the processes involved in galaxy formation in a *cosmological context* through *self-consistent* gravodynamical simulations. The method works as follows: initial conditions are set at high z, in a homogeneously sampled box, as a Monte Carlo realization of the field of primordial fluctuations to a given cosmological model; then the evolution of these fluctuations is numerically followed up to $z = 0$ by means of a computer code that solves, in a periodic box, the gravitational and hydrodynamical evolution equations. This method allows us to follow the evolution of the dynamical and thermo-hydrodynamical properties of matter in the universe: individual galaxy-like objects naturally appear as a consequence of this evolution. No prescriptions are needed as far as their mass assembly processes are concerned, only SF processes need further modelling. The important point here is that self-consistent simulations *directly* provide with complete six-dimensional phase space information on each constituent particle sampling a given galaxy-like object formed in the simulation, that is, they give directly the mass and velocity distributions of dark matter, gas and stars of each object.

Kobayashi (2005) has simulated the chemodynamical evolution of 74 fields with different cosmological cold dark matter (CDM) initial spectra set in slowly rotating spheres, each of them with a 1.5 Mpc comoving radius and vacuum boundaries. So, these simulations are not yet fully self-consistent. She succeeded in reproducing the observed global scaling relations shown by EGs, and, in particular, the FP relation, and the surface-brightness profiles, along with the colour–magnitude and the mass–metallicity relations. She also analyses the role of major merger events and the time-scales for SF in shaping the mass and sizes of remnants.

Concerning self-consistent hydrodynamical simulations, Sommer-Larsen, Gotz & Portinari (2002) present first results on early-type galaxy formation in a cosmological context. Meza et al. (2003) present results of the dissipative formation of a compact EG in the ΛCDM scenario. Kawata & Gibson (2003, 2005) and Gibson et al. (2006) have studied the X-ray and optical properties of virtual ellipticals formed in different simulations run with their chemodynamical Tree/SPH code. Romeo, Portinari & Sommer-Larsen (2005) analyse the galaxy stellar populations formed in their simulations of galaxy clusters. Naab et al. (2005) got, from cosmological initial conditions, a spheroidal system whose photometric and kinematical properties agree with observations of ellipticals in a scenario not including feedback from supernovae or active galactic nuclei (AGN) and not requiring recent major mergers. Interesting results on elliptical formation have also been

obtained by de Lucia et al. (2006), from a semi-analytic model of galaxy formation grafted to the *Millennium Simulation*.

However, detailed analyses of the mass and velocity distributions of samples of virtual ellipticals formed in fully self-consistent hydrodynamical simulations and, in particular, of the amount and distribution of dark matter relative to the bright matter distribution, as well as of the kinematics of the dark and bright components, and their successful comparison with observational data, were still missing. This is the work we present in this paper. To be specific, we have analysed the samples of virtual ellipticals formed in 10 self-consistent hydrodynamical simulations, run in the framework of a flat ΛCDM cosmological model characterized by cosmological parameters consistent with their last determinations (Spergel et al. 2006). Galaxy-like objects of different morphologies appear in these simulations at $z = 0$: disc-like objects, SO-like objects, ELOs and peculiars.

Our previous work has shown that these ELO samples have properties that agree with observational data, so that they have counterparts in the real world. In fact, an analysis of the structural and dynamical ELO parameters that can be constrained from observations (i.e. stellar masses, projected half-mass radii, central LOS velocity dispersions) has shown that they are consistent with those measured in the Sloan Digital Sky Survey (SDSS) Data Release 1 (DR1) elliptical sample (Sáiz, Domínguez-Tenreiro & Serna 2004), including the FP relation (Oñorbe et al. 2005), and their lack of evolution at low and intermediate redshifts (Domínguez-Tenreiro et al. 2006, hereafter DTal06). Also, their stellar populations have age distributions showing similar trends as those inferred from observations, i.e. most stars have formed at high z on short time-scales, and, moreover, more massive objects have older means and narrower spreads in their stellar age distributions than less massive ones[1] (Domínguez-Tenreiro, Sáiz & Serna 2004, hereafter DSS04).

This paper is organized as follows. In Section 2, we briefly describe the simulations and the SF modelling. In Section 3, the ELO sample and the generic structure of ELOs are described. A brief account on ELO formation is given in Section 4. The 3D orbital structure of the baryonic component is briefly described in Section 5. Section 6 is devoted to report on the dark matter and baryonic mass density profiles of the ELOs produced in the simulations. In Section 7, we report on the kinematics of the different ELO components. Finally, in Section 8 we summarize our results and discuss them in the context of theoretical results on halo structure and dissipation of the gaseous component and their connections with observational data.

2 THE SIMULATIONS

We have analysed ELOs identified in 10 self-consistent cosmological simulations run in the framework of the same global flat ΛCDM cosmological model, with $h = 0.65$, $\Omega_m = 0.35$ and $\Omega_b = 0.06$. The normalization parameter has been taken slightly high, $\sigma_8 = 1.18$, as compared with the average fluctuations of two-degree field galaxy redshift survey (2dFGRS) or SDSS galaxies (Spergel et al. 2006) to mimic an active region of the Universe (Evrard, Silk & Szalay 1990).

[1]This is equivalent to the *downsizing* concept introduced by Cowie et al. (1996) to mean that SF is stronger at low redshifts in smaller galaxies than in larger ones.

We have used a Lagrangian code (DEVA; Serna, Domínguez-Tenreiro & Sáiz 2003), particularly designed to study galaxy assembly in a cosmological context. Gravity is computed through an AP3M-like method, based on Couchman (1991). Hydrodynamics are computed through a smoothed particle hydrodynamics (SPH) technique where special attention has been paid to ensure that the implementation of conservation laws (energy, entropy and angular momentum) is as accurate as possible [see Serna et al. (2003) for details, in particular, for a discussion on the implications of violating some conservation laws]. Entropy conservation is assured by taking into consideration the space variation of the smoothing length (i.e. the so-called ∇h terms). Time-steps are individual for particles (to save CPU time, allowing a good time resolution) as well as masses. Time integration uses a PEC (predict–evaluate–correct) scheme. In any run, a homogeneously sampled periodic box of 10 Mpc side has been employed and 64^3 dark matter and 64^3 baryonic particles, with a mass of $m^{dark} = 1.29 \times 10^8$ and $m^b = 2{,}67 \times 10^7$ $M_\odot$, respectively, have been used. The gravitational softening used was $\epsilon = 2.3$ kpc. The cooling function is that from Tucker (1975) and Bond et al. (1984) for an optically thin primordial mixture of H and He ($X = 0.76$, $Y = 0.24$) in collisional equilibrium and in absence of any significant background radiation field with a primordial gas composition. Each of the 10 simulations started at a redshift $z_{in} = 20$.

SF processes have been included through a simple phenomenological parametrization, as that first used by Katz (1992, see also Tissera, Lambas & Abadi 1997; Serna et al. 2003 for details) that transforms cold locally collapsing gas at the scales the code resolves, denser than a threshold density, ρ_{thres}, into stars at a rate $d\rho_{star}/dt = c_*\rho_{gas}/t_g$, where t_g is a characteristic time-scale chosen to be equal to the maximum of the local gas-dynamical time, $t_{dyn} = (4\pi G\rho_{gas})^{-1/2}$ and the local cooling time; c_* is the average SF efficiency at resolution ϵ scales, i.e. the empirical Kennicutt–Schmidt law (Kennicutt 1998). It is worth noting that, in the context of the new sequential multi-scale SF scenarios (Vázquez-Semadeni 2004a,b; Ballesteros-Paredes et al. 2006, and references therein), it has been argued that this law, and particularly so the low c_* values inferred from observations, can be explained as a result of SF processes acting on dense molecular cloud core scales when conveniently averaged on disc scales (Elmegreen 2002; Sarson et al. 2004, see below). Supernova feedback effects or energy inputs other than gravitational have not been *explicitly* included in these simulations. We note that the role of discrete stellar energy sources at the scales resolved in this work is not yet clear, as some authors argue that stellar energy releases drive gas density structuration locally at sub-kpc scales (Elmegreen 2002). In fact, recent MHD simulations of self-regulating Type II supernova (SNII) heating in the interstellar medium (ISM) at scales <250 pc (Sarson et al. 2004) indicate that this process produces a Kennicutt–Schmidt like law on average. If this were the case, the Kennicutt–Schmidt law implemented in our code would already *implicitly* account for the effects stellar self-regulation has on the scales our code resolves, and our ignorance on sub-kpc scale processes would be contained in the particular values of ρ_{thres} and c_*.

Five out of the 10 simulations (the SF-A type simulations) share the SF parameters ($\rho_{thres} = 6 \times 10^{-25}$ gr cm^{-3}, $c_* = 0.3$) and differ in the seed used to build up the initial conditions. To test the role of SF parametrization, the same initial conditions have been run with different SF parameters ($\rho_{thres} = 1.8 \times 10^{-24}$ gr cm^{-3}, $c_* = 0.1$) making SF more difficult, contributing another set of five simulations (hereafter, the SF-B type simulations).

3 SIMULATED ELLIPTICAL-LIKE OBJECTS AT $Z = 0$: THE ELO SAMPLE

ELOs have been identified as those galaxy-like-objects having a prominent, relaxed spheroidal component, made out of stars, with no extended discs and very low cold gas content. Moreover, their dark matter haloes must also be relaxed to allow their meaningful analysis, excluding systems that have just merged or that are about to merge. It turns out that, at $z = 0$, 26 (17) objects out of the more massive formed in SF-A (SF-B) type simulations fulfil these conditions. ELOs form two samples (the SF-A and SF-B ELO samples) partially analysed in Sáiz et al. (2004), DSS04 and DTal06. In Oñorbe et al. (2005, 2006), it is shown that both samples satisfy dynamical FP relations.

ELOs are embedded in dark matter haloes whose virial radii[2] are in the range $527 > r_{\rm vir} > 191$ kpc. ELO stellar components have ellipsoidal shapes and have a lower limit in their stellar mass content of $3.8 \times 10^{10}\,{\rm M}_{\odot}$ [see Kauffmann et al. (2003) for a similar result in SDSS galaxies]. Inner discs, when present, are made out of cold gas. ELOs have also hot diffuse gas forming an extended halo (Sáiz, Domínguez-Tenreiro & Serna 2003). The number of dark and baryonic particles within $r_{\rm vir}$ is in the ranges (5.3×10^4, 2.4×10^3) and (3.1×10^4, 2.0×10^3), respectively, giving a lower limit in the virial masses of ELOs of $M_{\rm vir} > 3.7 \times 10^{11}\,{\rm M}_{\odot}$. Some ELOs show a clear net rotation, resulting in an average value of their spin parameter of $\bar{\lambda} = 0.033$. ELO mass function is consistent with that of a small group, that is a dense environment (Cuesta-Bolao & Serna, private communication). ELOs in the SF-B sample tend to be of later type than their corresponding SF-A counterparts because forming stars becomes more difficult; this is why many of the SF-B sample counterparts of the less massive ELOs in SF-A sample do not satisfy the selection criteria, and the SF-B sample has a lower number of ELOs than the SF-A sample.

4 A BRIEF ACCOUNT ON ELO FORMATION

The simulations unveil the physical patterns of ELO mass assembly, energy dissipation and SF rate histories (see Sierra-Glez.de Buitrago et al. 2003; DSS04; DTal06). Our simulations indicate that ELOs are assembled out of the mass elements that at high z are enclosed by those overdense regions R whose local coalescence length $L_{\rm c}(t, R)$ (Vergassola et al. 1994) grows much faster than average, and whose mass scale (total mass enclosed by R, M_R) is of the order of an EG virial mass. Analytical models, as well as N-body simulations, indicate that two different phases operate along halo mass assembly: first, a violent fast one, where the mass aggregation rates are high and, then, a slower one, with lower mass aggregation rates (Wechsler et al. 2002; Zhao et al. 2003; Salvador-Solé, Manrique & Solanes 2005). Our hydrodynamical simulations indicate that the fast phase occurs through a multiclump collapse (see Thomas, Greggio & Bender 1999) ensuing turnaround of the overdense regions, and it is characterized by the fast head-on (that is, with very low relative orbital angular momentum) fusions experienced by the nodes of the cellular structure these regions enclose, resulting in strong shocks and high cooling rates of their gaseous component, and, at the same time, in strong and very fast SF bursts that transform most of the available cold gas in R into stars. For the massive ELOs in this work, this happens between $z \sim 6$ and $\sim$2.5 and mainly corresponds to a cold mode of gas aggregation, as in Keres et al. (2005). Consequently, most of the dissipation involved in the mass assembly of a given ELO occurs in this violent early phase at high z; moreover, its rate history[3] is reflected by the SF rate history, as illustrated in fig. 1 of DTal06. The FP relation shown by EGs appears in this fast violent phase as a consequence of dissipation and homology breaking in the mass distribution (see Oñorbe et al. 2005, 2006; DTal06).

The slow phase comes after the fast phase. In this phase, the halo mass aggregation rate is low and the $M_{\rm vir}$ increment results from major mergers, minor mergers or continuous mass accretion. Our cosmological simulations show that the fusion rates are generally low and that these mergers generally imply only a modest amount of energy dissipation or SF. In fact, a strong SF burst and dissipation follow a major merger only if enough gas is still available after the early violent phase. This is unlikely in any case, and it becomes more and more unlikely as $M_{\rm vir}$ increases (see DSS04). A consequence of the lack of dissipation is that the FP is roughly preserved along the slow phase (see DTal06). We have to point out that mergers play an important role in this slow phase as far as mass assembly is concerned: $\sim$50 per cent of ELOs in the sample have experienced a major merger event at $2 < z < 0$, that results in the increase of the ELO mass content, size and stellar mean square velocity. Some of these mergers are multiple, and in some few cases either binary or multiple mergers involve disc galaxies, but none of the ELOs in our sample has been shaped by a merger of two or more adult disc virtual galaxies, maybe because our simulated box mimics a dense environment.

So, our simulations suggest that most of the stars of today ellipticals, or at least of those in dense environments, could have formed at high redshifts, while they are assembled later on [see de Lucia et al. (2006) for similar results from a semi-analytic model of galaxy formation grafted to the *Millennium Simulation*]. This formation scenario shares some aspects of both, the hierarchical merging and the monolithic collapse scenarios, but it has also significant differences, mainly that most stars belonging to EGs form out of cold gas that had never been shock heated at the halo virial temperature and then formed a disc, as the conventional recipe for galaxy formation propounds [see discussion in Keres et al. (2005) and references therein]. An important point is that our simulations indicate that this formation scenario follows from simple physical principles in the context of the current ΛCDM scenario.

5 THREE-DIMENSIONAL STRUCTURE OF THE BARYONIC CONSTITUENT

A quantitative description of ELO mass distributions is given by their 3D density profile and the structure of their constituent particles. We first address the structure of the baryonic particles.

5.1 Three-dimensional structure for gas particles

The gas structure is drawn in Fig. 1 for the second more massive object formed in a SF-B type simulation. The 3D density at a given distance, r, from the centre of the object has been calculated by binning on concentric spherical shells around r. In this figure, the line

[2]The virial radii, $r_{\rm vir}$, have been calculated using the Bryan & Norman (1998) fitting formula that yields, at $z = 0$, a value of $\Delta \simeq 100$ for the mean density within $r_{\rm vir}$ in units of the critical density.

[3]That is, the amount of cooling per time unit experienced by those gas particles that at $z = 0$ form the ELO stellar component.

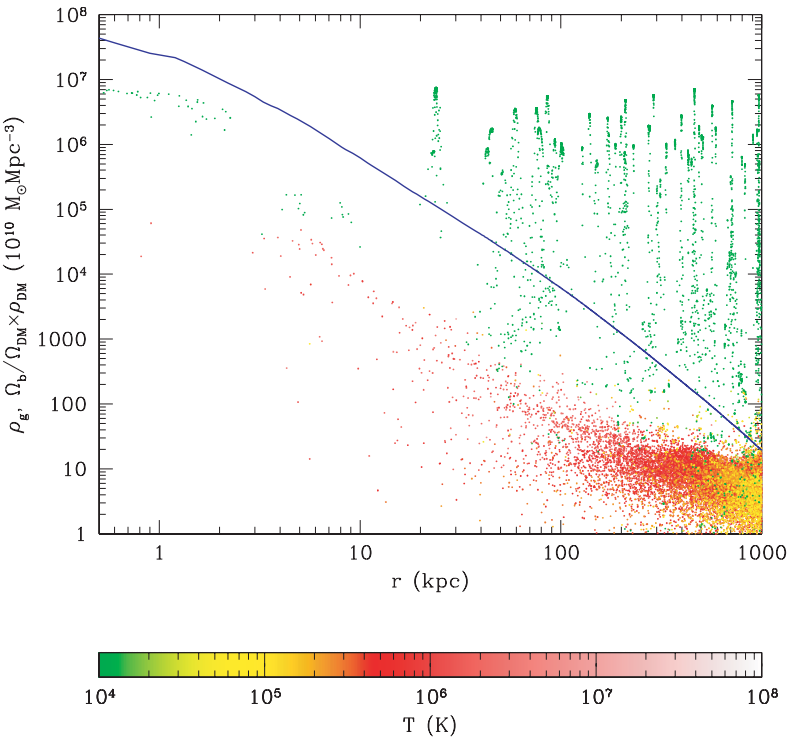

Figure 1. 3D gas (points) and dark matter (blue line) density for a typical ELO. Note the dense cold gas clumps embedded in the diffuse hot gas component. See text for an explanation.

is the density profile of dark matter around the object, multiplied by Ω_b/Ω_m. Points represent gas density at the positions of SPH particles, and colours stand for gas particle temperatures in accordance with the scale at the bottom of the figure.

We see in this figure that very less gas is left at positions with $r \leqslant 30$ kpc where stars dominate the mass density, that cold gas at $r \geqslant 30$ kpc is dense and clumpy, while hot gas (i.e. gaseous particles with $T > 3 \times 10^4$ K) is diffuse with an almost isothermal component at $100 \leqslant r \leqslant 400$ kpc, and a warm component at the outskirts of the configuration, reaching outside the virial radius (395.0 kpc). Two scales stand out in this configuration: the *ELO scale* or stellar component, with a size in this case of ∼30 kpc, and the *halo scale*, a halo of dark matter of 395.0 kpc. Cold dense gas particles are associated in most cases with small dark matter haloes (not seen in the figure); both gaseous particles in cold clumps and dark matter particles in their (sub)haloes are *shocked* particles, using the terminology of the adhesion model (see e.g. Vergassola et al. 1994). The configuration illustrated by this figure is generic for ELOs: we can distinguish an *ELO scale*, with typical sizes of no more than ∼10–40 kpc, and the *halo scale*, a halo of dark matter typically 10 times larger in size.

5.2 Stellar and gaseous particle orbits

ELO constituent particles of different kinds travel on orbits that have different characteristics. To analyse this point, in the upper panel of Fig. 2 we plot, for each star particle and each gaseous particle of a typical ELO, the cosine of the angle formed by its position ($\boldsymbol{r}_i$) and its velocity ($\boldsymbol{v}_i$) as a function of $\boldsymbol{r}_i$. Positions and velocities have been taken with respect to the centre of mass of the main baryonic object. In this plot, radial orbits have cosines $= \pm 1$, while circular orbits have cosines $= 0$. Starred (circular) symbols stand for stellar (gaseous) particles. We see that cold gas particles at $r \leqslant 4$ kpc form a disc in coherent circular motion; filled (open) symbols represent particles in corotation (counterrotation) with respect to this small disc. We can also see that stellar particle orbits at $\leqslant 3$ kpc scales do not show any preference, while those further away, as well as gaseous particles outside the disc, show a slight tendency to be on radial orbits providing anisotropy to the velocity dispersion. Stellar particles constitute a disordered or dynamically hot component, showing an important velocity dispersion and, also, in some cases, a coherent net rotation. In Section 7, these issues will be addressed in detail.

6 THE DARK MATTER AND BARYONIC MASS DISTRIBUTIONS

6.1 Dark matter profiles

Spherically averaged dark matter density profiles of relaxed haloes formed in N-body simulations have been found to be well fitted by

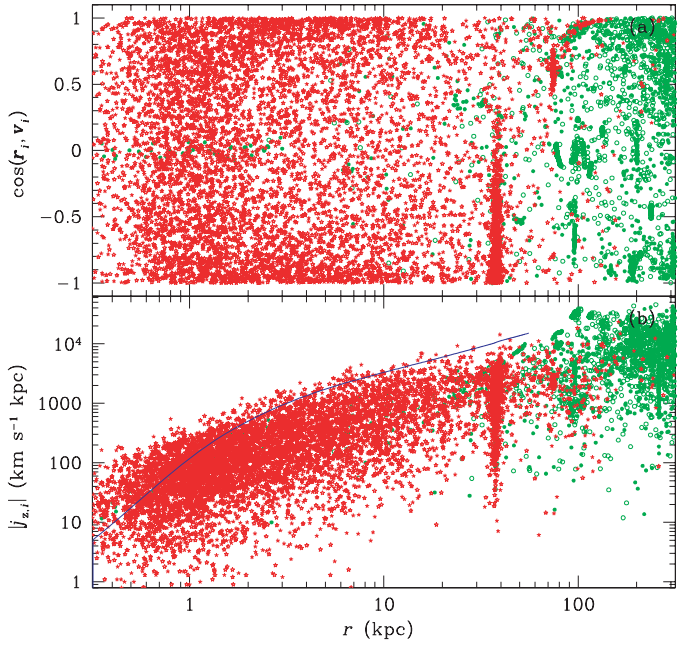

Figure 2. Upper panel: the cosine of the angle formed by the position and the velocity vectors for each gaseous (green circles) and stellar (starred red symbols) particle belonging to a typical ELO. Filled (open) symbols stand for particles in (counter) corotation with the small inner disc.

analytical expressions such that, once rescaled, give essentially a unique mass density profile, i.e. a two-parameter family. These two parameters are usually taken to be the total mass, $M_{\rm vir}$, and the concentration, c, or the energy content, E. These two parameters are, on their turn, correlated (i.e. the mass–concentration relation; see e.g. Bullock et al. 2001; Wechsler et al. 2002; Manrique et al. 2003) because the assembly process implies a given correlation between $M_{\rm vir}$ and E. Different authors propound slightly different fitting formulae, see Einasto (1965, 1968, 1969) or Navarro et al. (2004), Hernquist (1990, hereafter Hern90), Navarro, Frenk & White (1995, 1996, hereafter NFW), Tissera & Domínguez-Tenreiro (1998, hereafter TD), Moore et al. (1999) and Jing & Suto (2000, hereafter JS), that can be written as

$$\rho_{\rm h}^{\rm dark}(r) = 3c^3\rho_{\Delta}^{\rm aver} g(c) \times \rho(r/a_h), \qquad (2)$$

where $\rho_{\Delta}^{\rm aver}$ is the average density within the virial radii, $c \equiv r_{\rm vir}/a_h$ is the so-called concentration parameter and

$$\rho(y) = y^{-\alpha}(1+y)^{-\beta}, \qquad (3)$$

where $(\alpha,\beta) = (1,3)$ for Hern90; $(\alpha,\beta) = (1,2)$ for NFW; $(\alpha,\beta) = (2,2)$ for TD and $\beta = 3-\alpha$, with α left free, for the general formula found by JS (note that NFW can be considered as JS with $\alpha = 1$). In these fitting formulae, α is the inner slope ($r \ll a_h$), the outer slope ($r \gg a_h$) is $\alpha+\beta$ (3 for JS or NFW), so that a_h characterizes the scale where the slope changes. Other interesting scale is r_{-2}, the r value where the logarithmic slope, $\mathrm{d}\ln\rho/\mathrm{d}\ln r = -2$. We have $r_{-2} = a_h(2-\alpha)/(\alpha+\beta-2)$ for a profile given by equation (3), with $r_{-2} = a_h(2-\alpha)$ for JS and $r_{-2} = a_h$ for NFW. Navarro et al. (2004) propound a different fitting formula of the form

$$\rho(y) = \exp(-2\mu y^{1/\mu}), \qquad (4)$$

where $\mathrm{d}\ln\rho/\mathrm{d}\ln r = -2(r/a_h)^{1/\mu}$ and $r_{-2} = a_h$. Note that this fitting formula is similar to the Sérsic formula (equation 1), as Merritt et al. (2005) first pointed out. It was first used by Einasto (1965, 1968, 1969; see also Einasto & Haud 1989), so that we will refer to it as the *Einasto model* (hereafter Eina), in consistency with the terminology used by other authors (Merritt et al. 2006).

The $g(c)$ functions can be written as

$$g(y) = y^2/2(y+1)^2 \text{ (Hern90)} \qquad (5)$$

$$g(y) = \ln(y+1) - y/(y+1) \text{ (NFW)} \qquad (6)$$

$$g(y) = 9y/(1+y) \text{ (TD)} \qquad (7)$$

$$g(y) = (3-\alpha)^{-1}y^{3-\alpha}\ {}_2F_1(3-\alpha, 3-\alpha, 4-\alpha, -y) \text{ (JS)} \qquad (8)$$

$$g(y) = \rho_{-2}\exp(2\mu)/(3c^3\rho_{\Delta}) \text{ (Eina)} \qquad (9)$$

where ρ_{-2} is the average density within r_{-2} and ${}_2F_1$ is the hypergeometric function.

When processes other than gravitational are involved in mass assembly (e.g. cooling or heating), the dark matter density profiles could be modified (see Blumenthal et al. 1986; Dalcanton et al. 1997; TD; Gnedin et al. 2004). To analyse this point, we plot in Fig. 3 the dark matter density profiles for several typical ELOs, along with their best fit to different analytical profiles. The optimal fit has been obtained by minimizing the statistics:

$$\chi^2 = \Sigma_{i=1}^{N}\left[\log M(<r_i) - \log M_{\rm ELO}^{\rm dark}(<r_i)\right]^2/N \qquad (10)$$

where $M_{\rm ELO}^{\rm dark}(<r_i)$ is the ELO dark matter mass within a sphere of radius r_i centred at its centre of mass, $M(<r_i)$ is the integrated

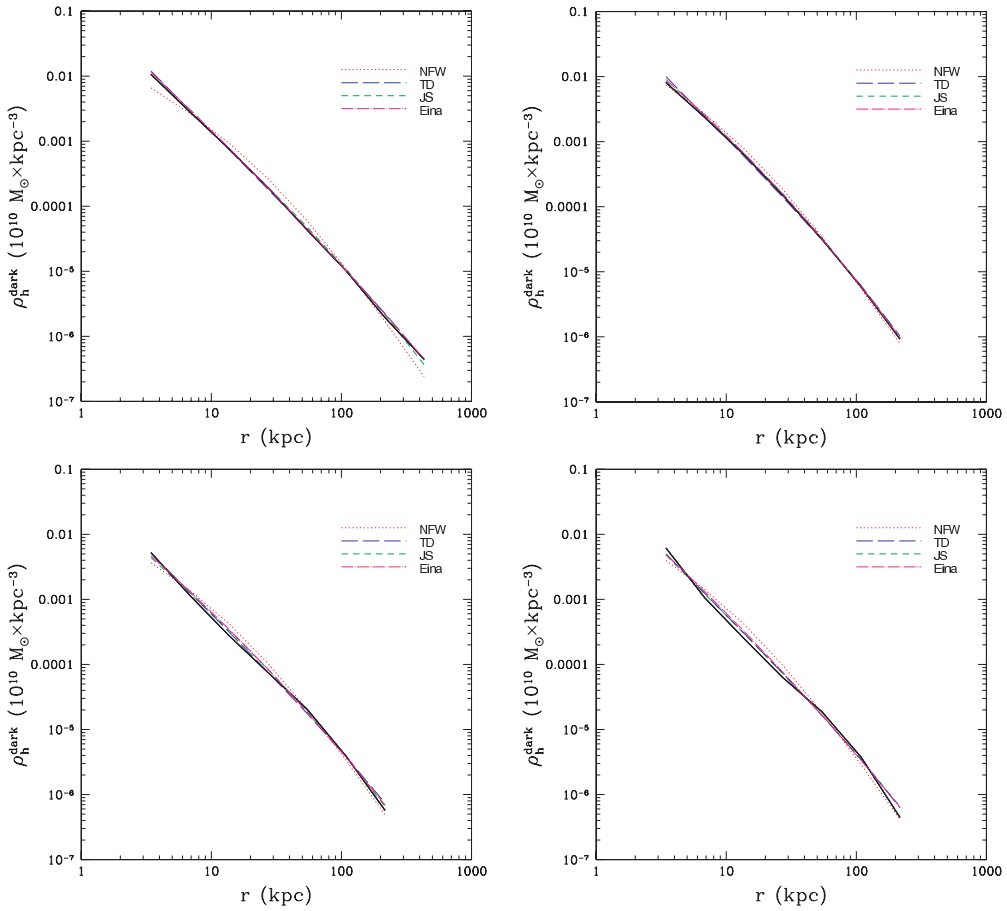

Figure 3. Dark matter density profiles (black full line) for several typical ELOs from SF-A and SF-B samples along with their best fits to different analytical profiles: NFW (red point line), TD (blue long-dashed line), JS (green short-dashed line) and Eina (magenta point-dashed line).

mass density profile corresponding to the different formulae above and the virial radii r_{vir} have been taken as outer boundaries of the fitting range. The *integrated* dark matter density profiles have been used as fitting formulae instead of the dark matter density profiles themselves because these latter are binning dependent. An updated version of the MINUIT software from the CERN (European Council for Nuclear Research) library has been used to make these fits as well as the others in this paper.

Note in Fig. 3 that the quality of the fits differs from one analytical profile to another. To quantify this effect, we plot in Fig. 4 the distributions of the χ^2 per degree of freedom (d.o.f.) statistics, normalized to $(\log M_{vir})^2$, resulting from the fits to the different profiles above, except for Hern90 one whose results are generally poorer. We see that the lower χ^2 per d.o.f. values generally correspond to either the Eina or the JS profiles, with the TD profiles in the third position. In Fig. 5, we draw the values of the μ (for Eina profiles) and α (for JS profiles) slopes corresponding to the optimal fits of SF-A sample dark matter haloes. A slight mass effect can be appreciated with lower mass ELOs having steeper dark matter haloes than more massive ones, presumably due to a more important pulling in of baryons on to dark matter as they fall to the ELO centre with decreasing ELO mass. That is, massive haloes are less concentrated than lighter ones, i.e. the mass–concentration relation. In any case, the profiles are always steeper than $\alpha = 1$ (i.e. the NFW profile; see Mamon & Łokas 2005a).

To further analyse this effect, we plot in Fig. 6 the ρ_{-2} density parameter versus the r_{-2} scale obtained from fits to the Einasto model. Blue triangles are measurements by Navarro et al. (2004) on to haloes formed in *N*-body simulations and the green line is their best fit. We see that at given r_{-2}, ρ_{-2} is higher in our hydrodynamical simulations than in Navarro et al. (2004), presumably due to the pulling in of dark matter by baryon infall. We also see that at given M_{vir}, r_{-2} is shorter in hydrodynamical simulations than in purely gravitatory ones by the same reason.

6.2 Projected stellar-mass density profiles

Authors now agree that the Sérsic law given in equation (1) (Sérsic 1968) is an adequate empirical representation of the optical surface brightness profiles of most ellipticals (see e.g. Caon et al. 1993;

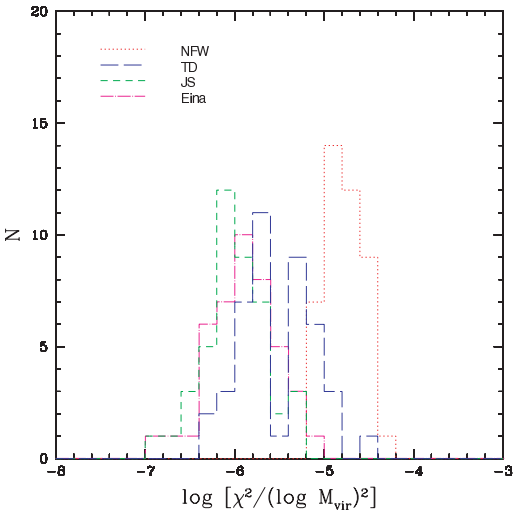

Figure 4. The distributions of the χ^2 per d.o.f., normalized to the logarithm of their respective mass square, for the fits of the dark matter density profiles of ELO haloes (SF-A and SF-B samples) to different analytical profiles.

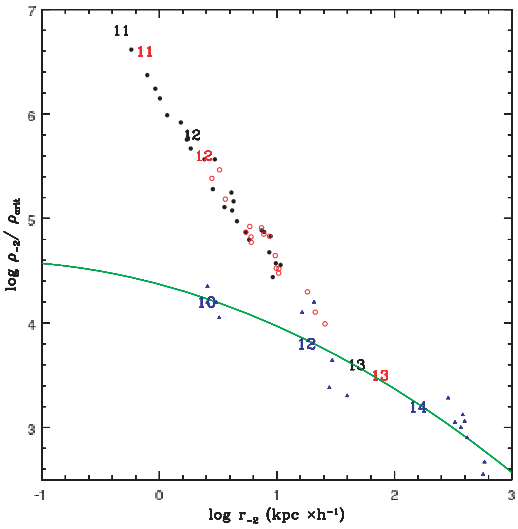

Figure 6. The ρ_{-2} density parameter versus the r_{-2} scale obtained from fits to the Einasto formula, for ELOs in both the SF-A sample (filled black circles) and the SF-B sample (open red circles). Blue triangles are measurements by Navarro et al. (2004), on to haloes formed in *N*-body simulations, with their fit by Mamon & Łokas (2005a) (green line). Numbers correspond to the logarithms of the virial masses (in units of $M_\odot$) of haloes formed in different simulations, according to their respective colours.

Bertin et al. 2002). Assuming that the stellar mass-to-light ratio $\gamma^{\rm star}$ does not appreciably change with ELO projected radius R,[4] the projected stellar *mass* profile, $\Sigma^{\rm star}(R)$, can be taken as a measure of the surface *brightness* profile and be written as

$$\Sigma^{\rm star}(R) = \gamma^{\rm star} I^{\rm light}(R). \qquad (11)$$

One can then expect that $\Sigma^{\rm star}(R)$ can be fitted by a Sérsic-like law. This is in fact the case as shown in Fig. 7 for several typical ELOs drawn from both SF-A and SF-B samples (see Kawata & Gibson, 2005, for a similar result concerning one virtual elliptical galaxy). Some remarks on how the fits have been made are in order. First, the $\Sigma^{\rm star}(R)$ profiles have been calculated by averaging on concentric rings centred at the projection of the centre-of-mass of

[4]Hereafter, we will use capital R to mean projected radii.

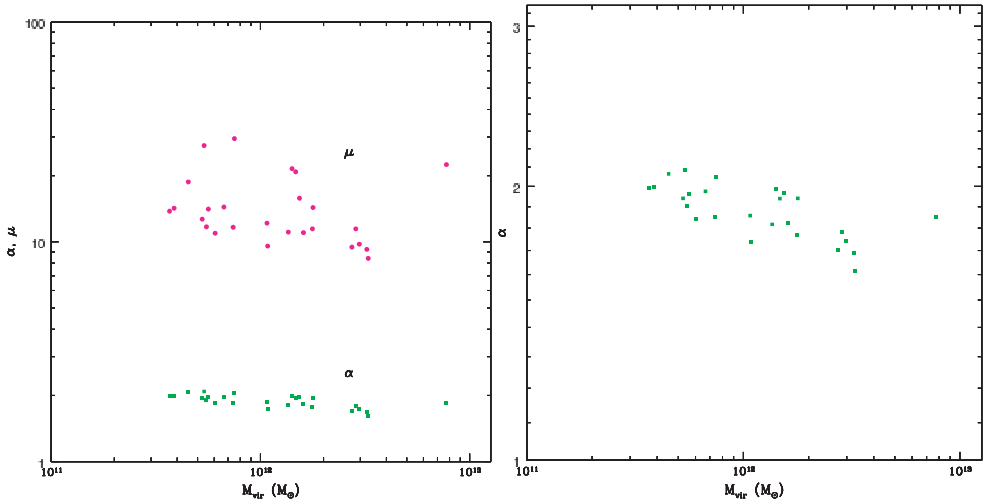

Figure 5. Left-hand panel: the optimal inner slope α of the general Jing & Suto profile for the dark matter haloes of ELOs (green filled squares) and the μ coefficient of the Einasto analytical profile (magenta filled circles) versus their virial mass for SF-A sample ELOs. Right-hand panel: zoom of the α versus virial mass plot to clarify the mass effect.

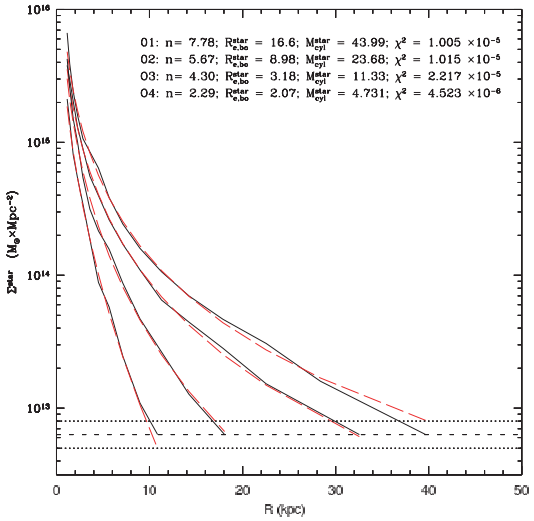

Figure 7. Projected stellar-mass density profiles for different ELOs along with their best fit by a Sérsic law. The corresponding shape parameter best values and minimal χ^2 per d.o.f are also shown.

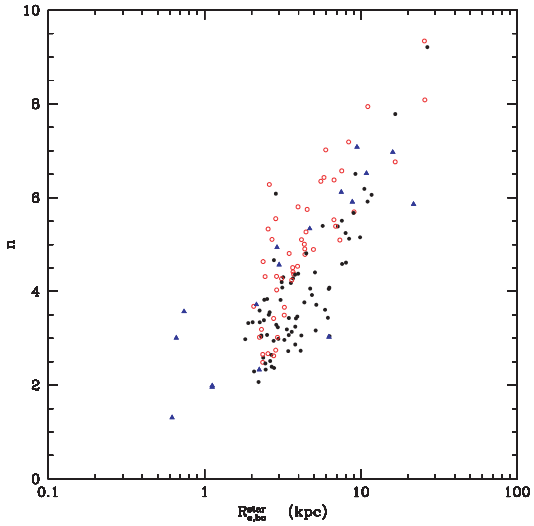

Figure 8. The Sérsic shape parameter n versus the projected stellar half-mass radii for SF-A sample (black filled circles) and SF-B sample (red open circles) ELOs. For each ELO, the results of projections along three orthogonal directions are shown. Blue filled triangles are data on n and R_e^{light} from D'Onofrio (2001).

the corresponding ELO. Three projections along orthogonal directions have been considered for each ELO. Also, because these projected densities are binning dependent and somewhat noisy, the integrated projected mass density in concentric cylinders of radius R and mass

$$M_{cyl}^{star}(R) = 2\pi \int_0^R \Sigma^{star}(R')R'\,dR' \qquad (12)$$

has been used as a fitting function, instead of $\Sigma^{star}(R)$ itself. Concerning the fitting range, we have adopted an outer boundary R_{max} such that the corresponding surface brightness $I^{light}(R_{max})$ (see equation 11) gives the standard value of $\mu_B = 27$ mag arcsec^{-2}. The values for the stellar mass-to-blue-light γ_B^{star} span a range from $\gamma_B^{star} =$ 2 to 12, depending on the details of its determination (see discussion in Mamon & Łokas 2005a), and best values of $\gamma_B^{star} = 5$ to 8. Their geometric mean $\gamma_B^{star} = 6.3$ has been used to make the fits drawn in Fig. 7, but the results of the fit do not significantly depend on the particular γ_B^{star} value used within its range of best values.

An interesting result is that the values of the shape parameter n we have obtained are consistent with observations, including their correlations with the effective radii R_e^{light}, luminosity L and velocity dispersion (Caon et al. 1993; Prugniel & Simien 1997; Graham 1998; Márquez et al. 2000; D'Onofrio 2001; Trujillo et al. 2001; Vazdekis, Trujillo & Yamada 2004; Graham et al. 2006), as illustrated in Fig. 8. In this figure, we plot the shape parameter n versus the ELO-projected stellar half-mass radii, $R_{e,bo}^{star}$, defined by the condition that $M_{cyl}^{star}(R_{e,bo}^{star})$ encloses half the total stellar mass of the system, assuming that γ_B^{star} does not depend on R, we will have $R_{e,bo}^{star} \simeq R_e^{light}$. Blue triangles are data on n and R_e^{light} from D'Onofrio (2001). Note that a slight effect resulting from the different SF parametrization in SF-A and SF-B sample ELOs is apparent in this plot, mainly due to the smaller sizes of SF-B sample ELOs as compared to their SF-A sample counterparts.

6.3 Baryonic 3D mass density profiles

In the last section, it has been shown that the projected stellar-mass density profiles are adequately described by the standard Sérsic profiles, that is, they are consistent with observational data. We now analyse the 3D mass density profiles of baryons.

We first analyse the baryon distribution at the ELO scale, where the main contribution to the mass density comes from stars. We lack any observational input on how the 3D stellar-mass density profiles $\rho^{star}(r)$ can be, except for a deprojection of the Sérsic profiles (Prugniel & Simien 1997; Lima Neto, Gerbal & Márquez 1999). In Fig. 9, we plot $\rho^{star}(r)$ for ELOs in the SF-A sample. Different colours have been used for ELOs in different mass intervals, and a clear mass effect can be seen in this figure, and particularly so at the inner regions, where at fixed r/r_{vir} the stellar-mass density of less massive ELOs can be a factor of 2 or so higher than that of more massive ones. This means that the mass homology is broken in the 3D stellar mass distribution.

To quantify the stellar three-dimensional mass density profiles of ELOs, they have been fit to JS and Eina analytical formulae through the statistics defined in equation (10) where $M_{ELO}^{dark}(<r_i)$ has been replaced by the ELO stellar mass within a sphere of radius r_i. The quality of the fits is illustrated in Fig. 10, and in Fig. 11 the values of the χ^2 per d.o.f. statistics are given, normalized to log M_{bo}^{star}. Both figures show that these profiles describe adequately well the spherically averaged stellar mass distribution in three dimensions, even if with very small r_{-2} values.

To study the possibility that the homology in the dark- versus bright-mass distribution is also broken, the stellar-to-dark density ratio profiles

$$f_\rho^{star}(r) = \rho^{star}(r)/\rho^{dark}(r) \qquad (13)$$

are plot versus either the radii (Fig. 12 upper panel) or the radii normalized to virial radii (Fig. 12 lower panel). We see that there is,

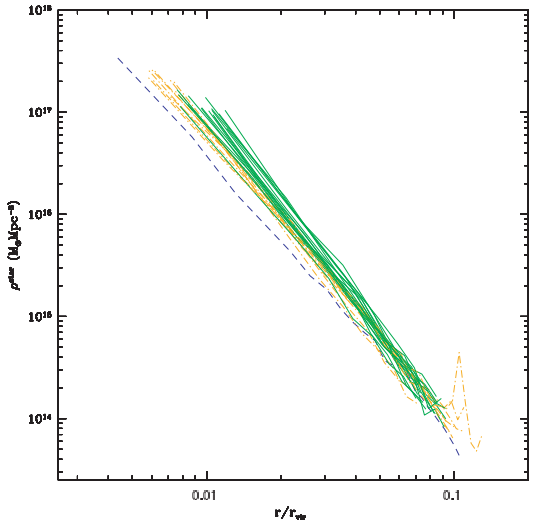

Figure 9. 3D stellar mass profiles for ELOs in the SF-A sample: full green lines, ELOs with $M_{\rm vir} < 1.5 \times 10^{12}\,{\rm M}_\odot$; orange point-dashed lines, ELOs with $1.5 \times 10^{12}\,{\rm M}_\odot \leqslant M_{\rm vir} < 5 \times 10^{12}\,{\rm M}_\odot$; blue dashed lines: ELOs with $M_{\rm vir} \geqslant 5 \times 10^{12}\,{\rm M}_\odot$. The stellar-mass density profiles show homology breaking.

in any case, a clear mass effects at the inner regions, with the stellar mass distribution relative to the dark mass one less concentrated with increasing ELO mass. For example, in Fig. 12 we see that the fraction of the ELO virial volume where $f^{\rm star}_{\rho}(r) > 1$ is smaller as the ELO mass grows; also, at fixed $r/r_{\rm vir}$, $f^{\rm star}\,(r)$ increases with decreasing ELO mass. So, the homology is broken in the 3D stellar-to-dark mass distribution, a fact that could be important to explain the tilt of the observed FP (see Oñorbe et al. 2005, 2006).

To further analyse this point and make the comparison with observational results easier, the dark-to-stellar mass ratio profiles, $M^{\rm dark}(<r)/M^{\rm tot}(<r)$, are drawn in Fig. 13 for the same ELOs, with the radii in units of the 3D stellar half-mass radii.[5] We see that there is, in any case, a positive gradient, and again a clear mass effect, with a tendency of the dark matter fraction at fixed values of $r/r^{\rm star}_{\rm e.bo}$ to be higher as the mass scale increases. To be more quantitative and to compare with observational data, we plot in Fig, 14, upper panel, the fraction of dark-to-total masses at $r/R^{\rm star}_{\rm e.bo} = 1$ for ELOs in the SF-A and SF-B samples, versus their stellar masses. The differences among results for both samples come from the smaller $R^{\rm star}_{\rm e.bo}$ values of SF-B sample ELOs as compared with their SF-A counterparts (see details in Oñorbe et al. 2006). Blue triangles with error bars are results from integral-field SAURON data and models by Cappellari et al. (2006). We see that these empirical determinations of the dark matter fraction at the centre of ellipticals is consistent with the values found in ELOs of both samples, including its growth with the mass scale.

In the lower panel of Fig. 14, we give the gradients of the $M^{\rm dark}(<r)/M^{\rm star}(<r)$ profiles as a function of their stellar masses. Blue triangles with error bars are the empirical mass-to-light gradients as determined by Napolitano et al. (2005) for EGs with isophotal shape $a_4 \times 100 < 0.1$, that is, boxy ellipticals. We have used as inner and outer radii $r/r^{\rm star,in}_{\rm e.bo} = 0.5$ and $r/r^{\rm star,out}_{\rm e.bo} = 4$, roughly the average values of the inner and outer radii these authors give in their table 1. We see that there is a mass effect and that our results are consistent with those found by these authors in the range of stellar mass values our samples span, especially when we consider that ELOs in our samples are boxy (see Section 7.2). A SF effect in the stellar mass distribution also appears in Fig. 14, again due to the compactness of the SF-B sample ELOs relative to their SF-A sample counterparts.

We now turn to analyse the baryon space distribution at halo scales. To have an insight on how baryons of any kind are distributed relative to the dark matter at the halo scale and beyond, the baryon fraction profile

$$f^{\rm ab}(r) = \rho^{\rm ab}(r)/\rho^{\rm tot}(r), \qquad (14)$$

where 'ab' stands for baryons of any kind (i.e. stars, cold gas and hot gas) and 'tot' stands for matter of any kind (i.e. dark plus baryons of any kind), is drawn in Fig. 15 for ELOs in the SF-A sample (black full lines) and in the SF-B sample (red point lines) in the same range of virial mass, $1.5 \times 10^{12}\,{\rm M}_\odot \leqslant M_{\rm vir} < 5 \times 10^{12}\,{\rm M}_\odot$. Despite individual characteristics, the $f^{\rm ab}\,(r)$ curves show a typical pattern in which their values are high at the centre, then they decrease and have a minimum lower than the global value, $f^{\rm ab}_{\rm cosmo} \equiv \Omega_{\rm b}/\Omega_{\rm m} = 0.171$, at a radius $r^{\rm ab}_{\rm min}$, then they increase again, reach a maximum value and then they decrease and fall to the $f^{\rm ab}_{\rm cosmo}$ value at a rather large r value, larger than the corresponding virial radii. This result, i.e. EGs are not baryonically closed, is also indicated by recent X-ray observations (Humphrey et al. 2006). Note (Fig. 16) that the increase of $f^{\rm ab}(r)$ at $r > r^{\rm ab}_{\rm min}$ is mainly contributed by hot gas, almost absent at $r < r^{\rm ab}_{\rm min}$, indicating that $r^{\rm ab}_{\rm min}$ separates the (inner) region where gas cooling has been possible from the (outer) region where gas has not had time enough to cool in the ELO lifetime. Note also in Fig. 16 that an important amount of hot gas is outside the spheres of radii $r_{\rm vir}$, that is, it is not bound to the self-gravitating configuration defined by the ELO halo. In fact, the mass of hot gas increases monotonically up to $r \simeq 4r_{\rm vir}$, and maybe also beyond this value, but it is difficult at these large radii to properly dilucidate whether or not a given hot gas mass element belongs to a given ELO or to another close one (to alleviate this difficulty, only those ELOs not having massive neighbours within radii of $6 \times r_{\rm vir}$ have been considered to draw this figure). Another important result is that the hot gas mass fraction, relative to the cold mass fraction at the ELO scale, increases with $M_{\rm vir}$ at given $r/r_{\rm vir}$, and the differences between massive and less massive ELOs can be as high as a factor of $\sim$2 at $r/r_{\rm vir} < 4$. We see that, in massive ELOs, this excess of baryons in the form of hot gas at the outer parts of their configurations compensates for the lack of baryons in the form of stars at the ELO scales.

6.4 Total three-dimensional mass density profiles

We now address the issue of the total mass (i.e. baryonic plus dark) density profiles. In Fig. 17, they are drawn for ELOs in the SF-A sample (upper panel) as well as for those in the SF-B sample (lower panel). In both the cases, the profiles corresponding to ELOs in different mass intervals have been drawn with different line and colour codes. Some important results are that (i) they are well fitted by power-law expressions $\rho^{\rm tot}(r) \propto r^{-\gamma}$ in a range of $r/r_{\rm vir}$ values larger than two decades; (ii) the slope of the power law increases with decreasing ELO mass and (iii) a slight SF effect appears, but only at the very inner regions, with SF-B sample ELOs showing a worse fit to a power law than their SF-A counterparts. Koopmans

[5]The effective or stellar half-mass radii $r^{\rm star}_{\rm e.bo}$ are defined as the radii of the spheres enclosing half the ELO stellar mass. This is the relevant 3D size parameter at ELO scales (see Oñorbe et al. (2006) for details).

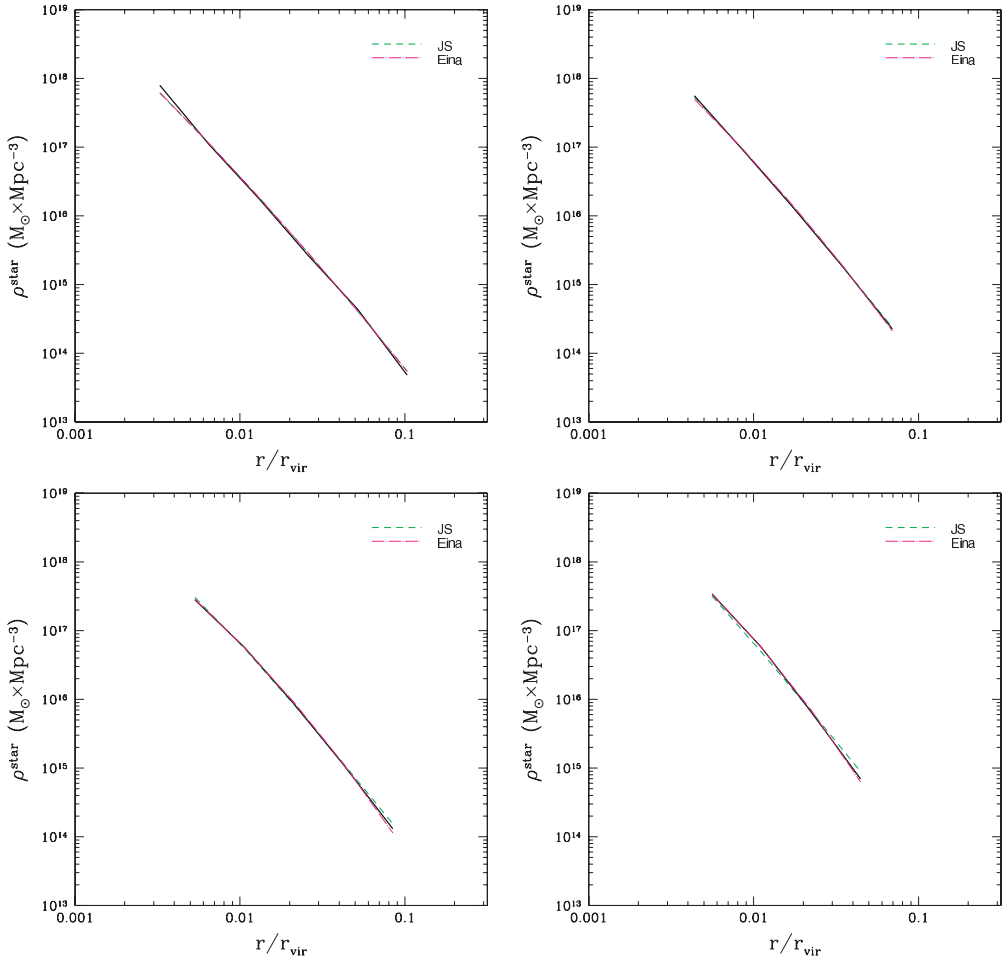

Figure 10. The stellar mass profiles for four typical ELOs in SF-A sample (black continuous lines) and their optimal fits to Einasto profiles (magenta point-dashed lines) and JS profiles (green dashed lines).

et al. (2006) have also found that the total mass density profiles of their massive ($\langle\sigma_{ap}\rangle = 263\ km\ s^{-1}$) lens EGs can be fit by power-law expressions within their Einstein radii ($\langle R_{Einst}\rangle = 4.2 \pm 0.4$ kpc, with $\langle R_{Einst}/R_e^{light}\rangle = 0.52 \pm 0.04$, i.e. the inner region), whose average slope is $\langle\gamma\rangle = 2.01^{+0.02}_{-0.03} \pm 0.05$ (68 per cent CL), with an intrinsic scatter of 0.12. To elucidate how well the total mass density profiles of ELOs compare with these results, we plot in Fig. 18 the slopes γ for ELOs, as well as for SLACS lens ellipticals (table 1, Koopmans et al. 2006), versus their central LOS stellar velocity dispersions. The fitting range for ELOs used to draw this figure is $r < R_{e,bo}^{star}$. We see that results for ELO and SLACS lens galaxy samples are consistent in the range of velocity dispersion values where they coincide.

7 KINEMATICS

7.1 Three-dimensional velocity distributions

Shapes and mass density profiles (i.e. positions) are related to the 3D velocity distributions of relaxed EGs through the Jeans equation (see Binney & Tremaine 1987). Observationally, information on such 3D distributions are not available for external galaxies, only the line-of-sight velocity distributions (LOSVD) can be inferred from their spectra (Binney & Tremaine 1987; de Zeeuw & Franx 1991; van der Marel & Franx 1993). The complete six-dimensional phase space information for each of the particles sampling the ELOs provided by numerical simulations allows us to calculate the 3D profiles for the velocity dispersion, $\sigma_{3D}(r)$, as well as the circular velocity profiles, $V_{cir}(r)$. In Fig. 19, we draw the $V_{cir}(r)$ profiles (full line), as well as their dark matter (short-dashed line) and baryonic contributions (stars, long-dashed line; stars plus cold gas, point line).

The $V_{cir}(r)$ profiles provide another measure of ELO mass distribution. We note in Fig. 19 that the baryon mass distribution is more concentrated than the dark matter one due to energy losses by the gaseous component before being transformed into stars. This is a general property of the circular velocity profiles of the ELO samples. Moreover, objects in SF-B sample are more concentrated than their SF-A sample counterparts

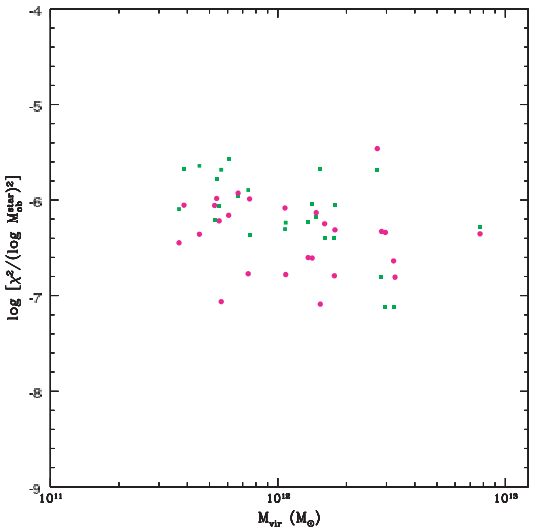

Figure 11. The χ^2 statistics (equation 10) corresponding to the fits of the stellar mass profiles for ELOs in the SF-A sample Einasto profiles (magenta filled circles) and JS profiles (green filled squares).

because of the SF implementation: the amount of baryons at their central volumes relative to dark matter is always lower in SF-A than in SF-B objects; this is a small-scale effect as $r \sim 30$ or 40 kpc radii enclose roughly similar amounts of baryons or dark matter in any cases.

In Fig. 20 we draw, for the same ELOs, the $\sigma_{3D}(r)$ profiles as measured by stars ($\sigma^{star}_{3D}(r)$, starred symbols and short-dashed lines) and by dark matter ($\sigma^{dark}_{3D}(r)$, open circles and long-dashed lines) as proof particles in the overall potential well. These profiles are in any case decreasing outwards, both for dark matter and for stellar components. An outstanding result illustrated by Fig. 20 is that $\sigma^{d}_{3D}(r)$ is always higher than $\sigma^{star}_{3D}(r)$ (because stars are made out of cooled gas), with $\sigma^{star}_{3D}(r)/\sigma^{dark}_{3D}(r) \sim 0.8$, consistent with the values found by Loewenstein (2000) on theoretical grounds and by Dekel et al. (2005) from pre-prepared simulations of mergers of disc galaxies. This is the so-called kinematical segregation (Sáiz 2003; Sáiz et al. 2004). To further analyse this issue, we plot in Fig. 21 the $\sigma^{star}_{3D}(r)/\sigma^{dark}_{3D}(r)$ ratios for the ELOS in both the SF-A sample and in the SF-B sample, with different colour and line codes depending on the ELO mass range. We see that the kinematical segregation does not show either a clear mass dependence or a radial dependence. Moreover, the SF parametrization effect is only mild.

Another relevant quantity is the anisotropy of the 3D velocity distributions of the ELO sample, defined as

$$\beta_{ani} = 1 - \frac{\sigma_t^2}{2\sigma_r^2}, \qquad (15)$$

where σ_r and σ_t are the radial and tangential velocity dispersions ($\sigma_t^2 = \sigma_\theta^2 + \sigma_\phi^2$), relative to the centre of the object. The anisotropy profile, $\beta_{ani}(r)$, is represented in Fig. 20 for typical ELOs in the sample, for their dark matter and stellar particle components. The anisotropy is always positive (i.e. an excess of dispersion in radial motions), and the profiles are almost constant, except at the innermost regions, and the stellar component is always more anisotropic than the dark matter one, presumably as a consequence of the

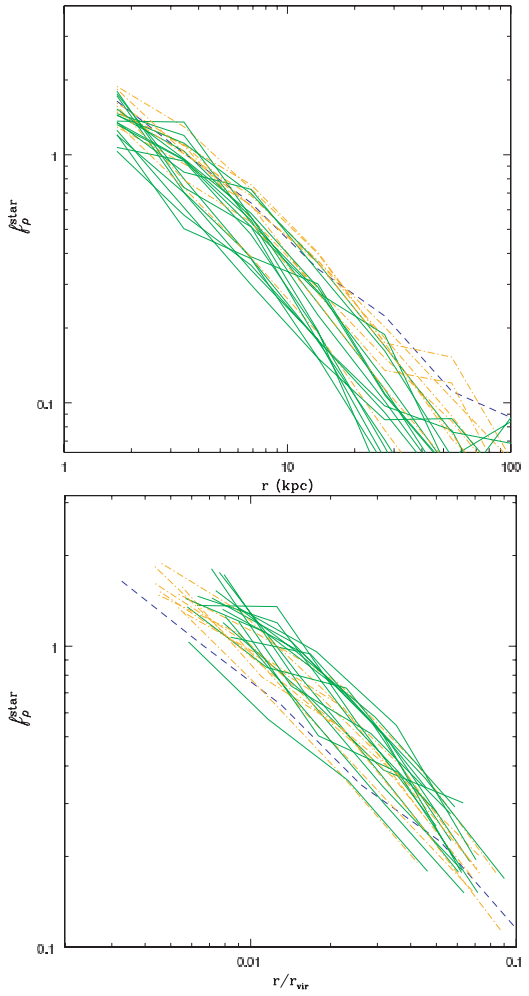

Figure 12. The stellar-to-dark mass profiles for ELOs in the SF-A sample. In the lower panel, radii are normalized to the virial radii. Line types and colours are the same as in Fig. 9.

mergers involved in the ELO mass assembly (see Section 4 and DTal06). In fact, the characteristics of the stellar anisotropy profiles [roughly constant and $\beta^{star}_{ani}(r) \simeq 0.5$ in most cases] are consistent with those found by Dekel et al. (2005), where they conclude that large radial anisotropy is generic to the stellar component of merger remnants of any kind.

7.2 Stellar LOS velocity and velocity dispersion profiles

The two last figures provide an illustration of the general characteristics of the lower order moments of the 3D velocity distribution. The profiles plotted in these figures are not observationally available, but only the lower order moments of the LOSVD are. We have measured the stellar LOS velocity and the stellar velocity dispersion profiles, $V^{star}_{LOS}(R)$ and $\sigma^{star}_{LOS}(R)$, along three orthogonal projections for all ELOs in the sample. To mimic observational techniques used in stellar kinematics of EGs, we have measured these profiles along

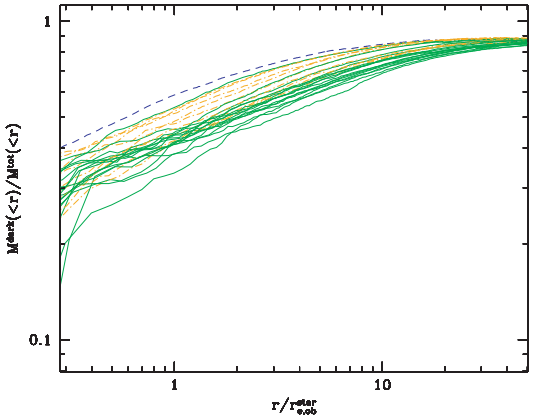

Figure 13. The fraction of dark-to-total mass profiles, $M^{\rm dark}(<r)/M^{\rm tot}(<r)$ for ELOs in the SF-A sample; different colours stand for different mass ranges, as in Fig. 9; radii are normalized to the 3D stellar half-mass radii.

the major and minor axes of projected ELOs, where the major axis is defined as that orthogonal to the ELO spin vector projected on the plane normal to the LOS, and the minor axis is parallel to the spin projection. We have found that in some cases ELOs do indeed show a clear rotation curve, while in most cases the rotation is only modest or even very low, as illustrated in Figs 22 and 23, respectively.

To quantify the amount of rotation in ELOs and its possible dependence on the mass scale, we plot in Fig. 24 the ratios $c_{\rm rot} = V_{\rm min}/(V^2_{\rm maj} + V^2_{\rm min})^{1/2}$ as a function of the ELO virial masses, for ELOs in both the SF-A and the SF-B samples [$V_{\rm maj}$ and $V_{\rm min}$ are the maximum values of the $V^{\rm star}_{\rm LOS}(R)$ profile when measured along the major and the minor axes, respectively]. When the ELO shows a clear rotation curve, $V_{\rm min}$ is much lower than $V_{\rm maj}$, and the $c_{\rm rot}$ ratio is low; by contrast, when the rotation is unimportant, then $V_{\rm min} \simeq V_{\rm maj}$ and $c_{\rm rot} \sim 0.7$. For a given ELO, the $c_{\rm rot}$ value depends on the direction taken as LOS direction, in such a way that it is maximum when the ELO spin is taken as LOS direction, and minimum when the LOS direction is normal to the ELO spin vector, that is, when rotation stands out. This is the LOS direction taken to draw this figure, where we see that there is not a clear mass dependence, that most ELOs are in between the two situations described above and that the values of the $c_{\rm rot}$ ratio of ELOs are typical of boxy ellipticals (see e.g. Binney & Merrifield, fig. 4.39).

We now comment on the major axis LOS stellar velocity dispersion profiles of ELOs (Figs 22 and 23). Their most outstanding feature is the decrease of the $\sigma^{\rm star}_{\rm LOS}$ (R) profiles in some cases and particularly so along some LOS directions at large R. These profiles are suited to compare with stellar kinematics data. In other cases, for example, to compare with planetary nebulae data, the LOS velocity dispersion profiles must be calculated by averaging over the LOS velocities of stars placed within cylindrical shells, with their axes in the LOS direction. Fig. 25 is a plot of such profiles normalized to $\sigma^{\rm star}_{\rm LOS}(R^{\rm star}_{\rm e,bo})$ for the SF-A sample ELOs; each panel corresponds to a different orthogonal projection.

To make clearer the decline of the $\sigma^{\rm star}_{\rm LOS}(R)$ profiles, in Fig. 26 we plot, at different R values, the averages of the stacked profiles shown in Fig. 25 with their dispersions (green points and error bars), as well as the averages of the profiles corresponding to young stars (age $\leqslant$3 Gyr, orange squares and error bars), normalized for each ELO

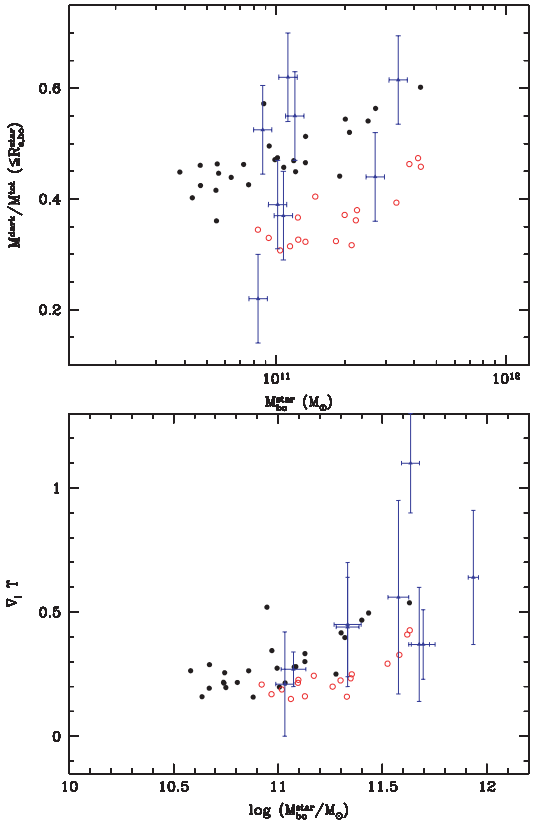

Figure 14. Upper panel: the fraction of dark-to-total mass at $r/R^{\rm star}_{\rm e,bo} = 1$ versus the ELO stellar masses. Filled (open) symbols: ELOs in SF-A (SF-B) sample. Points with error bars are the values corresponding to the SAURON sample of ellipticals. Lower panel: the gradients of the $M^{\rm dark}(<r)/M^{\rm star}(<r)$ profiles as a function of their stellar masses; blue triangles with error bars are the empirical mass-to-light gradients as determined by Napolitano et al. (2005) for galaxies with the $a_4 \times 100$ shape parameter lower than 0.1 (i.e. for boxy ellipticals).

to their corresponding $\sigma^{\rm star}_{\rm LOS}(R^{\rm star}_{\rm e,bo})$. The decline of these velocity dispersion profiles can be clearly appreciated, as well as the slightly larger decline of the profiles corresponding to the younger stellar populations. These results are consistent, within their dispersions, with that shown by Dekel et al. (2005) in their fig. 2 (lower panel). They are also marginally consistent with the decline shown by PN data in the NGC 821, 3379, 4494 and 4697 galaxies (Romanowsky et al. 2003; Romanowsky 2006). Note, however, that our ELOs are boxy, while the $a_4 \times 100/a$ shape parameters for these galaxies are 2.5, 0.2, 0.3 and 1.4, respectively, that is, they are rather discy ellipticals.

8 SUMMARY, DISCUSSION AND CONCLUSIONS

8.1 Summary: method and main results

This paper belongs to a series aimed at studying galaxy formation in a cosmological context through hydrodynamical simulations.

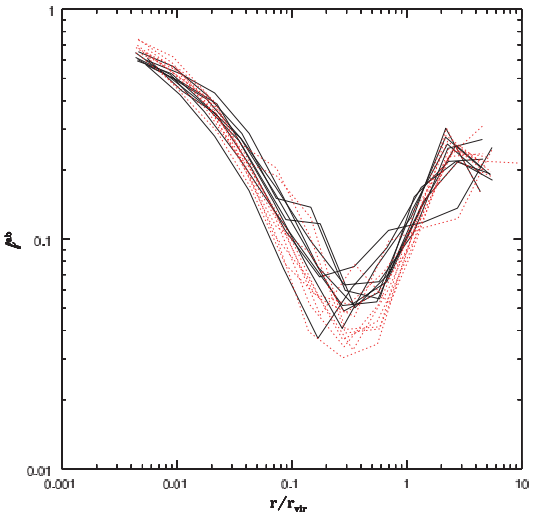

Figure 15. Baryon fraction profiles for ELOs in SF-A sample (black full lines) and SF-B sample (red point lines), in the same range of virial mass, $1.5 \times 10^{12}\,\mathrm{M}_{\odot} \leqslant M_{\mathrm{vir}} < 5 \times 10^{12}\,\mathrm{M}_{\odot}$.

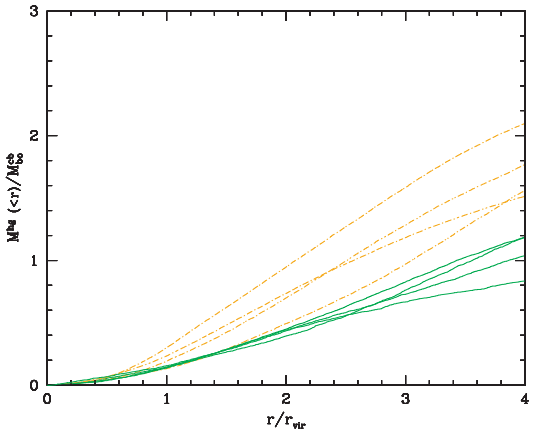

Figure 16. The $M^{\mathrm{HG}}(<r)/M^{\mathrm{cb}}_{\mathrm{bo}}$ profiles for typical ELOs. $M^{\mathrm{HG}}(<r)$ is the mass of hot gas within a sphere of radius r. Orange point-dashed lines: ELOs with $1.5 \times 10^{12} \leqslant M_{\mathrm{vir}} < 5 \times 10^{12}\,\mathrm{M}_{\odot}$; green full lines: ELOs with $M_{\mathrm{vir}} < 1.5 \times 10^{12}\,\mathrm{M}_{\odot}$. Only isolated ELOs have been considered.

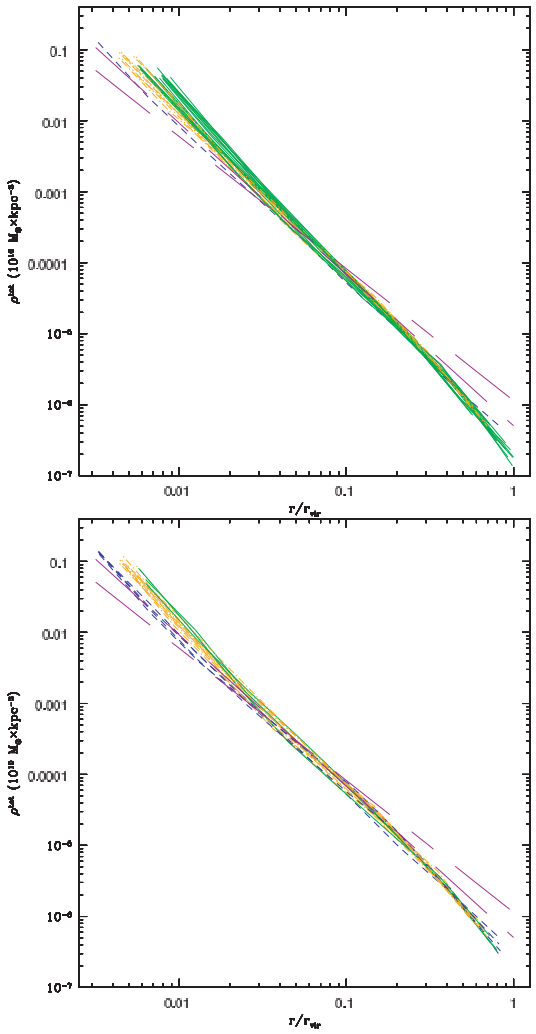

Figure 17. The total mass density profiles for ELOs in the SF-A sample (up) and in the SF-B sample (down). Green full lines: ELOs with $M_{\mathrm{vir}} < 1.5 \times 10^{12}$ M$_{\odot}$; orange point-dashed lines: ELOs with 1.5×10^{12} M$_{\odot}$ $\leqslant M_{\mathrm{vir}} < 5 \times 10^{12}$ M$_{\odot}$; blue dashed lines: ELOs with 5×10^{12} M$_{\odot}$ $\leqslant M_{\mathrm{vir}}$. The violet long-dashed lines are the one sigma interval for the slope resulting from fits to power-law profiles of lens ellipticals from Koopmans et al. (2006).

Here, we present an analysis of the sample of ELOs formed in 10 different cosmological simulations, run within the same global flat Λ cosmological model, roughly consistent with observations. The normalization parameter has been taken slightly high, $\sigma_8 = 1.18$, as compared with the average fluctuations of 2dFGRS or SDSS galaxies, to mimic an active region of the Universe. Newton laws and hydrodynamical equations have been integrated in this context, with a standard cooling algorithm and a SF parametrization through a Kennicutt–Schmidt like law, containing our ignorance about its details at sub-kpc scales, and where subresolution processes affecting SF are implicitly taken into account through the values given to these parameters. No further hypotheses to model the assembly processes have been made. Individual galaxy-like objects naturally appear as an output of the simulations, so that the physical processes underlying mass assembly can be studied. Five out of the 10 simulations (the SF-A type simulations) share the SF parameters and differ in the seed used to build up the initial conditions. To test the role of SF parametrization, the same initial conditions have been run with different SF parameters making SF more difficult, contributing another set of five simulations (the SF-B type simulations). ELOs have been identified in the simulations as those galaxy-like objects at $z = 0$ having a prominent, dynamically

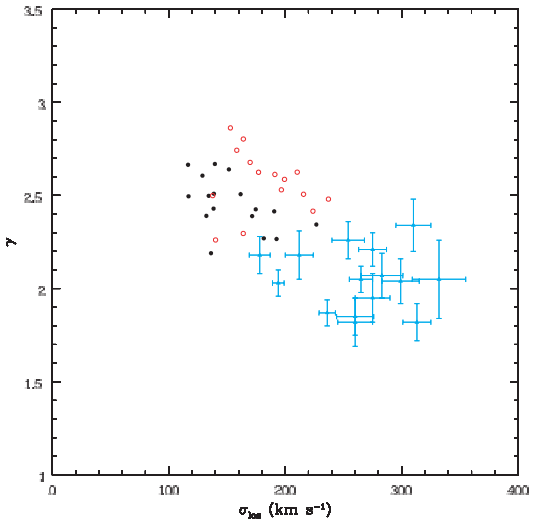

Figure 18. The logarithmic slopes corresponding to the total mass density profiles for ELOs in the SF-A (black filled circles) and the SF-B samples (red open circles), versus their central LOS stellar velocity dispersions. Triangles with error bars correspond to data on SLACS lens ellipticals, as given in table 1 of Koopmans et al. (2006).

relaxed spheroidal component made out of stars, with no extended discs and very low gas content. These stellar components are embedded in a dark matter halo that contributes an important fraction of the mass at distances from the ELO centre larger than ∼10–15 kpc on average, within which some clumps made out of cold dense gas and stars, associated in some cases with dark matter substructures, orbit. No ELOs with stellar masses below $3.8 \times 10^{10}\,M_{\odot}$ or virial masses below $3.7 \times 10^{11}\,M_{\odot}$ have been found that met the selection criteria [see Kauffmann et al. (2003) for a similar result in SDSS galaxies and Dekel & Birnboim (2006) and Cattaneo et al. (2006) for a possible physical explanation]. ELOs have also an extended halo of hot, diffuse gas. Stellar and dark matter particles constitute a dynamically hot component with an important velocity dispersion and, except in the very central regions, a positive anisotropy.

The first step in the program of studying the origins of EGs through self-consistent simulations is to make sure that they produce ELO samples that have counterparts in the real local Universe. This objective has been partially fulfilled in previous works. An analysis of the structural and dynamical ELO parameters that can be constrained from observations has shown that they are consistent with those measured in the SDSS DR1 elliptical sample (Sáiz et al. 2004), including the FP relation (Oñorbe et al. 2005, 2006). Also, ELO stellar populations have age distributions with the same trends as those inferred from observations, i.e. most stars have formed at high z on short time-scales and, moreover, more massive objects have older means and narrower spreads in their stellar age distributions than less massive ones (DSS04).

In this paper, we address the important issue of the amount and distribution of dark matter in virtual ellipticals and, in particular, its amount and distribution relative to the bright matter distribution. We also address the kinematics of the dark matter component and its relationship with the kinematics of the bright matter component. We want to answer the question of the mass and extension of dark matter haloes in EGs. To answer this question, we have first compared our virtual results with new observational data, obtaining a very satisfactory agreement.

(i) The projected stellar *mass* profile, $\Sigma^{\rm star}(R)$, can be adequately fitted by a Sérsic-like law. The shape parameter values n we have obtained are consistent with observations, including their correlations with the ELO luminosity, size and velocity dispersion.
(ii) The fraction of dark-to-total mass inside the projected half-mass radii is consistent with the observational ones obtained by Cappellari et al. (2006) from SAURON data.
(iii) The gradients of the dark-to-stellar $M^{\rm dark}(<r)/M^{\rm star}(<r)$ profiles as a function of their stellar masses are consistent with those observationally found by Napolitano et al. (2005) for boxy ellipticals.
(iv) The total mass (i.e. baryonic plus dark) density profiles can be well fitted by a power-law expression in a large range of $r/r_{\rm vir}$ values, with power-law slopes that are consistent with, within the dispersion or slightly higher than those observationally found by Koopmans et al. (2006) for massive lens ellipticals within their Einstein radii.
(v) The LOS velocity profiles along the major axis show, in some cases, a clear rotation, even if in most cases the rotation is modest or low. The values of the rotation ratio along the major and minor axis (a measure of the rotation in ELOs) do not depend on the mass scale.
(vi) The values spanned by the rotation ratios of ELOs are typical of boxy ellipticals.
(vii) The LOS velocity dispersion profiles, $\sigma_{\rm LOS}(R)$, decline outwards at large R, and the slope slightly increases when only the younger stellar populations are considered. These profiles are only marginally consistent with data on PNs at large radii, but these correspond to discy ellipticals while our virtual ellipticals are rather boxy.

These agreements strongly suggest that the intrinsic 3D dark and bright matter mass and velocity distributions we get in our simulations might also adequately describe real ellipticals. We now summarize our most important findings on the 3D mass and velocity structure of ELOs:

(i) ELOs are embedded in extended massive dark matter haloes.
(ii) The best fits of their spherically averaged dark matter density profiles to usual analytical formulae (Hern90; NFW; TD; JS; Eina) are generally provided by the two last formulae. The quality of the fits is good, so that ELO haloes form a two-parameter family where the two parameters are correlated. This is consistent with those produced in purely N-body simulations. The JS inner slope parameter, α, is always higher than the NFW value ($\alpha = 1$).
(iii) The slope parameters grow as the ELO mass scale decreases, indicating that the halo concentration grows when the mass decreases.
(iv) Haloes have suffered from adiabatic contraction. This can be made quantitative by comparing the plot of the density at the Einasto scale, ρ_{-2}, versus the scale $r_{-2} = a_h$, with the plot provided by Navarro et al. (2004) (results of purely N-body simulations).
(v) At the ELO scale, most baryons have turned into stars. The 3D stellar-mass density profiles can be fit by Eina or JS profiles, but with small r_{-2} values.
(vi) The mass distribution homology is broken in the stellar mass as well as in the dark- versus bright-mass distributions, with the stellar mass distribution relative to dark mass one less concentrated with increasing ELO mass. That is, massive ELOs miss baryons at

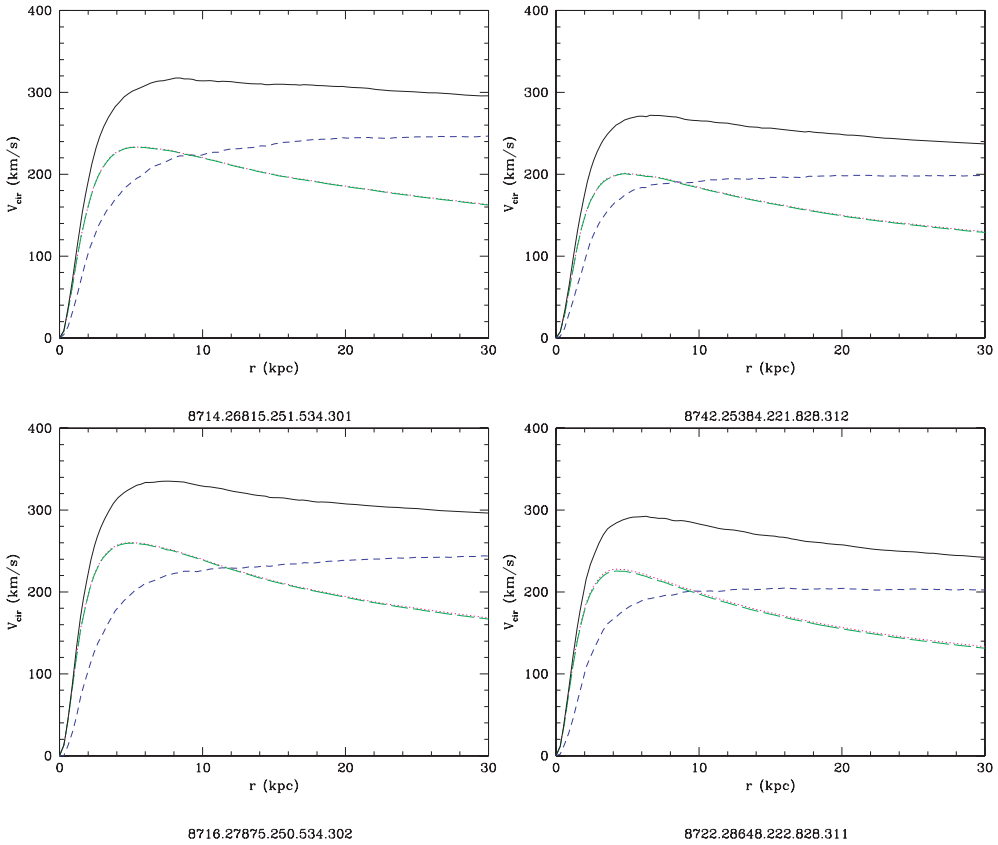

Figure 19. The circular velocity profiles of two typical ELOs in the SF-A sample (upper panels) and their SF-B sample counterparts (lower panels). Black continuous line: total mass; blue short-dashed line: dark matter contribution; green long-dashed line: stellar mass contribution; red point line: cold baryon contribution.

short scales as compared to less massive ones, when we normalize to the dark matter content. This result is consistent with the observational ones by Cappellari et al. (2006) from SAURON data, as well as by Napolitano et al. (2005) we quoted above.

(vii) At the halo scale, the baryon fraction profiles have been found to show a typical pattern, where their values are high at the centre, then they decrease and have a minimum roughly at $0.3 < r^{\rm ab}_{\rm min}/r_{\rm vir} < 0.7$, well below the global value, $\Omega_{\rm b}/\Omega_{\rm m} = 0.171$, then they increase again, reach a maximum value and then they decrease and fall to the global $\Omega_{\rm b}/\Omega_{\rm m}$ value well beyond the virial radii $r_{\rm vir}$. This suggests that the baryons that massive ELOs miss at short scales (stars) are found at the outskirts of the configuration as diffuse hot gas. This result could reflect the presence of a stable virial shock that prevents gas infall more efficiently as mass increases (Dekel & Birnboim 2006).

(viii) Concerning kinematics, ELO velocity dispersion profiles in three dimensions are slightly decreasing for increasing r, both for dark matter and for stellar particles, $\sigma^{\rm d}_{\rm 3D}(r)$ and $\sigma^{\rm star}_{\rm 3D}(r)$.

(ix) The dark and bright matter components of ELOs are kinematically segregated, as we have found that $(\sigma^{\rm d}_{\rm 3D}(r))^2 \sim (1.4\text{–}2)\,(\sigma^{\rm star}_{\rm 3D}(r))^2$, confirming previous results (Loewenstein 2000; Sáiz 2003; Dekel et al. 2005). This is so because stars are formed from gas that had lost energy by cooling.

(x) This kinematical segregation does not show any clear mass or radial dependence.

(xi) The anisotropy is always positive (i.e. an excess of radial motions) and almost non-varying with r inside the ELOs. Recall, however, that ELOs have been identified as dynamically relaxed objects: there are no recent mergers in our samples.

(xii) The stellar component generally shows more anisotropy than the dark component, maybe derived from the radial motion of the gas particles that gave rise to the stars.

8.2 Possible resolution effects

To make sure that the results we report in this paper are not unstable under resolution changes, a control simulation with 128^3 dark matter and 128^3 baryonic particles, a gravitational softening of $\epsilon = 1.15$ kpc and the other parameters as in SF-A type simulations (the S128 simulation) has been run. The results of its analysis have been compared with those of a 2×64^3 simulation (the S64 simulation), whose initial conditions have been built up by randomly choosing one out

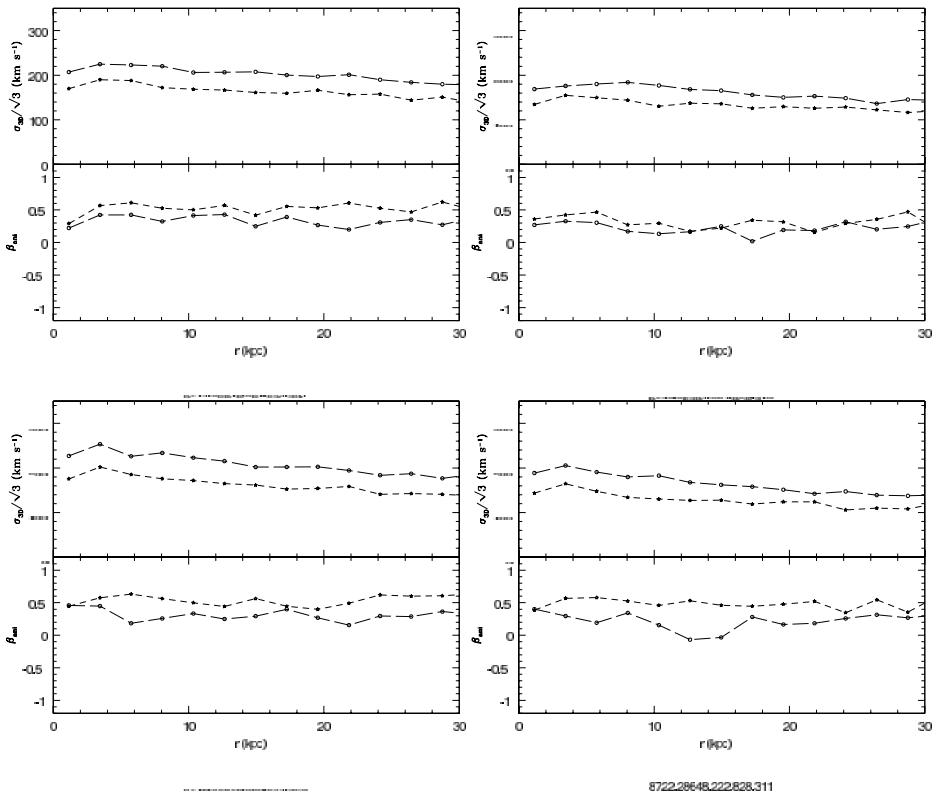

Figure 20. The $\sigma_{3D}(r)$ profiles of two typical ELOs in the SF-A sample (upper panels) and their SF-B sample counterparts (lower panels). Also shown are the anisotropy profiles $\beta_{ani}(r)$. Long-dashed lines: dark matter; short-dashed lines: stars.

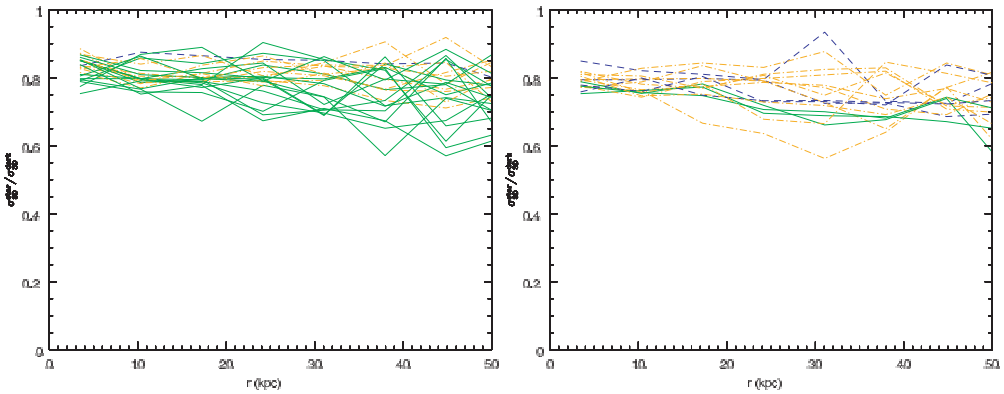

Figure 21. The $\sigma_{3D}^{star}(r)/\sigma_{3D}^{dark}(r)$ ratio profiles for ELOs in SF-A (left-hand panel) and SF-B (right-hand panel) samples. Different colour and line codes stand for ELO mass intervals, as in Fig. 9.

of eight particles in the S128 initial conditions, so that every ELO in S128 has a counterpart in the lower resolution simulation and conversely. Due to the very high CPU time requirements for S128, the comparison has been made at $z = 1$. The results of this comparison are very satisfactory, as illustrated in Fig. 27.

Otherwise, Figs 20 and 21 show that two-body relaxation effects (typically the most stringent requirement for convergence) have not been important at least for r larger than $\sim$1 kpc. In fact, two-body relaxation effects cause energy equipartition. But the values of the $\sigma_{3D}^{star}(r)/\sigma_{3D}^{dark}(r)$ ratios we have obtained ($\simeq$ 0.8) exclude energy

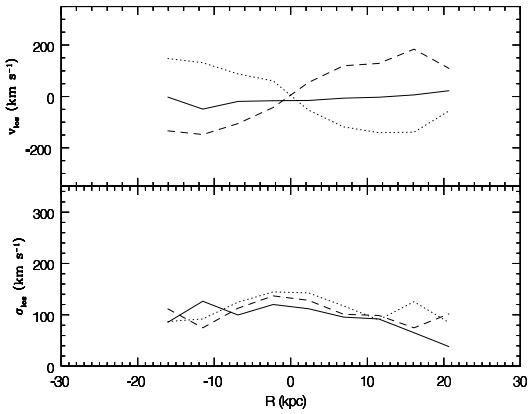

Figure 22. Upper panel, full line: the major axis stellar LOS velocity profile along the spin direction for an ELO in SF-A sample. Point and dashed lines: same as the continuous line taking the LOS direction normal to the ELO spin vector. This particular ELO rotates. Lower panel: same as the upper panel for the major axis LOS stellar velocity dispersion profiles.

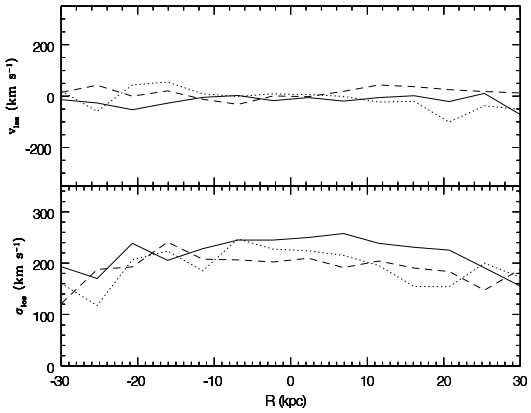

Figure 23. Same as the previous figure for another ELO. In this case, the rotation is only mild.

equipartition among dark matter and stellar particles in ELOs, because such equipartition would demand $\sigma^{star}_{3D}(r)/\sigma^{dark}_{3D}(r) = [m^{dark}/m^{star}]^{0.5} = 2{,}194$, where $m^{dark} = 1.29 \times 10^8$ M$_\odot$ and $m^{star} = 2.67 \times 10^7$ M$_\odot$ are the mass of dark and stellar particles, respectively. This result is important because it shows that two-body relaxation effects have played no important role in the gravitational interaction.

8.3 The physical processes underlying mass homology breaking and their observational implications

One of the most important findings of this paper is that the homology breaking ELO samples show both in the relative content and in the relative distributions of the baryonic and the dark mass components. As explained in Oñorbe et al. (2005, 2006), this has, as a consequence, the observed tilt of the FP relation relative to the virial one. Which are the physical processes underlying this breaking of homology? According to our simulations, they lie in

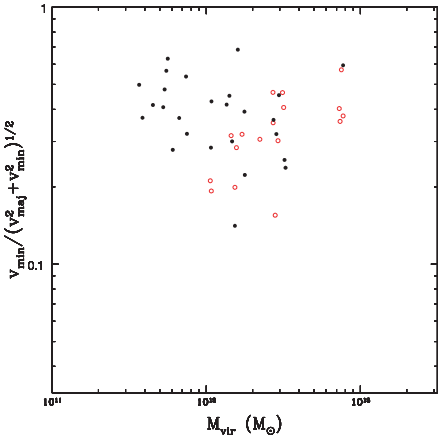

Figure 24. The c_{rot} ratios as a function of the virial mass for ELOs in the samples.

the systematic decrease, with increasing ELO mass, of the relative amount of dissipation experienced by the baryonic mass component along ELO stellar mass assembly (DTal06; Oñorbe et al, 2006). This possibility, already suggested by Bender, Burstein & Faber (1992), Guzmán, Lucey & Bower (1993) and Ciotti, Lanzoni & Renzini (1996), was first addressed through numerical methods by Bekki (1998). He studied elliptical formation through pre-prepared simulations of dissipative mergers of disc galaxies, where the rapidity of the SF in mergers is controlled by a free efficiency parameter C_{SF}. He shows that the SF rate history of galaxies determines the differences in dissipative dynamics, so that to explain the lack of homology in EGs he *needs to assume* that more luminous galaxies are formed by galaxy mergers with a shorter time-scale for gas transformation into stars. Recently, Kobayashi (2005) and Robertson et al. (2006) have confirmed the importance of dissipation and the time-scale for SF to explain mass homology breaking in ellipticals.

In this paper, we go a step further and study mass and velocity distributions of two samples of virtual ellipticals formed in self-consistent cosmological simulations. As explained in Section 3, the simulations provide us with clues on the physical processes involved in elliptical formation. They indicate that most of the dissipation involved in the mass assembly of a given ELO occurs in the violent early phase at high z and on very short time-scales (and earlier on shorter time-scales as the ELO mass grows, see details in DSS04 and DTal06), as a consequence of ELO assembly out of gaseous material and its transformation into stars. Moreover, the dissipation rate history is reflected by the SF rate history. During the later slower phase of mass assembly, ELO stellar mass growth essentially occurs without any dissipation, and the SF rate substantially decreases (see more details and fig. 1 in DTal06). So, the mass homology breaking appears in the early, violent phase of mass assembly, and it is essentially preserved during the later, slower phase. A consequence is that the dynamical plane appears in the violent phase and is roughly preserved along the slower phase, see discussion in DTal06 and Oñorbe et al. 2006. We see that our results on the role of dissipative dynamics essentially include previous ones, but they also add important new information. First, our results on the role of dissipative dynamics to break mass homology agree with the

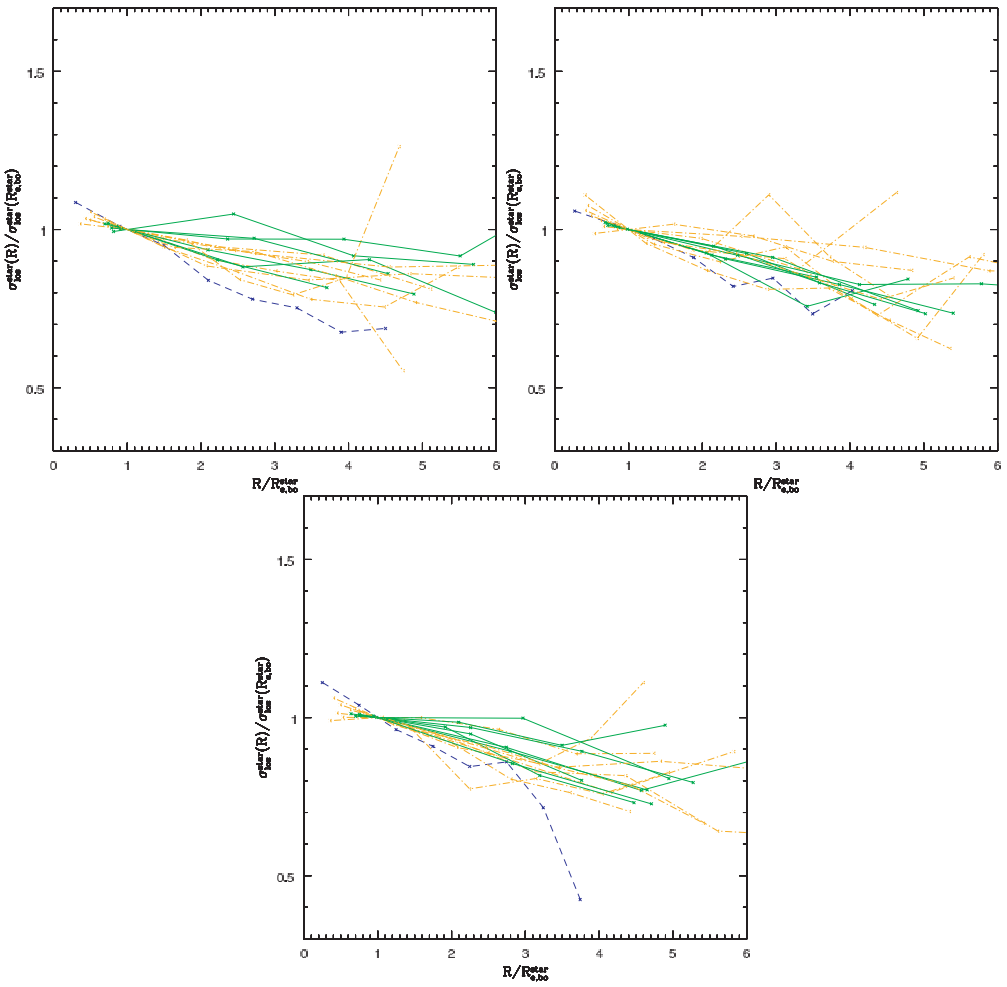

Figure 25. LOS velocity dispersion velocity profiles along three different orthogonal projections for ELOs in SF-A sample up to six effective radii. The profiles are normalized to their value at $R^{\rm star}_{\rm e,bo}$ for each ELO. Different colour and line codes stand for ELO mass intervals, as in Fig. 9.

previous ones, but it is important to note that, moreover, ELO stellar populations show age effects, that is, more massive objects produced in the simulations *do have* older means and narrower spreads in their stellar age distributions than less massive ones (see details DSS04); this is equivalent to downsizing (Cowie et al. 1996) and naturally appears in the simulations, so that it need not be considered as an additional assumption. Second, the preservation of the dynamical plane in the slow phase of mass aggregation in our simulations also agrees with previous work based on dissipationless simulations of pre-prepared mergers (Capelato et al. 1995; Dantas et al. 2003; González-García & van Albada 2003; Nipoti et al. 2003; Boylan-Kolchin et al. 2005). But, again, it is important to note that the important decrease of the dissipation rate in the slow phase of evolution naturally appears in the simulations and we do not have to assume this decrease. Also, the decrease of the merger rate in the later phase of mass assembly results from the global behaviour of the merger rate history in the particular cosmological context we have considered. Third, it turns out that the physical processes involved in ELO formation unveiled by our simulations, not only explain mass homology breaking (and its implications in the formation and preservation of the dynamical plane), and stellar age effects or downsizing in ellipticals, but also might explain other elliptical properties recently inferred from observations [e.g. the appearance of blue cores (Menanteau et al. 2004); the increase of the stellar mass contributed by the elliptical population since higher z, Bell et al. 2004; Conselice, Blackburne & Papovich 2005; Faber et al. 2005; see more details in DTal06].

8.4 Conclusions

We conclude that the simulations provide a unified scenario where most current observations on ellipticals can be interrelated. In

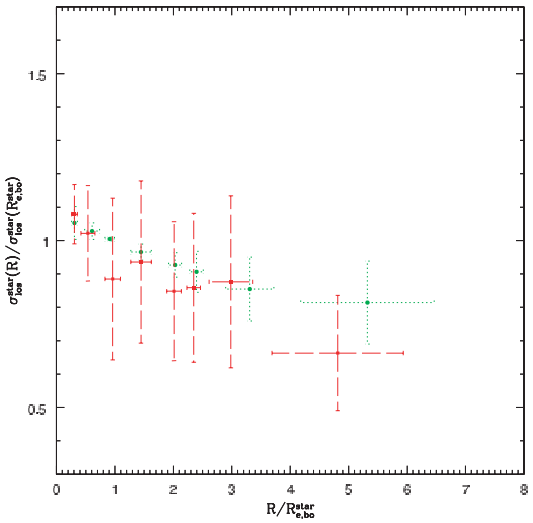

Figure 26. The SF-A sample average LOS velocity dispersion profiles normalized to their values at $R^{\rm star}_{\rm e,bo}$ for each ELO (green points) along with their 1σ dispersions. Orange points and error bars: the same for the young stellar particles, with the same normalization.

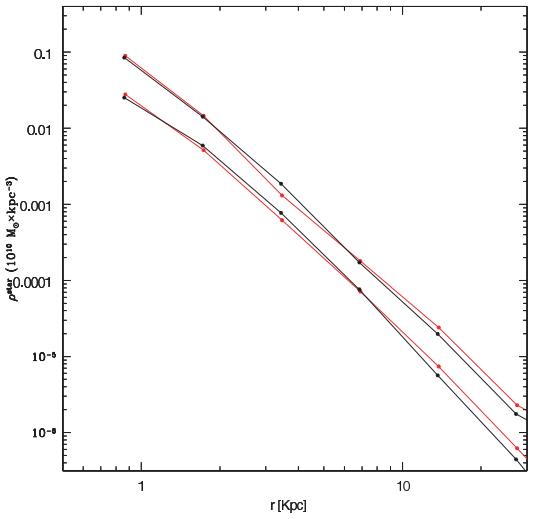

Figure 27. 3D stellar-mass density profiles for two ELOs identified at $z = 1$ in S128 (red lines) and their counterparts in S64 (black lines).

particular, this scenario proves the importance of dark matter haloes in relaxed virtual ellipticals, and suggests that real ellipticals must also have extended, massive dark matter haloes. Also, this scenario explains the homology breaking in the relative dark- to bright-mass content and distribution of ellipticals, that could have important implications to explain the physical origin of the FP relation and its preservation. It is worth mentioning that this scenario shares some characteristics of previously proposed scenarios, but it has also significant differences, mainly that most stars in EGs form out of cold gas that had never been shock heated at the halo virial temperature and then formed a disc, as the conventional recipe for galaxy formation propounds [see discussion in Keres et al. (2005), and references therein]. The scenario for elliptical formation emerging from our simulations has the advantage that it results from simple physical laws acting on initial conditions that are realizations of power spectra consistent with observations of CMB anisotropies.

ACKNOWLEDGMENTS

We thank H. Artal for computing assistance. This work was partially supported by the MCyT (Spain) through grants AYA-0973, AYA-07468-C03-02 and AYA-07468-C03-03 from the PNAyA, and also by the regional government of Madrid through the ASTROCAM Astrophysics network (S–0505/ESP–0237). We thank the Centro de Computación Científica (UAM, Spain) for computing facilities. AS thanks FEDER financial support from UE.

REFERENCES

Ballesteros-Paredes J., Klessen R. S., McLow M.-M., Vázquez-Semadeni E., 2006, preprint (astro-ph/0603357)
Bekki K., 1998, ApJ, 496, 713
Bell E. F. et al., 2004, ApJ, 608, 752
Bender R., Burstein D., Faber S. M., 1992, ApJ, 399, 462
Bergond G., Zepf S. E., Romanowsky A. J., Sharples R. M., Rhode K. L., 2006, A&A, 448, 155
Bernardi M. et al., 2003, AJ, 125, 1866
Bertin G., Ciotti L., Del Principe M., 2002, A&A, 386, 149
Binney J., Tremaine S., 1987, Galactic Dynamics. Princeton Univ. Press, Princeton, NJ
Binney J., Merrifield M., 1998, Galactic Astronomy. Princeton Univ. Press, Princeton, NJ
Blumenthal G. R., Faber S. M., Flores R., Primack J. R., 1986, ApJ, 301, 27
Bond J. R., Centrella J., Szalay A. S., Wilson J. R., 1984, MNRAS, 210, 515
Borriello A., Salucci P., Danese L., 2003, MNRAS, 341, 1109
Boylan-Kolchin M., Ma C. -P., Quataert E., 2005, MNRAS, 362, 184
Bryan G. L., Norman M. L., 1998, ApJ, 495, 80
Bullock J. S., Kolatt T. S., Sigad Y., Somerville R. S., Kravtsov A. V., Klypin A. A., Primack J. R., Dekel A., 2001, MNRAS, 321, 559
Busarello G., Capaccioli M., Capozziello S., Longo G., Puddu E., 1997, A&A, 320, 415
Caon N., Capaccioli M., D'Onofrio M., 1993, MNRAS, 265, 1013
Capelato H. V., de Carvalho R. R., Carlberg R. G., 1995, ApJ, 451, 525
Cappellari M. et al., 2006, MNRAS, 366, 1126
Cattaneo A., Dekel A., Devriendt J., Guiderdoni B., Blaizot J., 2006, MNRAS, 370, 1651
Ciotti L., Lanzoni B., Renzini A., 1996, MNRAS, 282, 1
Conselice C. J., Blackburne J. A., Papovich C., 2005, ApJ, 620, 564
Couchman H. M. P., 1991, ApJ, 368, L23
Cowie L. L., Songaila A., Hu E. M., Cohen J. G., 1996, AJ, 112, 839
Dalcanton J., Spergel D. N., Summers F. J., 1997, ApJ, 482, 659
Dantas C. C., Capelato H. V., Ribeiro A. L. B., de Carvalho R. R., 2003, MNRAS, 340, 398
Dekel A., Birnboim Y., 2006, MNRAS, 368, 2
Dekel A., Stoehr F., Mamon G. A., Cox T. J., Primack J. R., 2005, Nat, 437, 707
de Lucia G., Springel V., White S. D. M., Croton D., Kauffmann G., 2006, MNRAS, 366, 499
de Vaucouleurs G., 1948, Annales d'Astrophysique, 11, 247
de Zeeuw T., Franx M., 1991, ARA&A, 29, 239
de Zeeuw P. T. et al., 2002, MNRAS, 329, 513
Djorgovski S., Davis M., 1987, ApJ, 313, 59
Domínguez-Tenreiro R., Sáiz A., Serna A., 2004, ApJ, 611, L5 (DSS04)
Domínguez-Tenreiro R., Oñorbe J., Sáiz A., Artal H., Serna A., 2006, ApJ, 636, L77 (DTaI06)

D'Onofrio M., 2001, MNRAS, 326, 1517
Douglas N. et al., 2002, PASP, 114, 1234
Dressler A., Lynden-Bell D., Burstein D., Davies R. L., Faber S. M., Terlevich R., Wegner G., 1987, ApJ, 313, 42
Einasto J., 1965, Trudy Inst. Astrofiz., Alma–Ata, 5, 87
Einasto J., 1968, Tartu Astr. Obs. Publ., Vol. 36, 414
Einasto J., 1969, Astrofiz., 5, 137
Einasto J., Haud U., 1989, A&A, 223, 89
Elmegreen B., 2002, ApJ, 577, 206
Evrard A., Silk J., Szalay A. S., 1990, ApJ, 365, 13
Faber S. M., Dressler A., Davies R. L., Burstein D., Lynden-Bell D., 1987, in Faber S. M., ed., Nearly Normal Galaxies: From the Planck Time to the Present. Springer-Verlag, New York, p. 175
Faber S. M. et al., 2005, preprint (astro-ph/0506044)
Ferreras I., Saha P., Williams L. L. R., 2005, ApJ, 623, L5
Gerhard O., Kronawitter A., Saglia R. P., Bender R., 2001, AJ, 121, 1936
Gibson B. K., Sánchez-Blázquez P., Courty S., Kawata D., 2006, preprint, astro-ph/0611086
Gnedin O. Y., Kravtsov A. V., Klypin A. A., Nagai D., 2004, ApJ, 616, 16
González-García A. C., van Albada T. S., 2003, MNRAS, 342, 36
González-García A. C., Balcells M., Olshevsky V. S., 2006, MNRAS, 372, 78
Graham A. W., 1998, MNRAS, 295, 933
Graham A., Colless M., 1997, MNRAS, 287, 221
Graham A., Merritt D., Moore B., Diemond J., Terzić B., 2006, AJ, 132, 2711
Gustaffson M., Fairbairn M., Sommer-Larsen J., 2006, Phys. Rev. D, 74, 123522
Guzik J., Seljak U., 2002, MNRAS, 335, 311
Guzmán R., Lucey J., Bower R. G., 1993, MNRAS, 265, 731
Hernquist L., 1990, ApJ, 356, 359 (Hern90)
Hoekstra H., Yee H. K., Gladders M. D., 2004, ApJ, 606, 67
Humphrey P. J., Buote D. A., Gastaldello F., Zappacosta L., Bullock J. S., Brighenti F., Mathews W. G., 2006, ApJ, 646, 899
Jing Y. P., Suto Y., 2000, ApJ, 529, L69
Katz N., 1992, ApJ, 391, 502
Kauffmann G. et al., 2003, MNRAS, 341, 54
Kawata D., Gibson B. K., 2003, MNRAS, 346, 135
Kawata D., Gibson B. K., 2005, MNRAS, 358, 16
Kennicutt R., 1998, ApJ, 498, 541
Keres D., Katz N., Weinberg D. H., Davé R., 2005, MNRAS, 363, 2
Khochfar S., Burkert A., 2005, MNRAS, 359, 1379
Kobayashi C., 2005, MNRAS, 361, 1216
Koopmans L. V. E., Treu T., 2003, ApJ, 583, 606
Koopmans L. V. E., Treu T., Bolton A. S., Burles S., Moustakas L. A., 2006, ApJ, 649, 599
Kronawitter A., Saglia R. P., Gerhard O., Bender R., 2000, A&AS, 144, 53
Lima Neto G. B., Gerbal D., Márquez I., 1999, MNRAS, 309, 481
Loewenstein M., 2000, ApJ, 532, 17
Magorrian J., Ballantyne D., 2001, MNRAS, 322, 702
Mamon G. A., Łokas E. L., 2005a, MNRAS, 362, 95
Mamon G. A., Łokas E. L., 2005b, MNRAS, 363, 705
Manrique A., Raig A., Salvador-Solé E., Sanchis T., Solanes J. M., 2003, ApJ, 593, 26>
Márquez I., Lima Neto G. B., Capelato H., Durret F., Gerbal D., 2000, A&A, 353, 873
Menanteau F. et al., 2004, ApJ, 612, 202
Merritt D., Navarro J. F., Ludlow A., Jenkins A., 2005, ApJ, 624, L85
Merritt D., Graham A., Moore B., Diemond J., Terzić B., 2006, AJ, 132, 2685
Meza A., Navarro J. F., Steinmetz M., Eke V. R., 2003, ApJ, 590, 619
Moore B., Quinn T., Governato F., Stadel J., Lake G., 1999, MNRAS, 310, 1147
Myers S. T. et al., 1995, ApJ, 447, L5
Naab T., Burkert A., 2003, ApJ, 597, 893
Naab T., Trujillo I., 2006, MNRAS, 369, 625
Naab T., Johansson P. H., Efstathiou G., Ostriker J. P., 2005, preprint (astroph/0512235)
Naab T., Khochfar S., Burkert A., 2006, ApJ, 636, L81
Napolitano N. R. et al., 2005, MNRAS, 357, 691
Navarro J. F., Frenk C. S., White S. D. M., 1995, MNRAS, 275, 720
Navarro J. F., Frenk C. S., White S. D. M., 1996, ApJ, 462, 563
Navarro J. F. et al., 2004, MNRAS, 349, 1039
Nipoti C., Londrillo P., Ciotti L., 2003, MNRAS, 342, 501
Nipoti C., Londrillo P., Ciotti L., 2006, MNRAS, 370, 681
Oñorbe J., Domínguez-Tenreiro R., Sáiz A., Serna A., Artal H., 2005, ApJ, 632, L57
Oñorbe J., Domínguez-Tenreiro R., Sáiz A., Artal H., Serna A., 2006, MNRAS, 373, 503
O'Sullivan E., Ponman T. J., 2004a, MNRAS, 349, 535
O'Sullivan E., Ponman T. J., 2004b, MNRAS, 354, 935
Padmanabhan N. et al., 2004, New Astron., 9, 329
Pahre M. A., de Carvalho R. R., Djorgovski S. G., 1998, AJ, 116, 1606
Prugniel P., Simien F., 1997, A&A, 321, 111
Robertson B., Cox T. J., Hernquist L., Franx M., Hopkins P. F., Martini P., Springel V., 2006, ApJ, 641, 21
Romanowsky A. J., 2006, EAS Publication Ser., 20, 119
Romanowsky A. J., Kochanek C. S., 2001, ApJ, 553, 722
Romanowsky A. J., Douglas N. G., Arnaboldi M., Kuijken K., Merrifield M. R., Napolitano N. R., Capaccioli M., Freeman K. C., 2003, Sci, 301, 1696
Romeo A. D., Portinari L., Sommer-Larsen J., 2005, MNRAS, 361, 983
Sáiz A., 2003, PhD thesis, Universidad Autónoma de Madrid, Spain
Sáiz A., Domínguez-Tenreiro R., Tissera P. B., Courteau S., 2001, MNRAS, 325, 119
Sáiz A., Domínguez-Tenreiro R., Serna A., 2003, Ap&SS, 284, 411
Sáiz A., Domínguez-Tenreiro R., Serna A., 2004, ApJ, 601, L131
Salvador-Solé E., Manrique A., Solanes J. M., 2005, MNRAS, 358, 901
Sarson G. R., Shukurov A., Nordlund A., Gudiksen B., Brandenburg A., 2004, Ap&SS, 292, 267
Serna A., Domínguez-Tenreiro R., Sáiz A., 2003, ApJ, 597, 878
Sérsic J. L., 1968, Atlas de galaxias australes. Observatorio Astronómico, Córdoba, Argentina
Sierra-Glez.de Buitrago M. M., Domínguez-Tenreiro R., Serna A., 2003, in Gallego J., Zamorano J., Cardiel N. eds, Highlights of Spanish Astronomy III. Kluwer Academic Press, Dordrecht, p. 171,
Spergel D. N. et al., 2006, preprint (astro-ph/0603449)
Sommer-Larsen J., Gotz M., Portinari L., 2002, Ap&SS, 281, 519
Thomas D., Greggio L., Bender R., 1999, MNRAS, 302, 537
Tissera P. B., Lambas D. G., Abadi M. G., 1997, MNRAS, 286, 384
Tissera P. B., Domínguez-Tenreiro R., 1998, MNRAS, 297, 177 (TD)
Treu T., Koopmans L. V. E., 2004, ApJ, 611, 739
Trujillo I., Graham A. W., Caon N., 2001, MNRAS, 326, 869
Tucker W. H., 1975, Radiation Processes in Astrophysics. Wiley, New York
van den Bosch F. C., Norberg P., Mo H. J., Yang X., 2004, MNRAS, 352, 1302
Vazdekis A., Trujillo I., Yamada Y., 2004, ApJ, 601, L36
Vázquez-Semadeni E., 2004a, in Burton M., Jayawardhana R., Bourke T., eds, Proc. IAU Symp. 221, Star Formation at High Angular Resolution. Astron. Soc. Pac., San Francisco, p. 51
Vázquez-Semadeni E., 2004b, Ap&SS, 292, 187
Vergassola M., Dubrulle B., Frisch U., Noullez A., 1994, A&A, 289, 325
van der Marel R. P., Franx M., 1993, ApJ, 407, 525
Wechsler R. H., Bullock J. S., Primack J. R., Kravtsov A. V., Dekel A., 2002, ApJ, 568, 52
Zhao D. H., Mo H. J., Jing Y. P., Borner G., 2003, MNRAS, 339, 12

This paper has been typeset from a TEX/LATEX file prepared by the author.

Mon. Not. R. Astron. Soc. **373,** 503–520 (2006) doi:10.1111/j.1365-2966.2006.11084.x

Clues on regularity in the structure and kinematics of elliptical galaxies from self-consistent hydrodynamical simulations: the dynamical Fundamental Plane

J. Oñorbe,[1]★ R. Domínguez-Tenreiro,[1] A. Sáiz,[1]† H. Artal[1] and A. Serna[2]
[1]*Departamento de Física Teórica, C-XI. Universidad Autónoma de Madrid, Madrid E-28049, Spain*
[2]*Departamento de Física y A.C., Universidad Miguel Hernández, Elche, Spain*

Accepted 2006 September 15. Received 2006 September 11; in original form 2006 May 16

ABSTRACT

We have analysed the parameters characterizing the mass and velocity distributions of two samples of relaxed elliptical-like objects (ELOs) identified, at $z = 0$, in a set of self-consistent hydrodynamical simulations operating in the context of a concordance cosmological model. ELOs have a prominent, non-rotating, dynamically relaxed stellar spheroidal component, with very low cold gas content, and sizes of no more than ∼10–40 kpc (ELO or baryonic object scale), embedded in a massive halo of dark matter typically 10 times larger in size (halo scale). They have also an extended halo of hot diffuse gas. The parameters characterizing the mass, size and velocity dispersion both at the baryonic object and at the halo scales have been measured in the ELOs of each sample. At the halo scale, they have been found to satisfy virial relations; at the scale of the baryonic object, the (logarithms of the) ELO stellar masses, projected stellar half-mass radii, and stellar central line-of-sight (LOS) velocity dispersions define a flattened ellipsoid close to a plane (the intrinsic dynamical plane, IDP), tilted relative to the virial one, whose observational manifestation is the observed Fundamental Plane (FP). Otherwise, IDPs are not homogeneously populated, but ELOs, as well as elliptical (E) galaxies in the FP, occupy only a particular region defined by the range of their masses. The ELO samples have been found to show systematic trends with the mass scale in both, the relative content and the relative distributions of the baryonic and the dark mass ELO components, so that homology is broken in the spatial mass distribution (resulting in the IDP tilt), but ELOs are still a two-parameter family where the two parameters are correlated (causing its non-homogeneous population). The physical origin of these trends presumably lies in the systematic decrease, with increasing ELO mass, of the relative amount of dissipation experienced by the baryonic mass component along ELO stellar mass assembly. ELOs also show kinematical segregation, but it does not appreciably change with the mass scale.

The non-homogeneous population of IDPs explains the role played by $M_{\rm vir}$ to determine the correlations among intrinsic parameters. In this paper, we also show that the central stellar LOS velocity dispersion of ELOs, $\sigma^{\rm star}_{\rm los,\,0}$, is a fair empirical estimator of $M_{\rm vir}$, and this explains the central role played by $\sigma_{\rm los,0}$ at determining the observational correlations.

Key words: hydrodynamics – galaxies: elliptical and lenticular, cD – galaxies: haloes – galaxies: kinematics and dynamics – galaxies: structure – dark matter.

1 INTRODUCTION

Understanding how local galaxies of different Hubble types we observe today have formed is one of the most challenging open problems in cosmology. Among the different galaxy families, ellipticals (Es) are the easiest to study and are those that show the most precise regularities in their empirical properties, some times in the form of tight correlations among their observable parameters. The interest in these regularities lies in the fact that they could encode a lot of relevant informations on the physical processes underlying E formation and evolution.

The Sloan Digital Sky Survey (SDSS, York et al. 2000) has substantially improved the statistics on E samples. The sample selected

★E-mail: jose.onnorbe@uam.es
†Current address: Dept. of Physics, Mahidol University, Bangkok 10400, Thailand.

by Bernardi et al. (2003a), using morphological and spectral criteria, contains 9000 Es to date in the redshift range $0.01 \leqslant z \leqslant 0.3$ and in every environment from voids to groups to rich clusters. Analyses of their structural and dynamical parameters have shown that the distributions of their luminosities L, radii at half projected light $R_{\rm e}^{\rm light}$, and central line-of-sight (LOS) velocity dispersions $\sigma_{\rm los,0}$ (Bernardi et al. 2003b,c) are approximately Gaussian at any z. Moreover, a maximum likelihood analysis indicates that the pairs of parameters $\sigma_{\rm los,0}$–L and $R_{\rm e}^{\rm light}$–L, or their combinations, such as the mass-to-luminosity ratio within the effective radii $M_{\rm e}/L$ and L (where $M_{\rm e}$ is the dynamical mass defined as $M_{\rm e} = 2R_{\rm e}^{\rm light}\sigma^2_{\rm los,0}/G$), show correlations consistent with those previously established in literature, obtained from individual galaxy spectra of smaller samples, such as the Faber–Jackson relation (Faber & Jackson 1976), the D_n–$\sigma_{\rm los,0}$ relation (Dressler et al. 1987) and the surface brightness–$R_{\rm e}$ relation (Kormendy 1977; Kormendy & Djorgovski 1989), among others. Furthermore, early-type galaxies in the SDSS have been found to have roughly constant stellar-mass-to-light ratios (Kauffmann et al. 2003a,b; Padmanabhan et al. 2004).

The correlations involving two variables out of the three needed to fully characterize the structure and dynamics of an E galaxy are projections of the so-called Fundamental Plane (FP) relation (Djorgovski & Davis 1987; Dressler et al. 1987; Faber et al. 1987; Kormendy & Djorgovski 1989), involving the three or some or their combinations. The FP relation can be written as

$$\log_{10} R_{\rm e}^{\rm light} = a \log_{10} \sigma_{\rm los,0} + b \log_{10} \langle I^{\rm light} \rangle_{\rm e} + c, \qquad (1)$$

where $\langle I^{\rm light} \rangle_{\rm e}$ is the mean surface brightness within $R_{\rm e}^{\rm light}$. The values of the FP coefficients for the SDSS E sample are $a \simeq 1.5$, similar in the four SDSS bands, $b \simeq -0.77$, and $c \simeq -8.7$ (see their exact values in Bernardi et al. 2003c, table 2) with a small scatter. These SDSS results confirm previous ones, either in the optical (Lucey, Bower & Ellis 1991; Bender, Burstein & Faber 1992; de Carvalho & Djorgovski 1992; Jørgensen, Franx & Kjærgaard 1993, 1996; Prugniel & Simien 1996) or in the near-infrared (near-IR) wavelengths (Recillas-Cruz et al. 1990, 1991; Pahre, Djorgovski & de Carvalho 1995; Mobasher et al. 1999), even if the published values of a show larger values in the K band than at shorter wavelengths (see, for example, Pahre, de Carvalho & Djorgovski 1998).

The existence of the FP and its small scatter has the important implication that it provides us with a strong constraint when studying E galaxy formation and evolution (Bender, Burstein & Faber 1993; Guzmán, Lucey & Bower 1993; Renzini & Ciotti 1993). The physical origin of the FP is not yet clear, but it must be a consequence of the physical processes responsible for galaxy assembly. These processes built up early-type galaxies as dynamically hot systems whose configuration in phase space are close to equilibrium. Taking an E galaxy as a system in equilibrium, the virial theorem

$$M_{\rm vir} = c_{\rm F} \left(\sigma^{\rm tot}_{3,h}\right)^2 r^{\rm tot}_{\rm e,h}/G, \qquad (2)$$

where $M_{\rm vir}$ is its virial mass, $\sigma^{\rm tot}_{3,\rm h}$ is the average three-dimensional (3D) velocity dispersion of the whole E, including both dark and baryonic matter, $r^{\rm tot}_{\rm e,h}$ is the dynamical half-radius or radius enclosing half the total mass of the system, and $c_{\rm F}$ is a form factor of order unity, would imply a relation similar to equation (1) with $a = 2$ and $b = -1$ (known as the virial plane, Faber et al. 1987), should the dynamical mass-to-light ratios, $M_{\rm vir}/L$, and the mass structure coefficients,

$$c^{\rm vir}_{\rm M} = \frac{GM_{\rm vir}}{3\sigma^2_{\rm los,0} R_{\rm e}^{\rm light}}, \qquad (3)$$

be independent of the E luminosity or mass scale. The observational results described above mean that the FP is *tilted* relative to the virial plane and, consequently, that either $M_{\rm vir}/L$ or $c^{\rm vir}_{\rm M}$, or both, do depend on the E luminosity.

Different authors interpret the tilt of the FP relative to the virial relation as caused by different misassumptions that we comment on briefly (note that we can write $M_{\rm vir}/L = M^{\rm star}/L \times M_{\rm vir}/M^{\rm star}$, where $M^{\rm star}$ is the stellar mass of the E galaxy).

(1.1) A first possibility is that the tilt is due to systematic changes of stellar age and metallicity with galaxy mass, or, even, to changes of the slope of the stellar initial mass function (hereafter, IMF) with galaxy mass, resulting in systematic changes in the *stellar*-mass-to-light ratios, $M^{\rm star}/L$, with mass or luminosity (Zepf & Silk 1996; Pahre et al. 1998; Mobasher et al. 1999). However, these effects could explain at most only approximately one-third of the $\beta \neq 0$ value in the B band (Tinsley 1978; Dressler et al. 1987; Prugniel & Simien 1996; see also Renzini & Ciotti 1993; Trujillo, Burkert & Bell 2004). Furthermore, early-type galaxies in the SDSS have been found to have roughly constant stellar-mass-to-light ratios (Kauffmann et al. 2003a,b). Anyhow, the presence of a tilt in the K-band FP, where population effects are not important, indicates that it is very difficult that the tilt is caused by stellar physics processes alone, as Bender et al. (1992), Guzmán et al. (1993), Renzini & Ciotti (1993) and Pahre et al. (1998), among other authors, have suggested.

(1.2) A second possibility is that $M_{\rm vir}/L$ changes systematically with the mass scale because the total dark-to-visible mass ratio, $M_{\rm vir}/M^{\rm star}$ changes (see, for example, Renzini & Ciotti 1993; Ciotti, Lanzoni & Renzini 1996; Pahre et al. 1998; Padmanabhan et al. 2004).

Otherwise, a dependence of $c^{\rm vir}_M$ on the mass scale could be caused by systematic differences in:

(2.1) the dark versus bright matter spatial distribution;

(2.2) the kinematical segregation, the rotational support and/or velocity dispersion anisotropy in the stellar component (dynamical non-homology); or

(2.3) systematic projection or other geometrical effects.

Taking into account these effects in the FP tilt demands modelling of the galaxy mass and velocity 3D distributions and comparing the outputs with high-quality data. Bender et al. (1992) considered effects (2.1) and (2.2); Ciotti et al. (1996) explored (1.2)–(2.2) and concluded that a systematic increase in the dark matter content with mass, or differences in its distribution, as well as a dependence of the Sérsic (1968) shape parameter for the luminosity profiles with mass, may by themselves formally produce the tilt; and Padmanabhan et al. (2004) found evidence of effect (1.2) in SDSS data. Other authors have also shown that allowing for broken homology, either dynamical (Busarello et al. 1997), in the luminosity profiles (Trujillo et al. 2004), or both (Prugniel & Simien 1997; Graham & Colless 1997; Pahre et al. 1998), brings the observed FP closer to equation (3).

Observational methods suffer from some drawbacks to study in depth the physical origin of the FP tilt. For example, one drawback is the impossibility to get accurate measurements of the E 3D mass distributions (either dark, stellar or gaseous) and another is that the intrinsic 3D velocity distribution of galaxies is severely limited by projection. Only the line-of-sight velocity distributions (LOSVDs) can be inferred from galaxy spectra. Therefore, the interpretation of observational data is not always straightforward. To complement the information provided by data and circumvent these drawbacks, analytical modelling is largely used in the literature (Kronawitter

et al. 2000; Gerhard et al. 2001; Romanowsky & Kochanek 2001; Borriello, Salucci & Danese 2003; Padmanabhan et al. 2004; Mamon & Łokas 2005a,b). These methods give very interesting insights into mass and velocity distributions, as well as the physical processes causing them, but are somewhat limited by symmetry considerations and other necessary simplifying hypotheses. These difficulties and limitations could be circumvented should we have at our disposal complete information on the phase space of the galaxy constituents. This is not possible through observations, but can be attained, at least in a virtual sense, through numerical simulations.

Capelato, de Carvalho & Carlberg (1995) first addressed the origin of the FP through numerical simulations. By analysing the remnants of the dissipationless mergers of two equal-mass one-component King models, and varying their relative orbital energy and angular momentum, they show that the mergers of objects in the FP produce new objects in the FP. This result was extended by: Dantas et al. (2003), who used one- and two-component Hernquist models as progenitors; González-García & van Albada (2003), based on Jaffe (1983) models; and by Boylan-Kolchin, Ma & Quataert (2005), who used Hernquist + NFW models. Nipoti, Londrillo & Ciotti (2003) show, in turn, that the FP is well reproduced by dissipationless hierarchical equal-mass merging of one- and two-component galaxy models, and by accretion with substantial angular momentum, with the merging zeroth-order generation placed at the FP itself. They also found that both the Faber–Jackson and the Kormendy relations are not reproduced by the simulations, and concluded that dissipation must be a basic ingredient in E formation. In agreement with this conclusion, Dantas et al. (2002, 2003) have shown that the end products of dissipationless collapse generally do not follow an FP-like correlation. Bekki (1998) first considered the role of dissipation in E formation through preprepared simulations. He adopted the merger hypothesis (i.e. Es form by the mergers of two equal-mass gas-rich spirals) and he focused on the role of the time-scale for star formation (SF) in determining the structural and kinematical properties of the merger remnants. He concluded that the slope of the FP reflects the difference in the amount of dissipation the merger end products have experienced according to their luminosity (or mass). Recently, Robertson et al. (2006) have confirmed this conclusion on the role of dissipative dynamics to shape the FP, again through preprepared mergers of disc galaxies.

In this paper, we go a step further and we analyse the tilt of the FP in samples of virtual Es formed in a cosmological context through self-consistent hydrodynamical simulations. This numerical approach provides a convenient method to work out the clues of regularity and systematics of E galaxies, and to find out their links with the processes involved in galaxy assembly in a cosmological context. The important point for our current purposes is that they *directly* provide complete six-dimensional (6D) phase-space information on each constituent particle sampling a given galaxy-like object formed in the simulation: that is, they give directly the mass and velocity distributions of dark matter, gas and stars of each object.

Taking advantage of these possibilities, we have analysed 10 self-consistent hydrodynamical simulations run in the framework of a flat ΛCDM cosmological model, characterized by cosmological parameters consistent with their last determinations (Spergel et al. 2006). Galaxy-like objects of different morphologies form in these simulations at $z = 0$: irregulars, disc-like objects, S0-like objects and elliptical-like objects (hereafter, ELOs). ELOs have been identified as those objects having a prominent dynamically relaxed, roughly non-rotating stellar spheroidal component, with no extended discs and very low cold gas content; the stellar component has typical sizes of no more than ∼10–40 kpc, it dominates the mass density at these scales (hereafter, *ELO or baryonic object scale*) and it is embedded in a halo of dark matter typically 10 times larger in size (hereafter, *halo scale*). In a forthcoming paper (Oñorbe et al., in preparation), we report on an analysis of the mass and velocity distributions of the different ELO components: dark matter, stars, cold gas and hot gas. In this paper, we focus on the quantitative characterization of these mass and velocity distributions through their corresponding parameters, both at the ELO and at the halo scales. At the baryonic object scale, to characterize the structural and dynamical properties of ELOs, we will describe their 3D distributions of mass and velocity through the three intrinsic (that is, 3D) parameters (the stellar mass at the baryonic object scale, $M^{\rm star}_{\rm bo}$, the stellar half-mass radii at the baryonic object scale, $r^{\rm star}_{\rm e,bo}$, defined as those radii enclosing half the $M^{\rm star}_{\rm bo}$ mass, and the mean square velocity for stars, $\sigma^{\rm star}_{\rm 3,bo}$) whose observational projected counterparts (the luminosity L, effective projected size $R^{\rm light}_{\rm e}$, and the stellar central LOS velocity dispersion, $\sigma_{\rm los,0}$) enter the definition of the observed FP (equation 1). To help the reader, in Table 1 we give a list of the parameter names and symbols and in Table 2 a list of the profiles and ratios. These intrinsic parameters have been measured on ELOs, and their correlations have been looked for, and more specifically, the lower-dimensional regions (i.e. *dynamical planes*) they fill in the

Table 1. Parameter names and symbols.

Name	Symbol
Observational parameters	
Luminosity	L
Half projected light radius	$R^{\rm light}_{\rm e}$
Central LOS velocity dispersion	$\sigma_{\rm los,0}$
Dynamical mass	$M_{\rm e}$
Mean surface brightness within $R^{\rm light}_{\rm e}$	$\langle I^{\rm light}\rangle_{\rm e}$
Stellar mass	$M^{\rm star}$
Stellar-mass-to-light ratio	$\gamma^{\rm star}$
Halo scale parameters	
Virial mass	$M_{\rm vir}$
Virial radius	$r_{\rm vir}$
Dark mass inside virial radius	$M^{\rm dark}_{\rm h}$
Baryon mass inside virial radius	$M^{\rm ab}_{\rm h}$
Cold baryon mass inside virial radius	$M^{\rm cb}_{\rm h}$
Stellar mass inside virial radius	$M^{\rm star}_{\rm h}$
Total half-mass radius	$r^{\rm tot}_{\rm e,h}$
Cold baryon half-mass radius	$r^{\rm cb}_{\rm e,h}$
Stellar half-mass radius	$r^{\rm star}_{\rm e,h}$
Total 3D velocity dispersion	$\sigma^{\rm tot}_{\rm 3,h}$
Baryonic-object scale parameters	
Stellar mass	$M^{\rm star}_{\rm bo}$
Cold baryon mass	$M^{\rm cb}_{\rm bo}$
Stellar half-mass radius	$r^{\rm star}_{\rm e,bo}$
Cold baryon half-mass radius	$r^{\rm cb}_{\rm e,bo}$
Projected stellar half-mass radius	$R^{\rm star}_{\rm e,bo}$
Mean stellar 3D velocity dispersion	$\sigma^{\rm star}_{\rm 3,bo}$
Central LOS stellar velocity dispersion	$\sigma^{\rm star}_{\rm los,0}$
Mean projected stellar mass density within $R^{\rm star}_{\rm e,bo}$	$\langle\Sigma^{\rm star}\rangle_{\rm e}$

Table 2. Profiles and ratios.

Profiles		Ratios		
Name	Symbol[a]	Ratio definition	Ratio symbol	Logarithmic slope
Hot baryon mass profile	$M^{\rm hb}(r)$	$GM_{\rm vir}/(\sigma^{\rm tot}_{\rm 3,h})^2\, r^{\rm tot}_{\rm e,h}$	$c_{\rm F}$	$\beta_{\rm F}$
Circular velocity profile	$V_{\rm cir}(r)$	$r^{\rm tot}_{\rm e,h}/r^{\rm star}_{\rm e,bo}$	$c_{\rm rd}$	$\beta_{\rm rd}$
3D velocity dispersion profile	$\sigma_{\rm 3D}(r)$	$r^{\rm star}_{\rm e,bo}/R^{\rm star}_{\rm e,bo}$	$c_{\rm rp}$	$\beta_{\rm rp}$
Anisotropy profile	$\beta_{\rm ani}(r)$	$(\sigma^{\rm tot}_{\rm 3,h}/\sigma^{\rm star}_{\rm 3,bo})^2$	$c_{\rm vd}$	$\beta_{\rm vd}$
Projected mass density profile	$\Sigma(R)$	$(\sigma^{\rm star}_{\rm 3,bo})^2/3\ (\sigma^{\rm star}_{\rm los,0})^2$	$c_{\rm vpc}$	$\beta_{\rm vpc}$
Line-of-sight velocity profile Line-of-sight velocity dispersion profile	$V_{\rm los}(R)$ $\sigma_{\rm los}(R)$	$GM_{\rm vir}/3\ (\sigma^{\rm star}_{\rm los,0})^2\, R^{\rm light}_{\rm e} = c_{\rm F}\, c_{\rm rd}\, c_{\rm rp}\, c_{\rm vd}\, c_{\rm vpc}$	$c^{\rm vir}_{\rm M}$	$\beta_{\rm M}$

[a]To specify the constituent, a superscript has been added in the text to the profile symbols.

3D space of the $M^{\rm star}_{\rm bo}$, $r^{\rm star}_{\rm e,bo}$ and $\sigma^{\rm star}_{\rm 3,bo}$ parameters, because the observational manifestation of these dynamical planes is the FP relation. This information, combined with that on the mass, size and velocity dispersion parameters at the halo scale, allows us to test whether or not the $c^{\rm vir}_{\rm M}$ coefficients and the $M_{\rm vir}/M^{\rm star}$ ratios do systematically depend on the mass scale, so that the tilt and the scatter of the observed FP can be explained in terms of the regularities in the structural and dynamical properties of ELOs formed in self-consistent hydrodynamical simulations.

Fully consistent gravo-hydrodynamical simulations as a method to study E assembly have already proven to be useful. An analysis of ELO structural and kinematical properties that can be constrained from observations (i.e. stellar masses, projected half-mass radii, central LOS velocity dispersions) has shown that they have counterparts in the local Universe as far as these properties are concerned (Sáiz 2003; Sáiz, Domínguez-Tenreiro & Serna 2004, hereafter SDTS04), including the FP relation and some clues about its physical origin (Oñorbe et al. 2005), and its lack of dynamical evolution (Domínguez-Tenreiro et al. 2006, hereafter DTal06). Also, ELO stellar populations have age distributions showing similar trends to those inferred from observations (Domínguez-Tenreiro, Sáiz & Serna 2004, hereafter DSS04).

The paper is organized as follows. In Section 2, we briefly describe the simulations, the ELO samples and their generic properties. The ELO size and mass scales and their relations are analysed in Section 3. Section 4 is devoted to kinematics, and in Section 5 we report on what the intrinsic dynamical plane (IDP) ELOs show and its comparison with the observed FP, and we analyse its physical origin. Finally, in Section 6 we summarize our results and discuss them in the context of theoretical results on halo structure and dissipation of the gaseous component.

2 THE SIMULATIONS AND THE ELO SAMPLES

We have analysed ELOs identified in 10 self-consistent cosmological simulations run in the framework of the same global flat ΛCDM cosmological model, with $h = 0.65, \Omega_{\rm m} = 0.35, \Omega_{\rm b} = 0.06$. The normalization parameter has been taken slightly high, $\sigma_8 = 1.18$, as compared with the average fluctuations of Two-degree Field Galaxy Redshift Survey (2dFGRS) or SDSS galaxies (Lahav et al. 2002; Tegmark et al. 2004) or recent results from *WMAP* (Spergel et al. 2006) to mimic an active region of the Universe (Evrard, Silk & Szalay 1990).

We have used a Lagrangian code (DEVA, Serna, Domínguez-Tenreiro & Sáiz 2003) particularly designed to study galaxy assembly in a cosmological context. Gravity is computed through an adaptive particle-particle, particle-mesh (AP3M)–like method, based on Couchman (1991). Hydrodynamics is computed through a smoothed particle hydrodynamics technique where special attention has been paid to make the implementation of conservation laws (energy, entropy and angular momentum) as accurate as possible (see Serna et al. 2003 for details, in particular for a discussion on the observational implications of violating some conservation laws). Entropy conservation is assured by taking into consideration the space variation of the smoothing length (i.e. the so-called ∇h terms). Time-steps are individual for particles (to save CPU time, allowing a good time resolution), as well as masses. Time integration uses a predict-evaluate-correct scheme. In any run, a homogeneously sampled periodic box of 10-Mpc side has been employed, and 64^3 dark matter and 64^3 gas particles, with masses of 1.29×10^8 and $2.67 \times 10^7\ {\rm M}_\odot$, respectively, have been used. The gravitational softening used was $\epsilon = 2.3$ kpc. The cooling function is that from Tucker (1975) and Bond et al. (1984) for an optically thin primordial mixture of H and He ($X = 0.76, Y = 0.24$) in collisional equilibrium and in the absence of any significant background radiation field with a primordial gas composition. Each of the 10 simulations started at a redshift of $z_{\rm in} = 20$.

SF processes have been included through a simple phenomenological parametrization, like that first used by Katz (1992; see also Tissera, Lambas & Abadi 1997, Sáiz 2003 and Serna et al. 2003 for details), that transforms cold locally collapsing gas at the scales the code resolves, denser than a threshold density, $\rho_{\rm thres}$, into stars at a rate ${\rm d}\rho_{\rm star}/{\rm d}t = c_*\rho_{\rm gas}/t_{\rm g}$, where $t_{\rm g}$ is a characteristic time-scale chosen to be equal to the maximum of the local gas-dynamical time, $t_{\rm dyn} = (4\pi G\rho_{\rm gas})^{-1/2}$, and the local cooling time, and c_* is the average SF efficiency at resolution ϵ scales, i.e. the empirical Kennicutt–Schmidt law (Kennicutt 1998). It is worth noting that, in the context of the new sequential multiscale SF scenarios (Vázquez-Semadeni 2004a,b; Ballesteros-Paredes et al. 2006, and references therein), it has been argued that this law and particularly the low c_* values inferred from observations can be explained as a result of SF processes acting on dense molecular cloud core scales when conveniently averaged on disc scales (Elmegreen 2002; Sarson et al. 2004, see below). Supernova feedback effects or energy inputs other than gravitational have not been *explicitly* included in these simulations. We note that the role of discrete stellar energy sources at the scales resolved in this work is not yet clear, as some authors argue that stellar energy releases drive the structuring of gas density locally at sub-kpc scales (Elmegreen 2002). In fact, some magnetohydrodynamic (MHD) simulations of self-regulating Type II supernova (SNII) heating in the interstellar medium (ISM)

at scales <250 pc (Sarson et al. 2004) indicate that this process produces a Kennicutt–Schmidt-like law on average. If this were the case, the Kennicutt–Schmidt law implemented in our code would already *implicitly* account for the effects stellar self-regulation has on the scales our code resolves, and our ignorance of sub-kpc scale processes would be contained in the particular values of $\rho_{\rm thres}$ and c_*.

Five out of the 10 simulations (the SF-A type simulations) share the SF parameters ($\rho_{\rm thres} = 6 \times 10^{-25}\,{\rm gr\,cm^{-3}}, c_* = 0.3$) and differ in the seed used to build up the initial conditions. To test the role of SF parametrization, the same initial conditions have been run with different SF parameters ($\rho_{\rm thres} = 1.8 \times 10^{-24}\,{\rm gr\,cm^{-3}}$, $c_* = 0.1$) making SF more difficult, contributing another set of five simulations (hereafter, the SF-B type simulations).

ELOs have been identified in the simulations as those galaxy-like objects at $z = 0$ having a prominent, non-rotating, dynamically relaxed spheroidal component made out of stars, with no extended discs and very low cold gas content. It turns out that, at $z = 0$, 26 (17) objects out of the more massive formed in SF-A (SF-B) type simulations fulfil this identification criterion, forming two samples (the SF-A and SF-B ELO samples) partially analysed in SDTS04, in DSS04 and in DTal06. In Oñorbe et al. (2005), it is shown that both samples satisfy dynamical FP relations. ELOs in the SF-B sample tend to be of later type than their corresponding SF-A counterparts because forming stars becomes more difficult: this is why many of the SF-B sample counterparts of the less massive ELOs in the SF-A sample do not satisfy the selection criteria, and the SF-B sample has a lower number of ELOs that the SF-A sample.

A visual examination of ELOs indicates that the stellar component is embedded in a dark matter halo, contributing an important fraction of the mass at distances from the ELO centre larger than ∼15 kpc on average. ELOs have also a hot, extended, X-ray emitting halo of diffuse gas (Sáiz, Domínguez-Tenreiro & Serna 2003). Stellar and dark matter particles constitute a dynamically hot component with an important velocity dispersion and, except in the very central regions, a positive anisotropy. In Tables 3 and 4, different data on ELOs in the samples are given. In these tables, following the criterion introduced in Sáiz et al. 2001, ELOs have been labelled by a three-digit code formed by rounding their x, y and z coordinates in units where the simulated box has, at any redshift, a length of 1. The number of particles of each species sampling each ELO in the sample can be easily determined from these tables and the values of the masses of dark and baryonic particles. The spin parameters of the ELO samples have an average value of $\bar{\lambda} = 0.033$. ELO mass function is consistent with that of a small group environment (Cuesta-Bolao & Serna, private communication).

The simulations show the physical patterns of ELO mass assembly and SF rate histories (see DSS04 and DTal06 for more details). ELOs form out of the mass elements that at high z are enclosed by overdense regions whose mass scale (total mass they enclose) is of the order of an E galaxy total (i.e. including its halo) mass. Analytical models as well as N-body simulations indicate that two different phases operate along halo mass assembly: first, a violent fast one, where the mass aggregation rates are high, and then, a slower one, with lower mass aggregation rates (Wechsler et al. 2002; Zhao et al. 2003; Salvador-Solé, Manrique & Solanes 2005). Our hydrodynamical simulations indicate that the fast phase occurs through a multiclump collapse (see Thomas, Greggio & Bender 1999) ensuing turnaround of the overdense regions, and it is characterized by the fast head-on fusions experienced by the nodes of the cellular structure these regions enclose, resulting in strong shocks and high cooling rates of their gaseous component and, at the same time, in strong and very fast SF bursts that transform most of the available cold gas into stars. Consequently, most of the dissipation involved in the mass assembly of a given ELO occurs in this violent early phase at high z. The slow phase comes after the multiclump collapse. In this phase, the halo mass aggregation rate is low and the mass increments result from major mergers, minor mergers or continuous accretion. Our cosmological simulations show that the fusion rates are generally low and that a strong SF burst and dissipation follow a major merger only if enough gas is still available after the early violent phase. This is very unlikely in any case, and it becomes more and more unlikely as the ELO mass increases (see DSS04). Therefore, these mergers imply only a modest amount of energy dissipation or SF, but they play an important role in this slow phase: ∼50 per cent of ELOs in the sample have experienced a major merger event at $2 < z < 0$, which results in the increase of the ELO mass content, size and stellar mean square velocity. Therefore, our simulations indicate that most of the stars of today Es formed at high redshifts, while they are assembled later on (see de Lucia et al. 2006, for similar results from a semi-analytic model of galaxy formation grafted to the *Millennium Simulation*). This scenario shares some characteristics of previously proposed scenarios (see discussion and references in DTal06), but it has also significant differences, mainly that most stars form out of cold gas that was never shock heated at the halo virial temperature and then formed a disc, as the conventional recipe for galaxy formation propounds (see discussion in Keres et al. 2005 and references therein).

3 SIZE AND MASS SCALES

3.1 Masses and sizes at the scale of the virial radius

The virial radius describes the ELO size *at the scale of its dark matter halo*. It roughly encloses those particles that are bound into the self-gravitating configuration forming a given ELO system (i.e. a dark matter halo plus the main baryonic compact object plus the substructures and satellites hosted by the dark matter halo). The virial radii have been calculated using the Bryan & Norman (1998) fitting formula, which yields, at $z = 0$, a value of $\Delta \simeq 100$ for the mean density within $r_{\rm vir}$ in units of the critical density. The mass at the scale of $r_{\rm vir}$ is the virial mass, $M_{\rm vir}$, the total mass inside $r_{\rm vir}$ or halo total mass. The mass scales associated with the different constituents considered here are:[1] dark matter, $M_{\rm h}^{\rm dark}$; baryons of any kind, $M_{\rm h}^{\rm ab}$; cold baryons (that is, cold gas particles with $T \leqslant 3 \times 10^4$ K and stellar particles), $M_{\rm h}^{\rm cb}$; stars, $M_{\rm h}^{\rm star}$; and hot gas (that is, gaseous particles with $T > 3 \times 10^4$ K). A measure of the compactness of the mass distribution for the different ELO constituents, at the halo scale, is given by their respective half-mass radii, or radii enclosing half the mass of these constituents within $r_{\rm vir}$: for example, the overall half-mass radii, $r_{\rm e,h}^{\rm tot}$, are the radii of the sphere enclosing $M_{\rm vir}/2$, the stellar half-mass radii $r_{\rm e,h}^{\rm star}$ enclose $M_{\rm h}^{\rm star}/2$ and so on.

For each of the ELOs in our sample, their virial mass and radii are listed in Table 3, where also given are the masses within $r_{\rm vir}$ corresponding to different constituents and some relevant half-mass radii. All these mass scales are strongly correlated with $M_{\rm vir}$ as shown

[1] Note that we have used superscripts to mean the different ELO constituents and subscripts to distinguish between halo (h) or baryonic object (bo) scales (see Table 1).

Table 3. Masses, sizes and mean square velocities of ELOs at the halo scale ($z = 0$).

Run	ELO	$M_{\rm vir}$	$M_{\rm h}^{\rm dark}$	$M_{\rm h}^{\rm ab}$	$M_{\rm h}^{\rm cb}$	$M_{\rm h}^{\rm star}$	$r_{\rm vir}$	$r_{\rm e,h}^{\rm tot}$	$r_{\rm e,h}^{\rm cb}$	$r_{\rm e,h}^{\rm star}$	$\sigma_{\rm 3,h}^{\rm tot}$
8714	#173	772.82	678.31	94.51	70.65	66.69	527.00	222.54	64.80	51.63	302.43
	#353	322.18	285.71	36.47	31.60	29.61	394.00	110.99	18.62	16.11	261.18
	#581	177.03	156.26	20.77	18.94	17.59	322.00	101.54	19.05	16.07	202.53
	#296	153.52	134.38	19.14	16.79	15.56	308.00	92.12	17.09	13.20	201.13
	#373	74.00	64.23	9.77	8.35	7.66	241.00	66.65	6.70	5.79	162.36
	#772	60.71	52.16	8.55	7.50	6.89	226.00	56.57	6.58	5.40	159.75
	#284	53.76	46.03	7.73	6.86	6.15	217.00	67.69	6.34	4.96	149.92
8747	#288	285.17	251.80	33.37	29.83	28.27	378.00	112.14	25.87	22.65	241.90
	#115	178.07	157.31	20.77	17.62	16.14	323.00	95.56	11.28	8.24	220.92
	#189	45.15	38.62	6.53	5.77	5.42	205.00	58.45	4.88	4.45	145.62
	#915	38.63	32.47	6.17	5.51	5.05	194.00	47.74	4.14	3.59	141.02
8741	#011	273.34	237.46	35.87	30.12	29.42	373.00	102.20	21.83	20.37	246.70
	#017	141.44	121.97	19.47	16.33	15.29	299.00	89.04	17.01	13.93	197.56
	#930	135.71	118.56	17.15	13.70	12.67	295.00	89.82	20.45	15.95	209.05
	#945	107.34	93.26	14.08	12.63	11.59	273.00	78.06	11.07	9.00	184.78
	#097	108.18	95.20	12.97	11.33	10.45	274.00	73.36	9.80	8.45	185.69
	#907	55.15	47.67	7.48	6.35	5.81	219.00	50.61	4.32	3.77	160.98
8742	#234	296.59	260.31	36.29	29.86	28.80	383.00	101.79	15.71	14.62	258.68
	#283	160.41	137.78	22.63	16.60	16.10	312.00	87.69	9.47	8.90	235.18
	#254	147.26	128.57	18.69	16.98	15.37	303.00	100.62	17.43	12.99	190.07
	#092	75.03	64.57	10.46	9.14	8.46	242.00	84.18	9.84	8.52	151.06
8743	#238	327.12	289.42	37.70	33.03	30.92	396.00	116.33	24.41	20.78	255.62
	#328	66.83	56.77	10.06	8.63	8.36	233.00	56.61	5.64	5.44	167.70
	#515	56.33	48.75	7.58	6.79	6.40	220.00	56.20	4.66	4.34	158.78
	#437	52.65	45.23	7.42	6.78	6.31	215.00	54.73	8.00	6.83	152.63
	#421	36.75	31.44	5.31	4.69	4.29	191.00	46.77	4.33	3.82	141.13
8716	#173	753.34	673.07	80.28	64.75	54.89	523.00	230.70	39.85	24.19	300.90
	#253	312.64	281.54	31.10	27.42	24.03	390.00	109.32	8.85	6.72	261.01
	#581	170.89	151.97	18.92	17.26	14.68	319.00	100.06	8.65	6.07	207.37
	#296	153.65	135.26	18.39	16.36	13.34	308.00	93.98	8.39	5.07	205.79
8717	#317	739.03	673.61	65.41	62.44	56.86	519.00	157.32	30.96	24.15	345.96
	#288	280.20	249.36	30.85	28.17	24.27	376.00	108.00	14.90	9.54	245.54
	#348	222.99	197.69	25.30	23.15	19.23	348.00	111.59	14.26	8.81	222.23
8721	#011	271.20	237.67	33.53	28.36	26.61	372.00	105.34	9.83	7.90	248.27
	#945	107.97	94.22	13.75	12.44	10.20	274.00	78.03	5.60	3.73	187.11
	#097	106.32	93.99	12.33	10.54	8.99	272.00	73.94	5.14	3.83	185.74
8722	#293	729.97	658.54	71.42	65.54	58.46	516.00	151.34	28.27	20.95	332.75
	#234	292.30	259.61	32.69	27.44	25.72	381.00	100.25	7.96	6.87	261.70
	#283	157.20	136.37	20.83	15.78	13.95	310.00	86.88	4.84	3.62	237.45
	#254	145.18	127.78	17.40	16.04	13.13	302.00	102.94	6.47	4.33	193.14
8723	#647	773.24	689.69	83.55	71.59	59.77	527.00	182.08	92.82	44.22	325.39
	#238	318.02	285.59	32.44	29.60	24.81	392.00	107.38	12.58	8.06	260.00
	#563	271.83	240.05	31.78	27.93	24.49	372.00	110.79	24.03	15.38	240.78

Masses are given in $10^{10}\,{\rm M}_{\odot}$, distances in kpc, velocity dispersion in km s^{-1}.

in Fig. 1 for $M_{\rm h}^{\rm star}$. Note that the virial masses of ELOs have a lower limit of $3.7 \times 10^{11}\,{\rm M}_{\odot}$.

An important point is the amount of gas infall *relative* to the halo mass scale. As illustrated in Fig. 2 for $M_{\rm h}^{\rm cb}/M_{\rm vir}$, any of the ratios $M_{\rm h}^{\rm ab}/M_{\rm vir}$, $M_{\rm h}^{\rm cb}/M_{\rm vir}$ or $M_{\rm h}^{\rm star}/M_{\rm vir}$ decreases as $M_{\rm vir}$ increases, as observationally found at smaller scales (see Section 1). Note that we have in any case $M_{\rm h}^{\rm ab}/M_{\rm vir} < \Omega_{\rm b}/\Omega_{\rm m} = 0.171$, the average cosmic fraction, so that there is a lack of baryons within $r_{\rm vir}$ relative to the dark mass content that becomes more important as $M_{\rm vir}$ increases. Otherwise, heating processes along ELO assembly give rise to a hot gas halo around the objects, partially beyond the virial radii. The amount of hot gas mass outside the virial radii, normalized to the ELO stellar mass $M_{\rm bo}^{\rm star}$ (see Section 3.2), increases with the mass scale. It also increases relative to the cold gas content at the halo scale. To illustrate this point, in Fig. 3 we plot the integrated hot gas density profile normalized to the mass of cold baryons inside the virial radii, $M_{\rm h}^{\rm cb}$. The mass effect can be clearly appreciated in this figure, where we see the following.

(i) The mass of hot gas increases monotonically up to $r \simeq 4$ $r_{\rm vir}$ and maybe also beyond this value. However, it is difficult at these large radii to properly elucidate whether or not a given hot gas mass element belongs to a given ELO or to another close one. (To alleviate this difficulty, only those ELOs not having massive

Table 4. Masses, sizes and mean square velocities at the baryonic object scale, as well as projected radii and central stellar line-of-sight velocity dispersions ($z = 0$).

Run	ELO	$M_{\rm bo}^{\rm cb}$	$M_{\rm bo}^{\rm star}$	$r_{\rm e,bo}^{\rm star}$	$r_{\rm e,bo}^{\rm star}$	$\sigma_{3,\rm bo}^{\rm star}$	$\sigma_{\rm los,0}^{\rm star}$
8714	#173	43.12	42.59	13.01	12.72	351.93	226.67
	#353	25.62	25.17	8.25	7.95	297.11	192.47
	#581	13.72	13.45	6.75	6.66	222.42	136.18
	#296	12.21	11.95	4.76	4.69	225.95	138.39
	#373	7.38	7.23	3.85	3.83	186.95	116.88
	#772	5.62	5.51	2.33	2.30	181.59	107.28
	#284	5.70	5.48	2.81	2.74	169.09	103.74
8747	#288	20.11	20.05	7.84	7.81	269.58	171.50
	#115	12.21	12.17	2.94	2.96	259.05	161.63
	#189	4.74	4.68	2.57	2.61	169.93	104.81
	#915	4.52	4.32	2.23	2.19	164.69	99.61
8741	#011	19.10	19.10	5.36	5.35	279.61	174.62
	#017	10.34	10.15	4.15	4.09	224.37	139.54
	#930	8.95	8.85	4.68	4.70	214.97	138.64
	#945	10.00	9.89	4.58	4.62	209.68	128.84
	#097	9.46	9.34	5.00	5.05	206.21	132.19
	#907	5.63	5.55	2.57	2.60	187.67	119.71
8742	#234	27.42	27.13	9.33	9.23	287.18	190.47
	#283	13.51	13.44	4.28	4.30	246.54	151.56
	#254	10.91	10.81	4.50	4.50	221.72	134.23
	#092	6.55	6.38	3.14	3.17	177.69	108.46
8743	#238	20.97	20.88	6.76	6.79	289.43	181.53
	#328	7.76	7.60	3.40	3.36	187.15	116.49
	#515	5.74	5.63	2.60	2.62	185.04	114.13
	#437	4.79	4.70	2.36	2.40	172.71	105.13
	#421	3.91	3.81	2.11	2.14	161.41	102.09
8716	#173	39.13	38.07	7.07	6.75	355.08	237.07
	#253	22.98	22.54	4.40	4.28	305.37	199.34
	#581	13.03	12.46	3.35	3.18	243.71	152.89
	#296	10.87	10.43	2.52	2.50	241.58	140.14
8717	#317	42.28	41.55	8.12	7.77	387.30	223.73
	#288	18.63	18.25	3.48	3.45	286.59	169.81
	#348	15.36	14.84	3.73	3.57	261.06	158.31
8721	#011	21.73	21.37	3.34	3.31	287.47	177.04
	#945	9.99	9.30	2.55	2.44	226.33	128.90
	#097	8.62	8.34	2.34	2.36	213.00	133.46
8722	#293	43.56	42.75	9.40	9.09	365.95	215.68
	#234	22.40	22.28	3.53	3.57	313.03	196.62
	#283	12.67	12.51	2.10	2.13	262.81	163.89
	#254	11.97	11.52	2.64	2.62	237.10	137.68
8723	#647	34.01	33.43	5.86	5.76	336.69	210.25
	#238	20.09	19.91	3.78	3.74	297.51	191.05
	#563	13.67	13.44	2.41	2.45	274.84	164.01

Masses are given in $10^{10}\,{\rm M}_{\odot}$, distances in kpc, velocity dispersions in km s^{-1}.

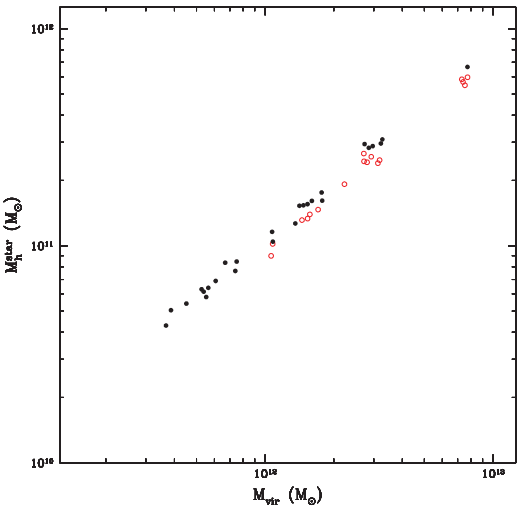

Figure 1. Masses at the halo scale of stars versus their corresponding virial masses: filled black symbols, SF-A sample ELOs; open red symbols, SF-B sample ELOs.

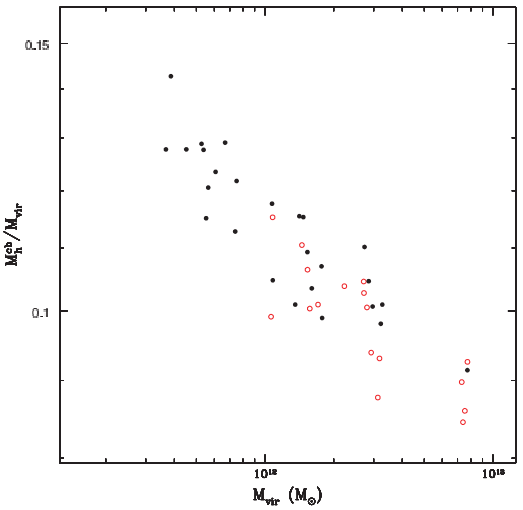

Figure 2. Masses of cold baryons inside the virial radii in units of the corresponding virial mass for the ELO sample: filled black symbols, SF-A sample ELOs; open red symbols, SF-B sample ELOs.

neighbours within radii of $6 \times r_{\rm vir}$ have been considered to draw this figure.)

(ii) The hot gas mass fraction increases with $M_{\rm vir}$ at given $r/r_{\rm vir}$. This suggests that the cold baryons that massive ELOs miss inside $r_{\rm vir}$ relative to less massive ones appear as a diffuse warm component at the outskirts of their configurations.

We now comment on length-scales. The overall half-mass radii $r_{\rm e,h}^{\rm tot}$ are closely correlated to $M_{\rm vir}$. Concerning baryon mass distributions, dissipation in shocks and gas cooling play now important roles to determine these mass distributions. Therefore, the $r_{\rm e,h}^{\rm star}$ radii depend on how much energy was radiated before gaseous particles became dense enough to be turned into stars. This, in turn, depends on the mass scale, on the one hand, and, in a given mass range, on the values of SF parameters, on the other hand. Therefore, more massive ELOs tend to have larger $r_{\rm e,h}^{\rm star}$ radii and, in a given mass range, SF-A sample ELOs tend to have larger $r_{\rm e,h}^{\rm star}$ radii than their SF-B sample counterparts, because the SF implementation in the code demands denser gas to form stars in the latter than in the former. This effect is more remarkable for sizes at the scale of the baryonic object, as we shall see in the next subsection.

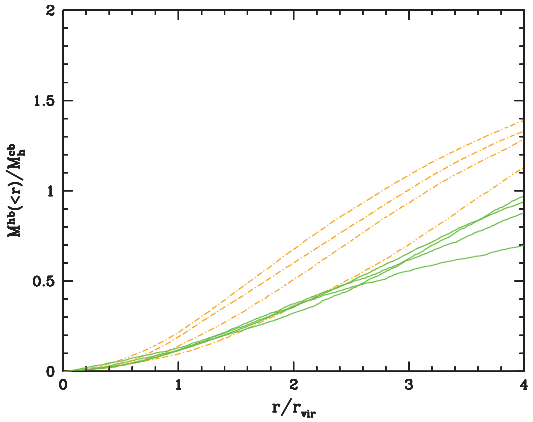

Figure 3. The hot gas density profile normalized to the mass of cold baryons inside the virial radii for isolated ELOs: orange point-dashed lines, ELOs in the mass interval $1.5 \times 10^{12}\,M_{\odot} \leqslant M_{\rm vir} < 5 \times 10^{12}\,M_{\odot}$; continuous green lines, ELOs in the mass interval $M_{\rm vir} < 1.5 \times 10^{12}\,M_{\odot}$.

3.2 Masses and sizes at the scale of the baryonic object

Let us now turn to the study of ELOs at the scale of the baryonic objects themselves: that is, at scales of some tens of kpc. Physically, the mass parameter at the ELO scale is $M^{\rm cb}_{\rm bo}$, the total amount of cold baryons that have reached the central volume of the haloes, forming an ELO. Most of these cold baryons have turned into stars, depending on the strength of the dynamical activity in the volume surrounding the proto-ELO at high z and, also, on the values of the SF parameters. $M^{\rm star}_{\rm bo}$ is the stellar mass. It can be estimated from luminosity data through modelling (see Kauffmann et al. 2003a, for example).[2] Effective or half-mass radii at the baryonic object scale, $r^{\rm cb}_{\rm e,bo}$ and $r^{\rm star}_{\rm e,bo}$, can be defined as those radii enclosing half the $M^{\rm cb}_{\rm bo}$ or $M^{\rm star}_{\rm bo}$ masses, respectively. These are the relevant size scales for the intrinsic ELOs, but the observationally relevant size scales are the *projected* half-mass radii. They are determined from $M_{\rm cyl}(R)$, the integrated projected mass density in concentric cylinders of radius R for the different constituents. For example, $r^{\rm cb}_{\rm e,bo}$ and $r^{\rm star}_{\rm e,bo}$ are the projected radii where $M^{\rm cb}_{\rm cyl}(R)$ and $M^{\rm star}_{\rm cyl}(R)$ are equal to $M^{\rm cb}_{\rm bo}/2$ and to $M^{\rm star}_{\rm bo}/2$, respectively. Significant parameters at the baryonic object scale are listed in Table 4. Note that ELOs have a lower limit in their stellar mass content of $3.8 \times 10^{10}\,M_{\odot}$ (see Kauffmann et al. 2003b for a similar result in SDSS early-type galaxies).

To illustrate how the halo total mass, $M_{\rm vir}$, determines the ELO structure at kpc scales, in Figs 4 and 5 we draw $M^{\rm star}_{\rm bo}$ and $r^{\rm star}_{\rm e,bo}$ versus $M_{\rm vir}$, respectively, for the ELO sample. A good correlation is apparent in Fig. 4, where it is shown that ELO stellar masses are mainly determined by the halo mass scale, $M_{\rm vir}$, with only a very slight dependence on the SF parametrization (SF-A type ELOs have a slightly higher stellar content than their SF-B counterparts, as expected). Fig. 5 shows also a good correlation between the length-scales for the stellar masses and $M_{\rm vir}$, but now the sizes depend also

[2] The results of these authors indicate that, for SDSS E galaxies, the stellar-mass-to-light ratio, $\gamma^{\rm star}$, can be taken to be constant in the range of absolute luminosities $M < -21$ (see Kauffmann et al. 2003b). The values of the logarithm of this ratio are $\log \gamma^{\rm star}_{r} \simeq 0.53$ and $\log \gamma^{\rm star}_{z} \simeq 0.25$, with dispersions $\sigma_S < 0.15$ and 0.1, in the r and z SDSS bands, respectively.

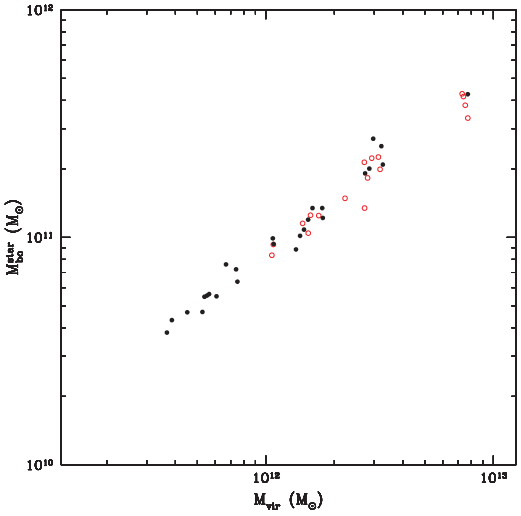

Figure 4. Stellar masses at the baryonic object scale scale versus halo mass for the ELO sample. Symbols are as in previous figures

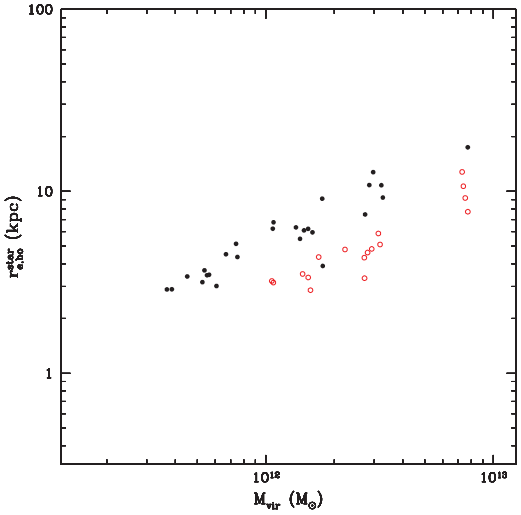

Figure 5. The 3D half-mass radii for stellar masses at the baryonic object scale versus halo mass for the ELO sample. Symbols are as in previous figures.

on the SF parameters. The physical foundations of this behaviour are the same as discussed in Section 3.1.

The observationally relevant scalelengths are the projected half-mass radii $R^{\rm star}_{\rm e,bo}$. Their correlations with their intrinsic 3D counterparts $R^{\rm star}_{\rm e,bo}$ are very good, as illustrated in Fig. 6, where the very low dispersion in the plots of the $c_{\rm rp} \equiv r^{\rm star}_{\rm e,bo}/R^{\rm star}_{\rm e,bo}$ ratios versus the stellar mass $M^{\rm star}_{\rm bo}$ can be appreciated. The results of a fit to a power law of the form $c_{\rm rp} = A_{\rm rp}\,(M^{\rm star}_{\rm bo})^{\beta_{\rm rp}}$[3] are given in Table 5, where we see

[3] We list the different ratio definitions we use in this paper and their corresponding logarithmic slopes in Table 2.

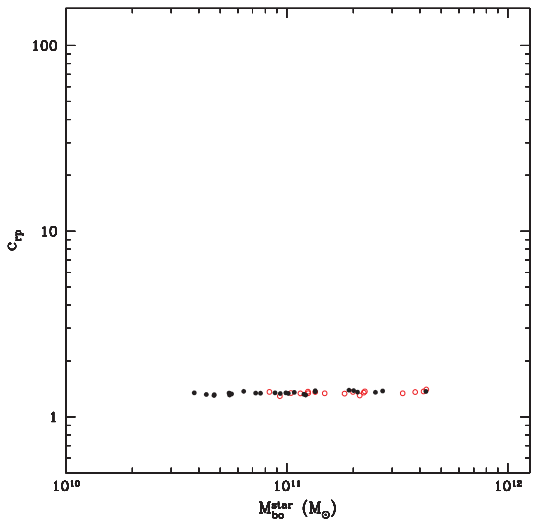

Figure 6. The $c_{rp} \equiv r_{e,bo}^{star}/R_{e,bo}^{star}$ ratios versus the stellar masses at the baryonic object scale. Symbols are as in previous figures.

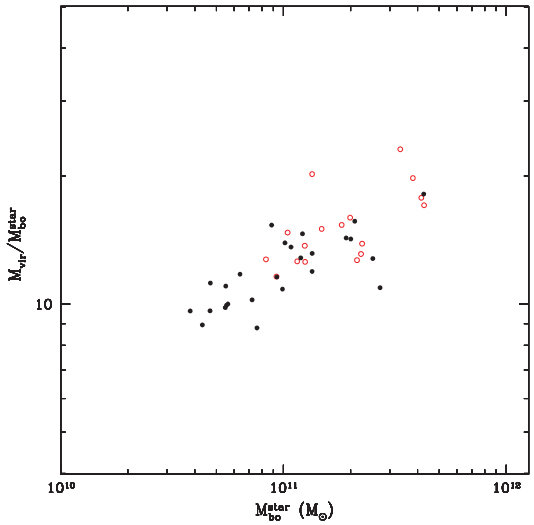

Figure 7. The M_{vir}/M_{bo}^{star} ratios as a function of the ELO mass scale. Symbols are as in previous figures.

Table 5. Slopes for linear fits.

	SF-A		SF-B	
M_1	0.256	±0.035	0.281	±0.048
β_{vir}	0.221	±0.083	0.237	±0.158
β_M	−0.204	±0.116	−0.247	±0.189
β_F	0.025	±0.048	0.022	±0.081
β_{vd}	0.021	±0.041	0.076	±0.075
β_{vpc}	−0.044	±0.029	−0.044	±0.093
β_{rd}	−0.225	±0.127	−0.316	±0.199
β_{rp}	0.019	±0.009	0.016	±0.017

Column 2: the slopes of the $\kappa_3^D = M_1\kappa_1^D + M_0$ relation (direct fits); the slopes of the M_{vir}/M_{bo}^{star} and $c_i \propto (M_{bo}^{star})^{\beta_i}$ scaling relations for the the SF-A sample, calculated in log–log plots through direct fits. Column 3: their respective 95 per cent confidence intervals. Columns 4 and 5: same as columns 2 and 3 for the SF-B sample.

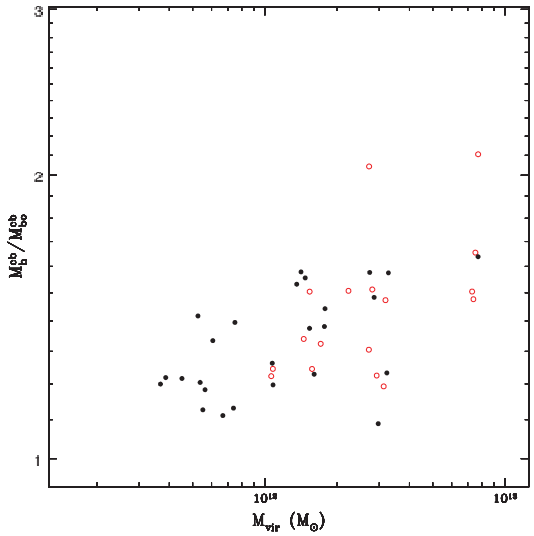

Figure 8. The M_h^{cb}/M_{bo}^{cb} ratios as a function of the ELO mass scale. Symbols are as in previous figures.

that the c_{rp} ratios show a very mild mass dependence in the SF-A sample and none in the SF-B sample. This result is important because it indicates that the observationally available *projected* radii $R_{e,bo}^{star}$ are robust estimators of the physically meaningful size scales $R_{e,bo}^{star}$.

We now address the correlations of normalized mass and size scales. The increasing behaviour of the M_{vir}/M_{bo}^{cb} and M_{vir}/M_{bo}^{star} ratios with increasing mass scale are very interesting. In particular, the last ratio (Fig. 7) follows the same trends as the empirical M_e/L versus L relation (see Bernardi et al. 2003b). The results of a fit to a power law of the form $M_{vir}/M_{bo}^{star} = A_{vir}(M_{vir}/M_{bo}^{star})^{\beta_{vir}}$ are given in Table 5, where we see that they do not depend on the SF parametrization.

To have an idea of how important cold baryon infall has been at the baryonic object scale relative to that at the halo scale, in Fig. 8 the M_h^{cb}/M_{bo}^{cb} ratios are drawn as a function of the ELO mass scale. We see that, in any case, more than half the mass of cold baryons inside the virial radii is concentrated in the central baryonic object, and that there is a mass effect, in the sense that this fraction grows with decreasing ELO mass scale, and no appreciable SF effect.

Concerning sizes, in Fig. 9 we plot the $c_{rd} \equiv r_{e,h}^{tot}/r_{e,bo}^{star}$ ratios versus the M_{bo}^{star} mass scale for ELOs in both the SF-A and the SF-B samples. In this figure, the effects of SF parametrization are clear: SF-A type ELOs have larger sizes relative to the halo size than SF-B type ELOs. There is also a clear mass effect, with more massive ELOs less concentrated relative to the total mass distribution than less massive ones (i.e. spatial homology breaking; note, how-

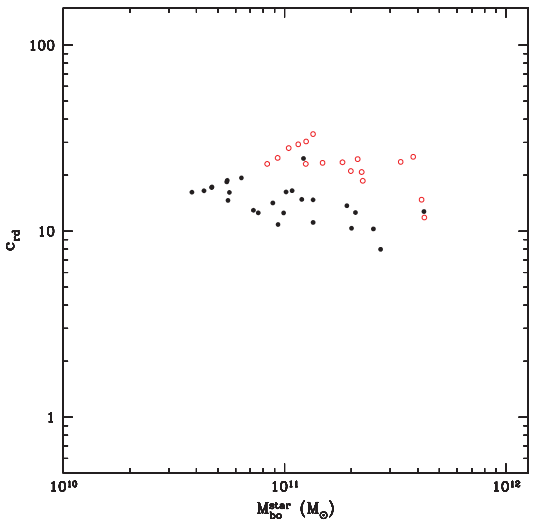

Figure 9. The $c_{rd} \equiv r_{e,h}^{tot}/r_{e,bo}^{star}$ ratios as a function of the ELO mass scale. Symbols are as in previous figures. Spatial homology breaking is clear in this figure.

ever that the scatter is important). Moreover, Fig. 9 suggests that this trend does not significantly depend on the SF parametrization. These indications are quantitatively confirmed through a fit to a power law $c_{rd} = A_{rd}(M_{vir}/M_{bo}^{star})^{\beta_{rd}}$ (see Table 5) and have interesting implications to explain the tilt of the observed FP.

4 KINEMATICS

4.1 Three-dimensional velocity distributions

Shapes and mass density profiles (i.e. positions) are related to the 3D velocity distributions of relaxed E galaxies through the Jeans equation (see Binney & Tremaine 1987). Observationally, the information on such 3D distributions is not available for external galaxies; only the LOSVDs can be inferred from their spectra. They have been found to be close to Gaussian (Binney & Tremaine 1987; van der Marel & Franx 1993), so that simple equilibrium models can be expected to adequately describe their dynamical state (de Zeeuw & Franx 1991). The complete 6D phase-space information for each of the particles sampling the ELOs provided by numerical simulations allows us to calculate the velocity profiles, $V_{cir}(r)$, the 3D profiles for the velocity dispersion, $\sigma_{3D}(r)$, and their corresponding anisotropy profiles. The anisotropy is defined as

$$\beta_{ani} = 1 - \frac{\sigma_t^2}{2\sigma_r^2}, \qquad (4)$$

where σ_r and σ_t are the radial and tangential velocity dispersions ($\sigma_t^2 = \sigma_\theta^2 + \sigma_\phi^2$), relative to the centre of the object. These profiles, as well as the LOS velocity $V_{los}(R)$ and LOS velocity dispersion $\sigma_{los}(R)$ profiles, are analysed in detail in Oñorbe et al. (in preparation). Fig. 10 illustrates the more outstanding results we have obtained: ELO velocity dispersion profiles in three dimensions are slightly decreasing for increasing r, both for dark matter and stellar particles, $\sigma_{3D}^{dark}(r)$ and $\sigma_{3D}^{star}(r)$. It has been found that $[\sigma_{3D}^{dark}(r)]^2 \sim (1.4\text{–}2)\,[\sigma_{3D}^{star}(r)]^2$, as Loewenstein (2000) had found on theoretical grounds. This

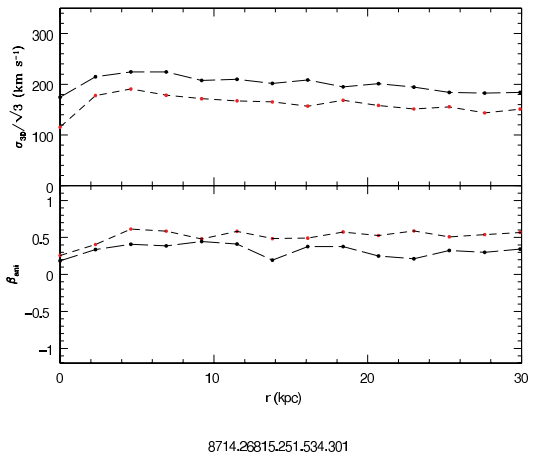

8714.26815.251.534.301

Figure 10. The $\sigma_{3D}(r)$ profiles of a typical ELO in the SF-A sample. Also shown are their anisotropy profiles $\beta_{ani}(r)$. Long-dashed lines, dark matter; short-dashed lines, stars.

is so because stars are formed from gas that has lost energy by cooling. This result on kinematical segregation is very interesting because it has the implication that the use of stellar kinematics to measure the total mass of Es could result in inaccurate values. The study of anisotropy has shown that it is always positive and almost non-varying with r (recall, however, that ELOs are non-rotating and that they have been identified as dynamically relaxed objects, so that there are not recent mergers in our samples). The stellar component generally shows more anisotropy than the dark component, possibly coming from the radial motion of the gas particles that gave rise to the stars.

4.2 Global parameters for the velocity distribution

Only for a limited number of Es are the $V_{los}(R)$ or $\sigma_{los}(R)$ profiles available. Observationally, a useful characterization of the velocity dispersion of an E galaxy is provided by its central stellar LOS velocity dispersion, $\sigma_{los,0}$. It corresponds to the velocity dispersion of the stellar (as opposed to dark matter or other) component. Due to its interest, $\sigma_{los,0}$ has deserved important attention in literature and it was measured for several E galaxy samples before the SDSS results (Djorgovski & Davis 1987; Dressler et al. 1987; Faber et al. 1987; Lucey et al. 1991; Jørgensen et al. 1993, 1996; Kelson et al. 1997, 2000; Bernardi et al. 2002). In Table 4, the values of $\sigma_{los,0}^{star}$ for the ELO sample are listed.[4] In Fig. 11 we show the good correlation between $\sigma_{los,0}^{star}$ and the virial mass M_{vir}.

Physically, a measure of the average dynamical state of stars in the ELO itself is provided by their mean square velocity relative to the ELO centre of mass, or average 3D velocity dispersion $\sigma_{3,bo}^{star}$, of which the observationally available $\sigma_{los,0}^{star}$ parameter is assumed to be a fair estimator. To test this point, in Fig. 12 we plot the $c_{vpc} \equiv (\sigma_{3,bo}^{star})^2/3(\sigma_{los,0}^{star})^2$ ratios versus the ELO mass scale. We see that no mass effect is apparent and this is quantitatively

[4] Recall that the central LOS velocity dispersion for the *stellar* component of ELOs is written as $\sigma_{los,0}^{star}$, with a 'star' superscript to distinguish it from that of the other ELO components.

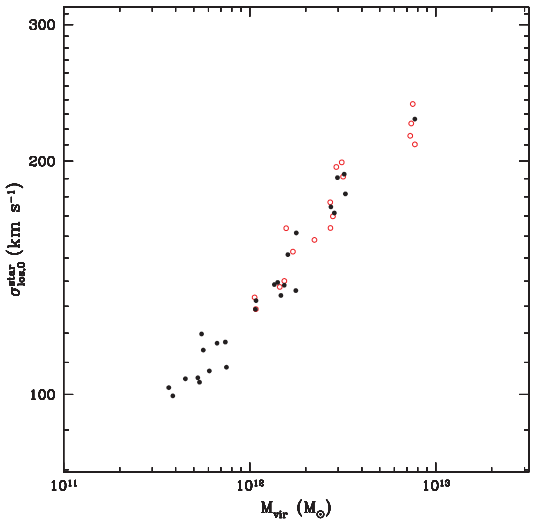

Figure 11. The correlation between the central line-of-sight velocity dispersion and the virial mass for the ELO samples. Symbols are as in previous figures.

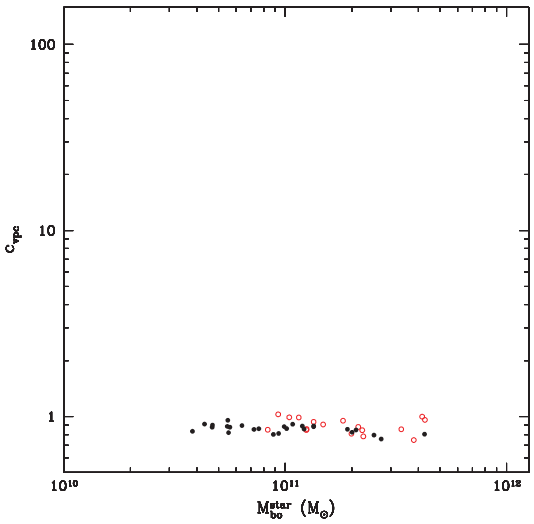

Figure 12. $c_{vpc} \equiv (\sigma^{star}_{3,bo})^2/3\ (\sigma^{star}_{los,0})^2$ ratios versus the ELO mass scale. Symbols are as in previous figures.

confirmed in Table 5, where the results of a fit of the form $c_{vpc} = A_{vpc}(M_{vir}/M^{star}_{bo})^{\beta_{vpc}}$ are given. We also see that due to radial anisotropy, $c_{vpc} < 1$, with no SF parametrization effect. Therefore, there is no mass bias when using $\sigma^{star}_{los,0}$ as an estimator for $\sigma^{star}_{3,bo}$, but some warnings are in order concerning anisotropy effects.

A significant velocity dispersion parameter for ELOs at the halo scale is $\sigma^{tot}_{3,h}$, the average 3D velocity dispersion of the whole E, including both dark and baryonic matter. According with equation (2), this is the velocity dispersion entering into the virial theorem for the whole ELO configuration. To test that this is in fact the case, in

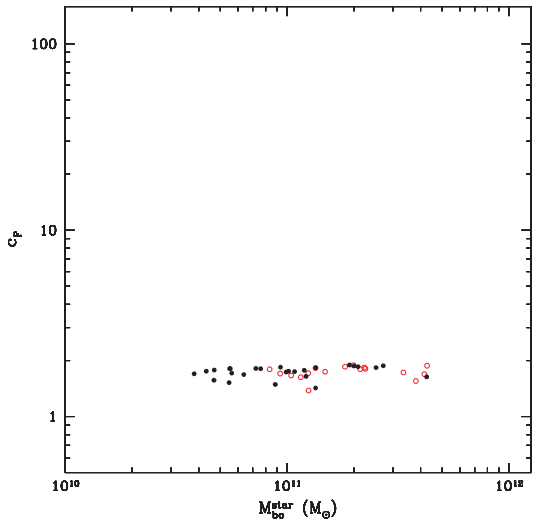

Figure 13. The $c_F \equiv GM_{vir}/(\sigma^{tot}_{3,h})^2\, r^{tot}_{e,h}$ form factors (see equation 2) versus the ELO mass scale. Symbols are as in previous figures. This figure confirms that $r^{tot}_{e,h}$ and $\sigma^{tot}_{3,h}$ are the size and velocity dispersion ELO parameters that must be used in the virial theorem.

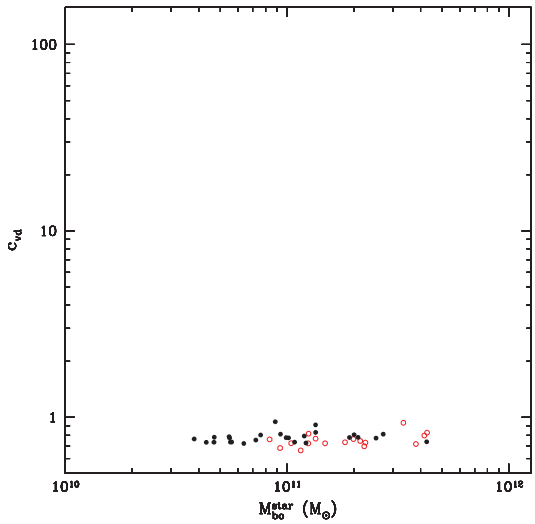

Figure 14. The $c_{vd} \equiv (\sigma^{tot}_{3,h}/\sigma^{star}_{3,bo})^2$ ratios (average kinematical segregation) as a function of the ELO mass scale. Symbols are as in previous figures. No dynamically broken homology can be seen in this figure, but the kinematical segregation between dark matter and stars is clear.

Fig. 13 we plot the $c_F \equiv GM_{vir}/(\sigma^{tot}_{3,h})^2 r^{tot}_{e,h}$ form factors (see equation 2) as a function of M^{star}_{bo}. The lack of any significant mass or SF parametrization effects in this figure is quantitatively confirmed through a fit to power laws of the form $c_F = A_F(M_{vir}/M^{star}_{bo})^{\beta_F}$, whose results in Table 5 are consistent with c_F being independent of the ELO mass scale or SF parameter values. Note also that the c_F values are as expected (Binney & Tremaine 1987).

Once we have confirmed that when writing the virial theorem for an ELO configuration, $\sigma^{\rm tot}_{3,\rm h}$ is the velocity dispersion one has to use, let us remind that one has to be careful when using $\sigma^{\rm star}_{\rm los,0}$ or $\sigma^{\rm star}_{3,\rm bo}$ as estimators for this physically meaningful quantity. In Fig. 14, we plot the $c_{\rm vd} \equiv (\sigma^{\rm tot}_{3,\rm h}/\sigma^{\rm star}_{3,\rm bo})^2$ ratios, which measure how dissipation and concentration affect, on average, the relative values of the dispersion at the halo scale (involving also dark matter) and at the baryonic object scale. No mass effects are apparent in this figure, but an average kinematical segregation is clear [see Table 5 for the results of a fit to the expression $c_{\rm vd} = A_{\rm vd}(M_{\rm vir}/M^{\rm star}_{\rm bo})^{\beta_{\rm vd}}$]. These are important results, which could have interesting observational implications.

5 THE INTRINSIC DYNAMICAL PLANES AND THE DYNAMICAL FUNDAMENTAL PLANES

5.1 The dynamical plane relations of ELO samples

In the last section, it has been shown that the mass, size and velocity dispersion parameters *at the halo scale* satisfy virial relations. This result is, however, at odds with the tilt of the observed FP of the Es discussed in Section 1, which involves the L,$R^{\rm light}_{\rm e}$ and $\sigma_{\rm los,0}$ observed variables, whose virtual counterparts describe the ELO at *the scale of the baryonic object*. Therefore, we have first to analyse whether or not the mass, size and velocity dispersion of ELOs at this scale define planes tilted relative to the virial one.

To this end, we have carried out a principal component analysis (PCA) of the SF-A and SF-B samples in the 3D variables $E \equiv \log_{10}M^{\rm star}_{\rm bo}$, $r \equiv \log_{10}r^{\rm star}_{\rm e,bo}$ and $v \equiv \log_{10}\sigma^{\rm star}_{3,\rm bo}$ through their 3×3 correlation matrix **C**. We have used 3D variables rather than projected ones to circumvent projection effects, which add noise to the correlations (see, for example, Fig. 12). We have found that, irrespective of the SF parametrization, one of the eigenvalues of **C** is considerably smaller than the others (see Table 6), so that ELOs populate in any case a flattened ellipsoid close to a two-dimensional (2D) plane in the (E, r, v) space that we call the IDP; the FP is the observed manifestation of this IDP. The eigenvectors of **C** indicate that the projection

$$E - \tilde{E} = \alpha^{\rm 3D}(r - \tilde{r}) + \gamma^{\rm 3D}(v - \tilde{v}), \quad (5)$$

where $\tilde{E}$, $\tilde{r}$ and $\tilde{v}$ are the mean values of the E, r and v variables, shows the IDP viewed edge-on. Table 6 gives the eigenvalues of the correlation matrix **C**(λ_1, λ_2, λ_3), the planes equation (5), as well as their corresponding thicknesses σ_{Erv}, both for the SF-A and SF-B samples. The IDPs are in fact tilted relative to the virial plane (characterized by $\alpha = 1, \gamma = 2$), and their scatter is very low as measured by their thicknesses σ_{Erv}. Note that the eigenvalues of the PCA analysis are not dependent on the SF parametrization.

In Fig. 15, we plot the (E, v), (E, r) and (r, v) projections of the IDPs corresponding both to the SF-A and the SF-B samples. We see that the three projections show correlations and that these are very tight for the first of them.

5.2 Comparing the IDP to the observed FP of elliptical galaxies

The next step is to compare the results on the IDPs we have found with the tilt and the scatter of the observed FP. We note that the r and v variables are not observationally available, so we have to use their projected counterparts. Assuming that the projected stellar *mass* density profile, $\Sigma^{\rm star}(R)$, can be taken as a measure of the surface *brightness* profile, then $\langle\Sigma^{\rm star}\rangle_{\rm e} = c\langle I^{\rm light}\rangle_{\rm e}$, with c a constant, and $R^{\rm star}_{\rm e,bo} \simeq R^{\rm light}_{\rm e}$ and we can look for an FP (hereafter, the dynamical FP) in the 3D space of the structural and dynamical parameters $R^{\rm star}_{\rm e,bo}$, $\langle\Sigma^{\rm star}\rangle_{\rm e}$ and $\sigma^{\rm star}_{\rm los,0}$, directly provided by the hydrodynamical simulations. To make this analysis as clear as possible, we transform to a κ-like orthogonal coordinate system, the dynamical $\kappa^{\rm D}_i$ system, $i = 1, 2, 3$, similar to that introduced by Bender et al. (1992), but using $R^{\rm star}_{\rm e,bo}$ instead of $R^{\rm light}_{\rm e}$ and $\langle\Sigma^{\rm star}\rangle_{\rm e}$ instead of $\langle I^{\rm light}\rangle_{\rm e}$, and, consequently, free of age, metallicity or IMF effects. The dynamical $\kappa^{\rm D}_i$ variables can be written as

$$\kappa^{\rm D}_1 \equiv \left[\log\left(\sigma^{\rm star}_{\rm los,0}\right)^2 + \log R^{\rm star}_{\rm e,bo}\right] \Big/ \sqrt{2}, \quad (6)$$

$$\kappa^{\rm D}_2 \equiv \left[\log\left(\sigma^{\rm star}_{\rm los,0}\right)^2 + 2\log\left\langle\sum{}^{\rm star}\right\rangle_{\rm e} - \log R^{\rm star}_{\rm e,bo}\right] \Big/ \sqrt{6}, \quad (7)$$

$$\kappa^{\rm D}_3 \equiv \left[\log\left(\sigma^{\rm star}_{\rm los,0}\right)^2 - \log\left\langle\sum{}^{\rm star}\right\rangle_{\rm e} - \log R^{\rm star}_{\rm e,bo}\right] \Big/ \sqrt{3}, \quad (8)$$

and they are related to the κ coordinates through the expressions: $\kappa_1 \simeq \kappa^{\rm D}_1$, $\kappa_2 \simeq \kappa^{\rm D}_2 - \sqrt{6}/3\log(M^{\rm star}_{\rm bo}/L)$ and $\kappa_3 \simeq \kappa^{\rm D}_3 + \sqrt{3}/3\log(M^{\rm star}_{\rm bo}/L)$. We discuss the tilt and the scatter of the dynamical FP separately. We first address the tilt issue. We use at this stage for the $R^{\rm star}_{\rm e,bo}$ and $\sigma^{\rm star}_{\rm los,0}$ variables the averages over three orthogonal LOS projections, to minimize the scatter in the plots caused by projection effects.

Fig. 16 plots $\kappa^{\rm D}_3$ versus $\kappa^{\rm D}_1$ (top) and $\kappa^{\rm D}_2$ versus $\kappa^{\rm D}_1$ (bottom) for ELOs in both the SF-A and SF-B samples. We also drew the 2σ concentration ellipses in the respective variables, as well as its major and minor axes, for the SDSS early-type galaxy sample in the SDSS z band (solid lines) and in the r band (point lines) as analysed by Bernardi et al. (2003b,c). The most outstanding feature of this figure (upper panel) is the good scaling behaviour of $\kappa^{\rm D}_3$ versus $\kappa^{\rm D}_1$, with a very low scatter (see the slopes M_1 in Table 5; note that the slopes for the SF-A and SF-B samples are consistent within their errors, while the zero-points depend on the SF parametrization through the ELO sizes). Another interesting feature of Fig. 16 is that it shows that most of the values of the $\kappa^{\rm D}_i$ coefficients are within the 2σ concentration ellipses in both plots for ELOs formed

Table 6. Results of PCA at $z = 0$.

Sample	No.	$\tilde{E}$	$\tilde{r}$	$\tilde{v}$	λ_1	λ_2	λ_3	$\alpha^{\rm 3D}$	$\gamma^{\rm 3D}$	σ_{Erv}
SF-A	26	10.993	0.746	2.335	0.128 93	0.003 55	0.000 13	0.427	2.066	0.011
SF-B	17	11.259	0.695	2.453	0.093 42	0.002 92	0.000 14	0.249	2.449	0.012

Column 2: ELO number in the sample.
Columns 3, 4 and 5: sample mean values of the E, r and v variables.
Columns 6, 7 and 8: eigenvalues of the correlation matrix.
Columns 9 and 10: coefficients of the plane (equation 5).
Column 11: IDP scatter in the E, r and v variables.

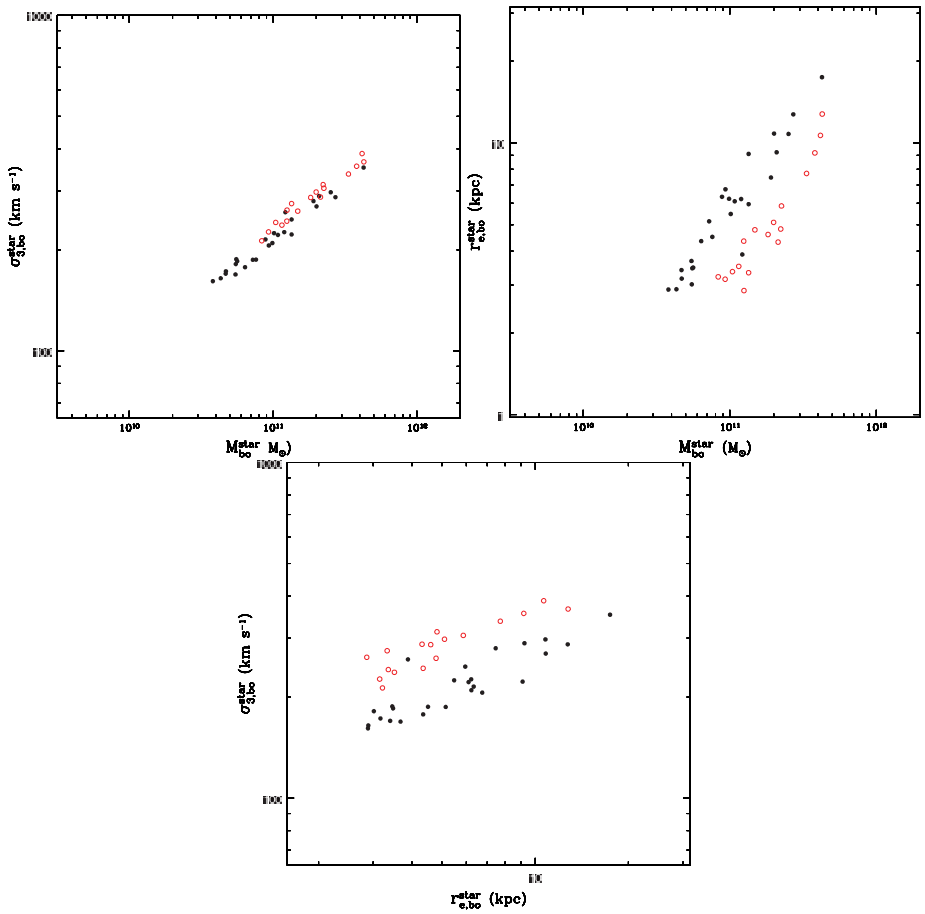

Figure 15. The IDPs for the SF-A and SF-B samples. Projections on the (E, v), (E, r) and (r, v) coordinate planes are shown.

in SF-A type simulations, with a slightly worse agreement for ELOs in the SF-B sample. This means that ELOs have counterparts in the real world (SDTS04). It is worth mentioning that these results are stable against slight changes in the values of the $\Omega_\Lambda, \Omega_{\rm baryon}$ or h parameters; for example, we have tested that using their preferred *WMAP* values (Spergel et al. 2003) shows results negligibly different to those plotted in Fig. 16. Finally, we note that either the dynamical or the observed FPs are not homogeneously populated: both SDSS Es and ELOs occupy only a region within these planes (see Fig. 16 lower panel, see also Guzmán et al. 1993; Márquez et al. 2000). This means that, from the point of view of their structure and dynamics, ELOs are a two-parameter family where the two parameters are not fully independent. Moreover, concerning ELOs, the occupied region changes when the SF parameters change. The reason for this change is that the ELO sizes decrease as SF becomes more difficult, because the amount of dissipation experienced by the stellar component along ELO assembly increases.

We now turn to consider the scatter of the dynamical FP for the ELO samples and compare it with the scatter of the FP for the SDSS E sample, calculated as the square root of the smallest eigenvalue of the 3×3 covariance matrix in the E (or $\log L$), $V \equiv \log \sigma^{\rm star}_{\rm los,0}$ and $R \equiv \log R^{\rm star}_{\rm e,bo}$ variables (Saglia et al. 2001). As Fig. 16 suggests, when projection effects are circumvented by taking averages over different directions, the resulting 3D orthogonal scatter for ELOs is smaller than for SDSS Es ($\sigma_{EVR} = 0.0164$ and $\sigma_{EVR} = 0.0167$ for the SF-A and SF-B samples, respectively, to be compared with $\sigma_{LVR} = 0.0489$ for the SDSS in the $\log L, V \equiv \log \sigma_{\rm los,0}$ and $R \equiv \log R^{\rm light}_{\rm e}$ variables). To estimate the contribution of projection effects to the observed scatter, we have calculated the orthogonal scatter for ELOs when no averages over projection directions for the $R^{\rm star}_{\rm e,bo}$ and $\sigma^{\rm star}_{\rm los,0}$ variables are made. The scatter ($\sigma_{EVR} = 0.0238$ and $\sigma_{EVR} = 0.0214$ for the SF-A and SF-B samples) increases, but it is still lower than observed. This indicates that a contribution from stellar population effects is needed to explain the scatter of the observed FP, as suggested by different authors (see, for example, Pahre et al. 1998; Trujillo et al. 2004).

5.3 Clues on the physical origin of the IDP tilt

We now address the issue of the physical origin of the tilt of ELO IDPs relative to the virial relation. As discussed in Section 1, a non-zero tilt can be caused by a mass dependence of the

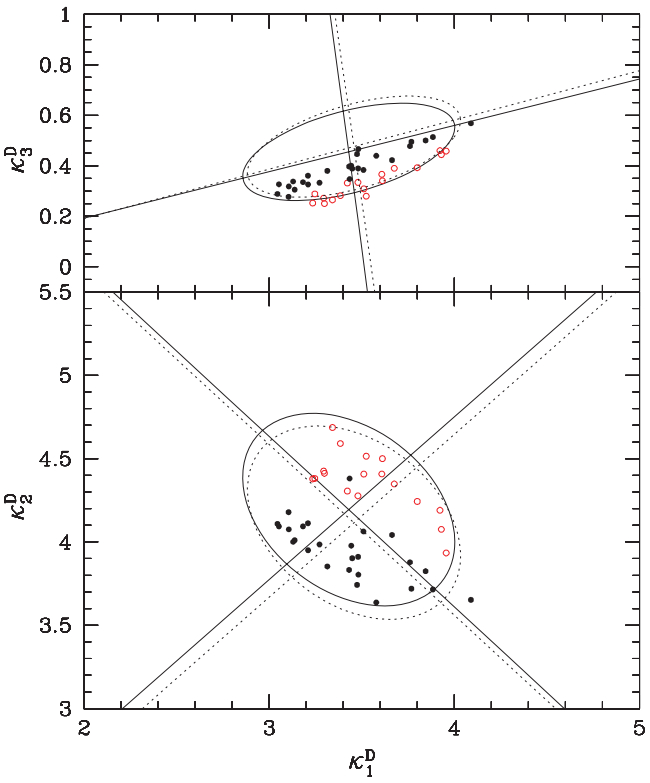

Figure 16. Dynamical Fundamental Plane in the κ^D system. Edge-on projection (top panel) and nearly face-on projection (bottom panel) of the dynamical FP of ELOs in the κ^D variables (black filled symbols, SF-A sample; red open symbols, SF-B sample). We also draw the respective concentration ellipses (with their major and minor axes) for the SDSS early-type galaxy sample from Bernardi et al. (2003b) in the *z* band (solid line) and the *r* band (dashed line). See text for more details.

mass-to-light ratio $M_{\rm vir}/L$, of the mass structure coefficients $c_{\rm M}^{\rm vir} \equiv \frac{GM_{\rm vir}}{3\sigma^2_{\rm los,0}R_{\rm e}^{\rm light}}$, or of both of them. We examine these possibilities in turn.

(i) We first note that the mass-to-light ratio can be written as

$$M_{\rm vir}/L = A_{\rm vir}\left(M_{\rm bo}^{\rm star}\right)^{\beta_{\rm vir}} \times \gamma^{\rm star}, \tag{9}$$

where $\gamma^{\rm star} \equiv M_{\rm bo}^{\rm star}/L$ is the stellar mass-to-light ratio, which, as already explained, can be considered to be independent of the E galaxy luminosity or ELO mass scale. Fig. 7 and the values of the $\beta_{\rm vir}$ slopes given in Table 5 indicate that the dark to bright mass content of ELOs increases with their mass, contributing a tilt to their IDPs. Similar results have also been found in preprepared simulations of dissipative mergers (Robertson et al. 2006).

(ii) Writing the $c_{\rm M}^{\rm vir}$ mass structure coefficients as power laws $c_{\rm M}{}^{\rm vir} = A_M(M_{\rm bo}^{\rm star})^{\beta_M}$, ELO homology would imply $\beta_M = 0$. To elucidate whether or not this is the case, the β_M slopes have been measured on the ELO samples through direct fits in log–log scales. The results are given in Table 5, where we see that the homology is in fact broken both for SF-A or SF-B samples. To deepen into the causes of this behaviour, we use equations (2) and (3) to write

$$c_{\rm M}^{\rm vir} = c_{\rm F}c_{\rm rd}c_{\rm rp}c_{\rm vd}c_{\rm vpc}, \tag{10}$$

where the $c_{\rm i}$ coefficients with i = rd, rp, vd, vpc have been defined in Section 3.2 and with $i = F$ in Section 4.2. Taking into account the power-law forms of these coefficients, we have

$$\beta_{\rm M} = \beta_{\rm F} + \beta_{\rm rd} + \beta_{\rm rp} + \beta_{\rm vd} + \beta_{\rm vpc}, \tag{11}$$

when the $\beta_{\rm i}$ slopes are calculated through direct fits. From Table 5, we see that the main contribution to the homology breaking comes from the $c_{\rm rd}$ coefficients (i.e. spatial homology breaking, see Section 3.2 and Oñorbe et al. 2005), while, as previously discussed, no dynamical homology breaking (see Section 4.2) or projection effects are important in our ELO samples.

6 SUMMARY, DISCUSSION AND CONCLUSIONS

6.1 Summary

We present an analysis of the sample of ELOs formed in 10 different cosmological simulations, run within the same global flat Λ cosmological model, roughly consistent with observations. The normalization parameter has been taken slightly high, $\sigma_8 = 1.18$, as compared with the average fluctuations of 2dFGRS or SDSS galaxies to mimic an active region of the Universe. Newton laws and hydrodynamical equations have been integrated in this context, with a standard cooling algorithm and an SF parametrization through a Kennicutt–Schmidt-like law, containing our ignorance about its

details at sub-kpc scales. No further hypotheses to model the assembly processes have been made. Individual galaxy-like objects naturally appear as an output of the simulations, so that the physical processes underlying mass assembly can be studied. Five out of the 10 simulations (the SF-A type simulations) share the SF parameters and differ in the seed used to build up the initial conditions. To test the role of SF parametrization, the same initial conditions have been run with different SF parameters making SF more difficult, contributing another set of five simulations (the SF-B type simulations). ELOs have been identified in the simulations as those galaxy-like objects at $z = 0$ having a prominent, non-rotating dynamically relaxed spheroidal component made out of stars, with no extended discs and very low gas content. This stellar component is embedded in a dark matter halo that contributes an important fraction of the mass at distances from the ELO centre larger than $\sim$10–15 kpc. No ELOs with stellar masses below 3.8×10^{10} $M_\odot$ or virial masses below 3.7×10^{11} $M_\odot$ have been found that met the selection criteria (see Kauffmann et al. 2003b for a similar result in SDSS galaxies, and see Dekel & Birnboim 2006 and Cattaneo et al. 2006 for a possible physical explanation). ELOs have also an extended halo of hot, diffuse gas. Stellar and dark matter particles constitute a dynamically hot component with an important velocity dispersion and, except in the very central regions, a positive anisotropy.

The information about position and velocity distributions of the ELO particles of different kinds (dark matter, stars, cold gas, hot gas) provided by the simulations allows a detailed study of their intrinsical 3D mass and velocity distributions, as well as a measure of the parameters characterizing their structure and dynamics. In a forthcoming paper, we report on the 3D mass density, circular velocity and velocity dispersion profiles, as well as the projected stellar mass density profiles and the LOS velocity dispersion profiles. In this paper, we focus on a parameter analysis to quantify some of the previous results.

Mass, size and velocity dispersion scales for their different components have been measured in the ELO samples, both at the scale of their halo and at the scale of the baryonic object (a few tens of kpc). At the *halo scale*, the masses of both cold gas and stars, $M_{\rm h}^{\rm cb}$ and $M_{\rm h}^{\rm star}$, respectively, have been found to be tightly correlated with the halo total mass, $M_{\rm vir}$, with the ratios $M_{\rm h}^{\rm cb}/M_{\rm vir}$ and $M_{\rm h}^{\rm star}/M_{\rm vir}$ decreasing as $M_{\rm vir}$ increases (that is, massive objects miss cold baryons within $r_{\rm vir}$ when compared with less massive ELOs), presumably because gas gets more difficulties to cool and fall as $M_{\rm vir}$ increases. The overall half-mass radii, $r_{\rm e,h}^{\rm tot}$ shows also a very tight correlation with $M_{\rm vir}$. Half-mass radii for the cold baryon or stellar mass distributions have a more complex behaviour, as in these cases gas heating in shocks and energy losses due to gas cooling are in competition to determine these distributions.

A very important result we have found when analysing ELOs at the *scale of the baryonic object*, is that $M_{\rm vir}$ plays an important role to determine the ELO structure also below a few tens of kpc scales. In fact, both the masses of cold baryons $M_{\rm bo}^{\rm cb}$ (i.e. those baryons that have reached the central regions of the configuration) and of stars $M_{\rm bo}^{\rm star}$ show a good correlation with $M_{\rm vir}$, and, moreover, the $M_{\rm bo}^{\rm cb}/M_{\rm vir}$ and $M_{\rm bo}^{\rm star}/M_{\rm vir}$ ratios (i.e. the relative content of cold baryons or stars versus total mass) decrease as $M_{\rm vir}$ increases. This is the same qualitative behaviour shown by these ratios observationally in the SDSS data and, also, by ELOs at the halo scale. The dependence of $M_{\rm bo}^{\rm cb}$ or $M_{\rm bo}^{\rm star}$ on the SF parametrization is only very slight, with SF-A type ELOs having slightly more stars than their SF-B type counterparts. The half-mass radii for cold baryon and stellar masses, $r_{\rm e,bo}^{\rm cb}$ and $r_{\rm e,bo}^{\rm star}$, show also a good correlation with $M_{\rm vir}$, but now the values of the SF parameters also play a role, because their change implies a change in the time interval during which gas cooling is turned on, and this changes the ELO stellar mass distribution, i.e. its length-scale, so that ELO compactness increases from SF-A to SF-B type simulations. Another important result is that, regardless of the SF parametrizations used in this work, the relative distributions of the stellar and dark mass components in ELOs show a systematic trend measured through the $c_{\rm rd} \equiv r_{\rm e,h}^{\rm tot}/r_{\rm e,bo}^{\rm star}$ ratios, with stars relatively more concentrated as $M_{\rm vir}$ decreases (i.e. a quantification of the spatial homology breaking). Note that, to compare with observational data, the relevant parameters are the *projected* half-mass radii, $r_{\rm e,bo}^{\rm star}$. We have checked that they show an excellent correlation with the corresponding 3D half-mass radii, with the $c_{\rm rp} \equiv r_{\rm e,bo}^{\rm star}/R_{\rm e,bo}^{\rm star}$ ratios showing no significant dependence on the ELO mass scale.

Concerning kinematics, a useful characterization of the ELO velocity dispersion is the central stellar LOS velocity dispersion, $\sigma_{\rm los,0}^{\rm star}$, whose observational counterpart can be measured from E spectra. A very important result is the very tight correlation we have found between $M_{\rm vir}$ and $\sigma_{\rm los,0}^{\rm star}$, confirming that the observationally measurable $\sigma_{\rm los,0}$ is a fair virial mass estimator. In addition, $\sigma_{\rm los,0}^{\rm star}$ is closely related to the mean square velocity of both, the whole E at the halo scale (including the dark matter), $\sigma_{\rm 3,h}^{\rm tot}$, and the stellar component of the central object, $\sigma_{\rm 3,bo}^{\rm star}$. We have also found that the $c_{\rm vd} \equiv (\sigma_{\rm 3,h}^{\rm tot}/\sigma_{\rm 3,bo}^{\rm star})^2$ or the $c_{\rm vpc} \equiv (\sigma_{\rm 3,bo}^{\rm star})^2/3(\sigma_{\rm los,0}^{\rm star})^2$ ratios are roughly independent of the ELO mass scale. Therefore, ELOs do not show dynamically broken homology, even if their stellar and dark components are kinematically segregated (i.e. $c_{\rm vd} \neq 1$). This could lead to inaccurate determinations of the total mass of Es when using stellar kinematics.

A very important result is that, irrespective of the SF parametrization, the (logarithms of the) ELO stellar masses $M_{\rm bo}^{\rm star}$, stellar half-mass radii $r_{\rm e,bo}^{\rm star}$ and stellar mean square velocity of the central object $\sigma_{\rm 3,bo}^{\rm star}$ define IDPs. These planes are tilted relative to the virial plane and the tilt does not significantly depend on the SF parametrization, but the zero-point does. Otherwise, the IDP is not homogeneously populated, but ELOs, as well as E galaxies in the FP (Guzmán et al. 1993), occupy only a particular region defined by the range of their masses.

6.2 Testing possible resolution effects

To make sure that the results we report in this paper are not unstable under resolution changes, a control simulation with 128^3 dark matter and 128^3 baryonic particles, a gravitational softening of $\epsilon = 1.15$ kpc and the other parameters as in SF-A type simulations (the S128 simulation) has been run. The results of its analysis have been compared with those of a 2×64^3 simulation (the S64 simulation), whose initial conditions have been built up by randomly choosing one out of eight particles in the S128 initial conditions, so that every ELO in S128 has a counterpart in the lower resolution simulation and conversely. Due to the very high CPU time requirements for S128, the comparison has been made at $z = 1$. The results of this comparison are very satisfactory, as Fig. 17 illustrates (compare with Fig. 7).

6.3 The dimensionality of ELO and elliptical samples in parameter space

The IDPs and their occupations (see Section 6.1) reflect the fact that dark matter haloes are a two-parameter family (for example, the virial mass and the energy content or the concentration; see, for example, Hernquist 1990; Navarro, Frenk & White 1995, 1996;

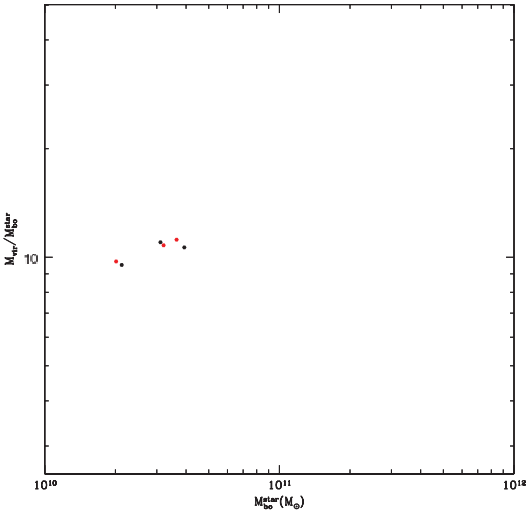

Figure 17. The $M_{\rm h}^{\rm cb}/M_{\rm bo}^{\rm cb}$ ratios as a function of the ELO mass scale for three ELOs identified at $z = 1$ in S128 (red) and their counterparts in S64 (black).

Manrique et al. 2003; Navarro et al. 2004) where the two parameters are correlated (see, for example, Bullock et al. 2001; Wechsler et al. 2002; Manrique et al. 2003). Adding gas implies that heating and cooling processes also play a role at determining the mass and velocity distributions, and, more particularly, the length-scales. However, as explained above, we have found that both the relative content and the relative distributions of the dark and baryonic mass components show systematic trends with the ELO mass scale, which can be written as power laws of the form $M_{\rm vir}/M_{\rm bo}^{\rm star} = A_{\rm vir}(M_{\rm bo}^{\rm star})^{\beta_{\rm vir}}$ and $r_{\rm e,h}^{\rm tot}/r_{\rm e,bo}^{\rm star} = A_{\rm rd}(M_{\rm bo}^{\rm star})^{\beta_{\rm rd}}$.

A first consequence of the regularity of the trends with the mass scale found in this paper is that no new parameters are added relative to the dark matter halo family, so that the baryonic objects are also a two-parameter family, and ELO structural and dynamical parameters define also a plane. A second consequence is that the plane is tilted relative to the halo plane (i.e. the virial plane) because $\beta_{\rm rd} - \beta_{\rm vir} \neq 0$. Finally, the plane is not homogeneously populated because of the mass-concentration halo correlation, which at the scale of the baryonic objects appears for example as a mass–size correlation. This explains the role played by $M_{\rm vir}$ to determine the intrinsic 3D correlations. In this paper, we also show that $\sigma_{\rm los,0}^{\rm star}$ is a fair empirical estimator of $M_{\rm vir}$, and this explains the central role played by $\sigma_{\rm los,0}$ in determining the observational correlations.

The FP shown by real E samples is the observational manifestation of the IDPs when using projected parameters $R_{\rm e,bo}^{\rm star}$, $\sigma_{\rm los,0}^{\rm star}$ and luminosity variables instead of stellar masses $M_{\rm bo}^{\rm star}$. We have taken advantage of the constancy of the stellar-mass-to-light ratios of Es in the SDSS (Kauffmann et al. 2003a,b) to put the E sample of Bernardi et al. (2003b,c) in the same projected variables we can measure in our virtual Es. We have found that the FPs shown by the two ELO samples are consistent with that shown by the SDSS E sample in the same variables, with no further need for any relevant contribution from stellar population effects to explain the observed tilt. These effects could, however, have contributed to the scatter of the observed FP, as the IDPs have been found to be thinner than the observed FP.

6.4 The physical origin of the tilt in a cosmological context

We now turn to discuss the physical origin of the trends given by the power laws $M_{\rm vir}/M_{\rm bo}^{\rm star} = A_{\rm vir}(M_{\rm bo}^{\rm star})^{\beta_{\rm vir}}$ and $r_{\rm e,h}^{\rm tot}/r_{\rm e,bo}^{\rm star} = A_{\rm rd}\,(M_{\rm bo}^{\rm star})^{\beta_{\rm rd}}$. As explained in Section 2, the simulations provide us with clues on the physical processes involved in E formation (see also DSS04 and DTal06). They also indicate that the dynamical plane appears at an early violent phase as a consequence of ELO assembly out of gaseous material, with cooling and on short time-scales, and it is preserved during a later, slower phase, where dissipationless merging plays an important role in stellar mass assembly (see more details in DTal06). Our simulations show that the physical origin of the trends above lie in the systematic decrease, with increasing ELO mass, of the relative amount of dissipation experienced by the baryonic mass component along ELO stellar mass assembly (DTal06; Oñorbe et al., in preparation). This possibility had been suggested by Bender et al. (1992), Guzmán et al. (1993) and Ciotti et al. (1996). Bekki (1998) first addressed it numerically in the framework of the merger hypothesis for E formation through preprepared simulations of dissipative mergers of disc galaxies, where the rapidity of the SF in mergers is controlled by a free efficiency parameter $C_{\rm SF}$. He shows that the SF rate history of galaxies determines the differences in dissipative dynamics, so that to explain the slope of the FP he *needs to assume* that more luminous galaxies are formed by galaxy mergers with a shorter time-scale for gas transformation into stars. Recently, Robertson et al. (2006) have confirmed these findings on the importance of dissipation to explain the FP tilt.

In this paper, we go a step further and analyse the FP of virtual Es formed in a cosmological context, where individual galaxy-like objects naturally appear as an output of the simulations. Our results essentially include previous ones and add important new information. First, our results on the role of dissipation to produce the tilt of the FP essentially agree with those obtained through dissipative preprepared mergers, but it is important to note that, moreover, more massive objects produced in the simulations *do have* older means and narrower spreads in their stellar age distributions than less massive ones (see details DSS04); this naturally appears in the simulations and need not be considered as an additional assumption. Secondly, the preservation of the FP in the slow phase of mass aggregation in our simulations also agrees with previous work based on dissipationless simulations of preprepared mergers (Capelato et al. 1995; Dantas et al. 2003; González-García & van Albada 2003; Boylan-Kolchin et al. 2005; Nipoti et al. 2003). Moreover, E properties recently inferred from observations (for example, the appearance of blue cores, Menanteau et al. 2004, and the increase of the stellar mass contributed by the E population since higher z, Bell et al. 2004; Conselice, Blackburne & Papovich 2005; Faber et al. 2005; see more details in DTal06) can also be explained in our simulations.

6.5 Conclusions

We conclude that the simulations provide a unified scenario where most current observations on Es can be interrelated. In particular, it explains the most important results relative to the physical origin of their FP relation (i.e. the FP tilt is due dissipative dynamics, and disipationless merging in the slow growth phase of mass assembly does not change the tilt). It is worth mentioning that this scenario shares some characteristics of previously proposed scenarios, but it

has also significant differences, mainly that most stars in E galaxies form out of cold gas that was never shock heated at the halo virial temperature and then formed a disc, as the conventional recipe for galaxy formation propounds (see discussion in Keres et al. 2005 and references therein). The scenario for E formation emerging from our simulations has the advantage that it results from simple physical laws acting on initial conditions that are realizations of power spectra consistent with observations of CMB anisotropies.

ACKNOWLEDGMENTS

This work was partially supported by the MCyT (Spain), through grants AYA-0973, AYA-07468-C03-02 and AYA-07468-C03-03 from the PNAyA, and also by the regional government of Madrid, through the ASTROCAM Astrophysics network. We thank the Centro de Computación Científica (UAM, Spain) for computing facilities. AS thanks FEDER financial support from the European Union.

REFERENCES

Ballesteros-Paredes J., Klessen R. S., McLow M.-M., Vázquez-Semadeni E., 2006, in Reipurth B., Jewitt D., Keil K., eds, Protostars an dPlanets V. Univ. Arizona Press, Tucson, in press (astro-ph/0603357)
Bekki K., 1998, ApJ, 496, 713
Bell E. F. et al., 2004, ApJ, 608, 752
Bender R., Burstein D., Faber S. M., 1992, ApJ, 399, 462
Bender R., Burstein D., Faber S. M., 1993, ApJ, 411, 153
Bernardi M., Alonso M. V., da Costa L. N., Willmer C. N. A., Wegner G., Pellegrini P. S., Rité C., Maia M. A. G., 2002, AJ, 123, 2990
Bernardi M. et al., 2003a, AJ, 125, 1817
Bernardi M. et al., 2003b, AJ, 125, 1849
Bernardi M. et al., 2003c, AJ, 125, 1866
Binney J., Tremaine S., 1987, Galactic Dynamics. Princeton Univ. Press, Princeton
Bond J. R., Centrella J., Szalay A. S., Wilson J. R., 1984, MNRAS, 210, 515
Borriello A., Salucci P., Danese L., 2003, MNRAS, 341, 1109
Boylan-Kolchin M., Ma C.-P., Quataert E., 2005, MNRAS, 462, 184
Bryan G. L., Norman M. L., 1998, ApJ, 495, 80
Bullock J. S., Kolatt T. S., Sigad Y., Somerville R. S., Kravtsov A. V., Klypin A. A., Primack J. R., Dekel A., 2001, MNRAS, 321, 559
Busarello G., Capaccioli M., Capozziello S., Longo G., Puddu E., 1997, A&A, 320, 415
Capelato H. V., de Carvalho R. R., Carlberg R. G., 1995, ApJ, 451, 525
Cattaneo A., Dekel A., Devriendt J., Guiderdoni B., Blaizot J., 2006, MNRAS, 370, 1651
Ciotti L., Lanzoni B., Renzini A., 1996, MNRAS, 282, 1
Conselice C. J., Blackburne J. A., Papovich C., 2005, ApJ, 620, 564
Couchman H. M. P., 1991, ApJ, 368, L23
de Carvalho R. R., Djorgovski S., 1992, ApJ, 389, L49
Dantas C. C., Capelato H. V., de Carvalho R. R., Ribeiro A. L. B., 2002, A&A, 384, 772
Dantas C. C., Capelato H. V., Ribeiro A. L. B., de Carvalho R. R., 2003, MNRAS, 340, 398
Dekel A., Birnboim Y., 2006, MNRAS, 368, 2
de Lucia G., Springel V., White S. D. M., Croton D., Kauffmann G., 2006, MNRAS, 366, 499
de Zeeuw T., Franx M., 1991, ARA&A, 29, 239
Djorgovski S., Davis M., 1987, ApJ, 313, 59
Domínguez-Tenreiro R., Sáiz A., Serna A., 2004, ApJ, 611, L5 (DSS04)
Domínguez-Tenreiro R., Oñorbe J., Sáiz A., Serna A., Artal H., 2006, ApJ, 636, L77 (DTal06)
Dressler A., Lynden-Bell D., Burstein D., Davies R. L., Faber S. M., Terlevich R., Wegner G., 1987, ApJ, 313, 42
Elmegreen B., 2002, ApJ, 577, 206
Evrard A., Silk J., Szalay A. S., 1990, ApJ, 365, 13
Faber S. M., Jackson R. E., 1976, ApJ, 204, 668
Faber S. M., Dressler A., Davies R. L., Burstein D., Lynden-Bell D., 1987, in Faber S. M., ed., Nearly Normal Galaxies. From the Planck Time to the Present. Springer-Verlag, New York, p. 175
Faber S. M. et al., 2005, ApJ, submitted (astro-ph/0506044)
Gerhard O., Kronawitter A., Saglia R. P., Bender R., 2001, AJ, 121, 1936
González-García A. C., van Albada T. S., 2003, MNRAS, 342, 36
Graham A., Colless M., 1997, MNRAS, 287, 221
Guzmán R., Lucey J., Bower R. G., 1993, MNRAS, 265, 731
Hernquist L., 1990, ApJ, 356, 359
Jaffe W., 1983, MNRAS, 202, 995
Jørgensen I., Franx M., Kjærgaard P., 1993, ApJ, 411, 34
Jørgensen I., Franx M., Kjærgaard P., 1996, MNRAS, 280, 167
Katz N., 1992, ApJ, 391, 502
Kauffmann G. et al., 2003a, MNRAS, 341, 33
Kauffmann G. et al., 2003b, MNRAS, 341, 54
Kelson D. D., van Dokkum P. G., Franx M., Illingworth G. D., Fabricant D., 1997, ApJ, 478, L13
Kelson D. D., Illingworth G. D., van Dokkum P. G., Franx M., 2000, ApJ, 531, 184
Kennicutt R., 1998, ApJ, 498, 541
Keres D., Katz N., Weinberg D., Davé R., 2005, MNRAS, 363, 2
Kormendy J., 1977, ApJ, 218, 333
Kormendy J., Djorgovski S., 1989, ARA&A, 27, 235
Kronawitter A., Saglia R. P., Gerhard O., Bender R., 2000, A&AS, 144, 53
Lahav O. et al., 2002, MNRAS, 333, 961
Loewenstein M., 2000, ApJ, 532, 17
Lucey J. R., Bower R. G., Ellis R. S., 1991, MNRAS, 249, 755
Mamon G. A., Łokas E. L., 2005a, MNRAS, 362, 95
Mamon G. A., Łokas E. L., 2005b, MNRAS, 363, 705
Manrique A., Raig A., Salvador-Solé E., Sanchis T., Solanes J. M., 2003, ApJ, 593, 26
Márquez I., Lima Neto G. B., Capelato H., Durret F., Gerbal D., 2000, A&A, 353, 873
Menanteau F. et al., 2004, ApJ, 612, 202
Mobasher B., Guzmán R., Aragón-Salamanca A., Zepf S., 1999, MNRAS, 304, 225
Navarro J. F., Frenk C. S., White S. D. M., 1995, MNRAS, 275, 720
Navarro J. F., Frenk C. S., White S. D. M., 1996, ApJ, 462, 563
Navarro J. F. et al., 2004, MNRAS, 349, 1039
Nipoti C., Londrillo P., Ciotti L., 2003, MNRAS, 342, 501
Oñorbe J., Domínguez-Tenreiro R., Sáiz A., Serna A., Artal H., 2005, ApJ, 632, L57
Oñorbe J., Domínguez-Tenreiro R., Sáiz A., Serna A., Artal H., 2006, MNRAS, submitted
Padmanabhan N. et al., 2004, New Astron., 9, 329
Pahre M. A., de Carvalho R. R., Djorgovski S. G., 1998, AJ, 116, 1606
Pahre M. A., Djorgovski S. G., de Carvalho R. R., 1995, ApJ, 453, L17
Prugniel P., Simien F., 1996, A&A, 309, 749
Prugniel P., Simien F., 1997, A&A, 321, 111
Recillas-Cruz E., Serrano P. G. A., Cruz-Gonzalez I., Carrasco L., 1990, A&A, 229, 64
Recillas-Cruz E., Serrano A., Cruz-Gonzalez I., Carrasco L., 1991, A&A, 249, 312
Renzini A., Ciotti L., 1993, ApJ, 416, L49
Robertson B., Cox T. J., Hernquist L., Franx M., Hopkins P. F., Martini P., Springel V., 2006, ApJ, 641, 21
Romanowsky A. J., Kochanek C. S., 2001, ApJ, 553, 722
Saglia R. P., Colless M., Burstein D., Davies R. L., McMahan R. K., Wegner G., 2001, MNRAS, 324, 389
Sáiz A., Domínguez-Tenreiro R., Tissera P. B., Courteau S., 2001, MNRAS, 325, 119
Sáiz A., 2003, PhD thesis, Universidad Autónoma de Madrid, Spain
Sáiz A., Domínguez-Tenreiro R., Serna A., 2003, Ap&SS, 284, 411
Sáiz A., Domínguez-Tenreiro R., Serna A., 2004, ApJ, 601, L131 (SDTS04)
Salvador-Solé E., Manrique A., Solanes J. M., 2005, MNRAS, 358, 901
Sarson G. R., Shukurov A., Nordlund A., Gudiksen B., Brandenburg A., 2004, Ap&SS, 292, 267

Serna A., Domínguez-Tenreiro R., Sáiz A., 2003, ApJ, 597, 878
Sérsic J. L., 1968, Atlas de galaxias australes Córdoba. Observatorio Astronómico, Argentina
Spergel D. N. et al., 2003, ApJS, 148, 175
Spergel D. N. et al., 2006, ApJ, submitted (astro-ph/0603449)
Tegmark M. et al., 2004, Phys. Rev. D, 69, 103501
Thomas D., Greggio L., Bender R., 1999, MNRAS, 302, 537
Tinsley B. M., 1978, ApJ, 222, 14
Tissera P. B., Lambas D. G., Abadi M. G., 1997, MNRAS, 286, 384
Trujillo I., Burkert A., Bell E. F., 2004, ApJ, 600, L39
Tucker W. H., 1975, Radiation Precesses in Astrophysics. Wiley, New York
van der Marel R. P., Franx M., 1993, ApJ, 407, 525
Vázquez-Semadeni E., 2004a, in Burton M., Jayawardhana R., Bourke T., eds, Proc. IAU Symp. 221, Star Formation at High Angular Resolution. Astron. Soc. Pac., San Francisco, p. 51
Vázquez-Semadeni E., 2004b, Ap&SS, 292, 187
Wechsler R. H., Bullock J. S., Primack J. R., Kravtsov A. V., Dekel A., 2002, ApJ, 568, 52
York D. G. et al., 2000, AJ, 120, 1579
Zepf S., Silk J., 1996, ApJ, 466, 114
Zhao D. H., Mo H. J., Jing Y. P., Borner G., 2003, MNRAS, 339, 12

This paper has been typeset from a TEX/LATEX file prepared by the author.

Bibliography

Aarseth S.J., Turner E.L., & Gott III J.R., 1979. N-body simulations of galaxy clustering. I - Initial conditions and galaxy collapse times. *ApJ*, 228:664–683.

Abraham R.G., Ellis R.S., Fabian A.C., Tanvir N.R., & Glazebrook K., 1999. The star formation history of the Hubble sequence: spatially resolved colour distributions of intermediate-redshift galaxies in the Hubble Deep Field. *MNRAS*, 303:641–658.

Abraham R.G., Tanvir N.R., Santiago B.X., Ellis R.S., Glazebrook K., & van den Bergh S., 1996. Galaxy morphology to I=25 mag in the Hubble Deep Field. *MNRAS*, 279:L47–L52.

Aceves H., Velázquez H., & Cruz F., 2006. Sérsic properties of disc galaxy mergers. *MNRAS*, 373:632–642.

Agertz O., Moore B., Stadel J., Potter D., Miniati F., Read J., Mayer L., Gawryszczak A., Kravtsov A., Nordlund Å., Pearce F., Quilis V., Rudd D., Springel V., Stone J., Tasker E., Teyssier R., Wadsley J., & Walder R., 2007. Fundamental differences between SPH and grid methods. *MNRAS*, 380:963–978.

Allen S.W., Schmidt R.W., Ebeling H., Fabian A.C., & van Speybroeck L., 2004. Constraints on dark energy from Chandra observations of the largest relaxed galaxy clusters. *MNRAS*, 353:457–467.

Allgood B., Flores R.A., Primack J.R., Kravtsov A.V., Wechsler R.H., Faltenbacher A., & Bullock J.S., 2006. The shape of dark matter haloes: dependence on mass, redshift, radius and formation. *MNRAS*, 367:1781–1796.

Arnaud M., 2005. X-ray observations of clusters of galaxies. In F. Melchiorri & Y. Rephaeli, editors, *Background Microwave Radiation and Intracluster Cosmology*, pages 77–+.

Avila-Reese V. & Vázquez-Semadeni E., 2001. Turbulent Dissipation in the Interstellar Medium: The Coexistence of Forced and Decaying Regimes and Implications for Galaxy Formation and Evolution. *ApJ*, 553:645–660.

Bacon R., Copin Y., Monnet G., Miller B.W., Allington-Smith J.R., Bureau M., Carollo C.M., Davies R.L., Emsellem E., Kuntschner H., Peletier R.F., Verolme E.K., & de Zeeuw P.T., 2001. The SAURON project - I. The panoramic integral-field spectrograph. *MNRAS*, 326:23–35.

Bagla J.S., 2005. Cosmological N-Body simulation: Techniques, Scope and Status. *Current Science*, 88:1088–1100.

Balcells M. & González A.C., 1998. Formation of Kinematic Subsystems in Stellar Spiral-Spiral Mergers. *ApJ*, 505:L109–L112.

Bardeen J.M., Bond J.R., Kaiser N., & Szalay A.S., 1986. The statistics of peaks of Gaussian random fields. *ApJ*, 304:15–61.

Barnes J. & Hut P., 1986. A Hierarchical O(NlogN) Force-Calculation Algorithm. *Nature*, 324:446–449.

Barnes J.E. & Hernquist L., 1992. Dynamics of interacting galaxies. *ARA&A*, 30:705–742.

Baugh C.M., 2006. A primer on hierarchical galaxy formation: the semi-analytical approach. *Reports of Progress in Physics*, 69:3101–3156.

Beckwith S.V.W., Stiavelli M., Koekemoer A.M., Caldwell J.A.R., Ferguson H.C., Hook R., Lucas R.A., Bergeron L.E., Corbin M., Jogee S., Panagia N., Robberto M., Royle P., Somerville R.S., & Sosey M., 2006. The Hubble Ultra Deep Field. *AJ*, 132:1729–1755.

Bekki K., 1998. The Fundamental Plane and Merger Scenario. I. Star Formation History of Galaxy Mergers and Origin of the Fundamental Plane. *ApJ*, 496:713–+.

Bell E.F., Naab T., McIntosh D.H., Somerville R.S., Caldwell J.A.R., Barden M., Wolf C., Rix H.W., Beckwith S.V., Borch A., Häussler B., Heymans C., Jahnke K., Jogee S., Koposov S., Meisenheimer K., Peng C.Y., Sanchez S.F., & Wisotzki L., 2006. Dry Mergers in GEMS: The Dynamical Evolution of Massive Early-Type Galaxies. *ApJ*, 640:241–251.

Bell E.F., Papovich C., Wolf C., Le Floc'h E., Caldwell J.A.R., Barden M., Egami E., McIntosh D.H., Meisenheimer K., Pérez-González P.G., Rieke G.H., Rieke M.J., Rigby J.R., & Rix H.W., 2005. Toward an Understanding of the Rapid Decline of the Cosmic Star Formation Rate. *ApJ*, 625:23–36.

Bell E.F., Wolf C., Meisenheimer K., Rix H.W., Borch A., Dye S., Kleinheinrich M., Wisotzki L., & McIntosh D.H., 2004. Nearly 5000 Distant Early-Type Galaxies in COMBO-17: A Red Sequence and Its Evolution since z˜1. *ApJ*, 608:752–767.

Bender R., 1988. Velocity anisotropies and isophote shapes in elliptical galaxies. *A&A*, 193:L7–L10.

Bender R., Burstein D., & Faber S.M., 1992. Dynamically hot galaxies. I - Structural properties. *ApJ*, 399:462–477.

Bender R. & Nieto J.L., 1990. Internal kinematics of low-luminosity ellipsoidal galaxies. *A&A*, 239:97–112.

Bender R., Saglia R.P., & Gerhard O.E., 1994. Line-of-Sight Velocity Distributions of Elliptical Galaxies. *MNRAS*, 269:785–+.

Bender R., Surma P., Doebereiner S., Moellenhoff C., & Madejsky R., 1989. Isophote shapes of elliptical galaxies. II - Correlations with global optical, radio and X-ray properties. *A&A*, 217:35–43.

Bergond G., Zepf S.E., Romanowsky A.J., Sharples R.M., & Rhode K.L., 2006. Wide-field kinematics of globular clusters in the Leo I group. *A&A*, 448:155–164.

Bernardeau F., Colombi S., Gaztañaga E., & Scoccimarro R., 2002. Large-scale structure of the Universe and cosmological perturbation theory. *Phys. Rep.*, 367:1–3.

Bernardi M., Alonso M.V., da Costa L.N., Willmer C.N.A., Wegner G., Pellegrini P.S., Rité C., & Maia M.A.G., 2002. Redshift-Distance Survey of Early-Type Galaxies. I. The ENEARc Cluster Sample. *AJ*, 123:2990–3017.

Bernardi M., Sheth R.K., Annis J., Burles S., Eisenstein D.J., Finkbeiner D.P., Hogg D.W., Lupton R.H., Schlegel D.J., SubbaRao M., Bahcall N.A., Blakeslee J.P., Brinkmann J., Castander F.J., Connolly A.J., Csabai I., Doi M., Fukugita M., Frieman J., Heckman T., Hennessy G.S., Ivezić Ž., Knapp G.R., Lamb D.Q., McKay T., Munn J.A., Nichol R., Okamura S., Schneider D.P., Thakar A.R., & York D.G., 2003a. Early-Type Galaxies in the Sloan Digital Sky Survey. I. The Sample. *AJ*, 125:1817–1848.

Bernardi M., Sheth R.K., Annis J., Burles S., Eisenstein D.J., Finkbeiner D.P., Hogg D.W., Lupton R.H., Schlegel D.J., SubbaRao M., Bahcall N.A., Blakeslee J.P., Brinkmann J., Castander F.J., Connolly A.J., Csabai I., Doi M., Fukugita M., Frieman J., Heckman T., Hennessy G.S., Ivezić Ž., Knapp G.R., Lamb D.Q., McKay T., Munn J.A., Nichol R., Okamura S., Schneider D.P., Thakar A.R., & York D.G., 2003b. Early-type Galaxies in the Sloan Digital Sky Survey. II. Correlations between Observables. *AJ*, 125:1849–1865.

Bernardi M., Sheth R.K., Annis J., Burles S., Eisenstein D.J., Finkbeiner D.P., Hogg D.W., Lupton R.H., Schlegel D.J., SubbaRao M., Bahcall N.A., Blakeslee J.P.,

Brinkmann J., Castander F.J., Connolly A.J., Csabai I., Doi M., Fukugita M., Frieman J., Heckman T., Hennessy G.S., Ivezić Ž., Knapp G.R., Lamb D.Q., McKay T., Munn J.A., Nichol R., Okamura S., Schneider D.P., Thakar A.R., & York D.G., 2003c. Early-Type Galaxies in the Sloan Digital Sky Survey. III. The Fundamental Plane. *AJ*, 125:1866–1881.

Bernardi M., Sheth R.K., Annis J., Burles S., Finkbeiner D.P., Lupton R.H., Schlegel D.J., SubbaRao M., Bahcall N.A., Blakeslee J.P., Brinkmann J., Castander F.J., Connolly A.J., Csabai I., Doi M., Fukugita M., Frieman J., Heckman T., Hennessy G.S., Ivezić Ž., Knapp G.R., Lamb D.Q., McKay T., Munn J.A., Nichol R., Okamura S., Schneider D.P., Thakar A.R., & York D.G., 2003d. Early-Type Galaxies in the Sloan Digital Sky Survey. IV. Colors and Chemical Evolution. *AJ*, 125:1882–1896.

Bertin G., Ciotti L., & Del Principe M., 2002. Weak homology of elliptical galaxies. *A&A*, 386:149–168.

Bertschinger E., 1995. COSMICS: Cosmological Initial Conditions and Microwave Anisotropy Codes. *ArXiv Astrophysics e-prints*.

Bertschinger E., 2001. Multiscale Gaussian Random Fields and Their Application to Cosmological Simulations. *ApJS*, 137:1–20.

Bertschinger E. & Gelb J.M., 1991. Cosmological N-body simulations. *Computers in Physics*, 5:164–175.

Binney J., 1976. Is the flattening of elliptical galaxies necessarily due to rotation. *MNRAS*, 177:19–29.

Binney J., 1978. On the rotation of elliptical galaxies. *MNRAS*, 183:501–514.

Binney J., 2005. Rotation and anisotropy of galaxies revisited. *MNRAS*, 363:937–942.

Binney J. & Tremaine S., 1987. *Galactic dynamics*. Princeton, NJ, Princeton University Press, 1987, 747 p.

Birnboim Y. & Dekel A., 2003. Virial shocks in galactic haloes? *MNRAS*, 345:349–364.

Blain A.W., Smail I., Ivison R.J., Kneib J.P., & Frayer D.T., 2002. Submillimeter galaxies. *Phys. Rep.*, 369:111–176.

Blanton M.R., Brinkmann J., Csabai I., Doi M., Eisenstein D., Fukugita M., Gunn J.E., Hogg D.W., & Schlegel D.J., 2003. Estimating Fixed-Frame Galaxy Magnitudes in the Sloan Digital Sky Survey. *AJ*, 125:2348–2360.

Bluck A.F.L., Conselice C.J., Bouwens R.J., Daddi E., Dickinson M., Papovich C., & Yan H., 2009. A surprisingly high pair fraction for extremely massive galaxies at z ˜ 3 in the GOODS NICMOS survey. *MNRAS*, pages L178+.

Blumenthal G.R., Faber S.M., Flores R., & Primack J.R., 1986. Contraction of dark matter galactic halos due to baryonic infall. *ApJ*, 301:27–34.

Bond J.R., Centrella J., Szalay A.S., & Wilson J.R., 1984. Cooling pancakes. *MNRAS*, 210:515–545.

Bond J.R., Efstathiou G., & Tegmark M., 1997. Forecasting cosmic parameter errors from microwave background anisotropy experiments. *MNRAS*, 291:L33–L41.

Borriello A., Salucci P., & Danese L., 2003. The fundamental plane of ellipticals - I. The dark matter connection. *MNRAS*, 341:1109–1120.

Bournaud F., Jog C.J., & Combes F., 2005. Galaxy mergers with various mass ratios: Properties of remnants. *A&A*, 437:69–85.

Boylan-Kolchin M., Ma C.P., & Quataert E., 2005. Dissipationless mergers of elliptical galaxies and the evolution of the fundamental plane. *MNRAS*, 362:184–196.

Bryan G.L. & Norman M.L., 1998. Statistical Properties of X-Ray Clusters: Analytic and Numerical Comparisons. *ApJ*, 495:80–+.

Buitrago F., Trujillo I., Conselice C.J., Bouwens R.J., Dickinson M., & Yan H., 2008. Size evolution of the most massive galaxies at $1.7 < z < 3$ from GOODS NICMOS survey imaging. *ArXiv e-prints*, 807.

Bullock J.S., Kolatt T.S., Sigad Y., Somerville R.S., Kravtsov A.V., Klypin A.A., Primack J.R., & Dekel A., 2001. Profiles of dark haloes: evolution, scatter and environment. *MNRAS*, 321:559–575.

Bullock J.S., Kravtsov A.V., & Weinberg D.H., 2000. Reionization and the Abundance of Galactic Satellites. *ApJ*, 539:517–521.

Bundy K., Ellis R.S., & Conselice C.J., 2005. The Mass Assembly Histories of Galaxies of Various Morphologies in the GOODS Fields. *ApJ*, 625:621–632.

Burkert A. & Naab T., 2005. The surprising anisotropy of fast rotating, discy elliptical galaxies. *MNRAS*, 363:597–602.

Busarello G., Capaccioli M., Capozziello S., Longo G., & Puddu E., 1997. The relation between the virial theorem and the fundamental plane of elliptical galaxies. *A&A*, 320:415–420.

Caldwell N., Rose J.A., & Concannon K.D., 2003. Star Formation Histories of Early-Type Galaxies. I. Higher Order Balmer Lines as Age Indicators. *AJ*, 125:2891–2926.

Caon N., Capaccioli M., & D'Onofrio M., 1993. On the Shape of the Light Profiles of Early Type Galaxies. *MNRAS*, 265:1013–+.

Capelato H.V., de Carvalho R.R., & Carlberg R.G., 1995. Mergers of Dissipationless Systems: Clues about the Fundamental Plane. *ApJ*, 451:525–+.

Capozziello S., Cardone V.F., Molinaro R., & Salzano V., 2007. The Sersic Virial Hyperplane. *ArXiv Astrophysics e-prints*.

Cappellari M., Bacon R., Bureau M., Damen M.C., Davies R.L., de Zeeuw P.T., Emsellem E., Falcón-Barroso J., Krajnović D., Kuntschner H., McDermid R.M., Peletier R.F., Sarzi M., van den Bosch R.C.E., & van de Ven G., 2006. The SAURON project - IV. The mass-to-light ratio, the virial mass estimator and the Fundamental Plane of elliptical and lenticular galaxies. *MNRAS*, 366:1126–1150.

Cappellari M., Emsellem E., Bacon R., Bureau M., Davies R.L., de Zeeuw P.T., Falcón-Barroso J., Krajnović D., Kuntschner H., McDermid R.M., Peletier R.F., Sarzi M., van den Bosch R.C.E., & van de Ven G., 2007. The SAURON project - X. The orbital anisotropy of elliptical and lenticular galaxies: revisiting the (V/σ, ϵ) diagram with integral-field stellar kinematics. *MNRAS*, 379:418–444.

Cassata P., Cimatti A., Franceschini A., Daddi E., Pignatelli E., Fasano G., Rodighiero G., Pozzetti L., Mignoli M., & Renzini A., 2005. The evolution of the galaxy B-band rest-frame morphology to z˜ 2: new clues from the K20/GOODS sample. *MNRAS*, 357:903–917.

Cen R., 1992. A hydrodynamic approach to cosmology - Methodology. *ApJS*, 78:341–364.

Cenarro A.J. & Trujillo I., 2009. Weak Velocity Dispersion Evolution of Spheroid-like Massive Galaxies since z˜2. *ArXiv e-prints*.

Ceverino D. & Klypin A., 2007. The role of stellar feedback in the formation of galaxies. *ArXiv e-prints*, 712.

Cimatti A., Daddi E., Mignoli M., Pozzetti L., Renzini A., Zamorani G., Broadhurst T., Fontana A., Saracco P., Poli F., Cristiani S., D'Odorico S., Giallongo E., Gilmozzi R., & Menci N., 2002. The K20 survey. I. Disentangling old and dusty star-forming galaxies in the ERO population. *A&A*, 381:L68–L72.

Cimatti A., Daddi E., Renzini A., Cassata P., Vanzella E., Pozzetti L., Cristiani S., Fontana A., Rodighiero G., Mignoli M., & Zamorani G., 2004. Old galaxies in the young Universe. *Nature*, 430:184–187.

Ciotti L., Lanzoni B., & Renzini A., 1996. The tilt of the fundamental plane of elliptical galaxies - I. Exploring dynamical and structural effects. *MNRAS*, 282:1–12.

Ciotti L., Lanzoni B., & Volonteri M., 2007. The Importance of Dry and Wet Merging on the Formation and Evolution of Elliptical Galaxies. *ApJ*, 658:65–77.

Ciotti L. & Ostriker J.P., 2001. Cooling Flows and Quasars. II. Detailed Models of Feedback-modulated Accretion Flows. *ApJ*, 551:131–152.

Clemens M.S., Bressan A., Nikolic B., & Rampazzo R., 2009. The history of star formation and mass assembly in early-type galaxies. *MNRAS*, 392:L35–L39.

Coe D., Benítez N., Sánchez S.F., Jee M., Bouwens R., & Ford H., 2006. Galaxies in the Hubble Ultra Deep Field. I. Detection, Multiband Photometry, Photometric Redshifts, and Morphology. *AJ*, 132:926–959.

Cole S., Aragon-Salamanca A., Frenk C.S., Navarro J.F., & Zepf S.E., 1994. A Recipe for Galaxy Formation. *MNRAS*, 271:781–+.

Colín P., Klypin A., Valenzuela O., & Gottlöber S., 2004. Dwarf Dark Matter Halos. *ApJ*, 612:50–57.

Conselice C.J., 2003. The Relationship between Stellar Light Distributions of Galaxies and Their Formation Histories. *ApJS*, 147:1–28.

Conselice C.J., 2006. Early and Rapid Merging as a Formation Mechanism of Massive Galaxies: Empirical Constraints. *ApJ*, 638:686–702.

Conselice C.J., Blackburne J.A., & Papovich C., 2005. The Luminosity, Stellar Mass, and Number Density Evolution of Field Galaxies of Known Morphology from z = 0.5 to 3. *ApJ*, 620:564–583.

Conselice C.J., Yang C., & Bluck A.F.L., 2008. The Structures of Distant Galaxies - III: The Merger History of over 20,000 Massive Galaxies at z <1.2. *ArXiv e-prints*.

Corbelli E. & Salucci P., 2000. The extended rotation curve and the dark matter halo of M33. *MNRAS*, 311:441–447.

Couchman H.M.P., 1991. Mesh-refined P3M - A fast adaptive N-body algorithm. *ApJ*, 368:L23–L26.

Couchman H.M.P., Thomas P.A., & Pearce F.R., 1995. Hydra: an Adaptive-Mesh Implementation of P 3M-SPH. *ApJ*, 452:797–+.

Cowie L.L., Songaila A., Hu E.M., & Cohen J.G., 1996. New Insight on Galaxy Formation and Evolution From Keck Spectroscopy of the Hawaii Deep Fields. *AJ*, 112:839–+.

Cox T.J., Dutta S.N., Di Matteo T., Hernquist L., Hopkins P.F., Robertson B., & Springel V., 2006. The Kinematic Structure of Merger Remnants. *ApJ*, 650:791–811.

Cyburt R.H., Fields B.D., & Olive K.A., 2003. Primordial nucleosynthesis in light of WMAP. *Physics Letters B*, 567:227–234.

Dalcanton J.J., Spergel D.N., & Summers F.J., 1997. The Formation of Disk Galaxies. *ApJ*, 482:659–+.

Dantas C.C., Capelato H.V., de Carvalho R.R., & Ribeiro A.L.B., 2002. Dissipationless collapse of spherical protogalaxies and the fundamental plane. *A&A*, 384:772–779.

Dantas C.C., Capelato H.V., Ribeiro A.L.B., & de Carvalho R.R., 2003. 'Fundamental Plane'-like relations from collisionless stellar dynamics: a comparison of mergers and collapses. *MNRAS*, 340:398–410.

Davies R.L., Efstathiou G., Fall S.M., Illingworth G., & Schechter P.L., 1983. The kinematic properties of faint elliptical galaxies. *ApJ*, 266:41–57.

Davis M., Efstathiou G., Frenk C.S., & White S.D.M., 1985. The evolution of large-scale structure in a universe dominated by cold dark matter. *ApJ*, 292:371–394.

de Avillez M.A. & Breitschwerdt D., 2007. The Generation and Dissipation of Interstellar Turbulence: Results from Large-Scale High-Resolution Simulations. *ApJ*, 665:L35–L38.

de Carvalho R.R. & Djorgovski S., 1992. Systematic differences between the field and cluster elliptical galaxies. *ApJ*, 389:L49–L53.

De Lucia G., Springel V., White S.D.M., Croton D., & Kauffmann G., 2006. The formation history of elliptical galaxies. *MNRAS*, 366:499–509.

De Propris R., Conselice C.J., Liske J., Driver S.P., Patton D.R., Graham A.W., & Allen P.D., 2007. The Millennium Galaxy Catalogue: The Connection between Close Pairs and Asymmetry; Implications for the Galaxy Merger Rate. *ApJ*, 666:212–221.

de Vaucouleurs G., 1948. Recherches sur les Nebuleuses Extragalactiques. *Annales d'Astrophysique*, 11:247–+.

de Zeeuw P.T., Bureau M., Emsellem E., Bacon R., Carollo C.M., Copin Y., Davies R.L., Kuntschner H., Miller B.W., Monnet G., Peletier R.F., & Verolme E.K., 2002. The SAURON project - II. Sample and early results. *MNRAS*, 329:513–530.

de Zeeuw T. & Franx M., 1991. Structure and dynamics of elliptical galaxies. *ARA&A*, 29:239–274.

Dehnen W., 2000. A Very Fast and Momentum-conserving Tree Code. *ApJ*, 536:L39–L42.

Dekel A. & Birnboim Y., 2006. Galaxy bimodality due to cold flows and shock heating. *MNRAS*, 368:2–20.

Dekel A., Birnboim Y., Engel G., Freundlich J., Goerdt T., Mumcuoglu M., Neistein E., Pichon C., Teyssier R., & Zinger E., 2009. Cold streams in early massive hot haloes as the main mode of galaxy formation. *Nature*, 457:451–454.

Dekel A., Stoehr F., Mamon G.A., Cox T.J., Novak G.S., & Primack J.R., 2005. Lost and found dark matter in elliptical galaxies. *Nature*, 437:707–710.

di Serego Alighieri S., Vernet J., Cimatti A., Lanzoni B., Cassata P., Ciotti L., Daddi E., Mignoli M., Pignatelli E., Pozzetti L., Renzini A., Rettura A., & Zamorani G., 2005. The evolution of early-type galaxies at $z \sim 1$ from the K20 survey. *A&A*, 442:125–136.

Djorgovski S. & Davis M., 1987. Fundamental properties of elliptical galaxies. *ApJ*, 313:59–68.

Dolag K., Bartelmann M., & Lesch H., 1999. SPH simulations of magnetic fields in galaxy clusters. *A&A*, 348:351–363.

Dolag K., Borgani S., Schindler S., Diaferio A., & Bykov A.M., 2008. Simulation techniques for cosmological simulations. *ArXiv e-prints*, 801.

Domínguez-Tenreiro R., Oñorbe J., Sáiz A., Artal H., & Serna A., 2006. The Lack of Structural and Dynamical Evolution of Elliptical Galaxies since $z\tilde{1}.5$: Clues from Self-Consistent Hydrodynamic Simulations. *ApJ*, 636:L77–L80.

Domínguez-Tenreiro R., Oñorbe J., Serna A., & González-García A.C., 2008. Downsizing in Elliptical Galaxies: Some Clues from Self-consistent Hydrodynamical Simulations. In J.H. Knapen, T.J. Mahoney, & A. Vazdekis, editors, *Pathways Through an Eclectic Universe*, volume 390 of *Astronomical Society of the Pacific Conference Series*, pages 468–+.

Domínguez-Tenreiro R., Sáiz A., & Serna A., 2004. Elliptical Galaxies at z = 0 from Self-consistent Hydrodynamic Simulations: Clues on Age Effects in Their Stellar Populations. *ApJ*, 611:L5–L8.

Domínguez-Tenreiro R., Serna A., Sáiz A., & Sierra-Glez. de Buitrago M.M., 2003. Clues on the Hubble sequence formation from self-consistent hydrodynamical simulations. *Ap&SS*, 284:397–400.

Domínguez-Tenreiro R., Tissera P.B., & Sáiz A., 1998. Disk Formation in Hierarchical Hydrodynamical Simulations:A Way Out of the Angular Momentum Catastrophe. *ApJ*, 508:L123–L127.

D'Onofrio M., 2001. 2D modelling of the light distribution of early-type galaxies in a volume-limited sample - II. Results for real galaxies. *MNRAS*, 326:1517–1532.

Douglas N.G., Arnaboldi M., Freeman K.C., Kuijken K., Merrifield M.R., Romanowsky A.J., Taylor K., Capaccioli M., Axelrod T., Gilmozzi R., Hart J., Bloxham G., & Jones D., 2002. The Planetary Nebula Spectrograph: The Green Light for Galaxy Kinematics. *PASP*, 114:1234–1251.

Douglas N.G., Napolitano N.R., Romanowsky A.J., Coccato L., Kuijken K., Merrifield M.R., Arnaboldi M., Gerhard O., Freeman K.C., Merrett H.R., Noordermeer E., & Capaccioli M., 2007. The PN.S Elliptical Galaxy Survey: Data Reduction, Planetary Nebula Catalog, and Basic Dynamics for NGC 3379. *ApJ*, 664:257–276.

Dressler A., Lynden-Bell D., Burstein D., Davies R.L., Faber S.M., Terlevich R., & Wegner G., 1987. Spectroscopy and photometry of elliptical galaxies. I - A new distance estimator. *ApJ*, 313:42–58.

Drory N., Bender R., Feulner G., Hopp U., Maraston C., Snigula J., & Hill G.J., 2004. The Munich Near-Infrared Cluster Survey (MUNICS). VI. The Stellar Masses of K-Band-selected Field Galaxies to z˜1.2. *ApJ*, 608:742–751.

Dunkley J., Komatsu E., Nolta M.R., Spergel D.N., Larson D., Hinshaw G., Page L., Bennett C.L., Gold B., Jarosik N., Weiland J.L., Halpern M., Hill R.S., Kogut A., Limon M., Meyer S.S., Tucker G.S., Wollack E., & Wright E.L., 2009. Five-Year Wilkinson Microwave Anisotropy Probe Observations: Likelihoods and Parameters from the WMAP Data. *ApJS*, 180:306–329.

Efstathiou G., 2000. A model of supernova feedback in galaxy formation. *MNRAS*, 317:697–719.

Efstathiou G., Davis M., White S.D.M., & Frenk C.S., 1985. Numerical techniques for large cosmological N-body simulations. *ApJS*, 57:241–260.

Efstathiou G. & Rees M.J., 1988. High-redshift quasars in the Cold Dark Matter cosmogony. *MNRAS*, 230:5P–+.

Eggen O.J., Lynden-Bell D., & Sandage A.R., 1962. Evidence from the motions of old stars that the Galaxy collapsed. *ApJ*, 136:748–+.

Einasto J., 1969. N/a. *Astrofizika*, 5:137–+.

Einasto J. & Haud U., 1989. Galactic models with massive corona. I - Method. II - Galaxy. *A&A*, 223:89–106.

Ellis R. & Silk J., 2007. New Frontiers in Cosmology and Galaxy Formation: Challenges for the Future. *ArXiv e-prints*, 712.

Elmegreen B.G., 2002. Star Formation from Galaxies to Globules. *ApJ*, 577:206–220.

Elmegreen B.G., 2003. Gas phase processes affecting galactic evolution. *Ap&SS*, 284:819–832.

Emsellem E., Cappellari M., Krajnović D., van de Ven G., Bacon R., Bureau M., Davies R.L., de Zeeuw P.T., Falcón-Barroso J., Kuntschner H., McDermid R., Peletier R.F., & Sarzi M., 2007. The SAURON project - IX. A kinematic classification for early-type galaxies. *MNRAS*, 379:401–417.

Emsellem E., Cappellari M., Peletier R.F., McDermid R.M., Bacon R., Bureau M., Copin Y., Davies R.L., Krajnović D., Kuntschner H., Miller B.W., & de Zeeuw P.T., 2004. The SAURON project - III. Integral-field absorption-line kinematics of 48 elliptical and lenticular galaxies. *MNRAS*, 352:721–743.

Ettori S., De Grandi S., & Molendi S., 2002. Gravitating mass profiles of nearby galaxy clusters and relations with X-ray gas temperature, luminosity and mass. *A&A*, 391:841–855.

Evrard A.E., 1988. Beyond N-body - 3D cosmological gas dynamics. *MNRAS*, 235:911–934.

Evrard A.E., Silk J., & Szalay A.S., 1990. The morphology-density relation for galaxies in a cold dark matter-dominated universe. *ApJ*, 365:13–21.

Evrard A.E., Summers F.J., & Davis M., 1994. Two-fluid simulations of galaxy formation. *ApJ*, 422:11–36.

Faber S.M., Dressler A., Davies R.L., Burstein D., & Lynden-Bell D., 1987. Global scaling relations for elliptical galaxies and implications for formation. In S.M. Faber, editor, *Nearly Normal Galaxies. From the Planck Time to the Present*, pages 175–183.

Faber S.M. & Jackson R.E., 1976. Velocity dispersions and mass-to-light ratios for elliptical galaxies. *ApJ*, 204:668–683.

Faber S.M., Willmer C.N.A., Wolf C., Koo D.C., Weiner B.J., Newman J.A., Im M., Coil A.L., Conroy C., Cooper M.C., Davis M., Finkbeiner D.P., Gerke B.F., Gebhardt K., Groth E.J., Guhathakurta P., Harker J., Kaiser N., Kassin S., Kleinheinrich M., Konidaris N.P., Kron R.G., Lin L., Luppino G., Madgwick D.S., Meisenheimer K., Noeske K.G., Phillips A.C., Sarajedini V.L., Schiavon R.P., Simard L., Szalay A.S., Vogt N.P., & Yan R., 2007. Galaxy Luminosity Functions to z˜1 from DEEP2 and COMBO-17: Implications for Red Galaxy Formation. *ApJ*, 665:265–294.

Fall S.M., 1978. On the evolution of galaxy clustering and cosmological N-body simulations. *MNRAS*, 185:165–178.

Ferguson H.C., Dickinson M., & Williams R., 2000. The Hubble Deep Fields. *ARA&A*, 38:667–715.

Ferreras I., Saha P., & Williams L.L.R., 2005. Stellar and Total Mass in Early-Type Lensing Galaxies. *ApJ*, 623:L5–L8.

Fixsen D.J., Cheng E.S., Gales J.M., Mather J.C., Shafer R.A., & Wright E.L., 1996. The Cosmic Microwave Background Spectrum from the Full COBE FIRAS Data Set. *ApJ*, 473:576–+.

Folkes S., Ronen S., Price I., Lahav O., Colless M., Maddox S., Deeley K., Glazebrook K., Bland-Hawthorn J., Cannon R., Cole S., Collins C., Couch W., Driver S.P., Dalton G., Efstathiou G., Ellis R.S., Frenk C.S., Kaiser N., Lewis I., Lumsden S., Peacock J., Peterson B.A., Sutherland W., & Taylor K., 1999. The 2dF Galaxy Redshift Survey: spectral types and luminosity functions. *MNRAS*, 308:459–472.

Fontana A., Pozzetti L., Donnarumma I., Renzini A., Cimatti A., Zamorani G., Menci N., Daddi E., Giallongo E., Mignoli M., Perna C., Salimbeni S., Saracco P., Broadhurst T., Cristiani S., D'Odorico S., & Gilmozzi R., 2004. The K20 survey. VI. The distribution of the stellar masses in galaxies up to $z \sim 2$. *A&A*, 424:23–42.

Foot R., 2004. Mirror Matter-Type Dark Matter. *International Journal of Modern Physics D*, 13:2161–2192.

Freedman W.L., Madore B.F., Gibson B.K., Ferrarese L., Kelson D.D., Sakai S., Mould J.R., Kennicutt Jr. R.C., Ford H.C., Graham J.A., Huchra J.P., Hughes S.M.G., Illingworth G.D., Macri L.M., & Stetson P.B., 2001. Final Results from the Hubble Space Telescope Key Project to Measure the Hubble Constant. *ApJ*, 553:47–72.

Frenk C.S., White S.D.M., Bode P., Bond J.R., Bryan G.L., Cen R., Couchman H.M.P., Evrard A.E., Gnedin N., Jenkins A., Khokhlov A.M., Klypin A., Navarro J.F., Norman M.L., Ostriker J.P., Owen J.M., Pearce F.R., Pen U.L., Steinmetz M., Thomas P.A., Villumsen J.V., Wadsley J.W., Warren M.S., Xu G., & Yepes G., 1999. The Santa Barbara Cluster Comparison Project: A Comparison of Cosmological Hydrodynamics Solutions. *ApJ*, 525:554–582.

Gallazzi A., Charlot S., Brinchmann J., & White S.D.M., 2006. Ages and metallicities of early-type galaxies in the Sloan Digital Sky Survey: new insight into the physical origin of the colour-magnitude and the $Mg_2 - \sigma_V$ relations. *MNRAS*, 370:1106–1124.

Gavazzi R., Treu T., Rhodes J.D., Koopmans L.V.E., Bolton A.S., Burles S., Massey R.J., & Moustakas L.A., 2007. The Sloan Lens ACS Survey. IV. The Mass Density Profile of Early-Type Galaxies out to 100 Effective Radii. *ApJ*, 667:176–190.

Gelb J.M. & Bertschinger E., 1994. Cold dark matter. 1: The formation of dark halos. *ApJ*, 436:467–490.

Gerhard O., Kronawitter A., Saglia R.P., & Bender R., 2001. Dynamical Family Properties and Dark Halo Scaling Relations of Giant Elliptical Galaxies. *AJ*, 121:1936–1951.

Gibson B.K., Sánchez-Blázquez P., Courty S., & Kawata D., 2007. Chemodynamical Simulations of Elliptical Galaxies. In *EAS Publications Series*, volume 24 of *EAS Publications Series*, pages 133–138.

Gingold R.A. & Monaghan J.J., 1977. Smoothed particle hydrodynamics - Theory and application to non-spherical stars. *MNRAS*, 181:375–389.

Gnedin O.Y., Kravtsov A.V., Klypin A.A., & Nagai D., 2004. Response of Dark Matter Halos to Condensation of Baryons: Cosmological Simulations and Improved Adiabatic Contraction Model. *ApJ*, 616:16–26.

Goetz M., Huchra J.P., & Brandenberger R.H., 1998. Group Identification in N-Body Simulations: SKID and DENMAX Versus Friends-of-Friends. *ArXiv Astrophysics e-prints*, 9811393.

González-García A.C. & Balcells M., 2005. Elliptical galaxies from mergers of discs. *MNRAS*, 357:753–772.

González-García A.C., Balcells M., & Olshevsky V.S., 2006. Line-of-sight velocity distributions of elliptical galaxies from collisionless mergers. *MNRAS*, 372:L78–L82.

González-García A.C., Oñorbe J., Domínguez-Tenreiro R., & Gómez-Flechoso M.Á., 2009. Shape and kinematics of elliptical galaxies: evolution due to merging at $z < 1.5$. *A&A*, 497:35–40.

González-García A.C. & van Albada T.S., 2003. Mergers between elliptical galaxies and the thickening of the Fundamental Plane. *MNRAS*, 342:L36–L40.

González-García A.C. & van Albada T.S., 2005. Encounters between spherical galaxies - I. Systems without a dark halo. *MNRAS*, 361:1030–1042.

Gottlöber S., Klypin A., & Kravtsov A.V., 2001. Merging History as a Function of Halo Environment. *ApJ*, 546:223–233.

Gottlöeber S., Yepes G., Wagner C., & Sevilla R., 2006. The MareNostrum Universe. *ArXiv Astrophysics e-prints*.

Graham A. & Colless M., 1997. Some effects of galaxy structure and dynamics on the Fundamental Plane. *MNRAS*, 287:221–239.

Graham A.W., 1998. Some effects of galaxy structure and dynamics on the Fundamental Plane - II. A Virgo-Fornax distance modulus. *MNRAS*, 295:933–945.

Graham A.W., 2002. The 'Photometric Plane' of elliptical galaxies. *MNRAS*, 334:859–864.

Graham A.W., Merritt D., Moore B., Diemand J., & Terzić B., 2006. Empirical Models for Dark Matter Halos. III. The Kormendy Relation and the $\log(\rho_e)$-$\log(R_e)$ Relation. *AJ*, 132:2711–2716.

Gurbatov S.N., Saichev A.I., & Shandarin S.F., 1989. The large-scale structure of the universe in the frame of the model equation of non-linear diffusion. *MNRAS*, 236:385–402.

Gustafsson M., Fairbairn M., & Sommer-Larsen J., 2006. Baryonic pinching of galactic dark matter halos. *Phys. Rev. D*, 74(12):123522–+.

Guzik J. & Seljak U., 2002. Virial masses of galactic haloes from galaxy-galaxy lensing: theoretical modelling and application to Sloan Digital Sky Survey data. *MNRAS*, 335:311–324.

Guzman R., Lucey J.R., & Bower R.G., 1993. The Fundamental Relations of Elliptical Galaxies. *MNRAS*, 265:731–+.

Hao C.N., Mao S., Deng Z.G., Xia X.Y., & Wu H., 2006. Isophotal shapes of elliptical/lenticular galaxies from the Sloan Digital Sky Survey. *MNRAS*, 370:1339–1350.

Hau G.K.T. & Forbes D.A., 2006. Radial kinematics of isolated elliptical galaxies. *MNRAS*, 371:633–642.

Heitmann K., Lukic Z., Fasel P., Habib S., Warren M.S., White M., Ahrens J., Ankeny L., Armstrong R., O'Shea B., Ricker P.M., Springel V., Stadel J., & Trac H., 2007. The Cosmic Code Comparison Project. *ArXiv e-prints*, 706.

Heitmann K., Ricker P.M., Warren M.S., & Habib S., 2005. Robustness of Cosmological Simulations. I. Large-Scale Structure. *ApJS*, 160:28–58.

Hernquist L., 1990. An analytical model for spherical galaxies and bulges. *ApJ*, 356:359–364.

Hernquist L., 1993. Some cautionary remarks about smoothed particle hydrodynamics. *ApJ*, 404:717–722.

Hernquist L. & Katz N., 1989. TREESPH - A unification of SPH with the hierarchical tree method. *ApJS*, 70:419–446.

Heymans C., Bell E.F., Rix H.W., Barden M., Borch A., Caldwell J.A.R., McIntosh D.H., Meisenheimer K., Peng C.Y., Wolf C., Beckwith S.V.W., Häußler B., Jahnke K., Jogee S., Sánchez S.F., Somerville R., & Wisotzki L., 2006. A weak lensing estimate from GEMS of the virial to stellar mass ratio in massive galaxies to z ˜ 0.8. *MNRAS*, 371:L60–L64.

Hoekstra H., Yee H.K.C., & Gladders M.D., 2004. Properties of Galaxy Dark Matter Halos from Weak Lensing. *ApJ*, 606:67–77.

Hopkins P.F., Cox T.J., & Hernquist L., 2008a. Dissipation and the Fundamental Plane: Observational Tests. *ArXiv e-prints*, 806.

Hopkins P.F., Lauer T.R., Cox T.J., Hernquist L., & Kormendy J., 2008b. Dissipation and Extra Light in Galactic Nuclei: III. 'Core' Ellipticals and 'Missing' Light. *ArXiv e-prints*.

Hubble E.P., 1936. Realm of the Nebulae. *Yale University Press*.

Huchra J.P. & Geller M.J., 1982. Groups of galaxies. I - Nearby groups. *ApJ*, 257:423–437.

Humphrey P.J., Buote D.A., Gastaldello F., Zappacosta L., Bullock J.S., Brighenti F., & Mathews W.G., 2006. A Chandra View of Dark Matter in Early-Type Galaxies. *ApJ*, 646:899–918.

Hyde J.B. & Bernardi M., 2008a. Curvature in the scaling relations of early-type galaxies. *ArXiv e-prints*.

Hyde J.B. & Bernardi M., 2008b. The luminosity and stellar mass Fundamental Plane of early-type galaxies. *ArXiv e-prints*.

Iliev I.T., Ciardi B., Alvarez M.A., Maselli A., Ferrara A., Gnedin N.Y., Mellema G., Nakamoto T., Norman M.L., Razoumov A.O., Rijkhorst E.J., Ritzerveld J., Shapiro P.R., Susa H., Umemura M., & Whalen D.J., 2006. Cosmological radiative transfer codes comparison project - I. The static density field tests. *MNRAS*, 371:1057–1086.

Illingworth G., 1977. Rotation in 13 elliptical galaxies. *ApJ*, 218:L43–L47.

Iocco F., Mangano G., Miele G., Pisanti O., & Serpico P.D., 2008. Primordial Nucleosynthesis: from precision cosmology to fundamental physics. *ArXiv e-prints*, 809.

Jaffe W., 1983. A simple model for the distribution of light in spherical galaxies. *MNRAS*, 202:995–999.

Jesseit R., Naab T., Peletier R.F., & Burkert A., 2007. 2D kinematics of simulated disc merger remnants. *MNRAS*, 376:997–1020.

Jimenez R., Bernardi M., Haiman Z., Panter B., & Heavens A.F., 2007. The Ages, Metallicities, and Star Formation Histories of Early-Type Galaxies in the SDSS. *ApJ*, 669:947–951.

Jimenez R., Panter B., Heavens A.F., & Verde L., 2005. Baryonic conversion tree: the global assembly of stars and dark matter in galaxies from the Sloan Digital Sky Survey. *MNRAS*, 356:495–501.

Jimenez R., Verde L., & Oh S.P., 2003. Dark halo properties from rotation curves. *MNRAS*, 339:243–259.

Jing Y.P. & Suto Y., 2000. The Density Profiles of the Dark Matter Halo Are Not Universal. *ApJ*, 529:L69–L72.

Jones B.J.T. & Wyse R.F.G., 1985. The ionisation of the primeval plasma at the time of recombination. *A&A*, 149:144–150.

Jorgensen I., Franx M., & Kjaergaard P., 1993. Sources of scatter in the fundamental plane and the Dn-sigma relation. *ApJ*, 411:34–42.

Jorgensen I., Franx M., & Kjaergaard P., 1996. The Fundamental Plane for cluster E and S0 galaxies. *MNRAS*, 280:167–185.

Juneau S., Glazebrook K., Crampton D., McCarthy P.J., Savaglio S., Abraham R., Carlberg R.G., Chen H.W., Le Borgne D., Marzke R.O., Roth K., Jørgensen I., Hook I., & Murowinski R., 2005. Cosmic Star Formation History and Its Dependence on Galaxy Stellar Mass. *ApJ*, 619:L135–L138.

Kang X., van den Bosch F.C., & Pasquali A., 2007. On the origin of the dichotomy of early-type galaxies: the role of dry mergers and active galactic nucleus feedback. *MNRAS*, 381:389–400.

Kartaltepe J.S., Sanders D.B., Scoville N.Z., Calzetti D., Capak P., Koekemoer A., Mobasher B., Murayama T., Salvato M., Sasaki S.S., & Taniguchi Y., 2007. Evolution of the Frequency of Luminous ($\geq L_V^*$) Close Galaxy Pairs at $z < 1.2$ in the COSMOS Field. *ApJS*, 172:320–328.

Katz N., Hernquist L., & Weinberg D.H., 1992. Galaxies and gas in a cold dark matter universe. *ApJ*, 399:L109–L112.

Katz N., Keres D., Dave R., & Weinberg D.H., 2003. How Do Galaxies Get Their Gas? In J.L. Rosenberg & M.E. Putman, editors, *The IGM/Galaxy Connection. The Distribution of Baryons at z=0*, volume 281 of *Astrophysics and Space Science Library*, pages 185–+.

Katz N., Weinberg D.H., & Hernquist L., 1996. Cosmological Simulations with TreeSPH. *ApJS*, 105:19–+.

Kauffmann G., Heckman T.M., White S.D.M., Charlot S., Tremonti C., Brinchmann J., Bruzual G., Peng E.W., Seibert M., Bernardi M., Blanton M., Brinkmann J., Castander F., Csábai I., Fukugita M., Ivezic Z., Munn J.A., Nichol R.C., Padmanabhan N., Thakar A.R., Weinberg D.H., & York D., 2003a. Stellar masses and star formation histories for 10^5 galaxies from the Sloan Digital Sky Survey. *MNRAS*, 341:33–53.

Kauffmann G., Heckman T.M., White S.D.M., Charlot S., Tremonti C., Peng E.W., Seibert M., Brinkmann J., Nichol R.C., SubbaRao M., & York D., 2003b. The dependence of star formation history and internal structure on stellar mass for 10^5 low-redshift galaxies. *MNRAS*, 341:54–69.

Kawata D. & Gibson B.K., 2003. Multiwavelength cosmological simulations of elliptical galaxies. *MNRAS*, 346:135–152.

Kawata D. & Gibson B.K., 2005. Self-regulated active galactic nuclei heating in elliptical galaxies. *MNRAS*, 358:L16–L20.

Kelson D.D., Illingworth G.D., van Dokkum P.G., & Franx M., 2000. The Evolution of Early-Type Galaxies in Distant Clusters. III. M/L_V Ratios in the z=0.33 Cluster CL 1358+62. *ApJ*, 531:184–199.

Kelson D.D., van Dokkum P.G., Franx M., Illingworth G.D., & Fabricant D., 1997. Evolution of Early-Type Galaxies in Distant Clusters: The Fundamental Plane from Hubble Space Telescope Imaging and Keck Spectroscopy. *ApJ*, 478:L13+.

Kennicutt Jr. R.C., 1998. The Global Schmidt Law in Star-forming Galaxies. *ApJ*, 498:541–+.

Kereš D., Katz N., Fardal M., Dave R., & Weinberg D.H., 2008. Galaxies in a simulated ΛCDM Universe I: cold mode and hot cores. *ArXiv e-prints*.

Kereš D., Katz N., Weinberg D.H., & Davé R., 2005. How do galaxies get their gas? *MNRAS*, 363:2–28.

Khochfar S. & Burkert A., 2003. The Importance of Spheroidal and Mixed Mergers for Early-Type Galaxy Formation. *ApJ*, 597:L117–L120.

Khochfar S. & Burkert A., 2005. On the origin of isophotal shapes in elliptical galaxies. *MNRAS*, 359:1379–1385.

Khosroshahi H.G., Wadadekar Y., Kembhavi A., & Mobasher B., 2000. A Near-Infrared Photometric Plane for Elliptical Galaxies and Bulges of Spiral Galaxies. *ApJ*, 531:L103–L106.

Kimm T. & Yi S.K., 2007. Intrinsic Axis Ratio Distribution of Early-Type Galaxies from the Sloan Digital Sky Survey. *ApJ*, 670:1048–1055.

Kobayashi C., 2005. GRAPE-SPH chemodynamical simulation of elliptical galaxies - II. Scaling relations and the fundamental plane. *MNRAS*, 361:1216–1226.

Kochanek C.S. & Dalal N., 2003. CDM Substructure in Gravitational Lenses: Tests and Results. In S.H. Holt & C.S. Reynolds, editors, *The Emergence of Cosmic Structure*, volume 666 of *American Institute of Physics Conference Series*, pages 103–112.

Komatsu E., Dunkley J., Nolta M.R., Bennett C.L., Gold B., Hinshaw G., Jarosik N., Larson D., Limon M., Page L., Spergel D.N., Halpern M., Hill R.S., Kogut A., Meyer S.S., Tucker G.S., Weiland J.L., Wollack E., & Wright E.L., 2009. Five-Year Wilkinson Microwave Anisotropy Probe Observations: Cosmological Interpretation. *ApJS*, 180:330–376.

Koopmans L.V.E. & Treu T., 2003. The Structure and Dynamics of Luminous and Dark Matter in the Early-Type Lens Galaxy of 0047-281 at z = 0.485. *ApJ*, 583:606–615.

Koopmans L.V.E., Treu T., Bolton A.S., Burles S., & Moustakas L.A., 2006. The Sloan Lens ACS Survey. III. The Structure and Formation of Early-Type Galaxies and Their Evolution since z ˜ 1. *ApJ*, 649:599–615.

Kormendy J., 1977. Brightness distributions in compact and normal galaxies. II - Structure parameters of the spheroidal component. *ApJ*, 218:333–346.

Kormendy J. & Bender R., 1996. A Proposed Revision of the Hubble Sequence for Elliptical Galaxies. *ApJ*, 464:L119+.

Kormendy J. & Djorgovski S., 1989. Surface photometry and the structure of elliptical galaxies. *ARA&A*, 27:235–277.

Kowalski M., Rubin D., Aldering G., Agostinho R.J., Amadon A., Amanullah R., Balland C., Barbary K., Blanc G., Challis P.J., Conley A., Connolly N.V., Covarrubias R., Dawson K.S., Deustua S.E., Ellis R., Fabbro S., Fadeyev V., Fan X., Farris B., Folatelli G., Frye B.L., Garavini G., Gates E.L., Germany L., Goldhaber G., Goldman B., Goobar A., Groom D.E., Haissinski J., Hardin D., Hook I., Kent S., Kim A.G., Knop R.A., Lidman C., Linder E.V., Mendez J., Meyers J., Miller G.J., Moniez M., Mourão A.M., Newberg H., Nobili S., Nugent P.E., Pain R., Perdereau O., Perlmutter S., Phillips M.M., Prasad V., Quimby R., Regnault N., Rich J., Rubenstein E.P., Ruiz-Lapuente P., Santos F.D., Schaefer B.E., Schommer R.A., Smith R.C., Soderberg A.M., Spadafora A.L., Strolger L.G., Strovink M., Suntzeff N.B., Suzuki N., Thomas R.C., Walton N.A., Wang L., Wood-Vasey W.M., & Yun J.L., 2008.

Improved Cosmological Constraints from New, Old, and Combined Supernova Data Sets. *ApJ*, 686:749–778.

Kronawitter A., Saglia R.P., Gerhard O., & Bender R., 2000. Orbital structure and mass distribution in elliptical galaxies. *A&AS*, 144:53–84.

La Barbera F., Busarello G., Merluzzi P., de la Rosa I.G., Coppola G., & Haines C.P., 2008. The SDSS-UKIDSS Fundamental Plane of Early-Type Galaxies. *ApJ*, 689:913–918.

La Barbera F., Covone G., Busarello G., Capaccioli M., Haines C.P., Mercurio A., & Merluzzi P., 2005. New insights into the structure of early-type galaxies: the Photometric Plane at z˜ 0.3. *MNRAS*, 358:1116–1132.

Larson R.B., 1974. Dynamical models for the formation and evolution of spherical galaxies. *MNRAS*, 166:585–616.

Lauer T.R., 1985. Boxy isophotes, discs and dust lanes in elliptical galaxies. *MNRAS*, 216:429–438.

Le Fèvre O., Abraham R., Lilly S.J., Ellis R.S., Brinchmann J., Schade D., Tresse L., Colless M., Crampton D., Glazebrook K., Hammer F., & Broadhurst T., 2000. Hubble Space Telescope imaging of the CFRS and LDSS redshift surveys - IV. Influence of mergers in the evolution of faint field galaxies from z˜1. *MNRAS*, 311:565–575.

Lee J.H., Lee M.G., & Hwang H.S., 2006. The Nature of Blue Early-Type Galaxies in the GOODS Fields. *ApJ*, 650:148–165.

Li Y., Mac Low M.M., & Klessen R.S., 2005a. Control of Star Formation in Galaxies by Gravitational Instability. *ApJ*, 620:L19–L22.

Li Y., Mac Low M.M., & Klessen R.S., 2005b. Star Formation in Isolated Disk Galaxies. I. Models and Characteristics of Nonlinear Gravitational Collapse. *ApJ*, 626:823–843.

Liddle A.R. & Lyth D.H., 2000. *Cosmological Inflation and Large-Scale Structure*. Cosmological Inflation and Large-Scale Structure, by Andrew R. Liddle and David H. Lyth, pp. 414. ISBN 052166022X. Cambridge, UK: Cambridge University Press, April 2000.

Lima Neto G.B., Gerbal D., & Márquez I., 1999. The specific entropy of elliptical galaxies: an explanation for profile-shape distance indicators? *MNRAS*, 309:481–495.

Loewenstein M., 2000. Heating of Intergalactic Gas and Cluster Scaling Relations. *ApJ*, 532:17–27.

Lucey J.R., Bower R.G., & Ellis R.S., 1991. The fundamental plane of cluster ellipticals. *MNRAS*, 249:755–762.

Lucy L.B., 1977. A numerical approach to the testing of the fission hypothesis. *AJ*, 82:1013–1024.

Lukić Z., Heitmann K., Habib S., Bashinsky S., & Ricker P.M., 2007. The Halo Mass Function: High-Redshift Evolution and Universality. *ApJ*, 671:1160–1181.

Magorrian J. & Ballantyne D., 2001. Mass profiles and anisotropies of early-type galaxies. *MNRAS*, 322:702–714.

Maio U., Dolag K., Ciardi B., & Tornatore L., 2007. Metal and molecule cooling in simulations of structure formation. *MNRAS*, 379:963–973.

Mamon G.A. & Łokas E.L., 2005a. Dark matter in elliptical galaxies - I. Is the total mass density profile of the NFW form or even steeper? *MNRAS*, 362:95–109.

Mamon G.A. & Łokas E.L., 2005b. Dark matter in elliptical galaxies - II. Estimating the mass within the virial radius. *MNRAS*, 363:705–722.

Manrique A., Raig A., Salvador-Solé E., Sanchis T., & Solanes J.M., 2003. On the Origin of the Inner Structure of Halos. *ApJ*, 593:26–37.

Márquez I., Lima Neto G.B., Capelato H., Durret F., & Gerbal D., 2000. Gravo-thermal properties and formation of elliptical galaxies. *A&A*, 353:873–886.

Márquez I., Lima Neto G.B., Capelato H., Durret F., Lanzoni B., & Gerbal D., 2001. Energy, entropy and mass scaling relations for elliptical galaxies. Towards a physical understanding of their photometric properties. *A&A*, 379:767–780.

Martin C.L. & Kennicutt Jr. R.C., 2001. Star Formation Thresholds in Galactic Disks. *ApJ*, 555:301–321.

Martínez-Serrano F.J., Serna A., Domínguez-Tenreiro R., & Mollá M., 2008. Chemical evolution of galaxies - I. A composition-dependent SPH model for chemical evolution and cooling. *MNRAS*, 388:39–55.

Massey R., Rhodes J., Leauthaud A., Capak P., Ellis R., Koekemoer A., Réfrégier A., Scoville N., Taylor J.E., Albert J., Bergé J., Heymans C., Johnston D., Kneib J.P., Mellier Y., Mobasher B., Semboloni E., Shopbell P., Tasca L., & Van Waerbeke L., 2007. COSMOS: Three-dimensional Weak Lensing and the Growth of Structure. *ApJS*, 172:239–253.

Matsushita K., 2001. Origin of the Scatter in the X-Ray Luminosity of Early-Type Galaxies Observed with ROSAT. *ApJ*, 547:693–704.

Matteucci F., 2003. What determines galactic evolution? *Ap&SS*, 284:539–548.

Mayer L., Quinn T., Wadsley J., & Stadel J., 2004. The Evolution of Gravitationally Unstable Protoplanetary Disks: Fragmentation and Possible Giant Planet Formation. *ApJ*, 609:1045–1064.

McCarthy P.J., Le Borgne D., Crampton D., Chen H.W., Abraham R.G., Glazebrook K., Savaglio S., Carlberg R.G., Marzke R.O., Roth K., Jørgensen I., Hook I., Murowinski R., & Juneau S., 2004. Evolved Galaxies at $z > 1.5$ from the Gemini Deep Deep Survey: The Formation Epoch of Massive Stellar Systems. *ApJ*, 614:L9–L12.

McIntosh D.H., Bell E.F., Rix H.W., Wolf C., Heymans C., Peng C.Y., Somerville R.S., Barden M., Beckwith S.V.W., Borch A., Caldwell J.A.R., Häußler B., Jahnke K., Jogee S., Meisenheimer K., Sánchez S.F., & Wisotzki L., 2005. The Evolution of Early-Type Red Galaxies with the GEMS Survey: Luminosity-Size and Stellar Mass-Size Relations Since z=1. *ApJ*, 632:191–209.

McKee C.F. & Ostriker E.C., 2007. Theory of Star Formation. *ARA&A*, 45:565–687.

Menanteau F., Abraham R.G., & Ellis R.S., 2001. Evidence for evolving spheroidals in the Hubble Deep Fields North and South. *MNRAS*, 322:1–12.

Menanteau F., Ford H.C., Illingworth G.D., Sirianni M., Blakeslee J.P., Meurer G.R., Martel A.R., Benítez N., Postman M., Franx M., Ardila D.R., Bartko F., Bouwens R.J., Broadhurst T.J., Brown R.A., Burrows C.J., Cheng E.S., Clampin M., Cross N.J.G., Feldman P.D., Golimowski D.A., Gronwall C., Hartig G.F., Infante L., Kimble R.A., Krist J.E., Lesser M.P., Miley G.K., Rosati P., Sparks W.B., Tran H.D., Tsvetanov Z.I., White R.L., & Zheng W., 2004. Internal Color Properties of Resolved Spheroids in the Deep Hubble Space Telescope Advanced Camera for Surveys Field of UGC 10214. *ApJ*, 612:202–214.

Menanteau F., Martel A.R., Tozzi P., Frye B., Ford H.C., Infante L., Benítez N., Galaz G., Coe D., Illingworth G.D., Hartig G.F., & Clampin M., 2005. The Nature of Blue Cores in Spheroids: A Possible Connection with Active Galactic Nuclei and Star Formation. *ApJ*, 620:697–702.

Merritt D., Graham A.W., Moore B., Diemand J., & Terzić B., 2006. Empirical Models for Dark Matter Halos. I. Nonparametric Construction of Density Profiles and Comparison with Parametric Models. *AJ*, 132:2685–2700.

Merritt D., Navarro J.F., Ludlow A., & Jenkins A., 2005. A Universal Density Profile for Dark and Luminous Matter? *ApJ*, 624:L85–L88.

Meza A., Navarro J.F., Steinmetz M., & Eke V.R., 2003. Simulations of Galaxy Formation in a ΛCDM Universe. III. The Dissipative Formation of an Elliptical Galaxy. *ApJ*, 590:619–635.

Michard R. & Prugniel P., 2004. Peculiarities and populations in elliptical galaxies. I. An old question revisited. *A&A*, 423:833–847.

Miyoshi K. & Kihara T., 1975. Development of the correlation of galaxies in an expanding universe. *PASJ*, 27:333–346.

Mobasher B., Dickinson M., Ferguson H.C., Giavalisco M., Wiklind T., Stark D., Ellis R.S., Fall S.M., Grogin N.A., Moustakas L.A., Panagia N., Sosey M., Stiavelli M., Bergeron E., Casertano S., Ingraham P., Koekemoer A., Labbé I., Livio M., Rodgers B., Scarlata C., Vernet J., Renzini A., Rosati P., Kuntschner H., Kümmel M., Walsh J.R., Chary R., Eisenhardt P., Pirzkal N., & Stern D., 2005. Evidence for a Massive Poststarburst Galaxy at z˜6.5. *ApJ*, 635:832–844.

Mobasher B., Guzman R., Aragon-Salamanca A., & Zepf S., 1999. The near-infrared Fundamental Plane of elliptical galaxies. *MNRAS*, 304:225–234.

Monaghan J.J., 1992. Smoothed particle hydrodynamics. *ARA&A*, 30:543–574.

Moore B., Ghigna S., Governato F., Lake G., Quinn T., Stadel J., & Tozzi P., 1999a. Dark Matter Substructure within Galactic Halos. *ApJ*, 524:L19–L22.

Moore B., Quinn T., Governato F., Stadel J., & Lake G., 1999b. Cold collapse and the core catastrophe. *MNRAS*, 310:1147–1152.

Moriondo G., Cimatti A., & Daddi E., 2000. The morphology of extremely red objects. *A&A*, 364:26–42.

Murali C., Katz N., Hernquist L., Weinberg D.H., & Davé R., 2002. The Growth of Galaxies in Cosmological Simulations of Structure Formation. *ApJ*, 571:1–14.

Murante G., Giovalli M., Gerhard O., Arnaboldi M., Borgani S., & Dolag K., 2007. The importance of mergers for the origin of intracluster stars in cosmological simulations of galaxy clusters. *MNRAS*, 377:2–16.

Myers S.T., Fassnacht C.D., Djorgovski S.G., Blandford R.D., Matthews K., Neugebauer G., Pearson T.J., Readhead A.C.S., Smith J.D., Thompson D.J., Womble D.S., Browne I.W.A., Wilkinson P.N., Nair S., Jackson N., Snellen I.A.G., Miley G.K., de Bruyn A.G., & Schilizzi R.T., 1995. 1608+656: A Quadruple-Lens System Found in the CLASS Gravitational Lens Survey. *ApJ*, 447:L5+.

Naab T. & Burkert A., 2003. Statistical Properties of Collisionless Equal- and Unequal-Mass Merger Remnants of Disk Galaxies. *ApJ*, 597:893–906.

Naab T., Johansson P.H., Ostriker J.P., & Efstathiou G., 2007. Formation of Early-Type Galaxies from Cosmological Initial Conditions. *ApJ*, 658:710–720.

Naab T., Khochfar S., & Burkert A., 2006. Properties of Early-Type, Dry Galaxy Mergers and the Origin of Massive Elliptical Galaxies. *ApJ*, 636:L81–L84.

Napolitano N.R., Capaccioli M., Romanowsky A.J., Douglas N.G., Merrifield M.R., Kuijken K., Arnaboldi M., Gerhard O., & Freeman K.C., 2005. Mass-to-light ratio gradients in early-type galaxy haloes. *MNRAS*, 357:691–706.

Navarro J.F., Abadi M.G., & Steinmetz M., 2004a. Tidal Torques and the Orientation of Nearby Disk Galaxies. *ApJ*, 613:L41–L44.

Navarro J.F., Frenk C.S., & White S.D.M., 1995. Simulations of X-ray clusters. *MNRAS*, 275:720–740.

Navarro J.F., Frenk C.S., & White S.D.M., 1996. The Structure of Cold Dark Matter Halos. *ApJ*, 462:563–+.

Navarro J.F., Hayashi E., Power C., Jenkins A.R., Frenk C.S., White S.D.M., Springel V., Stadel J., & Quinn T.R., 2004b. The inner structure of ΛCDM haloes - III. Universality and asymptotic slopes. *MNRAS*, 349:1039–1051.

Navarro J.F. & White S.D.M., 1994. Simulations of dissipative galaxy formation in hierarchically clustering universes-2. Dynamics of the baryonic component in galactic haloes. *MNRAS*, 267:401–412.

Nieto J.L. & Bender R., 1989. Boxiness in elliptical galaxies. *A&A*, 215:266–271.

Nipoti C., Londrillo P., & Ciotti L., 2003. Galaxy merging, the fundamental plane of elliptical galaxies and the M_{BH}-σ_0 relation. *MNRAS*, 342:501–512.

Oñorbe J., Domínguez-Tenreiro R., Artal H., & Serna A., 2006. Dark haloes in ellipticals and the tilt of the Fundamental Plane: some clues from self-consistent hydrodynamical simulations. In G.A. Mamon, F. Combes, C. Deffayet, & B. Fort, editors, *EAS Publications Series*, volume 20 of *EAS Publications Series*, pages 275–276.

Oñorbe J., Domínguez-Tenreiro R., Artal H., & Serna A., 2007. Elliptical Galaxies Since z $\tilde{1}$.5: The Evolution of The Fundamental Planes. In F. Combes & J. Palous, editors, *IAU Symposium*, volume 235 of *IAU Symposium*, pages 420–420.

Oñorbe J., Domínguez-Tenreiro R., & Sáiz A., 2006. The Fundamental Plane of Elliptical Galaxies: Clues from Hydrodynamical Simulations. In *Proceedings of Bernard's Cosmic Stories: from primordial fluctuations to the birth of stars and galaxies.June 26-30, 2006. UIMP, VALENCIA, SPAIN. Meeting abstracts, http://www.astro.rug.nl/˜bernard60/index.php, p.77.1.*

Oñorbe J., Domínguez-Tenreiro R., Sáiz A., Artal H., & Serna A., 2006. Clues on regularity in the structure and kinematics of elliptical galaxies from self-consistent hydrodynamical simulations: the dynamical Fundamental Plane. *MNRAS*, 373:503–520.

Oñorbe J., Domínguez-Tenreiro R., Sáiz A., & Serna A., 2007. Bright and dark matter in elliptical galaxies: Mass and velocity distributions from self-consistent hydrodynamical simulations. *MNRAS*, 376:39–60.

Oñorbe J., Domínguez-Tenreiro R., Sáiz A., Serna A., & Artal H., 2005. Clues on the Physical Origin of the Fundamental Plane from Self-Consistent Hydrodynamical Simulations. *ApJ*, 632:L57–L60.

Oñorbe J., Domínguez-Tenreiro R., & Serna A., 2008. The Luminous Matter Profiles in Ellipticals since z 1.5: The Photometric Plane and its Evolution. In J.H. Knapen, T.J. Mahoney, & A. Vazdekis, editors, *Pathways Through an Eclectic Universe*, volume 390 of *Astronomical Society of the Pacific Conference Series*, pages 498–+.

O'Sullivan E. & Ponman T.J., 2004a. The isolated elliptical NGC 4555 observed with Chandra. *MNRAS*, 354:935–944.

O'Sullivan E. & Ponman T.J., 2004b. XMM-Newton and Chandra observations of three X-ray-faint early-type galaxies. *MNRAS*, 349:535–546.

Outram P.J., Shanks T., Boyle B.J., Croom S.M., Hoyle F., Loaring N.S., Miller L., & Smith R.J., 2004. The 2dF QSO Redshift Survey - XIII. A measurement of Λ from the quasi-stellar object power spectrum, $P^S(k_\parallel, k_\perp)$. *MNRAS*, 348:745–752.

Padmanabhan N., Seljak U., Strauss M.A., Blanton M.R., Kauffmann G., Schlegel D.J., Tremonti C., Bahcall N.A., Bernardi M., Brinkmann J., Fukugita M., & Ivezić Ž., 2004. Stellar and dynamical masses of ellipticals in the Sloan Digital Sky Survey. *New Astronomy*, 9:329–342.

Padmanabhan T., 1993. *Structure Formation in the Universe*. Structure Formation in the Universe, by T. Padmanabhan, pp. 499. ISBN 0521424860. Cambridge, UK: Cambridge University Press, June 1993.

Padoan P., Juvela M., Goodman A.A., & Nordlund Å., 2001. The Turbulent Shock Origin of Proto-Stellar Cores. *ApJ*, 553:227–234.

Pahre M.A., de Carvalho R.R., & Djorgovski S.G., 1998. Near-Infrared Imaging of Early-Type Galaxies. IV. The Physical Origins of the Fundamental Plane Scaling Relations. *AJ*, 116:1606–1625.

Pahre M.A., Djorgovski S.G., & de Carvalho R.R., 1995. The Near-Infrared Fundamental Plane of Elliptical Galaxies. *ApJ*, 453:L17+.

Papovich C., Dickinson M., Giavalisco M., Conselice C.J., & Ferguson H.C., 2005. The Assembly of Diversity in the Morphologies and Stellar Populations of High-Redshift Galaxies. *ApJ*, 631:101–120.

Patton D.R., Pritchet C.J., Carlberg R.G., Marzke R.O., Yee H.K.C., Hall P.B., Lin H., Morris S.L., Sawicki M., Shepherd C.W., & Wirth G.D., 2002. Dynamically Close Galaxy Pairs and Merger Rate Evolution in the CNOC2 Redshift Survey. *ApJ*, 565:208–222.

Peacock J.A., 1999. *Cosmological Physics*. Cosmological Physics, by John A. Peacock, pp. 704. ISBN 052141072X. Cambridge, UK: Cambridge University Press, January 1999.

Pedersen K., Rasmussen J., Sommer-Larsen J., Toft S., Benson A.J., & Bower R.G., 2006. Discovery of a very extended X-ray halo around a quiescent spiral galaxy The missing link of galaxy formation. *New Astronomy*, 11:465–470.

Peebles P.J.E., 1974. The Gravitational-Instability Picture and the Nature of the Distribution of Galaxies. *ApJ*, 189:L51+.

Peebles P.J.E., 1980. *The large-scale structure of the universe*. Research supported by the National Science Foundation. Princeton, N.J., Princeton University Press, 1980. 435 p.

Peebles P.J.E., 2002. When did the Large Elliptical Galaxies Form? In N. Metcalfe & T. Shanks, editors, *A New Era in Cosmology*, volume 283 of *Astronomical Society of the Pacific Conference Series*, pages 351–+.

Pellegrini S., 2005. The X-ray emission properties and the dichotomy in the central stellar cusp shapes of early-type galaxies. *MNRAS*, 364:169–178.

Percival W.J., Cole S., Eisenstein D.J., Nichol R.C., Peacock J.A., Pope A.C., & Szalay A.S., 2007. Measuring the Baryon Acoustic Oscillation scale using the Sloan Digital Sky Survey and 2dF Galaxy Redshift Survey. *MNRAS*, 381:1053–1066.

Pipino A., Silk J., & Matteucci F., 2009. Supermassive black holes, star formation and downsizing of elliptical galaxies. *MNRAS*, 392:475–482.

Pointecouteau E., Arnaud M., & Pratt G.W., 2005. The structural and scaling properties of nearby galaxy clusters. I. The universal mass profile. *A&A*, 435:1–7.

Power C. & Knebe A., 2006. The impact of box size on the properties of dark matter haloes in cosmological simulations. *MNRAS*, 370:691–701.

Power C., Navarro J.F., Jenkins A., Frenk C.S., White S.D.M., Springel V., Stadel J., & Quinn T., 2003. The inner structure of ΛCDM haloes - I. A numerical convergence study. *MNRAS*, 338:14–34.

Pratt G.W. & Arnaud M., 2005. XMM-Newton observations of three poor clusters: Similarity in dark matter and entropy profiles down to low mass. *A&A*, 429:791–806.

Press W.H. & Schechter P., 1974. Formation of Galaxies and Clusters of Galaxies by Self-Similar Gravitational Condensation. *ApJ*, 187:425–438.

Primack J.R., 2004. Summary talk: How serious are the problems faced by CDM: cusps, thin disks, and halo substructure. In S. Ryder, D. Pisano, M. Walker, & K. Freeman, editors, *Dark Matter in Galaxies*, volume 220 of *IAU Symposium*, pages 53–+.

Prugniel P. & Simien F., 1996. The fundamental plane of early-type galaxies: stellar populations and mass-to-light ratio. *A&A*, 309:749–759.

Prugniel P. & Simien F., 1997. The fundamental plane of early-type galaxies: non-homology of the spatial structure. *A&A*, 321:111–122.

Prunet S., Pichon C., Aubert D., Pogosyan D., Teyssier R., & Gottloeber S., 2008. Initial Conditions For Large Cosmological Simulations. *ApJS*, 178:179–188.

Ravindranath S., Giavalisco M., Ferguson H.C., Conselice C., Katz N., Weinberg M., Lotz J., Dickinson M., Fall S.M., Mobasher B., & Papovich C., 2006. The Morphological Diversities among Star-forming Galaxies at High Redshifts in the Great Observatories Origins Deep Survey. *ApJ*, 652:963–980.

Recillas-Cruz E., Serrano A., Cruz-Gonzalez I., & Carrasco L., 1991. The manifold of early-type galaxies from IR photometry in clusters of galaxies - The Virgo cluster. *A&A*, 249:312–322.

Recillas-Cruz E., Serrano P.G.A., Cruz-Gonzalez I., & Carrasco L., 1990. The manifold of early-type galaxies from IR photometry - The Coma cluster. *A&A*, 229:64–74.

Reese E.D., Carlstrom J.E., Joy M., Mohr J.J., Grego L., & Holzapfel W.L., 2002. Determining the Cosmic Distance Scale from Interferometric Measurements of the Sunyaev-Zeldovich Effect. *ApJ*, 581:53–85.

Renzini A. & Ciotti L., 1993. Transverse Dissections of the Fundamental Planes of Elliptical Galaxies and Clusters of Galaxies. *ApJ*, 416:L49+.

Riess A.G., Strolger L.G., Casertano S., Ferguson H.C., Mobasher B., Gold B., Challis P.J., Filippenko A.V., Jha S., Li W., Tonry J., Foley R., Kirshner R.P., Dickinson M., MacDonald E., Eisenstein D., Livio M., Younger J., Xu C., Dahlén T., & Stern

D., 2007. New Hubble Space Telescope Discoveries of Type Ia Supernovae at $z \geq 1$: Narrowing Constraints on the Early Behavior of Dark Energy. *ApJ*, 659:98–121.

Rix H.W. & White S.D.M., 1992. Optimal estimates of line-of-sight velocity distributions from absorption line spectra of galaxies - Nuclear discs in elliptical galaxies. *MNRAS*, 254:389–403.

Robertson B., Cox T.J., Hernquist L., Franx M., Hopkins P.F., Martini P., & Springel V., 2006. The Fundamental Scaling Relations of Elliptical Galaxies. *ApJ*, 641:21–40.

Roettiger K., Stone J.M., & Burns J.O., 1999. Magnetic Field Evolution in Merging Clusters of Galaxies. *ApJ*, 518:594–602.

Romanowsky A.J., 2006. Elliptical Galaxy Halo Masses from Internal Kinematics. In G.A. Mamon, F. Combes, C. Deffayet, & B. Fort, editors, *EAS Publications Series*, volume 20 of *EAS Publications Series*, pages 119–126.

Romanowsky A.J., Douglas N.G., Arnaboldi M., Kuijken K., Merrifield M.R., Napolitano N.R., Capaccioli M., & Freeman K.C., 2003. A Dearth of Dark Matter in Ordinary Elliptical Galaxies. *Science*, 301:1696–1698.

Romanowsky A.J. & Kochanek C.S., 2001. Dynamics of Stars and Globular Clusters in M87. *ApJ*, 553:722–732.

Romeo A.D., Portinari L., & Sommer-Larsen J., 2005. Simulating galaxy clusters - II. Global star formation histories and the galaxy populations. *MNRAS*, 361:983–996.

Rothberg B. & Joseph R.D., 2006. A Survey of Merger Remnants. III. Are Merger Remnants Supported by Rotation or Anisotropy? *AJ*, 132:976–988.

Ryden B.S., Forbes D.A., & Terlevich A.I., 2001. Structural evolution in elliptical galaxies: the age-shape relation. *MNRAS*, 326:1141–1148.

Saglia R.P., Colless M., Burstein D., Davies R.L., McMahan R.K., & Wegner G., 2001. The peculiar motions of early-type galaxies in two distant regions - VI. The maximum-likelihood Gaussian algorithm. *MNRAS*, 324:389–419.

Saitoh T.R., Daisaka H., Kokubo E., Makino J., Okamoto T., Tomisaka K., Wada K., & Yoshida N., 2008. Toward first-principle simulations of galaxy formation: I. How should we choose star formation criteria in high-resolution simulations of disk galaxies? *ArXiv e-prints*, 802.

Sáiz A., Domínguez-Tenreiro R., & Serna A., 2003. Early-type galaxies at low Z from self-consistent hydrodynamical simulations. *Ap&SS*, 284:411–414.

Sáiz A., Domínguez-Tenreiro R., & Serna A., 2004. Elliptical Galaxies at z=0 from Self-consistent Hydrodynamical Simulations: Comparison with Sloan Digital Sky Survey Structural and Kinematical Data. *ApJ*, 601:L131–L134.

Sakai S., Mould J.R., Hughes S.M.G., Huchra J.P., Macri L.M., Kennicutt Jr. R.C., Gibson B.K., Ferrarese L., Freedman W.L., Han M., Ford H.C., Graham J.A., Illingworth G.D., Kelson D.D., Madore B.F., Sebo K., Silbermann N.A., & Stetson P.B., 2000. The Hubble Space Telescope Key Project on the Extragalactic Distance Scale. XXIV. The Calibration of Tully-Fisher Relations and the Value of the Hubble Constant. *ApJ*, 529:698–722.

Salvador-Solé E., Manrique A., González-Casado G., & Hansen S.H., 2007. The Nature of Dark Matter and the Density Profile and Central Behavior of Relaxed Halos. *ApJ*, 666:181–188.

Salvador-Solé E., Manrique A., & Solanes J.M., 2005. Scale radii and aggregation histories of dark haloes. *MNRAS*, 358:901–912.

Scannapieco C., Tissera P.B., White S.D.M., & Springel V., 2008. Effects of Supernova Feedback on the Formation of Galaxies. *ArXiv e-prints*.

Schiavon R.P., Faber S.M., Konidaris N., Graves G., Willmer C.N.A., Weiner B.J., Coil A.L., Cooper M.C., Davis M., Harker J., Koo D.C., Newman J.A., & Yan R., 2006. The DEEP2 Galaxy Redshift Survey: Mean Ages and Metallicities of Red Field Galaxies at z ˜ 0.9 from Stacked Keck DEIMOS Spectra. *ApJ*, 651:L93–L96.

Scoville N., Abraham R.G., Aussel H., Barnes J.E., Benson A., Blain A.W., Calzetti D., Comastri A., Capak P., Carilli C., Carlstrom J.E., Carollo C.M., Colbert J., Daddi E., Ellis R.S., Elvis M., Ewald S.P., Fall M., Franceschini A., Giavalisco M., Green W., Griffiths R.E., Guzzo L., Hasinger G., Impey C., Kneib J.P., Koda J., Koekemoer A., Lefevre O., Lilly S., Liu C.T., McCracken H.J., Massey R., Mellier Y., Miyazaki S., Mobasher B., Mould J., Norman C., Refregier A., Renzini A., Rhodes J., Rich M., Sanders D.B., Schiminovich D., Schinnerer E., Scodeggio M., Sheth K., Shopbell P.L., Taniguchi Y., Tyson N.D., Urry C.M., Van Waerbeke L., Vettolani P., White S.D.M., & Yan L., 2007. COSMOS: Hubble Space Telescope Observations. *ApJS*, 172:38–45.

Seljak U., Makarov A., McDonald P., Anderson S.F., Bahcall N.A., Brinkmann J., Burles S., Cen R., Doi M., Gunn J.E., Ivezić Ž., Kent S., Loveday J., Lupton R.H., Munn J.A., Nichol R.C., Ostriker J.P., Schlegel D.J., Schneider D.P., Tegmark M., Berk D.E., Weinberg D.H., & York D.G., 2005. Cosmological parameter analysis including SDSS Lyα forest and galaxy bias: Constraints on the primordial spectrum of fluctuations, neutrino mass, and dark energy. *Phys. Rev. D*, 71(10):103515–+.

Serna A., Domínguez-Tenreiro R., & Sáiz A., 2003. Conservation Laws in Smooth Particle Hydrodynamics: The DEVA Code. *ApJ*, 597:878–892.

Sérsic J.L., 1968. *Atlas de galaxias australes*. Cordoba, Argentina: Observatorio Astronomico, 1968.

Silk J., 2005. Ultraluminous starbursts from supermassive black hole-induced outflows. *MNRAS*, 364:1337–1342.

Silk J. & Bouwens R., 2001. The formation of galaxies. *New Astronomy Review*, 45:337–350.

Silk J. & Rees M.J., 1998. Quasars and galaxy formation. *A&A*, 331:L1–L4.

Sirko E., 2005. Initial Conditions to Cosmological N-Body Simulations, or, How to Run an Ensemble of Simulations. *ApJ*, 634:728–743.

Slyz A.D., Devriendt J.E.G., Bryan G., & Silk J., 2005. Towards simulating star formation in the interstellar medium. *MNRAS*, 356:737–752.

Solanes J.M., Manrique A., González-Casado G., & Salvador-Solé E., 2005. Implications of Halo Inside-Out Growth for the X-Ray Properties of Nearby Galaxy Systems within the Preheating Scenario. *ApJ*, 628:45–60.

Sommer-Larsen J., Götz M., & Portinari L., 2002. CDM, Feedback and the Hubble Sequence. *Ap&SS*, 281:519–524.

Spergel D.N., Bean R., Doré O., Nolta M.R., Bennett C.L., Dunkley J., Hinshaw G., Jarosik N., Komatsu E., Page L., Peiris H.V., Verde L., Halpern M., Hill R.S., Kogut A., Limon M., Meyer S.S., Odegard N., Tucker G.S., Weiland J.L., Wollack E., & Wright E.L., 2007. Three-Year Wilkinson Microwave Anisotropy Probe (WMAP) Observations: Implications for Cosmology. *ApJS*, 170:377–408.

Spergel D.N., Verde L., Peiris H.V., Komatsu E., Nolta M.R., Bennett C.L., Halpern M., Hinshaw G., Jarosik N., Kogut A., Limon M., Meyer S.S., Page L., Tucker G.S., Weiland J.L., Wollack E., & Wright E.L., 2003. First-Year Wilkinson Microwave Anisotropy Probe (WMAP) Observations: Determination of Cosmological Parameters. *ApJS*, 148:175–194.

Springel V., White S.D.M., Jenkins A., Frenk C.S., Yoshida N., Gao L., Navarro J., Thacker R., Croton D., Helly J., Peacock J.A., Cole S., Thomas P., Couchman H., Evrard A., Colberg J., & Pearce F., 2005. Simulations of the formation, evolution and clustering of galaxies and quasars. *Nature*, 435:629–636.

Squires G., Kaiser N., Fahlman G., Babul A., & Woods D., 1996. A Weak Gravitational Lensing Analysis of Abell 2390. *ApJ*, 469:73–+.

Stadel J., Katz N., Weinberg D., & Hernquist L., 1997. *Overview of SKID (http://www-hpcc.astro.washington.edu/tools/SKID.html).*

Stanford S.A., Dickinson M., Postman M., Ferguson H.C., Lucas R.A., Conselice C.J., Budavári T., & Somerville R., 2004. The Evolution of Early-Type Field Galaxies Selected from a NICMOS Map of the Hubble Deep Field North. *AJ*, 127:131–155.

Stinson G., Seth A., Katz N., Wadsley J., Governato F., & Quinn T., 2006. Star formation and feedback in smoothed particle hydrodynamic simulations - I. Isolated galaxies. *MNRAS*, 373:1074–1090.

Stoehr F., 2006. Circular velocity profiles of dark matter haloes. *MNRAS*, 365:147–152.

Suto Y., 2003. Simulations of Large-Scale Structure in the New Millennium. *ArXiv Astrophysics e-prints.*

Tegmark M., Strauss M.A., Blanton M.R., Abazajian K., Dodelson S., Sandvik H., Wang X., Weinberg D.H., Zehavi I., Bahcall N.A., Hoyle F., Schlegel D., Scoccimarro R., Vogeley M.S., Berlind A., Budavari T., Connolly A., Eisenstein D.J., Finkbeiner D., Frieman J.A., Gunn J.E., Hui L., Jain B., Johnston D., Kent S., Lin H., Nakajima R., Nichol R.C., Ostriker J.P., Pope A., Scranton R., Seljak U., Sheth R.K., Stebbins A., Szalay A.S., Szapudi I., Xu Y., Annis J., Brinkmann J., Burles S., Castander F.J., Csabai I., Loveday J., Doi M., Fukugita M., Gillespie B., Hennessy G., Hogg D.W., Ivezić Ž., Knapp G.R., Lamb D.Q., Lee B.C., Lupton R.H., McKay T.A., Kunszt P., Munn J.A., O'Connell L., Peoples J., Pier J.R., Richmond M., Rockosi C., Schneider D.P., Stoughton C., Tucker D.L., vanden Berk D.E., Yanny B., & York D.G., 2004. Cosmological parameters from SDSS and WMAP. *Phys. Rev. D*, 69(10):103501–+.

Thacker R.J. & Couchman H.M.P., 2000. Implementing Feedback in Simulations of Galaxy Formation: A Survey of Methods. *ApJ*, 545:728–752.

Thomas D., Greggio L., & Bender R., 1999. Constraints on galaxy formation from alpha-enhancement in luminous elliptical galaxies. *MNRAS*, 302:537–548.

Thomas D., Maraston C., & Bender R., 2002. The Epoch(s) of Early-Type Galaxy Formation in Clusters and in the Field. In R.E. Schielicke, editor, *Reviews in Modern Astronomy*, volume 15 of *Reviews in Modern Astronomy*, pages 219–+.

Thomas D., Maraston C., Bender R., & Mendes de Oliveira C., 2005. The Epochs of Early-Type Galaxy Formation as a Function of Environment. *ApJ*, 621:673–694.

Tinsley B.M., 1978. Evolutionary synthesis of the stellar population in elliptical galaxies. II - Late M giants and composition effects. *ApJ*, 222:14–22.

Tissera P.B. & Dominguez-Tenreiro R., 1998. Dark matter halo structure in CDM hydrodynamical simulations. *MNRAS*, 297:177–194.

Tissera P.B., Lambas D.G., & Abadi M.G., 1997. Analysis of galaxy formation with hydrodynamics. *MNRAS*, 286:384–392.

Tortora C., Napolitano N.R., Romanowsky A.J., Capaccioli M., & Covone G., 2009. Central mass-to-light ratios and dark matter fractions in early-type galaxies. *ArXiv e-prints*.

Treu T., 2004. The Formation of Early-type Galaxies: Observations to z $\sim$ 1. In J.S. Mulchaey, A. Dressler, & A. Oemler, editors, *Clusters of Galaxies: Probes of Cosmological Structure and Galaxy Evolution*, pages 177–+.

Treu T., Ellis R.S., Liao T.X., van Dokkum P.G., Tozzi P., Coil A., Newman J., Cooper M.C., & Davis M., 2005. The Assembly History of Field Spheroidals: Evolution of Mass-to-Light Ratios and Signatures of Recent Star Formation. *ApJ*, 633:174–197.

Treu T. & Koopmans L.V.E., 2004. Massive Dark Matter Halos and Evolution of Early-Type Galaxies to z ˜ 1. *ApJ*, 611:739–760.

Trujillo I., Burkert A., & Bell E.F., 2004. The Tilt of the Fundamental Plane: Three-Quarters Structural Nonhomology, One-Quarter Stellar Population. *ApJ*, 600:L39–L42.

Trujillo I., Conselice C.J., Bundy K., Cooper M.C., Eisenhardt P., & Ellis R.S., 2007. Strong size evolution of the most massive galaxies since z ˜ 2. *MNRAS*, 382:109–120.

Trujillo I., Graham A.W., & Caon N., 2001. On the estimation of galaxy structural parameters: the Sérsic model. *MNRAS*, 326:869–876.

Tucker W., 1975. *Radiation processes in astrophysics*. Cambridge, Mass., MIT Press, 1975. 320 p.

van de Ven G., van Dokkum P.G., & Franx M., 2003. The Fundamental Plane and the evolution of the M/L ratio of early-type field galaxies up to z˜ 1. *MNRAS*, 344:924–934.

van den Bosch F.C., Norberg P., Mo H.J., & Yang X., 2004. Probing dark matter haloes with satellite kinematics. *MNRAS*, 352:1302–1314.

van der Marel R.P. & Franx M., 1993. A new method for the identification of non-Gaussian line profiles in elliptical galaxies. *ApJ*, 407:525–539.

van der Marel R.P. & van Dokkum P.G., 2007. Dynamical Models of Elliptical Galaxies in z = 0.5 Clusters. I. Data-Model Comparison and Evolution of Galaxy Rotation. *ApJ*, 668:738–755.

van der Wel A., Franx M., van Dokkum P.G., & Rix H.W., 2004. The Fundamental Plane of Field Early-Type Galaxies at z = 1. *ApJ*, 601:L5–L8.

van der Wel A., Holden B.P., Zirm A.W., Franx M., Rettura A., Illingworth G.D., & Ford H.C., 2008. Recent Structural Evolution of Early-Type Galaxies: Size Growth from z=1 to z=0. *ArXiv e-prints*, 808.

van Dokkum P.G., 2005. The Recent and Continuing Assembly of Field Elliptical Galaxies by Red Mergers. *AJ*, 130:2647–2665.

van Dokkum P.G. & Ellis R.S., 2003. On the Assembly History of Early-Type Galaxies in the Hubble Deep Field-North. *ApJ*, 592:L53–L57.

van Dokkum P.G., Franx M., Kelson D.D., & Illingworth G.D., 1998. Luminosity Evolution of Early-Type Galaxies to Z = 0.83: Constraints on Formation Epoch and Omega. *ApJ*, 504:L17+.

van Dokkum P.G., Franx M., Kelson D.D., & Illingworth G.D., 2001. Luminosity Evolution of Field Early-Type Galaxies to Z=0.55. *ApJ*, 553:L39–L42.

van Dokkum P.G. & van der Marel R.P., 2007. The Star Formation Epoch of the Most Massive Early-Type Galaxies. *ApJ*, 655:30–50.

Vazdekis A., Trujillo I., & Yamada Y., 2004. A Correlation between Light Profile and [Mg/Fe] Abundance Ratio in Early-Type Galaxies. *ApJ*, 601:L33–L36.

Vázquez-Semadeni E., Gazol A., & Scalo J., 2000. Is Thermal Instability Significant in Turbulent Galactic Gas? *ApJ*, 540:271–285.

Vergassola M., Dubrulle B., Frisch U., & Noullez A., 1994. Burgers' equation, Devil's staircases and the mass distribution for large-scale structures. *A&A*, 289:325–356.

Wada K. & Norman C.A., 2001. Numerical Models of the Multiphase Interstellar Matter with Stellar Energy Feedback on a Galactic Scale. *ApJ*, 547:172–186.

Wechsler R.H., Bullock J.S., Primack J.R., Kravtsov A.V., & Dekel A., 2002. Concentrations of Dark Halos from Their Assembly Histories. *ApJ*, 568:52–70.

Weinberg D.H., Hernquist L., & Katz N., 1997. Photoionization, Numerical Resolution, and Galaxy Formation. *ApJ*, 477:8–+.

Weinberg S., 1972. *Gravitation and Cosmology: Principles and Applications of the General Theory of Relativity*. Gravitation and Cosmology: Principles and Applications of the General Theory of Relativity, by Steven Weinberg, pp. 688. ISBN 0-471-92567-5. Wiley-VCH , July 1972.

White S.D.M., 1976. The dynamics of rich clusters of galaxies. *MNRAS*, 177:717–733.

White S.D.M. & Rees M.J., 1978. Core condensation in heavy halos - A two-stage theory for galaxy formation and clustering. *MNRAS*, 183:341–358.

Wiklind T., Dickinson M., Ferguson H.C., Giavalisco M., Mobasher B., Grogin N.A., & Panagia N., 2008. A Population of Massive and Evolved Galaxies at $z \geq 5$. *ApJ*, 676:781–806.

Wuyts S., van Dokkum P.G., Kelson D.D., Franx M., & Illingworth G.D., 2004. The Detailed Fundamental Plane of Two High-Redshift Clusters: MS 2053-04 at z=0.58 and MS 1054-03 at z=0.83. *ApJ*, 605:677–688.

Yepes G., 2001. Cosmological numerical simulations: past, present and future. In *Historical Development of Modern Cosmology, ASP Conference Proceedings. Vol 252. p.335.*

York D.G., Adelman J., Anderson Jr. J.E., Anderson S.F., Annis J., Bahcall N.A., Bakken J.A., Barkhouser R., Bastian S., Berman E., Boroski W.N., Bracker S., Briegel C., Briggs J.W., Brinkmann J., Brunner R., Burles S., Carey L., Carr M.A., Castander F.J., Chen B., Colestock P.L., Connolly A.J., Crocker J.H., Csabai I., Czarapata P.C., Davis J.E., Doi M., Dombeck T., Eisenstein D., Ellman N., Elms B.R., Evans M.L., Fan X., Federwitz G.R., Fiscelli L., Friedman S., Frieman J.A., Fukugita M., Gillespie B., Gunn J.E., Gurbani V.K., de Haas E., Haldeman M., Harris F.H., Hayes J., Heckman T.M., Hennessy G.S., Hindsley R.B., Holm S., Holmgren D.J., Huang C.h., Hull C., Husby D., Ichikawa S.I., Ichikawa T., Ivezić Ž., Kent S., Kim R.S.J., Kinney E., Klaene M., Kleinman A.N., Kleinman S., Knapp G.R., Korienek J., Kron R.G., Kunszt P.Z., Lamb D.Q., Lee B., Leger R.F., Limmongkol S., Lindenmeyer C., Long D.C., Loomis C., Loveday J., Lucinio R., Lupton R.H., MacKinnon B., Mannery E.J., Mantsch P.M., Margon B., McGehee P., McKay T.A., Meiksin A., Merelli A., Monet D.G., Munn J.A., Narayanan V.K., Nash T., Neilsen E., Neswold R., Newberg H.J., Nichol R.C., Nicinski T., Nonino M., Okada N., Okamura S., Ostriker J.P., Owen R., Pauls A.G., Peoples J., Peterson R.L., Petravick D., Pier J.R., Pope A., Pordes R., Prosapio A., Rechenmacher R., Quinn T.R., Richards G.T., Richmond M.W., Rivetta C.H., Rockosi C.M., Ruthmansdorfer K., Sandford D., Schlegel D.J., Schneider D.P., Sekiguchi M., Sergey G., Shimasaku K., Siegmund W.A., Smee S., Smith J.A., Snedden S., Stone R., Stoughton C., Strauss M.A., Stubbs C., SubbaRao M., Szalay A.S., Szapudi I., Szokoly G.P., Thakar A.R., Tremonti C., Tucker D.L., Uomoto A., Vanden Berk D., Vogeley M.S., Waddell P., Wang S.i., Watanabe M., Weinberg D.H., Yanny B., & Yasuda N., 2000. The Sloan Digital Sky Survey: Technical Summary. *AJ*, 120:1579–1587.

Zel'Dovich Y.B., 1970. Gravitational instability: An approximate theory for large density perturbations. *A&A*, 5:84–89.

Zepf S.E. & Silk J., 1996. On the Effects of Bursts of Massive Star Formation during the Evolution of Elliptical Galaxies. *ApJ*, 466:114–+.

Zhang Y.Y., Böhringer H., Finoguenov A., Ikebe Y., Matsushita K., Schuecker P., Guzzo L., & Collins C.A., 2006. X-ray properties in massive galaxy clusters: XMM-Newton observations of the REFLEX-DXL sample. *A&A*, 456:55–74.

Zhao D.H., Mo H.J., Jing Y.P., & Börner G., 2003. The growth and structure of dark matter haloes. *MNRAS*, 339:12–24.

Zwicky F., 1933. Die Rotverschiebung von extragalaktischen Nebeln. *Helvetica Physica Acta*, 6:110–127.